



THE UNIVERSITY OF QUEENSLAND
A U S T R A L I A

**Development of High Total Pressure Scramjet Flow
Conditions using the X2 Expansion Tube**

David E. Gildfind

A thesis submitted for the degree of Doctor of Philosophy at

The University of Queensland in February, 2012

Division of Mechanical Engineering, School of Engineering

In memory of my Grandfather,

Joseph Winn

Declaration by Author

This thesis is composed of my original work, and contains no material previously published or written by another person except where due reference has been made in the text. I have clearly stated the contribution by others to jointly-authored works that I have included in my thesis.

I have clearly stated the contribution of others to my thesis as a whole, including statistical assistance, survey design, data analysis, significant technical procedures, professional editorial advice, and any other original research work used or reported in my thesis. The content of my thesis is the result of work I have carried out since the commencement of my research higher degree candidature and does not include a substantial part of work that has been submitted to qualify for the award of any other degree or diploma in any university or other tertiary institution. I have clearly stated which parts of my thesis, if any, have been submitted to qualify for another award.

I acknowledge that an electronic copy of my thesis must be lodged with the University Library and, subject to the General Award Rules of The University of Queensland, immediately made available for research and study in accordance with the Copyright Act 1968.

I acknowledge that copyright of all material contained in my thesis resides with the copyright holder(s) of that material. Where appropriate I have obtained copyright permission from the copyright holder to reproduce material in this thesis.

David E. Gildfind

Statement of Contributions and List of Publications

Statement of Contributions to Jointly Authored Works Contained in the Thesis

No jointly-authored works.

Statement of Contributions by Others to the Thesis as a Whole

No contributions by others.

Statement of Parts of the Thesis Submitted to Qualify for the Award of Another Degree

None.

Published Works by the Author Incorporated into the Thesis

None.

Additional Published Works by the Author Relevant to the Thesis but not Forming Part of it

P.A. Jacobs, R.J. Gollan, D.F. Potter, D.E. Gildfind, T.N. Eichmann, B.F. O'Flaherty, and D.R. Buttsworth. CFD Tools for Design and Simulation of Transient Flows in Hypersonic Facilities. *Proceedings of the AVT-186 RTO AVT/VKI Lecture Series*, the von Karman Institute, Rhode St., Genèse, Belgium, 29 March – 1 April 2010.

D.E. Gildfind, R.G. Morgan, M. McGilvray, P.A. Jacobs, T. Eichmann, R.J. Stalker, and P. Teakle. Design of Lightweight Pistons for the X2 and X3 Expansion Tube Free-Piston Drivers. *Proceedings of the 17th Australasian Fluid Mechanics Conference*, Auckland, New Zealand, 5–9 December, 2010.

D.E. Gildfind, R.G. Morgan, M. McGilvray, P.A. Jacobs, R.J. Stalker, and T.N. Eichmann. Free-Piston Driver Optimisation for Simulation of High Mach Number Scramjet Flow Conditions. *Proceedings of the 28th International Symposium on Shock Waves*, Manchester, United Kingdom, 17–22 July, 2011. *Proceedings published in: Shock Waves*, Editor: K. Kontis, Heidelberg: Springer, 2012, ISBN:978-3-642-25687-5.

D.E. Gildfind, R.G. Morgan, M. McGilvray, and P.A. Jacobs. High Mach Number and Total Pressure Flow Conditions for Scramjet Testing. *Proceedings of the 28th International Symposium on Shock Waves*, Manchester, United Kingdom, 17–22 July, 2011. *Proceedings published in:* Shock Waves, Editor: K. Kontis, Heidelberg: Springer, 2012, ISBN:978-3-642-25687-5.

R.G. Morgan, U.A. Sheikh, and D.E. Gildfind. Standing Shock Formation in a Non-Reflected Shock Tube. *Proceedings of the 28th International Symposium on Shock Waves*, Manchester, United Kingdom, 17–22 July, 2011. *Proceedings published in:* Shock Waves, Editor: K. Kontis, Heidelberg: Springer, 2012, ISBN:978-3-642-25687-5.

D.E. Gildfind, R.G. Morgan, M. McGilvray, P.A. Jacobs, R.J. Stalker, and T.N. Eichmann. Free-Piston Driver Optimisation for Simulation of High Mach Number Scramjet Flow Conditions. *Shock Waves*, 21:6, pp 559-572, 2011.

D.E. Gildfind, R.G. Morgan, M. McGilvray, P.A. Jacobs. Simulation of High Mach Number Scramjet Flow Conditions using the X2 Expansion Tube. *Proceedings of the 18th AIAA International Space Planes and Hypersonic Systems and Technologies Conference*, Tours, France, 24–28 September, 2012.

Acknowledgements

I'll never know if I managed to grab any of that high hanging fruit, but if I didn't manage, it was not for lack of support from the following people:

- Richard Morgan, who welcomed me into a great research group and started me on a broad and interesting topic. He is always available, involved, and looking out for his students, but still provides them freedom to chart their own course.
- Matthew McGilvray, who has brought all his energy and enthusiasm to the project, performed the unpleasant task of checking through my work with a fine toothed comb, and helped to push things along in general.
- Peter Jacobs, for his generous help with all aspects of the CFD analysis, for his insights into various things hypersonic, and for providing a sounding board over coffee on innumerable occasions.
- Brian Loughrey, Frans de Beurs, Keith Hitchcock, Neil Duncan, and Gary Manning for technical assistance with X2. To Brian in particular, who seemingly can make anything, and will be sorely missed now that he has retired.
- Troy Eichmann, for optics and instrumentation advice in general, Labview help specifically, and for giving me that sample of dehydrated bullsh\$t for people ‘who are full of it’, now mounted on the office wall, which continues to provide visitors ongoing amusement. To that I say: “*Ha, ha, very funny*”.
- Ray Stalker, for inventing the free-piston driven shock tunnel back in the 1960’s, and then explaining all that maths to me in 2010. And who did some independent calculations for X2’s new piston mass, and then reassured me that 10 kg ‘sounded about right’, which gave me much needed confidence to proceed with design and manufacture.
- Steve Kimball, the most competent and nicest IT guy around.
- Rose Clements for administrative support.
- Other current and former members of the Centre for Hypersonics, as well as the frequent visitors to our lab, for their assistance, support, banter, insults, in alphabetical order: David Buttsworth, Wilson Chan, Andrew

Dann, Luke Doherty, Carolyn Jacobs, Hadas Porat, Daniel Potter, Andrew Ridings, Umar Sheikh, James Turner, Dylan Wise, and Fabian Zander.

- The X2 expansion tube, for not letting me down even once during months and months of experiments.
- My parents, for their complete faith in me at all times. My Dad always smiles proudly and tells me that I do great work. I know he probably hasn't read it. That's why I call it faith and why I appreciate it all the more.
- Celine, for keeping me smiling, keeping me well fed, and giving me plenty of motivation to get the task finished.

In keeping with the general theme of this thesis, these acknowledgements have spanned two pages, and are perhaps a bit wordier than they need to be. So I would like to finish with an apology to all readers of this document who find it a bit long, I'll try to make the next one shorter.

Abstract

The objective of this thesis was to use the X2 expansion tube to produce the high Mach number and high total pressure scramjet flow conditions associated with access to space. Initial experimental attempts to produce a Mach 13 condition indicated that the existing free-piston driver arrangement, based on a 35 kg piston and 100% helium driver gas, did not produce high pressure driver gas for sufficient duration. Following expansion of the driver gas, the expansion wave processing the driver gas reflected off the piston face, interfering with the test gas prior to its arrival in the test section. The result was significant attenuation of the primary shock prior to its arrival in the test section. It was determined that a tuned driver condition could provide a significantly longer duration of high pressure driver gas; achieving this operating condition subsequently became the first major task of the investigation.

Tuned operation involves configuring the driver so that the piston is moving sufficiently fast following primary diaphragm rupture that the piston displacement compensates for driver gas loss to the driven tube. This can result in approximately constant driver pressures for a relatively long duration of time. An analysis of X2's free-piston driver indicated that for X2's relatively short (4.5 m) compression tube, tuned operation requires a very lightweight piston (≈ 10 kg). The tuned piston must be light so that it can be first accelerated to a high speed (>200 m/s), and then brought to rest, over the short compression tube length. A new 10.5 kg lightweight piston for X2 was developed, and three new tuned driver conditions were developed.

The theoretical performance envelope of X2 with the new driver was then investigated, and a set of new scramjet flow conditions was proposed based on analytical relations which were later refined using the 1-D CFD code L1d2. The final task in this study was to assess the new flow conditions both experimentally in X2, and numerically using a hybrid 1-D L1d2/2-D axisymmetric Eilmer3 CFD model. Four flow conditions were considered: Mach 10, 12.5, and 15 conditions in X2 without a nozzle, and a Mach 10 condition with a nozzle.

The experimental and numerical results indicated that the predicted primary wave processes were achieved. The detailed CFD analysis further predicted that the target test flow Mach number, velocity, temperature, and static pressure, were

all approximately achieved at each condition. It is estimated that the maximum test flow total pressures were 3.75, 8.79, and 10.4 GPa, at Mach 10, 12.5, and 15 respectively. At these relatively low enthalpies (4.05, 6.68, and 10.4 MJ/kg respectively), these are the highest total pressure scramjet flows that have been reported in the literature to date.

Several challenges remain to be addressed following this experimental campaign. Satisfactory experimental Pitot pressure measurements could not be achieved in these harsh, short duration test flows, and therefore CFD Pitot calculations could not be experimentally validated. Partial impact pressure measurements with 15 deg half angle cone probes, specially developed for this experimental campaign, *did* demonstrate reasonable correlation with an equivalent pressure calculation from the CFD simulation results. Hence, there are reasons to be confident that better measurement techniques will demonstrate that good agreement exists with the experiment. This is based on a) matched wave processes, b) matched and steady tube wall static pressure measurements, c) correlation with cone probe pressure measurements, and d) the high fidelity of the CFD simulations.

Two other obvious limiting features of these test flows are the short test times and small core flow diameters (40-80 mm). X2 is a medium sized facility, and test time and core flow size are directly dependent on tube length and diameter. The purpose of this investigation was to demonstrate proof of concept, and this has been achieved. UQ's X3 facility is much larger than X2, and when these conditions are scaled upwards it is expected that test flow duration and core flow diameter will correspondingly increase to meet the requirements for actual scramjet testing.

In summary, this study has shown, for the first time, that an expansion tube *can* be configured to achieve the high Mach number, GPa total pressure, flow conditions associated with scramjet access to space. The CFD predicts some unsteadiness in these test flows; in the worst case, future testing may simply need to adapt to these imperfect test flows, since no ground testing technique, other than the expansion tube, is currently conceived which can produce flows even close to these total pressures. One of ground testing's most important functions is validation of CFD models, and these test flows can provide experimental data which permit validation of CFD models very close to the true flight conditions.

Keywords

hypersonic, experimental, expansion tube, free-piston driver, scramjet, ground testing, high total pressure, high Mach number, numerical simulation

Australian and New Zealand Standard Research Classifications
(ANZSRC)

090107 Hypersonic Propulsion and Hypersonic Aerodynamics (100%)

Contents

Preliminary Pages	i
Declaration by Author	i
Statement of Contributions and List of Publications	ii
Acknowledgements	iv
Abstract	vi
Australian and New Zealand Standard Research Classifications	ix
List of Figures	xxiv
List of Tables	xxvi
Nomenclature	xxvii
1 Introduction	1
1.1 Chapter Overview	1
1.2 Scramjet Engines	1
1.2.1 Concept	1
1.2.2 Potential Applications	3
1.2.3 Scramjets for Access to Space	3
1.2.4 Key Scramjet Design Challenges	5
1.3 Scramjet Flight Regime	6
1.3.1 Proposed Ascent Trajectory	6
1.3.2 Binary Scaling and Total Pressures	8
1.4 Objective of this Thesis	9
1.4.1 Target Flow Conditions	10
1.5 Structure of this Thesis	12
1.6 Original Scientific Contributions of this Study	15
2 Ground Testing of Scramjet Engines	18
2.1 Chapter Overview	18
2.1.1 Introduction	18

2.1.2	Blow Down Facilities	20
2.1.3	Impulse Facilities - Basic Shock Tube	21
2.1.4	Impulse Facilities - Reflected Shock Tunnel	22
2.1.5	Impulse Facilities - Expansion Tube	23
3	Expansion Tube Theory and Operation	27
3.1	Chapter Overview	27
3.2	Analytical Model of Expansion Tube	27
3.2.1	Basic Operation	27
3.2.2	Flow Properties in the Shock Tube	28
3.2.3	Flow Properties in the Acceleration Tube	31
3.3	Unsteady Expansion Process	32
3.4	Primary Driver	33
3.5	Area Change at Primary Driver	35
3.6	Secondary Driver	36
3.7	Flow Properties in the Secondary Driver	37
3.7.1	Unsteady Expansion at Secondary Diaphragm	38
3.7.2	Reflected Normal Shock at Secondary Diaphragm	38
3.7.3	Correct Solution at Secondary Diaphragm	41
3.7.4	Solution Across Tertiary Diaphragm	41
3.8	Test Time and Wave Processes	41
3.9	Diaphragm Rupture Disturbances	43
3.9.1	Primary Diaphragm Pre-Scoring	43
3.9.2	Test Flow Frequency Focussing	43
3.9.3	Thin Mylar Diaphragm Rupture	45
3.10	Mirels Effect - Boundary Layer Mass Entrainment	47
3.11	Steady Expansion Contoured Nozzle	50
3.11.1	General Characteristics	50
3.11.2	Estimate of Flow Properties	51
3.12	Unsteady vs. Steady Expansion of Test Flow	52
3.13	UQ Expansion Tube Facilities	54
3.13.1	X2 Expansion Tube	54
3.13.2	X3 Expansion Tube	55
3.14	Computational Fluid Dynamics Analysis	58
4	Tuned Operation of the X2 Free-Piston Driver	60
4.1	Chapter Overview	60
4.2	Case Study: X2 Mach 13 Optimised Flow Condition	61

4.2.1	Introduction	61
4.2.2	X2 Perfect Gas Quasi-1D Parametric Optimisation Tool . .	62
4.2.2.1	Optimisation variables	62
4.2.2.2	Flow solver	63
4.2.2.3	Objective function	64
4.2.2.4	Optimiser	65
4.2.3	Optimised Tunnel Configuration and Predicted Flow	65
4.2.4	Experimental Results and Comparison with L1d2 Analysis .	66
4.2.5	Requirement for a Tuned Free-Piston Driver	71
4.3	Tuned Free-Piston Driver Operation	71
4.3.1	Piston Over-Drive Parameter, β	71
4.3.2	Piston Soft Landing Condition	75
4.4	Stalker Analysis	78
4.4.1	Methodology	78
4.4.2	Results	81
4.5	Target Piston Mass	85
4.6	Conclusion	86
5	Design and Stress Analysis of a Lightweight Piston for X2	87
5.1	Chapter Overview	87
5.2	Introduction	87
5.3	Overview of the Existing 35 kg X2 Piston	88
5.4	Overview of the New Lightweight 10.5 kg X2 Piston	88
5.5	Materials	90
5.5.1	Piston Body (PNo. X2-LWP-001-1/Appendix A.2)	90
5.5.2	Load Ring (PNo. X2-LWP-003-0/Appendix A.4)	90
5.5.3	Brass Holder (PNo. X2-LWP-005-0/Appendix A.6)	91
5.5.4	Wear rings and chevron seal (PNo. X2-LWP-002-0/ Appendix A.3; X2-LWP-004-0/Appendix A.5)	91
5.5.5	Steel Tunnel Parts	91
5.6	Load Cases	92
5.7	Finite Element Analysis Analysis software	92
5.8	Strength Criteria	92
5.9	Deflection Criteria	93
5.10	Symmetric Finite Element Solid Model - Static Analysis	93
5.10.1	Introduction	93
5.10.2	Finite Element Mesh	94

5.10.3	Interfaces	94
5.10.4	Loads and Boundary Conditions - LC1 Driver Pressure	96
5.10.5	Loads and Boundary Conditions - LC2 Reservoir Pressure	97
5.11	Results	99
5.11.1	80 MPa Driver Pressure Loading	99
5.11.2	20 MPa reservoir pressure loading	99
5.12	Analytical Stress Analysis	99
5.12.1	Overview	99
5.12.2	Buckling Analysis	99
5.12.3	Reservoir Hoop Stress Finite Element Model Validation	104
5.13	Piston Impact	104
5.14	Dynamic Pressure Loading	105
5.15	Fatigue	106
5.16	Operational Experience	106
5.17	Recommendations	106
5.18	Conclusion	108
6	Commissioning of a New Lightweight Piston for X2	109
6.1	Chapter Overview	109
6.2	Introduction	109
6.3	Target Performance for New Tuned Driver	110
6.3.1	Required Shock Strength	110
6.3.2	Over-Drive and Driver Gas Useful Supply Duration	112
6.3.3	Target Condition: Piston Soft Landing	112
6.3.4	Buffer Length	113
6.4	X2 Driver Description	113
6.5	X2 Driver Design Variables	114
6.6	Tuned Driver Condition General Design Process	116
6.7	X2 Driver Analytical Model	118
6.7.1	Overview	118
6.7.2	Piston Motion Before Diaphragm Rupture	119
6.7.3	Piston Motion After Diaphragm Rupture	120
6.7.4	Model Validation	123
6.7.5	Analytically Calculated Tuned Driver Conditions	126
6.8	Condition Refinement with L1d2	127
6.8.1	General Approach	127
6.8.2	L1d2 Simulation Results	130

6.9	Blanked-Off Driver Experiments	137
6.9.1	Overview	137
6.9.2	Polytropic Index - an Indication of Driver Heat Loss	138
6.10	Rupturing Diaphragm Experimental Results	142
6.10.1	Overview	142
6.10.2	Experimental Setup	142
6.10.3	Nylon Stud Sizing	144
6.10.4	Rupturing Diaphragm Experimental Results	147
6.11	Conclusion	148
7	Theoretical Performance Envelope of X2 with Tuned Driver	151
7.1	Chapter Overview	151
7.2	Equilibrium Gas Analysis with NASA CEA	151
7.3	Expansion Tube Design Variables	153
7.3.1	Items 1 to 3	153
7.3.2	Item 4	153
7.3.3	Items 5 to 8	154
7.3.4	Item 9	154
7.3.5	Item 10	155
7.3.6	Item 11	155
7.3.7	Parametric Design Variables	155
7.4	Analysis Limitations	156
7.5	Driver Performance Calculation	157
7.5.1	Methodology	157
7.5.2	Results	160
7.6	Predicted Test Flow Properties - Basic Expansion Tube	161
7.6.1	Overview	161
7.6.2	Shock Tube Flow Processes	163
7.6.3	Acceleration Tube Flow Processes	163
7.6.4	X2 Mach 10 Contoured Nozzle	164
7.6.5	Results - X2 Performance Envelope - Basic Expansion Tube	165
7.7	Predicted Test Flow Properties - Expansion Tube with Secondary Driver	168
7.7.1	General Design Philosophy	168
7.7.2	Secondary Driver Tube Shock Speed	169
7.7.3	Test Gas Tube Shock Speed	169
7.7.4	Acceleration Tube Flow Processes	171

7.7.5	Results - X2 Performance Envelope - Expansion Tube with Secondary Driver	171
7.8	Selected Flow Conditions	172
7.9	Conclusion	180
8	2-D Axisymmetric CFD Analysis using Eilmer3, and Comparison with Experimental Results	183
8.1	Chapter Overview	183
8.2	Previous Work	184
8.3	The Eilmer3 Code	188
8.4	Eilmer3 2-D Axisymmetric model of X2	188
8.5	Conical Glancing Impact Pressure Probe Measurements	192
8.6	Results and Discussion	199
8.6.1	Results Overview	199
8.6.2	Mach 10 without Nozzle (x2-scr-m10p0-rev-1)	200
8.6.2.1	Critical Wave Processes	200
8.6.2.2	Visualisation of Flow Development	205
8.6.2.3	Tube Wall Static Pressure Traces	208
8.6.2.4	Test Flow Properties	215
8.6.3	Mach 10 with Nozzle (x2-scr-m10p0-noz-rev-1)	218
8.6.3.1	Critical Wave Processes	218
8.6.3.2	Tube Wall Static Pressure Measurements	221
8.6.3.3	Test Flow Properties at the Nozzle Inlet	226
8.6.3.4	Test Flow Properties at the Nozzle Exit	228
8.6.3.5	Visualisation of Flow Development Through the Nozzle	230
8.6.4	Mach 12.5 and 15 Flow Conditions	235
8.6.5	Grid Sensitivity Check	239
8.7	Additional Comments Regarding Acceleration Tube Transducer Signal Noise	241
8.8	Conclusion	243
9	Test Flow Disturbances Originating at the Primary Driver	247
9.1	Chapter Overview	247
9.2	Fixed Volume Primary Driver Model	247
9.3	Iris Opening Primary Diaphragm Model	254
9.4	Results and Discussion	259
9.4.1	Critical Wave Processes	261

9.4.2	Visualisation of Flow Development	263
9.4.2.1	Tube Wall Static Pressure Traces	268
9.4.2.2	Test Flow Properties	273
9.5	Grid Sensitivity Check	275
9.6	Conclusion	277
10	Conclusion	280
11	Recommendations for Further Work	284
References		287
Appendices		305
A	X2 Lightweight Piston Drawing Set	306
A.1	X2-LWP-000-1: X2 Lightweight Piston Assembly	307
A.2	X2-LWP-001-1: X2 Lightweight Piston Body	308
A.3	X2-LWP-002-0: Wear Ring	313
A.4	X2-LWP-003-0: Load Ring	314
A.5	X2-LWP-004-0: Chevron Seal	315
A.6	X2-LWP-005-0: Brass Holder	316
B	Material and Physical Properties	317
B.1	7075-T6 Aluminium Alloy Rod	317
B.2	C95800 Copper Alloy	317
B.3	Nylon 6 Oil Filled Cast	318
C	X2 Equilibrium Gas Operational Envelope - Results	319
D	L1d2 Validation of Hornung Free-Piston Dynamics Model	323
E	X2 Compression Ratio Volumetric Correction Factors	331
E.1	Driver Volume: No Buffer	331
E.2	Driver Volume: Rubber Buffer	331
E.3	Driver Volume: Nylon Stud Buffer	332
E.4	Driver Volume: L1d2 Buffer	334
E.5	Driver Volume: Correction Factors	335
E.5.1	No Buffer Correction	336
E.5.2	Rubber Buffer Correction	337
E.5.3	Nylon Stud Correction	337

F Nylon Studs: Allowable Piston Impact Speed	339
G Stainless Steel Pitot Cap Drawing	342
H 15 Deg Conical Glancing Impact Pressure Probe Drawing	344
I Results, Mach 12.5 Flow Condition, X2 <i>without</i> Nozzle	346
J Results, Mach 15.0 Flow Condition, X2 <i>without</i> Nozzle	355
K Grid Sensitivity Analysis	364
L X2 Diaphragm Holder and Buffer Drawing Set	394
L.1 X2-DIA-000-0: Diaphragm Holder and Buffer Assembly	395
L.2 X2-DIA-001-0: Diaphragm Holder Back Plate	400
L.3 X2-DIA-002-0: Diaphragm Holder Front Plate	402
L.4 X2-DIA-004-0: Diaphragm Holder Buffer	404
L.5 X2-DIA-005-0: Diaphragm Holder Bumper	405
L.6 X2-DIA-006-0: Diaphragm Holder Front Tube Adaptor	407
L.7 X2-DIA-007-0: Diaphragm Holder Fixing Ring	409
L.8 X2-DIA-008-0: Diaphragm Holder Buffer Template	410
L.9 X2-DIA-009-0: Mylar diaphragm template	411
M Uncertainty Analysis	412
M.1 Introduction	412
M.2 Facility Geometry	412
M.3 Reservoir Fill Pressure	413
M.4 Compression Tube Fill Pressure	413
M.5 Secondary Driver Fill Pressure	413
M.6 Shock Tube Fill Pressure	413
M.7 Acceleration Tube Fill Pressure	414
M.8 Primary Diaphragm Rupture Pressure	414
M.9 Mylar Diaphragm Rupture Pressures	414
M.10 Tube Fill Temperatures	415
M.11 Piston Maximum Displacement Measurement	415
M.12 Shock Speeds	417
M.13 PCB Transducer Sensitivities	417
M.13.1 Air Rig Calibrations	417
M.13.2 Oil Rig Calibrations	420

List of Figures

1.1	Specific impulse for various engines	2
1.2	Representative scramjet ascent trajectory	8
1.3	Comparison of proposed ascent trajectories	9
1.4	Effect of model scale on simulation total pressure requirements . . .	10
2.1	Total pressure capability for various hypersonic facilities	20
3.1	Idealised x - t schematic of expansion tube flow processes	28
3.2	Required initial driver/test gas pressure ratio vs. test gas shock Mach number	34
3.3	Idealised x - t schematic of expansion tube flow processes with secondary driver	38
3.4	Reflected shock / unsteady expansion solutions following diaphragm rupture	39
3.5	Thin mylar diaphragm rupture schematic	46
3.6	Sketch of flow behind a shock wave in a low pressure shock tube . .	48
3.7	Mirels schematic of flow between shock and contact surface	49
3.8	Total pressure and total enthalpy ratios across unsteady expansion .	53
3.9	Schematic of the X2 expansion tube	56
3.10	Schematic of X3 (upgraded configuration)	57
3.11	X3's new nozzle, test section, and dumptank	58
4.1	0-D analytical model optimisation process	63
4.2	Shock speed vs. position for Mach 13 flow condition	67
4.3	L1d2 calculated x - t diagrams for Mach 13 flow condition	68
4.4	L1d2 predicted shock speed vs. time for Mach 13 flow condition .	69
4.5	L1d2 predicted shock speed vs. position for longer driver	70
4.6	Free-piston driver schematic	72
4.7	Effect of piston over-driving on driver pressure	73
4.8	x - t diagram explanation of tuned free-piston driver wave processes .	74

4.9	Characteristics of piston motion	77
4.10	Variation in driver pressure after piston rupture using Stalker analysis	79
4.11	Driver pressure analysis for $\pm 10\%$ pressure variation, $k = 1$	80
4.12	Stalker analysis results for X2 driver (part 1 of 2)	83
4.13	Stalker analysis results for X2 driver (part 2 of 2)	84
5.1	X2 existing 35 kg piston	89
5.2	Piston assembly section view	89
5.3	Lightweight piston views	90
5.4	Solid mesh, 1/24 th segment model, piston with accessories	95
5.5	Solid mesh, 1/24 th segment model, piston body only	95
5.6	Loads and boundary conditions, LC1 80 MPa driver pressure	97
5.7	Loads and boundary conditions, LC2 20 MPa reservoir pressure	98
5.8	Piston launcher schematic	98
5.9	Von Mises Stress, linear piston material model, 80 MPa driver pressure	100
5.10	Von Mises Stress, non-linear material model, 80 MPa driver pressure	101
5.11	Von Mises Stress, linear material model, 20 MPa reservoir pressure	102
5.12	Piston deflection, linear material model, 20 MPa reservoir pressure .	103
5.13	Column instability modes	104
5.14	Newly manufactured piston, mass = 10.524 kg	107
6.1	Assumed tube configuration for L1d2 analyses of X2	114
6.2	Piston launcher for X2	115
6.3	X2 free-piston driver condition development process	117
6.4	Entropy rise across a shock in helium/argon driver gas	125
6.5	Example of nylon stud length measurement	131
6.6	L1d2 driver response for tuned driver condition LWP-1.2mm-Rev-0	132
6.7	L1d2 driver response for tuned driver condition LWP-2.0mm-Rev-0	133
6.8	L1d2 driver response for tuned driver condition LWP-2.5mm-Rev-0	134
6.9	Correction to L1d2 calculated piston inflection location	137
6.10	L1d2 predicted driver pressure for Table 6.7 driver cases	138
6.11	Comparison of experimental and numerical driver pressures for new tuned lightweight piston driver conditions	139
6.12	Measurement of location of piston maximum displacement.	142
6.13	Staggered buffer rod arrangement prior to blanked-off driver shot. .	143
6.14	Measurement of location of piston maximum displacement - example.	143
6.15	Maximum piston impact speed for X2 6 nylon stud buffer	146
6.16	Example of shattered nylon studs	147

6.17	Comparison of experimental, L1d2 predicted, and analytical required shock speeds for new X2 tuned driver conditions	149
7.1	X2 performance envelope for new tuned driver, basic expansion tube	166
7.2	X2 performance envelope for new tuned driver, expansion tube with nozzle	167
7.3	Procedure to calculate fill pressures p_1 , p_5 , and p_7	173
7.4	Shock and acceleration tube fill pressures for Mach 10.0 flow	174
7.5	Shock and acceleration tube fill pressures for Mach 12.5 flow	175
7.6	Shock and acceleration tube fill pressures for Mach 15.0 flow	176
7.7	L1d2 predicted x - t diagram for flow condition x2-scr-m10p0-0	179
7.8	Secondary driver shocks speeds for driver condition LWP-2.0mm-0 .	180
7.9	Comparison of L1d2 and Equilibrium 0-D analysis shock speeds . .	181
8.1	X2 2-D axisymmetric hybrid model geometry	189
8.2	X2 nozzle geometry	192
8.3	Stainless steel 4-hole swirl cap after a single Mach 12.5 shot	194
8.4	High speed camera footage of X2 expansion tube flow over two Pitot probes	195
8.5	Various Pitot probe configurations	196
8.6	Conical probe arrangement in test section, X2 <i>without</i> nozzle.	197
8.7	Conical probe arrangement in test section, X2 <i>with</i> nozzle.	199
8.8	x - t diagram for Mach 10 flow condition, flow condition x2-scr-m10p0-rev-1	203
8.9	Primary shock speed vs. axial position for Mach 10 flow condition, flow condition x2-scr-m10p0-rev-1	204
8.10	Flow development in shock and acceleration tubes for Mach 10 flow condition, flow condition x2-scr-m10p0-rev-1	207
8.11	Direction of velocity vectors, contact surface-steady reference frame, flow condition x2-scr-m10p0-rev-1	209
8.12	Static pressures at secondary driver transducers $sd1$, $sd2$, and $sd3$, flow condition x2-scr-m10p0-rev-1	211
8.13	Static pressures at shock tube transducers $st1$, $st2$, and $st3$, flow condition x2-scr-m10p0-rev-1	212
8.14	Static pressures at acceleration tube transducers $at4$, $at5$, and $n1$, flow condition x2-scr-m10p0-rev-1	213
8.15	Computed and experimental test flow properties at the acceleration tube exit, x2-scr-m10p0-rev-1	216

8.16	Radial variation in flow properties during the test time, flow condition x2-scr-m10p0-rev-1	219
8.17	Primary shock speed vs. position for Mach 10 flow condition, x2-scr-m10p0-noz-rev-1	221
8.18	<i>x-t</i> diagram for Mach 10 flow condition, x2-scr-m10p0-noz-rev-1	222
8.19	Static pressures at secondary driver transducers <i>sd1</i> , <i>sd2</i> , and <i>sd3</i> , flow condition x2-scr-m10p0-noz-rev-1	223
8.20	Static pressures at secondary driver transducers <i>st1</i> , <i>st2</i> , and <i>st3</i> , flow condition x2-scr-m10p0-noz-rev-1	224
8.21	Static pressures at secondary driver transducers <i>at4</i> , <i>at5</i> , and <i>n1</i> , flow condition x2-scr-m10p0-noz-rev-1	225
8.22	Computed and experimental test flow properties at the acceleration tube exit, flow condition x2-scr-m10p0-noz-rev-1	227
8.23	Radial variation in flow properties during the test time, flow condition x2-scr-m10p0-noz-rev-1	229
8.24	Computed and experimental test flow properties at the nozzle exit, flow condition x2-scr-m10p0-noz-rev-1	231
8.25	Computed and experimental cone static pressures at the nozzle exit, flow condition x2-scr-m10p0-noz-rev-1	233
8.26	Radial variation in flow properties at nozzle exit during the test time, flow condition x2-scr-m10p0-noz-rev-1	234
8.27	Flow development in nozzle, flow condition x2-scr-m10p0-noz-rev-1	237
9.1	X2 2-D axisymmetric fixed volume driver CFD model geometry	249
9.2	L1d2 predicted X2 driver gas slug pressure and temperature at diaphragm rupture	251
9.3	<i>x-t</i> diagram calculated using L1d2 for fixed volume driver scaling	252
9.4	<i>x-t</i> diagram comparing shock speeds for different assumed driver lengths of a fixed volume driver, calculated with L1d2 for flow condition x2-scr-m10p0-rev-1.	253
9.5	<i>x-t</i> diagram with sound speed mapped for flow condition x2-scr-m10p0-rev-1, calculated with L1d2 assuming a fixed volume driver.	253
9.6	Schematic of rupturing diaphragm.	255
9.7	Diaphragm opening time curves	256
9.8	Primary shock speed vs. position for Mach 10 flow condition x2-scr-m10p0-rev-1	261

9.9	Flow development in secondary driver, shock, and acceleration tubes, full facility CFD model, flow condition x2-scr-m10p0-rev-1	265
9.10	Detail view of primary diaphragm opening process	267
9.11	Static pressures at secondary driver transducers $sd1$, $sd2$, and $sd3$, for flow condition x2-scr-m10p0-rev-1	269
9.12	Static pressures at shock tube transducers $st1$, $st2$, and $st3$, for flow condition x2-scr-m10p0-rev-1.	270
9.13	Static pressures at acceleration tube transducers $at4$, $at5$, and $n1$, for flow condition x2-scr-m10p0-rev-1.	271
9.14	Computed and experimental test flow properties at the acceleration tube exit	274
D.1	Analytical piston dynamics model validation test case 1	324
D.2	Analytical piston dynamics model validation test case 2	325
D.3	Analytical piston dynamics model validation test case 3	326
D.4	Analytical piston dynamics model validation test case 4	327
D.5	Analytical piston dynamics model validation test case 5	328
D.6	Analytical piston dynamics model validation test case 6	329
D.7	Analytical piston dynamics model validation test case 7	330
E.1	Driver geometry - no buffer.	332
E.2	Buffer geometry - rubber buffer.	333
E.3	Buffer geometry - nylon studs.	334
E.4	Buffer geometry - L1d2.	336
F.1	Example of a buffer comprised of 6×50 mm DIA nylon studs.	339
I.1	$x-t$ diagram for Mach 12.5 flow condition, flow condition x2-scr-m12p5-rev-1	348
I.2	Primary shock speed vs. position for Mach 12.5 flow condition, flow condition x2-scr-m12p5-rev-1	349
I.3	Static pressures at secondary driver transducers $sd1$, $sd2$, and $sd3$, flow condition x2-scr-m12p5-rev-1	350
I.4	Static pressures at shock tube transducers $st1$, $st2$, and $st3$, flow condition x2-scr-m12p5-rev-1	351
I.5	Static pressures at acceleration tube transducers $at4$, $at5$, and $n1$, flow condition x2-scr-m12p5-rev-1	352
I.6	Computed and experimental test flow properties at the acceleration tube exit	353

I.7	Radial variation in flow properties during the test time, flow condition x2-scr-m12p5-rev-1	354
J.1	<i>x-t</i> diagram for Mach 15.0 flow condition, x2-scr-m15p0-rev-1	357
J.2	Primary shock speed vs. position for Mach 15.0 flow condition, x2-scr-m15p0-rev-1	358
J.3	Static pressures at secondary driver transducers <i>sd1</i> , <i>sd2</i> , and <i>sd3</i> , flow condition x2-scr-m15p0-rev-1	359
J.4	Static pressures at shock tube transducers <i>st1</i> , <i>st2</i> , and <i>st3</i> , flow condition x2-scr-m15p0-rev-1	360
J.5	Static pressures at acceleration tube transducers <i>at4</i> , <i>at5</i> , and <i>n1</i> , flow condition x2-scr-m15p0-rev-1	361
J.6	Computed and experimental test flow properties at the acceleration tube exit, flow condition x2-scr-m15p0-rev-1	362
J.7	Radial variation in flow properties during the test time, flow condition x2-scr-m15p0-rev-1	363
K.1	Grid convergence check, x2-scr-m10p0-rev-1, hybrid CFD model	365
K.2	Grid sensitivity check, transducer pressure histories, x2-scr-m10p0-rev-1, hybrid CFD model	366
K.3	Grid sensitivity check, radial variation in flow properties across tube exit, 25% of test time, x2-scr-m10p0-rev-1, hybrid CFD model	367
K.4	Grid sensitivity check, radial variation in flow properties across tube exit, 50% of test time, x2-scr-m10p0-rev-1, hybrid CFD model	368
K.5	Grid sensitivity check, radial variation in flow properties across tube exit, 75% of test time, x2-scr-m10p0-rev-1, hybrid CFD model	369
K.6	Grid convergence check, x2-scr-m10p0-noz-rev-1, hybrid CFD model, flow at nozzle inlet	370
K.7	Grid sensitivity check, transducer pressure histories, x2-scr-m10p0-noz-rev-1, hybrid CFD model, flow at nozzle inlet	371
K.8	Grid sensitivity check, radial variation in flow properties across nozzle inlet, 25% of test time, x2-scr-m10p0-noz-rev-1, hybrid CFD model	372
K.9	Grid sensitivity check, radial variation in flow properties across nozzle inlet, 50% of test time, x2-scr-m10p0-noz-rev-1, hybrid CFD model	373
K.10	Grid sensitivity check, radial variation in flow properties across nozzle inlet, 75% of test time, x2-scr-m10p0-noz-rev-1, hybrid CFD model	374
K.11	Grid convergence check, x2-scr-m10p0-noz-rev-1, nozzle CFD model, flow at nozzle exit	375

K.12 Grid sensitivity check, radial variation in flow properties across nozzle exit, 25% of test time, x2-scr-m10p0-noz-rev-1, hybrid CFD model	376
K.13 Grid sensitivity check, radial variation in flow properties across nozzle exit, 50% of test time, x2-scr-m10p0-noz-rev-1, hybrid CFD model	377
K.14 Grid sensitivity check, radial variation in flow properties across nozzle exit, 75% of test time, x2-scr-m10p0-noz-rev-1, hybrid CFD model	378
K.15 Grid convergence check, x2-scr-m12p5-rev-1, hybrid CFD model . . .	379
K.16 Grid sensitivity check, transducer pressure histories, x2-scr-m12p5-rev-1, hybrid CFD model	380
K.17 Grid sensitivity check, radial variation in flow properties across tube exit, 25% of test time, x2-scr-m12p5-rev-1, hybrid CFD model . . .	381
K.18 Grid sensitivity check, radial variation in flow properties across tube exit, 50% of test time, x2-scr-m12p5-rev-1, hybrid CFD model . . .	382
K.19 Grid sensitivity check, radial variation in flow properties across tube exit, 75% of test time, x2-scr-m12p5-rev-1, hybrid CFD model . . .	383
K.20 Grid convergence check, x2-scr-m15p0-rev-1, hybrid CFD model . . .	384
K.21 Grid sensitivity check, transducer pressure histories, x2-scr-m15p0-rev-1, hybrid CFD model	385
K.22 Grid sensitivity check, radial variation in flow properties across tube exit, 25% of test time, x2-scr-m15p0-rev-1, hybrid CFD model . . .	386
K.23 Grid sensitivity check, radial variation in flow properties across tube exit, 50% of test time, x2-scr-m15p0-rev-1, hybrid CFD model . . .	387
K.24 Grid sensitivity check, radial variation in flow properties across tube exit, 75% of test time, x2-scr-m15p0-rev-1, hybrid CFD model . . .	388
K.25 Grid convergence check, x2-scr-m10p0-rev-1, full facility CFD model	389
K.26 Grid sensitivity check, transducer pressure histories, x2-scr-m10p0-rev-1, full facility CFD model	390
K.27 Grid sensitivity check, radial variation in flow properties across tube exit, 25% of test time, x2-scr-m10p0-rev-1, full facility CFD model .	391
K.28 Grid sensitivity check, radial variation in flow properties across tube exit, 50% of test time, x2-scr-m10p0-rev-1, full facility CFD model .	392
K.29 Grid sensitivity check, radial variation in flow properties across tube exit, 75% of test time, x2-scr-m10p0-rev-1, full facility CFD model .	393
M.2 Compressed air calibration apparatus.	419
M.3 Hydraulic oil calibration apparatus.	420

List of Tables

1.1	Target flow conditions.	11
3.1	Representative flow condition illustrating enthalpy/total pressure multiplication	53
4.1	Mach 13 calculated flow condition	66
4.2	Critical driver geometries for X2	82
5.1	Piston acceleration due to LC1 80 MPa driver pressure	97
6.1	Nominal X2 free-piston driver configuration	111
6.2	X2 L1d2 geometry details	114
6.3	X2 simplified model parameters	124
6.4	X2 Hornung/L1d2 comparison cases.	124
6.5	X2 driver configuration case ID's	126
6.6	X2 analytical model results.	128
6.7	X2 lightweight piston finalised driver conditions.	130
6.8	X2 PCB transducer configuration	144
6.9	X2 buffer nylon stud length comparison.	146
7.1	Experimentally measured shock speeds, 150 kPa helium initial fill .	161
7.2	CEA calculation of shocked gas properties, 150 kPa helium	162
7.3	X2 lightweight piston driver condition performance calculations. .	162
7.4	Proposed scramjet flow conditions based on equilibrium calculations	178
7.5	Revised scramjet flow conditions	182
8.1	Adjustments to L1d2 primary diaphragm loss factor, K/L	190
8.2	Correlation factors for partial impact cone probes.	198
8.3	Test flow properties for Mach 10 flow condition, flow condition x2-scr-m10p0-rev-1	201

8.4	Test flow properties for Mach 10 flow condition, x2-scr-m10p0-noz-rev-1	220
8.5	Comparison of average test flow properties between nozzle inlet and exit, flow condition x2-scr-m10p0-noz-rev-1.	235
8.6	Comparison of average test flow properties	239
9.1	Test flow properties for Mach 10 flow condition, flow condition x2-scr-m10p0-rev-1, full facility CFD model	260
B.1	Mechanical and physical properties of 7075-T6 rod	317
B.2	Mechanical and physical properties of C95800 copper alloy	317
B.3	Mechanical and physical properties of Nylon 6 oil filled cast	318
C.1	Required p_1 and p_5 to achieve flow conditions for X2-LWP-1.2mm-0	320
C.2	Required p_1 and p_5 to achieve flow conditions for X2-LWP-2.0mm-0	321
C.3	Required p_1 and p_5 to achieve flow conditions for X2-LWP-2.5mm-0	322
I.1	Test flow properties for Mach 12.5 flow condition, x2-scr-m12p5-rev-1	347
J.1	Test flow properties for Mach 15.0 flow condition, x2-scr-m15p0-rev-1	356
M.1	Summary of experimentally measured PCB sensitivities	418

Nomenclature, Units

1-D	:	one dimensional
2-D	:	two dimensional
a	:	speed of sound, m/s; piston acceleration , m/s ²
A	:	tube area, piston area, m ²
D	:	(effective) tube diameter; piston diameter, m
e	:	strain at failure
E	:	modulus of elasticity, N/m ²
F	:	force on piston face, N; stress, N/m ²
G	:	shear modulus, N/m ²
h	:	specific enthalpy, J/kg
H	:	total enthalpy, J/kg
k	:	piston kinetic energy safety factor
K	:	penalty factor
l	:	length, m
L	:	length, m; piston position from driver area change, m
m	:	piston mass, kg
M	:	Mach number; piston mass, kg
n	:	polytropic index; number of items
P	:	force, N
q	:	dynamic pressure, Pa
r	:	radius, m
\bar{r}	:	shear modulus, N/m ²
R	:	gas constant, J/kg · K
t	:	time, s; thickness, m
T	:	temperature, K
u	:	flow velocity, m/s; flow velocity in x -direction, m/s; piston velocity, m/s
U	:	piston velocity, m/s

v	: flow velocity in y -direction, m/s
V	: free stream velocity, m/s
\mathbf{V}_{css}	: velocity vector in the contact surface-steady frame of reference, m/s
w	: flow velocity in z -direction, m/s
W	: shock speed, m/s; work done, J
x	: position, m
z	: piston non-dimensionalised time

Greek

β	: piston over-drive parameter
γ	: ratio of specific heats
λ	: compression ratio for the free-piston driver
μ, ν	: Poisson's ratio
π	: 3.14159...
ρ	: density, kg/m ³
σ	: piston mass per unit area, kg/m ² , stress, N/m ²
Δ	: change in value

Subscripts

*	: throat
0	: initial value, stagnation condition
1	: initial test gas
2	: shock processed test gas
3	: expanded primary driver/secondary driver gas
4	: driver gas at primary diaphragm rupture
5	: initial acceleration gas
6	: shock processed acceleration gas
7	: expanded test gas
∞	: free stream conditions
A	: reservoir
<i>actual</i>	: actual value
<i>av</i>	: average value

<i>buf</i>	:	acoustic buffer
<i>Buffer</i>	:	buffer
<i>c</i>	:	contact surface
<i>corrected</i>	:	corrected value
<i>cr</i>	:	critical compressive value
<i>cs</i>	:	contact surface
<i>cy</i>	:	compressive yield allowable
<i>D</i>	:	driver, dynamic value
<i>Drv</i>	:	driver
<i>exp</i>	:	experimental value
<i>ff</i>	:	piston front face
<i>H</i>	:	hoop; total enthalpy, J/kg
<i>i</i>	:	inlet, inner
<i>imp</i>	:	piston impact
<i>L</i>	:	value as a function of piston position, <i>L</i>
<i>L1d2</i>	:	L1d2 calculated value
<i>m</i>	:	contact surface at maximum separation from shock, instant when piston acceleration is zero
<i>max</i>	:	maximum value
<i>mid</i>	:	piston mid length
<i>NoBuffer</i>	:	no buffer
<i>noz</i>	:	nozzle
<i>Nylon</i>	:	nylon stud
<i>o</i>	:	outlet, outer
<i>p</i>	:	piston, induced mass flow behind shock
<i>r</i>	:	reflected shock, condition when density is a maximum in driver, value at rupture
<i>ref</i>	:	reference value
<i>rupt</i>	:	diaphragm rupture
<i>R</i>	:	reflected
<i>s</i>	:	shock; nylon stud value
<i>S</i>	:	static value
<i>sd</i>	:	secondary driver
<i>sd1</i>	:	initial secondary driver gas
<i>sd2</i>	:	shock processed secondary driver gas
<i>sd3</i>	:	expanded primary driver gas
<i>st</i>	:	shock tube

t	:	tangent value
$target$:	target value
tu	:	tensile ultimate allowable
tt	:	test time
ty	:	tensile yield allowable
T	:	target value
$u + a$:	$u + a$ reflected characteristic wave
x	:	value as a function of piston position, x

Superscripts

*	:	sonic value
---	---	-------------

Acronyms and Abbreviations

sx	:	steady expansion
usx	:	unsteady expansion
s	:	shock
rs	:	reflected shock
cs	:	contact surface
sd	:	secondary driver
CEA	:	NASA equilibrium gas solver
L1d2	:	1-D Lagrangian transient compressible flow solver
LOx	:	Liquid oxygen augmentation
Eilmer3	:	2-D/3-D Navier-Stokes transient compressible flow solver
mb_cns	:	2-D/3-D Navier-Stokes transient compressible flow solver
SSTO	:	Single-stage-to-orbit
UQ	:	The University of Queensland
DSTO	:	Defence Science and Technology Organisation
TOGW	:	Takeoff gross weight

Chapter 1

Introduction

1.1 Chapter Overview

The scramjet engine is proposed as a propulsion source for access to space launch vehicles. Air breathing flight at high Mach numbers involves new flight conditions, and there exists a corresponding need to reproduce these flight conditions in ground-based test facilities in order to assess new designs. This thesis is concerned with using expansion tube facilities to produce flow conditions for the testing of new access to space scramjet engine designs. The chapter begins with a general discussion on the scramjet engine concept and outlines its potential applications. The discussion then focuses on the proposed use of the scramjet engine as part of a multi-stage launch vehicle, and describes details of the specific high Mach number, high total pressure, flight regime that this entails. The objective of this thesis is then introduced - i.e. to produce these types of flow conditions in an expansion tube facility - and specific target flow conditions are calculated. Finally, an overview of the thesis structure is presented, followed by a summary of its original scientific contributions.

1.2 Scramjet Engines

1.2.1 Concept

Traditional subsonic air-breathing engines, such as aircraft turbojet engines, mechanically compress air before it enters the combustion chamber. For a mechanical compressor to operate at supersonic speeds, the flow is normally slowed to subsonic speeds before it enters the compressor. This incurs losses which become prohibitive at high supersonic and hypersonic speeds. However, at these higher speeds, there

is sufficient compression of air due to the vehicle bow and engine inlet shocks to remove the requirement for a mechanical compressor [1].

Ramjets, which are the engines of choice between Mach 3-6, transform supersonic flow at the engine inlet into subsonic flow through a normal shock wave system [2]. However, beyond approximately Mach 6, decelerating the flow to subsonic speeds produces excessive temperatures, excessive wall heat transfer rates, excessive performance losses due to the normal shock wave system, and excessive chemical dissociation [2]. In addition, loss of total pressure reduces the pressure recovery and thrust developed. At these higher Mach numbers, it is preferable that the flow through the combustor should remain supersonic, thus leading to the supersonic combustion ramjet (SCramjet) engine.

The scramjet engine is thus proposed as an efficient source of air-breathing propulsion for hypersonic aircraft for flight speeds exceeding approximately Mach 5 [3]. The key characteristic of the scramjet engine is that thrust is achieved by supersonic combustion of atmospheric oxygen, as opposed to a rocket which must carry the oxidiser on-board. This provides the advantages of reduced size and mass, with a corresponding order of magnitude increase in specific impulse as compared to conventional rockets [4]. A comparison of theoretical engine performance as a function of Mach number is shown in Figure 1.1:

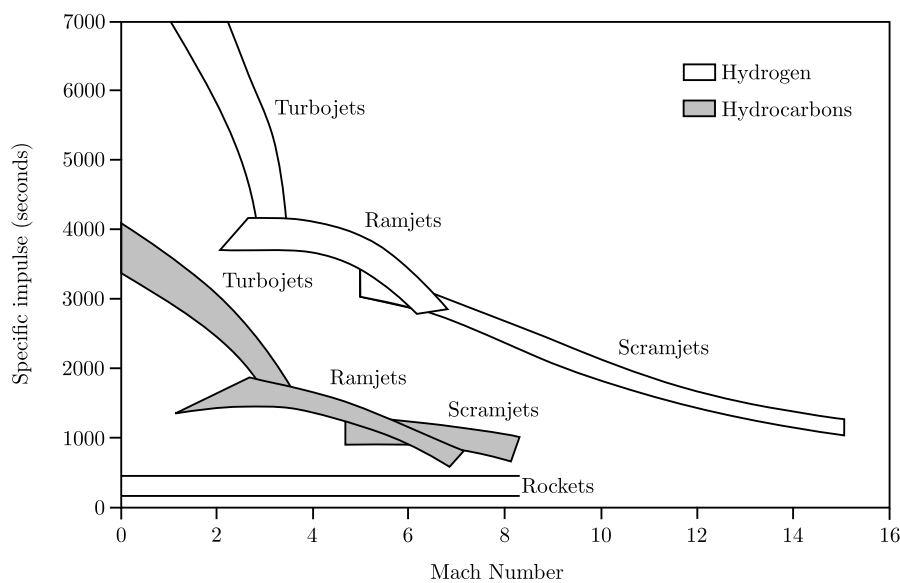


Figure 1.1: Specific impulse for various engines (adapted from Kors [5]).

1.2.2 Potential Applications

Billig [6] notes four main applications for supersonic combustion:

1. Primary propulsion for missiles.
2. Primary propulsion for hypersonic airplanes and trans-atmospheric accelerators.
3. Thrust augmentation for fuel-rich rockets.
4. External burning devices for thrust production (or drag reduction) and/or lateral control.

Based upon the above, scramjets are most likely to find application in missiles, hypersonic aircraft, and space launch vehicles. Given the large investment required to develop scramjet technology, they are most likely to be first used in military and space programs, which typically have much of their funding provided by governments. Once the technology has matured, it may later filter down to commercial applications. This thesis considers scramjet propulsion at the high Mach numbers which are associated with access to space, therefore the discussion will now focus directly upon this application.

1.2.3 Scramjets for Access to Space

Kumar [7] outlines several benefits of air-breathing launch systems over traditional rocket powered systems:

- Safety. Air-breathers have significantly lower power densities than rockets (i.e. maximum propellant flow rates of 7,500 lb/sec for rockets vs. 120 lb/sec for air-breathers). Air-breathers also have the potential to abort.
- Mission flexibility. Air-breathers may have the capacity for horizontal take-off and landing, and also the ability to achieve alternate orbits.
- Robustness. Higher margins of safety are feasible since weight-growth sensitivity is less (one pound of dry weight increase to an air-breathing engine adds 3.7 pounds to its takeoff gross weight (TOGW), compared to 10 pounds extra TOGW for a rocket system). Generally, thrust levels are also lower.
- Reliability. Probability of system failure is reduced since thermal loads and pressure requirements on the fuel pump are lower (however thermal loads on air-breathers will be higher than for rockets).
- Operating costs. These may potentially be an order of magnitude less [8, 9].

Smart and Tetlow [10] argue that hypersonic air breathing launch systems are only suitable for use in a multi-staged launch vehicle, where they will only operate for part of the flight. Rockets (or possibly turbojets) would be used for the initial phase of the flight, then the air breathing engine, and finally a liquid fuelled rocket would be used for the last phase, to insert the payload into orbit [10]. As part of a multi-stage launch vehicle, options exist for both reusable and single use scramjet stages. Semple [11] argues that it is desirable to make the scramjet stage expendable, since this will allow the use of ablation cooling to deal with the significant aerodynamic heating of the engine. However, Tetlow and Doolan [4] argue that the high structural mass of scramjets compared to rockets will make it economically infeasible to treat the scramjet stage as expendable, since structure is more expensive than propellant (i.e. it is cheaper to burn an equivalent mass of fuel than dispose of structure). Tetlow and Doolan [4] further argue that in any case, re-usability of scramjets will be more practical than rockets since scramjets will have fewer moving parts.

Alternatively, single-stage-to-orbit (SSTO) vehicles are proposed, and these drove the National Aero-Space Plane (NASP) program in the late 1980's. These vehicles would complete their full mission cycle as a single vehicle, unlike the multi-stage vehicles typical of current space access (i.e. the space shuttle). Studies such as Moses et al. [12] propose an integrated lifting body, where initial propulsion is achieved with turbojet/ramjet engines powering the craft to Mach 4 (perhaps with assistance from a rocket both at takeoff and through the transonic regime), followed by main engine ramjet/scramjet operation to approximately Mach 12-15. At very high Mach numbers, there may be some liquid oxygen (LO_x) augmentation to increase the scramjet thrust in the thinner atmosphere, followed by a pull-up manoeuvre and rocket operation to reach space. Cockrell et al. [13] note that system studies indicate that LO_x augmentation may be necessary to achieve efficient orbital insertion for SSTO vehicles.

To date, several scramjet engines have been successfully flight tested, including the following:

1. The first scramjet to successfully achieve thrust was the hydrocarbon-fuelled HyShot 2 at Mach 8, which was designed by NAL and launched by The University of Queensland (UQ) on 30 July 2002 [14, 15].
2. The hydrogen-fuelled NASA X-43 sustained Mach 7 scramjet powered flight for ten seconds on March 27, 2004 [9], and Mach 10 flight for approximately 10-12 seconds on November 16, 2004 [16].

3. On 25 March 2006, UQ and Australia's Defence Science and Technology Organisation, DSTO, launched the Hyshot III scramjet aboard a two-stage Terrier-Orion rocket. The engine was designed by the British research organisation QinetiQ. After initially rising to 330km, the rocket reached a peak speed of Mach ≈ 8 during its free fall. The scramjet was operated for 6 seconds while the vehicle was at Mach = 7.6 [17]
4. On 15 June 2007, DSTO launched the hydrogen-fuelled HyCause Mach 10 scramjet [18, 19].
5. Most recently, the hydrocarbon-fuelled U.S. Air Force X-51A achieved scramjet ignition and acceleration for 200 seconds on May 26 2010 [20]. The X-51A, attached to a solid rocket army tactical missile, was initially released from a B-52 aircraft at 50,000 ft [20]. The solid rocket booster was used to accelerate the X-51A to Mach 4.8, whereupon the X-51A separated. After slowing to Mach 4.73, the scramjet engine was ignited and accelerated the vehicle to approximately 70,000 ft and a peak speed of Mach 5 [21]. The flight was terminated after 200 seconds following the loss of telemetry [20, 21] and the acceleration was less than planned (0.15g compared to 0.22g) [21]. Although the vehicle did not reach its target speed and burn time (Mach 6 and 300 seconds respectively), the test was still considered very successful by the Air Force [21].

1.2.4 Key Scramjet Design Challenges

At the high Mach numbers considered in this thesis, the bulk of the flow through the engine may be hypersonic. Combustion in this flow environment is referred to as hypersonic combustion, and is characterised by high local Mach numbers, shallow Mach angles, reduced effect of heat release due to combustion, and fully three-dimensional flow fields [22].

Due to its high mass-specific energy content, and rapid ignition and reaction, hydrogen is the only fuel expected to be viable at the upper Mach limit of scramjet combustion [23, 1, 24, 25] (approximately Mach 15 [3, 4]). Heat release due to combustion is inversely proportional to the square of free stream Mach number [13]. At speeds of approximately Mach 8, combustion energy is significant compared to the total enthalpy of the flow (approximately 50%), and large relative pressure rises are possible in the combustion chamber [22]. At Mach 15, combustion energy is only approximately 25% of the total free stream kinetic energy [13], and approaching Mach 25, heat release from combustion may be as little as only

10% of the total enthalpy of the flow [22]. The result is that small changes in specific impulse at high Mach numbers can make big differences in terms of gross take off weights, thus requiring highly optimised designs [13].

Fuel mixing with hydrogen becomes an extreme problem at Mach 12 and above. Various hydrogen injection schemes involve sonic flow through an injector [26, 27], which places an approximate limit on hydrogen injection speed (depending on its temperature). At Mach 12, the velocity of injected hydrogen is approximately the same as the combustor air stream flow [22]. Mixing at or above Mach 12 becomes difficult to predict, and depending on the degree of intake compression, dissociation may begin to occur due to high temperatures in the combustor [22, 1]. Viscous aero-heating of the engine walls also needs to be tackled since temperatures exceed material limits, and wall cooling effects can dominate the design process of hypersonic combustors [1]. Drag through the combustion chamber of the scramjet engine is considered a key source of inefficiency in a scramjet, and it is therefore desirable to reduce the length of the combustion chamber, for example, by upstream injection of fuel at the intake [28].

Considering the above, useful scramjet propulsion beyond Mach 15 is considered unlikely. For this reason, flow conditions beyond Mach 15 are not considered in this investigation.

1.3 Scramjet Flight Regime

1.3.1 Proposed Ascent Trajectory

A potential application of scramjet technology of great interest is payload delivery to orbit. However, the requirement that the scramjet must operate within a suitable air-breathing corridor imposes several limitations on the final launch vehicle configuration [29], including the following:

1. Additional sources of propulsion are required for the initial acceleration to scramjet ignition, and for propulsion once the vehicle leaves the atmosphere.
2. Upper altitude limit: The scramjet is an air-breathing engine, and as such, for a given Mach number it is required to fly at altitudes sufficiently low that it can capture and process sufficient airflow [30], and maintain sufficient static pressure for supersonic combustion. Typical trajectory studies generally consider a dynamic pressure of approximately 25 kPa as a realistic lower limit for combustion (for example [29, 31]), although some trajectory studies

have considered even lower dynamic pressures (for example, Ardema et al. with a 5 kPa limit [32]; Tetlow and Doolan with a 9.5 kPa limit [4]).

3. Lower altitude limit: Increasing the flight dynamic pressure directly benefits thrust generation [33]. However, at the high dynamic pressures which are required for sufficient thrust in order to power, for example, a large SSTO, aerodynamic heating presents severe structural challenges [34]. Airframe structural loading and aerodynamic heating impose upper limits on the dynamic pressures (corresponding to lower limits on altitude) at which the vehicle can operate [33]. As flight speed approaches Mach 20, heat transfer rates begin to rise rapidly, and there comes a point where heating becomes the limiting design constraint [35]. At this point the launch vehicle must rapidly ascend to higher altitude and lower densities to prevent catastrophic heating, and therefore must depart from the constant dynamic pressure ascent trajectory [35].

Considering the above, proposed scramjet ascent trajectories typically target a constant dynamic pressure phase during the bulk of the scramjet burn cycle. The requirement for high thrust demands that dynamic pressures be kept as high as structural limitations will allow [33]. Thrust and structural limitations therefore define an operational band within which the scramjet must operate during the ascent. An example of a representative ascent trajectory is illustrated in Figure 1.2.

Figure 1.2 describes a representative ascent trajectory whereby the scramjet burn cycle occurs along the 2000 psf (95.8 kPa) dynamic pressure isobar. There are several authors who also consider this dynamic pressure to be an approximate maximum practical limit [6, 30, 33]. Figure 1.2 is only one proposed trajectory, but it provides a useful and rational basis upon which to develop flow conditions. It does not take into account specific vehicle operational parameters, and is simply an approximate flight path.

Others have used optimisation to develop more mission-specific trajectories, which consider a greater number of parameters such as payload size, aerodynamics, structural loads, structural weight, cost, and so forth [4, 6, 11, 12, 29, 33, 36, 37]. Figure 1.3 shows several proposed ascent trajectories plotted along with the reference ascent trajectory from Figure 1.2, and also shows the space shuttle launch trajectory for comparison. It can be seen that all of the scramjet trajectories follow a high dynamic pressure trajectory. The optimised trajectory from Tetlow and Doolan [4]

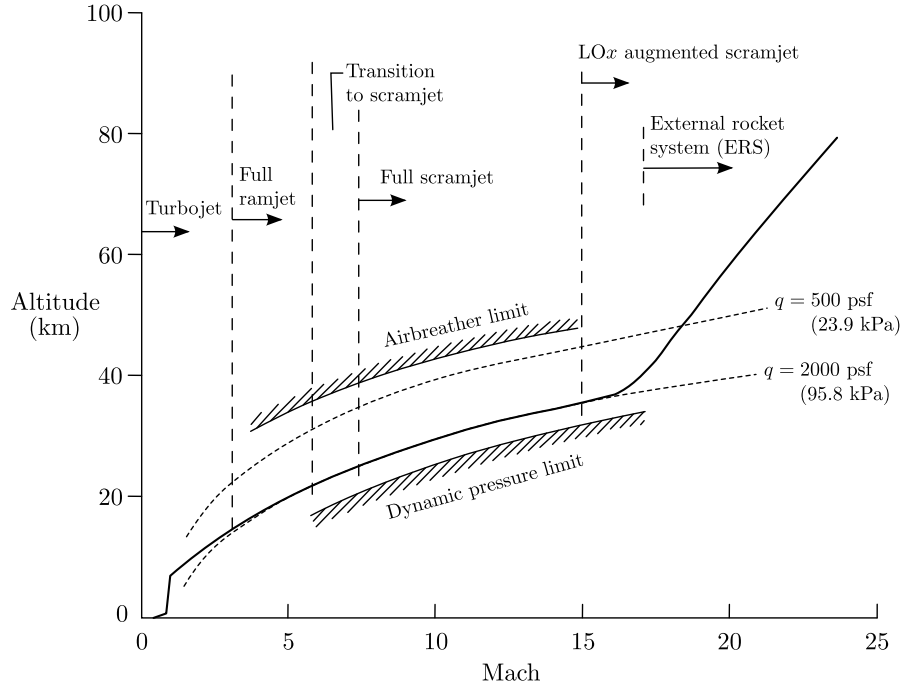


Figure 1.2: Representative scramjet ascent trajectory (adapted from Hunt and Martin [29]).

reaches the highest dynamic pressure of those trajectories shown, and also includes the detailed effects of decelerations during coasting phases of the flight.

1.3.2 Binary Scaling and Total Pressures

Current impulse facilities are not capable of testing payload-to-orbit full scale scramjets due to test time and size restrictions, therefore subscale models are commonly used. For ground testing of sub-scale scramjet-powered vehicles, pressure-length scaling is applied in order to maintain similarity for many of the flight parameters, such as Reynolds number, binary reaction rates, viscous effects, ignition time, and the fuel mixing process [38, 39, 40]. This involves increasing static pressure, p , by inverse proportion to model scale (represented by a characteristic length parameter, L), such that the product pL remains equal to that for the full scale model.

The effect of pressure length scaling is to increase the total pressure requirement as model size reduces, placing greater demands on the total pressure performance of the impulse facility. Figure 1.4 shows how total pressure varies with model scale, for different free stream Mach numbers, at a constant dynamic pressure of 2000 psf (95.8 kPa, from the representative ascent trajectory in Figure 1.2; note: total pressure denotes calculations following an isentropic compression of atmospheric

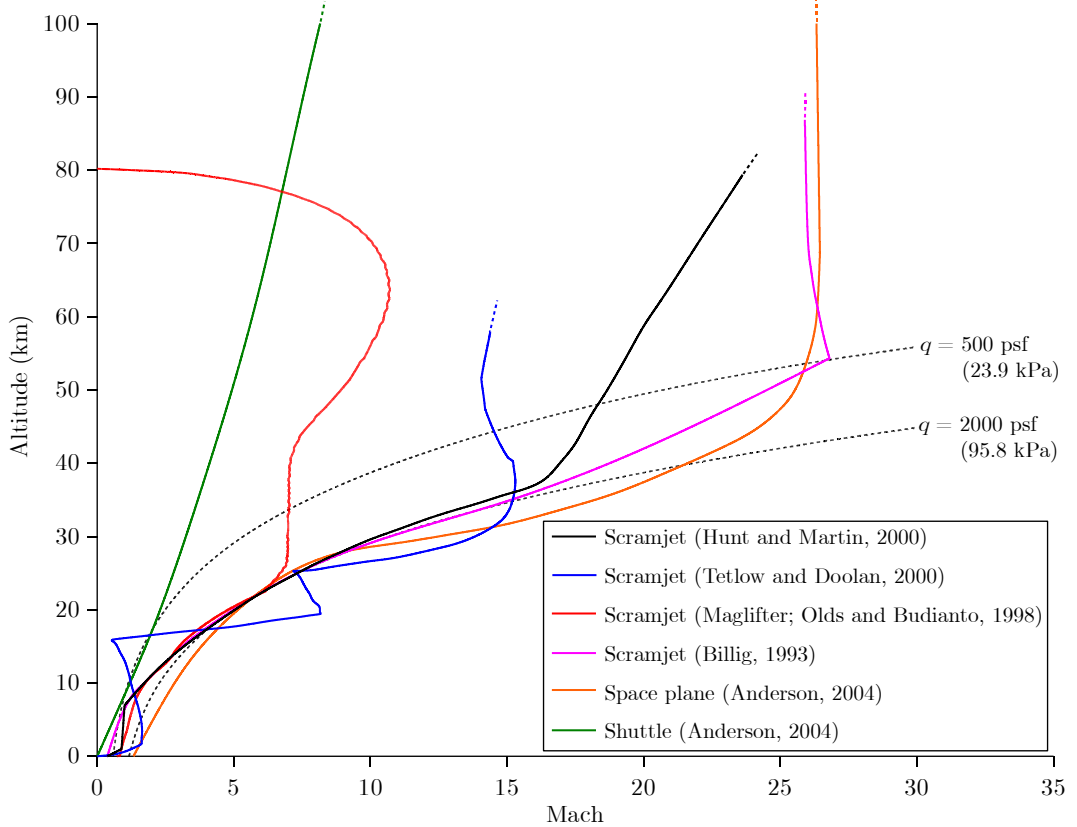


Figure 1.3: Comparison of proposed ascent trajectories (adapted from [29, 36, 33, 6, 37]).

air from flight velocity to stagnation, assuming shifting chemical equilibrium in accordance with Chinitz et al. [41]).

1.4 Objective of this Thesis

There are various ground-based test facilities available to simulate hypersonic flows, however expansion tubes are currently the only type of facility thought to have the potential to simulate high Mach number scramjet flight, characterised by total pressures of the order of gigapascals. Chapter 2 discusses ground-based testing of hypersonic flows in more detail. The core objective of this PhD thesis was to produce high Mach number, high total pressure, scramjet flow conditions using The University of Queensland's (UQ) X2 expansion tube impulse test facility.

The study attempted to simulate scramjet flow conditions at Mach 10, 12.5, and 15, along a 2000 psf (95.8 kPa) dynamic pressure ascent trajectory (see Figure 1.2), which was considered to address a representative range of flight speeds. Calculation

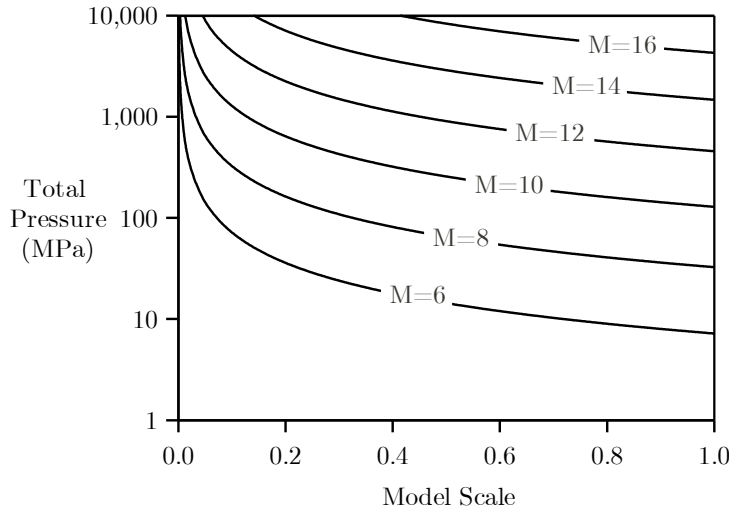


Figure 1.4: Effect of model scale on free stream simulation total pressure requirements, based on p - L scaling for a 2000 psf (95.8 kPa) constant dynamic pressure ascent trajectory (consistent with Hunt and Martin [29]). Calculations assume that atmospheric sound speed and density vary in accordance with the American Standard Atmosphere [42]; total pressure is calculated using NASA code CEA [43] assuming shifting chemical equilibrium in accordance with Chinitz et al. [41].

of these flow conditions is presented in Section 1.4.1, and the three target flow conditions are summarised in Table 1.1.

The key challenge which arose in the process of trying to develop these flow conditions was the need to modify the free-piston driver of X2; as a consequence, this task features prominently in this document. This and other aspects of the solution process are summarised in Section 1.5, which presents an overview of the thesis structure and outlines the path taken to achieving the core objective of the study.

1.4.1 Target Flow Conditions

Using the reference trajectory detailed in Figure 1.2, three flow conditions were targeted by this thesis, as shown in Table 1.1. The total pressure requirements at 1:10 model scale are also shown for reference. The flow conditions are calculated as follows:

1. Assume a dynamic pressure of 95.8 kPa (2000 psf).
2. Assume that altitude, sound speed, and density, vary in accordance with the American Standard Atmosphere [42].
3. Calculate the corresponding Mach number at each altitude increment using

Mach [-]	Altitude [m]	ρ [kg/m ³]	a [m/s]	T [K]	V [m/s]	h MJ/(kgK)	Full Scale Model		1:10 Scale Model	
							p [kPa]	p_0 [MPa]	p [kPa]	p_0 [MPa]
10.0	29,108	0.02112	301	226	3,011	4.760	1.368	129	13.68	1,282
12.5	32,104	0.01334	303	229	3,789	7.408	0.876	616	8.76	6,008
15.0	34,605	0.00900	308	235	4,614	10.88	0.608	2,547	6.08	24,172

Table 1.1: Target flow conditions.

the following equation:

$$q = \frac{1}{2}\rho V^2 = \frac{1}{2}\rho (Ma)^2 \rightarrow M = \sqrt{\frac{2q}{\rho a^2}} \quad (1.1)$$

4. Linearly interpolate flow properties for the given Mach number of interest.

Referring to Table 1.1, it can be seen that total pressure, p_0 , becomes very high at Mach 15 (2.5 GPa), and increases dramatically for 1:10 model scale (24.2 GPa). Besides static and total pressures, other flow parameters do not need to vary with model scale. The objective of this study was to first match the free stream flow condition parameters of velocity and Mach number (and therefore enthalpy), since these define the key free stream characteristics. The corresponding static pressure was then assessed, and different methods of varying the test flow static pressure were considered.

1.5 Structure of this Thesis

The remainder of this thesis is organised as follows:

Chapter 2 describes the different types of ground-based test facilities available to simulate hypersonic flows. The capabilities of each facility are compared and their applicability for scramjet testing is considered. The difference between direct-connect and free stream scramjet engine testing is explained, and previous scramjet testing by different international facilities is reviewed. It is shown that the expansion tube is currently the only facility understood to be capable of replicating the high total pressure flow conditions characteristic of scramjet-powered access to space.

Only one previous scramjet combustion study using expansion tubes is identified in the literature, which demonstrated that expansion tubes can indeed be used to test scramjet combustion. However, this study did not investigate combustion at the high total pressures targeted by the present study. It is determined that the uniquely high total pressure capability of expansion tubes has yet to be applied to scramjet testing, therefore the present study stands to yield valuable new understanding in this field.

Chapter 3 presents a detailed discussion about expansion tube facilities. Analytical relations are reviewed and important aspects of expansion tube performance are considered. The discussion concludes with a review firstly of UQ's X2 and X3 expansion tube experimental facilities, and secondly of UQ's transient CFD analysis codes, L1d2 and Eilmer3, which have been used in the present study to predict expansion tube performance.

Chapter 4 begins by describing an initial attempt, at the beginning of this study, to simulate a high total pressure Mach 13 scramjet flow condition using X2 with its existing free-piston driver configuration. The new flow condition was developed using analytical techniques. It was found that shock speeds attenuated significantly down the length of the tube, and the target flow condition was not achieved. Results are presented of a detailed analysis of the flow processes using the 1-D Lagrangian transient CFD code L1d2, which models the full piston dynamics and longitudinal wave processes. It is shown that shock attenuation occurs because the volume of high pressure driver gas downstream of the piston expands too rapidly, and as a result a strong $u + a$ expansion wave is reflected from the piston face and interrupts downstream flow processes.

The concept of a tuned free-piston driver is then introduced, whereby the piston

has sufficient velocity at the moment of diaphragm rupture to temporarily compensate for driver gas loss to the driven tube, thus maintaining driver pressure for longer. Tuned operation involves high piston speeds, which presents challenges in terms of accelerating the piston to high speed over a relatively short distance, and then stopping it again without causing damage to the piston or to the facility. It is determined that a tuned free-piston driver for X2 requires a much lighter piston, of at most approximately 10 kg (compared to the 35 kg piston previously used). Chapter 4 concludes by presenting an analysis which outlines the requirements to achieve tuned operation of the X2 free-piston driver.

Chapter 5 details the design and stress analysis of a new 10.5 kg lightweight piston for X2. The chapter details the piston design requirements, which include applied loads, failure criteria, and safety factors. Finite element analysis is used to demonstrate that the piston meets these design requirements. The chapter concludes by reporting on the condition of the piston after over 300 experimental shots in X2, including a number of shots at its maximum driver pressure loading. The piston is reported to be undamaged with no signs of structural distress, thus validating the design methodology used.

Chapter 6 details the commissioning of the new 10.5 kg lightweight piston for X2. As a first step, feasible driver configurations were calculated using an analytical model. Driver configurations were then fine-tuned using the 1-D Lagrangian code L1d2. The reservoir loss factor in L1d2, which is very important in terms of establishing the correct reservoir fill pressure, was determined based on blanked-off driver tests (i.e. using a non-rupturing diaphragm). An iterative approach was adopted until good correlation was obtained between blanked-off driver experiments and L1d2, whereupon full experiments were performed using rupturing diaphragms. The new driver conditions were found to operate smoothly without causing damage to the facility, and were also shown to avoid the shock attenuation which had been a problem with the previous 35 kg free-piston driver configuration. Three new tuned driver conditions are presented based on 1.2, 2.0, and 2.5 mm thick steel primary diaphragms.

Chapter 7 investigates the theoretical operating range of X2 using the newly developed tuned free-piston driver conditions detailed in Chapter 6, for air test gas. The analysis uses classical 0-D analytical techniques to predict the performance of the X2 expansion tube facility across a range of likely configuration options. In order to improve the accuracy of predictions, the NASA equilibrium gas solver, CEA, is used to calculate equilibrium gas properties across normal shocks and

through unsteady expansions. The facility is considered with and without a nozzle. Test time and Mirels effects, both dependant on tube length, are ignored; these influences are taken into consideration in 1-D L1d2 calculations at the end of the chapter, and in 2-D axisymmetric Eilmer3 CFD calculations in Chapter 8.

Chapter 8 presents experimental results for the new flow conditions proposed in Chapter 7. A hybrid L1d2/Eilmer3 CFD model is used to simulate each test condition, and the CFD results are compared to experiment. Mach 10, 12.5, and 15 flow conditions for X2 *without* nozzle, and a Mach 10 condition for X2 *with* nozzle, are each analysed. It is shown that shock speeds and tube wall static pressure traces agree well with CFD, indicating that target wave processes have been achieved. Making Pitot measurements proved difficult in these short duration, extremely harsh, scramjet flows; in order to achieve a similar measurement, partial impact 15 deg cone pressure probes were developed. It is determined that while these probes produced more consistent traces, and have much improved survivability, their response is too slow for these very short duration ($\approx 50\mu\text{s}$) scramjet test flows. The chapter concludes by arguing that gigapascal total pressure, relatively steady scramjet flows have been achieved. However, further work is required to make more reliable Pitot measurements, and the flow conditions now need to be scaled up to a larger facility (such as UQ's X3 expansion tube) in order to achieve longer test times and larger core flow diameters.

The hybrid CFD model in Chapter 8 uses the 1-D code L1d2 (which includes full piston dynamics) to calculate an inflow to a 2-D axisymmetric model spanning the shock and acceleration tubes. The primary source of 2-D disturbances in the driver gas is the expansion of the driver gas through the area change and rupturing primary diaphragm; these 2-D effects are not captured in the hybrid model, so it cannot predict the subsequent effect of these disturbances on the test flow. **Chapter 9** therefore uses a full facility 2-D axisymmetric Eilmer3 model to simulate the Mach 10 X2 flow condition (X2 without nozzle). Eilmer3 does not presently include piston dynamics, so a fixed volume driver is assumed. The primary diaphragm is modelled as an iris opening diaphragm, and it is believed that representative disturbances are introduced to the driver gas. Results from this full facility simulation are compared to the Mach 10 hybrid CFD results from Chapter 8, and also to experimental results. It is argued that the full facility CFD simulation results indicate that 2-D noise originating from the driver does not appear to corrupt the useful portion of the test flow, and that the hybrid model calculations from Chapter 8 therefore remain valid.

Chapter 10 presents the conclusions from this study, followed by *Chapter 11* which presents recommendations for further work.

1.6 Original Scientific Contributions of this Study

This study has produced the following original contributions to scientific knowledge:

- The expansion tube configuration for these scramjet flow conditions is characterised by the use of a secondary driver to maintain an acoustic buffer, and the use of a very dense air test gas to achieve high test flow density. Extensive analysis of the longitudinal wave processes typical of these flow processes has been performed using L1d2, for example, Sections 4.2.4 and 7.8. In particular, the reflected shock which develops at the secondary diaphragm and reflects from the primary driver/secondary driver gas interface, has been shown to have an important interaction with the test flow, as discussed in Section 7.8.
- Chapter 5 details the design of a new lightweight piston for X2. For its loading and size, this is the lightest piston currently being operated in comparable impulse facilities around the world. The literature does not contain other examples of the detailed design methodology for such a piston, including validation of the design process. Therefore the work presented in Chapter 5 constitutes a new and validated set of guidelines as a basis for future and more advanced lightweight piston designs (i.e. a lightweight filament wound carbon composite piston for X3).
- Chapter 6 details the commissioning of the new lightweight piston for X2. This work is unique in so far as the piston is lighter and therefore undergoes higher accelerations than other pistons in comparable impulse facilities. Operating the piston at these speeds achieves very high performance levels for a compression tube which is significantly shorter than that of comparable facilities.
- Chapter 7 presents a novel approach to expansion tube performance analysis. This chapter contains calculations of the full performance envelope of the facility for varying helium secondary driver fill pressures. By then solving for the shock and acceleration tube air fill pressures which achieve target flow conditions, and repeating this analysis for varying secondary driver fill

pressures, the analysis demonstrates the effect of the secondary driver on the resulting flow conditions. Ignoring longitudinal waves processes, but taking into account equilibrium gas properties, it is seen that the secondary driver fill pressure presents a mechanism for adjusting the test flow static pressure, which is normally fixed by the free-piston driver configuration. Since the development of tuned free-piston driver conditions can be laborious and higher risk with very light pistons, using the secondary driver to modify test flow static pressure potentially reduces the number of tuned free-piston driver operating conditions required to achieve various target test flow conditions.

- Chapter 8, Section 8.7, details a new Mylar diaphragm holder which is designed to perform two functions; firstly, to firmly support the Mylar diaphragm in a cartridge unit prior to insertion into the tube, thus ensuring it is properly supported and not damaged during insertion; secondly, the cartridge unit allows the two adjacent tubes to be axially decoupled, thus preventing transmission of axial stress waves downstream of the diaphragm station. Initial experimentation with the lightweight free-piston driver indicated that the high piston deceleration introduced large magnitude stress waves into the tube which arrived at the relatively sensitive acceleration tube wall static pressure sensors before the test flow, thus corrupting the measured pressure signal. The new diaphragm holder almost entirely eliminated the observable effects of these stress waves in the transducer signals. This work both highlights the need to consider tube decoupling in the design of impulse facilities, and also provides a practical design concept which can be retrofitted to an existing facility without significant modification. Vibration isolation is an ongoing challenge with impulse facilities, and this design presents a new approach to achieve this goal across a secondary/tertiary diaphragm station in an expansion tube.
- The expansion tube configuration used for this thesis employs a helium-filled secondary driver, primarily to act as an acoustic buffer to prevent transmission of noise (of radial origin) in the driver gas to the test gas. Hybrid 1-D/2-D CFD analysis of new flow conditions has been performed to accompany experimental results; see Chapter 8. However, these hybrid models do not reveal the effectiveness of the secondary driver, since they rely on the 1-D L1d2 code to calculate flow processes upstream of the shock tube. It was therefore considered beneficial to attempt to include the primary sources of driver noise into one of the CFD models (in this case, the Mach 10 flow

condition for X2 without a nozzle). Chapter 9 shows that this was achieved by modelling a fixed volume driver with an area change, and incorporating an iris opening primary diaphragm model. These two features provide a representative source of radial disturbances into the driver gas, which specifically permit the effectiveness of the secondary driver as an acoustic buffer to be assessed for the example Mach 10 flow condition. CFD modelling of the driver flow processes in an expansion tube, with secondary driver, and including diaphragm rupture, has not previously been undertaken.

- The new scramjet flow conditions presented in Chapter 8 represent the highest published total pressure scramjet flow conditions yet to be achieved in a ground test facility, and are the first published example of the use of an expansion tube to achieve multi-gigapascal total pressures for scramjet flight conditions. This outcome represents the successful achievement of the core objective of this thesis.

Chapter 2

Ground Testing of Scramjet Engines

2.1 Chapter Overview

This chapter presents a discussion on the various options available for ground testing of scramjet engines. The chapter begins with a discussion of different types of hypersonic facilities, outlining their generic capabilities and limitations. It is shown that the expansion tube is currently the only hypersonic ground test facility thought to have the potential to achieve the gigapascal test flow total pressures characteristic of high Mach number scramjet flight. However, in practice scramjet flow conditions at these total pressures have yet to be developed, thereby indicating the need to develop this capability for expansion tube facilities and thus justifying the research topic of this thesis.

2.1.1 Introduction

Ground testing is much cheaper than flight testing, particularly for research and technology development [44]. Anderson et al. argue that CFD codes can provide valuable insight into complex hypersonic flows, and can be useful for parametric design studies, however the codes must be benchmarked against experimental data [45]. CFD codes generally do not model turbulence directly [45], and empirical correlations used for turbulence calculations are based on incompressible flow [45].

Considering scramjet engines, despite the availability of predictive CFD tools, at best these tools model combustion physics crudely [45]; combustion occurs at a molecular level, however CFD codes treat the flow as continuous. In many cases effective phenomenological models are simply not available and experiments must be relied upon. These are some of the reasons that having a ground testing capability spanning the entire scramjet flight regime is necessary for scramjet development.

Figure 1.2 previously illustrated a representative flight envelope for scramjets used for payload delivery to orbit, which will be the most extreme application of the technology. The figure provides an indication of the range of conditions which hypersonic ground test facilities must be able to simulate. Since air-breathing scramjets must fly within the atmosphere, where air densities are comparatively high, then at Mach numbers exceeding 10 the total pressures, which increase exponentially with Mach number, become extremely high (refer to Table 1.1).

Figure 2.1 shows the performance of various international hypersonic test facilities, measured in terms of Mach number and total pressure. In relation to scramjet engine testing, shaded bands in Figure 2.1 indicate two types of study:

1. ‘Direct connect’ combustion simulation, which aims to simulate flow at the combustor entrance that has already been compressed by the vehicle bow and intake shocks. Since this approach bypasses inlet losses, it allows maximum flight Mach number simulation [46]. Although useful, this type of simulation fails to capture complex flow effects upstream of the intake due to scramjet integration within the overall flight vehicle. These effects can potentially have a critical effect on subsequent flow through the scramjet [47].
2. Freestream engine simulation, which aims to simulate the full free stream flow conditions. This allows full assessment of the scramjet performance, including the effects of engine integration into the flight vehicle. This type of test is typically restricted to small scale or small engines [46].

Bakos et al. [50] identified several key elements of hypersonic combustion (i.e. scramjets operating in the hypervelocity regime of $Mach > 10$). These included fuel penetration, turbulent mixing rates, combustion efficiency, film cooling requirements, and internal losses. Bakos et al. [50] stated that these phenomena could not be extrapolated from supersonic and low hypersonic data ($Mach < 8$), therefore any suitable ground test facility needs to produce the actual high Mach number flows experienced in flight. Considering this, and referring to Figure 2.1, at first glance it is clear that above approximately Mach 10, only impulse facilities, which operate for a very short time, are capable of producing high total pressure hypervelocity flows [45]. The various facilities are now discussed below, where it is concluded that only expansion tube facilities can potentially produce the flow conditions targeted by this thesis.

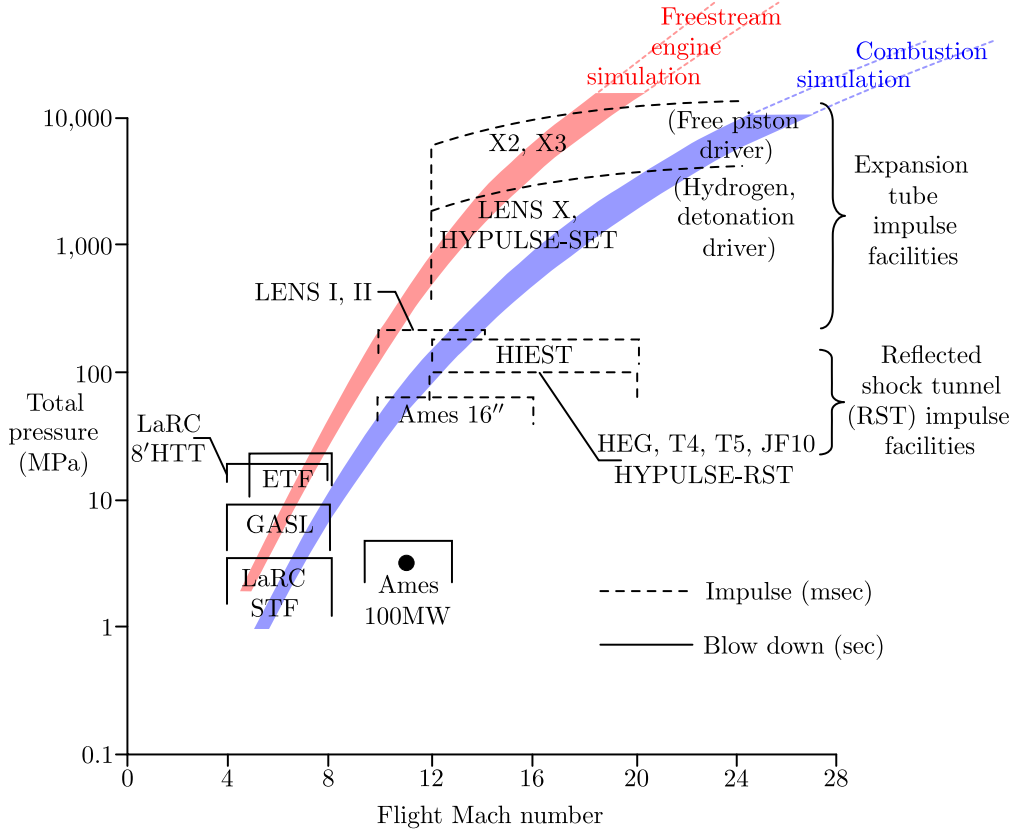


Figure 2.1: Total pressure capability for various hypersonic facilities used for scramjet work (adapted from [45]; updated with [48, 49]).

2.1.2 Blow Down Facilities

Considering Figure 2.1, it can be seen that blow down facilities are limited to approximately Mach 8 (NASA Ames has a capability of approximately Mach 10, but its maximum total pressure is comparatively low). Blow down facilities are long duration facilities, where heat is added to the test gas initially, and then it is expanded isentropically through a nozzle [51]. These facilities are not capable of simulating high Mach number scramjet flows for several reasons:

1. Hypervelocity flows have impractically large power requirements [51].
2. The test gas is required to be contained at or near stagnation conditions, which imposes excessive facility structural requirements [51].
3. At high Mach numbers, the process of heating the test gas causes blow down facilities to suffer from problems with dissociation of oxygen and creation of atomic oxygen and nitrogen oxides. The rapid expansion of this gas can

prevent recombination reactions from taking place, with nitrogen oxides remaining in the test gas [52]. Fischer and Rock [52] analytically studied the effect of NO dissociation and found the effects become evident at Mach 8, leading to slightly enhanced combustion.

Some examples of blow down facilities include:

- The NASA Langley Direct-Connect Supersonic Combustion Test Facility (DCSCTF), which utilises hydrogen-air combustion to energise the test gas and achieve enthalpies equivalent to Mach 4-7.5 [13]. This facility is used to test ramjet and scramjet combustor models for mixing, ignition, flame holding, and combustion characteristics [53].
- The Italian SCIROCCO facility, with potential operation for up to 30 minutes, and the ability to vary free stream Mach number during the test [54].
- The NASA Langley Research Center Arc-Heated Scramjet Test Facility (AH-STF), in which incoming air is heated by an electric arc to near 4400K to achieve the stagnation enthalpies for Mach number simulations up to approximately Mach 8 [52].

2.1.3 Impulse Facilities - Basic Shock Tube

The most simple impulse facility is the shock tube. In essence it is comprised of a tube with a diaphragm separating a region of high pressure driver gas from a region of low pressure test gas [55]. When the diaphragm is ruptured/removed, a shock wave propagates into the test gas [55]. The effect of the shock is to increase the temperature and pressure of the test gas, and also to induce a mass motion behind the shock, in the direction of the shock, which is used as test flow. The test flow properties are a function purely of the properties of the original driver and test gases [55], and the geometry.

The basic shock tube is not capable of producing the high enthalpy and high total pressure flow simulations required for scramjet testing. The total enthalpy that can be added to the flow by the shock is limited by radiation effects [56, 57], and driver gas pressures are limited by structural strength considerations. In that respect, the basic shock tunnel is of no use to the present study, however the more sophisticated impulse facilities, which will actually have application in this study, are all developments on the basic shock tube concept.

A key attribute of impulse facilities is that they have a very short test time (in the order of milliseconds or less), therefore it is necessary that measurements have a very high frequency (in the order of a MHz [58]). However, the short duration of such tests is beneficial in the sense that model cooling can be met by simple heat sink approaches [22]. In the short test times considered, wall reactivity may not accurately be modelled due to low wall temperatures (especially where dissimilar materials are used), however in this instance CFD can be used to a first order to correct for wall thermal effects [22].

2.1.4 Impulse Facilities - Reflected Shock Tunnel

The reflected shock tunnel (RST) is a shock tube facility which operates by processing the test gas with two shocks. The first shock traverses the shock tube and processes the test gas, just like a basic shock tube. However, when this shock reaches the end of the tube, it hits a fixed boundary and reflects back upstream. The reflected shock processes the test gas for a second time, and due to the fixed boundary condition of the tube end, stagnates the gas. The stagnation enthalpy and pressure of this gas depend on the temperature, pressure, and composition of the driver gas, the diaphragm rupture pressure, and the initial pressure in the shock tube [59]. The stagnated test gas temporarily acts as a reservoir of hot, high pressure gas, which is then expanded isentropically through a nozzle to the desired condition [58].

Since the RST fully stagnates the test gas prior to expansion to the test section, its performance at high Mach numbers is limited by several factors:

- The facility must structurally contain the full total pressure of the stagnated test gas, severely limiting allowable total pressures, as evidenced by RST facility limitations in Figure 2.1. Development work on the National Aerospace Plane (NASP) in the late 1980's emphasised that impulse wind tunnel facilities would be required for ground testing of hypersonic combustion, which is associated with access to space flight [22]. It was originally thought that RSTs could achieve the necessary performance, and the Rocketdyne Hypersonic Flow Laboratory (RHYFL) RST facility was a direct outcome of the NASP project [22] (although its development was later suspended prior to its completion [60]). However it became clear, in practise, that RSTs could not achieve the required total pressures at the higher Mach numbers [41]. Generally, RSTs are structurally limited to 150-300 MPa total pressure [61],

and nozzle erosion, throat melting, and ablation of the tube, also become performance-limiting factors at high total pressures and enthalpies[61, 59].

- Since all of the energy is added across a shock, both reflected and non-reflected shock tunnels are limited by the total enthalpy that they can simulate [56, 57]. Any technique which relies on a steady expansion from stagnation conditions will be limited by the degree to which O₂ recombination occurs in the test gas [45]. Enthalpy range will also be limited by radiation losses from the stagnation region [62], however this phenomenon does not impact the current study since it is only observed at much higher speeds (i.e. superorbital speeds) than those at which scramjets will be tested.
- RSTs are capable of simulating direct-connect scramjet conditions above Mach 10, but are incapable of simulating free stream conditions above Mach 10, and therefore cannot capture the significant effects of scramjet integration into the flight vehicle.

In Australia, the first scramjet ground testing was performed by Stalker and Morgan (from UQ) in 1981, using the T3 RST facility at ANU in Canberra [63]. In 1987 UQ commissioned its own RST in Brisbane - T4 - which was developed specifically for scramjet testing [63]. The facility has a free-piston driver, a maximum total pressure of approximately 90 MPa, and a test time of approximately 1 ms at a flow enthalpy of 15 MJ/kg (3.5 km/s) [40]. T4 is capable of testing scramjets at up to Mach 10 and 50 kPa dynamic pressure (or at higher Mach numbers for lower density flows). Routine combustion experiments are now performed on complete flow path scramjet models [63]. The core experimental measurements are typically static pressures through the engine, although UQ has also developed expertise at force measurements using multi-component force balances [63].

As can be seen in Figure 2.1, one of the highest performance RST facilities is the HIEST facility in Japan, which has a maximum stagnation pressure of 150 MPa, a maximum enthalpy of 25 MJ/kg, and a test time of approximately 2 ms at this condition [64]. HIEST has been used for scramjet testing at Mach 8 [64]. It is noted, however, that even at its highest performance condition, the total pressure is still far too low for the required target flow conditions of this thesis.

2.1.5 Impulse Facilities - Expansion Tube

The expansion tube varies from an RST in that there is the addition of a second low pressure acceleration tube after the shock tube. The shock tube test gas is

separated from the acceleration tube gas by a thin secondary diaphragm, usually a light film material like Mylar.

As can be seen from the x - t diagram in Figure 3.1, A normal shock wave is generated following rupture of the primary diaphragm. This shock travels along the shock tube until it reaches the secondary diaphragm. The secondary diaphragm ruptures upon impact, whereupon a new shock is generated in the acceleration tube. Behind this new shock, the test gas is processed by an unsteady expansion as it flows into the low pressure acceleration tube. This unsteady expansion is the fundamental mechanism underpinning the expansion tube concept.

Expansion tubes are capable of achieving much higher total pressures and temperatures than other facilities because the test gas is never stagnated. Instead, total enthalpy and total pressure are added to the test gas by the unsteady expansion as the test gas accelerates into the low pressure acceleration tube. A feature of flow through an unsteady expansion is that total pressure and temperature increase in supersonic flow, whereas they drop in subsonic flow. Therefore, if the Mach number of the primary shock is sufficiently high, and the change in velocity is positive, then there will be a large increase in total pressure and temperature. Since the shock wave is no longer the only mechanism used to add energy to the test flow, levels of dissociation and radiative losses in the expanded test gas can be minimised [57, 60, 65, 66].

Since the unsteady expansion process relies on the transfer of energy from the unexpanded upstream test gas to the expanded downstream test gas, only part of the test gas is processed this way, therefore test time is reduced [40]. Developing flow conditions for expansion tubes is also complicated by the fact that there are theoretically limitless ways to achieve a desired flow condition, by varying how the shock and the unsteady expansion add energy to the test flow, and in practise developing stable operating conditions has proven difficult [57].

Minimal dissociation in the test flow is an important characteristic of expansion tubes which makes them desirable for scramjet testing. This compares to RST facilities, where at high enthalpy levels significant dissociated species are formed in the nozzle reservoir which do not fully recombine during the nozzle expansion (dissociated species such as atomic oxygen and nitric oxide may comprise up to 50% of the flow leaving the nozzle exit) [65]. The effect of these dissociated species on combustion is to produce additional heat, increase ignition rate, and possibly to affect mixing [65].

Several studies have compared RST and expansion tube flows to determine the

effect of dissociation products in the RST test flow. Bakos and Morgan [65] found that the presence of dissociated oxygen leads to a rise in combustor exit pressures (a maximum of 11% at Mach 17 [65]). Jachimowski [67] compared scramjet combustion in expansion tube flows and RST flows, both at Mach 17, and found that the presence of dissociated oxygen enhanced combustion, and therefore needed to be taken into account.

Although expansion tubes do not suffer from the severe contaminants and compromised gas compositions that facilities such as arc tunnels and RSTs suffer from (i.e. combustion products in the heated test gas, dissociation products), other flow contaminants exist, such as diaphragm materials, driver gas, and/or anomalous dissociation products [22]. Further, there can still be uncertainties in the test flow condition due to the complexity of the flow processes.

Expansion tubes have traditionally been used to simulate low density flows at high enthalpies, such as planetary entry at up to 13 km/s [57]. Very little work is published on scramjet flow condition development in expansion tubes. In the 1990's the HYPULSE impulse facility was used in expansion tube mode to simulate scramjet freestream flight and combustor entrance flow conditions for flight speeds up to Mach 19 [68]. Bakos et al. reported that total pressures in excess of 1.3 GPa were achieved in these tests, which made use of a Shock Induced Detonation (SID) driver, and they predicted even higher performance with a free-piston driver [68].

UQ's X2 expansion tube has previously been used by McGilvray et al. [69] to conduct a complete nose-to-tail test of a hydrogen-fueled 2D scramjet at Mach 10.1, a velocity of 3,190 m/s, a static pressure of 2.31 kPa, and a maximum enthalpy of 5.3 MJ/kg; this corresponds to an isentropic equilibrium total pressure of 272 MPa (calculated by the author). This flow condition was selected since the same scramjet design had already been tested using the T4 RST. The T4 testing was conducted with a model $2.5\times$ larger, therefore the X2 static pressure was increased by approximately $2.5\times$ in order to preserve the $p\cdot L$ product. The study by McGilvray et al. permitted comparison and validation of the X2 expansion tube test with the established and independent T4 facility [69]. Combustion was achieved for the engine, and the X2 and T4 results agreed within the bounds of experimental uncertainty [69].

Referring to Figure 1.4, it is clear that even with moderate pressure-length scaling, scramjet flight in excess of Mach 10 involves total pressures in the order of gigapascals. Figure 2.1 illustrates that only expansion tubes are currently considered to be capable of producing flow conditions with total pressures above approxi-

mately 300 MPa. This is the primary reason that expansion tubes are the subject of flow condition development for the present study. The McGilvray study [58] demonstrated that scramjet combustion testing was possible in the X2 expansion tube at Mach 10, at a flow condition approaching the performance limit of the T4 RST. The present study revisits the X2 expansion tube facility, but now seeks to develop scramjet flow conditions at order of magnitude higher total pressures.

Chapter 3

Expansion Tube Theory and Operation

3.1 Chapter Overview

This chapter presents a more detailed discussion of expansion tube facilities. Analytical relations are reviewed in order to explain the fundamental physical processes underpinning the expansion tube concept. Important aspects of expansion tube performance are considered, such as the choice of primary driver, tube length with respect to test time, wave processes, boundary layer effects, diaphragm rupture disturbances, and the use of an over-tailored helium secondary driver to both increase performance and to avoid test flow unsteadiness. The discussion concludes with a review of The University of Queensland's X2 and X3 expansion tube experimental facilities.

3.2 Analytical Model of Expansion Tube

3.2.1 Basic Operation

Figure 3.1 shows an idealised schematic of an expansion tube. The example shown has a free-piston driver with an area reduction at the primary diaphragm, which is typical of the expansion tube facilities used at UQ. The following discussion begins with a calorically perfect gas analysis of expansion tube principals. These principals were initially derived by Trimpf [70].

A light, low pressure driver gas initially fills the compression tube volume between the piston and the primary diaphragm. A reservoir filled with high pressure air

s = shock

rs = reflected shock

cs = contact surface

sx = steady expansion

usx = unsteady expansion

$u + a$ = reflected $u + a$ characteristic

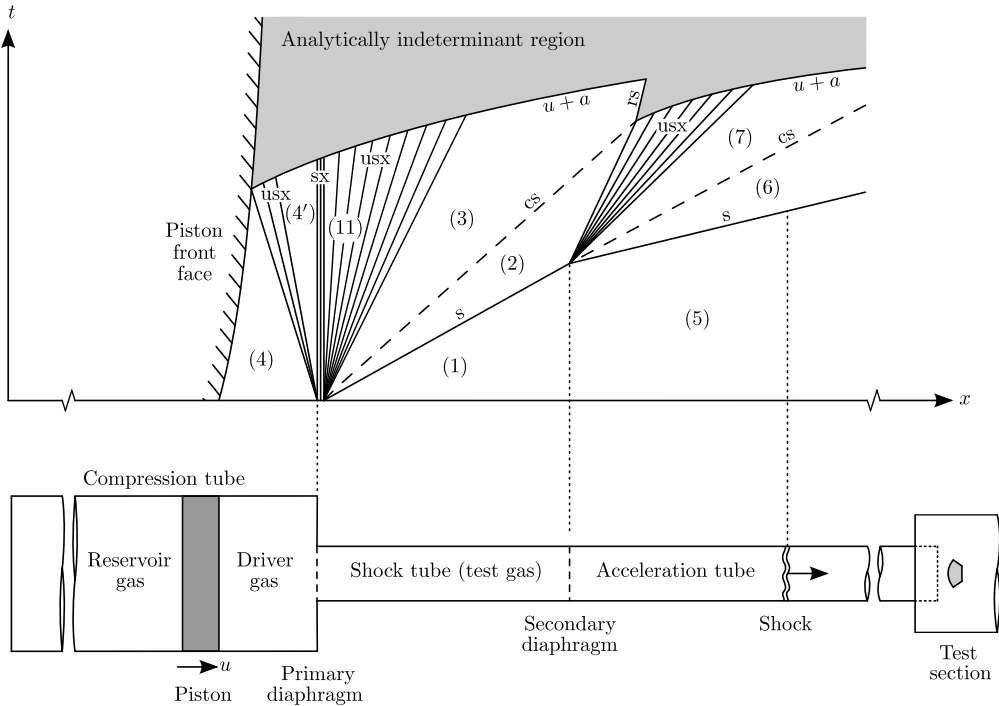


Figure 3.1: Idealised distance-time ($x-t$) schematic of expansion tube flow processes (adapted from [51, 61, 62, 66, 71, 72, 73, 74]).

pushes against the piston, which is initially restrained from moving. Upon piston release, the reservoir gas accelerates the piston along the compression tube, which in turn compresses the driver gas. As the piston approaches the end of the tube, the volumetric compression ratio of the driver gas begins to rise rapidly. The driver gas pressure eventually exceeds the pressure in the reservoir, and the piston begins to decelerate. Towards the end of the piston stroke, the piston has considerable kinetic energy, which is configured to increase the driver gas pressure up to levels far in excess of the initial reservoir gas pressure. The primary diaphragm eventually ruptures once a pre-determined driver gas pressure is attained, whereupon flow processes are initiated in the shock tube.

3.2.2 Flow Properties in the Shock Tube

As can be seen from the $x-t$ diagram in Figure 3.1, upon rupture of the primary diaphragm a normal shock wave is generated in the shock tube. High pressure driver gas flows through the area change into the shock tube. The approximately stagnant driver gas (Region 4) is first processed by an unsteady expansion, which

starts the gas moving towards the area change. For large area changes this $u - a$ wave imparts little velocity to the driver gas, therefore stagnation properties of the expanded driver gas (Region 4', typically with $M_{4'} \approx 0.05 - 0.1$) remain approximately unchanged to those in Region 4 [75].

$$T_4 \approx T_{4'} \approx T_{4',0} \quad (3.1)$$

The area change from the compression tube to the shock tube throttles the flow of driver gas into the shock tube, resulting in sonic flow across the throat. The driver gas in Region 4' is processed by a steady expansion across the area change, producing Region 11 in Figure 3.1. Across this steady expansion, total pressure is unchanged, and normal Mach relations apply:

$$M_{11} = 1.0 \quad (3.2)$$

$$\frac{T_{11,0}}{T_{11}} = 1 + \frac{\gamma_{11} - 1}{2} M_{11}^2 \quad (3.3)$$

Gas stagnation properties across the steady expansion between Regions 4' and 11 are constant:

$$T_{11,0} = T_{4',0} \quad (3.4)$$

Substituting Equations 3.1, 3.2 and 3.4 into Equation 3.3, and assuming perfect gas relations ($\gamma_4 = \gamma_{11}$):

$$T_{11} = \frac{2T_4}{\gamma_4 + 1} \rightarrow a_{11} = \left(\frac{2\gamma_4 R_4 T_4}{\gamma_4 + 1} \right)^{1/2} \quad (3.5)$$

Driver temperature at rupture, T_4 , can be determined from driver initial fill pressure, $T_{4,0}$, and compression ratio at rupture, λ . Noting that the expansions between Regions 4 and 11 are isentropic, and substituting Equation 3.5, static pressure in Region 11 is as follows:

$$p_{11} = p_4 \left(\frac{T_{11}}{T_4} \right)^{\frac{\gamma_4}{\gamma_4 - 1}} = p_4 \left(\frac{2}{\gamma_4 + 1} \right)^{\frac{\gamma_4}{\gamma_4 - 1}} \quad (3.6)$$

After the driver gas exits the throat and enters the much lower pressure shock tube, it undergoes a strong unsteady expansion, resulting in Region 3 flow. Flow through

the unsteady expansion is as follows, assuming once more that $\gamma_3 = \gamma_{11} = \gamma_4$, and noting that for sonic flow $u_{11} = a_{11}$:

$$u_3 + \frac{2a_3}{\gamma_3 - 1} = u_{11} + \frac{2a_{11}}{\gamma_{11} - 1} \rightarrow u_3 = \frac{a_{11}(\gamma_4 + 1) - 2a_3}{\gamma_4 - 1} \quad (3.7)$$

The normal shock which processes gas in Region 1 results in Region 2 flow governed by the following equation:

$$u_2 = \frac{a_1}{\gamma_1} \left(\frac{p_2}{p_1} - 1 \right) \left[\frac{2\gamma_1 / (\gamma_1 + 1)}{p_2/p_1 + (\gamma_1 - 1) / (\gamma_1 + 1)} \right]^{1/2} \quad (3.8)$$

Temperature and pressure across the unsteady expansion is given by isentropic relations, again assuming $\gamma_{11} = \gamma_4$:

$$\frac{p_3}{p_{11}} = \left(\frac{T_3}{T_{11}} \right)^{\frac{\gamma_{11}}{\gamma_{11}-1}} \rightarrow T_3 = T_{11} \left(\frac{p_3}{p_{11}} \right)^{\frac{\gamma_4-1}{\gamma_4}} \quad (3.9)$$

Substituting Equations 3.5 and 3.6 into 3.9:

$$T_3 = T_{11} \left(\frac{p_3}{p_{11}} \right)^{\frac{\gamma_4-1}{\gamma_4}} \quad (3.10)$$

Across the contact surface, pressure is constant. Substituting $p_2 = p_3$, and Equations 3.5 and 3.6, into Equation 3.10, assuming that $\gamma_3 = \gamma_4$, and rearranging in terms of sound speed:

$$a_3 = \sqrt{\gamma_3 R_3 T_3} = \sqrt{\gamma_4 R_4 T_4} \left(\frac{p_2}{p_4} \right)^{\frac{\gamma_4-1}{2\gamma_4}} = a_4 \left(\frac{p_2}{p_4} \right)^{\frac{\gamma_4-1}{2\gamma_4}} \quad (3.11)$$

Flow velocity in Regions 2 and 3 is constant. Substituting Equations 3.5 and 3.11 into Equation 3.7, setting it equal to Equation 3.8, and simplifying:

$$\frac{a_4}{\gamma_4 - 1} \left[(\gamma_4 + 1)^{1/2} - \sqrt{2} (p_2/p_4)^{\frac{\gamma_4-1}{2\gamma_4}} \right] = \frac{a_1}{\gamma_1} \left(\frac{p_2}{p_1} - 1 \right) \left[\frac{\gamma_1 / (\gamma_1 + 1)}{p_2/p_1 + (\gamma_1 - 1) / (\gamma_1 + 1)} \right]^{1/2} \quad (3.12)$$

The only unknown in Equation 3.12 is the shock processed test gas pressure, p_2 . A numerical solution of Equation 3.12 will yield p_2 , whereupon the remaining flow properties can be calculated. T_3 is given by Equation 3.9; u_2 is given by Equation 3.8; pressure and velocity across the driver/test gas interface are constant, hence

$p_2 = p_3$ and $u_3 = u_2$; test gas shock Mach number, $M_{s,1}$, and shock processed test gas temperature, T_2 , are given by Equations 3.13 and 3.14 respectively:

$$M_{s,1} = \sqrt{\frac{\gamma_1 + 1}{2\gamma_1} \left(\frac{p_2}{p_1} - 1 \right) + 1} \quad (3.13)$$

$$T_2 = T_1 \left(\frac{p_2}{p_1} \right) \left[\frac{\frac{\gamma_1 + 1}{\gamma_1 - 1} + \frac{p_2}{p_1}}{1 + \frac{\gamma_1 + 1}{\gamma_1 - 1} \frac{p_2}{p_1}} \right] \quad (3.14)$$

3.2.3 Flow Properties in the Acceleration Tube

In the present analysis it is assumed that when the normal shock in the shock tube reaches the secondary diaphragm, the diaphragm ruptures instantaneously. Further, the diaphragm is assumed to be massless. Following diaphragm rupture, a new shock propagates down the acceleration tube. The high pressure shock-processed test gas encounters the low pressure acceleration tube fill gas, whereupon it undergoes an unsteady expansion. Flow properties across the unsteady expansion are as follows:

$$u_2 + \frac{2a_2}{\gamma_2 - 1} = u_7 + \frac{2a_7}{\gamma_7 - 1} \rightarrow u_7 = u_2 + \frac{2a_2}{\gamma_2 - 1} - \frac{2\sqrt{\gamma_7 R_7}}{\gamma_7 - 1} \sqrt{T_7} \quad (3.15)$$

The normal shock processes the acceleration gas in Region 5, inducing mass motion of velocity u_6 :

$$u_6 = \frac{a_5}{\gamma_5} \left(\frac{p_6}{p_5} - 1 \right) \left[\frac{2\gamma_5 / (\gamma_5 + 1)}{p_6/p_5 + (\gamma_5 - 1) / (\gamma_5 + 1)} \right]^{1/2} \quad (3.16)$$

Noting that the unsteady expansion is isentropic and that pressure is constant across the contact surface (i.e. $p_7 = p_6$):

$$\frac{p_7}{p_2} = \left(\frac{T_7}{T_2} \right)^{\frac{\gamma_2}{\gamma_2 - 1}} \rightarrow T_7 = T_2 \left(\frac{p_6}{p_2} \right)^{\frac{\gamma_2 - 1}{\gamma_2}} \quad (3.17)$$

Across the contact surface velocity is constant, i.e. $u_6 = u_7$. Equating 3.15 and 3.16, assuming ideal gases (i.e. $\gamma_7 = \gamma_2 = \gamma_1$), substituting Equation 3.17, and simplifying:

$$\frac{a_5}{\gamma_5} \left(\frac{p_6}{p_5} - 1 \right) \left[\frac{2\gamma_5 / (\gamma_5 + 1)}{p_6/p_5 + (\gamma_5 - 1) / (\gamma_5 + 1)} \right]^{\frac{1}{2}} = u_2 + \frac{2 \left[a_2 - \sqrt{\gamma_1 R_1 T_2} (p_6/p_2)^{\frac{\gamma_1 - 1}{2\gamma_1}} \right]}{\gamma_1 - 1} \quad (3.18)$$

Numerical solution of Equation 3.18 will yield p_6 . Flow properties in the expanded test gas are then given by Equations 3.17 and 3.16 previously, and Equations 3.19 and 3.20 below:

$$M_{s,5} = \sqrt{\frac{\gamma_5 + 1}{2\gamma_5} \left(\frac{p_6}{p_5} - 1 \right) + 1} \quad (3.19)$$

$$T_6 = T_5 \left(\frac{p_6}{p_5} \right) \left[\frac{\frac{\gamma_5 + 1}{\gamma_5 - 1} + \frac{p_6}{p_5}}{1 + \frac{\gamma_5 + 1}{\gamma_5 - 1} \frac{p_6}{p_5}} \right] \quad (3.20)$$

3.3 Unsteady Expansion Process

Trimpi [70] compares the velocity and total enthalpy relations for steady and unsteady expansions:

Steady expansion:

$$du = - \left(\frac{dh}{u} \right)_s \quad (3.21)$$

$$dH = 0 \quad (3.22)$$

Unsteady expansion:

$$du = - \left(\frac{dh}{a} \right)_s \quad (3.23)$$

$$dH = - (M - 1) dh \quad (3.24)$$

Considering the steady expansion equations, Equations 3.21 and 3.22, two points are noted. Firstly, the velocity increment, du , due to a given reduction in static enthalpy, dh , is proportional to the current velocity, u . As velocity increases, the total velocity increment as a function of static enthalpy reduction itself reduces. Equation 3.22 also indicates that there is no change in total enthalpy through the steady expansion.

Considering the unsteady expansion equation for velocity, Equation 3.23, it can be seen that for a given static enthalpy reduction, dh , the unsteady expansion produces a velocity increase proportional to the speed of sound, a , which corresponds to a significantly greater velocity increase than the steady expansion. The total enthalpy equation, Equation 3.24, indicates that the unsteady expansion results in a total enthalpy increase proportional to the Mach number. Therefore, the higher the Mach number, the greater the enthalpy multiplication. This is the fundamental relation which differentiates expansion tubes from other impulse facilities.

3.4 Primary Driver

Equation 3.25 from [55] can be used to calculate shock strength in a basic shock tube assuming ideal gas behaviour. A basic shock tube is comprised of two equal diameter tubes initially separated by a diaphragm. p_4/p_1 is the initial driver/test gas pressure ratio across the diaphragm prior to rupture; p_2/p_1 is the pressure ratio across the normal shock which propagates into the shock tube following diaphragm rupture, and is related to the Mach number of the shock by Equation 3.26; a_1/a_4 is the ratio between test and driver gas sound speeds, and is dependant on the fill gas compositions and temperatures.

It can be seen from Equation 3.25 that the essential performance parameters governing shock strength are the primary diaphragm pressure ratio at rupture (p_4/p_1), and the sound speed ratio (a_1/a_4). The latter parameter is critical since in order to achieve a specific shock speed, increasing the driver gas speed of sound results in a correspondingly enormous reduction in the required primary diaphragm pressure ratio. This is illustrated in Figure 3.2, which relates diaphragm pressure ratio to shock tube Mach number for different initial driver gas temperatures. The example shown is for air test gas initially at 300K, and helium driver gas at varying initial fill temperatures. It can be seen that raising the temperature of the helium driver gas can reduce the required diaphragm pressure ratio by orders of magnitude.

$$\frac{p_4}{p_1} = \frac{p_2}{p_1} \left[1 - \frac{(\gamma_4 - 1)(a_1/a_4)(p_2/p_1 - 1)}{\sqrt{2\gamma_1 [2\gamma_1 + (\gamma_1 + 1)(p_2/p_1 - 1)]}} \right]^{\frac{-2\gamma_4}{\gamma_4 - 1}} \quad (3.25)$$

$$M_{s,1} = \sqrt{\frac{\gamma_1 + 1}{2\gamma_1} \left(\frac{p_2}{p_1} - 1 \right) + 1} \quad (3.26)$$

The simplified ideal gas analysis shown in Figure 3.2 clearly indicates that there

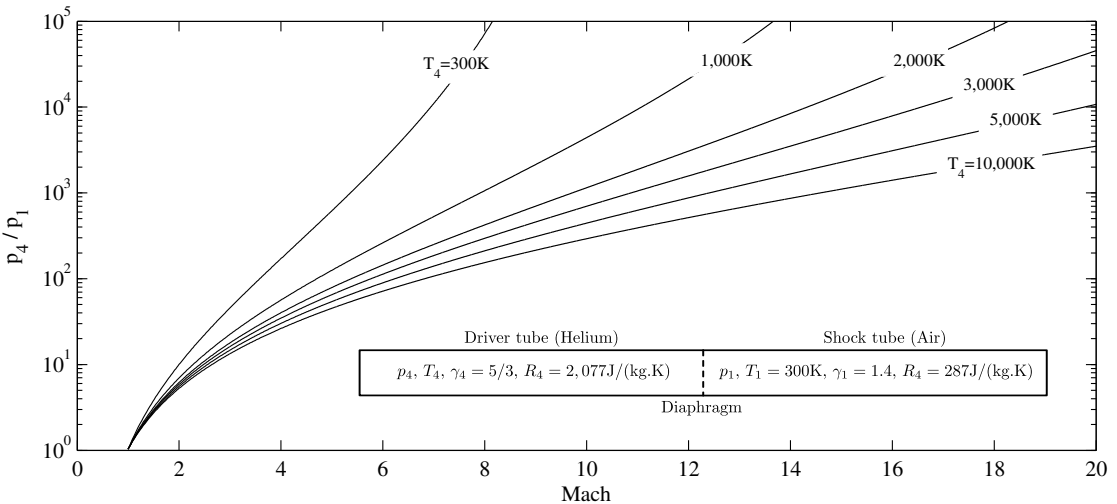


Figure 3.2: Required initial driver/test gas pressure ratio vs. test gas shock Mach number for ideal helium driver/air test gas constant area shock tube. Each curve represents a different initial driver gas temperature (and hence sound speed ratio, a_1/a_4).

is a significant performance advantage by increasing driver gas sound speed at diaphragm rupture. There are several ways to increase the driver gas speed of sound:

1. Using lighter driver gases with higher sound speeds [61]. Hydrogen would be an ideal driver gas except that it is dangerous and therefore expensive to use [66]. Helium is also effective, especially when heated, and is therefore commonly used.
2. Electrical heating of the driver gas to increase its sound speed. As indicated in Section 2.1.2, heating via this method can have impractical power requirements.
3. Combustion heating of the driver gas to increase its sound speed. Morgan [56] indicates that the high molecular weight of combustion products in a detonation driver make them disadvantageous for very high enthalpy flows.
4. Compressively heating a light driver gas using a free-piston driver. This is considered the key to achieving the full performance of a driver, however its cost can typically exceed the combined costs of all other components in an impulse facility [61]. The operation of the piston needs to be tuned in order to achieve relatively constant driver gas conditions [61], and also to prevent damage to the piston/buffer. By maintaining sufficient piston speed after diaphragm rupture, it is possible to maintain reasonably constant pressure to allow for sufficient test time [76]; for a given compression ratio, increasing

the length of the driver also directly increases the volume of compressively heated driver gas available, thereby increasing potential test times.

5. A comparably high sound speed can be achieved without a free-piston driver, however the solution is expensive and complicated. An example is the Large Energy National Shock Tunnel Facility (LENS), which consists of two reflected shock tunnels; LENS I, which uses a heated fixed volume driver, and LENS II, which uses a non-heated fixed volume driver and may also be operated in expansion tube mode [77]. Both facilities can use hydrogen for the driver gas [77]. Considering the LENS I facility, the driver gas is heated to 750°F and can be compressed up to 30,000 psi [78]; using a hydrogen driver gas at these conditions achieves a high sound speed without the need for free-piston compressive heating, and the large fixed volume driver ensures that useful driver gas is supplied for a relatively long duration. Aspects of such a system which drive up its cost include the heated driver and its large power requirement, structural requirements to contain the large volume of compressed driver gas, and the additional operational safety considerations raised by using hydrogen gas for this application.

It is noted that whilst increasing the sound speed of the driver gas increases the strength of the generated shock, this driver performance comes at a cost. Increased sound speed of the driver gas results in a faster expansion of the available gas volume, therefore the duration of time for which the driver gas can drive flow processes downstream is correspondingly decreased.

3.5 Area Change at Primary Driver

An area change at the primary diaphragm has a couple of advantages. Firstly, if all other initial conditions are equal, a stronger shock will be produced at the primary diaphragm [76, 79]. The area change allows the driver gas to be accelerated by a steady expansion in the subsonic region, thus conserving total pressure. The unsteady expansion is constrained to Mach = 1 at the throat of the area change, therefore delivering the maximum theoretical total pressure. Secondly, when coupled with a moving piston, the area change permits relatively steady delivery of gas through the throat, at manageable piston velocities, and with relatively small driver volumes [62]. To achieve the same test time without an appropriate area change would require a facility several times longer [74, 76].

However, the use of an area change drives up the cost of the impulse facility significantly [61], especially when a single free-piston driver is employed [76]. The design cost of a primary diaphragm station with an area change is high since it requires a large amount of high quality steel, forged and machined to shape, to cope with the large stresses at the section change [76]. Finally, flow through the area change also introduces radial waves into the driver gas, which can potentially be transmitted into the test gas and act as an additional source of noise in the test flow.

3.6 Secondary Driver

The shock-heated secondary driver was originally proposed by Henshall [80] and evaluated experimentally by Stalker and Plumb [81]. Morgan and Stalker [62] first utilised a secondary driver with an expansion tube in order to achieve super-orbital flows. The secondary driver is an additional section of tube which is located between the primary driver and the shock tube. It is typically filled with helium and is run in the over-tailored mode. Referring to Figure 3.3, the tube is over-tailored when the shock processed gas in Region $sd2$ has a higher sound speed than the expanded driver gas in Region $sd3$ (i.e. $a_{sd2} > a_{sd3}$). Since pressure and velocity are equal across the contact surface, and sound speed is increased, the higher sound speed in Region $sd2$ results in a stronger shock propagating into the test gas [62].

This shock-strengthening mechanism can be explained in more qualitative terms. Considering a 100% helium primary driver coupled to a 100% helium secondary driver, the static pressure of the shock-processed secondary driver gas (region $sd2$) is theoretically equal to the static pressure of the expanded driver gas (region $sd3$). In order to achieve a reasonable sound speed increase from region $sd3$ to $sd2$, it may be necessary to expand the primary driver gas to a substantially lower static pressure than would otherwise be the case if it were driving a shock directly into the test gas. Despite the lower static pressure of the region $sd2$ gas, a stronger shock may be achieved in the test gas because the higher sound speed permits a more rapid transfer of energy from the secondary driver gas to the test gas. However, this higher shock strength is achieved at a cost; the duration of the flow processes which this flow mechanism can drive is correspondingly reduced. This is analogous to a 100% helium primary driver, which for the same amount of piston compressive work, and the same compression ratio and rupture pressure, can drive a much stronger shock than a 100% argon primary driver, but only for a much

shorter duration since the helium driver gas expands more rapidly.

As will be seen in Section 3.9, Morgan [57] also noted that operation in the over-tailored mode provides the acoustic buffer effect described by Paull and Stalker [72] which can improve test flow quality [56]. The secondary driver has four disadvantages which need to be weighed against its benefits before it is used:

1. The additional tube requires the addition of another thin Mylar (or similar) diaphragm to the tube, which complicates the operation of the facility, interferes with flow processes, and adds contaminants and debris to the flow [56].
2. For a given total tube length, the secondary driver reduces the length of the remaining tubes, and consequently also the available test time [56].
3. Application of this driver configuration to the higher density, lower speed scramjet flows (as compared to the super-orbital flows considered by [62]) may allow further time for upstream waves to interfere with flow development.
4. Running a secondary driver in over-tailored mode reduces the maximum duration of downstream flow processes which can be driven as compared to the primary driver alone, even if the facility is correspondingly lengthened to incorporate the secondary driver.

A parameter referred to as the ‘driver equivalent Mach number’ has been proposed by Morgan [56] to measure the performance advantage of the secondary driver. This parameter is calculated by dividing the flow speed behind the secondary shock by the primary driver sound speed. The secondary driver is seen to offer performance benefits when the driver equivalent Mach number exceeds 2, while 4 is treated as a practical upper limit due to viscosity and facility limitations [56].

3.7 Flow Properties in the Secondary Driver

High total pressure scramjet flow conditions typically require the initial fill pressure of the air test gas to be relatively high. Referring to Figure 3.3, when the normal shock in the secondary driver arrives at and ruptures the secondary diaphragm, the shock processed secondary driver gas may be processed by a reflected shock instead of an unsteady expansion. This is because the density in the test gas is sufficient to require this additional shock processing to raise the static pressure

s = shock
 rs = reflected shock
 cs = contact surface
 sx = steady expansion
 usx = unsteady expansion
 $u + a$ = reflected $u + a$ characteristic

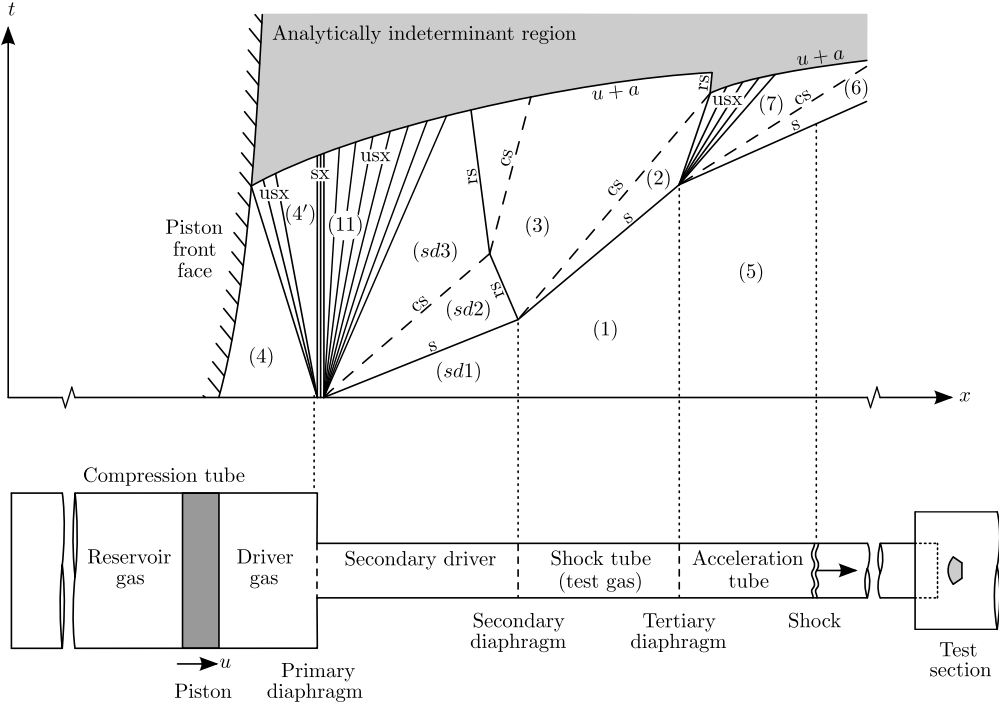


Figure 3.3: Idealised distance-time (x - t) schematic of expansion tube flow processes with secondary driver (adapted from [51, 61, 62, 66, 71, 72, 73, 74]).

of the secondary driver gas (Region 7 in Figure 3.3) to the same pressure as the shock processed test gas (Region 6 in Figure 3.3).

In order to determine whether an unsteady expansion or reflected shock arises at the secondary diaphragm, it is necessary to consider both cases and then select the appropriate result. Figure 3.4 shows the two different cases.

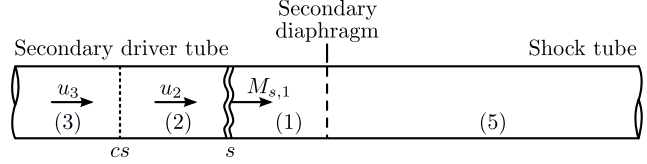
3.7.1 Unsteady Expansion at Secondary Diaphragm

The methodology to calculate flow conditions for the unsteady expansion case was presented in Section 3.2.3.

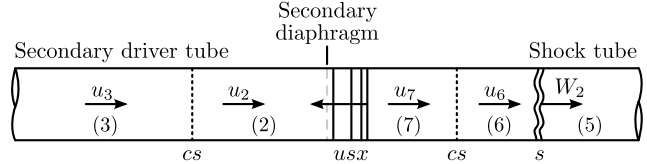
3.7.2 Reflected Normal Shock at Secondary Diaphragm

It is assumed that a reflected shock arises at the secondary diaphragm. Although the shock may travel from left to right in the laboratory reference system, in the shock steady coordinate system it travels from right to left into the Region 2 flow, as shown in Figure 3.4. Let W be the velocity of the gas *ahead* of the shock wave, and u_p be the velocity of the induced mass flow *behind* the shock wave, both

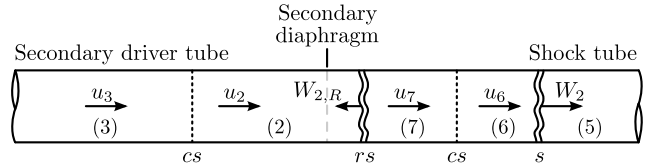
(a) Prior to shock arrival at secondary diaphragm.



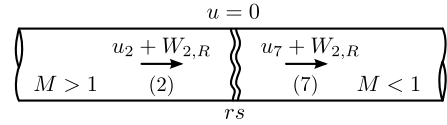
(b) After diaphragm rupture; $u_7 > u_2$.



(c) After diaphragm rupture; $u_7 < u_2$.



(d) Reflected shock from (c) in shock steady coordinate system.



s = shock; cs = contact surface; usx = unsteady expansion; rs = reflected shock

Figure 3.4: Reflected shock and unsteady expansion solutions following secondary diaphragm rupture.

relative to the shock wave:

$$W = u_2 - W_{2,R} \rightarrow W_{2,R} = u_2 - W \quad (3.27)$$

$$W - u_p = u_7 - W_{2,R} \rightarrow W_{2,R} = u_7 - W + u_p \quad (3.28)$$

Equating 3.27 and 3.28:

$$u_2 - W = u_7 - W + u_p \rightarrow u_p = u_2 - u_7 \quad (3.29)$$

Mass induced flow velocity is given by:

$$u_p = \frac{a_2}{\gamma_2} \left(\frac{p_7}{p_2} - 1 \right) \left(\frac{\frac{2\gamma_2}{\gamma_2 + 1}}{\frac{p_7}{p_2} + \frac{\gamma_2 - 1}{\gamma_2 + 1}} \right)^{\frac{1}{2}} \quad (3.30)$$

Flow in Region 6 is given by:

$$u_7 = u_6 = \frac{a_5}{\gamma_5} \left(\frac{p_6}{p_5} - 1 \right) \left(\frac{\frac{2\gamma_5}{\gamma_5 + 1}}{\frac{p_6}{p_5} + \frac{\gamma_5 - 1}{\gamma_5 + 1}} \right)^{\frac{1}{2}} \quad (3.31)$$

Noting that $u_6 = u_7$ and $p_6 = p_7$, assuming that $\gamma_2 = \gamma_1$, and substituting Equations 3.30 and 3.31 into 3.29:

$$\frac{a_2}{\gamma_1} \left(\frac{p_6}{p_2} - 1 \right) \left(\frac{\frac{2\gamma_1}{\gamma_1 + 1}}{\frac{p_6}{p_2} + \frac{\gamma_1 - 1}{\gamma_1 + 1}} \right)^{\frac{1}{2}} = u_2 - \frac{a_5}{\gamma_5} \left(\frac{p_6}{p_5} - 1 \right) \left(\frac{\frac{2\gamma_5}{\gamma_5 + 1}}{\frac{p_6}{p_5} + \frac{\gamma_5 - 1}{\gamma_5 + 1}} \right)^{\frac{1}{2}} \quad (3.32)$$

Numerical solution of Equation 3.32 will yield p_6 and therefore p_7 . Equation 3.31 will then provide u_6 and u_7 ; temperatures T_6 and T_7 , and shock Mach numbers $M_{2,r}$ and M_5 , are obtained from the following equations:

$$T_6 = T_5 \left(\frac{p_6}{p_5} \right) \left(\frac{\frac{\gamma_5 + 1}{\gamma_5 - 1} + \frac{p_6}{p_5}}{1 + \frac{\gamma_5 + 1}{\gamma_5 - 1} \frac{p_6}{p_5}} \right) \quad (3.33)$$

$$T_7 = T_2 \left(\frac{p_7}{p_2} \right) \left(\frac{\frac{\gamma_1 + 1}{\gamma_1 - 1} + \frac{p_7}{p_2}}{1 + \frac{\gamma_1 + 1}{\gamma_1 - 1} \frac{p_7}{p_2}} \right) \quad (3.34)$$

$$M_{2,r} = \sqrt{\frac{\gamma_1 + 1}{2\gamma_1} \left(\frac{p_7}{p_5} - 1 \right) + 1} \quad (3.35)$$

$$M_5 = \sqrt{\frac{\gamma_5 + 1}{2\gamma_5} \left(\frac{p_6}{p_5} - 1 \right) + 1} \quad (3.36)$$

3.7.3 Correct Solution at Secondary Diaphragm

Solutions are first performed for both the unsteady expansion and reflected shock cases. The correct solution is the one which correctly satisfies all boundary conditions; i.e. the *incorrect* solution will be either an unsteady expansion which has associated $u_7 < u_2$ (an *expansion* which *slows* the flow), or a reflected shock which has $u_7 > u_2$ (a *reflected shock* which *speeds up* the flow).

3.7.4 Solution Across Tertiary Diaphragm

For an expansion tube with a secondary driver, the acceleration tube will always have a comparatively low pressure, so there will be an unsteady expansion at the tertiary diaphragm. Flow properties in the acceleration tube are therefore calculated in accordance with Section 3.2.3, making appropriate substitutions.

3.8 Test Time and Wave Processes

The available test time is the period between the arrival of the accelerator gas / test gas contact surface, and the arrival of any waves which disrupt the uniform test flow. Referring to either Figure 3.1 or Figure 3.3, there are generally three wave processes which may terminate the test flow, as follows:

1. The downstream edge of the unsteady expansion wave at the tertiary diaphragm. The arrival of this wave signals the end of the nominal test time.
2. An unsteady expansion reflecting off a contact surface as a $(u+a)$ characteristic: referring to Figure 3.3, these waves are produced when the upstream edge of an unsteady expansion (usx) reflects off a density discontinuity [74]. The reflected $(u + a)$ characteristic is a very fast wave, which races downstream. It can potentially overtake other flow features and reach the acceleration tube exit early enough to disrupt the test flow [74]. Given that test time can depend greatly on the location of the contact surfaces, it is therefore important to accurately estimate their progression [72].
3. An unsteady expansion reflecting off the piston head as a $(u + a)$ characteristic: the finite volume of the driver tube can result in pressure in the driver section decaying rapidly after diaphragm rupture, and this decay is also transferred downstream as a reflected $(u + a)$.

Test time will be maximised if the downstream edge of each reflected unsteady expansion arrives at the same time or after the adjacent contact surface arrives, which is dependant on tube length configuration [74]. Optimum tube configuration achieves simultaneous arrival of these wave disturbances [51], since the arrival of either disturbance ends the test time.

In terms of determining the minimum amount of test time that is required for a simulation, transient flow phenomena need to be accounted for. Considering scramjet engines, some important flow processes in the combustor take significant time to become established (i.e. reach steady state), even in steady flow [82]. When transient effects such as nozzle start-up are also accounted for, flow establishment time increases even further.

Jacobs [82] found that establishment time for inviscid flow features, such as shock waves and pressure distribution, were fairly insensitive to inlet flow conditions, however, viscous flow features, such as heat transfer and skin friction, were much more sensitive. Anderson [22] indicates that viscous phenomena are the slowest fluid-dynamic processes to reach steady state, and are best established using heat transfer rate. Fortunately, heat flux can be accurately measured in an impulse facility, and provides the best confirmation of flow establishment and also nozzle starting [22].

Several rules of thumb are indicated regarding flow establishment times:

- $tu/L \geq 2$ for attached turbulent flow [22].
- $tu/L \geq 3$ for attached laminar flow [22].
- $tu/L \geq 4$ for mixing [58].

where t is the test time, u is the steady test gas velocity, and L is the characteristic length of the model, which depends on which part of the model is being assessed. These rules of thumb serve only as a guide to the level of test time required, but as stated above, experimental verification of flow establishment also needs to be produced in order to demonstrate that steady state processes are present. The requirements above are somewhat eased for an expansion tube by virtue of the fact that flow establishment commences with the arrival of the shocked accelerator gas, and therefore is already partially under way upon arrival of the test gas.

3.9 Diaphragm Rupture Disturbances

The complex flow processes that occur in an expansion tube can result in a deterioration in the quality of the test flow. These processes need to be considered, and in several cases actively mitigated against, in order to achieve acceptable test flows. Erdos and Bakos [44] identify the following sources of noise at the test section:

- Primary, secondary, and tertiary diaphragm rupture.
- Stress waves and vibrations.
- Tube and nozzle wall boundary layers.
- Surface roughness, steps, and gaps.

3.9.1 Primary Diaphragm Pre-Scoring

Diaphragm rupture events are normally the largest source of test flow noise. Considering primary diaphragm rupture, pre-scoring of the diaphragm generally ensures no large fragments of diaphragm traverse the tube and hit the model. However, it is considered likely that particulates from the ragged edges of the primary diaphragm are carried down the tube by the driver gas [44]. Over time these particulates can cause surface roughness in the tube which contributes to acoustic disturbances [44].

3.9.2 Test Flow Frequency Focussing

Paull and Stalker [72] conducted a detailed investigation into the cause of the test flow disturbances which had, until that point in time, rendered many expansion tube test flows unusable. Whilst the classical theory had indicated that expansion tubes had the potential to simulate a wide range of flow conditions [70, 72], actual testing found that many flow conditions had unacceptable levels of noise in the test flow [72]. Paull and Stalker first made the distinction between high enthalpy and low enthalpy flow conditions. They noted that only the high enthalpy conditions had acceptable quality test flows, and then investigated the physical processes responsible for this difference [72].

It was determined that the unsteady expansion at the secondary diaphragm, which produces a large drop in the sound speed of the test gas, has the effect of focussing all frequency components of noise present in the test gas into a narrow bandwidth

of frequencies [72]. This is later characterised as strong disturbances in the test flow. It was also shown that this focussing effect only occurs for lateral acoustic waves (radial waves in an axisymmetric facility); the effect does not occur for longitudinal waves.

This frequency focussing effect is fundamental to the unsteady expansion process, and occurs for both high and low enthalpy flow conditions. The reason that high enthalpy flow conditions have acceptable test flow quality is because for these conditions the test gas has very low levels of noise *prior* to the unsteady expansion, so that even after frequency focussing has occurred, noise levels remain acceptably low. In contrast, low enthalpy flows typically already have high levels of noise in the test gas prior to the unsteady expansion, and after frequency focussing these disturbances become unacceptably large. The characteristic difference between these two types of flows was the relative ratio between the sound speeds of the shock processed test gas, a_2 , and the expanded driver gas, a_3 (refer Figure 3.1).

Paull and Stalker determined that operating an expansion tube in a suitably over-tailored configuration (i.e. $a_2 > a_3$ in Figure 3.1) can prevent acoustic disturbances present in the expanded driver gas from penetrating the test gas, the effect being likened to an ‘acoustic buffer’ [72]. The required ratio a_2/a_3 increases where higher frequency noise is to be suppressed, or where the driver gas sound speed is lower. In practise, Paull and Stalker [72] indicate that this acoustic buffer will be effective for $a_2/a_3 > 1.25$. This ratio is also supported by Morgan [57], which was published several years later following greater experience with the concept.

Paull and Stalker concluded that successful expansion tube operation would be limited to high enthalpy conditions (where the shock-processed test gas is very hot and therefore has a high sound speed) unless some means of reducing the noise in the driver gas could be devised. This seems unlikely in a free-piston driven expansion tube; aside from the diaphragm rupture process itself, the expansion of driver gas through the area change is a fundamental source of radial disturbances (see Chapter 9).

However, Morgan [57] noted that this sound speed increase could alternatively be achieved by using a helium secondary driver; refer Section 3.6. The helium secondary driver not only produces a stronger shock in the test gas, it is easily configured to achieve a sound speed increase compared to the expanded driver gas [57]. The shock-processed test gas may therefore have a comparatively slow sound speed (for example, for a high density air scramjet condition), since noise in the expanded driver gas is instead suppressed by the upstream shock-processed helium.

3.9.3 Thin Mylar Diaphragm Rupture

Considering the rupture of the thin Mylar (or similar material) secondary or tertiary diaphragms, the diaphragm rupture has a significant effect on the test flow. In a typical thin Mylar diaphragm rupture event, the diaphragm is instantaneously loaded to many orders of magnitude above its normal ‘static’ rupture pressure (which would be a membrane failure mode). This causes the diaphragm to fail by shearing around its periphery, before it has time to deform and fail from the centre (as it would under static loading). Following diaphragm rupture at the periphery, the predominant movement of the diaphragm mass can then be accurately tracked by an inertial model [62].

Wegener et al. [83] recorded holographic images of a light cellophane diaphragm being ruptured by a shock wave in the X1 expansion tube, finding that the shear stresses around the periphery of the diaphragm indeed caused it to break around its edge before it had time to develop sufficient membrane stress to fail at its centre. Following rupture, the diaphragm flattened out and became planar, and after moving about $\frac{1}{4}$ diameter along the tube, it began to fragment [83]. Beyond fragmentation, it is thought that a diaphragm may either vaporise or burn, with products being drawn into the tube wall boundary layer [44], or else gas may simply pass through gaps in the shattered diaphragm.

The preceding paragraph discusses the fate of the thin Mylar diaphragm. The effect of the diaphragm on the flow itself is to cause a reflected shock after arrival of the incident shock [84]. Experimental studies have found that the reflected shock strength is primarily dependant on diaphragm mass [83, 85, 86], and is not as dependant on actual strength or brittleness of the diaphragm material [85]. Generally the thicker/heavier the diaphragm, the more the flow quality decreases [83].

The reflected shock processes the test gas, and particularly in relation to the test gas, can cause significant oxygen dissociation [84]. The reflected shock is eliminated by the unsteady expansion [84], however, the attenuation of this reflected shock strongly depends on the diaphragm mass and corresponding diaphragm hold time [83]. Figure 3.5 below shows a schematic of the Mylar diaphragm rupture process in an expansion tube. This is the diaphragm separating the test and acceleration gases, and would be either the secondary diaphragm in Figure 3.1, or the tertiary diaphragm in Figure 3.3.

Any dissociation in the shock heated gas due to the reflected shock at the di-

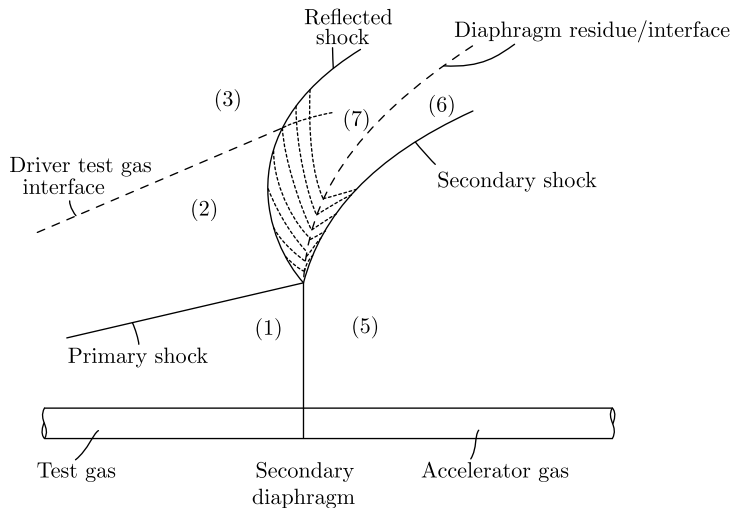


Figure 3.5: Thin mylar diaphragm rupture schematic (adapted from [62]).

aphragm may only be partially eliminated by recombination in the unsteady expansion, since chemical processes in the flow may freeze before equilibrium is reached [83]. Considering the test gas in particular, the test flow in an expansion tube originates as shock heated gas which is initially close to the secondary diaphragm (or tertiary diaphragm where a secondary driver is employed), and non-ideal diaphragm rupture processes can therefore have a significant effect on the final state of much of the test gas [83]. It is noted that this will be less of a problem at lower flow enthalpies, such as those speeds at which scramjets will be tested.

Several approaches are suggested to reduce the influence of the thin Mylar diaphragm rupture on flow quality. Furukawa et al. [85] concluded that reducing the diaphragm mass increases its acceleration, thus alleviating the diaphragm-originated disturbances. Roberts et al. [87] found that pre-deformation of the diaphragm, and minimising its thickness, both reduced its impact on flow properties and reduced the diaphragm holding time. In terms of diaphragm pre-stressing, anecdotal experience at UQ indicates that thin Mylar diaphragm rupture stresses are highly variable. It is therefore difficult to pre-stress the diaphragms close to their rupture pressures prior to operation without having a high proportion of diaphragms prematurely rupturing, which results in aborted experiments.

Self-opening diaphragms have been proposed, which remove the diaphragm just prior to shock arrival [88]. Whilst such devices were reported to prevent reflected shocks being formed, their operation has only been demonstrated for shock waves

up to Mach 3.5, and they are not in common use [88].

Based on the above, it is therefore important to understand and to be able to accurately model the thin Mylar diaphragm rupture process [89]. Inertial diaphragm models (where diaphragm mass is accounted for) have been developed for numerical expansion tube simulations [83, 90]. Such models predict significant differences in test gas composition compared to traditional holding time models (where no diaphragm mass is assumed), indicating the importance of correct diaphragm representation [73]. Diaphragm inertia models have been found to be effective immediately after rupture, however the assumption of uniform shock properties between the diaphragm and the reflected shock then results in a deterioration in accuracy [83].

Finally, the high total pressure flow conditions targeted by this study involve large test gas fill pressures (of the order of several atmospheres) in the shock tube (and also secondary driver). With the acceleration tube at a comparatively low pressure (100's Pa), the result is that the secondary and tertiary diaphragms are required to resist a pressure difference of up to several atmospheres. If a single Mylar diaphragm is used to resist this pressure, it needs to be relatively thick (typically 0.1 mm for X2; thicker in the large diameter X3 facility). There is concern that such thick diaphragms do not fragment and vaporise like normal thin Mylar diaphragms, but instead remain in relatively large pieces as they travel down the tube. This may create disturbances in the test flow, and also cause damage to the model or other objects in the test section.

In order to prevent this behaviour, it may be necessary to develop a multiple diaphragm arrangement, whereby several thinner Mylar diaphragms are used to resist a stepped pressure differential. Such an arrangement would be trialled in parallel with a thick single Mylar diaphragm. The differences in measured test flows between the two arrangements would provide a useful indication of how critical is the diaphragm thickness for this type of high total pressure flow simulation.

3.10 Mirels Effect - Boundary Layer Mass Entrainment

Considering a shock and a contact surface moving down a shock tube, the boundary layer which develops behind the shock acts as an aerodynamic sink, and to a varying extent, entrains mass from the region in-between [74]. First observations

of this phenomenon are attributed to Donaldson and Sullivan [91] and Hollyer [92], although Duff [93] provided the first useful explanation of the phenomenon.

Duff [93] observed in his experiments that the distance between the contact surface and the shock became independent of tube length for $L \gg D$, and that shock speed decreased along the tube in a nonlinear manner, unlike in the ideal scenario where the shock departs from the contact surface at a constant rate along the tube (i.e. per Figures 3.1 or 3.3). Duff did not identify an analytical solution to the problem, but attributed it to flow being captured in the laminar boundary layer, as shown in Figure 3.6.

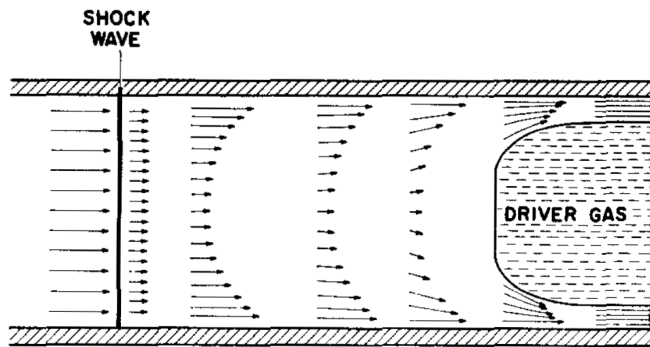


Figure 3.6: Sketch of flow behind a shock wave in a low pressure shock tube, in shock stationary coordinates (flow is moving from right to left in the laboratory frame of reference). Arrow length represents fluid velocity; arrow density represents fluid density. Taken from [93].

Mirels [94] first developed the methodology to describe the laminar boundary layer behind the shock. In [95] he presented a methodology to determine shock attenuation for thin laminar boundary layers, which was correlated by experiment in [96]. He investigated the phenomenon further in [97] (laminar) and [98] (laminar and turbulent). Mirels' main publications regarding boundary layer mass loss are [99] and [100], which look at the effect on shock tube test time of laminar and turbulent boundary layers respectively. These two papers are considered to be the defining work on this phenomenon, thus leading to its characterisation as the Mirels effect.

In the first paper [99], which deals with laminar boundary layers, he characterises the boundary layer profile, imposes mass continuity, and determines a maximum separation distance, l_m , between the shock and the contact surface (which occurs when the excess mass flow in the boundary layer equals the mass flow entering the shock; see Figure 3.7). He then outlines a methodology to determine the separation distance between the shock and the contact surface as a function of

time, thus allowing test time to be calculated [99]. This separation imposes an upper bound on the test time in shock tubes.

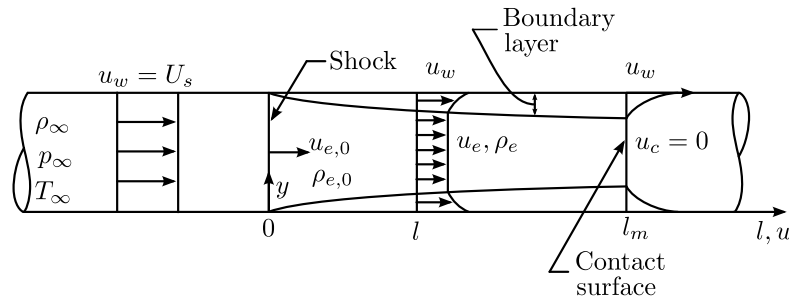


Figure 3.7: Mirels schematic of flow between shock and contact surface in shock-stationary coordinate system (flow is moving from right to left in the laboratory frame of reference). Taken from [99].

In [100] Mirels develops an equivalent methodology for a turbulent boundary layer, although its suitability for various tube configurations is limited to the specific empirical relationships presented in his paper. An improved turbulent boundary layer model was proposed by Petersen and Hanson [101], which can otherwise be used directly with the Mirels methodology. [101] improves the compressible, frictional term, and is suited to high pressure shock tubes, which makes it relevant to this high total pressure investigation. [74] and [102] indicate that turbulent boundary layer theory is applicable if the product of shock tube filling pressure, and shock tube inside diameter, is greater than 0.17 m.kPa.

It was already noted in Section 3.8 that it is important to accurately estimate contact surface progression through the tube in order to quantify locations of reflected ($u + a$) characteristics, therefore capturing the Mirels effect is important for expansion tube performance calculations. Subsequent experimentation and numerical analyses have shown good agreement with Mirels for shock tubes with both laminar and turbulent boundary layers (for example, [56, 86, 103, 104, 105]).

Depending on the specific flow condition, boundary layer effects impose a fundamental limit on the diameter/length ratio for an expansion tube facility, particularly the low pressure acceleration tube. The longer the tube, the greater the diameter it must be in order to limit the boundary layer effects to acceptable levels. This is the primary reason that longer facilities, required for longer test times, must also have larger diameter tubes; the other fundamental reason why larger diameter tubes are used is to permit testing with larger models.

3.11 Steady Expansion Contoured Nozzle

3.11.1 General Characteristics

The purpose of using a contoured nozzle is primarily to increase the test gas core flow size, although the test time may also increase slightly [106, 107]. Hypersonic nozzles are characterised by being purely diverging, with fully hypersonic flow throughout [108].

The difficulty with contoured nozzles is that they are optimised for a single nozzle inlet Mach profile. Whilst the contoured nozzle may produce a uniform exit flow at the design Mach number, it is more susceptible to flow non-uniformities at off-design conditions [108]. Further, these nozzles are susceptible to shock generation at the wall contour, and the high Mach numbers through the nozzle encourage growth of boundary layers, which may already be thick at the acceleration tube exit [108].

A steady expansion nozzle increases the size of model which can be tested, which has practical benefits in terms of model size and instrumentation. However, increasing model size does not assist with meeting pressure length (p - L) scaling targets (as discussed in Section 1.3.2), since the corresponding reduction in flow static pressure (proportional to D^2) is greater than the increase in model size (proportional to D). This results in a reduction of the p - L term through the nozzle, which is proportional to D for $M \gg 1$. However, due to the very high levels of total pressure achievable, the reduction of this p - L term due to nozzle expansion may not matter.

X2 has an operational contoured nozzle which is full capture and shock free [71]. The preliminary design of the nozzle used the method of characteristics, targeting an exit flow Mach number of 10 for an inflow Mach number of 7.3, and a 0 deg flow angle, assuming inviscid and irrotational flow [71]. This shape was then further optimised using a Nelder-Mead technique matched with the compressible flow solver SM_3D+ [71]. The nozzle was tested in [71] for three conditions (two air and one Titan atmosphere) and found to produce acceptable results.

Other facilities have incorporated contoured nozzles with expansion tubes. A 4:1 area ratio contoured nozzle was incorporated into HYPULSE for a Mach 14 enthalpy condition, where nozzle inflow was characterised by a thick, turbulent boundary layer, with some transient effects [106]. At this condition, the nozzle established steady flow in 0.3 ms, followed by constant Mach flow for 0.5 ms.

However, due to differences between the actual nozzle inflow conditions and those assumed during its design, and also difficulty in holding machining tolerances on the nozzle internal contour, the HYPULSE nozzle did not deliver uniform core flow [106, 109]. Bakos et. al [106] also suggested that an improved contour may be achieved by machining a mandrel and winding fiberglass around it. Later nozzle design on HYPULSE successfully utilised this fiberglass construction technique for a Mach 15 nozzle [109]. This particular nozzle was also assessed at off-design conditions, with poor results once more indicating the need for specific nozzles for different Mach numbers [109]. In relation to X2, this further suggests that it may be problematic to operate the facility with the current nozzle at the higher of the Mach numbers which this thesis intends to target.

As part of its upgrade, X3 has been modified to incorporate a Mach 10 nozzle manufactured by filament winding of fiberglass around a mandrel [110], as recommended by Bakos et. al [106]. X3's nozzle has been geometrically scaled directly from the X2 nozzle, resulting in a nominal length of 3.0075m [110]. However, the available filament-winding machine is only 2.5m long, therefore the scaled up nozzle has been truncated to 2.5m, with length removed from the expanded exit side [110]. This is expected to have minimal effect on the flow since the affected part of the nozzle would only be trying to expand the large boundary layers (occupying approximately 50% of the overall diameter at this point along the nozzle) [110]. CFD analysis supported this assessment, with negligible impact identified [110]. Several commissioning shots of X3 with the new nozzle were performed in October and November 2011. The nozzle is shown in Figure 3.11.

3.11.2 Estimate of Flow Properties

For idealised supersonic flow in a diverging nozzle, the Mach number depends only on cross-sectional area. Consider a diverging nozzle with inlet and outlet areas, A_i and A_o respectively, and a reference area where the flow is sonic (choked), A^* . Mach numbers at the inlet and outlet, M_i and M_o respectively, are related to A^* as follows:

$$\left(\frac{A_i}{A^*}\right)^2 = \frac{1}{M_i^2} \left[\frac{2}{\gamma + 1} \left(1 + \frac{\gamma - 1}{2} M_i^2 \right) \right]^{\frac{(\gamma+1)}{(\gamma-1)}} \quad (3.37)$$

$$\left(\frac{A_o}{A^*}\right)^2 = \frac{1}{M_o^2} \left[\frac{2}{\gamma + 1} \left(1 + \frac{\gamma - 1}{2} M_o^2 \right) \right]^{\frac{(\gamma+1)}{(\gamma-1)}} \quad (3.38)$$

Solving for A^* in Equations 3.37 and 3.38 and equating both expressions yields the following general relation for the nozzle:

$$\frac{1}{A_i M_i} \left[\frac{2}{\gamma + 1} \left(1 + \frac{\gamma - 1}{2} M_i^2 \right) \right]^{\frac{(\gamma+1)}{2(\gamma-1)}} = \frac{1}{A_o M_o} \left[\frac{2}{\gamma + 1} \left(1 + \frac{\gamma - 1}{2} M_o^2 \right) \right]^{\frac{(\gamma+1)}{2(\gamma-1)}} \quad (3.39)$$

Assuming constant γ through the nozzle, then for any M_i , M_o can be calculated by solving Equation 3.39. This formulation is approximate and will only provide indicative estimates. The flow processes through the contoured nozzle are complex; the startup is unsteady and boundary layer development will have a varying impact on the performance of the nozzle.

3.12 Unsteady vs. Steady Expansion of Test Flow

High total pressure scramjet flow conditions typically involve processing a high density test gas with a strong but relatively slow shock. In order to produce a high Mach number test flow to meet the target flow condition, the flow must be expanded to increase the Mach number. In an expansion tube, part of this expansion is done through the acceleration tube by the unsteady expansion, whilst the remaining expansion may be done through a nozzle by an isentropic steady expansion. These steady and unsteady expansions process the flow differently, with the unsteady expansion increasing total pressure and total enthalpy (in supersonic flow only), whilst the steady expansion theoretically keeps these properties constant.

To illustrate the enthalpy and total pressure multiplication effects of the unsteady expansion, a representative acceleration tube inlet flow was analytically expanded to different Mach numbers through an unsteady expansion, assuming a 0-D perfect gas analysis. The analysis considers the X2 expansion tube with secondary driver installed per Figure 3.3. The unsteady expansion at the tertiary diaphragm processes the shock tube flow in Region 2 from Figure 3.3, resulting in Region 7 flow. The assumed Region 2 flow properties are shown in Table 3.1, and represent theoretical Region 2 flow conditions for a Mach 13 condition calculated for X2 with secondary driver (see Section 4.2). The total pressure and total enthalpy ratios across the unsteady expansion are shown in Figure 3.8 for different final Mach numbers.

Observing Figure 3.8, it can be seen that both ratios equal one for Mach = 1.69, which represents no expansion of the flow. At Mach 15, these ratios increase markedly

Notation	Description	Value
p_2	Static pressure	11.2 MPa
$p_{2,0}$	Total pressure	54.6 MPa
T_2	Static temperature	1,990 K
a_2	Speed of sound	894 m/s
u_2	Flow speed	1,510 m/s
M_2	Flow Mach number	1.69
$H_{0,2}$	Total enthalpy	3.14 MJ/kg

Table 3.1: Representative flow condition (based on X2 Mach 13 condition per Section 4.2; flow properties are for Region 2 in Figure 3.3).

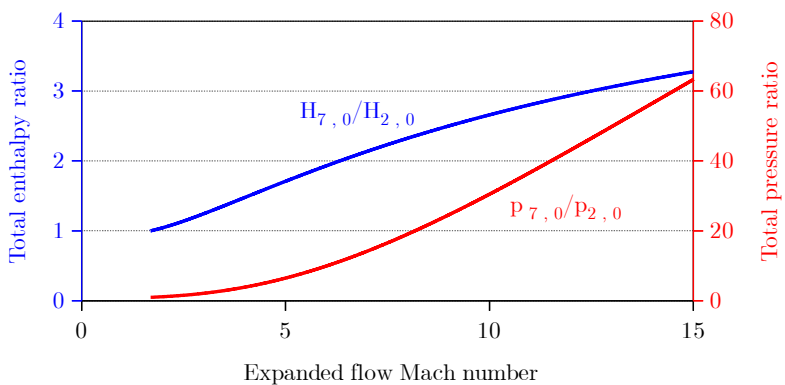


Figure 3.8: Total pressure and total enthalpy ratios across an unsteady expansion for representative acceleration tube inflow conditions.

($p_{07}/p_{02} = 63$; $H_{07}/H_{02} = 3.27$). What should be inferred from this plot is that there is considerable capacity to increase total pressure and total enthalpy across the unsteady expansion, particularly at higher Mach numbers.

In the extreme case, where there is no nozzle, and the final Mach number is obtained solely through the unsteady expansion, then the total pressure of the test flow will be maximised. On the other hand, if a large proportion of the flow expansion occurs in the nozzle, then there will be a significantly lower test flow total pressure. Since this investigation will target flow conditions with very high total pressures, it may be necessary to either avoid the use of a nozzle, or else use a nozzle with a relatively small area ratio, in order to achieve the targeted very high total pressures.

Finally, the total pressure and total enthalpy increases across the unsteady expansion come at the cost of reduced test time and reduced core flow size as compared to expansion through a nozzle. Considering all of these interacting effects, a nozzle may or may not be advantageous.

3.13 UQ Expansion Tube Facilities

3.13.1 X2 Expansion Tube

X2 was commissioned in 1995 [111] and was originally configured with a compound driver in order to act as a prototype for the larger X3 expansion tube. Due to the size of X3, a single stage piston driver was considered at the time to be too expensive, so the compound piston was proposed in order to reduce costs [111, 76, 112]. The two-stage (compound) free-piston driver consists of a light aluminium outer piston, which carries a heavy stainless steel inner piston, and compresses the driver gas in two stages.

The first stage of the compression involves both inner and outer pistons. This stage takes advantage of the fact that for most of the piston cycle there is little compression of the gas, therefore stress levels in this first stage are low, and the structure can be lighter and correspondingly cheaper [76]. The outer piston is light, and most of the reservoir gas energy in this stage is transferred into kinetic energy in the heavier inner piston [74]. When the two stage piston reaches the buffer, the outer piston is stopped, and the inner piston continues the compression to the final burst pressure [76].

The advantage of the compound driver is that it can achieve similar compression ratios to a single piston driver, but with a much shorter compression tube (for an inner/outer piston diameter ratio of 2, compression tube length can be reduced by approximately 75%). Further, the large diameter section of the compression tube can be made of thinner steel, since it does not have to contain the large pressures at the primary diaphragm.

The compound piston driver has three distinct disadvantages as compared to the single piston driver. Firstly, it is a more complicated device to operate [111]. Secondly, without the area change of the single piston, a longer slug of driver gas is required for adequate test time. Thirdly, there is a reduction in the maximum pressures and densities which can be achieved [111, 112]. For these reasons, X2 was subsequently reconfigured with a single stage 35 kg piston, with an area ratio of 9 across the primary diaphragm. The installation of the new driver was completed in April 2004 [111].

X2 currently has a full capture, shock free, contoured nozzle, which was designed for a Mach 7.3 inflow. This nozzle has already been discussed in Section 3.11.

X2 was successfully used for scramjet testing by McGilvray [58]. These tests required more space in the test section to fit and to access the scramjet engine, so the larger dumptank previously used with X3 (see Section 3.13.2) was adapted to X2. A schematic of X2 is shown in Figure 3.9. Facility geometry is described as required throughout this document, but key information is summarised in the following figures: Figure 6.1 details the driver geometry (where $x = 0$ is located at the upstream face of the piston); Figure 9.1 details the full driven tube geometry and transducer locations (where $x = 0$ is

located at the primary diaphragm); Figure 8.2 details the nozzle geometry (where $x = 0$ is located at the nozzle inlet plane).

3.13.2 X3 Expansion Tube

The development of X3 began in 1994, with targeted dimensions of approximately 65m total length, and a bore of 182.6mm [57]. As discussed in Section 3.13.1, to save manufacturing costs, X3 was originally developed with a two-stage free-piston driver, the prototype of which was tested in X2. The two stage piston comprised a 200kg inner piston, 100 kg outer piston, and a primary diaphragm rupture pressure up to 100 MPa [57]. The commissioning tests for X3 were conducted in January 2001, with the first experiments conducted in May 2001 [111]. X3 has since been used successfully for several aerothermodynamic test campaigns, where simulations have typically targeted high enthalpy superorbital speeds [58].

Several difficulties with the original configuration of X3 have, however, led to two major upgrades to the facility, which were completed in 2011. The first upgrade involved the development of a new single-stage free-piston driver. The original dual-stage arrangement proved complicated to operate, and the requirement to decelerate the outer piston with a buffer arrangement set upper limits on the piston velocity, which in turn limited performance in the tube [58]. The use of a single piston also introduces an area change to the primary diaphragm, and thus also provides the corresponding performance benefits this entails (as discussed in Section 3.5). The new configuration of X3 is shown in Figure 3.10.

X3 has also been modified to incorporate a contoured Mach 10 nozzle, manufactured from fiberglass using fiber-winding around a mandrel [110], similar to the technique discussed in [109] and [106]. The development of this nozzle was discussed previously in Section 3.11.

Finally, since the original X3 dumptank was moved to X2, another dumptank was sourced for X3. This replacement dumptank is the dumptank that was originally used on the T3 reflected shock tunnel, previously operated at ANU in Canberra. A new test section has also been manufactured which approximately doubles the volume of the dumptank vacuum, provides optical access to experiments, and permits testing of scramjet model designs. The new nozzle, test section, and dumptank, are shown in Figure 3.11.

At the time of writing a number of shots have been successfully performed with the new driver, nozzle, and test section. Mach 10 test flows of approximately 1 ms duration have already been achieved. The upgraded facility theoretically has class leading performance capabilities and will be in high demand once fully operational.

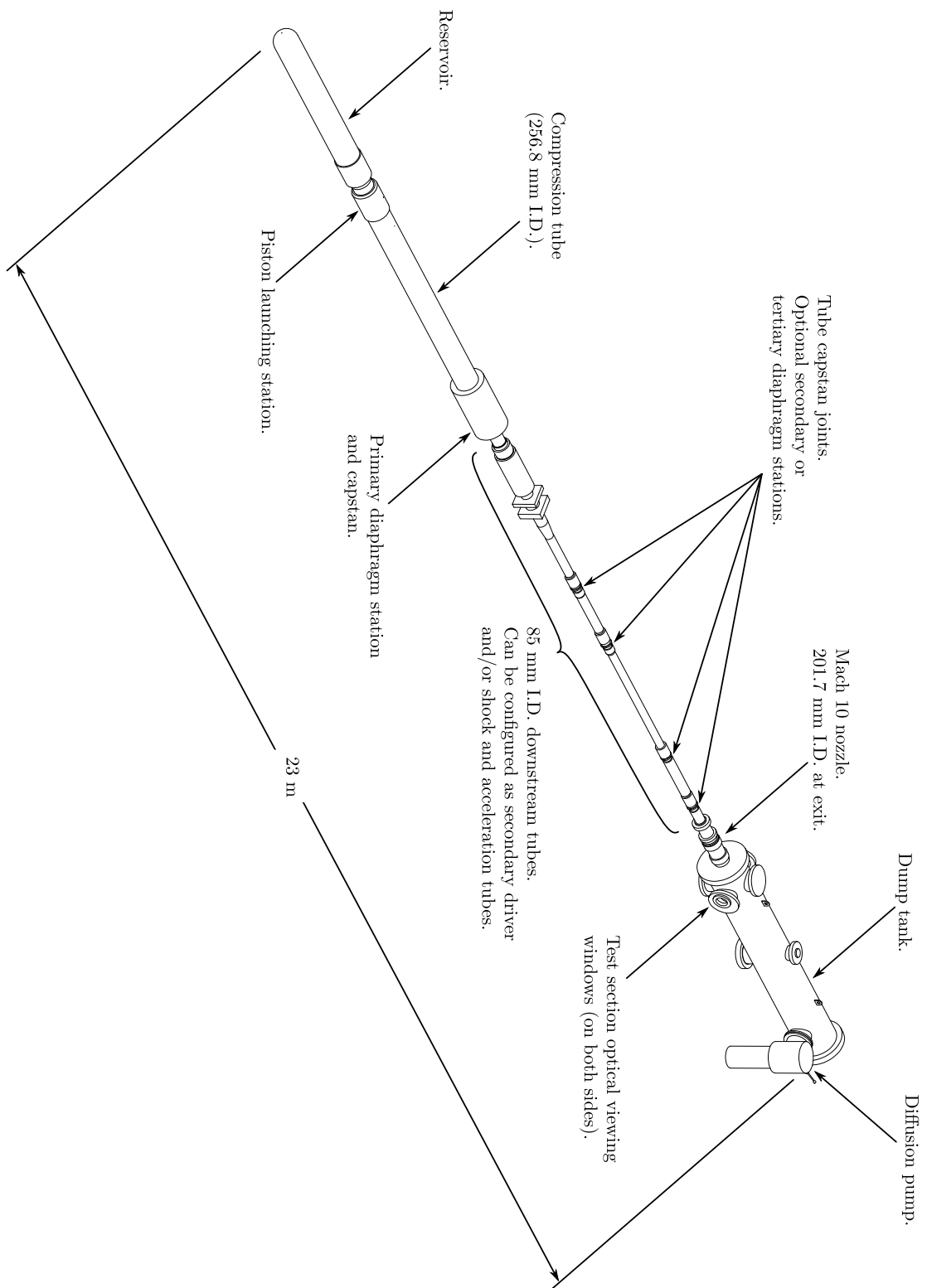


Figure 3.9: Schematic of the X2 expansion tube; shown to scale; with nozzle attached.

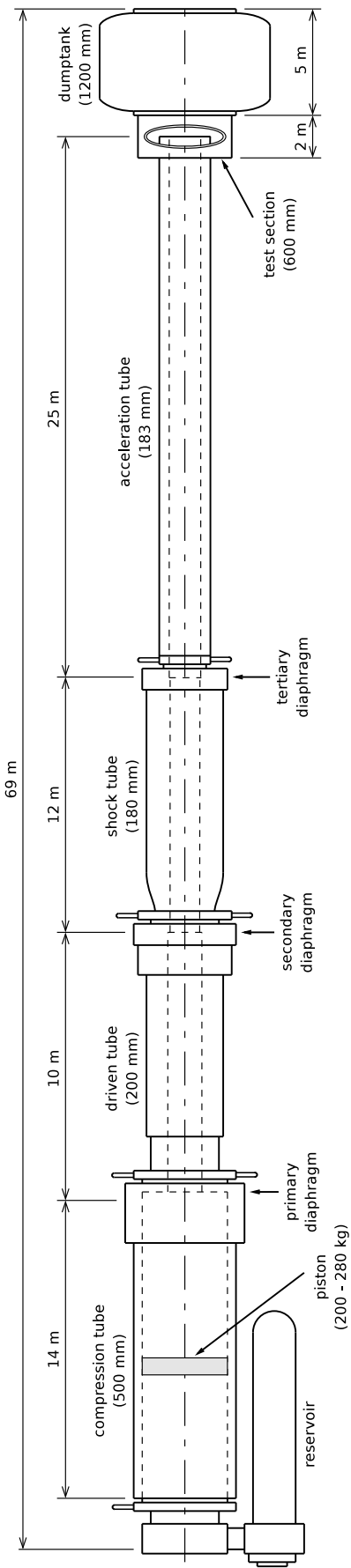


Figure 3.10: Schematic of X3 (upgraded configuration; no nozzle; longitudinal axis compressed to fit detail on page).

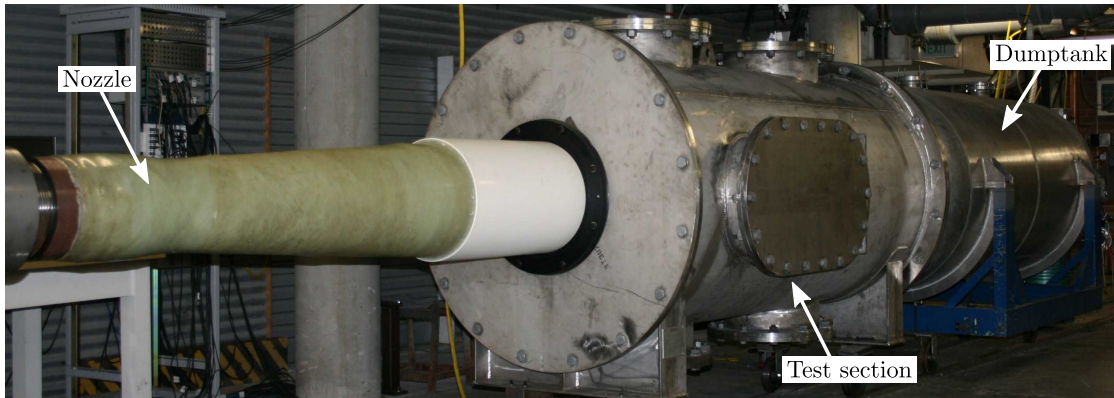


Figure 3.11: X3's new nozzle, test section, and dumptank.

3.14 Computational Fluid Dynamics Analysis

Computational fluid dynamics (CFD) has served several functions during the course of this study. CFD was used to predict expansion tube flows to assist with condition development, and following experimental validation, to reveal full facility test flow characteristics. The UQ Centre for Hypersonics has two CFD codes which were used for this study:

1. The quasi-one-dimensional Lagrangian transient flow code L1d2 [90, 113]. This code was developed primarily to analyse the UQ impulse facilities. The code models longitudinal unsteady wave processes and the full piston dynamics, and includes piston friction, flow chemistry, and pipe-flow viscous effects along the tube walls [113]. Gradual area changes can be handled by the code, however 2-D and 3-D physical processes, such as flow through the launcher, cannot be directly modelled.

To simulate the effect of complex flow paths, L1d2 uses loss regions, which apply a loss factor over a finite length of the tube where an area contraction etc. is present. Representative loss factors can only be determined from experimental data, therefore development of loss factors must occur in conjunction with experimental testing. There is no guarantee that a loss region will model a disturbed flow region with useful accuracy; however, experience indicates that the modelling tool is quite effective once tuned for a given test condition.

2. The 2-D/3-D Navier-Stokes transient compressible flow solver Eilmer3 [114]. This code can model flows that include shocks, expansions, shear layers, boundary layers, and includes several turbulence models [114].

Comparing the two codes, L1d2 can be used to quickly estimate flow processes in an expansion tube, however, as a one-dimensional code it cannot capture detailed flow

phenomena across the diameter of the tube, and therefore loses accuracy in non-uniform flows, for example flows with large boundary layers. Eilmer3 has much more capability in regards to analysing 2-D/3-D flows, however this comes at the cost of significantly greater processing time.

Previous work by Stewart et al. [60] compared the two predecessor codes to L1d2 and Eilmer3, respectively L1d and MB_CNS [115], for simulations of UQ's X2 expansion tube. It found that L1d was around 300 times faster to run, with the two solvers predicting only approximately 2% difference in shock speed and flow velocity, and 10% difference in static pressure. Stewart et al. concluded that L1d was an adequate tool for modelling of expansion tubes, including making general performance predictions, and noted that in larger facilities (in their case RHYFL-X, although the larger X3 facility is analogous) viscous effects and three-dimensional phenomena responsible for discrepancies between the two types of solvers would be less significant.

Scott et al. [111] also used both L1d and MB_CNS to simulate air and Titan conditions in X2, finding good agreement between both of the codes and the experimental data, indicating the value of these two codes as predictive tools for expansion tube analysis.

Chapter 4

Tuned Operation of the X2 Free-Piston Driver

4.1 Chapter Overview

Early on in this study, attempts were made to simulate a high total pressure Mach 13 scramjet flow condition using X2 with its existing driver configuration. Results were unexpected; it was found that shock speeds attenuated significantly down the length of the tube, and the target flow condition was not achieved. Further investigation indicated that the existing free-piston driver configuration used for X2 was not suited for these new scramjet flow conditions since it did not produce high pressure driver gas for sufficient duration. It was determined that the driver needed to be operated in a ‘tuned’ condition, whereby the piston has sufficient velocity at the moment of diaphragm rupture to temporarily compensate for driver gas loss to the driven tube, thus maintaining driver pressure for longer. Tuned operation involves high piston speeds, which presents challenges in terms of accelerating the piston to high speed over a relatively short distance, and then stopping it again without causing damage to the piston or to the facility. It was concluded that a tuned free-piston driver for X2 would require a much lighter piston, of at most approximately 10 kg (compared to the 35 kg piston previously used). This chapter firstly presents the results of the Mach 13 flow condition experiments, and secondly presents the analysis outlining the requirements to achieve tuned operation of the X2 free-piston driver.

4.2 Case Study: X2 Mach 13 Optimised Flow Condition

4.2.1 Introduction

Well established analytical techniques are available which can be used to predict the flow processes in an expansion tube; see Chapter 3. These techniques make various simplifying assumptions about the flow physics, however they enable rapid and straightforward performance predictions to be made for this complex class of facility. At the early stages of this study, an analytical model of X2 was developed in order to predict the test flow properties and test time for an arbitrary set of tunnel configuration parameters. An heuristic optimisation algorithm was then used to calculate the tunnel configuration parameters which would most closely achieve a user-specified set of test flow properties.

As an initial exercise, this optimisation tool was used to calculate the required tunnel parameters to achieve a Mach 13 scramjet flow condition, with target flow properties calculated using the methodology detailed in Section 1.4.1. The standard X2 free-piston driver configuration was used (35 kg piston, 100% helium driver gas, diaphragm rupture pressure of 15.5 MPa, and a compression ratio at rupture of 42). Tunnel fill pressures and tube arrangement were calculated using the code, with the results indicating that the test flow properties could be closely matched.

The calculated Mach 13 flow condition was then performed experimentally using X2, but with unexpected results. It was found that experimentally measured shock speeds were much lower than those predicted by the analytical model. An investigation into reasons for the discrepancy, using the more sophisticated L1d2 1-D CFD code, determined that the free-piston driver was not producing high pressure driver gas for a sufficient duration of time.

Following primary diaphragm rupture an unsteady expansion causes a rapid pressure drop in the driver gas, which is transmitted downstream as a strong $u + a$ wave. This $u + a$ wave may interfere with downstream flow processes before or during the test time. For the Mach 13 case, this wave was arriving at the shock and causing significant shock attenuation prior to the shock arriving at the test section, thus preventing the target flow condition from being achieved.

Considering the high speed flow conditions for which X2 has typically been used (such as planetary entry between 6 and 10 km/s), critical flow processes occur in the test section before the reflected $u + a$ wave from the driver reaches the test section. However, for high total pressure scramjet flow conditions, slow shocks in the dense test gas take more time to traverse the tube; early driver gas pressure loss manifests itself in shock waves which rapidly weaken *before* critical flow processes reach the test section. These flow processes

require driver pressure to be maintained at target levels for a much longer duration.

This section details the process used to calculate the Mach 13 flow condition, and then compares theoretical predictions to experimental results. Results of the L1d2 analysis are presented, and used to explain the reason for the discrepancy between theory and experiment. It is finally demonstrated that these high Mach number, high total pressure scramjet flow conditions require a free-piston driver which supplies high pressure driver gas for a significantly greater duration of time; the technique to achieve this is later detailed in Section 4.3.

The Mach 13 analytical and experimental results discussed in the present section were not used for the final flow condition testing conducted for this thesis. However, it is considered instructive to review this experience with the Mach 13 flow condition as a case study since it was the catalyst to develop a new ‘tuned’ free-piston driver configuration for X2, which has constituted an unanticipated but major component of the research efforts of this thesis.

4.2.2 X2 Perfect Gas Quasi-1D Parametric Optimisation Tool

An analytical model of the X2 expansion tube facility, operating with a secondary driver and Mach 10 nozzle, was developed in MATLAB. A Simulated Annealing optimisation algorithm was used to target desired flow conditions. Mach 13 flow condition properties were calculated using the methodology detailed in Section 1.4.1; the optimiser was then used to calculate the tunnel parameters which would produce this condition. A general overview of the optimisation is now presented. The analytical model was based on relations detailed in Chapter 3. In order to improve the test time estimates, the model also incorporated both Mirels Effect (to more accurately calculate contact surface location; see Section 3.10) and some wave interaction. Figure 4.1 summarises the 0-D analytical model optimisation process. Individual components of Figure 4.1 are then detailed separately.

4.2.2.1 Optimisation variables

Referring to Figure 4.1, there are four optimisation variables:

1. Tube length parameter.
2. Secondary driver fill pressure (100% helium).
3. Shock tube fill pressure (100% air).
4. Acceleration tube fill pressure (100% air).

The latter three variables are self-explanatory. The first variable - the tube length parameter - is a parameter varying between 0 and 1, which defines the tube configuration

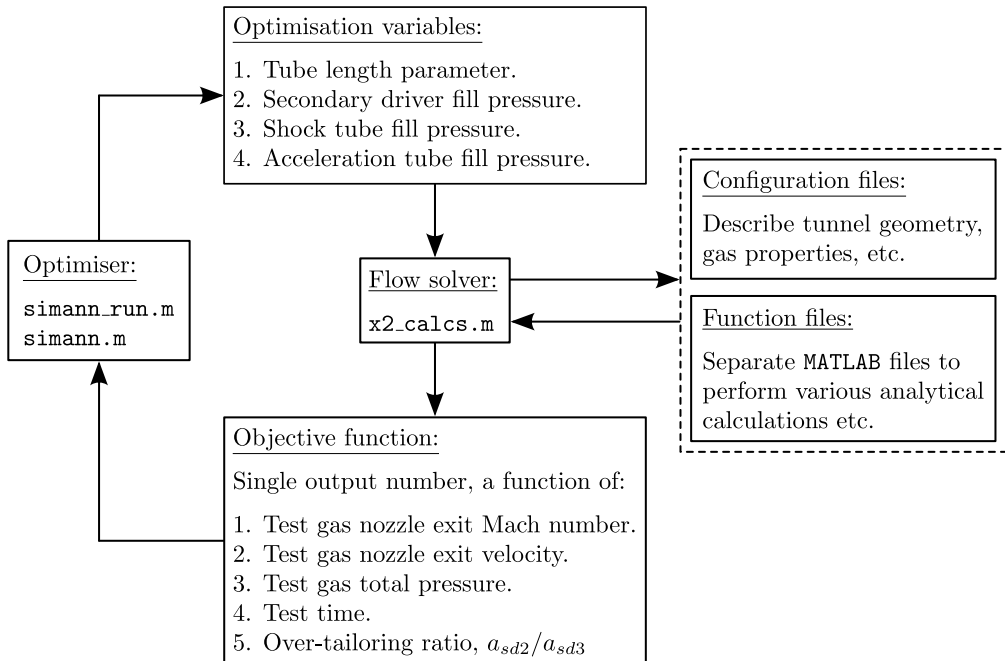


Figure 4.1: 0-D analytical model optimisation process.

for the tunnel. This parameter refers to a data file which contains all possible combinations of three tubes that can be constructed for X2 from the five currently available tube length segments at the UQ X-lab facility (this data file is calculated by a separate code). These combinations are arranged in an ordered array. The row number for the array is normalised by the total number of rows, and the selected configuration is the normalised row number closest to the value of the tube length parameter.

The benefit of this system is that it only identifies feasible tube lengths given the available hardware. The problem with this approach is that the tube length variable is discontinuous (with potentially many values) therefore making it poorly suited to optimisation. However, the optimisation algorithm used - Simulated Annealing - is very robust, and can handle such discontinuities provided that it is configured suitably, and that sufficient solution iterations can be performed.

4.2.2.2 Flow solver

This is a MATLAB function which takes as input the optimisation variables and calculates the facility response using a perfect gas 0-D analysis. It also takes into account Mirels Effect, and some wave interaction. The configuration of the tunnel and gas properties etc. are mostly defined in separate configuration files. The output of the flow solver is a summary of the tube flow properties, and also the calculated objective function value. The code takes of the order ~ 1 s to compute, thereby providing a practical foundation for a global search algorithm. Even a 1-D code such as L1d2 has a computation time

of order ~ 1 hour, therefore a global optimisation requiring of order $\sim 1,000 - 10,000$ iterations would take too long.

4.2.2.3 Objective function

The present problem is essentially a design problem, where the objective is to develop a flow condition which has several different performance measures, each of which needs to be met. Figure 4.1 details five performance measures which were selected for optimisation. Some of these measures require a specific value to be targeted, others require that a parameter be maximised, and so forth. The target values for each of the performance measures is detailed below.

1. Test gas nozzle outlet Mach number; target $M_{7,T} = 13.0$.
2. Test gas nozzle velocity; target $u_{7,T} = 3,952$ m/s.
3. Test gas total pressure; maximise $p_{7,0}$.
4. Test time; maximise t_{tt} .
5. Over-tailoring ratio, $a_{sd2}/a_{sd3} \geq 1.25$.

The objective function, OF , is a single number which was derived from the above variables as follows:

$$OF = (10 + |u_{7,T} - u_7|) \times \left(\frac{1}{p_{7,0}} \right) \times (0.1 + |M_{7,T} - M_7|) \times \left(\frac{1}{t_{tt}} \right) \times K_{buf} \quad (4.1)$$

where $K_{buf} = 1$ for $a_{sd2}/a_{sd3} \geq 1.25$, otherwise $K_{buf} = 1,000$.

Given that the optimisation algorithm seeks purely to minimise the objective function, the construction of Equation 4.1 becomes clear. It can be seen that each of the bracketed expressions reduces when the targeted parameter is approached. Considering velocity and Mach expressions, to avoid each of these two bracketed expressions going to zero, which would focus the optimiser's efforts excessively on these two parameters, error values were included (10 m/s and 0.1 respectively). These values reduce the relative sensitivity of the objective function to these specific parameters.

It can be seen that maximising total pressure and test time reduces the objective function, hence their positions on the denominator. Finally, K_{buf} causes a step increase in the objective function if the requirement $a_{sd2}/a_{sd3} \geq 1.25$ is *not* met, thus moving the optimiser away from such solutions.

It is finally noted that this objective function derivation is far from ideal, and is only a work-around to solve the current problem at hand. Additionally, there are more sophisticated methods to perform Multi-objective Optimisation, which aim to develop

Pareto fronts [116]. These are curves showing a range of optimised solutions based on the different design variables, where a given variable is optimised without disadvantage to the others. However, these methods were considered too complex for the task at hand, and further, are currently incapable of handling many performance variables.

4.2.2.4 Optimiser

The solution space for this problem is complicated because the problem is highly nonlinear and discontinuous. For example, the imposition of $K_{buf} = 1,000$ for $a_{sd2}/a_{sd3} < 1.25$ is a three order of magnitude penalty applied to the objective function whenever the acoustic buffer requirement is not met. Similarly, the tube length parameter is a continuous variable, but it points to discrete tube combinations, therefore while this parameter may itself vary within small bounds, there may be no actual change in the corresponding tube configuration. Moreover, when the tube configuration does change, the result is a discontinuous change to a new set of discrete tube lengths.

A Simulated Annealing optimisation algorithm was selected over iterative improvement schemes since this algorithm effectively samples the full search space without getting stuck at local minima [117]. However, since it only considers a single design point at a time, Simulated Annealing generally requires fewer iterations than other global search algorithms such as genetic algorithms. For the purposes of this study, the success of the optimisation algorithm was measured by whether the solution was convincingly optimal. It is shown below that the results of the optimisation process indicate that the optimisation algorithm works fairly effectively since target flow conditions are approximately achieved. The efficiency of the overall process was not assessed, since overall computation time was not prohibitive in an absolute sense.

4.2.3 Optimised Tunnel Configuration and Predicted Flow Properties

The calculated X2 configuration parameters to achieve the Mach 13 condition are summarised in Table 4.1. Results are for the 100% helium, 35 kg piston mass, free-piston driver. At diaphragm rupture it is assumed that driver pressure and temperature are respectively 15.5 MPa and 2,500 K. This rupture pressure is based on previous experimental physical testing; the temperature is an empirical estimate based on experimental shock speed measurements for previous super-orbital flow condition experiments.

The tube lengths specified in Table 4.1 are combinations of existing tube segments which can potentially be specified by reconfiguring the current X2 expansion tube configuration. However, it was not considered necessary to make these changes to the X2 expansion tube for this short preliminary experimental testing campaign, therefore the tube configuration was left unchanged. Actual tube lengths used are shown in brackets in Table

4.1, where applicable. The use of a shorter shock tube in the eventual configuration resulted in a shorter predicted test time (also shown in brackets in Table 4.1). For the purposes of these experiments this was considered acceptable since the experiments were primarily undertaken in order to confirm the predicted shock speeds as a preliminary check of the methodology.

Symbol	Value	Units	Description
p_{sd1}	150	kPa	Secondary driver fill pressure, 100% helium.
p_1	330	kPa	Shock tube fill pressure, 100% air.
p_5	254	Pa	Acceleration tube fill pressure, 100% air.
L_{sd}	3.424	m	Secondary driver tube length.
L_{st}	2.416	m	Shock tube length ($L_{st} = 1.301$ m actually used).
L_{at}	3.139	m	Acceleration tube length ($L_{at} = 4.254$ m actually used).
M_7	9.33	-	Mach number at nozzle inlet.
u_7	3.890	km/s	Flow velocity at nozzle inlet.
$p_{7,0}$	1,450	MPa	Total pressure at nozzle inlet.
M_{noz}	13.4	-	Mach number at nozzle exit; target $M_{noz,T} = 13.0$.
u_{noz}	3.950	km/s	Flow velocity at nozzle exit; target $u_{noz,T} = 3,952$ m/s.
$p_{noz,0}$	1,450	MPa	Total pressure at nozzle exit.
t_{tt}	0.178	ms	Test time ($t_{tt} = 0.0845$ s for actual tube configuration).
a_{sd2}/a_{sd3}	1.26	-	Acoustic buffer ratio; target > 1.25 .

Table 4.1: Mach 13 calculated flow condition (see [118], Table 7, for flow condition details). All calculations assume perfect and ideal gases and ignore secondary wave processes. The X2 Mach 10 nozzle was used for these calculations and subsequent experiments.

4.2.4 Experimental Results and Comparison with L1d2 CFD Analysis

The Mach 13 flow condition detailed in Table 4.1 was attempted using X2. Experimentally measured shock speeds are used to assess the flow condition in the present case study. Figure 4.2 shows three sets of shock speeds:

1. Experimental shock speeds. Shock speeds are calculated by dividing the distance between two adjacent transducers (from the same tube) by the difference in shock arrival times at each, which assumes constant velocity. Shock speeds are averaged across X2 shots x2s1362, x2s1363, and x2s1364.
2. Required shock speeds. These are the predicted shock speeds for the Mach 13 condition described in Table 4.1, and are based on the 0-D perfect gas analysis.
3. L1d2 shock speed. This is the predicted shock speed as it travels along the length of the facility as calculated using the 1-D Lagrangian CFD code, L1d2. The shock has been tracked as it progresses across the cells of the CFD model; the curve is discontinuous due to the finite CFD model grid resolution and finite solution time

step size, however it provides sufficient detail to identify the key wave processes. The code is discussed in Section 3.14; the results shown are for an equilibrium gas calculation.

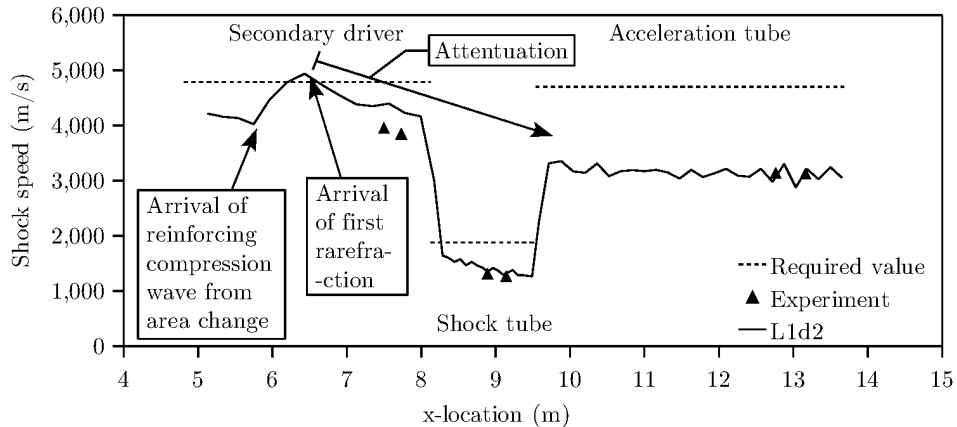


Figure 4.2: Shock speed vs. position for Mach 13 flow condition. Primary diaphragm is located at $x = 4.810$ m. Experimental shock speeds are averaged over three shots, with maximum experimental uncertainty of $\pm 3\%$. Each experimental shock speed is plotted at the x -location mid-point of the two transducers across which it was measured.

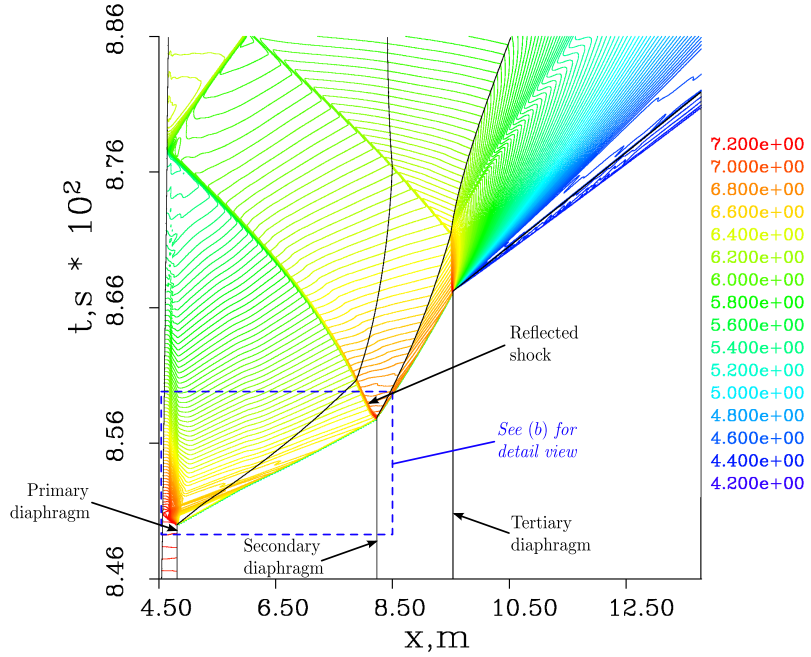
Referring to Figure 4.2, it can be seen that experimental shock speeds do not match required shock speeds. There is significant shock attenuation along the secondary driver and shock tube, and the final shock speeds through the acceleration tube are significantly below the required values. However, the L1d2 predicted shock speed matches the experiment quite closely. Unlike the 0-D perfect gas analytical calculations, L1d2 captures unsteady wave processes and includes piston dynamics, which turn out to be important for the present flow condition.

Detailed analysis with L1d2 indicated that the cause of the shock attenuation is the pressure drop in the driver gas. Figure 4.3 shows x - t diagrams for the Mach 13 condition, calculated using L1d2, for (a) the full-facility, and (b) a detailed view local to the driver. Referring to Figures 4.2 and 4.3(b), two key driver wave processes are observed:

1. The offset of the primary diaphragm from the area change causes the shock to be initially weaker. Figure 6.1 shows the L1d2 X2 analysis geometry. When the expansion arrives at the area change, a reinforcing compression wave propagates downstream and increases the shock speed. This is illustrated in both Figures 4.2 and 4.3(b). Note: L1d2 requires that the area change be modelled gradually, as shown in Figure 6.1. Whilst the area change in the actual facility is abrupt, the effect of the offset should be sufficiently accounted for with the idealised L1d2 model.

(a) x - t diagram, X2 Mach 13 flow condition, 35 kg piston, 100% helium driver.

```
x2_tune_log_p.ge log-p,Pa L1D:space-time-plot
x1 x2 dx 4.50e+00 1.38e+01 2.00e+00 y1 y2 dy 8.46e-02 8.86e-02 1.00e-03
v1 v2 dv 4.20e+00 7.20e+00 2.50e-02
```



(b) x - t diagram, X2 Mach 13 flow condition, detail view from (a).

```
x2_tune_log_p.ge log-p,Pa L1D:space-time-plot
x1 x2 dx 4.50e+00 8.50e+00 1.00e+00 y1 y2 dy 8.49e-02 8.60e-02 2.00e-04
v1 v2 dv 4.20e+00 7.20e+00 1.00e-02
```

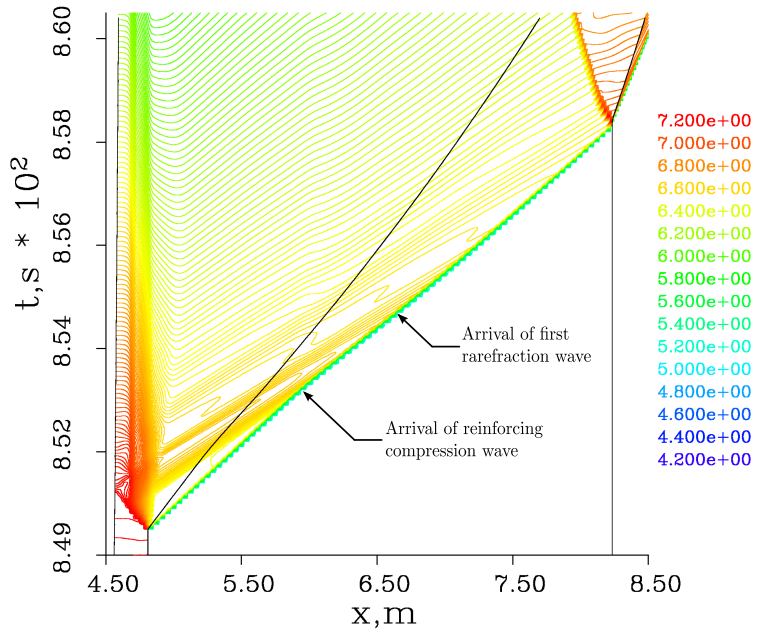


Figure 4.3: L1d2 calculated x - t diagram for Mach 13 flow condition. Contours of log of static pressure are shown.

- Once the unsteady expansion reaches the piston face, a strong rarefaction wave ($u+a$ characteristic) is sent downstream which weakens the shock upon its arrival. This is the first of a continuous stream of rarefaction waves which arise due to the expansion of the driver gas, which rapidly weaken the shock and cause the observed attenuation.

Delayed arrival of the reinforcing compression wave, as described in Item 1, explains why the experimental shock speed is initially slower than the required shock speed. Early arrival of the rarefaction wave, as described in Item 2, explains the subsequent significant shock attenuation.

Note: the L1d2 predicted shock speed in the secondary driver is higher than corresponding experimentally measured shock speeds, and remains marginally higher across the shock tube; this may be due to L1d2 underestimating driver heat loss during the piston compression process, thereby over-estimating driver temperature at rupture. L1d2 uses velocity-dependant pipe flow models to estimate driver heat loss, and for a relatively slow process such as piston compression, will tend to underestimate heat loss. A higher driver gas temperature results in a higher sound speed, which in turn will produce a stronger shock. This discrepancy is not a serious concern since the general shock behaviour is consistent and the discrepancy is not of a large magnitude.

For high total pressure flow conditions such as this Mach 13 condition, slow shocks in the dense test gas take more time to traverse the tube. Figure 4.4 shows the L1d2 calculated shock speed vs. time. This clearly illustrates the significant duration of time required for the shock to traverse the relatively short shock tube (1.301 m long), as compared to the much longer secondary driver (3.424 m long; the faster shock speeds in the secondary driver for the Mach 13 condition are still quite slow in comparison to those generated for superorbital flow conditions).

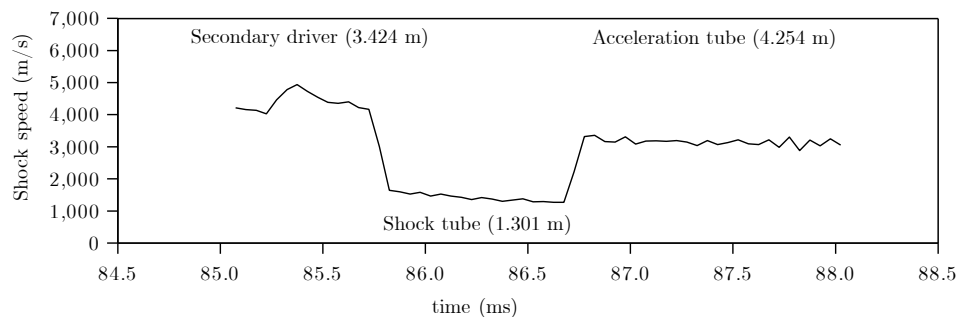


Figure 4.4: L1d2 predicted shock speed vs. time for Mach 13 flow condition. $t = 0$ corresponds to piston launch in the L1d2 model.

Finally, the driver upstream of the compression tube area change was scaled lengthwise in L1d2 by $10\times$ in order to delay reflection of the unsteady expansion from the piston face. Fill pressures and the diaphragm rupture pressure were left unchanged; the piston mass was increased by $10\times$ to ensure similar dynamic behaviour. Whilst this process is not a precisely consistent scaling exercise, it does capture the effect of an increased driver gas volume at diaphragm rupture. Figure 4.5 shows the shock speed vs. position for both scaled and unscaled driver geometries, and demonstrates that a longer driver prevents shock attenuation. The shock speed is much closer to required values; the difference may be explained by viscous effects, non-linear scaling effects, and other secondary wave processes.

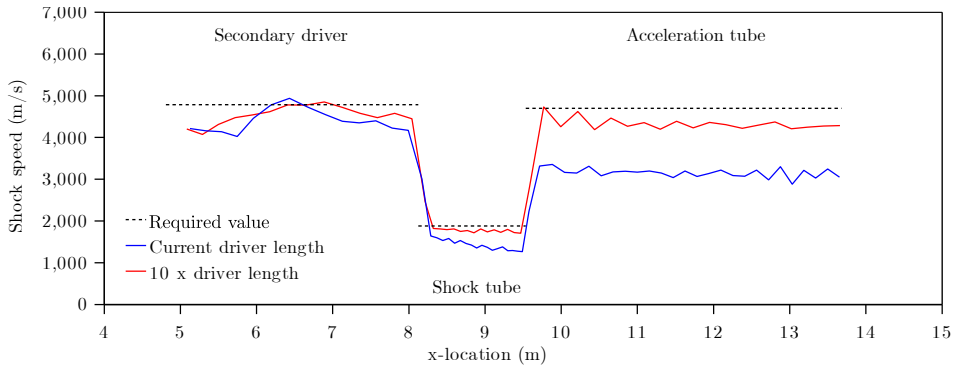


Figure 4.5: L1d2 predicted shock speed vs. position for Mach 13 flow condition. The current driver performance is compared to a driver scaled in length by $10\times$ (all components upstream of the compression tube area change). Fill pressures are unchanged; piston mass is increased by $10\times$.

It is noted that the driver pressure loss which caused the shock attenuation observed in Figure 4.2 has also been present for other flow conditions used with the 35 kg piston and 100% helium driver gas. The transmission of a reflected $u + a$ characteristic does not render a flow condition unusable. The driver performance is acceptable so long as required test flow properties are met, the test flow is sufficiently steady, and the test time is of sufficient duration. Indeed, Mach 10 scramjet testing has previously been performed successfully using X2 with this free-piston driver configuration; see McGilvray [58]. The pressure drop becomes a problem when increasingly higher total pressures are sought, since it manifests itself as a significant reduction in the peak performance of the driver (which is not immediately evident based on the initial driver gas properties at diaphragm rupture). Addressing this performance deficit was therefore essential if X2 was to be used to simulate scramjet flow conditions such as those detailed in Table 1.1.

4.2.5 Requirement for a Tuned Free-Piston Driver

This Mach 13 flow condition case study indicates that for high Mach number, high total pressure scramjet flow conditions, the existing free-piston driver used for X2 does not supply useful driver gas for sufficient duration to permit critical flow processes to reach the test section without interruption. Fortunately, order of magnitude increases in the duration of useful driver gas supply can potentially be achieved by operating a ‘tuned’ free-piston driver. For tuned operation, the driver is configured so that at the moment of diaphragm rupture the piston has a velocity such that the mass of driver gas displaced by the piston front face approximately matches driver gas mass loss to the driven tube [119, 120]. In doing so, driver pressure can be maintained for significantly increased duration. However, tuned operation raises several challenges, including how to accelerate the piston to the required high speeds at the time of diaphragm rupture, and then how to stop it safely before it hits the end of the compression tube. The remainder of this chapter discusses the tuned free-piston driver concept and considers the basic requirements for its implementation in X2.

4.3 Tuned Free-Piston Driver Operation

4.3.1 Piston Over-Drive Parameter, β

Figure 4.6 is an idealised representation of free-piston driver behaviour during the compression process leading to diaphragm rupture. Following diaphragm rupture, hot, high pressure driver gas flows into the driven tube. In order to achieve a high temperature in the driver gas, large compression ratios are typically used, therefore the volume of driver gas at diaphragm rupture is relatively small [119]. If the piston is moving with relatively low velocity at this point, the driver gas slug has approximately constant volume. The unsteady expansion will therefore lead to a rapid pressure drop in the driver gas [119]. The effect of this pressure drop is then transmitted downstream as a reflected $u + a$ characteristic, potentially interfering with downstream flow processes before or during test time.

The concept of tuned piston operation was originally proposed by Stalker in [119] and [120], and it attempts to increase the duration over which driver gas is maintained at a useful pressure. It involves configuring the driver so that diaphragm rupture occurs while the piston still has sufficient velocity to approximately compensate for driver gas loss to the driven tube [119].

The following analysis assumes that gases are ideal and perfect, neglects friction and other losses, and ignores secondary wave processes. A large area change is assumed to exist at the primary diaphragm, resulting in choked (sonic) flow across the throat.

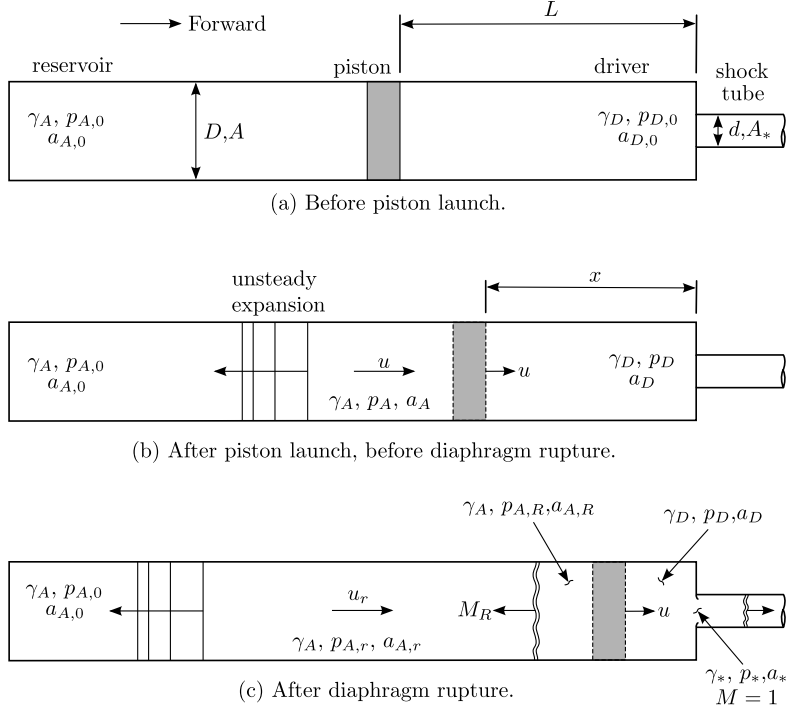


Figure 4.6: Free-piston driver schematic.

Considering mass flow through the driver throat:

$$\rho_* a_* A_* = \frac{\rho_* a_* A_*}{\rho_D a_D A} \rho_D a_D A = \frac{\rho_*}{\rho_D} \sqrt{\frac{T_*}{T_D}} A_* \rho_D a_D \quad (4.2)$$

Assuming driver gas velocity is sufficiently low that total pressure and temperature are approximately equal to stagnation quantities, and applying isentropic relations for flow through a duct:

$$\rho_* a_* A_* = \left(\frac{2}{\gamma_D + 1} \right)^{\frac{\gamma_D + 1}{2(\gamma_D - 1)}} A_* \rho_D a_D \quad (4.3)$$

Following diaphragm rupture, there is a piston speed at which the mass flow of driver gas displaced by the piston matches the mass flow of driver gas to the driven tube. This piston speed is referred to as the reference velocity, U_{ref} :

$$\rho_D U_{ref} A = \rho_* a_* A_* = \left(\frac{2}{\gamma_D + 1} \right)^{\frac{\gamma_D + 1}{2(\gamma_D - 1)}} A_* \rho_D a_D \quad (4.4)$$

Solving for U_{ref} :

$$U_{ref} = \frac{A}{\rho_D} \left(\frac{2}{\gamma_D + 1} \right)^{\frac{\gamma_D + 1}{2(\gamma_D - 1)}} \frac{A_*}{A} \rho_D a_D \quad (4.5)$$

Relating driver gas density, ρ_D in Equation 4.5, to initial driver fill conditions and diaphragm rupture pressure:

$$U_{ref} = \left(\frac{2}{\gamma_D + 1} \right)^{\frac{\gamma_D + 1}{2(\gamma_D - 1)}} \frac{A_*}{A} \sqrt{\gamma_D R_D T_{D,0} \left(\frac{p_{rupt}}{p_{D,0}} \right)^{\frac{\gamma_D - 1}{\gamma_D}}} \quad (4.6)$$

Itoh et al. [121] non-dimensionalised the *actual* piston speed at the moment of diaphragm rupture, u_{rupt} , by the reference speed U_{ref} , to produce the piston over-drive parameter, β :

$$\beta = \frac{u_{rupt}}{U_{ref}} \quad (4.7)$$

Stalker [120] essentially proposed the idea of configuring the driver such that $\beta > 1$, thereby ‘over-driving’ the piston. For $\beta > 1$, the piston will actually momentarily continue to increase the driver pressure following diaphragm rupture, before pressure begins to fall again. The duration of time over which this variation in driver pressure is within acceptable limits (typically considered to be around 10% of the target pressure [122, 120, 119, 121]), can correspond to a significantly extended period of useful supply time. This concept is explained schematically in Figure 4.7.

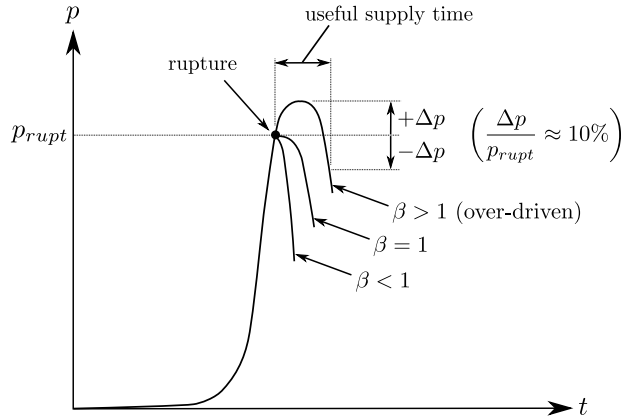


Figure 4.7: Effect of piston over-driving on driver pressure. Time is normalised.

Figure 4.8 schematically shows the operation of (a) a relatively slow free-piston driver (i.e. approximately constant volume after diaphragm rupture), and (b) a tuned free-piston driver, in terms of $x-t$ diagrams. In order to more clearly illustrate the tuned driver concept, the example only shows the wave processes for a simple shock tube, however, the principle also applies to the more complex wave processes which occur in an expansion tube (such as that shown in Figure 3.3).

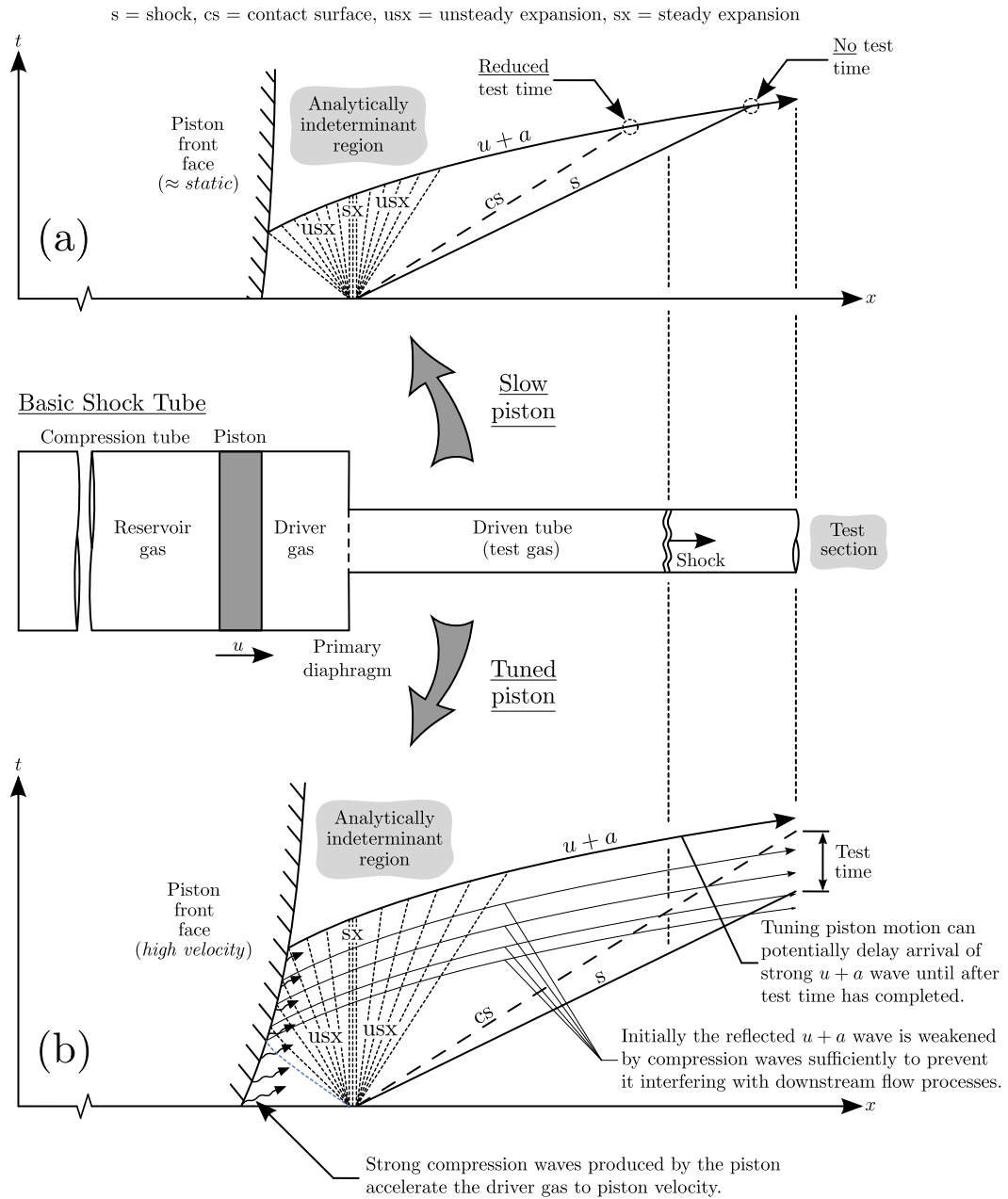


Figure 4.8: $x-t$ diagrams showing wave processes for (a) a relatively slow free-piston driver (i.e. approximately constant volume after diaphragm rupture), and (b) a tuned free-piston driver. The example only shows the wave processes for a simple shock tube, however, the principle also applies to the more complex wave processes which occur in an expansion tube.

If the piston is moving relatively slowly compared to driver flow processes (Figure 4.8a), the driver gas can be considered to have approximately constant volume. In this case the unsteady expansion in the driver gas reflects off the piston front face as a strong $u + a$ wave. This and subsequent rarefaction waves quickly travel downstream, interrupting any flow processes which they encounter. If the $u + a$ wave reaches the contact surface before the test time is complete then the test time will be reduced; if it reaches the normal shock, there will be no useful test flow.

If the piston is moving sufficiently fast (Figure 4.8b), the strong compression waves it produces will weaken the initial unsteady expansion and delay transmission of a strong reflected $u + a$ wave. If the piston has sufficient speed, the strong compression waves it produces will actually initially increase average driver pressure (i.e. it will be ‘over-driven’ per Figure 4.7; these initially strong compression waves will cause a corresponding increase in the initial shock strength, although in the physical machine the process is complicated by secondary wave processes which occur in the driver). It is only once the piston has slowed such that the compression waves do not sufficiently weaken the unsteady expansion, that the reflected $u + a$ waves develop enough strength to significantly interrupt downstream flow processes. Tuned driver operation does not eliminate reflected $u + a$ waves, but instead aims to weaken the waves to the point that their interference with the test flow is kept to an acceptable level.

4.3.2 Piston Soft Landing Condition

Over-driving the piston in accordance with Section 4.3.1 results in the piston having a relatively large velocity (typically 100 – 300 m/s [75, 123]) at the moment when the diaphragm ruptures. For high enthalpy and/or high total pressure flow conditions, the driver sound speed a_D in Equation 4.5 needs to be maximised, and the required piston speed increases accordingly. However, it is also necessary to stop the piston before it collides with the end of the compression tube, which can prove challenging since the distance available to decelerate the piston is relatively small for the high compression ratios required for driver performance. Several authors have attempted to analytically calculate driver configurations which simultaneously achieve over-driving and a soft landing for the piston:

1. Stalker [120] considers a moment in time following diaphragm rupture when the driver gas pressure is at a maximum. Initially assuming that the driver pressure remains constant, the total work done by the piston to push the entire remaining volume of driver gas through the area change is calculated. This work term is then related by a factor k to the kinetic energy of the piston at the moment of peak driver pressure. The equations for driver pressure as a function of time (which is no longer assumed to be constant), *after diaphragm rupture*, are

analytically derived for the case when this work-energy relation is maintained, thus ensuring that there is approximately sufficient driver gas available (subject to the factor k) to slow the piston down before it hits the end of the tube. This methodology makes several simplifying assumptions in its calculation of the work term, such as constant driver and reservoir pressures after rupture (even though both pressure loads are actually highly variable since, among other reasons, the piston is constantly decelerating).

Stalker [120] proposed that the driver should be configured such that at the moment of maximum driver pressure, the kinetic energy of the piston should be less than the amount of work required to expel the remaining high pressure driver gas from the compression tube (Stalker indicates that making the kinetic energy equal to half of the work term will provide a margin of safety against piston impact). The result will be that the piston will momentarily come to rest at some point prior to reaching the end of the tube.

2. Hornung [124] developed a general set of equations describing piston motion both pre- and post- diaphragm rupture. These equations make fewer simplifications about pressure loads on the piston, and are not limited to the single soft-landing case used by Stalker. Later, Hornung and Belanger [123] used a more simplified analysis, which assumed that the driver gas applies a constant acceleration to the piston following diaphragm rupture, and derived the equations which ensure the piston is brought to rest by the time it reaches the end of the tube based on this assumption.
3. Itoh et al. [121] characterised the three different types of piston response which are possible, after diaphragm rupture, as the piston approaches the end of the compression tube. These are shown in Figure 4.9, and are defined as being either ‘piston rebound’, ‘soft landing’, or ‘direct impact’. The assumptions of Stalker [120] and Hornung and Belanger [123] do not account for the highly variable acceleration which the piston may be subject to following diaphragm rupture. Following rupture, the driver gas can vary significantly depending on driver gas sound speed, compression ratio, degree of over-drive, and so forth. Additionally, there remains a large reservoir pressure force acting on the upstream face of the piston. Even if the piston is brought to rest momentarily towards the end of the tube, it will normally accelerate again towards the downstream end of the tube due to the large residual expanded reservoir pressure force acting on it. Particularly for lightweight pistons, acceleration to a high velocity can occur over very short distances.

Per Figure 4.9, Itoh et al. [121] define the soft landing condition as a possible condition at the end of the deceleration phase, where acceleration and velocity of the piston are both simultaneously zero (referred to as an ‘inflection’ point).

If this occurs, then the piston will momentarily come to rest, before it is once more accelerated forward by the residual expanded reservoir gas pressure. If the buffer at the end of the compression tube is sized such that it extends to this inflection point, then the piston can be ‘caught’ at this inflection point, and will be subsequently supported against the accelerating force of the expanded residual reservoir gas. Itoh et al. proposed targeting the soft landing condition, and solved Hornung’s [124] equations to achieve it.

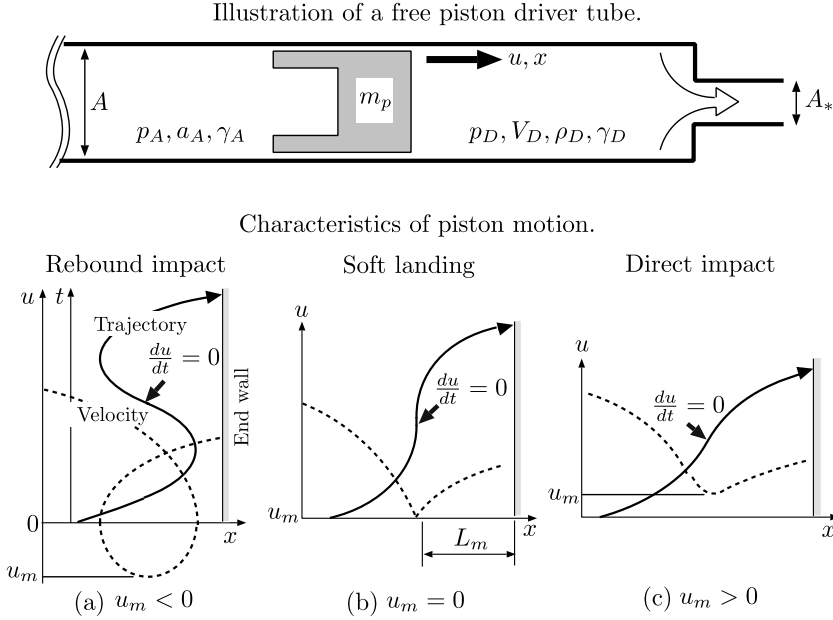


Figure 4.9: Characteristics of piston motion (adapted from [121]). Subscript m refers to the instant when piston acceleration is zero; if $u_m = 0$ then the piston has an inflection point where it can theoretically be ‘caught’ by an appropriately sized buffer, thus avoiding impact.

The above three studies of piston behaviour provide the foundation for the present investigation into tuning the free-piston driver of the X2 expansion tube. The methodology developed by Stalker [120] provides the basic fundamental insights into how driver configuration must be designed to safely achieve tuned operation. It is also sufficiently simple to be suitable for an initial parametric study to determine the feasible performance limits of X2, including the corresponding piston masses required. Hornung [124] provides the analytical tools to more accurately estimate piston response. Itoh et al. [121] provide a clear definition of the target piston response.

Beyond analytical approaches, the complexity of the actual driver geometry, as well as other secondary effects, are modelled with improved accuracy by using numerical codes (such as L1d2 [113]). Such codes are very useful for fine tuning piston response, as well as for understanding experimental results. However, the analytical models described

above are more appropriate at the initial stage to first develop an understanding the general problem, and then to identify the approximate solution to the problem from the practically unlimited potential solutions. Numerical analysis and experimentation are then required to make further progress with the specific detailed driver configuration.

The remainder of this chapter presents the results of an analysis to calculate basic requirements for a tuned free-piston driver for X2, using the methodology developed by Stalker [120]. It is shown that a lightweight piston is a fundamental requirement. Chapter 5 discusses the design and stress analysis of a new lightweight piston for X2. Chapter 6 then applies principles developed by Hornung [124] and Itoh et al. [121], followed by CFD analysis and experimental testing, to develop new tuned free-piston driver conditions for X2 with the new lightweight piston.

4.4 Stalker Analysis

4.4.1 Methodology

The methodology developed by Stalker [120] was used to determine the necessary piston mass for tuned operation of the X2 free-piston driver. The methodology and results are outlined in this section. Ideal gases and lossless processes are assumed. Figure 4.6 defines parameters used in the derivations.

Stalker considers a moment of time following diaphragm rupture when density is at a maximum in the driver, defines this as condition r , and sets $t = 0$ at this time:

$$\frac{d\rho_D}{dt} = 0 \quad (4.8)$$

$$(u)_r = U_r = - \left(\frac{dx}{dt} \right)_r \quad (4.9)$$

At this moment in time, the following equality is applied:

$$(p_{D,r} - p_{A,r}) V_r = k\sigma A U_r^2 \quad (4.10)$$

$$\sigma = m_p/A \quad (4.11)$$

The left hand side of Equation 4.10 represents the total work required to expel the entire remaining volume of driver gas in front of the piston, based on the pressure difference across the piston at condition r . This assumes constant reservoir and driver pressures acting on the piston, which is a significant simplification since both of these pressures will vary as the piston slows down. The right hand side of Equation 4.10 represents the

kinetic energy of the piston, factored by k . The work done equals the kinetic energy for $k = \frac{1}{2}$, although Stalker typically nominates $k = 1$ to provide a margin of safety [125]. Equating the total pressure force acting on the piston to mass \times acceleration, and applying Equation 4.10, Stalker eventually arrives at the following non-dimensionalised relationship between driver density and time:

$$\frac{\rho_D}{\rho_{D,r}} = \frac{1}{1 - z + \frac{k}{2}z^2} \exp \left[\frac{-2}{\sqrt{2k-1}} \left\{ \tan^{-1} \frac{kz-1}{\sqrt{2k-1}} - \tan^{-1} \frac{-1}{\sqrt{2k-1}} \right\} \right] \quad (4.12)$$

$$z = \frac{U_r t}{x_r} \quad (4.13)$$

$$\frac{x}{x_r} = \frac{k}{2}z^2 - z + 1 \quad (4.14)$$

$$\frac{u}{U_r} = 1 - kz \quad (4.15)$$

Inspection of Equation 4.12 indicates that the non-dimensionalised driver density after diaphragm rupture is only dependant on the value of k . Setting $k = 1$, and assuming $\gamma_D = \frac{5}{3}$, the ratio $p_D/p_{D,r}$ is plotted in Figure 4.10. It is emphasised that this plot is only applicable *after diaphragm rupture*, for a driver configuration which satisfies Equation 4.10, and is subject to several simplifying assumptions that have already been noted.

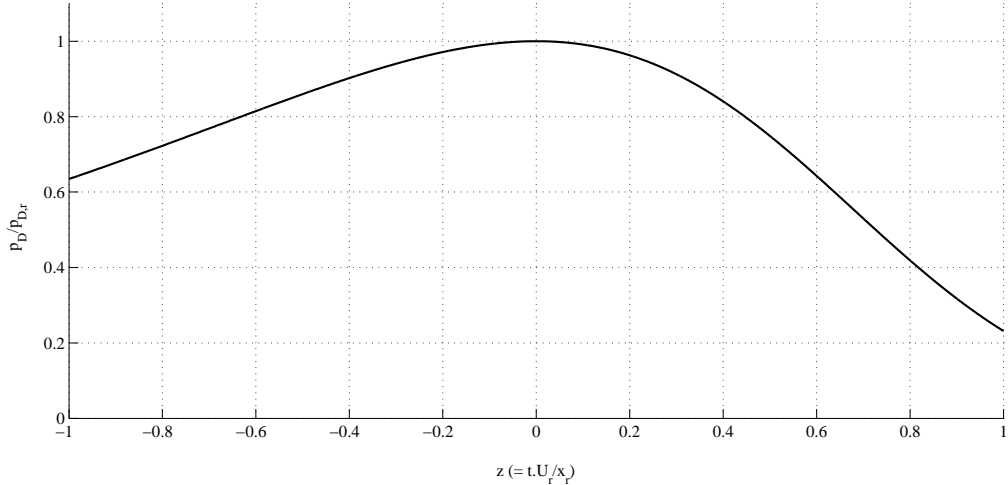


Figure 4.10: Variation in driver pressure after piston rupture using Stalker analysis [120] for $k = 1$.

Referring to Figure 4.10, since peak driver pressure occurs at $z = 0$, logic dictates that diaphragm rupture must occur for $z \leq 0$. For rupture at $z = 0$, driver pressure will immediately drop. However, for rupture at $z < 0$, driver pressure will continue to

increase momentarily, before dropping again, thus providing the mechanism for increased driver supply duration. This is referred to as ‘over-driving’ by Itoh et al. [121] and was previously described in Figure 4.7.

Figure 4.11 shows how a $\pm 10\%$ driver pressure variation can be used to establish increased duration of useful driver gas supply. For $k = 1$, corresponding z values can be solved for. Subsequently, Equations 4.12 to 4.15 can be used to predict corresponding driver performance and configuration requirements:

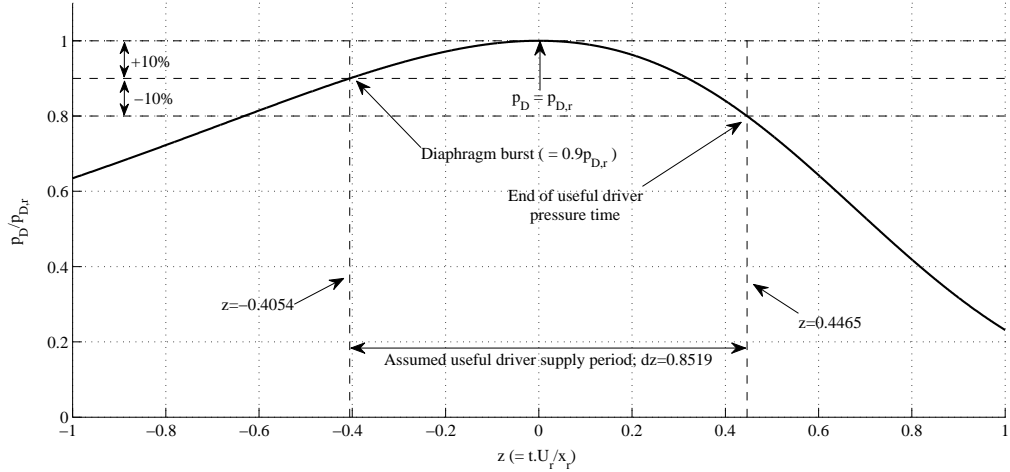


Figure 4.11: Driver pressure analysis for $\pm 10\%$ permissible pressure variation, $k = 1$.

From Equation 4.13:

$$\Delta t = \Delta z \frac{x_r}{U_r} = 0.8519 \frac{x_r}{U_r} \quad (4.16)$$

From Equation 4.15:

$$u_{rupt} = (1 - 1 \times -0.4054) U_r = 1.4054 U_r \quad (4.17)$$

Quantities at condition ‘ r ’ are determined as follows:

$$x_r = \left(\frac{p_{D,0}}{p_{D,r}} \right)^{\frac{1}{\gamma}} L = \frac{L}{\lambda_r} \quad (4.18)$$

where, for 10% driver pressure increase following diaphragm rupture:

$$\lambda_r = \lambda / 0.9^{\frac{1}{\gamma}} \quad (4.19)$$

$$U_r = \left(\frac{2}{\gamma_D + 1} \right)^{\frac{\gamma_D + 1}{2(\gamma_D - 1)}} \frac{A_*}{A} \sqrt{\gamma_D R_D T_{D,0} \left(\frac{p_{D,r}}{p_{D,0}} \right)^{\frac{\gamma_D - 1}{\gamma_D}}} \quad (4.20)$$

It is assumed that the reservoir gas, which acts on the piston rear face, is expanded to the piston velocity by an unsteady expansion. The reservoir pressure is therefore dependant on the piston velocity as follows:

$$p_A = p_{A,0} \left[1 - \frac{\gamma_A - 1}{2} \left(\frac{u}{a_{A,0}} \right) \right]^{2\gamma_A/(\gamma_A-1)} \quad (4.21)$$

Substituting Equation 4.21 into Equation 4.10 and solving for initial reservoir fill pressure:

$$p_{A,0} = \left(p_{D,r} - \frac{m_p U_r^2 k \lambda_r}{LA} \right) \left[1 - \frac{\gamma_A - 1}{2} \left(\frac{u}{a_{A,0}} \right) \right]^{-2\gamma_A/(\gamma_A-1)} \quad (4.22)$$

Summing forces on the piston and assuming isentropic compression of the driver gas:

$$\frac{du}{dt} = \frac{A}{m_p} \left\{ p_{A,0} \left[1 - \frac{\gamma_A - 1}{2} \frac{u}{a_{A,0}} \right]^{2\gamma_A/(\gamma_A-1)} - p_{D,0} \left(\frac{L}{x} \right)^{\gamma_D} \right\} \quad (4.23)$$

Typically, λ , driver and reservoir gas compositions, compression tube area, and diaphragm rupture pressure, will be initially specified for a driver. This leaves piston mass, m_p , and initial reservoir fill pressure, $p_{A,0}$, as the two remaining unknowns in Equations 4.22 and 4.23. These unknowns can be solved iteratively as follows:

1. Choose a piston mass.
2. Calculate reservoir fill pressure with Equation 4.22.
3. Calculate piston response with Equation 4.23, and calculate u_{rupt} at x_{rupt} .
4. Iterate through piston mass until $u_{rupt} = 1.4054U_r$.

4.4.2 Results

The methodology detailed in Section 4.4.1 was applied to the X2 driver geometry in order to determine what level of driver performance could be expected for tuned operation of different driver configurations. Whilst the Stalker analysis in Section 4.4.1 may be subject to several simplifying assumptions, the results in Section 4.4.2 provide useful information about general trends and performance limitations of the X2 driver, and generally indicate the requirement for a lighter piston. The calculations use the driver tube CAD geometry from [126], ignore the presence of the buffer, assume the piston face extends 100 mm forward of the piston launcher front face, and calculate an average compression tube length based on volume \div area (to account for any area changes at the primary diaphragm). Table 4.2 summarises the critical driver geometric features for X2.

Description	Value
Compression tube volume	0.2261 m ³
Compression tube diameter	0.2568 m
Compression tube average length	4.366m
Shock tube diameter	0.0850 m
Compression/shock tube area ratio	9.128
Nominal piston mass	35kg

Table 4.2: Critical driver geometries for X2.

Results from the Stalker analysis of the X2 free-piston driver are presented in Figures 4.12 and 4.13. The plots show the variation of several tunnel parameters required for tuned operation of the driver. These results are based on several already stated assumptions, but illustrate approximate trends.

It is noted that reservoir pressures are calculated assuming the reservoir is infinitely long, the same diameter as the compression tube, and has no area changes. The actual X2 reservoir is slightly wider than the compression tube, however it has a significant narrowing at the slotted piston launcher, which throttles flow to the piston; this is discussed in more detail in Sections 6.4 and 6.6. Consequently, the reservoir pressures shown in Figure 4.13 are likely to be significantly underestimated. Numerical analyses with high fidelity models are required to produce more accurate estimates.

The basic conclusion from the results in Figures 4.12 and 4.13 is that tuned operation of the X2 free-piston driver requires the use of a much lighter piston. A light piston is required for two reasons. Firstly, it must be accelerated over a relatively short distance to a high velocity in order to achieve an over-driven condition. This is only possible with a lightweight piston or else the required reservoir pressure accelerating the piston becomes excessive. Secondly, for high compression ratios there is only a small distance left to decelerate the piston following diaphragm rupture. For a given driver pressure force and a piston moving at high speed, a lighter piston will stop over a shorter distance.

Review of Figure 4.13 indicates that the X2 piston would need to be < 5 kg for a 100% helium driver in order to achieve similar shock strength to the nominal driver configuration ($\lambda \approx 42$ and 15.5 MPa rupture pressure). By inspection this is an unfeasibly low mass. However, it can be seen that reasonable performance should still be possible with a moderately heavier piston and some addition of argon gas to slow the driver gas sound speed. Establishment of a target mass is considered in Section 4.5.

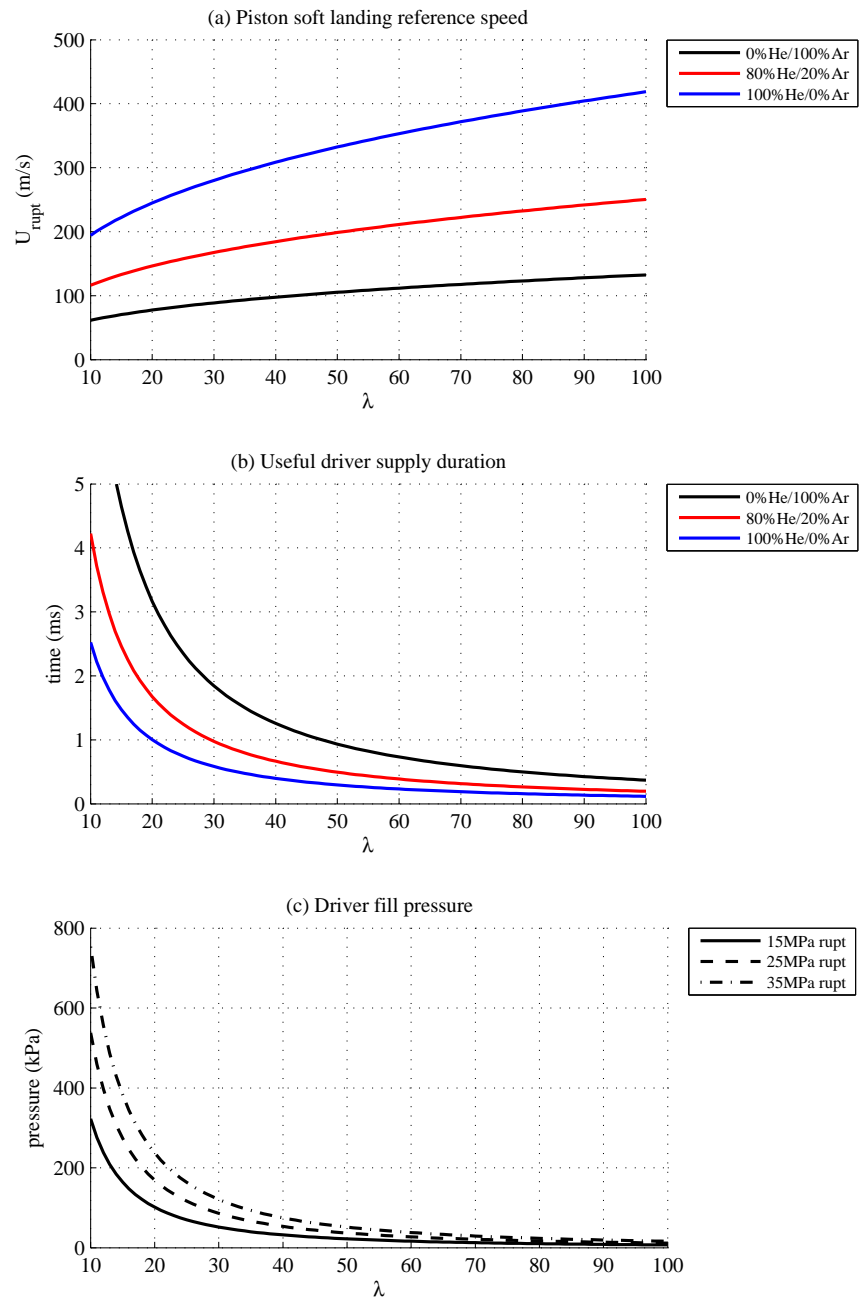


Figure 4.12: Stalker analysis results for X2 driver (part 1 of 2).

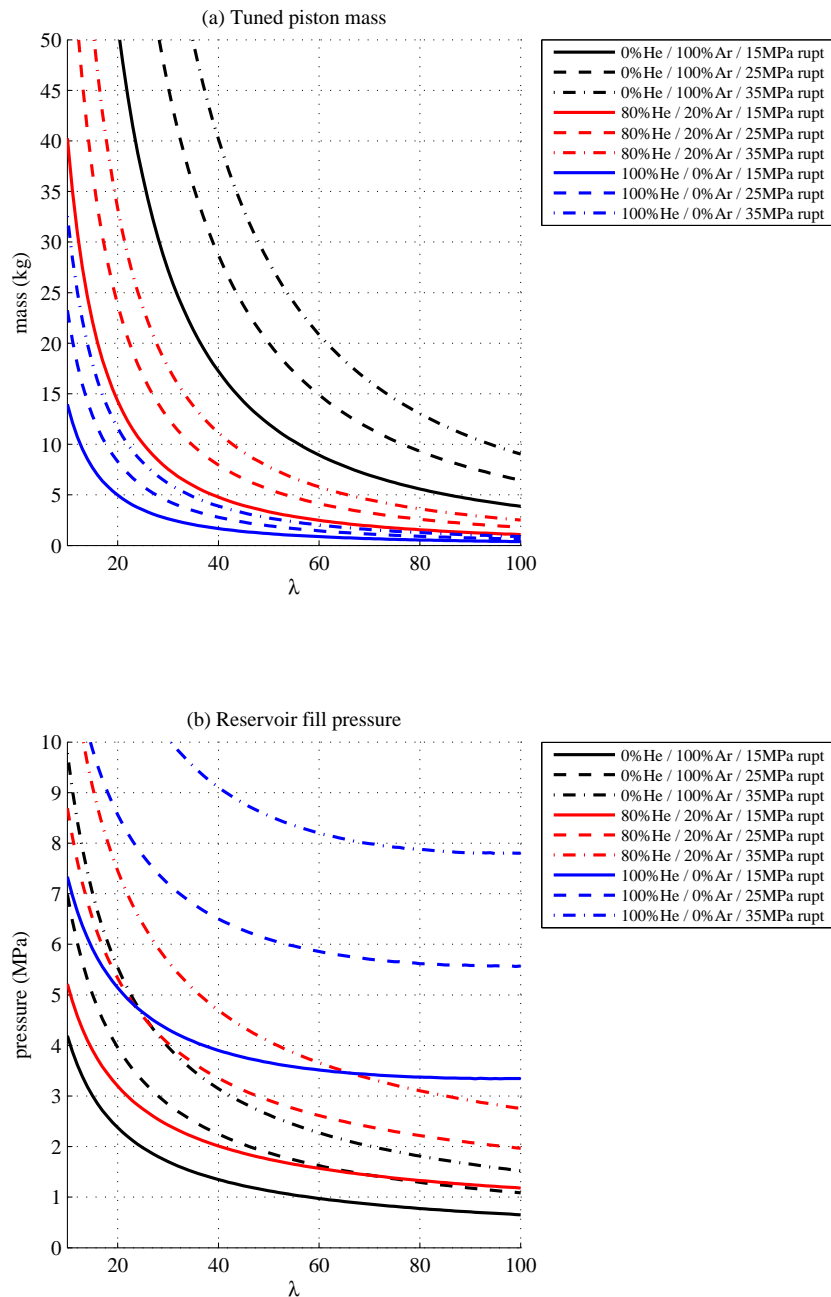


Figure 4.13: Stalker analysis results for X2 driver (part 2 of 2).

4.5 Target Piston Mass

Considering the Mach 13 flow condition detailed in Table 4.1 (refer also to Table 7 in [118]), the required flow condition shock speeds can be used to estimate the time it would take for the shock to traverse the entire length of the tube (assuming the shock maintains its required speed, and discounting the nozzle at the end of the tube):

$$t_{shk} = \sum \frac{L_i}{u_{s,i}} = \frac{3.424}{4,789} + \frac{1.301}{1,878} + \frac{4.254}{4,698} = 2.3 \text{ ms} \quad (4.24)$$

where i refers to the tube being considered.

Similarly, if it is assumed that a $u + a$ wave reflects from the piston face and traverses each tube through the gas region with the higher theoretical sound speed (see Figure 3.3; region pairs considered are $sd2/sd3$, $2/3$, and $6/7$), a conservative lower bound on the time it takes this wave to traverse the facility can be estimated:

$$t_{u+a} = \sum \frac{L_i}{u_i + \max|a_i|} = \frac{3.424}{3,420 + 2,850} + \frac{1.301}{1,510 + 3,540} + \frac{4.254}{3,890 + 2,100} = 1.5 \text{ ms} \quad (4.25)$$

The difference between these two times provides an estimate of the maximum duration that driver gas would need to be maintained at full pressure in order to avoid the shock attenuation which was observed experimentally in Figure 4.2; $t_{drv,min} = 2.3 - 1.8 = 0.5 \text{ ms}$. In reality the required duration is less because the $u + a$ wave partially traverses the gas region with the slower sound speed in each tube, the actual flow temperatures (and therefore sound speeds) can be significantly less when real gas effects are accounted for, and there is a finite delay between diaphragm rupture and generation of the $u + a$ wave.

Referring to Figure 4.12, a 10 kg piston with an 80% helium / 20% argon driver gas composition has a corresponding compression ratio of between approximately 23 (15 MPa rupture pressure) and 42 (35 MPa rupture pressure). Referring to Figure 4.13, these compression ratios correspond to a useful driver gas supply duration of between approximately 1.4 and 0.7 ms respectively. This indicates that the required driver gas supply time, $t_{drv,min}$, can be satisfied, which itself was calculated very conservatively.

Therefore, a 10 kg piston operating at these tuned conditions is expected to have sufficient supply time for the target scramjet flow conditions characteristic of that detailed in Table 1.1. It should also be possible to achieve reasonable performance with a 10 kg piston mass at the higher rupture pressures (a peak driver pressure of 40 MPa is possible with X2). However, the addition of argon makes it unlikely that the same initial shock strength can be achieved with a tuned 10 kg piston, as is possible with the existing 100% helium driver with 35 kg piston and 15.5 MPa rupture pressure.

4.6 Conclusion

The reference Mach 13 case study described in Section 4.2 indicated the requirement to develop a ‘tuned’ free-piston driver for X2 in order to increase the duration of supply of high pressure driver gas. An analysis following the arguments of Stalker [120] has shown that for reasonable performance, a piston mass $\lesssim 10$ kg is required.

Chapter 5

Design and Stress Analysis of a Lightweight Piston for X2

5.1 Chapter Overview

A new lightweight 10.5 kg piston has been designed and manufactured for X2. The 10.5 kg piston retains the interfacing geometry of the existing 35 kg piston. Strength was assessed using a symmetric finite element solid model for (a) an 80 MPa ultimate driver pressure load (the strength critical load) and (b) a 20 MPa reservoir pressure load (the deflection critical load). The piston was not assessed for impact; the design relies on avoiding impact into the end of the tube at high velocities. If high speed impact occurs, the tube will contain the piston, but the piston will potentially be irreparably damaged. Blow out panels in the test section protect against over-pressure from reservoir gas if the piston fails catastrophically. The 2× safety factor applied for static analyses is expected to provide coverage against the higher stresses that may occur due to the dynamic nature of the applied loading. At the time of writing, the piston has been successfully used for over 300 shots, including several at 100% of limit load. It has shown no signs of damage or structural distress, thus supporting the methodologies used in its design.

5.2 Introduction

An analysis following the arguments of Stalker [120] indicated that a piston weighing less than approximately 10 kg was required in order to develop a tuned free-piston driver for X2; see Chapter 4. A new piston was subsequently designed and is now discussed in the present chapter. The new piston retains the interfacing geometry of the existing 35 kg piston, but has had significant amounts of mass removed where practical.

The piston strength was assessed for two load cases: an 80 MPa ultimate pressure load

applied to the front face of the piston to represent driver gas loading, and a 20 MPa ultimate pressure load applied inside the piston to represent reservoir pressure loading for the piston on the launcher. The piston was analysed using a symmetric solid finite element model.

The 80 MPa driver pressure load case was shown to be critical. The Von Mises stress was determined to be generally less than the allowable yield stress of the piston. Some locations on the solid model had stresses slightly exceeding the yield stress. The model was therefore re-analysed using a non-linear material model, where it was shown that peak stresses fell below the ultimate allowable stress in all places. The piston was shown to be able to resist the 20 MPa reservoir pressure loading with minimal deformation (<0.05 mm) at the seals, indicating a low risk of pre-launch due to leakage past the launcher seals.

The piston was not assessed for impact or dynamic pressure loading. The design relies on avoiding piston impact into the end of the tube at high velocities. If high speed impact occurs, the tube will contain the piston, but the piston will potentially be irreparably damaged. The 2 \times safety factor applied in static stress analyses is expected to provide coverage against the higher stresses that may occur under the actual dynamic pressure loading conditions. Further, the piston material is expected to have higher strength at high strain rates, which will provide further protection against failure.

At the time of writing, over 300 shots have been performed using the piston, including shots to 100% limit load. No signs of structural damage or distress have been identified. Note: the original stress report for this piston design is provided in [127] and contains the complete set of design data and stress analysis results.

5.3 Overview of the Existing 35 kg X2 Piston

The existing piston arrangement is shown in Figures 5.1 and 5.2 (CAD models are taken from [126]). The axis system is shown in both figures; y corresponds to the forward (driver gas exposed) face of the piston. Referring to Figure 5.2, it can be seen that there is a large mass of aluminium that could potentially be removed whilst preserving interfacing geometries.

5.4 Overview of the New Lightweight 10.5 kg X2 Piston

Detailed drawings for the new lightweight piston are provided in Appendix A. An assembly view of the lightweight piston, and a view of just the piston body, are shown

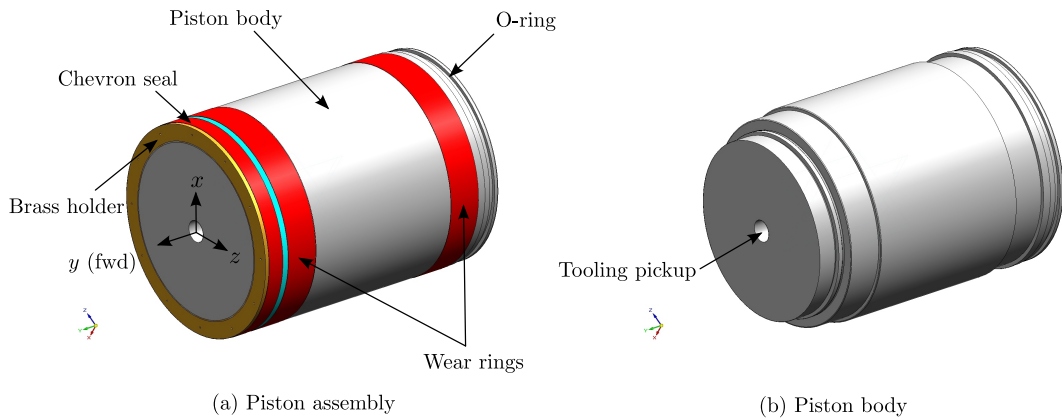


Figure 5.1: X2 existing 35 kg piston.

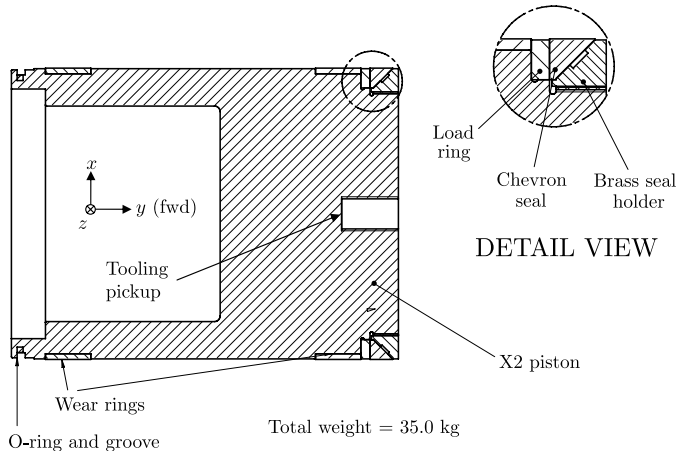


Figure 5.2: Piston assembly section view.

in Figure 5.3. The final manufactured piston mass was 10.524 kg, which is slightly less than the nominal CAD mass (10.683 kg). Referring to Figure 5.2, the approximate 25kg weight reduction was achieved by making the following modifications:

1. Reducing the depth of the piston head.
2. Reducing the hole depth of the tooling pickup.
3. Reducing the width of the wear rings (from 40mm to 30mm).
4. Removing material from the piston outer surface between the two wear rings.
5. Cutting out material from underneath the wear bands.

The addition of brakes can help to prevent the rebound motion identified in Figure 4.9, thereby making available a much wider range of driver operating conditions. However,

incorporating brakes into the piston would have added significant weight and complexity to the design, therefore the decision was made not to use them.

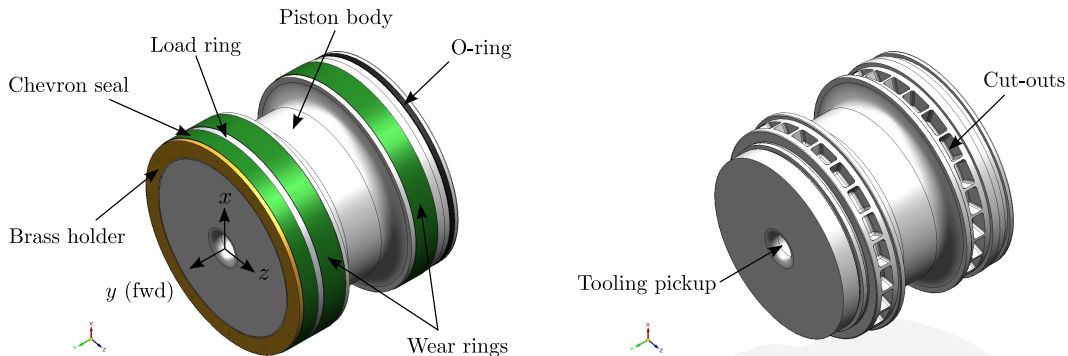


Figure 5.3: Lightweight piston views.

5.5 Materials

5.5.1 Piston Body (PNo. X2-LWP-001-1/Appendix A.2)

The piston was manufactured from 7075-T6 aluminium alloy rod, for its high strength-to-weight ratio, and for its reasonable material cost. For the purposes of this design, detailed material and physical properties were taken from MIL-HDBK-5H [128], Table 3.7.4.0(d). Material allowables are observed to reduce with increasing rod diameter; the largest quoted rod diameter was therefore conservatively used (4"), and it was assumed that these properties were applicable to the larger diameter rod required for this piston (approximately 10" diameter). The more conservative A-basis allowables were used, and the minimum of L and L-T orientation allowables was assumed to apply in all directions. Finally, it was assumed that quoted material allowables are true stresses, which is reasonable given the relatively small elongation at failure. In addition to these assumptions, any potential discrepancies between assumed and actual material mechanical properties were considered to be acceptable in light of the large ($2\times$) safety factor applied to loads used for certification of the design. Assumed material and physical properties are presented in Table B.1 of Appendix B.1.

5.5.2 Load Ring (PNo. X2-LWP-003-0/Appendix A.4)

The load ring is manufactured from existing commercial aluminium alloy plate sourced from the UQ mechanical engineering workshop; the specific alloy is unknown. It is not a highly stressed component, and its design is acceptable by inspection. The stiffness and

mass properties of the load ring were assumed to be the same as those shown in Table B.1, which is reasonable since density and stiffness do not vary significantly between different alloys of aluminium.

5.5.3 Brass Holder (PNo. X2-LWP-005-0/Appendix A.6)

The brass holder is manufactured from cast aluminium bronze, specification C95810. Material properties for C95800 series copper alloy were used for the analysis, and were taken from [3]. Properties are presented in Table B.2 of Appendix B.1. Detailed stress analysis of this component was not performed; the only material properties required were those relevant to the piston finite element stress model (i.e. stiffness and density properties).

The brass holder design remains unchanged from the existing 35 kg X2 piston. Although the pressure loads are the same for both heavy and lightweight X2 pistons, inertial loads are greater for the lightweight piston, therefore the strength of the brass holder cannot be passed by comparison to the heavy piston. However, two points are noted: firstly, a very similar design is used for the similarly sized T4 RST piston, which is subjected to approximately $2\times$ the maximum driver pressure of X2. Secondly, neither of the brass holders in either facility has shown signs of structural distress after a large number of load cycles. On that basis the risk of catastrophic failure of the brass holder was considered to be remote. The strength of the component was instead confirmed by ongoing inspection of the part during the commissioning process of the new lightweight piston, which included driver pressures up to the design limit.

5.5.4 Wear rings and chevron seal (PNo. X2-LWP-002-0/ Appendix A.3; X2-LWP-004-0/Appendix A.5)

The wear rings and chevron seal are all machined from Nylon 6 oil filled cast. Only the stiffness properties are required for these parts, since they are not strength critical. Properties are shown in Table B.3 of Appendix B.1.

5.5.5 Steel Tunnel Parts

The steel tube walls are modelled in ANSYS as rigid boundaries. Steel is significantly stiffer than Aluminium, and the cylindrical shape is intrinsically stiff, therefore this assumption was considered to be reasonable.

5.6 Load Cases

Two load cases were used to assess the piston design:

1. LC1: Driver pressure loading. The maximum operational driver pressure for X2 is 40 MPa. This pressure acts on the front face of the piston, and tends to accelerate it in the upstream direction. For design purposes a 2 \times safety factor was applied to this load, giving an ultimate driver pressure of 80 MPa.

Note: the reservoir pressure force, which acts in the opposite direction to the driver pressure force and therefore will reduce the magnitude of inertial loads to the piston for this load case, is conservatively ignored.

2. LC2: Reservoir pressure loading. The maximum operational reservoir pressure loading for X2 is 10 MPa, which acts on the upstream and inside surfaces of the piston when it is initially held in the launcher, and immediately after it is launched. Once the piston starts moving the reservoir pressure force correspondingly reduces. For design purposes a 2 \times safety factor is applied to this load, giving an ultimate reservoir pressure of 20 MPa.

5.7 Finite Element Analysis Analysis software

ANSYS Workbench 11.0 was used to perform the simulation.

5.8 Strength Criteria

Material *yield* was assumed to have occurred when the calculated Von Mises stress exceeded the material *yield* stress; material *failure* was assumed to have occurred when the calculated Von Mises stress exceeded the material *ultimate tensile* stress. Material yield and ultimate tensile stresses were assumed to be 414 MPa and 471 MPa respectively per Table B.1 in Appendix B.1. Two analyses were performed for both load cases:

1. Material yield at ultimate load: A linear material static analysis was performed at ultimate load (2 \times safety factor). It is the nature of finite element models (particularly solid models) that very localised stress peaks are observed due to the nature of the element formulation and the discreet nature of the finite element mesh, especially around complex geometry. These are not necessarily truly representative of the actual state of stress. To pass this criteria, the calculated Von Mises stress was permitted to exceed the material yield stress *only* if this occurred in very localised regions. If these localised regions did exist, the Von Mises stress was not permitted to exceed 1.5 \times the material allowable yield stress. This was to

conservatively ensure that at *limit* load (i.e. the maximum *actual* operating load, i.e. with $1\times$ safety factor) there would be no material yield.

In reality, even if the structure actually has a tendency to develop these stress concentrations, at the onset of yield the load will redistribute to the stiffer material which has not yielded. So long as this redistribution is confined to very small regions, there will be no gross yield of the structure. If the calculated Von Mises stress exceeded the yield stress at anything other than a small localised region, the piston body was considered to have failed this criteria, regardless of by how little it failed.

2. Material failure at ultimate load: a non-linear material static analysis was performed at ultimate load ($2\times$ safety factor). To pass this criteria the calculated Von Mises stress had to be less than the material ultimate tensile stress across the entire piston body.

By satisfying these two failure criteria (for both LC1 and LC2 load cases), it was demonstrated firstly that the piston would be able to sustain ultimate loading ($2\times$ safety factor) without failure, and in the worst case, only with very localised yielding, and secondly, that the piston would be able to sustain limit loading with zero yield ($1\times$ safety factor). Considering the $2\times$ safety factor used to calculate ultimate loading, the conservative material allowables selected, and the conservative yield criteria, there was generally a large amount of conservatism applied to the design.

5.9 Deflection Criteria

Deflection criteria were only applied to LC2. The radial expansion of the piston skirt inner surface, in the vicinity of the launcher D-ring seals, was not permitted to exceed 0.1 mm under ultimate reservoir pressure loading. This criteria was established in order to reduce the probability of leakage of reservoir gas across the launcher seals while the piston is awaiting launch with the reservoir at full pressure. Swelling of the piston skirt may cause leakage of reservoir air into the downstream vacuum cavity, which increases the chances that the piston will be inadvertently pre-launched.

5.10 Symmetric Finite Element Solid Model - Static Analysis

5.10.1 Introduction

The lightweight piston is axisymmetric except for two features:

1. Venting holes in the brass holder, spaced at 30° intervals around the axis of symmetry. These structural details will not affect the strength of the piston body and can be ignored.
2. Outer surface cut-outs in the piston body (pocketing beneath the wear rings) spaced at 15° intervals around the axis of symmetry. These cut outs were incorporated for weight saving purposes, but could not be axisymmetric whilst still supporting the wear bands.

To account for the structural pocketing, a static analysis of a $1/24^{\text{th}}$ slice of the piston was analysed. The chevron seal, load ring, and wear rings, were incorporated in the finite element model in order to more accurately simulate the boundary conditions on the piston body. For example, considering the reservoir pressure load case, if a rigid support is not applied at the wear strip locations, but instead directly to the piston body, then this will permit significant load transfer to the tunnel walls. However, in reality there are comparatively soft wear rings between the tunnel walls and the piston body. For the small deformations associated with the piston swelling up due to reservoir pressure loading, the expansion of the piston body will be accommodated by compression in the soft wear strips, therefore the actual load transfer to the tunnel will be negligible.

It is noted that the brass holder is screwed onto the piston body. In the finite element model these two items were modelled as being bonded along the mid-thread surface. The brass holder was given appropriate material properties. This arrangement was used so that the pressure load acting on the brass holder would be transferred into the piston body in a realistic manner. The actual thread was not assessed for strength; as indicated in Section 5.5.3, the same brass holder arrangement is used on the heavy X2 piston, and a similar brass holder arrangement is used at up to $2\times$ higher maximum driver pressure loading in the T4 RST, therefore the risk of catastrophic failure was considered to be remote. The strength of the component was confirmed by ongoing inspection during the commissioning process of the new piston.

5.10.2 Finite Element Mesh

ANSYS was used to automatically generate a solid tetrahedral element mesh with element global edge length of 1.5 mm. The mesh, which has 125,775 nodes and 54,462 elements, is shown in Figure 5.4 (with accessories) and Figure 5.5 (piston body only).

5.10.3 Interfaces

Different interface options are available in ANSYS, such as a bonded interface (surfaces stuck together), a frictionless interface (surfaces must remain on the same plane), a compression only interface (surfaces can separate but not pass through each other) etc.

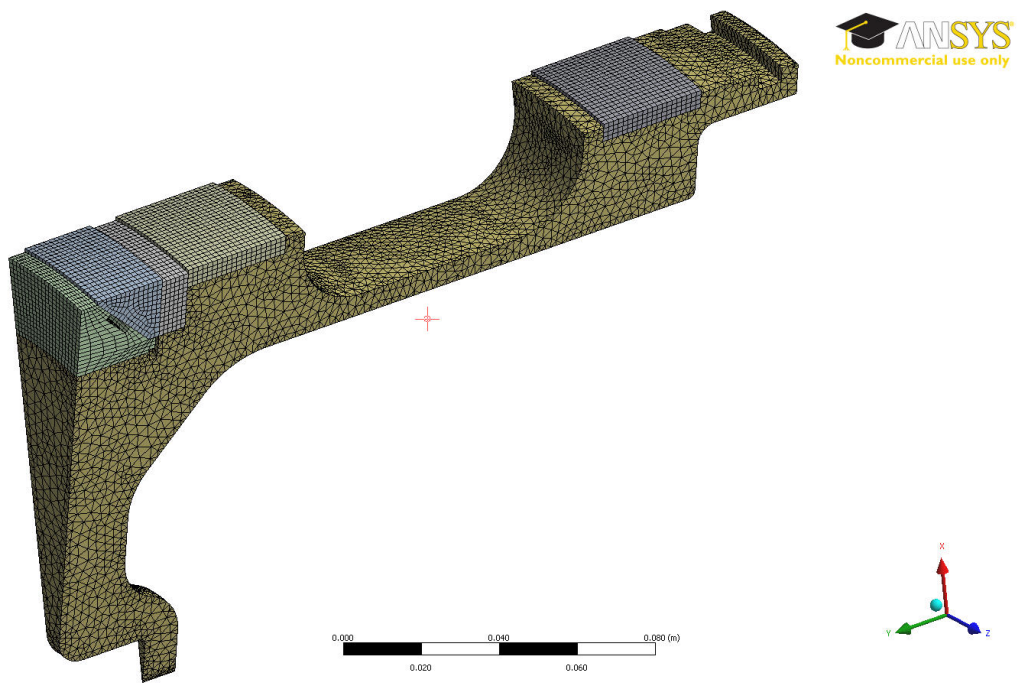


Figure 5.4: Solid mesh, 1/24th segment model, piston with accessories.

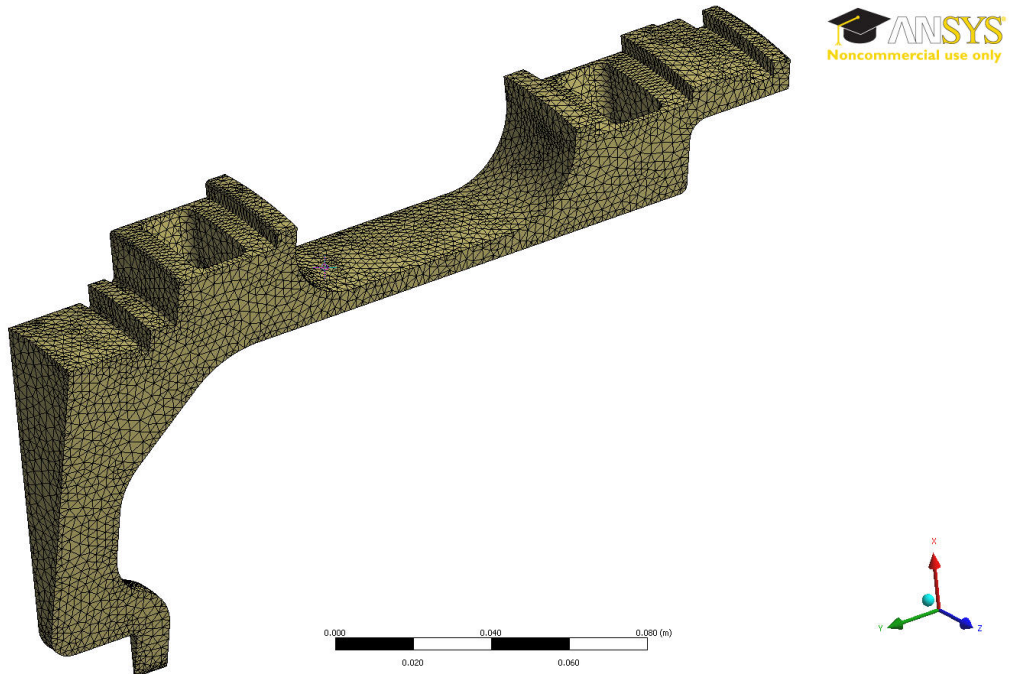


Figure 5.5: Solid mesh, 1/24th segment model, piston body only.

The type of interface determines whether the analysis is linear or not, since a contact-type interface must be solved iteratively. Two types of interface were selected in ANSYS:

1. Bonded interface: used for interfaces between the piston body and the wear rings, the piston body and the load ring, and the piston body and the brass holder.
2. No separation interfaces: used for all other interfaces, such as between the chevron seal and the brass holder, the wear ring edges and the piston, the piston and the side of the load ring etc.

5.10.4 Loads and Boundary Conditions - LC1 Driver Pressure

Loads and boundary conditions for LC1 are summarised in Figure 5.6. Both radial cut planes are planes of symmetry; the piston geometry may slide in-plane, but not across-plane. A sliding constraint is also applied along the centreline axis.

The surfaces which interface with the tunnel (the two wear rings and the chevron seal) were also assigned frictionless, no separation constraints (coloured blue). This constraint mechanism is only approximate, since it can apply both tensile and compressive forces to these surfaces; the actual tunnel can only react compressive force. However, the chevron seal and wear rings are very soft compared to the metallic components, therefore even if tensile stress arises within them, the small displacements involved will not result in large forces. This simplification was therefore considered acceptable, and is preferable since a compression-only support introduces contact non-linearity, which in this case would increase solution complexity considerably.

An 80 MPa ultimate pressure loading was applied normal to all surfaces along the front face of the piston (coloured red). Resistance to the pressure load was achieved by applying an inertial body load to the structure in the opposing direction. This load is applied as an acceleration, and coupled with the pressure force on the piston face, produces the state of stress in the piston which would result if its mass were steadily accelerating due to an applied pressure force at one end. Load will be a maximum at the piston face, and reduce to zero at the opposite end of the piston. In reality, the driver pressure load builds up rapidly against the piston face (over a duration of order 1 ms). This impulsive loading introduces a transient state of stress which the present static analysis does not account for; the implications of this simplification are considered in Section 5.14.

The acceleration of the piston is calculated in Table 5.1. It is noted that the discrete nature of the finite element mesh is such that this acceleration cannot perfectly balance the applied pressure force, therefore an additional support is required in the direction of the applied load. An elastic support of stiffness $1 \times 10^7 \text{ N/m}^3$ was applied to the rear face of the piston (not visible in Figure 5.6) to resist small residual forces, in order to

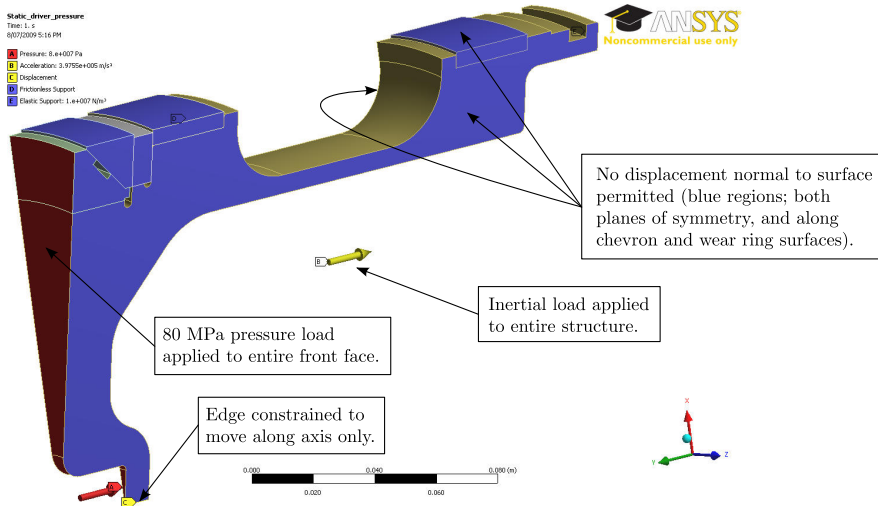


Figure 5.6: Loads and boundary conditions, LC1 80 MPa driver pressure load case.

avoid rigid body motion. Preliminary analysis indicated that there was indeed a small residual load resisted by this support. A correction was iteratively calculated to the acceleration body force to minimise this residual load, with the corrected acceleration being $397,552 \text{ m/s}^2$. Comparing this to Table 5.1, this constitutes a 1.3% discrepancy.

Notation	Description	Value	Units	Comments
p	Driver pressure	80×10^6	Pa	Ultimate load.
D	Piston diameter	0.2558	m	Outer diameter of brass holder.
A	Piston area	0.05139	m^2	$A = \pi D^2 / 4$
F	Force on piston face	4,111,317	N	$F = PA$
m	Piston mass	10.478 ¹	kg	From ANSYS geometry.
a	Piston acceleration	392,376	m/s^2	$a = F/m$

¹ The piston geometry used for the finite element analysis has slightly larger pocketing, hence the mass is lower. This pocketing was increased for manufacturing reasons.

Table 5.1: Calculation of piston acceleration due to LC1 80 MPa driver pressure load case.

5.10.5 Loads and Boundary Conditions - LC2 Reservoir Pressure

Figure 5.7 shows the loads and boundary conditions for the reservoir pressure load case. The constraints are unchanged compared to those described in Section 5.10.4, except that a rigid constraint against motion along the axis of symmetry (to prevent rigid body motion) replaces the rear elastic constraint used for LC1. The reservoir pressure was applied normal to the inside surface of the piston along the entire constant radius section. Referring to the launcher design illustrated in Figure 5.8, the actual reservoir

pressure load only acts between the two o-ring seals, therefore the assumed loading area is conservatively large.

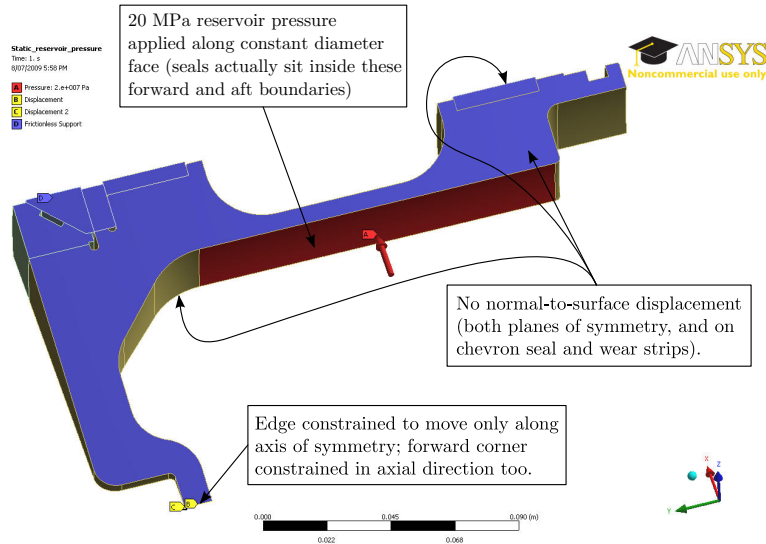


Figure 5.7: Loads and boundary conditions, LC2 20 MPa reservoir pressure load case.

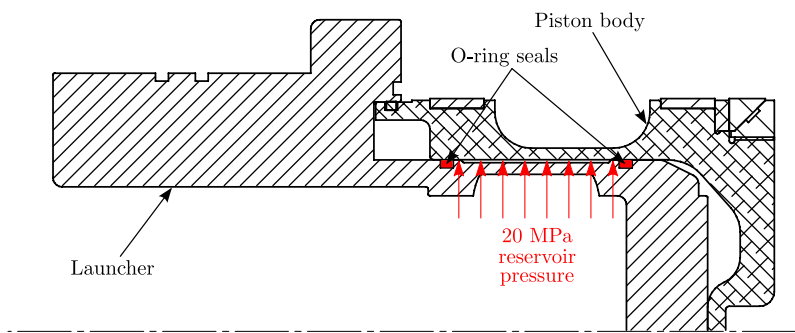


Figure 5.8: Piston launcher schematic.

It is noted that once the piston is released from the launcher, the reservoir gas fills the entire cavity inside the piston, and acts across the entire inner surface. This load case was not assessed since it is similar to the driver pressure load case, but only 25% of the magnitude (and in the opposite direction). The piston strength with respect to this post-launch reservoir pressure loading is acceptable by comparison to the driver pressure load case, LC1.

5.11 Results

5.11.1 80 MPa Driver Pressure Loading

Figure 5.9 shows multiple views of Von Mises stress distributions calculated from the linear material analysis, with red indicating stresses exceeding the yield allowable (414 MPa). Figure 5.10 shows the same stress distributions, but instead calculated using a non-linear material model, with red indicating stresses exceeding the ultimate tensile allowable (471 MPa). It is clear that where yield stress was locally exceeded in Figure 5.9 (linear material model), that these loads redistribute in Figure 5.10 (non-linear material model). Calculated stresses in the non-linear model do not exceed the ultimate tensile stress (471 MPa), therefore the piston will not fail.

In Figure 5.9 (the linear material analysis) the Von Mises stress exceeds the material yield stress by less than 10%. By inspection, at limit load (40 MPa driver pressure) the Von Mises stress will fall well below the material yield stress at all locations.

5.11.2 20 MPa reservoir pressure loading

Figure 5.11 shows a Von Mises stress plot for the piston body. The model was run with a linear material model. It can be seen that the yield stress is not exceeded and therefore the piston has sufficient strength to easily resist applied reservoir pressure loads.

Figure 5.12 shows an exaggerated deformation plot for the piston body. It can be seen that the maximum displacement is approximately 0.3 mm at the centre of the piston skirt, but only approximately 0.1 mm in the vicinity of the seals. Considering that the limit (maximum operating) reservoir pressure load is 10 MPa, deflections around the seals are predicted to not exceed 0.05 mm. By inspection this should not lead to leakage past the D-ring launcher seals, nor lead to other interfacing problems generally.

5.12 Analytical Stress Analysis

5.12.1 Overview

This section details two additional strength checks which were performed using traditional stress analysis techniques.

5.12.2 Buckling Analysis

By inspection the thinned skirt on the piston is the most critical location for instability failure. Referring to the piston drawings in Appendix A.2, tube dimensions are as follows:

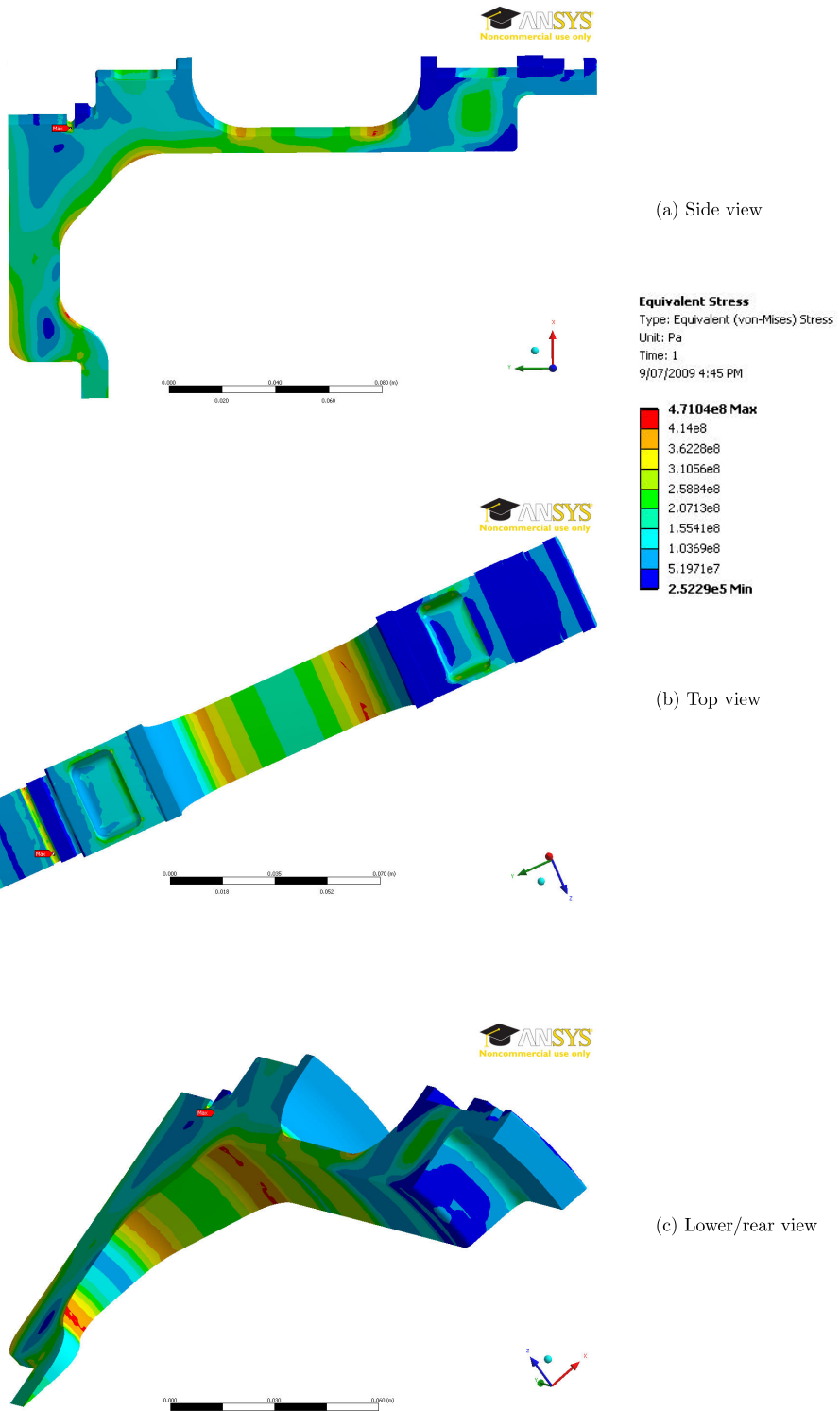


Figure 5.9: Von Mises stress distribution (Pa), linear piston body material model, LC1 80 MPa driver pressure load case.

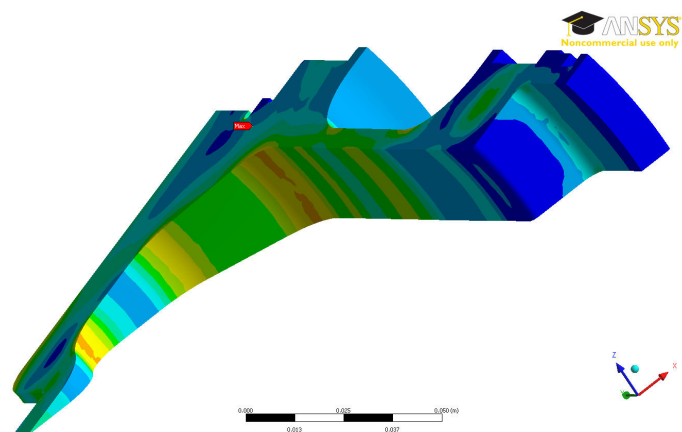
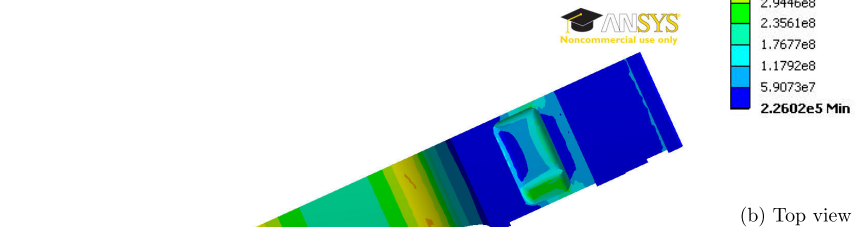
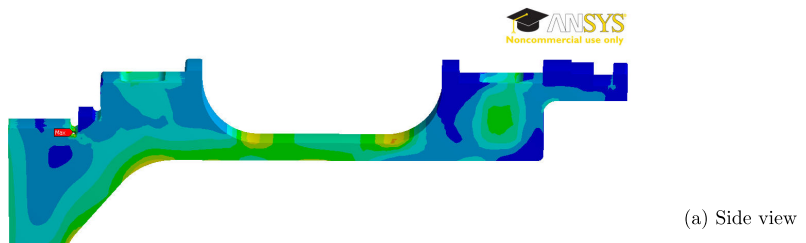


Figure 5.10: Von Mises stress distribution (Pa), *non-linear* piston body material model, LC1 80 MPa driver pressure load case.

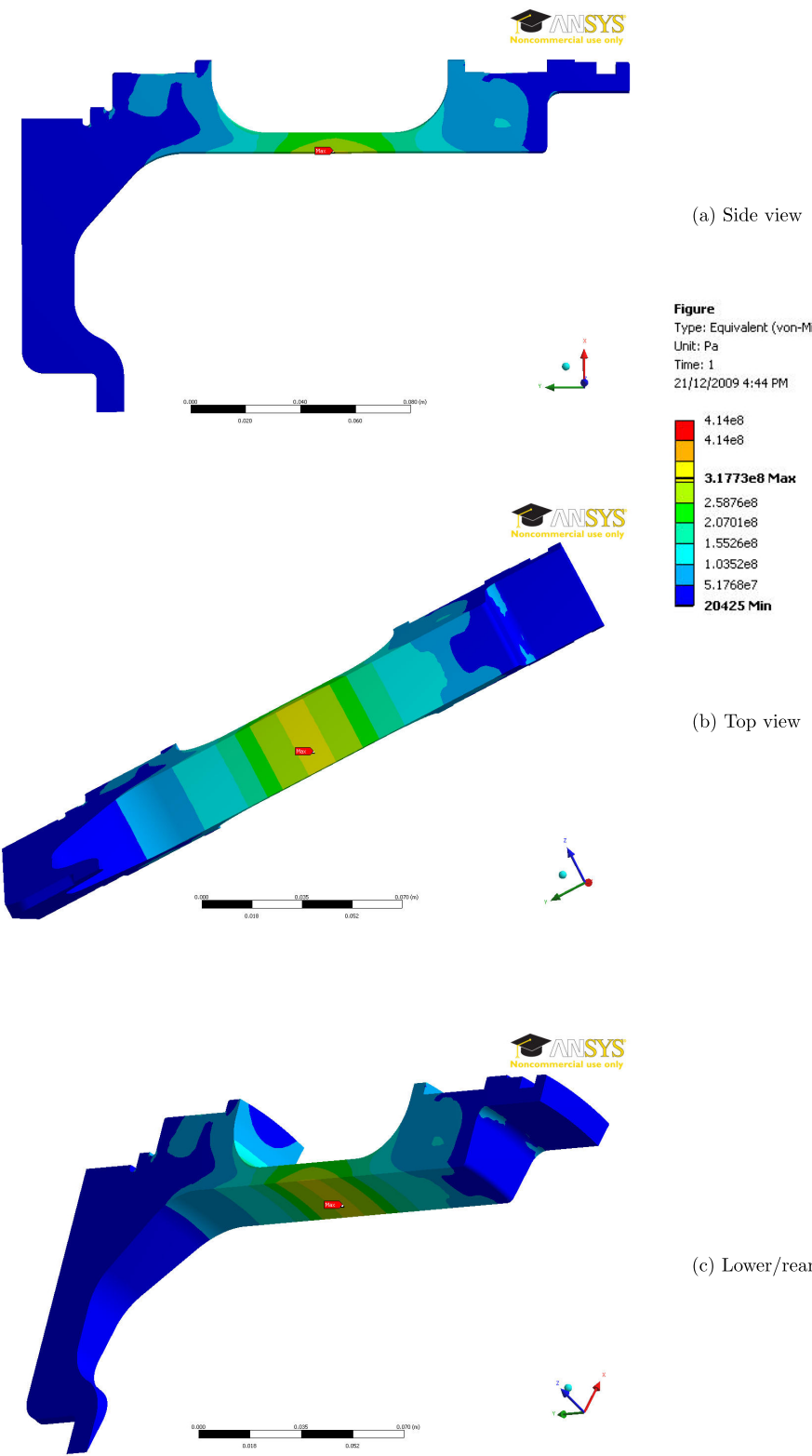


Figure 5.11: Von Mises stress distribution (Pa), linear piston body material model, 20 MPa reservoir pressure.

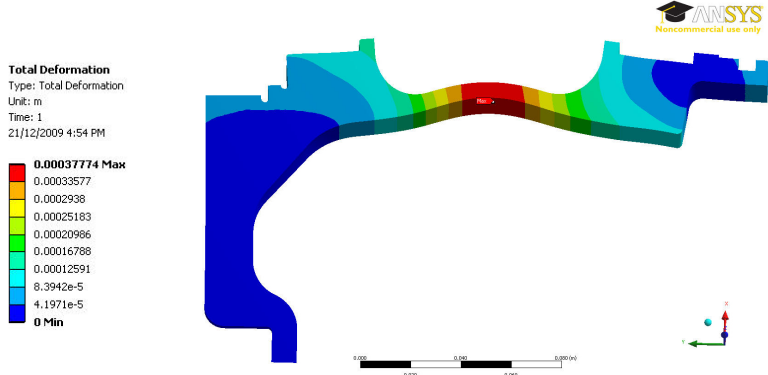


Figure 5.12: Piston deflection (m), exaggerated, linear piston body material model, 20 MPa reservoir pressure.

- Mean radius, $r = \frac{203 + 190}{2 \times 2} = 98.25$ mm.
- Thickness, $t = \frac{203 - 190}{2} = 6.5$ mm.
- Length, $L = 152 - 66 = 86$ mm (this length conservatively includes both 20 mm radii).

By inspection the column is short, and therefore will not fail by column buckling. However, it is still necessary to assess the piston for axisymmetric instability failure (refer Figure 5.13). A simple but accurate methodology to calculate this stress is not available. However, a conservative approximation is now determined based on Young and Budynas [129] (Table 15.2, Case 15) for local elastic instability failure of thin-walled circular tubes under uniform compression. Critical compressive stress due to local instability, σ_{cr} , is calculated as follows:

$$\sigma_{cr} = \frac{1}{\sqrt{3}} \frac{E}{\sqrt{1 - \nu^2}} \frac{t}{r} \quad (5.1)$$

applicable for $r/t > 10$ (thin walled) and $L > 2 \times 1.72\sqrt{rt}$ (i.e. a single buckling wavelength).

Referring to Equation 5.1, and considering the geometry of the piston, $r/t = 98.25/6.5 = 15.1 > 10$, therefore the cylinder may be considered to be thin walled. However, $2 \times 1.72\sqrt{rt} = 2 \times 1.72\sqrt{98.25 \times 6.5} = 86.9 < L$, which indicates that the piston skirt is slightly shorter than the actual wavelength associated with the instability failure. This suggests that the cylinder is probably too short to fail by local instability. However, the failing stress is still calculated to confirm this mode of failure is not critical. Substituting material properties from Table B.1 and the above geometric properties into Equation 5.1:

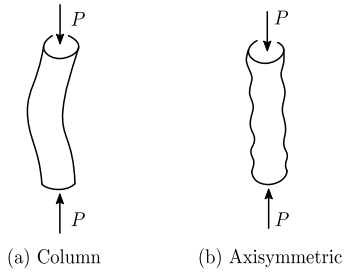


Figure 5.13: Column instability modes (taken from [130]).

$$\sigma_{cr} = \frac{1}{\sqrt{3}} \frac{71 \times 10^9}{\sqrt{1 - 0.33^2}} \frac{6.5}{98.25} = 2,873 \text{ MPa} \quad (5.2)$$

Young and Budynas [129] state that the stress calculated in Equation 5.2 should be scaled by 0.4-0.6 for an actual failing stress, giving $\sigma_{cr} = 0.4 \times 2,873 = 1,149 \text{ MPa}$. Clearly, since this stress far exceeds the material yield stress (414 MPa), and considering the conservative assumptions underlying this calculation, the piston will not fail due to local instability.

5.12.3 Reservoir Hoop Stress Finite Element Model Validation

Since hoop stress is easily estimated, it serves as a useful basis to validate the finite element model. Considering the minimum thickness section along the piston skirt, and the 20 MPa reservoir pressure, hoop stress is now determined.

Substituting the mean piston wall thickness, and the 20 MPa reservoir pressure, the idealised hoop stress may be determined:

$$\sigma_H = \frac{pD}{2t} = \frac{PD_i}{D_i - D_o} = \frac{20 \times 10^6}{(203 - 190)} = 292 \text{ MPa} \quad (5.3)$$

Comparison of Equation 5.3 with Figure 5.11 indicates good correlation (292 MPa from the classical analysis compared to 318 MPa from the finite element analysis). The piston is not a simple pressure vessel, and therefore some discrepancy should be expected. However, this check provides additional confidence in the basic geometry, materials, and load descriptions of the finite element model.

5.13 Piston Impact

The piston has not been assessed for impact into the end of the tube. It was not considered feasible to design a lightweight piston which could sustain significant impact

velocities into rigid metal. Instead, an intrinsic limitation of the piston is that driver conditions must be designed such that impact into the end of the tube is avoided.

There remains the possibility that the lightweight piston may accidentally hit the end of the tube at high speed, most likely due to either operator error or unintentional pre-launch. If this occurs, depending on the impact speed, the piston could potentially be irreparably damaged, and the primary concern is instead that the facility can contain the impact, and that personnel are not injured. It is noted that the facility has been designed to safely contain impact of heavy solid pistons (including the 35 kg X2 piston) into the end of the tube. By comparison, the lightweight piston presents a less severe impact case, for two reasons:

1. For a given impact velocity it has significantly less kinetic energy due to its lighter mass.
2. It is much more likely to be able to absorb impact energy through deformation of its thinner side walls.
3. In the event that the piston were to fail catastrophically, thereby allowing high pressure reservoir gas to flow past the piston, blow out panels in the test section protect against over-pressure.

5.14 Dynamic Pressure Loading

This analysis only considers static loading. In reality, driver pressure loading on the piston is characterised by a very rapid ramping upwards of pressure loading acting on the front face of the piston, over a very short duration (of order 1 ms). Some preliminary dynamic analyses of ramped driver pressure loading using the ANSYS implicit solver indicated that peak stresses were, momentarily, approximately double those calculated by static analysis. However, these stresses had a duration in the order of microseconds and therefore present a significantly different failure problem. Whilst this analysis has not accounted for this type of loading, two factors provide confidence that the current design is structurally safe:

1. The $2\times$ safety factor used to calculate ultimate loads, and the selection of conservative static material allowables, both provide a large margin of safety to accommodate the assumption of static loading.
2. Typically metals exhibit increased strength at very high strain rates. Referring to Johnson [131], below the recrystalline temperature of most metals and for large strains (0.05 to 0.5), the ratio of dynamic yield stress, σ_D , to static yield stress, σ_S , is approximately $1 < \sigma_A/\sigma_S < 2$; that is to say, low temperature metals typically demonstrate higher strength at high strain rates. At high temperatures, this ratio

increases significantly [131]. Whilst Aluminium is generally considered to have a relatively low strain sensitivity, it still demonstrates the same trend towards higher yield strength at high strain rates [132]. Therefore the higher material strength at high strain rates will at least partially compensate for higher transient stresses that may occur.

5.15 Fatigue

The piston has not been assessed for fatigue failure. Fatigue can be categorised as either high cycle or low cycle. High cycle fatigue is not applicable to this piston, since the number of loading cycles is relatively low (1000's of cycles at most). Low cycle fatigue, which involves loading approaching or exceeding the elastic limit of the piston material, is also not applicable since the piston peak stresses should not exceed approximately 50% of the yield stress allowable. The piston will be examined regularly during service to identify cracks or other evidence of damage. If evidence of fatigue cracking emerges, then more effort will be directed to determining the fatigue properties of the piston.

5.16 Operational Experience

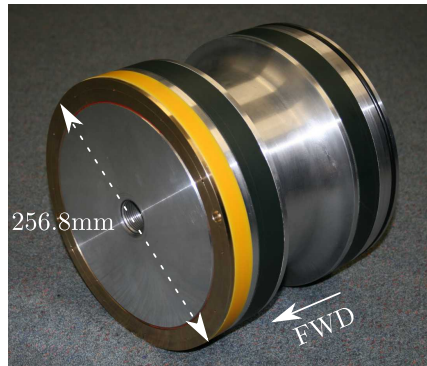
A piston was manufactured in accordance with the Appendix A drawing set. The final manufactured mass was 10.524 kg, which was approximately 1.5% lighter than the estimated mass. At the time of writing the piston had been used for over 300 shots, with a peak measured driver pressure of 40.49 MPa (shot x2s1344). Upon removal from the facility for inspection, there were no visible signs of damage or structural distress on the piston. Additionally, the piston has been operated to a peak reservoir pressure of 6.94 MPa with no pre-launch occurring, indicating that the piston is not deflecting excessively around the seals when subject to internal reservoir pressure loading.

5.17 Recommendations

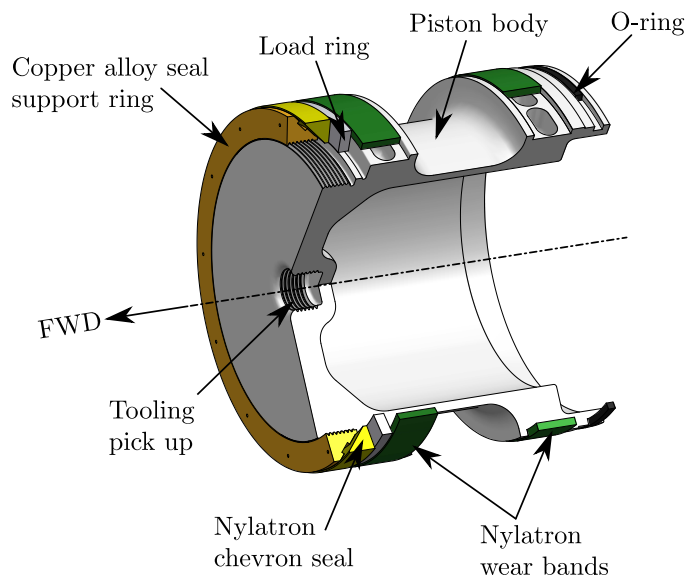
The primary limitation of the present analysis is the failure to accurately quantify and assess the piston structural response to dynamic loading, firstly from driver pressure loads, and secondly from impact of the piston into the buffer/tube end. Future work would involve developing analysis techniques using an explicit finite element solver to better understand the piston response to these applied loads. Such analyses would equally depend on obtaining accurate and representative material property data for high strain rate loading.



(a) Piston body, machined from 7075-T6 Aluminium. Note: material removal across piston skirt, and circumferential pocketing.



(b) Fully assembled piston.



(c) Cutaway view of piston assembly. Note: Ø190.0mm aft internal cavity which interfaces with piston launcher.

Figure 5.14: Newly manufactured piston, mass = 10.524 kg.

5.18 Conclusion

A new lightweight piston for X2 was designed and manufactured for use with tuned free-piston driver conditions. The new piston retains the interfacing geometry of the existing 35 kg piston, but has had significant amounts of mass removed where practical. The piston strength was assessed for two load cases: an 80 MPa ultimate pressure load applied to the front face of the piston to represent driver gas loading, and a 20 MPa reservoir pressure loading applied inside the piston to represent pressure loading when the piston is on the launcher. The piston was shown to have adequate strength to resist both load cases, which are $2\times$ design limit, and to also meet deflection requirements for the reservoir pressure load case.

The piston was not numerically assessed for impact or dynamic pressure loading. The design relies on avoiding piston impact into the end of the tube at high velocities. If this occurs, the tube will contain the piston, but the piston could potentially be irreparably damaged. It is noted that nylon studs have been used as the buffer for testing with this piston to date (see Section 6.10.3); the energy absorbing capability of the nylon buffer studs indicates that speeds of around ≈ 100 m/s would be survivable, so it would have to be a very major impact to cause piston failure. The $2\times$ safety factor applied in static analyses is expected to provide coverage against the higher transient stresses that may occur under the actual dynamic pressure loading conditions. Further, the piston material is expected to have higher strength at high strain rates, which will provide further protection against failure.

Initial service experience at driver pressures up to 100% of limit load indicates that the piston has sufficient strength to resist the maximum applied loading and to meet deflection requirements. It is recommended that future work should involve analysis of the piston response to dynamic pressure and impact loading using an explicit finite element code. Coupled with accurate material properties for high strain rate loading, this will provide a better understanding of the response of the piston to the applied loads, permitting a more optimised design in future.

Chapter 6

Commissioning of a New Lightweight Piston for X2

6.1 Chapter Overview

This chapter details the commissioning of a new 10.5 kg lightweight piston for X2. The lightweight piston was required in order to develop a tuned free-piston driver for use with high Mach number, high total pressure scramjet flow conditions. The chapter outlines the incremental approach which was used to develop new driver conditions. As a first step, feasible driver configurations were calculated using an analytical model based on Hornung’s free-piston driver equations of motion [124]. Driver configurations were then fine-tuned using the 1-D Lagrangian code L1d2 [113]. The reservoir loss factor in L1d2, which is very important in terms of establishing the correct reservoir fill pressure, was determined based on blanked-off driver tests (i.e. using a non-rupturing diaphragm). An iterative approach was adopted until good correlation was obtained between blanked-off driver experiments and L1d2, whereupon full experiments were performed using rupturing diaphragms. The new driver conditions were found to operate smoothly without causing damage to the facility, and were also shown to avoid the shock attenuation which had been a problem with the previous 35 kg free-piston driver configuration (see Section 4.2). Three new tuned driver conditions are presented based on 1.2, 2.0, and 2.5 mm thick steel primary diaphragms, corresponding to primary diaphragm rupture pressures of $p_4 = 15.5$, 27.9, and 35.7 MPa respectively.

6.2 Introduction

This chapter details the process used to develop a high performance tuned free-piston driver for X2 using a new lightweight (10.524 kg) piston. The lightweight piston was required in order to achieve ‘tuned’ piston dynamics [120, 124, 121], which typically

involve running the piston at comparatively high velocities around the period of diaphragm rupture. High piston speeds momentarily compensate for driver gas loss into the driven tube, and can significantly extend the period of time at which driver gas pressure is maintained at usefully high levels [120]. However, high piston speeds pose several challenges to safe driver operation, and require significantly different driver operational parameters, of which a lightweight piston is a key aspect.

The design of the piston is described in assembly drawing X2-LWP-001-1 (refer Appendix A). The piston stress analysis is presented in Chapter 5. The piston is functionally identical to the existing 35 kg piston which has previously been used in X2. A modification to the piston launcher was required to correctly seat the lightweight piston, however this does not affect ongoing use with the existing 35 kg piston.

The piston is rated to withstand the deceleration arising from a 40 MPa driver pressure load, as well as to resist, with negligible deformation, a 10 MPa reservoir pressure load when restrained on the X2 launcher (deformation must be minimal since leakage around the launcher D-ring seals could result in pre-launch). Stress analysis of the piston entailed applying a 2 \times safety factor to both of these loads (i.e. the piston was assessed with 80 MPa driver and 20 MPa reservoir pressure loads).

It is impractical to design a free-piston driver which survives a significant impact velocity of the piston into the end of the tube, therefore it is necessary to ensure that a soft landing condition is instead achieved. The structural response of the piston to impact loading against a typical X2 nitrile or polyurethane buffer has not been assessed. An appropriately sized buffer comprised of nylon studs can prevent damage to an aluminium piston for impact speeds up to approximately 100 m/s, however such impact speeds are undesirable for several reasons: the machine and piston will be highly loaded by the impact; the studs will be plastically deformed and it is likely that nylon fragments will be sent down the tube; full buffer replacement will be required after each shot.

The purpose of this chapter is to detail the process used to safely develop tuned driver conditions with the new lightweight piston. The final goal was to achieve safe, repeatable, high performance (i.e. high compression ratio, high sound speed, long duration) driver conditions for use with high total pressure flow conditions.

6.3 Target Performance for New Tuned Driver

6.3.1 Required Shock Strength

The original motivation to develop a tuned driver for X2 was the previous failure to achieve required shock speeds for the Mach 13 flow condition discussed in Section 4.2. The nominal driver performance targeted for the new tuned driver was therefore the

capacity to achieve the basic shock strength of the existing 35 kg piston, 100% helium, X2 driver condition, except with sufficiently increased driver gas supply duration to prevent shock attenuation characteristic of early driver pressure loss. For reference, the nominal driver configuration is outlined in Table 6.1. This shall henceforth be referred to as the X2 35 kg piston driver condition; characteristically similar driver conditions shall be referred to as heavy piston driver conditions.

Reservoir fill pressure, $p_A = 1.1 \text{ MPa}$
Driver fill pressure, $p_{4,0} = 30 \text{ kPa}$
Primary diaphragm rupture pressure, $p_r = 15.5 \text{ MPa}$
Compression ratio at rupture, $\lambda_r = 42.5 [-]$
Driver gas composition, 100% helium
Piston mass, 35 kg

Table 6.1: Nominal X2 free-piston driver configuration.

For X2's relatively short (4.5 m) compression tube, two characteristics of a tuned driver condition will generally differ from a heavy piston driver condition:

1. The driver gas sound speed typically needs to be reduced via the addition of argon in order to slow the rate of mass flow to the driven tube, thereby reducing the piston velocity required to match this mass flow rate; refer Section 4.3.
2. For a given primary diaphragm rupture pressure, a lower compression ratio is used in order to increase the volume of the driver gas slug at around the time of diaphragm rupture. This increases the distance available to decelerate the high velocity piston if direct impact into the end of the compression tube is to be avoided (see Figure 4.9c).

Both of these factors reduce the sound speed of the driver gas at rupture, thereby reducing the shock strength for a given diaphragm rupture pressure. In order to restore the performance of the tuned driver, it is necessary to operate at higher rupture pressures.

For a tuned condition the driver gas at the time of rupture typically has a significantly lower temperature due to the characteristically lower compression ratios used. Additionally, the piston compression process for tuned operation with a lightweight piston occurs over a comparatively shorter duration. These two factors will result in proportionally less heat loss from the driver as compared to the slow compression to higher temperatures for the heavy piston driver. The tuned driver is therefore likely to operate more closely to its theoretically ideal level as compared to the high compression ratio, heavy piston driver conditions, which potentially have significantly greater heat loss.

With nominal target performance levels based on the X2 35 kg piston driver condition, it is still desirable to develop a range of different driver performance levels. This expands

the facility operational envelope. For this reason, a range of different tuned conditions was investigated based on different diaphragm thicknesses. Three conditions were developed for this study, however future work may seek to broaden this range of available conditions in the longer term.

6.3.2 Over-Drive and Driver Gas Useful Supply Duration

The over-drive parameter β , referred to previously in Section 4.3.1, was selected such that driver pressure would not increase by more than 10% following diaphragm rupture. The driver gas useful supply time was defined as the period of time between diaphragm rupture and the moment when driver pressure had dropped to 90% of the diaphragm rupture pressure; refer Figure 4.7. For the purpose of examining trend behaviour, preliminary study with the analytical model (see Section 6.7) targeted over-pressure ratios up to 1.20, however these were not intended for implementation in actual testing.

6.3.3 Target Condition: Piston Soft Landing

In order to prevent damage to the facility, it is necessary to configure the free-piston driver such that the piston does not hit the buffer at the end of the compression tube with any significant velocity. In this context significant velocity implies speeds in excess of 5 – 10 m/s. A simple rubber buffer will typically disintegrate above these speeds, and if additional kinetic energy remains following disintegration of the buffer, the result may be significant damage to the piston and to the facility. Nylon studs can be configured to prevent damage to the aluminium piston at impact speeds up to approximately 100 m/s, however the nylon studs will be destroyed by such an impact. For this reason the soft landing condition previously defined in Section 4.3.2 was selected as the target piston response for this study. This involves firstly developing a condition whereby the piston motion has an ‘inflection point’ as described in Figure 4.9, and then sizing a buffer to catch the piston at this inflection point.

Note: it is possible to incorporate brakes in a piston to prevent it from being pushed back upstream, which can occur if the driver pressure remains high after the piston has initially decelerated to rest. Eventually the driver pressure vents, and the large residual reservoir pressure will re-accelerate the piston towards the downstream end of the tube. At this point most of the driver gas will have vented to the driven tube, and the driver pressure will be insufficient to provide a significant resisting force to the piston. Under these circumstances, the piston can hit the end of the tube with a high velocity, causing significant damage. This behaviour is referred to as a ‘rebound’ motion, and was explained previously schematically in Figure 4.9a.

The purpose of brakes is to prevent this rebound motion, thus significantly broadening the range of operating conditions for which the piston can be used. For the X2 lightweight

piston, brakes were not used for two reasons: firstly, the piston is compact, and brakes would have been difficult to incorporate, would have added to the weight of the piston, and would have increased the complexity of the stress analysis; secondly, X2's piston is reloaded by pushing it back up the compression tube, and brakes could have made this process difficult and possibly even impractical.

6.3.4 Buffer Length

The Itoh et al. [121] soft landing criteria (refer Figure 4.9b) indicates that buffer length should be varied such that the upstream edge of the buffer meets the downstream face of the piston when the piston is located at its inflection point. However, since the buffer also serves the function of absorbing impact energy of the piston, it cannot be made too short. For this analysis, 50 mm was selected as the minimum approximate buffer length, which also happens to be the approximate length of the buffer used with the X2 35 kg piston driver condition.

It is noted that the detailed buffer design, including material selection, is not made at this preliminary stage. The buffer design is refined once the driver condition is ready to be experimentally assessed; for detailed buffer sizing relating to this investigation see Section 6.10.3.

6.4 X2 Driver Description

The L1d2 representation of the X2 driver geometry is described in Figure 6.1 and Table 6.2. This geometry was also used for the analytical model detailed in Section 6.7. Reservoir and driver volume calculations are shown in Table 6.2. This geometry is a fairly representative 2-D approximation of the actual driver geometry. The primary deviations from the actual geometry are as follows:

1. Driver area change: the area change in the actual geometry is discrete (occurs across a single streamwise plane). However, area changes cannot be discontinuous with L1d2, and are therefore modelled gradually as shown in Figure 6.1.
2. The buffer, which is not accounted for in the L1d2 model, is located in the driver space and occupies a significant proportion of the driver gas volume when the piston is towards the end of its stroke, around the moment of diaphragm rupture. The presence of the buffer in the physical machine can be accounted for after the L1d2 simulation is completed, for example, when required buffer length is calculated from L1d2 results; see Section 6.10.3.
3. Piston launcher: with X2, reservoir gas must pass through an area change and also through a slotted launcher (refer Figure 6.2). Pressure loss through this

convoluted 3-D flow path is accounted for in L1d2 by using a loss factor; this is discussed further in Section 6.6.

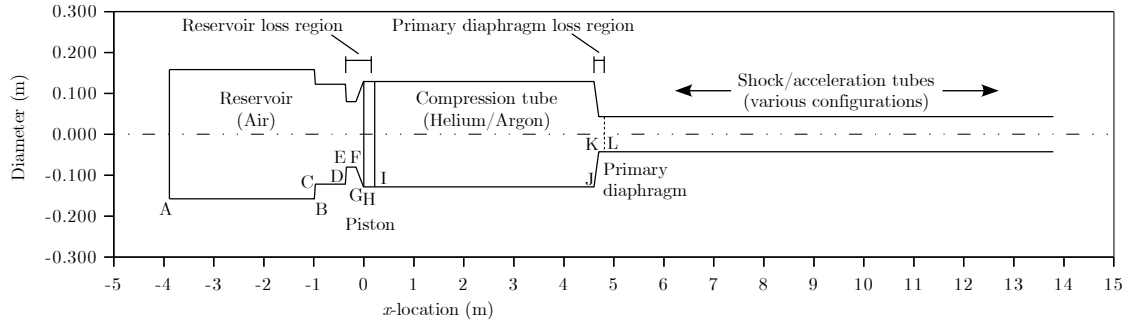


Figure 6.1: Assumed tube configuration for L1d2 analyses of X2. $x = 0$ corresponds to the upstream face of the piston.

ID	x-location (m)	Diameter (m)	Comment	Volume (m ³)
A	-3.890	0.316	Start of reservoir	Segment Total
B	-0.990	0.316		0.2274
C	-0.970	0.244		0.0012
D	-0.370	0.244		0.0281
E	-0.350	0.160		0.0007
F	-0.157	0.160		0.0039
G	-0.010	0.257		0.0051 Reservoir volume: $\Sigma = 0.2669 \text{ m}^3$
H	0.000	0.257	End of reservoir / start of piston	0.0005
I	0.221	0.257	End of piston / start of compression tube	
J	4.600	0.257		0.2268
K	4.700	0.085	Beginning of area change	0.0025 Compression tube volume: $\Sigma = 0.2299 \text{ m}^3$
L	4.810	0.085	Primary diaphragm	0.0006
Length of reservoir (LH wall to piston rear face):				3.890 m
Length of compression tube (piston RH face to primary diaphragm):				4.589 m

Table 6.2: X2 L1d2 geometry details (refer Figure 6.1 for location ID's). $x = 0$ corresponds to the upstream face of the piston.

6.5 X2 Driver Design Variables

There are practically limitless combinations of parameters which will lead to tuned operation of a free-piston driver, but several design constraints reduce the design space to a more manageable scale:

1. Piston mass: minimum piston mass is limited by structural and interface requirements. For initial analytical calculations the piston mass was assumed to be 10.683 kg in accordance with drawing X2-LWP-001-1; the final manufactured assembly mass was later measured to be 10.524 kg per Chapter 5; this lower final mass was used for all subsequent L1d2 simulations.



Figure 6.2: Piston launcher for X2 (shown detached from tunnel; downstream face is prominent). Note: the launcher inserts into the piston; reservoir gas must channel through the slots in the launcher, with potentially significant total pressure losses to the flow.

2. Driver pressure: the compression tube is limited by the magnitude of pressure it can structurally contain (40 MPa for X2).
3. Reservoir pressure: the reservoir fill pressure, which accelerates the piston down the compression tube, is limited by reservoir structural strength (hydraulic testing of X2's reservoir was undertaken to certify its maximum pressure rating to 8 MPa in order to permit operation of these driver conditions [118], however it has been designed for 10 MPa and will be re-rated accordingly at a future date).
4. Compression tube length and diameter: there is significant expense involved with changing the fundamental configuration of the facility, therefore compression tube geometry was assumed to be fixed.

Several variables remained available for driver condition design:

1. Reservoir fill pressure (0 to 8 MPa).
2. Driver fill pressure (<1 MPa).
3. Driver gas composition (helium and argon). The required piston speed for tuned operation depends on the speed of sound of the compressed driver gas. Reducing the sound speed (through the addition of argon to helium), reduces the required piston speed, however shock strength is also reduced; see Section 3.4.

4. Primary diaphragm thickness and material. In this study, diaphragm thickness was limited to 1.2, 2.0 and 2.5 mm thick, cold-rolled steel sheet. Each was pre-scored to 0.2 mm depth. Experimental testing has previously been used to determine the rupture pressure of the pre-scored 1.2 mm thick diaphragms (15.5 MPa); rupture pressures for the 2.0 and 2.5 mm thick scored diaphragms were estimated to be 27.9 and 35.7 MPa, respectively, by interpolation based on relative scored thicknesses.
5. Compression ratio. Reducing the compression ratio also reduces the required piston speed, since the driver gas is at a lower temperature when the diaphragm ruptures. However, a low compression ratio increases the amount of compressive work done to the driver gas, which is limited by driver performance restrictions.
6. Buffer length (the distance from the extreme end of the tube to the location where the piston makes contact with the buffer).

6.6 Tuned Driver Condition General Design Process

The process used to develop new driver conditions is outlined in Figure 6.3. The first step was to develop a rapidly solved perfect gas analytical model of the free-piston compression process. The piston equations of motion were obtained from Hornung [124] and used to predict piston motion and driver pressure before and after diaphragm rupture. The analytical model, described in Section 6.7, was used to manually identify a range of potential tuned driver solutions. The computational time was sufficiently small that each solution could be quickly identified.

Whilst the 0-D model proved capable of modelling the driver compression process fairly effectively, it could not make an accurate prediction of the required reservoir gas fill pressure. The reservoir gas expansion process was assumed to be an ideal unsteady expansion as shown in Figure 4.6b. With X2, reservoir gas must pass through an area change and also through a slotted launcher (refer Figure 6.2). This convoluted flow path has the effect of throttling the expansion process, significantly reducing the strength of the reservoir pressure force eventually acting on the piston. Further, X2's reservoir has finite length, and the unsteady expansion through the reservoir eventually reflects from the upstream end and causes a further pressure drop. Both of these factors necessitate a much better predictive tool for the reservoir gas flow.

L1d2 was used to fine tune the free-piston driver configuration prior to any experimental testing. The code is capable of capturing the longitudinal unsteady wave processes which occur during piston operation and includes piston friction, flow chemistry, and pipe-flow viscous effects along the tube walls. Gradual area changes can be handled by the code, however 3-D physical processes, such as flow through the launcher, cannot be directly

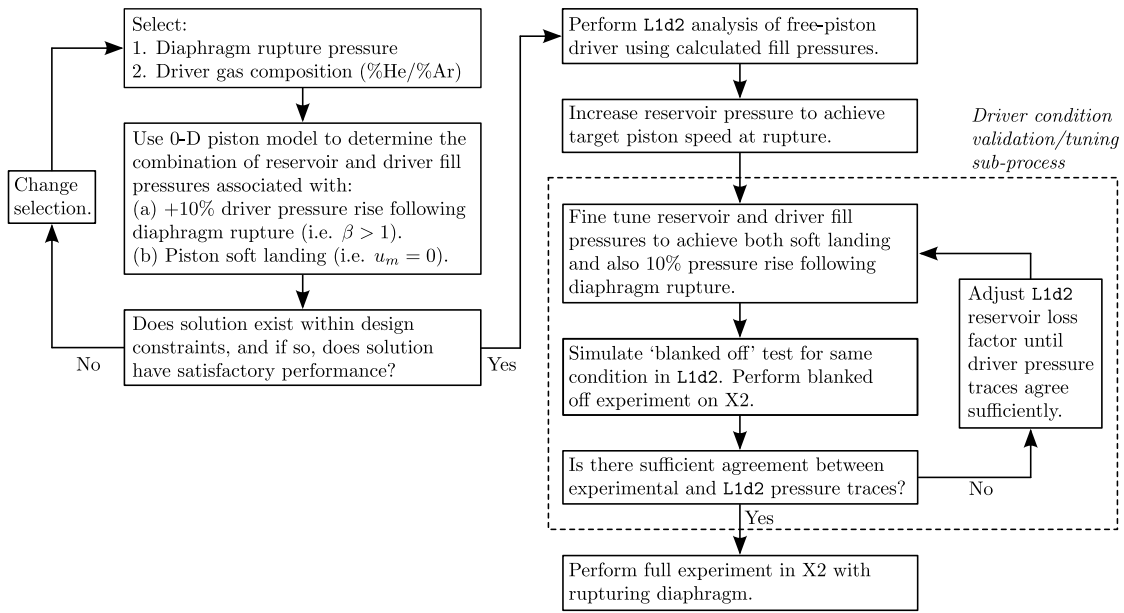


Figure 6.3: X2 free-piston driver condition development process.

modelled. To simulate the effect of these complex flow paths, L1d2 uses loss regions, which apply a loss factor over a finite length of the tube where an area contraction etc. is present. Representative loss factors can only be determined from experimental data, therefore development of loss factors must occur in conjunction with experimental testing. There is no guarantee that a loss region will model a disturbed flow region with useful accuracy; however, ongoing experience indicates that the modelling tool is quite effective once tuned for a given test condition. A more detailed explanation of L1d2 loss regions is presented in Section 8.4. Reservoir and primary diaphragm loss regions are identified on the L1d2 driver geometry shown in Figure 6.1.

Considering the X2 35 kg piston driver, the driver has been configured such that the amount of reservoir gas energy imparted to the piston is only a little greater than that required to rupture the steel diaphragm; for example, if the reservoir fill pressure is lowered by 10-20%, the piston will not have enough energy to raise driver pressure to the diaphragm rupture pressure, therefore the diaphragm will not rupture. The result is that during normal operation the piston does not have significant energy following diaphragm rupture. Further, since the piston is heavy, this energy is not associated with a high velocity, therefore the risk of significant impact velocities into the end of the compression tube are low.

A key characteristic which differentiates tuned free-piston driver operation with the lightweight piston is that the piston is given significantly greater energy than that which is required to break the diaphragm, since it must also have sufficient energy to continue

to push driver gas through the throat of the driver, at full pressure, *after* the diaphragm has broken. The lightweight tuned piston has to be accelerated to much higher velocities, be decelerated over a very short distance, and has significantly greater energy than that required to rupture the diaphragm. The risk of facility damage due to uncertainties in the analysis are much greater, therefore predictive tools must be as accurate as possible. To achieve this accuracy with L1d2, a series of blanked-off driver tests was performed.

A blanked-off driver test involves operating a free-piston driver condition using a stiff, non-rupturing diaphragm, typically manufactured from thick steel. For this commissioning process, a PCB pressure transducer was located in the diaphragm, so that driver pressure could be measured during the piston compression process. During a blanked-off driver test the piston bounces back and forth until it comes to rest. So long as the driver pressure does not exceed the facility or piston pressure limits, no damage will be done to either. A corresponding analysis can be performed with L1d2. The L1d2 model is then tuned, primarily by applying and adjusting loss factors, until an acceptable level of correlation is obtained between the experimental and numerical pressure traces.

This validation methodology is very effective, since it allows full correlation of the driver pressure trace right up until the moment when the diaphragm rupture pressure is reached. At this point with a normal experiment, the diaphragm would then rupture, initiating shock tube flow. If strong agreement can be obtained with the blanked-off driver tests, then it increases confidence that the post-diaphragm rupture piston dynamics will also be predicted with good accuracy.

Once blanked-off driver tests had satisfactorily demonstrated the performance of the L1d2 model, the full diaphragm rupturing experiment could finally be performed. This design process eventually yielded three driver configurations which were considered to be feasible and which are summarised in Table 6.7. The three conditions each used an 80% helium / 20% argon driver gas mix. The primary feature characterising the three conditions was the thickness of the cold-rolled steel diaphragm for each; 1.2 mm, 2.0 mm and 2.5 mm.

6.7 X2 Driver Analytical Model

6.7.1 Overview

An analytical model of X2 was created using MATLAB to provide a rapidly solved tool to predict piston motion before and after diaphragm rupture. The model was based on the free-piston driver equations of motion developed by Hornung [124], which are now detailed in the present section. An initial validation of the model was performed by first nominating some arbitrary but representative test conditions, and comparing

analytically calculated solutions with those from an equivalent model developed using the 1-D CFD code L1d2 [113]. Unless otherwise noted, all equations and the methodology in this section are taken from Hornung [124]. Ideal gases are assumed. Relevant piston dynamics parameters which are referred to in this section are shown in Figure 4.6 of Chapter 4. The piston is initially a distance L from the end of the compression tube; the varying magnitude of this distance is denoted by x .

6.7.2 Piston Motion Before Diaphragm Rupture

Per Figure 4.6, the piston is initially at rest, held in place on the launcher. Upon release, the large reservoir pressure force accelerates the piston, simultaneously beginning the compression of the driver gas. The reservoir air behind the piston is expanded through an unsteady expansion, from stagnant conditions up to the piston velocity, u . The pressure of this expanded reservoir gas, which acts on the upstream surfaces of the piston, is as follows:

$$p_A = p_{A,0} \left[1 - \left(\frac{\gamma_A - 1}{2} \right) \frac{u}{a_{A,0}} \right]^{\frac{2\gamma_A}{\gamma_A - 1}} = p_{A,0} \left[1 + \left(\frac{\gamma_A - 1}{2} \right) \frac{1}{a_{A,0}} \frac{dx}{dt} \right]^{\frac{2\gamma_A}{\gamma_A - 1}} \quad (6.1)$$

Assuming steady isentropic compression of the driver gas, pressure on the downstream face of the piston is a function of piston position only:

$$p_D = p_{D,0} \left(\frac{L}{x} \right)^{\gamma_D} \quad (6.2)$$

Summing forces across the piston, the equation of motion for the piston can be determined:

$$-M \frac{d^2x}{dt^2} = (p_A - p_D) \frac{\pi D^2}{4} \quad (6.3)$$

Substituting Equations 6.1 and 6.2 into 6.3, and rearranging:

$$\frac{d^2x}{dt^2} = -\frac{\pi D^2}{4M} \left\{ p_{A,0} \left[1 + \frac{1}{a_{A,0}} \left(\frac{\gamma_A - 1}{2} \right) \frac{dx}{dt} \right]^{\frac{2\gamma_A}{\gamma_A - 1}} - p_{D,0} \left(\frac{L}{x} \right)^{\gamma_D} \right\} \quad (6.4)$$

The time variable response of the piston is easily solved numerically using Equation 6.4 for the following initial conditions:

$$x(0) = L \quad (6.5)$$

$$\frac{dx}{dt}(0) = 0 \quad (6.6)$$

Equation 6.4 is based on several simplifying assumptions. These are considered below:

1. *Assumption: the reservoir is a constant diameter which is equal to the compression tube diameter.* For X2 the reservoir is actually larger diameter than the compression tube. Additionally, flow of reservoir gas is effectively throttled through the slotted piston launcher; refer Figure 6.2. The effect of this throttling is to cause a total pressure loss resulting in a reduction in the pressure force acting on the upstream surfaces of the piston.
2. *Assumption: the reservoir is sufficiently long that the unsteady expansion does not reflect from the upstream end prior to critical flow processes completing.* Analysis with L1d2 indicates that for many potential X2 driver configurations the unsteady expansion can reach the upstream end of the reservoir before critical flow processes have completed, which will result in a reduction in the reservoir pressure force acting on the piston.
3. *Assumption: the driver gas compression process is isentropic and steady.* The piston compresses the driver gas through a series of continuous compression waves which travel back and forth through the driver gas. This results in unsteady driver pressure and therefore unsteady piston acceleration.
4. *Assumption: the piston is continually accelerating in the downstream direction up until diaphragm rupture.* In reality, prior to diaphragm rupture there is a period when the driver gas pressure force exceeds the reservoir pressure force, and the piston begins to decelerate. During this period the piston imparts its kinetic energy into the driver gas, eventually raising the driver gas pressure to its rupture pressure. The velocity of the reservoir gas immediately adjacent to the upstream surfaces of the piston must match the piston velocity. Therefore, as the piston decelerates, it transmits compression waves into the reservoir gas. The reservoir gas applies a corresponding inertia force to the piston. This inertia force is neglected, and therefore the reservoir pressure force is under-predicted during the piston deceleration phase prior to diaphragm rupture. At this stage of the piston stroke the piston dynamics is dominated by the driver pressure, therefore the effect of this approximation is small.

The above factors do not negate the value of this analytical predictive tool for determining an approximate set of favourable driver conditions from the unlimited possible permutations. However, these considerations do indicate the benefit, at a subsequent stage in the analysis, in undertaking a more detailed analysis of the driver response using the L1d2 numerical solver, which better represents these important phenomena.

6.7.3 Piston Motion After Diaphragm Rupture

For typical driver configurations, the piston is decelerating at the moment of diaphragm rupture. As discussed in Section 6.7.2, a series of compression waves are transmitted into

the expanded reservoir gas in order to slow it to the corresponding piston speed. These compression waves converge into shocks of increasing strength. Hornung [124] introduces this effect at the moment of diaphragm rupture. Hornung assumes that a single reflected shock is generated upstream of the piston which has exactly the strength required to fully stagnate the reservoir gas from its velocity at the moment the diaphragm ruptures. The pressure of this shock-processed reservoir gas is assumed to act on the upstream surfaces of the piston for the remainder of the piston stroke. Noting that the ratio $u_r/a_{A,0}$ will be known from the final calculation prior to diaphragm rupture, and the generated shock Mach number can be calculated by solving the following equation given by Hornung [124]:

$$M_R^2 - \frac{(\gamma_A + 1)(u_r/a_{A,0})}{2 + (\gamma_A - 1)(u_r/a_{A,0})} M_R - 1 = 0 \quad (6.7)$$

$$\rightarrow M_R = \frac{(\gamma_A + 1)(u_r/a_{A,0})}{4 + 2(\gamma_A - 1)(u_r/a_{A,0})} + \left\{ \frac{1}{4} \left[\frac{(\gamma_A + 1)(u_r/a_{A,0})}{2 + (\gamma_A - 1)(u_r/a_{A,0})} \right]^2 + 1 \right\}^{\frac{1}{2}} \quad (6.8)$$

The pressure of reservoir gas which has been processed by the shock is then given by Hornung [124] based on normal shock relations. This pressure force is assumed to act on the upstream surfaces of the piston for the entire period of time following diaphragm rupture.

$$p_{A,R} = p_{A,0} \left[1 - \left(\frac{\gamma_A - 1}{2} \right) \frac{u_r}{a_{A,0}} \right]^{\frac{2\gamma_A}{\gamma_A - 1}} \left[1 + \frac{2\gamma_A}{\gamma_A + 1} (M_R^2 - 1) \right] \quad (6.9)$$

Considering the driver gas downstream of the piston, it is assumed that the pressure is sufficiently high to produce choked (sonic) flow across the area change into the driven tube. This assumption relies on the area ratio being sufficiently large, which is an appropriate assumption for the X2 driver (with area ratio exceeding 9:1). For sonic flow of driver gas into the driven tube:

$$\rho_* a_* A_* = \rho_* a_* A_* \frac{\rho_D a_D A}{\rho_D a_D A} = \frac{\rho_*}{\rho_D} \frac{\sqrt{\gamma_* R_* T_*}}{\sqrt{\gamma_D R_D T_D}} \frac{A_*}{A} \rho_D a_D A = \frac{\rho_*}{\rho_D} \left(\frac{T_*}{T_D} \right)^{\frac{1}{2}} \frac{A_*}{A} \rho_D a_D A \quad (6.10)$$

Assuming that the piston is moving at low subsonic speeds into the driver gas, stagnated flow properties can be assumed to equal static flow properties:

$$\frac{\rho_{D,0}}{\rho_*} \approx \frac{\rho_D}{\rho_*} = \left(\frac{\gamma_D + 1}{2} \right)^{1/(\gamma_D - 1)} \quad (6.11)$$

$$\frac{T_{D,0}}{T_*} \approx \frac{T_D}{T_*} = \left(\frac{\gamma_D + 1}{2} \right) \quad (6.12)$$

Substituting Equations 6.11 and 6.12 into 6.10, and equating the result to mass flow lost from the driver:

$$\frac{dm}{dt} = -\rho_* a_* A_* = -\left(\frac{2}{\gamma_D + 1}\right)^{\frac{\gamma_D + 1}{2(\gamma_D - 1)}} A_* \rho_D a_D \quad (6.13)$$

$$\rightarrow \frac{dm}{dt} = -\left(\frac{2}{\gamma_D + 1}\right)^{\frac{\gamma_D + 1}{2(\gamma_D - 1)}} \frac{\pi d^2}{4} \frac{p_D}{R_D T_D} \sqrt{\gamma_D R_D T_D} \quad (6.14)$$

The following isentropic relation is assumed:

$$\frac{p_D}{p_{D,r}} = \left(\frac{\rho_D}{\rho_{D,r}}\right)^{\gamma_D} \quad (6.15)$$

The density of the driver gas can be related to the total mass of gas in the compression tube both generally (Equation 6.16), and at the moment of diaphragm rupture (Equation 6.17):

$$\rho_D = \frac{4m}{\pi D^2 x} \quad (6.16)$$

$$\rho_{D,r} = \frac{4m_r}{\pi D^2 x_r} \quad (6.17)$$

Substituting Equations 6.16 and 6.17 into 6.15:

$$\frac{p_D}{p_{D,r}} = \left(\frac{x_r}{m_r}\right)^{\gamma_D} \left(\frac{m}{x}\right)^{\gamma_D} \quad (6.18)$$

Substituting Equation 6.18 into 6.14, an expression for driver gas mass flow rate after diaphragm rupture is obtained:

$$\frac{dm}{dt} = -\frac{\sqrt{\pi \gamma_D}}{2} \left(\frac{2}{\gamma_D + 1}\right)^{\frac{\gamma_D + 1}{2(\gamma_D - 1)}} \frac{d^2}{D^2} \sqrt{p_{D,r}} \left(\frac{x_r}{m_r}\right)^{\frac{\gamma_D}{2}} \left(\frac{m}{x}\right)^{\frac{\gamma_D + 1}{2}} \quad (6.19)$$

With expressions for pressures on both sides of the piston now derived, summing forces across the piston yields the equation of motion for the piston after diaphragm rupture:

$$M \frac{d^2 x}{dt^2} = (p_D - p_{A,R}) \frac{\pi D^2}{4} \quad (6.20)$$

Substituting Equation 6.18 into 6.20, and rearranging:

$$\frac{d^2 x}{dt^2} = \left[p_{D,r} \left(\frac{x_r}{m_r}\right)^{\gamma_D} \left(\frac{m}{x}\right)^{\gamma_D} - p_{A,R} \right] \frac{\pi D^2}{4M} \quad (6.21)$$

Equations 6.19 and 6.21 can be solved numerically to yield an estimate of piston motion after diaphragm rupture. The initial conditions for the solution directly follow from

calculated properties at the moment of diaphragm rupture. Once again, the equations make several assumptions which affect the accuracy of the solution:

1. *Assumption: the piston is moving significantly slower than the speed of sound of the driver gas.* This assumption is acceptable where helium is the driver gas, although it becomes less reliable if the driver gas sound speed is reduced significantly by the addition of argon.
2. *Assumption: the reservoir pressure acting on the upstream surfaces of the piston can be calculated by assuming that a single shock is reflected from the piston.* This assumption does not account for the time-variable change in the reservoir pressure, nor the effect of the piston accelerating forward again if the driver pressure drops sufficiently, nor the fixed length and 2D geometry of the driver configuration.
3. *Assumption: flow into the driven tube remains sonic.* This assumes that there is sufficient pressure difference between the compression tube and the smaller diameter driven tube to sustain sonic flow. This assumption is reasonable for the period up until the driver pressure drops significantly.

6.7.4 Model Validation

The CFD code L1d2 was used to validate the analytical model described in this chapter. The L1d2 model geometry was based on the analytical model so that, where possible, it was subject to the same assumptions. All options in L1d2 were set to ideal cases (no piston friction, no viscous effects, the diaphragm was located directly at the area change, etc). The reservoir was modelled as sufficiently long to delay the reflection of the unsteady expansion from the upstream end, thereby preventing this reflected wave from affecting critical flow processes. The geometry for this validation L1d2 model was different to the more representative L1d2 model outlined in Figure 6.1; the purpose was simply to check the results from the analytical model.

Assumed geometric features and ideal gas properties are outlined in Table 6.3. An assumed length, fill gas type, and fill pressure, were specified for the driven tube, and the downstream edge was modelled as a free end. This was to enable calculations in L1d2 following diaphragm rupture; the same information was not required for the analytical model.

A total of seven models were analysed, as outlined in Table 6.4. Calculations were performed for the analytical and L1d2 models for seven arbitrary but representative conditions. Results from the seven models are presented in Appendix D. It can be seen in Appendix D that piston velocity vs. position along the compression tube is modelled well by the analytical solver compared to L1d2. L1d2 predicts a slightly slower piston response as the deceleration begins. Several reasons have been identified for this:

Piston mass, $m_p = 10.683$ m
Piston length, $L_p = 0.221$ m
Diameter of driver tube, $D_{drv} = 0.2568$ m
Diameter of shock tube, $D_{shk} = 0.085$ m
Compression tube length, $L_{drv} = 4.469$ m
Assumed reservoir tube length (L1d2 only), $L_{res} = 5$ m
Assumed reservoir tube fill gas (L1d2 only), 100% Air
Assumed reservoir diameter (L1d2 only), $D_{res} = 0.2568$ m
Assumed buffer width, $w_{buf} = 0.075$ m
Assumed shock tube length (L1d2 only), $L_{shk} = 5$ m
Assumed shock tube fill gas (L1d2 only), 100% Air
Assumed shock tube fill pressure (L1d2 only), 10 kPa
Ratio of specific heats for Air, $\gamma_{Air} = 1.4$
Ratio of specific heats for Helium, $\gamma_{He} = 1.667$
Ratio of specific heats for Argon, $\gamma_{Ar} = 1.667$
Specific gas constant for Air, $R_{Air} = 287$ J/(kg.K)
Specific gas constant for Helium, $R_{He} = 2077$ J/(kg.K)
Specific gas constant for Argon, $R_{Ar} = 208$ J/(kg.K)

Table 6.3: X2 simplified model parameters.

Run ID [-]	p_{res} [MPa]	p_{drv} [kPa]	p_{rupt} [MPa]	He [%]	Ar [%]	Comments [-]
1	1.5	30	15	100	0	Arbitrary case, high sound speed, low velocity
2	1.5	30	15	90	10	Arbitrary case, medium sound speed, low velocity
3	1.5	30	15	0	100	Arbitrary case, low sound speed, low velocity
4	7.0	100	30	100	0	Arbitrary case, high sound speed, high velocity
5	7.0	100	30	90	10	Arbitrary case, medium sound speed, high velocity
6	7.0	100	30	0	100	Arbitrary case, low sound speed, high velocity
7	8.6	269	35.65	90	10	Sample optimised case, medium sound speed, high velocity

Table 6.4: X2 Hornung/L1d2 comparison cases.

- Driver gas compression process: the analytical model assumes that the driver gas compresses isentropically and steadily. However, where the piston is moving very quickly, the action of compression waves travelling back and forth across the driver volume becomes significant. Considering Case 1 as an example (refer Figure D.3), where the piston speed is comparatively slower and the driver gas has a high speed of sound, the behaviour of the compression waves does not significantly impact on the compression process, and the analytical and L1d2 models correlate well.

However, considering Case 6 (refer Figure D.6), where piston speed is high, and the 100% argon driver gas has a slow sound speed, strong compression waves in the driver gas are evident. The result is significantly poorer correlation between the analytical and L1d2 models. Figure 6.4 shows how the normalised entropy increases across a shock wave, as a function of pressure ratio across the shock. If the compression waves through the driver are assumed to be shock waves, it can be seen that for $p_2/p_1 < 2$ the entropy rise is minimal. Considering that a full high speed

piston stroke will only involve the driver gas being processed by a limited number of shocks, then it is reasonable to assume the compression process is isentropic for $p_2/p_1 < 2$. By inspection, for Case 6 (Figure D.6) $p_2/p_1 > 2$, therefore assuming an isentropic compression in this instance may be problematic. Fortunately such a configuration is unlikely to be used in practise, however the above discussion helps to explain the difference between analytical and L1d2 predictions for some of the cases considered.

2. Reservoir gas expansion process: the analytical model assumes that the reservoir gas can be modelled with an unsteady expansion until diaphragm rupture. Between the moment the piston starts to decelerate, and the point of diaphragm rupture, this assumption neglects the inertial effect of expanded reservoir gas piling into the upstream face of the decelerating piston, thus underestimating the reservoir gas pressure force. After diaphragm rupture, a single reverse shock is assumed to arise from the upstream face of the piston, stagnating the expanded reservoir gas as if the piston was stopped instantly. This assumption overestimates reservoir gas force.

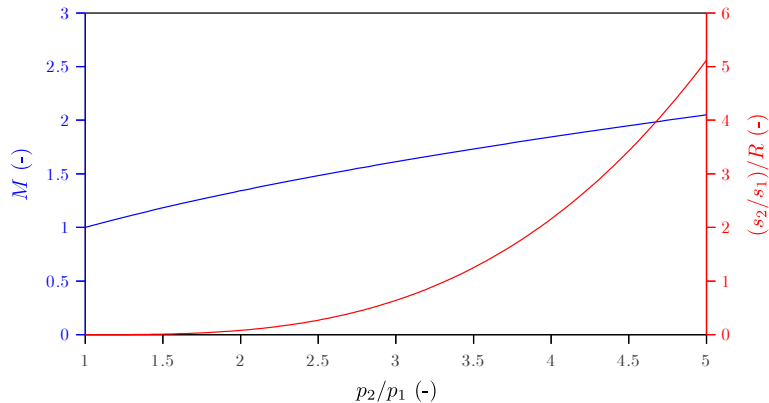


Figure 6.4: Entropy rise across a shock in helium/argon driver gas (i.e. $\gamma = 5/3$). p_2/p_1 is the pressure ratio across the shock, M is the shock Mach number, and $(s_2 - s_1)/R$ is the normalised entropy rise. Calculations use the ideal gas shock relations $\frac{p_2}{p_1} = 1 + \frac{2\gamma}{(\gamma + 1)}(M_1^2 - 1)$ and $\frac{(s_2 - s_1)}{R} = \frac{2}{3} \frac{\gamma}{(\gamma + 1)^2} (M_1^2 - 1)^3$ from Anderson [55].

Considering the cases in Appendix D where piston speed is high, and/or a slow speed of sound driver gas has been used, the effects of these assumptions become more significant. Importantly, these models do not account for the finite length of the reservoir or pressure loss through the piston launcher. However, the analytical model still provides

potentially useful approximate predictions of the piston response, and is similarly useful for identifying driver parameters that are close to the optimum solution.

6.7.5 Analytically Calculated Tuned Driver Conditions

The MATLAB analytical model was used to calculate a series of driver conditions with varying levels of performance and operational severity. Driver configurations were differentiated in terms of the following parameters:

1. Primary diaphragm rupture pressure: 15.5 MPa (1.2 mm thick; 1.0 mm at score), 27.9 MPa (2.0 mm thick; 1.8 mm at score), and 35.7 MPa (2.5 mm thick; 2.3 mm at score).
2. Driver gas composition: 0% He/100% Ar, 80% He/20% Ar, 90% He/10% Ar, 95% He/5% Ar, and 100% He/0% Ar.
3. Over-pressure ratio: $p_{max}/p_r = 1.00, 1.05, 1.10$, and 1.20 .
4. Occurrence of an inflection point (simultaneous occurrence of $u = 0$ and $a = 0$).

Table 6.5 details all attempted combinations of the above parameters. For some parameter combinations a valid solution to the problem did not exist; these cases are marked ‘ \times ’.

%He	%Ar	p_r [MPa]	p_{max}/p_r			
			1.00	1.05	1.10	1.20
0	100	15.5	1	2	3	4
		27.9	5	6	7	8
		35.7	9	10	11	12
80	20	15.5	13	14	15	16
		27.9	17	18	19	20
		35.7	21	22	23	24
90	10	15.5	25	26	27	28
		27.9	29	30	31	32
		35.7	33	34	35	36
95	5	15.5	37	\times	\times	\times
		27.9	38	39	40	41
		35.7	42	43	44	45
100	0	15.5	\times	\times	\times	\times
		27.9	\times	\times	\times	\times
		35.7	\times	\times	\times	\times

Table 6.5: X2 driver configuration case ID's (' \times ' indicates no solution found).

The optimisation was performed manually, since attempts to implement a numerical solver proved to be inefficient and not particularly effective. Where diaphragm rupture pressure, driver gas composition, and over-pressure ratio (p_{max}/p_r) are pre-defined, and where an inflection point is desired, there is only one solution to piston speed which

will achieve these targets. Therefore, manually solving for the targeted conditions above was not difficult. The procedure for solving the condition was to select a representative driver fill pressure, and then increase reservoir pressure until diaphragm rupture and then over-driving were observed. Then driver and reservoir fill pressures were adjusted until an inflection point was achieved, whilst simultaneously achieving the target pressure variation after diaphragm rupture. Results of the analytical model study are shown in Table 6.6.

It is noted that X2 is rated for a maximum driver pressure of 40 MPa. Referring to Table 6.5, the maximum diaphragm thickness used is 2.5mm, which has an assumed burst pressure of 35.7 MPa. Since the tuned driver conditions attempt to ‘over-drive’ the piston, driver pressure can potentially continue to rise *after* diaphragm rupture. Assuming a 10% pressure rise after rupture, the 2.5 mm diaphragm will have a rupture pressure rising to approximately 40 MPa, which explains why this was the thickest diaphragm to be considered. An over-pressure ratio of $p_{max}/p_r = 1.2$ is also considered in Tables 6.5 and 6.6, which would drive the pressure above 40 MPa for the 2.5 mm diaphragm. However, this over-pressure ratio is only included in order to examine trends; this level of driver pressure variation is otherwise unacceptably large for normal flow condition simulation.

6.8 Condition Refinement with L1d2

6.8.1 General Approach

The results shown in Table 6.6 are applicable to a highly idealised driver model. The next step was to adapt these results to the more representative detailed L1d2 model of X2 (refer to Figure 6.1 and Table 6.2). This model, unlike that used for the validation analysis described in Section 6.7, attempts to capture the full response of the X2 driver.

It is already known that the idealised representation of the reservoir in the analytical model will underestimate the required reservoir pressure. This is because it does not capture the total pressure loss through the launcher, does not account for the finite length of the reservoir, and does not account for the detailed effects of compression of the reservoir gas behind the piston as it begins to decelerate towards the end of the piston stroke. These factors affect the final response of the piston significantly. Therefore, further detailed analysis was required with the L1d2 model in order to determine a driver configuration which was more likely to work.

It is not practical to apply numerical optimisation to fine tuning of the L1d2 model. Such a model would be difficult to set up, and would have to be expertly configured in order to identify a solution within a reasonable time frame. Therefore manual fine-tuning of

the L1d2 driver configurations was performed. The analytical model detailed in Section 6.7 was used to establish the starting point for this process, and fine tuning of the L1d2 model was then performed as follows:

1. Increase reservoir pressure until the target piston over-pressure ratio was obtained.
2. Adjust driver pressure to achieve an inflection point.
3. Repeat Steps 1 and 2 until a reasonable response was obtained.

Referring to Section 6.6 and Figure 6.1, the L1d2 X2 driver model incorporates a loss factor across the reservoir in order to capture the total pressure loss which occurs through the area change and slotted launcher. Prior to experimental testing of a given tuned condition, a blanked-off driver experiment was performed at that condition. A corresponding blanked-off driver L1d2 simulation was performed (achieved simply by re-running the simulation with such a high primary diaphragm rupture pressure that it would not rupture). Driver pressure from the experiment was compared to the L1d2 driver pressure. If the two traces did not correlate closely, the L1d2 model was re-run with different reservoir loss factors and the process repeated until the two traces matched.

By modifying the reservoir loss factor, the calculated L1d2 driver condition usually was no longer tuned. Therefore the reservoir and driver fill pressures were once more fine-tuned in L1d2 to achieve a tuned condition. Then another blanked-off driver experiment was performed, and the whole process repeated until the tuned driver condition had a corresponding blanked-off driver pressure trace which closely matched experiment. This process is referred to as the ‘Driver condition validation/tuning sub-process’, and is identified in Figure 6.3. It was found that the L1d2 lightweight piston tuned driver models required a reservoir loss factor of approximately 3, as compared to 0.7 for the L1d2 X2 35 kg piston driver model. These higher loss factors result from the high fill pressures and much faster reservoir flow for the tuned driver.

Only three of the cases from Table 6.6 were fully developed using L1d2 through to the full rupturing diaphragm experimental stage. Most of the cases in this table were not useful, primarily due to the following reasons:

1. *The inflection point was too close to the end of the tube:* Considering X2, the primary diaphragm is located upstream of the area change, therefore there is a volume of driver gas which resides downstream of the buffer. In some cases a theoretical solution from the analytical model was not practical for the actual X2 geometry because the driver gas volume was less than the volume of the small diameter section of tube upstream of the diaphragm (downstream of the area change); this implies that the theoretical inflection point exists downstream of the area change. In other cases the inflection point was theoretically located upstream

of the area change, but the distance L_m was impractically small, and therefore would leave no space for a sensibly sized buffer.

2. *The compression ratios were too low:* Many of the cases in Table 6.6 have a compression ratio, λ , too low to produce reasonable strength shocks, and therefore were not explored further.
3. *The reservoir fill pressures were excessive:* Many of the higher performance cases required reservoir pressures which are too high for application in X2.

Considering the above, the three driver conditions which were eventually developed are detailed in the next section. The blanked-off driver testing used to validate the L1d2 models prior to full experimental testing is detailed in Section 6.9

6.8.2 L1d2 Simulation Results

The tuned driver condition design process detailed in Sections 6.6 and 6.8.1 yielded three new tuned driver conditions. These conditions are detailed in Table 6.7.

Driver condition ID ID [–]	Piston mass [kg]	Diaphragm thickness ¹ [mm]	Rupture pressure [MPa]	Fill pressures			Buffer Length ² [mm]
				$p_{A,0}$ [MPa]	$p_{D,He,0}$ [kPa]	$p_{D,Ar,0}$ [kPa]	
LWP-1.2mm-Rev-0	10.524	1.2	15.5 ³	4.94	88.2	22.1	100
LWP-2.0mm-Rev-0	10.524	2.0	27.9 ⁴	6.85	74.3	18.5	45
LWP-2.5mm-Rev-0	10.524	2.5	35.7 ⁴	6.08	61.7	15.5	45

¹ Diaphragms are manufactured from cold-rolled steel and pre-scored to 0.2 mm depth.

² Buffer is comprised of 6 × 50 mm diameter nylon studs; length is measured in accordance with Figure 6.5.

³ Previously established by experimental testing.

⁴ Interpolated by ratio of scored thicknesses (i.e. nominal thickness minus 0.2 mm) from 1.2 mm thick diaphragm.

Table 6.7: X2 lightweight piston finalised driver conditions.

The L1d2 analyses were used to predict an inflection point for the piston, which was then used to determine the required buffer length. However, the actual L1d2 simulations do not place the buffer at this point, and instead permit the piston to move some distance further downstream. This has no bearing on the L1d2 results now presented, since critical flow processes, which influence the driver performance, complete before the piston reaches the inflection point.

The buffer lengths specified in Table 6.7 do not directly correspond to the inflection points calculated by L1d2. For each driver condition, the location of the inflection point predicted by the L1d2 analysis was used to calculate the actual physical buffer length, however a correction had to be applied to the L1d2 result in order to account for the modified geometry used to model the area change. This correction was based on achieving equal driver gas volumes, and is discussed in Section 6.10.3.

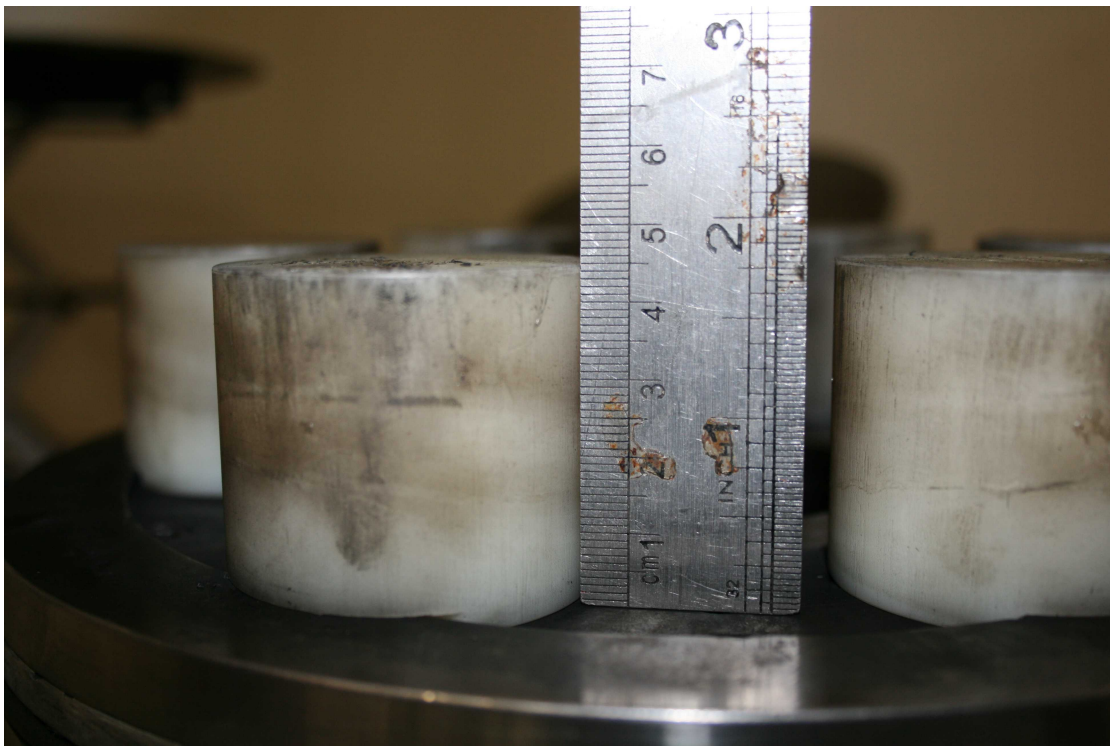


Figure 6.5: Example of nylon stud length measurement; buffer pre-shot x2s1351; 45 mm stud length.

Comparing the tuned conditions from Table 6.7 with the X2 35 kg piston driver condition in Table 6.1, it is clear that the higher piston speeds and lower compression ratios require much higher reservoir fill pressures (approximately 4 to 6 \times higher). This follows, since the tuned conditions tend to require that significantly greater work be done on the driver gas to compress the larger initial mass of gas up to the diaphragm rupture pressure, and then to drive this larger compressed volume through the area change.

Figures 6.6, 6.7, and 6.8, detail the predicted L1d2 piston motion and driver pressure responses for the three new tuned conditions. The quantity p_{max} is calculated from the blue curves; quantities with subscript ‘r’ are calculated from the red curves. Each of these conditions was also conducted experimentally; experimental results are later detailed in Section 6.10.

The first plot in each figure - *plot (a)* - shows the driver pressure vs. time. Two curves are shown, which correspond to the driver pressure at two locations, $x = 4.625$ m (blue curves), and $x = 4.800$ m (red curves). Referring to Figure 6.9 and Table 6.2, the blue curve measures the pressure just downstream of the beginning of the area change; the red curve measures the pressure just upstream of the diaphragm, inside the smaller diameter tube.

The red curves show the driver pressure at the diaphragm. In each of the three plots, it can be seen that the rupture pressure (15.5 MPa) is approximately triggered by the

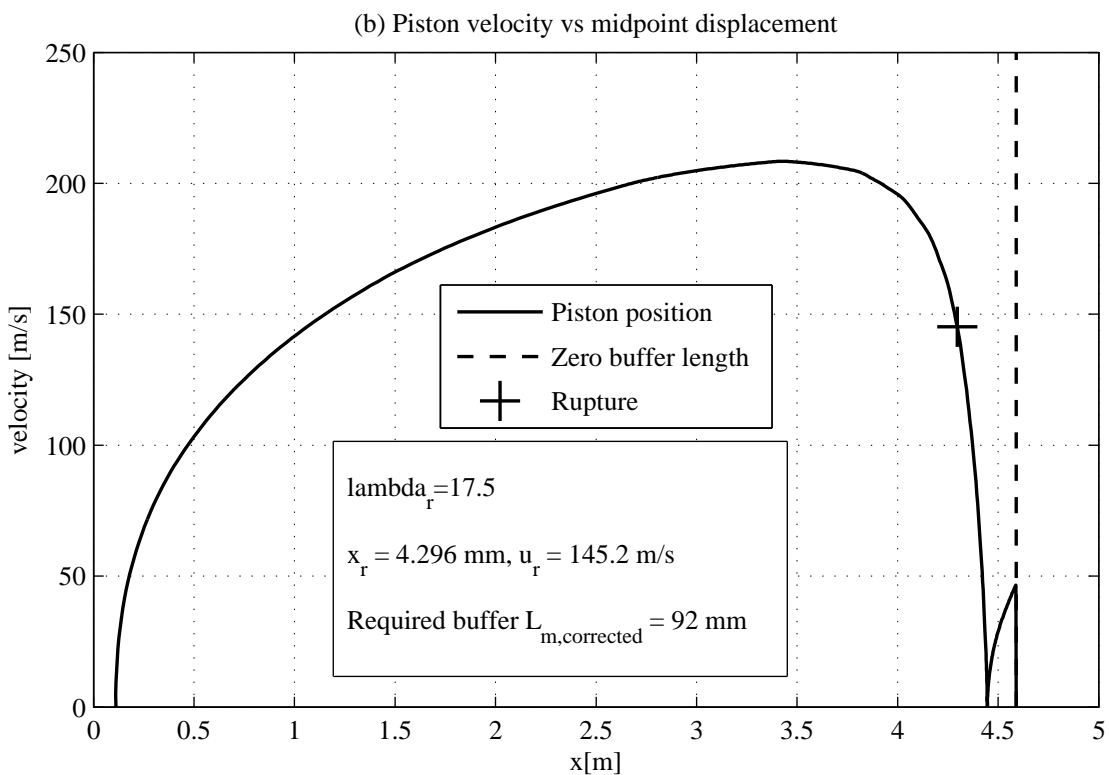
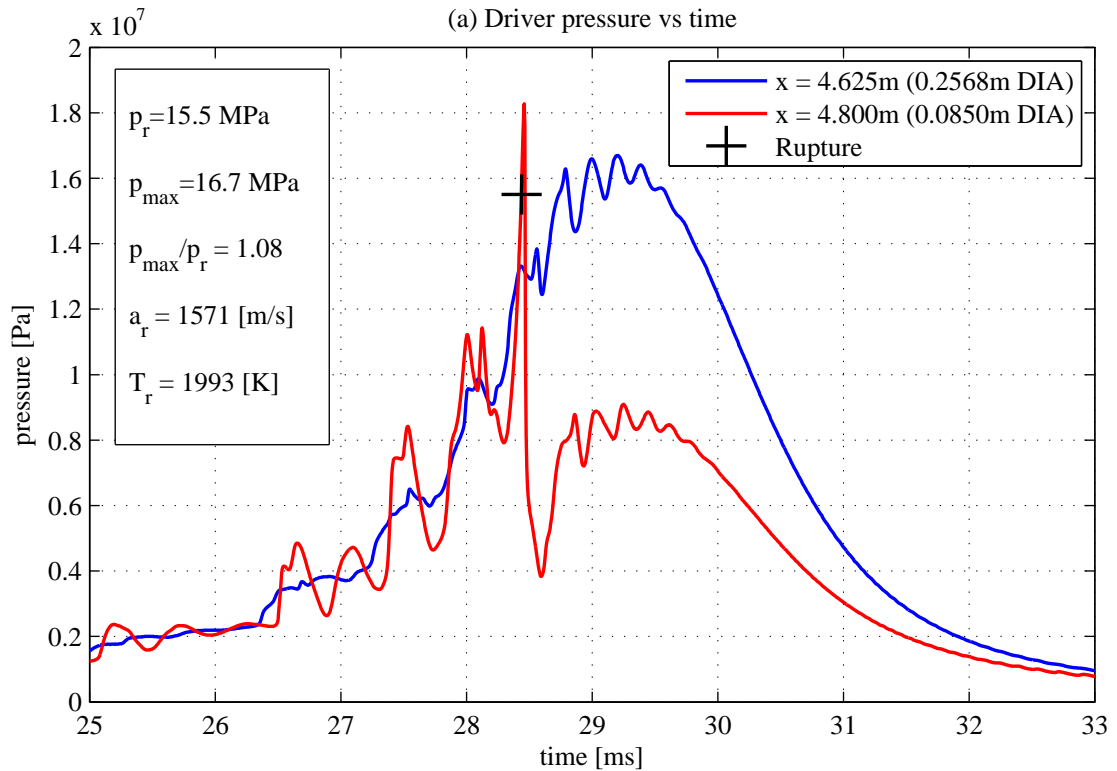


Figure 6.6: L1d2 predicted driver response for tuned driver condition LWP-1.2mm-Rev-0 ($p_{A,0} = 4.94 \text{ MPa}$, $p_{D,He,0} = 88.2 \text{ kPa}$, $p_{D,Ar,0} = 22.1 \text{ kPa}$, $p_r = 15.5 \text{ MPa}$); refer to also to Table 6.7.

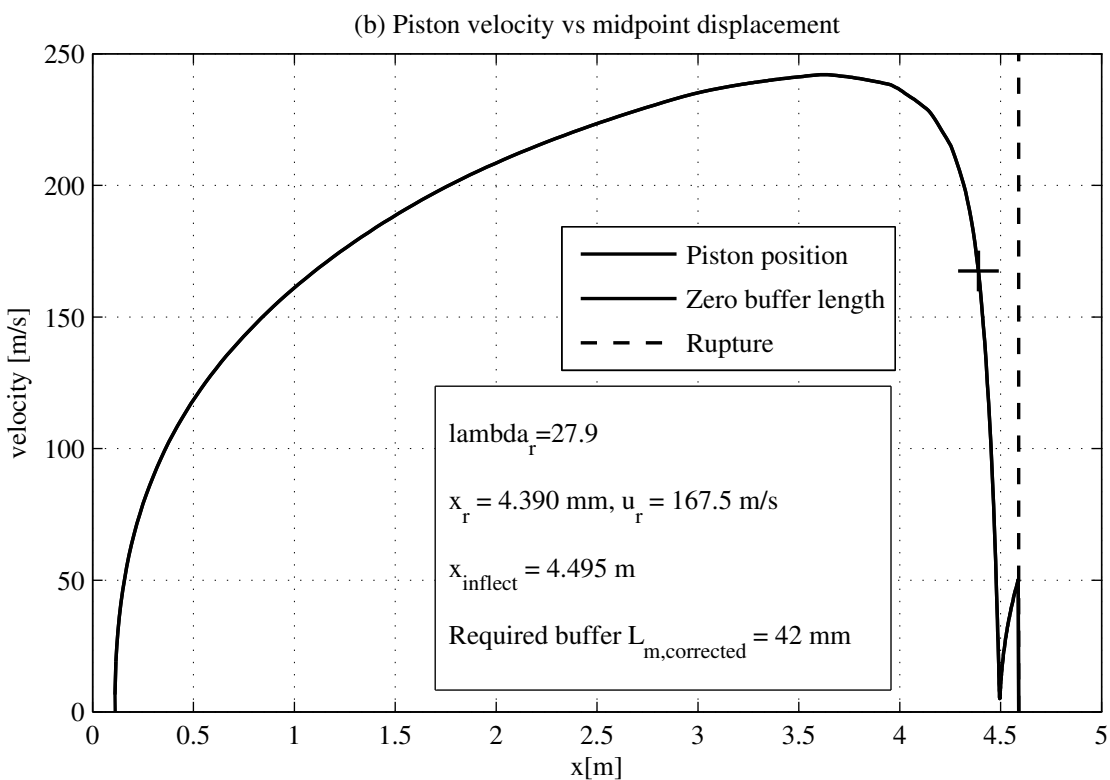
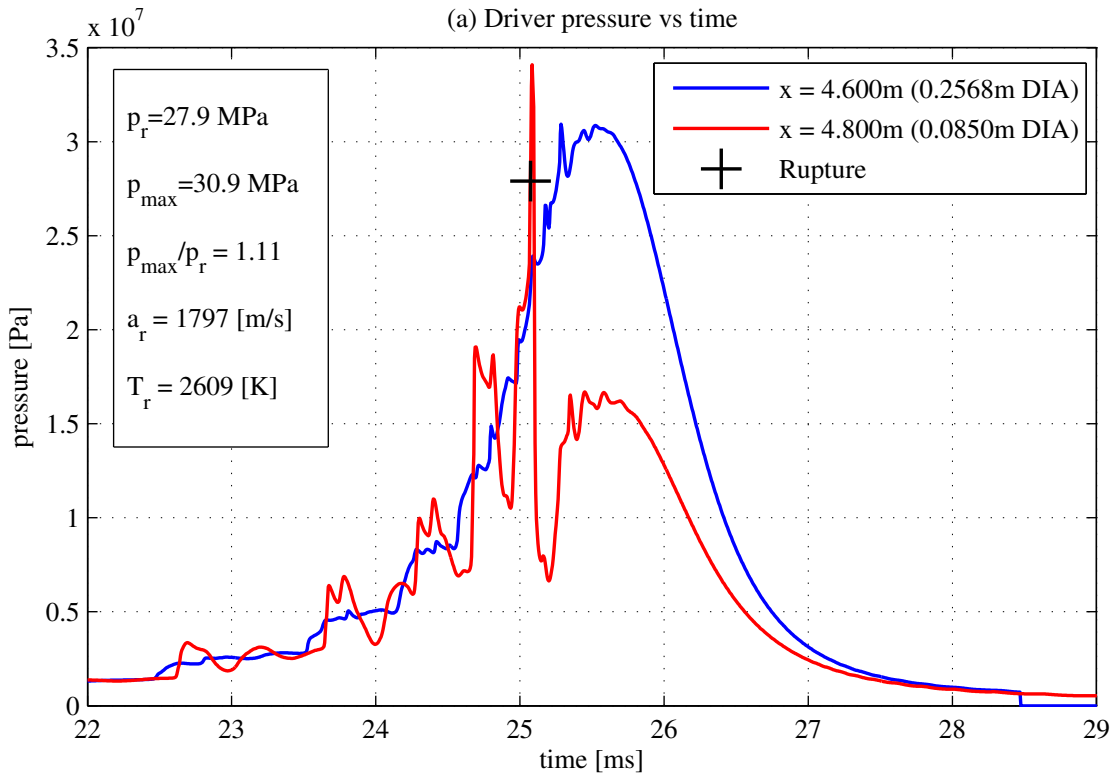


Figure 6.7: L1d2 predicted driver response for tuned driver condition LWP-2.0mm-Rev-0 ($p_{A,0} = 6.85 \text{ MPa}$, $p_{D,He,0} = 74.3 \text{ kPa}$, $p_{D,Ar,0} = 18.5 \text{ kPa}$, $p_r = 27.9 \text{ MPa}$); refer to also to Table 6.7.

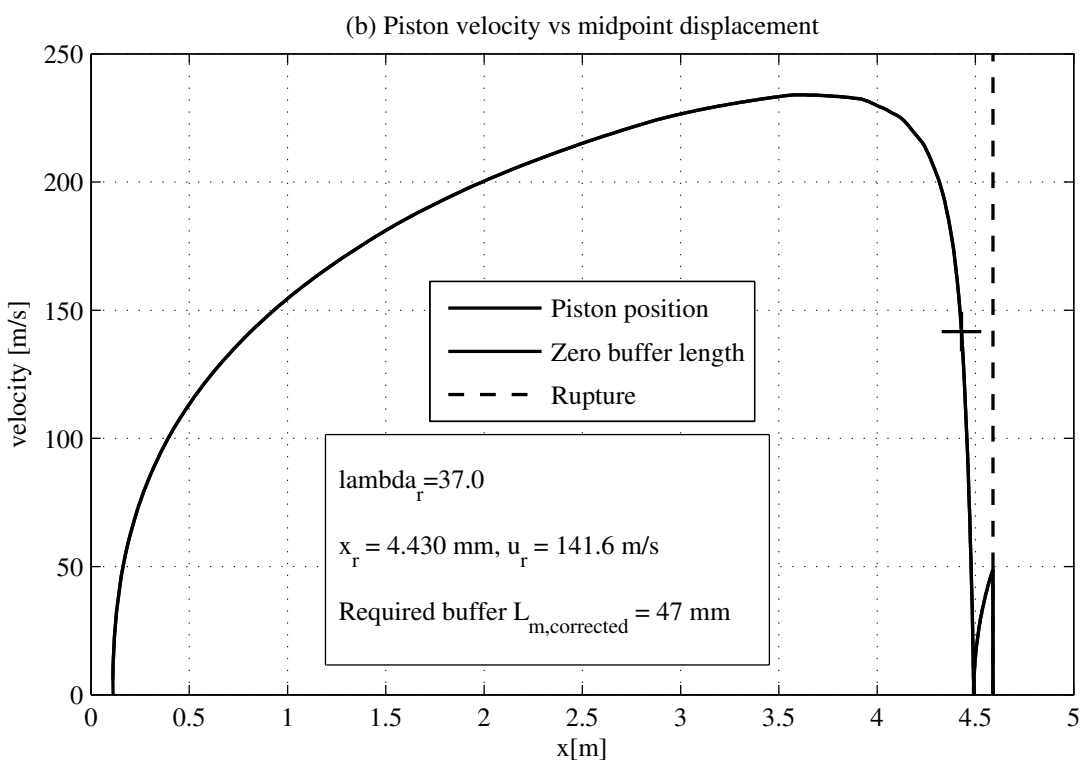
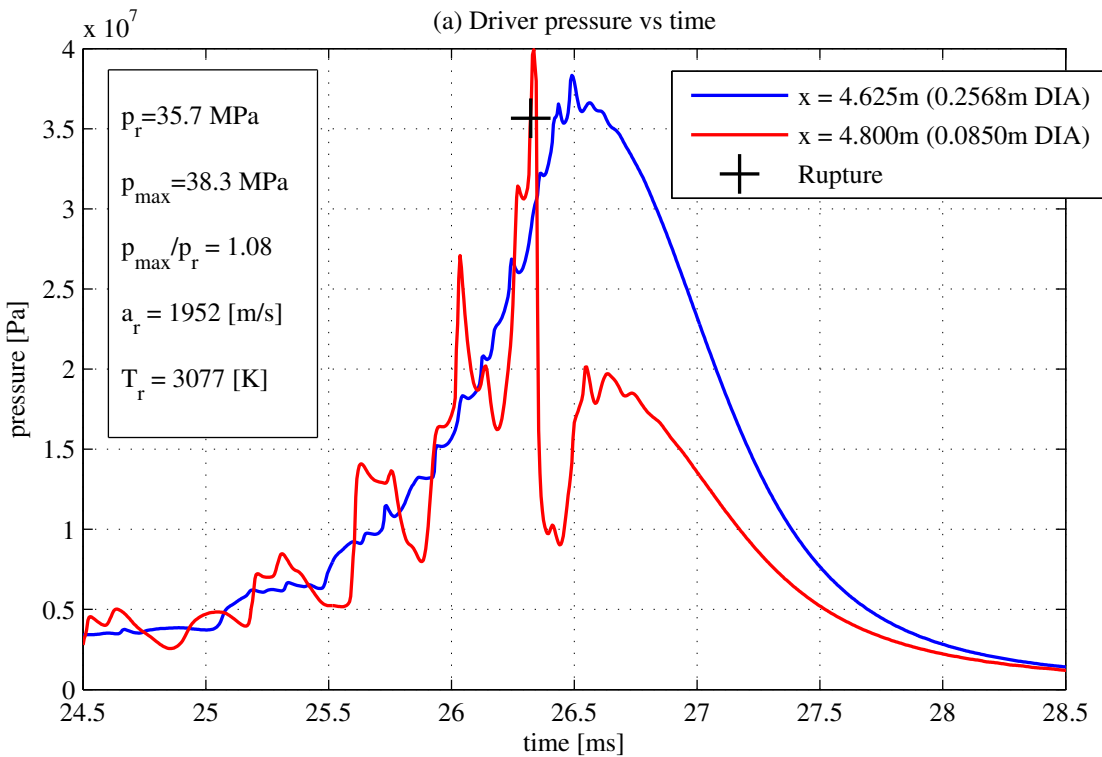


Figure 6.8: L1d2 predicted driver response for tuned driver condition LWP-2.5mm-Rev-0 ($p_{A,0} = 6.08 \text{ MPa}$, $p_{D,He,0} = 61.7 \text{ kPa}$, $p_{D,Ar,0} = 15.5 \text{ kPa}$, $p_r = 35.7 \text{ MPa}$); refer to also to Table 6.7.

red curve. Up until the moment the diaphragm ruptures, the pressure in the entire compression tube is approximately equal. Following rupture, flow through the area change is subject to a steady expansion, therefore the driver pressure downstream of the area change immediately drops. Also evident is the significant unsteadiness of the red pressure traces up until the moment the diaphragm ruptures; this unsteadiness is primarily due to frequency focussing through the area change. Whilst some frequency focussing is observed to occur in actual experiments (see Section 6.10.4), the 1-D code exaggerates this effect.

The blue curves show the driver pressure upstream of the area change. This gas initially has very similar mean pressure magnitude to the gas downstream of the area change (i.e. the red curves), however it is more steady. Since this gas is upstream of the steady expansion, the magnitude of the pressure remains high following diaphragm rupture. Over-driving is evident on each curve, with a period of continuing driver pressure rise following diaphragm rupture. It can be seen from the plots that following diaphragm rupture the driver pressure is sustained within approximately $\pm 5\text{-}10\%$ of the rupture pressure for 0.5-1.0 ms, depending on the condition.

It is noted that since the diaphragm rupture is, by necessity, triggered by the pressure at the diaphragm (the red curves), that triggering can therefore occur due to one of the large pressure spikes. This has the potential to cause an early trigger, however review of the three sets of plots indicates that this has not caused a premature trigger for either of the three new conditions.

The second plot in each figure - *plot (b)* - shows the velocity of the piston midpoint from the moment of launch until the piston reaches the end of the start of the area change (this is referred to as the *zero buffer length* position, since there would be no room to locate a buffer with the piston at this location). This is not the actual position of the area change, but the position of the midpoint of the piston when the piston is located with its upstream face coincident with the area change plane.

The position of the piston at the moment of diaphragm rupture is marked by a '+'. It can be seen from the three sets of plots that piston velocity exceeds 200 m/s for each driver case, and that the piston retains approximately two thirds of its velocity when the diaphragm ruptures. Deceleration is highest following rupture since this is the period of peak driver pressure (i.e. peak load acting on the piston).

The compression ratio at the moment of diaphragm rupture is denoted by 'lambda'. This is calculated by dividing the initial L1d2 driver volume by the driver volume at the moment of diaphragm rupture, using the L1d2 analysis geometry defined in Figure 6.1 and Table 6.2. The parameter ' $L_{m,\text{corrected}}$ ' is the calculated position of the piston front face when the piston momentarily arrives at the inflection point (when there is approximately simultaneous occurrence of zero velocity and zero acceleration, which is

evident on each figure). Since the L1d2 driver geometry at the area change has been modified to suit the gradual area change requirements of the 1-D code, the calculated L1d2 piston position, in absolute terms, is not the actual piston position for the real facility geometry. A corrected position is therefore calculated, which attempts to relate the L1d2 piston position (with the gradual area change), to the actual geometry (with the abrupt area change).

Figure 6.9 presents a schematic comparing the L1d2 analysis geometry to the actual geometry at the area change. There is no physical buffer present in either model (which would occupy part of the driver volume if present). Considering the L1d2 analysis results, at the point of inflection the piston midpoint location is defined as $x = x_{m,L1d2}$. Assuming the piston front face is upstream of the start of the area change ($x = 4.600$ mm), the volumes of driver gas contained between the piston and the diaphragm based on (a) L1d2, and (b) actual driver geometries, are respectively as follows:

$$\begin{aligned}
 V_{m,L1d2} &= \pi \frac{0.085^2}{4} \times (4.810 - 4.700) \\
 &\quad + \frac{\pi}{3} \left(\frac{0.085^2}{4} + \frac{0.085}{2} \times \frac{0.2568}{2} + \frac{0.2568^2}{4} \right) \times 0.100 \\
 &\quad + \pi \frac{0.2568^2}{4} \times \left(4.600 - x_{m,L1d2} - \frac{0.221}{2} \right) \\
 &= 0.2356 - 0.05179 \times x_{m,L1d2} \text{ [m}^3\text{]} \tag{6.22}
 \end{aligned}$$

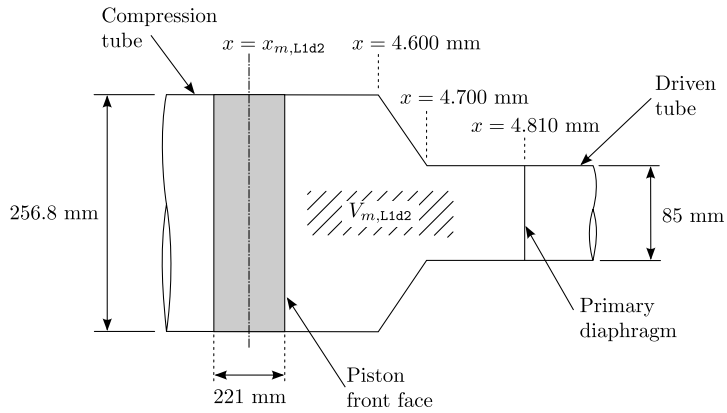
$$\begin{aligned}
 V_{m,\text{corrected}} &= \pi \frac{0.085^2}{4} \times (4.810 - 4.700) \\
 &\quad + \pi \frac{0.2568^2}{4} \times L_{m,\text{corrected}} \\
 &= 0.0006242 + 0.05179 \times L_{m,\text{corrected}} \text{ [m}^3\text{]} \tag{6.23}
 \end{aligned}$$

Equating $V_{m,\text{corrected}}$ to $V_{m,L1d2}$, the corrected piston inflection point is then determined:

$$L_{m,\text{corrected}} = 4.537 - x_{m,L1d2} \text{ [m]} \tag{6.24}$$

Figure 6.10 summarises the L1d2 predicted driver pressure responses for the three new tuned driver cases. It can be seen that piston over-drive results in an approximate 5-10% further increase in pressure following diaphragm rupture. The predicted driver pressure response for the original 35 kg piston 100% helium driver condition is also shown; it can be seen that the driver pressure drops rapidly compared to the tuned driver conditions.

(a) L1d2 calculated piston inflection location based on L1d2 analysis geometry.



NOT TO SCALE

(b) Corrected piston inflection location based on actual geometry.

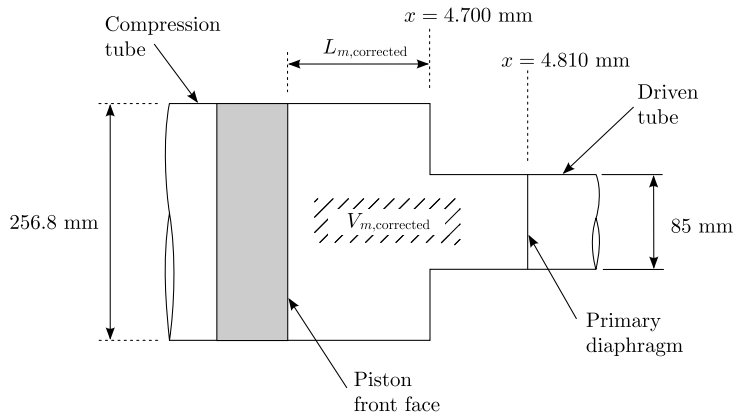


Figure 6.9: Piston mid-point position is calculated using L1d2. Volumes of driver gas are calculated assuming no buffer using both the L1d2 geometry and the actual geometry, and the two volumes are then equated. The corrected length $L_{m,corrected}$ is then solved for; see Equation E.3.

6.9 Blanked-Off Driver Experiments

6.9.1 Overview

Blanked-off tests were performed for each condition prior to performing diaphragm rupturing experiments. Figures 6.11(a-c) compare pressure traces between L1d2 predictions and representative experimental measurements. Blanked-off driver simulation is achieved in L1d2 by making the primary diaphragm burst pressure so high that it will not rupture. No other simulation parameters require modification. Close correlation is observed for the average experimental and L1d2 pressure magnitudes. There is some difference in the secondary wave processes; it was found that L1d2 had difficulty predicting the detailed unsteady behaviour of the driver pressure through the sharp area change to the primary

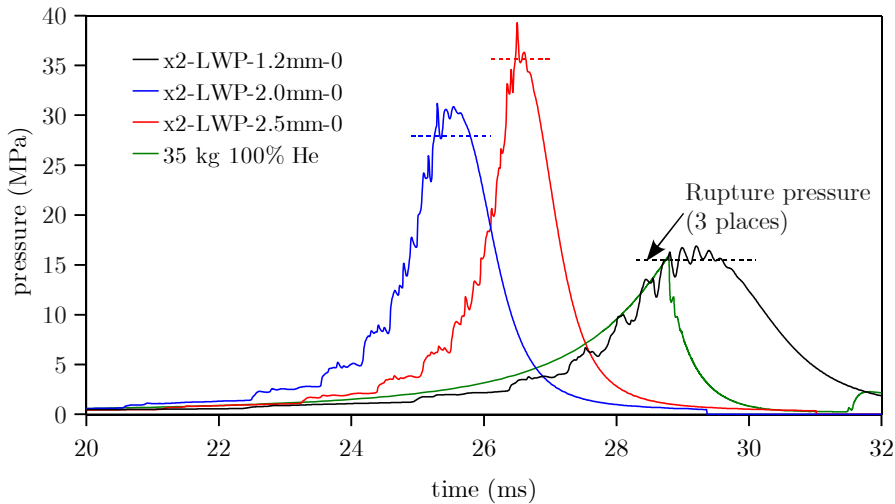


Figure 6.10: L1d2 predicted driver pressure for the driver cases detailed in Table 6.7. Driver pressure for previous 35 kg piston 100% helium driver condition is shown for comparison (green curve); this pressure history is time-referenced to align its rupture time with driver condition X2-LWP-1.2mm-0 (which has the same rupture pressure).

diaphragm. The L1d2 pressure traces are taken just before the compression tube area reduces.

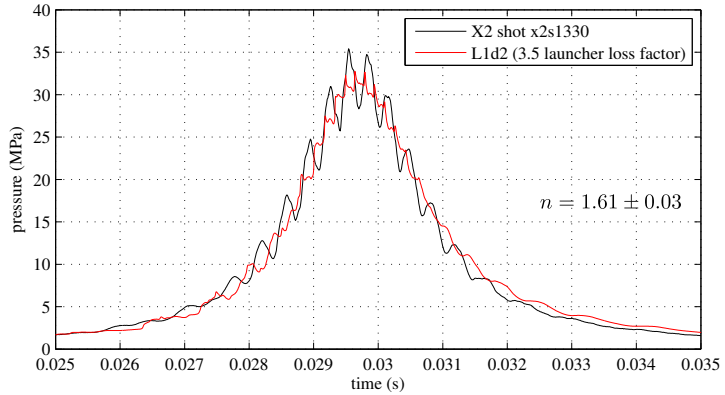
It was found that loss factors had to be increased from 0.5 (which is used with the existing 35 kg piston L1d2 model) to between 3.1 and 3.5 for the lightweight piston driver conditions, in order to obtain good agreement between numerical and experimental blanked-off driver pressure traces. This is not surprising, since the reservoir pressures and piston velocity and acceleration are much higher than for the X2 35 kg driver condition.

It is also noted that for blanked-off driver experimental tests with 2.0 and 2.5 mm steel diaphragms, the driver fill pressure was scaled upwards to ensure peak driver pressure did not exceed the facility limit of 40 MPa. Since reservoir pressure has proven most difficult to predict accurately, the reservoir pressure was not scaled. Prior to the rapid increase in driver pressure as the piston nears the end of its stroke, piston dynamics is primarily dependent on reservoir pressure (i.e. driver pressures are low for most of the piston stroke). Therefore these scaled blanked-off driver tests still permit reasonable verification of most of the compression process.

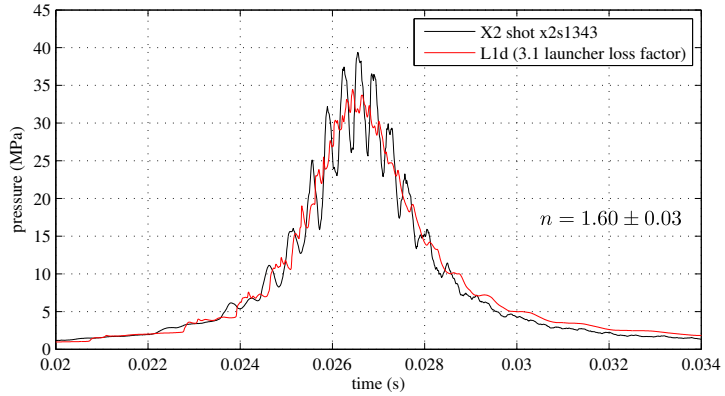
6.9.2 Calculation of Polytropic Index - an Indication of Driver Heat Loss

A polytropic index, n , was calculated for the blanked-off tests. A polytropic process is one which follows the relation $pV^n = C$, where n and C are constants [133]. If

(a) Driver condition X2-LWP-1.2mm-0 ($1.00 \times p_{D,0} / 1.00 \times p_{A,0}$).



(b) Driver condition X2-LWP-2.0mm-0 ($1.62 \times p_{D,0} / 1.00 \times p_{A,0}$).



(c) Driver condition X2-LWP-2.5mm-0 ($1.70 \times p_{D,0} / 1.00 \times p_{A,0}$).

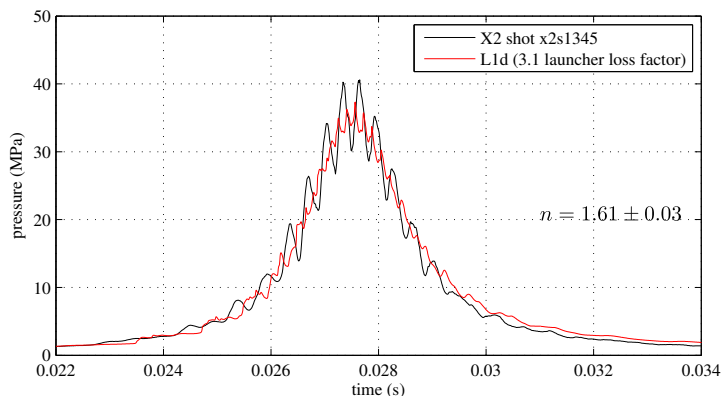


Figure 6.11: Comparison of experimental and numerical driver pressures for new tuned lightweight piston driver conditions (refer Table 6.7). Driver fill pressures for both case X2-LWP-2.0mm-0 and X2-LWP-2.5mm-0 have been scaled upwards, in both L1d2 simulation and experiment, in order to ensure peak driver pressure does not exceed facility maximum pressure rating of 40 MPa. Experimental pressure traces have been time-referenced to match L1d2 predictions. n is the calculated experimental polytropic index (see Section 6.9.2).

$n = \gamma = C_p/C_v$, then the process is adiabatic. If heat loss occurs (which is expected in a true compression process), then $n < \gamma$. Therefore, comparison between n and γ provides an indication of heat loss in the driver during the piston compression process. For the blanked-off driver experiments conducted for the lightweight piston, the polytropic index was calculated as follows (in accordance with Doolan and Morgan [76]):

$$n = \frac{\ln \left| \frac{p_{max}}{p_{D,0}} \right|}{\ln |\lambda_{exp}|} \quad (6.25)$$

The calculated experimental polytropic index is shown for each blanked-off driver experiment in Figure 6.11(a-c). These values ($n = 1.60, 1.61, 1.60$) are representative of those calculated for the entire series of blanked-off driver experiments, and compare to $\gamma = 5/3 = 1.67$ for helium/argon. This indicates that heat loss in the driver is not excessive, which is to be expected for the following reasons:

1. The piston stroke is very rapid, thereby limiting the time available for heat loss.
2. The driver gas volume is quite large compared to its surface area, and the compression tube is short; for much longer tubes and smaller pistons, there is greater opportunity for heat loss.
3. The addition of argon to the driver gas reduces its tendency to shed heat compared to a pure helium driver.

L1d2 uses a pipe flow model to calculate heat loss, therefore it does not predict heat loss well for a compression process where the gas is very hot, but is only moving with relatively low velocity (i.e. for a heavy, slow piston). Consideration of the experimental polytropic index is important since it indicates whether or not heat loss is significant. Since heat loss was determined to be relatively low for these experiments, the L1d2 simulations, which generally underestimate the heat loss, can still be expected to be applicable.

Figures 6.6(b), 6.7(b), and 6.8(b), show the L1d2 predicted piston velocity-displacement trajectory for each of the three driver conditions from Table 6.7. It can be seen that the deceleration of the piston prior to reaching the inflection point is significant and that incorrectly locating the buffer too far forward of the tube end may result in very high speed impact. Driver heat loss is very important in this respect, since significant heat loss will result in a smaller driver gas volume at the end of the piston stroke; if left unaccounted for, this may result in the buffer being located too far forward and consequently a significant impact velocity. The three calculated polytropic indices in Figure 6.11 correspond to a compressed volume of driver gas which will be approximately 11-12% smaller than that predicted for an adiabatic isentropic compression. This implies

that the buffer should be made at least 10% shorter than that predicted directly from L1d2 results.

Finally, the L1d2 piston velocity-displacement plots (Figures 6.6(b), 6.7(b), and 6.8(b)) indicate that where there is uncertainty regarding precise buffer length, it is better to have a too-short rather than too-long buffer for these driver conditions, since the piston re-acceleration due to residual reservoir pressure (once it has passed the inflection point) is much lower than its earlier deceleration due to the much higher pressure driver gas (as it approaches the inflection point). It is seen in Section 6.10.3 and Table 6.9 that final buffer lengths for the new tuned driver conditions were eventually made approximately 20% shorter than that predicted from L1d2 results. These buffers were found to catch the piston close enough to its inflection point to avoid any impact damage, which supports the above arguments.

Two parameters affect the accuracy of calculated n values:

- Measured piston rebound point: this was difficult to determine accurately. A staggered arrangement of rods was used (see Figures 6.12 and 6.13). This permitted piston maximum displacement to be measured directly (from the impacted rod) and indirectly (from the non-impacted rods). This approach indicated that some of the longer rods were contacting the piston during a point in the stroke where it was moving very fast, thus imparting so much inertia to the rods that there was sufficient energy to keep deforming them after loss of contact with the piston (which is slowed by the driver gas). Figure 6.14 shows an example of rod displacement on a staggered assembly, where the longest rod has deformed past several of the shorter non-impacted rods.

A rubber buffer was used to mount the staggered rod assembly. This buffer reduces the volume of driver gas for a given piston position and therefore was accounted for in volumetric compression ratio calculations. Appendix E.2 details the geometry of the rubber buffer, and the methodology to calculate the volume of driver gas for a given piston position. Piston position was then measured experimentally in accordance with Figure 6.12, and Equation E.1 was used to calculate the driver gas volume.

- Measured peak pressure, p_{max} : This was the peak value from the experimental blanked-off driver test. Due to the presence of strong compression waves in the driver gas, the peak pressure is unlikely to coincide with the peak volumetric compression ratio. In these calculations the peak *mean* pressure is used; this was determined by visually identifying the approximately bell-shaped curve which the secondary wave processes are centred about, and observing its maximum value. This assumption is considered to be appropriate since the piston speed is low at

this point in its stroke, and the strong fluctuations in the driver gas therefore cannot be a result of direct physical oscillation of the piston itself.

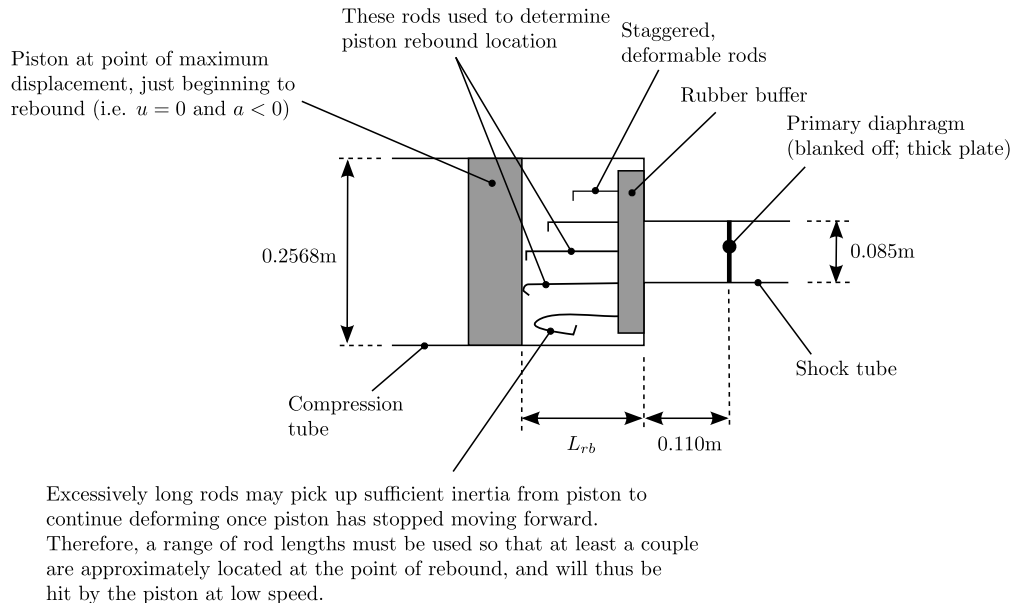


Figure 6.12: Measurement of location of piston maximum displacement.

6.10 Rupturing Diaphragm Experimental Results

6.10.1 Overview

The newly developed tuned driver conditions detailed in Table 6.7 were assessed experimentally with rupturing diaphragms once the blanked-off driver tests were shown to satisfactorily match L1d2 predictions. Downstream of the primary diaphragm, the Mach 13 fill conditions from Table 4.1 were used; this would give a comparison of driver performance between the new tuned driver conditions (with theoretically extended driver gas supply duration) and the existing X2 35 kg piston driver condition. This section details the results of these tests.

6.10.2 Experimental Setup

Downstream of the primary diaphragm, X2 was configured in accordance with the Mach 13 flow condition detailed in Table 4.1. Upstream of the primary diaphragm, the three different driver configurations from Table 6.7 were separately considered.

Shocks speeds were used for assessment of the tuned driver. These were calculated by measuring the time of flight between two adjacent transducers in a given tube, and

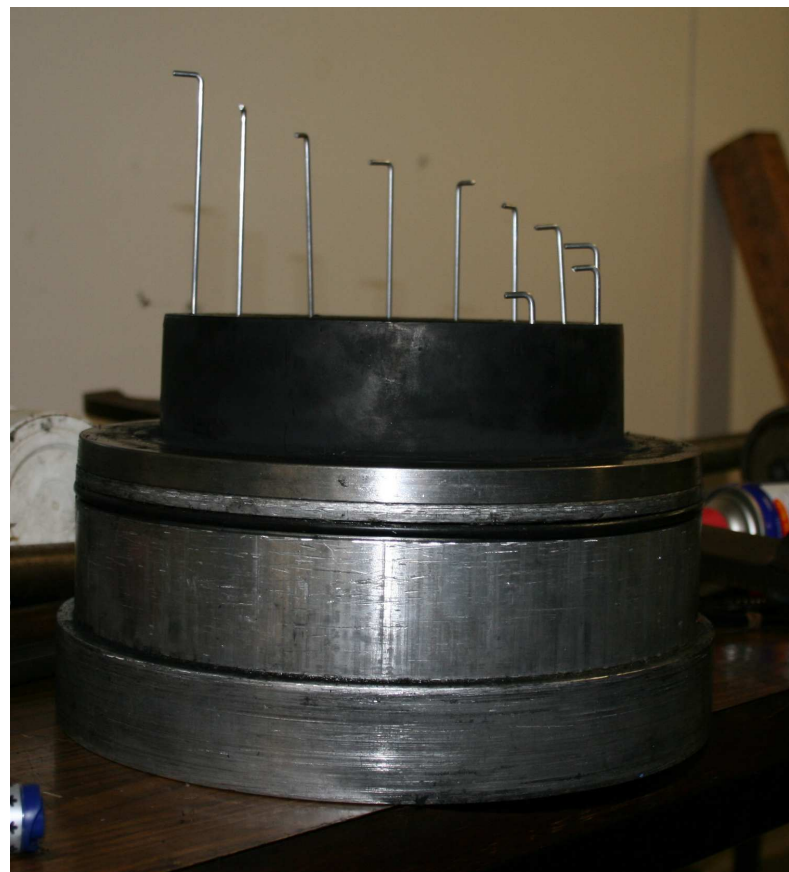


Figure 6.13: Example of staggered buffer rod arrangement prior to blanked-off driver shot.

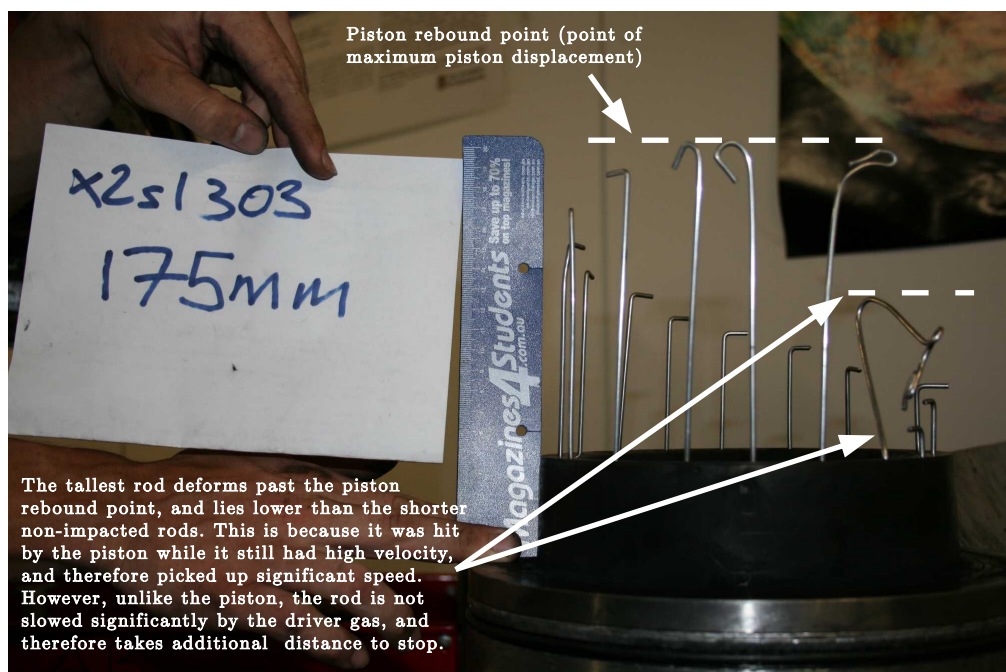


Figure 6.14: Measurement of location of piston maximum displacement - example.

then using the measured transducer spacing to determine the shock speed. Defining the x -location of the primary diaphragm as $x = 4.810$ mm, the transducer locations are defined in Table 6.8

	Transducer ID	x -loc (m)
Secondary driver	st1	7.382
	st2	7.614
	st3	7.846
Shock tube	at1	8.765
	at2	9.015
	at3	9.265
Acceleration tube	al3	10.831
	al4	12.673
	al5	12.854

Table 6.8: X2 PCB transducer configuration (primary diaphragm located at $x = 4.810$ m).

Primary diaphragms were manufactured from cold-rolled steel sheet, scored to a depth of 0.2 mm (i.e. leaving $(t - 0.2)$ mm remaining thickness at the score, for thicknesses of 1.2, 2.0, and 2.5 mm in accordance with Table 6.7). Secondary and tertiary diaphragms were cut from 0.1 mm thick Mylar; this relatively heavy diaphragm material was required in order to resist large initial fill pressure differences between tubes.

6.10.3 Nylon Stud Sizing

For these initial tests a buffer comprised of sacrificial nylon studs was used. Nylon studs have the capacity to absorb a significant amount of energy through plastic deformation. They are very useful during driver commissioning when analytical uncertainties are not fully understood and there is a chance of high speed piston impact. Once commissioning is complete the nylon stud buffers are not as practical as a rubber/nitrile buffer, primarily for two reasons:

1. *The nylon studs are easily damaged:* They have the capacity to absorb a lot of energy if the piston impacts at very high speed; in such cases the nylon will undergo significant deformation. However, at lower speeds the nylon is more brittle, and is liable to crack or become loose at the bolted attachment. A rubber buffer cannot absorb the energy of a high speed impact, however it can sustain a greater number of repeated low speed impacts typical of normal operation.
2. *Following completion of the piston stroke, there is a large residual reservoir pressure force acting on the upstream surfaces of the piston:* There is a varying degree of leakage of this gas over the piston wear rings and chevron seal. When a rubber buffer is used, the rubber forms a seal between the downstream face of the piston, and the downstream driven tube; the nylon studs do not provide such a seal.

Operation with nylon studs can result in a large quantity of air flowing into the downstream driven tube and dump tank, and where high reservoir pressures are used this can result in the dumptank pressure rising above atmospheric pressure. Once the pressure inside the facility exceeds atmospheric, the dumptank may be pushed off the tube exit, and/or rupture of the dumptank over-pressure safety blow-off diaphragms may occur. Either of these events are not dangerous, but are undesirable and to be avoided.

Appendix F derives an equation to estimate the maximum allowable impact speed that a given configuration of nylon buffers can absorb. Considering a typical configuration for X2, the impact speed for different stud diameters and lengths is calculated using Equation F.11. The following configuration is assumed for the driver:

1. Compression tube diameter, $D = 0.2568$ m.
2. Piston mass, $m_p = 10.524$ kg.
3. Stud diameter, $D_s = 40$ mm, 50 mm, and 60 mm.
4. Number of studs, $n = 6$.
5. $\sigma_{av} = 40$ MPa. Table H-3 from [134] indicates that the ultimate stress of nylon generally varies between 40-80 MPa; a 40 MPa assumed yield stress is considered to provide an indicative value for the purposes of these calculations; this yield stress is in approximate agreement with other published nylon material properties. So long as the nylon does not become volumetrically blocked, the nylon will plastically deform long before the piston body stress approaches the aluminium allowable, which is an order of magnitude higher than the nylon. Therefore damage to the piston or facility should be avoided.

It is noted that 6×50 mm DIA nylon studs were used for the experiments presently considered. Figure 6.15 indicates that an impact speed of approximately 70 m/s can be tolerated with the 45 mm nylon stud buffer, and greater than 100 m/s with the 100 mm buffer. This buffer arrangement therefore provides a considerable margin of safety in the event of an unexpectedly high impact speed.

The nylon stud lengths quoted Table 6.7 differ from the predicted inflection points calculated from L1d2 in Figures 6.6 to 6.8. These latter values have had correction factors applied to account for the modified L1d2 geometry, however they do not account for the presence of the nylon studs themselves. The effectively incompressible nylon studs require the piston to be positioned further from the end of the tube in order to preserve the driver gas volume which was used to calculate L_m . The position was determined by equating Equation E.2 and E.1 and solving for L_s :

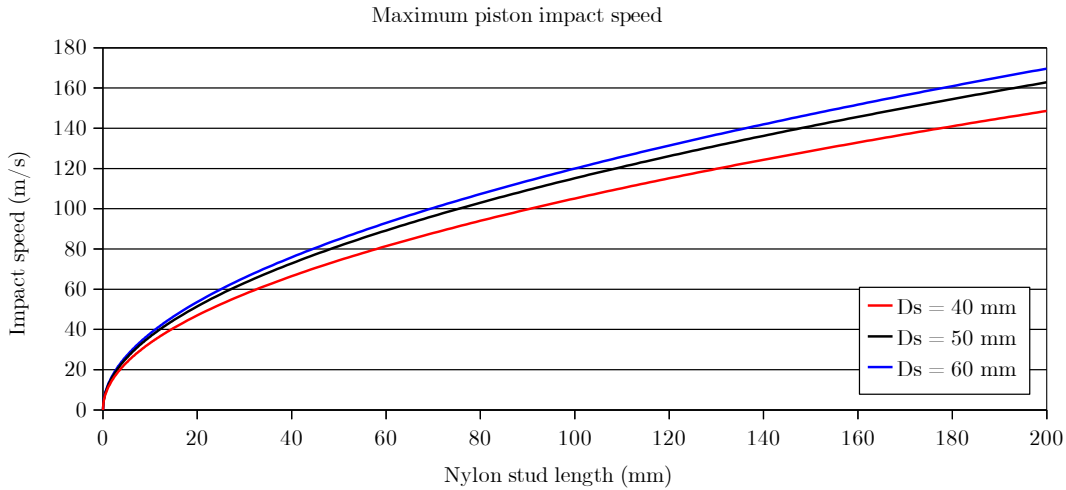


Figure 6.15: Maximum piston impact speed that can be absorbed by a 6 nylon stud buffer arrangement in X2. D_s is the stud diameter. See also Figure 6.14.

$$L_s = 1.295 L_m \quad (6.26)$$

Driver condition	L_m (mm)	L_s (mm) per Equation 6.26	L_s per Table 6.7
X2-LWP-1.2mm-0	92	120	100
X2-LWP-2.0mm-0	42	54	45
X2-LWP-2.5mm-0	47	61	45

Table 6.9: X2 buffer nylon stud length comparison.

Inspection of Table 6.9 indicates that the nylon studs used for actual experimental testing were less than those calculated using Equation 6.26. Inspection of the piston velocity curves in Figures 6.6, 6.7, and 6.8, indicates that piston deceleration prior to arrival at the inflection point is much higher than its re-acceleration downstream of this point. Therefore, if a buffer is too long by a given length ΔL , then the impact speed is likely to be much higher than if it is too short by the same amount. Where there is uncertainty in regards to the location of the piston inflection point, it is safer to make the buffer too short, rather than too long. In the first set of experiments, which attempted driver condition X2-LWP-1.2mm-0, 100 mm studs were used, with no resulting damage. For the next set of experiments for driver condition X2-LWP-2.0mm-0, the stud lengths were reduced by proportionally the same amount ($0.83\times$); for the final set of experiments for driver condition X2-LWP-2.5mm-0 the same studs were used since the predicted lengths were very similar, and these were also found to be satisfactory.

It is finally noted that it was found to be important to use relatively long bolts to firmly attach the nylon studs to the buffer plate. For initial testing with driver condition X2-LWP-2.0mm-0, very short bolts were used due to a concern that longer bolts may be driven into the piston body if a high speed impact occurred. However, it was found that having only a short threaded attachment led to shattering of four of the six studs; refer Figure 6.16. Whilst this was initially thought to be due to a high impact speed, further analysis and testing indicated that there were simply insufficient bolt threads in the nylon stud. Even at low speed impact there is a sizeable load transferred into the nylon studs, and a strong attachment is required. Lengthening of the bolts and installation with Lok-tite was found to prevent the nylon studs shattering and to permit repeated operation with a given set of studs.



Figure 6.16: Example of shattered nylon studs due to insufficient attaching bolt threads; buffer arrangement post- shot x2s1346.

6.10.4 Rupturing Diaphragm Experimental Results

Figure 6.17 shows averaged experimental shock speeds for each of the three driver conditions described in Table 6.7. Analytically calculated required shock speeds for the Mach 13 condition (see Table 4.1), and L1d2 predicted shock speeds, are both shown for comparison. The secondary driver shock speed is lower than the 0-D analytical pre-

dition due to the primary diaphragm being offset from the area change in the driven tube, which delays the shock reaching its full strength; refer Section 4.2.4 and Figure 4.2. Figure 6.17 indicates that this wave process is captured reasonably well by L1d2. L1d2 shock speeds in the shock and acceleration tubes are also seen generally to match experiment closely; the primary discrepancy is for driver case X2-LWP-2.5mm-0, where L1d2 predicts slightly higher shock speeds in the shock and acceleration tubes than those observed experimentally.

It can be seen that there is no longer the characteristic shock attenuation which was observed with the 35 kg piston driver (refer Figure 4.2). None of these new driver conditions caused any damage to the facility, indicating that the combined analytical/numerical/experimental development process managed to safely determine tuned, workable, driver conditions.

Referring to Figure 6.17, it can be seen that driver condition X2-LWP-1.2mm-0 has significantly lower shock speeds than the analytical required values to achieve the original Mach 13 condition. This is due to the low compression ratio of the driver gas at rupture, and the 20% argon gas composition, factors which both lead to a significant reduction in the sound speed of the driver gas.

Driver condition X2-LWP-2.0mm-0 achieved shock speeds much closer to required values due to the higher diaphragm rupture pressure and higher compression ratio. Little further improvement was observed with driver condition X2-LWP-2.5mm-0, which used the thickest diaphragm (2.5mm). This is likely to be due to the lower compression ratio at rupture. For condition X2-LWP-2.5mm-0 there was also evidence of debris detaching from the diaphragm during rupture and hitting objects in the test section. Therefore, condition X2-LWP-2.0mm-0 was considered preferable to X2-LWP-2.5mm-0 due to its cleaner operation and almost equivalent performance.

6.11 Conclusion

This chapter details the development of three new tuned driver conditions for the X2 expansion tube. Three soft landing conditions were achieved for 1.2, 2.0, and 2.5 mm thick steel diaphragms, detailed in Table 6.7. The 2.5 mm condition had little performance gain over the 2.0 mm condition, and there was also evidence of steel debris associated with unclean diaphragm rupture. Therefore the 2.0 mm condition, LWP-2.0mm-Rev-0, is presently considered the best option in terms of high performance and practical application; the 1.2 mm condition, LWP-1.2mm-Rev-0, operated very cleanly, and may be appropriate where lower static pressures are required. Further work may involve developing circular rubber buffers for these conditions which will have equal length and equivalent volume to the nylon studs. Additionally, development of additional driver

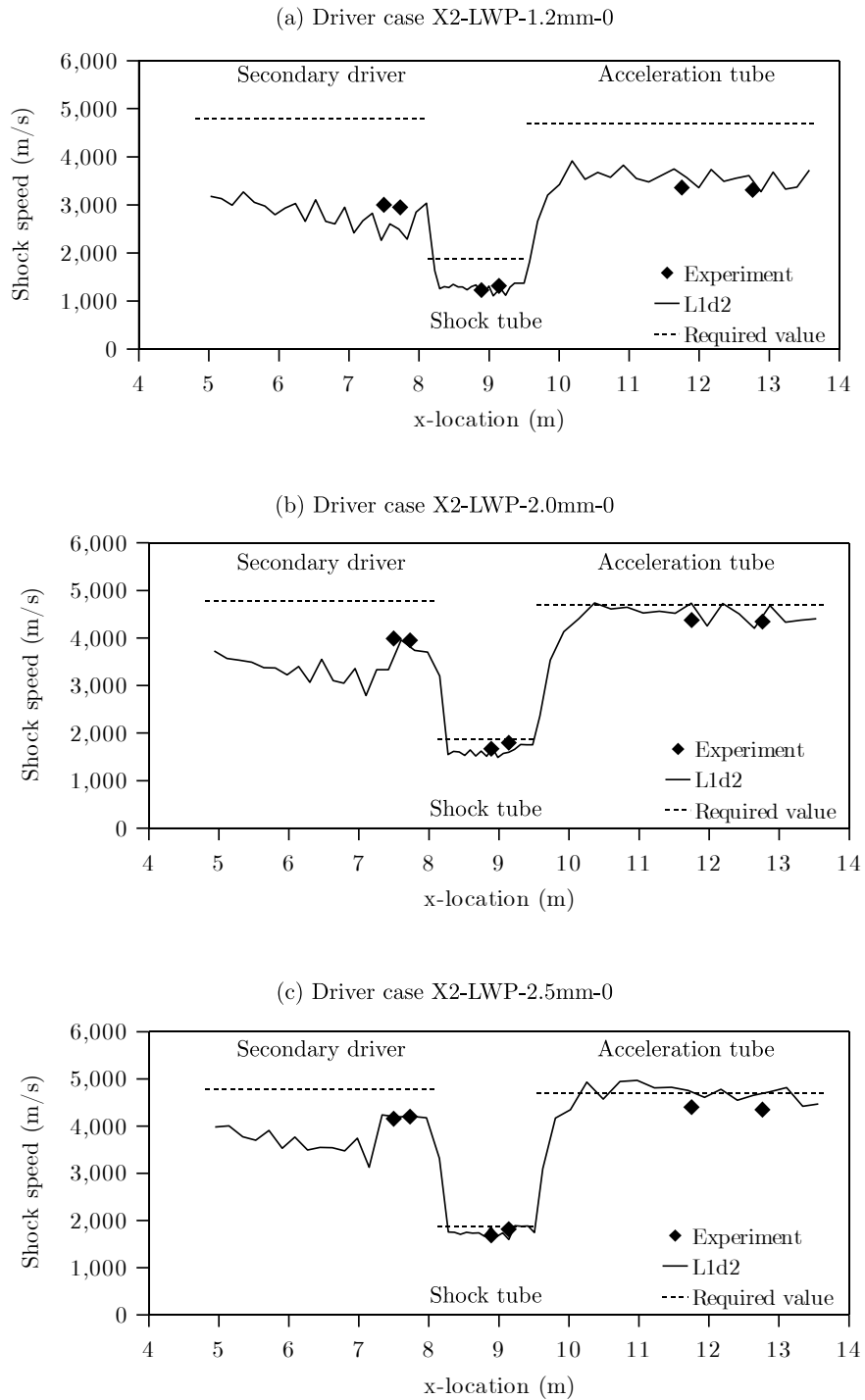


Figure 6.17: Comparison of experimental, L1d2 predicted, and analytical required shock speeds for new X2 tuned driver conditions (refer Table 6.7). Experimentally determined shock speeds shown are averaged speeds for three shots at each condition. Maximum experimental uncertainty of $\pm 2\%$.

conditions for different thickness diaphragms, different compression ratios at rupture, and/or different % argon content, will extend the range of conditions available with the new lightweight piston.

Chapter 7

Theoretical Performance Envelope of X2 with the New Tuned Driver

7.1 Chapter Overview

This chapter investigates the theoretical operating range of X2 using the newly developed tuned free-piston driver conditions detailed in Table 6.7. The analysis uses classical 0-D analytical techniques to predict the performance of the X2 expansion tube facility across a range of likely configuration options. In order to improve the accuracy of predictions, the NASA equilibrium gas solver, CEA [43], is used to calculate equilibrium gas properties across normal shocks and through unsteady expansions. The facility is considered with and without a nozzle. Test time and Mirels effects, both dependant on tube length, are ignored; these influences are taken into consideration in 2-D axisymmetric Eilmer3 CFD calculations in Chapter 8.

7.2 Equilibrium Gas Analysis with NASA CEA

At normal room temperature and pressure, air is comprised primarily of O₂ (20% by volume) and N₂ (79% by volume), with the remaining 1% consisting of Ar, He, CO₂, H₂O, and other trace species. The chemical behaviour of air is governed by these first two diatomic molecules. Between 3 K and 600 K, the assumption that air is a calorically perfect gas is valid [55]. Between 600 K and 2000 K, the ratio of specific heats, γ , is no longer constant, and air is said to be thermally perfect. Above 2000 K chemical reactions begin to occur in the air and γ can vary significantly [55]. For air at temperatures exceeding approximately 2,500 K, the O₂ and N₂ can chemically react, changing the composition and therefore properties of the gas [55]. For example, dissociation can occur (i.e. O₂ \rightleftharpoons 2O above 2500 K, and N₂ \rightleftharpoons 2N above 4000 K) and dissociated species can then react with each other (N + O \rightleftharpoons NO and N + O \rightleftharpoons NO⁺ + e⁻ are the most

common reactions)[55]. Above 9000 K, the dissociated N and O both begin to ionise (i.e. $\text{N} \rightarrow \text{N}^+ + e^-$ and $\text{O} \rightarrow \text{O}^+ + e^-$).

Expansion tube operation typically involves generation of high Mach number shock waves which produce very high temperatures in the shocked gas; for scramjet air flow conditions, these temperatures can well exceed that at which air becomes chemically reactive. Expansion tube analytical relations such as those derived by Trimpi [70] assume that gases remain calorically perfect throughout all flow processes. This assumption can lead to significant inaccuracies at more extreme parts of the facility operating envelope. In order to improve estimates of flow processes, performance calculations in this chapter instead use equilibrium gas properties (thermal and chemical).

A gas is said to be in chemical equilibrium if the various forward and reverse reactions are occurring in equal amounts, in which case the various species are also present in fixed amounts. These chemical processes are driven primarily by molecular collisions, which occur over a finite duration of time. If a gas has had sufficient time to achieve this equilibrium state, then its composition is purely a function of its pressure and temperature [55]. If insufficient time has passed, then the gas is said to be in chemical non-equilibrium. At low pressures and high temperatures the relative collision frequency is low, and the time to reach equilibrium increases [55]. Thermal non-equilibrium is also a finite rate process. Such conditions exist immediately behind a shock wave, however the present study does not take into consideration these non-equilibrium regions in expansion tube flows; their effect on overall flow processes may be significant depending on the Damkohler Number, but are not considered in this section in order to permit multiple computations which will be used to define performance envelopes.

CEA (Chemical Equilibrium with Applications) [43], a widely accepted code developed by NASA, was used to determine equilibrium gas properties. CEA directly calculates shocked gas properties for a specified shock speed through a specified media. It also calculates equilibrium gas properties for a gas at varying pressure but specified and constant entropy, thus being able to provide a case consistent set of gas properties through an unsteady expansion. Both of these capabilities permitted an iterative scheme to be developed which could predict the basic set of flow processes occurring in the expansion tube using full equilibrium gas properties.

7.3 Expansion Tube Design Variables

An expansion tube is defined by many variables, which make its design and configuration a complex task. Important design variables include:

1. Compression tube diameter and length.
2. Total facility length.
3. Secondary driver, shock, and acceleration tube lengths and diameters.
4. Piston mass.
5. Primary diaphragm rupture pressure.
6. Buffer length.
7. Reservoir fill pressure.
8. Driver fill pressure and helium/argon composition.
9. Contoured hypersonic nozzle.
10. Secondary driver fill pressure.
11. Shock and acceleration tube fill pressures and compositions.

7.3.1 Items 1 to 3

The most expensive part of an expansion tube facility is the free-piston driver [76, 61]. The size and pressure rating of this component will be determined largely by the available budget. It is preferable to maximise the diameter of the compression tube in order to have a large area change at the primary diaphragm (to maximise performance, the compression tube diameter needs to be at least approximately $3\times$ that of the driven tube), to maximise the length of the compression tube, and to have a high pressure rating. The driven tubes should be as long as space permits, with potential to modify individual tube lengths and therefore the spacing between secondary and tertiary diaphragms. However, tubes with insufficient diameter/length ratios will incur undesirable boundary layer effects, therefore maximum length is also constrained by the driven tube inner diameter. Once these components have been designed and manufactured, modifications are expensive, inconvenient, and unlikely to occur as part of normal operation. Hence for an established facility such as X2, these can usually be considered as fixed parameters, with only secondary and tertiary diaphragm locations having the potential to be normal operational variables.

7.3.2 Item 4

In order to achieve a tuned free-piston driver the piston mass must be optimised, which depends on driver gas γ , λ , and p_4 , compression tube L and D , and the available reservoir

pressure and volume. For the UQ expansion tube facilities, this leads to a low required piston mass, and the design challenge is therefore to minimise the total mass of the piston body and accessory components (such as seals and brakes). Whilst there is a lower limit on the specific piston mass which should be targeted at a given operating condition, in most cases this limit will be unfeasibly low once structural strength and interface requirements are taken into consideration. Therefore, the piston should be made as light as possible subject to it having the strength to survive the maximum operational driver pressure, braking loads, etc., and this final weight will be higher than its theoretically optimum weight would be for tuned operation. Piston mass will therefore not normally be a variable during routine operation of the facility.

7.3.3 Items 5 to 8

The upper limit of the primary diaphragm rupture pressure is determined by the driver pressure rating, but otherwise this is a parameter that is easily varied. For tuned piston operation, the performance of the driver will depend on the primary diaphragm rupture pressure, the compression ratio at rupture, and the driver gas specific gas constant (the combination of these second two factors determines the sound speed at rupture).

The normal procedure for developing a tuned driver condition is to select a diaphragm rupture pressure and then to determine a combination of driver gas composition and compression ratio which maximises driver gas sound speed at rupture, whilst simultaneously achieving a soft landing. The buffer length needs to be sized to catch the piston at the correct point in its motion. Reservoir pressure is simply that which achieves the required piston speed at rupture; maximum reservoir pressure therefore sets a limit on the possible piston speed for a given mass of piston.

For a tuned driver this is not straightforward (refer Chapter 6), since the problem is nonlinear and therefore condition scaling is not appropriate. However, once new driver conditions have been successfully commissioned, they can subsequently be varied on a shot-by-shot basis from there onwards. Over time the goal should be to develop a spread of driver conditions with incrementally different performance levels.

7.3.4 Item 9

A contoured hypersonic nozzle has a fixed area ratio and is optimised to operate at a single inlet Mach number (although it may have acceptable off-design performance depending on the specific flow condition). The expense of designing and manufacturing a nozzle is such that a facility will only have, at most, a few nozzles. The nozzle should be matched against inlet Mach number, and will be used where a large test flow core size is required, or a lower static pressure, or longer test time. Since a larger core flow

and longer test time are usually desirable, then if a nozzle is available it would normally be used unless it prevents target static pressure being achieved. As such it is therefore not a variable which significantly complicates the tunnel operation.

7.3.5 Item 10

The purpose of the secondary driver is twofold. For low enthalpy conditions, it is used as an acoustic buffer to prevent transmission of primary driver acoustic disturbances to the test flow, and to allow for the use of higher values of a_4 . For high enthalpy conditions it can increase the shock strength in the test gas [57]. In both cases the secondary driver should be configured to produce a sizable sound speed increase compared to the expanded primary driver gas. This requirement immediately sets a limit on the upper fill pressure of helium. For high enthalpy conditions it will be necessary to run low fill pressures in order to achieve a worthwhile shock strength increase. For low enthalpy conditions, the fill pressure should be just sufficiently low to achieve an acoustic buffer ratio of approximately $a_{sd2}/a_{sd3} > 1.25 \sim 1.50$. Hence in both cases the suitable fill pressure ranges are not broad, and this is not necessarily a variable that would normally be finely tuned.

7.3.6 Item 11

These fill gases are easily and finely tunable variables which directly influence the test flow properties. For scramjet conditions both shock and accelerator gases are air; the focus of this chapter is to examine how the test flow properties vary across a representative range of fill pressures in both tubes.

7.3.7 Parametric Design Variables

The above discussion demonstrates that for an established facility such as X2, the number of practical design variables becomes greatly reduced. This chapter aims to examine what operational envelope is realistically available for X2 with the new driver conditions described in Table 6.7. The facility is initially considered without a secondary driver, and its performance is calculated across a representative range of shock and acceleration tube fill pressures. Contour plots of test flow Mach number, velocity, and static pressure, show the theoretical range of test flow properties available with the three new driver conditions.

Importantly, the plots show that for a given driver condition, only two out of three target flow properties (Mach number, velocity, and static pressure) can theoretically be achieved at once. In order to obtain all three, the driver also needs to be specifically configured, which involves a large effort when a tuned driver condition is required. Therefore driver

performance can be seen as the primary static pressure control for the facility. It is also shown that for X2 configured to achieve the target scramjet flow conditions in Table 1.1, the value of a_4 has to be so high that an acoustic buffer from driver disturbances is not achieved (i.e. $a_2/a_3 \not> 1$ in Figure 3.1), and usable flow conditions would not arise. These scramjet flow conditions *cannot* be achieved simultaneously with an effective acoustic buffer *unless* a secondary driver is used.

The introduction of a suitably configured secondary driver achieves the acoustic buffer for each driver condition (i.e. $a_{sd2}/a_{sd3} > 1$). However, having secondary driver fill pressure as another variable prevents the X2 operational envelope from being presented on a single 2-D contour plot. Instead, a selection of representative secondary driver fill pressures was considered separately for each new driver condition, and a contour plot was produced for each combination of driver condition / secondary driver fill pressure. From the contour plots, the corresponding shock and acceleration fill pressures to achieve the target Mach number and velocity for each target flow condition were calculated; the resulting static pressure isobar passing through the intersection of these two contours was then identified.

It is shown that the introduction of a secondary driver configured to achieve $a_{sd2}/a_{sd3} > 1$ reduces the theoretical test flow static pressure for a given driver condition and target Mach number and velocity, however, this fill pressure can potentially be used for fine adjustment of the static pressure without modifying the primary driver. Finally, four different flow conditions are identified for further detailed analysis and experimental testing.

7.4 Analysis Limitations

The analysis contained in this chapter makes several key simplifications which affect the accuracy of the predictions:

1. The primary driver gas pressure and temperature are assumed to be constant following diaphragm rupture, and are derived from experimental shock speed measurements. Whilst driver pressure is actually unsteady, the assumption of constant driver conditions is reasonable since the driver is tuned and will approximately maintain these target levels for sufficient duration not to interfere with the test flow for most sensible facility configurations.
2. Mirels effects. If a tube has sufficient length, mass entrainment in the boundary layer will result in shock attenuation and acceleration of the trailing contact surface [99, 100]. Many of the predicted conditions will not be achieved if tube lengths are excessive.

3. Test time. It is assumed that tube lengths are configured to achieve usable test time. If tubes are too short then test time will be insufficient; too long, and upstream wave processes may interfere with the test flow before its arrival at the test section.
4. Wave processes. The analysis presented in this chapter does take into account some of the critical wave processes; for example, the reflected shock at the secondary diaphragm for high shock tube fill pressures with a secondary driver. However, as is discussed in Section 7.8, this reflected shock causes a delayed boost in the shock strength through the shock tube, which significantly increases the subsequent downstream shock strength. Effects such as this can be significant, but were ignored in the present study due to the impracticality of considering all such effects in such a broad study. However, it illustrates the requirement for more detailed analysis once basic flow conditions are selected, and indicates one aspect of the study that could be improved in future.

The purpose of this chapter is to provide an indication of the available performance envelope of X2 for the three new tuned driver conditions. The secondary driver is then considered in order to provide some understanding of how this complicating feature affects the final conditions that can be achieved. Whilst the results of this analysis provide guidance on how to develop new flow conditions, detailed flow condition development will benefit greatly from 1-D and 2-D axisymmetric CFD analysis, primarily to capture wave processes neglected in the 0-D analysis.

7.5 Driver Performance Calculation

7.5.1 Methodology

The three new driver conditions detailed in Table 6.7 are considered in the present analysis. These conditions (with 10.524 kg piston) have a significantly longer useful driver gas supply duration as compared to the previous pure helium driver (with 35.0 kg piston). Comparing a tuned driver condition to the nominal helium driver condition, in order to achieve similar shock strength performance, it is necessary to run the driver at much higher reservoir pressures, and with a thicker diaphragm. However, the end result is a free-piston driver with similar performance, but the capability to drive a strong, slow, shock, the entire length of the tunnel, without the previously observed shock attenuation due to driver pressure drop.

In order to perform a 0-D analysis of the tunnel, an approximation of the free-piston driver performance is made. Referring to Figure 3.3 on page 38, the driver gas flow across the area change at the primary diaphragm (from the 0.2568 m diameter compression

tube to the 0.085 m diameter driven tube) is choked. The driver gas undergoes a steady expansion across the area change followed by an unsteady expansion down the adjacent tube. The flow properties of the driver gas after the initial *steady expansion* (Region 11 in Figure 3.3) are approximately independent of the initial fill conditions in the adjacent tube. The flow properties of the driver gas after it has been processed by the *unsteady expansion* (Region 3) are then dependent on the fill conditions in the driven tube.

Considering Figure 3.3, driver gas from Region 11 is processed by an unsteady expansion, resulting in Region 3 flow. Flow properties across the unsteady expansion are related as follows:

$$u_3 + \frac{2a_3}{\gamma_3 - 1} = u_{11} + \frac{2a_{11}}{\gamma_{11} - 1} \quad (7.1)$$

Flow across the area change from the compression tube is assumed to be sonic (choked):

$$u_{11} = a_{11} \quad (7.2)$$

Noting that the driver gas is a mixture of helium and argon - two monatomic gases - the ratio of specific heats and gas constants are assumed to be constant throughout the entire series of flow processes:

$$\gamma_{11} = \gamma_3 = \gamma_4 \quad (7.3)$$

The specific gas constant for the mixture is calculated from the partial pressures and gas constants of the component gases. Once more, this property is assumed to remain constant throughout the various flow regions:

$$R_{11} = R_3 = R_4 = \frac{\sum_{i=1}^n p_i}{\sum_{i=1}^n \frac{p_i}{R_i}} \quad (7.4)$$

Expanding sound speed terms, substituting Equations 7.2, 7.3, and 7.4, into 7.1, and solving for T_{11} :

$$T_{11} = \left[\frac{u_3 (\gamma_4 - 1)}{(\gamma_4 + 1) \sqrt{\gamma_4 R_4}} + \frac{2\sqrt{T_3}}{\gamma_4 + 1} \right]^2 \quad (7.5)$$

Static pressure in the Region 11 expanded driver gas is calculated assuming an isentropic unsteady expansion:

$$T_{11} = T_3 \left(\frac{p_{11}}{p_3} \right)^{\frac{\gamma_4 - 1}{\gamma_4}} \quad (7.6)$$

Subscripting initial fill pressure and temperature in the compression tube with ‘*i*’, temperature and pressure at diaphragm rupture is assumed to vary isentropically during the free-piston compression process. This assumption is considered to be reasonable since the lightweight piston compression process is very fast, with heat loss subsequently low. Blanked-off driver test results were used to calculate polytropic indices of between 1.60 and 1.61 in Section 6.9.2. These are close to the ideal $\gamma = 5/3$ for helium, and therefore indicate that there was not excessive driver heat loss during the piston compression process. Thus, driver pressure and temperature are assumed to follow isentropic relations as follows:

$$T_4 = T_{4,i} \left(\frac{p_4}{p_{4,i}} \right)^{\frac{\gamma_4 - 1}{\gamma_4}} \quad (7.7)$$

An unsteady expansion wave passes from the primary diaphragm through the Region 4 driver gas. This $u - a$ wave, which propagates through the approximately stagnated driver gas, is weak for area ratios in excess of 4, and therefore has little effect on total pressure and total temperature [75]. Therefore Region 4 is assumed to have identical stagnated properties to Region 4' in Figure 3.3:

$$T_{04'} = T_{04} \quad (7.8)$$

Stagnation properties remain constant through the isentropic steady expansion between Regions 4' and 11:

$$T_{04'} = T_{011} = T_{04} \quad (7.9)$$

Applying standard Mach relations for total temperature in Regions 4 and 11, noting that flow in Region 11 is sonic ($M_{11} = 1$), and flow in region 4 is assumed to be stagnant ($M_4 = 0$), substituting Equation 7.3, and noting Equation 7.9:

$$\frac{T_{011}}{T_{11}} = 1 + \frac{\gamma_{11} - 1}{2} M_{11}^2 \rightarrow T_{011} = T_{11} \left(1 + \frac{\gamma_4 - 1}{2} \times 1^2 \right) \rightarrow T_{011} = T_{11} \left(\frac{\gamma_4 + 1}{2} \right) \quad (7.10)$$

$$\frac{T_{04}}{T_4} = 1 + \frac{\gamma_4 - 1}{2} M_4^2 \rightarrow T_{04} = T_4 \left(1 + \frac{\gamma_4 - 1}{2} \times 0^2 \right) \rightarrow T_{04} = T_4 \quad (7.11)$$

$$\rightarrow T_4 = T_{11} \left(\frac{\gamma_4 + 1}{2} \right) \quad (7.12)$$

Equating 7.7 and 7.12, and solving for T_{11} :

$$T_{11} = \left(\frac{2}{\gamma_4 + 1} \right) \left(\frac{p_4}{p_{4,i}} \right)^{\frac{\gamma_4 - 1}{\gamma_4}} T_{4,i} \quad (7.13)$$

Equating 7.13 and 7.5, and solving for p_4 :

$$p_4 = p_{4,i} \left[\frac{u_3 (\gamma_4 - 1)}{\sqrt{2\gamma_4 R_4 T_{4,i} (\gamma_4 + 1)}} + \sqrt{\frac{2T_3}{T_{4,i} (\gamma_4 + 1)}} \right]^{\frac{2\gamma_4}{\gamma_4 - 1}} \quad (7.14)$$

Equating 7.5 and 7.6, and solving for p_{11} :

$$p_{11} = p_3 \left[\frac{u_3 (\gamma_4 - 1)}{\sqrt{T_3} (\gamma_4 + 1) \sqrt{\gamma_4 R_4}} + \frac{2}{\gamma_4 + 1} \right]^{\frac{2\gamma_4}{\gamma_4 - 1}} \quad (7.15)$$

Finally, applying isentropic gas relations between Regions 4 and 11:

$$\frac{p_4}{p_{11}} = \left(\frac{T_4}{T_{11}} \right)^{\frac{\gamma_4}{\gamma_4 - 1}} \quad (7.16)$$

Substituting Equations 7.12, 7.14, and 7.15, into 7.16, and simplifying:

$$\left[\frac{u_3 (\gamma_4 - 1)}{\sqrt{2T_{4,i}\gamma_4 R_4 (\gamma_4 + 1)}} + \sqrt{\frac{2T_3}{T_{4,i} (\gamma_4 + 1)}} \right] - \left(\frac{p_3}{p_{4,i}} \right)^{\frac{\gamma_4 - 1}{2\gamma_4}} \left[\frac{u_3 (\gamma_4 - 1)}{\sqrt{2T_3\gamma_4 R_4 (\gamma_4 + 1)}} + \sqrt{\frac{2}{\gamma_4 + 1}} \right] = 0 \quad (7.17)$$

γ_4 , R_4 , and $p_{4,i}$, are known from the initial conditions in the driver. Once the shock speeds in the driven tube have been measured experimentally, u_2 and p_2 can be calculated using CEA2 for known initial conditions in the driven tube; it is then assumed that $u_3 = u_2$ and $p_3 = p_2$ across the interface. T_3 can then be solved numerically by substitution of these five parameters into Equation 7.17. p_{11} , p_4 , T_{11} , T_4 , and u_{11} , can subsequently be solved by substitution of known parameters into Equations 7.15, 7.14, 7.13, 7.12, and 7.2, respectively.

7.5.2 Results

Region 11 properties are now calculated for the three driver conditions from Table 6.7. Several repeat experimental measurements were made of shock speeds, through a tube initially filled with 150 kPa helium, as part of the lightweight piston commissioning process detailed in Chapter 4. Shock speeds were measured between two pairs of transducers (st1-st2 and st2-st3), providing two shock speed calculations per shot. Assuming that the shock speeds are constant through this section of the driven tube, an average was

made of all shock speeds for a given driver condition. Table 7.1(a to c) shows individual and averaged experimental shock speeds for each driver condition. It can be seen that shock speeds are fairly consistent, with standard deviations all less than 2.0% of average shock speed.

(a) X2-LWP-1.2mm-0		(b) X2-LWP-2.0mm-0		(c) X2-LWP-2.5mm-0					
Shot ID	Shock speeds (m/s)		Shot ID	Shock speeds (m/s)		Shot ID	Shock speeds (m/s)		
	Transducer pair st1-st2	st2-st3		Transducer pair st1-st2	st2-st3		Transducer pair st1-st2	st2-st3	
x2s1332	3,007	2,988	x2s1350	3,973	3,946	x2s1356	4,128	4,143	
x2s1333	3,029	3,017	x2s1351	3,986	3,946	x2s1357	4,128	4,234	
x2s1334	2,907	2,840	x2s1352	4,007	3,973	x2s1358	4,173	4,234	
x2s1361	2,982	2,986	x2s1353	3,986	3,939	x2s1359	4,165	4,195	
x2s1362	3,013	2,918	x2s1354	3,993	3,946				
x2s1363	3,017	2,940	x2s1355	3,993	3,966				
x2s1364	2,974	2,994							
Mean = 2,972 m/s, σ = 53 m/s		Mean = 3,971 m/s, σ = 23 m/s		Mean = 4,175 m/s, σ = 43 m/s					

Table 7.1: Experimentally measured shock speeds, 150 kPa helium initial fill, three different tuned driver conditions.

The average shock speeds in Table 7.1 were analysed using CEA for helium at 150 kPa and 300 K, with results shown in Table 7.2. The methodology derived in Section 7.5.1 was then used to predict expanded driver gas properties (Region 11 of Figure 3.3). Final results are summarised in Table 7.3. It can be seen that rupture pressures predicted using this technique differ from those assumed in Table 6.7; this will be primarily due to losses during the piston compression process and the expansion through the area change. Driver properties in Table 7.3 are now used to estimate downstream flow processes for various configurations of the X2 expansion tube facility.

7.6 Predicted Test Flow Properties - Basic Expansion Tube

7.6.1 Overview

This section outlines the methodology used to predict downstream flow processes for X2 running in basic expansion tube mode. A 0-D analysis of flow processes downstream of the primary diaphragm was made using expanded driver gas properties calculated in Table 7.3. Where applicable, ideal gas analytical relations were modified to incorporate equilibrium gas properties calculated using the NASA code CEA [43]. Following an explanation of the methodology in Sections 7.6.2 and 7.6.3, results are presented in Section 7.6.5.

(a) X2-LWP-1.2mm-0

(b) X2-LWP-2.0mm-0

(c) X2-LWP-2.5mm-0

INITIAL GAS (1)		INITIAL GAS (1)		INITIAL GAS (1)	
MACH NUMBER1	2.9162	MACH NUMBER1	3.8964	MACH NUMBER1	4.0966
U1, M/SEC	2972.00	U1, M/SEC	3971.00	U1, M/SEC	4175.00
P, BAR	1.5000	P, BAR	1.5000	P, BAR	1.5000
T, K	300.00	T, K	300.00	T, K	300.00
RHO, KG/CU M	2.4070-1	RHO, KG/CU M	2.4070-1	RHO, KG/CU M	2.4070-1
H, KJ/KG	9.6074	H, KJ/KG	9.6074	H, KJ/KG	9.6074
U, KJ/KG	-613.58	U, KJ/KG	-613.58	U, KJ/KG	-613.58
G, KJ/KG	-9202.73	G, KJ/KG	-9202.73	G, KJ/KG	-9202.73
S, KJ/(KG) (K)	30.7078	S, KJ/(KG) (K)	30.7078	S, KJ/(KG) (K)	30.7078
M, (1/n)	4.003	M, (1/n)	4.003	M, (1/n)	4.003
Cp, KJ/(KG) (K)	5.1932	Cp, KJ/(KG) (K)	5.1932	Cp, KJ/(KG) (K)	5.1932
GAMMAS	1.6667	GAMMAS	1.6667	GAMMAS	1.6667
SON VEL,M/SEC	1019.1	SON VEL,M/SEC	1019.1	SON VEL,M/SEC	1019.1
SHOCKED GAS (2)--INCIDENT--EQUILIBRIUM		SHOCKED GAS (2)--INCIDENT--EQUILIBRIUM		SHOCKED GAS (2)--INCIDENT--EQUILIBRIUM	
U2, M/SEC	1005.12	U2, M/SEC	1188.92	U2, M/SEC	1230.34
P, BAR	15.570	P, BAR	28.092	P, BAR	31.092
T, K	1053.17	T, K	1682.14	T, K	1832.49
RHO, KG/CU M	7.1172-1	RHO, KG/CU M	8.0394-1	RHO, KG/CU M	8.1678-1
H, KJ/KG	3920.94	H, KJ/KG	7187.32	H, KJ/KG	7968.12
U, KJ/KG	1733.23	U, KJ/KG	3693.05	U, KJ/KG	4161.53
G, KJ/KG	-30168.6	G, KJ/KG	-49289.9	G, KJ/KG	-53985.5
S, KJ/(KG) (K)	32.3686	S, KJ/(KG) (K)	33.5746	S, KJ/(KG) (K)	33.8084
M, (1/n)	4.003	M, (1/n)	4.003	M, (1/n)	4.003
(dLV/dLP)t	-1.00000	(dLV/dLP)t	-1.00000	(dLV/dLP)t	-1.00000
(dLV/dLT)p	1.0000	(dLV/dLT)p	1.0000	(dLV/dLT)p	1.0000
Cp, KJ/(KG) (K)	5.1932	Cp, KJ/(KG) (K)	5.1932	Cp, KJ/(KG) (K)	5.1932
GAMMAS	1.6667	GAMMAS	1.6667	GAMMAS	1.6667
SON VEL,M/SEC	1909.5	SON VEL,M/SEC	2413.3	SON VEL,M/SEC	2518.8
P2/P1	10.380	P2/P1	18.728	P2/P1	20.728
T2/T1	3.511	T2/T1	5.607	T2/T1	6.108
M2/M1	1.0000	M2/M1	1.0000	M2/M1	1.0000
RH02/RH01	2.9569	RH02/RH01	3.3400	RH02/RH01	3.3934
V2, M/SEC	1966.88	V2, M/SEC	2782.08	V2, M/SEC	2944.66

Table 7.2: CEA calculation of shocked gas properties, 150 kPa helium, three different tuned driver conditions.

(a) Inputs

Parameter	Units	X2-LWP-1.2mm-0	X2-LWP-2.0mm-0	X2-LWP-2.5mm-0
u_2	m/s	1,967	2,782	2,945
p_2	MPa	1.557	2.809	3.109
γ_4	-	5/3	5/3	5/3
$T_{4,i}$	K	300	300	300
$R_{4,He}$	J/(kg.K)	2,077	2,077	2,077
$R_{4,Ar}$	J/(kg.K)	208	208	208
$p_{4,i,He}$	kPa	88.2	74.3	61.7
$p_{4,i,Ar}$	kPa	22.1	18.5	15.4

(b) Outputs

Parameter	Units	X2-LWP-1.2mm-0	X2-LWP-2.0mm-0	X2-LWP-2.5mm-0
u_3	m/s	1,967	2,782	2,945
p_3	MPa	1.557	2.809	3.109
T_3	K	865	1,174	1,316
R_4	J/(kg.K)	741.7	744.1	743.2
$p_{4,i}$	kPa	110.3	92.8	77.1
p_4	MPa	8.837	23.68	26.22
λ_4	-	13.88	27.81	33.04
T_4	K	1,732	2,753	3,089
T_{11}	K	1,299	2,065	2,317
p_{11}	MPa	4.305	11.54	12.77
a_{11}	m/s	1,267	1,600	1,694
u_{11}	m/s	1,267	1,600	1,694

Table 7.3: X2 lightweight piston driver condition performance calculations.

7.6.2 Shock Tube Flow Processes

Referring to Figure 3.1, the monatomic driver gas in Region 11 is processed by an unsteady expansion, which results in Region 3 flow. Equation 7.1 applies through the unsteady expansion. Assuming $\gamma_3 = \gamma_4$, expanding the sound speed term a_3 , and solving for T_3 :

$$T_3 = T_{3,u_3} = \frac{(\gamma_4 - 1)^2}{4\gamma_4 R_4} \left(u_{11} - u_3 + \frac{2a_{11}}{\gamma_4 - 1} \right)^2 \quad (7.18)$$

Assuming the process is isentropic, temperature across the unsteady expansion can be determined from the pressure change. Solving for T_3 in Equation 7.6:

$$T_3 = T_{3,p_3} = T_{11} \left(\frac{p_3}{p_{11}} \right)^{\frac{\gamma_4 - 1}{\gamma_4}} \quad (7.19)$$

CEA is used to calculate the equilibrium gas properties of the shock processed air. For a given driver condition from Table 7.3, and shock tube fill pressure, the shock speed can be obtained as follows:

1. Assume a shock actually forms in the shock tube (a reasonable assumption so long as the shock tube fill pressure is less than the Region 11 static pressure).
2. Start with a shock speed just above Mach= 1, which is the minimum possible speed.
3. Use CEA to calculate u_2 and p_2 for the shocked test gas.
4. Noting that $p_3 = p_2$, substitute p_3 and the expanded driver gas properties from Table 7.3 into Equation 7.19 and calculate $T_3 = T_{3,p_3}$.
5. Noting that $u_3 = u_2$, substitute u_3 and the expanded driver gas properties from Table 7.3 into Equation 7.18 and calculate $T_3 = T_{3,u_3}$.
6. Calculate the difference between the two T_3 estimates, $\Delta_{u_3,p_3} = T_{3,u_3} - T_{3,p_3}$.
7. Using a marching solver, incrementally increase the assumed shock speed, repeating Steps 4 to 6, until Δ_{u_3,p_3} changes sign. At the cusp of this sign change, $T_{3,u_3} = T_{3,p_3}$; the corresponding shock speed is the solution.

7.6.3 Acceleration Tube Flow Processes

When the normal shock wave in the test gas arrives at the secondary diaphragm, rupture is assumed to occur instantaneously and the diaphragm is assumed to be massless. A new shock wave forms in the acceleration tube; this shock processes accelerator gas in Region 5 of Figure 3.1, producing Region 6 flow. Region 2 shock processed test gas undergoes an unsteady expansion upon arrival at the low pressure acceleration tube,

producing Region 7 flow. Static pressures and velocities are assumed to be equal for Regions 6 and 7; i.e. $p_6 = p_7$ and $u_6 = u_7$. Following the methodology from McIntyre et al. [135], the differential change in gas velocity through the unsteady expansion, du , is related to the change in speed of sound, da , as follows:

$$du = -\frac{2}{(\gamma - 1)}da \quad (7.20)$$

Referring to Equation 7.20, γ and c_p are not constant, however the entropy remains constant through the expansion. A code such as CEA may be used to generate a series of self-consistent gas properties for the isentropic expansion between an initial known pressure p_2 (calculated in Section 7.6.2) to an arbitrary pressure $p_7 (= p_6)$, with sufficient resolution to accurately capture changes in γ and c_p . The temperature and velocity of the gas can then be calculated using updated values for γ and c_p by stepping through the expansion until the pressure, p_7 , is reached [135]. The actual magnitude of p_7 is the final expanded pressure which has corresponding $u_7 = u_6$ (calculated in accordance with Equation 7.20) when the test gas is expanded to pressure $p_7 = p_6$. For known Region 2 and 5 flow properties, the shock speed through the acceleration tube is iterated through until these equalities are met. The general procedure to calculate Region 6 and 7 flow properties is as follows:

1. Assume there is a sufficient pressure drop between Regions 2 and 7 for Region 2 gas to undergo an unsteady expansion upon arrival at the acceleration tube.
2. Start with an acceleration tube shock speed just above Mach = 1.
3. Use CEA to calculate u_6 and p_6 for known initial fill properties in Region 5 and the shock speed from Step 2.
4. Using CEA, calculate a set of self consistent flow properties for a gas expanded from known Region 2 pressure and temperature to the calculated accelerator gas pressure p_6 from Step 3.
5. Calculate the velocity of the test gas once it has expanded to pressure p_6 using Equation 7.20.
6. Calculate the difference between the expanded test gas velocity, u_7 , and the shock processed accelerator gas velocity, u_6 , i.e. $\Delta_{u_6,u_7} = u_6 - u_7$.
7. Using a marching solver, incrementally increase the assumed shock speed, repeating Steps 3 to 6 until Δ_{u_6,u_7} changes sign. At the cusp of this sign change, $u_6 = u_7$ and the corresponding shock speed is the solution.

7.6.4 X2 Mach 10 Contoured Nozzle

The contoured Mach 10 nozzle for X2 has inlet and outlet diameters of $D_i = 85$ mm and $D_o = 201.8$ mm respectively. Assuming constant γ through the nozzle, then for any M_i ,

M_o can be calculated by solving Equation 3.39. The nozzle is optimised for $M_i = 7.3$ and $M_o = 10.0$, and it is not expected to perform well off-design. Often an ‘effective’ area ratio is calculated for a nozzle based on experimental measurements; this is not attempted here. The nozzle is assessed over such a broad range of off-design operating conditions that a correction based on a very narrow selection of actual experimental results is considered to be unhelpful. Instead, the geometric area ratio for the nozzle is used, $A_o/A_i = (201.8/85)^2 = 5.64$.

7.6.5 Results - X2 Performance Envelope - Basic Expansion Tube

Region 7 test flow properties (refer Figure 3.1) were calculated for a broad range of shock and acceleration tube fill pressures ($p_1 = 1\text{-}1,000 \text{ kPa}$ and $p_5 = 1\text{-}1,000 \text{ Pa}$). These calculations were used to generate contours of Mach number, velocity, and static pressure. Results are shown in Figures 7.1(a-c) for the three tuned driver conditions from Table 6.7 for X2 without a nozzle; Figure 7.2 shows the test flow properties if X2 is operated with the existing Mach 10 nozzle.

The target flow conditions in Table 1.1 are each characterised by three test flow properties: Mach number, velocity, and static pressure. Inspection of the Figure 7.1 and 7.2 contour plots indicates that for each driver condition, only two out of the three target flow properties can, in general, be achieved simultaneously. Of these three properties, Mach number and velocity are considered the two most important properties to match; firstly, matching Mach number and velocity ensures that the target flow enthalpy is achieved; secondly, static pressure is a scalable parameter which will vary depending on $p\text{-}L$ scaling for the specific test article.

In Figures 7.1 (a-c) and 7.2(a-c), Points ‘A’, ‘B’, and ‘C’ represent combinations of shock and acceleration tube fill pressures, p_1 and p_5 , which respectively achieve target Mach number and velocity for the Mach 10.0, 12.5, and 15.0 flow conditions in Table 1.1. The corresponding static pressure isobars which intersect each of these design points are not equal to the target static pressures shown in Table 1.1; actual static pressures are presented in Appendix C. In Figures 7.1(b & c) and 7.2(b & c), the Mach 10 flow condition (Point ‘A’, coloured grey) occurs outside of the domain of the contour plots; however, these Mach 10 conditions have also been calculated and are presented in the Appendix.

In most cases, the static pressure associated with each target flow condition is higher than the target static pressure; this indicates potential for $p\text{-}L$ scaling. In order to adjust the test flow static pressure whilst maintaining target Mach number and velocity, the normal approach would be to adjust the performance of the driver; comparison between Figures 7.1 and 7.2 indicates that a nozzle can significantly reduce the test flow static

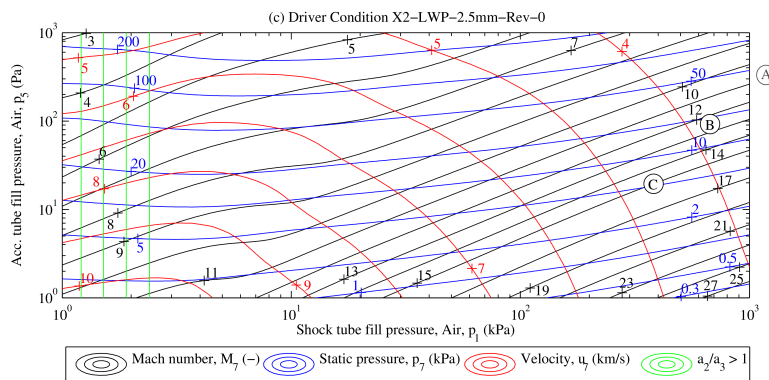
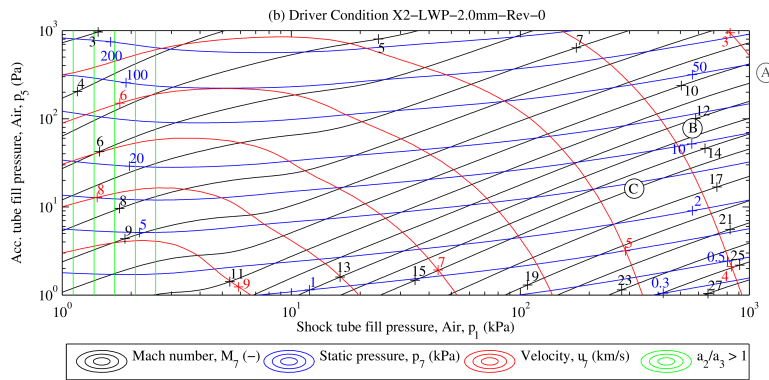
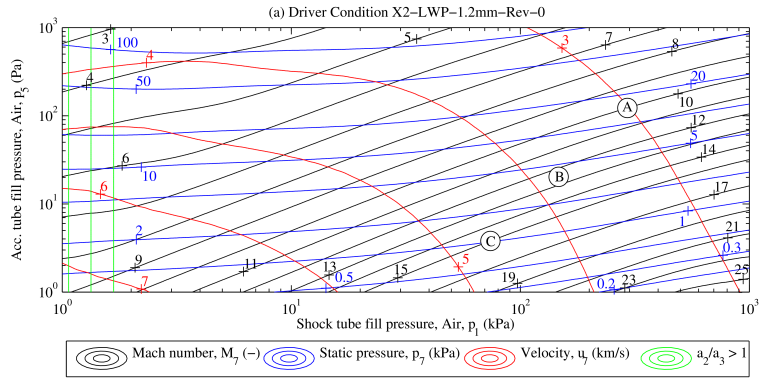


Figure 7.1: X2 performance envelope calculations for the new driver conditions detailed in Table 6.7. Analysis uses equilibrium gas properties calculated with CEA. Properties shown are for the test flow (Region 7 in Figure 3.1). Points 'A', 'B', and 'C' respectively represent the Mach 10.0, 12.5, and 15.0 target flow conditions from Table 1.1 in terms of velocity and Mach number; the corresponding static pressure for each flow condition differs from the Table 1.1 target value and depends on the particular driver used. In plots (b) and (c), Point 'A' occurs outside of the domain shown and is thus coloured grey; however, these flow condition details were also calculated and are provided in Appendix C.

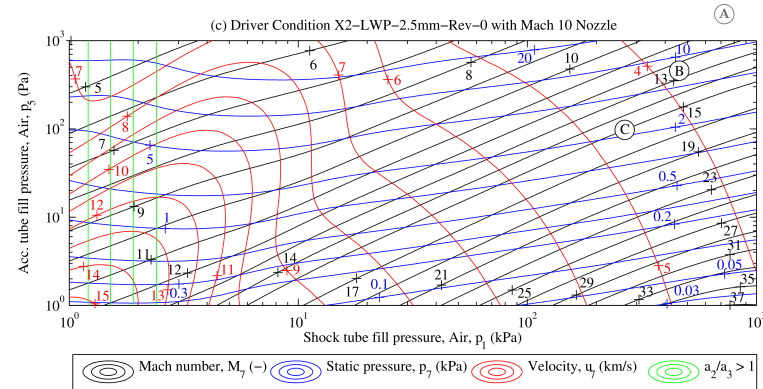
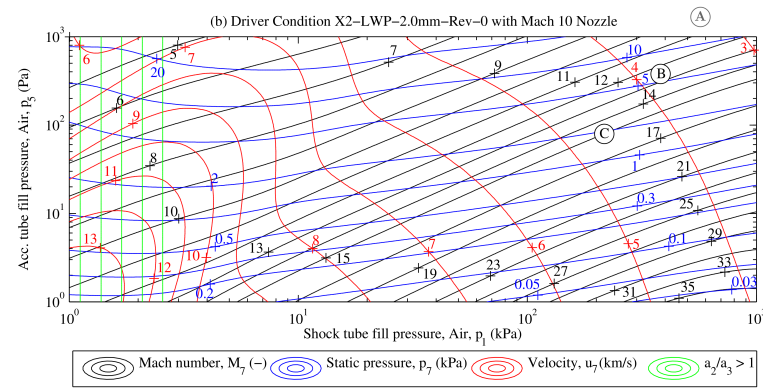
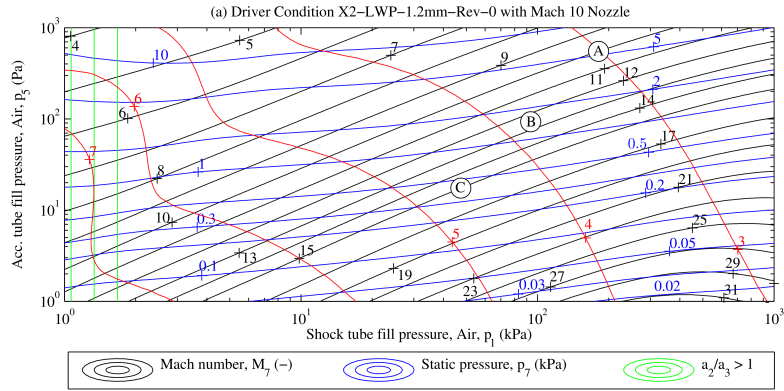


Figure 7.2: X2 performance envelope calculations for the new driver conditions detailed in Table 6.7 with Mach 10 nozzle. A steady expansion through a contoured Mach 10 nozzle with area ratio $(201.8/85)^2 = 5.64$ is applied to Region 7 test flow properties from Figure 7.1. Although equilibrium gas properties were used in the calculation of test flow properties in Figure 7.1, the subsequent nozzle expansion applied here assumes that the air test gas is calorically perfect and that the nozzle behaves in accordance with ideal 1-D theory per Section 7.6.4. Points 'A', 'B', and 'C' respectively represent the Mach 10.0, 12.5, and 15.0 target flow conditions from Table 1.1 in terms of velocity and Mach number; the corresponding static pressure for each flow condition differs from the Table 1.1 target value and depends on the particular driver used. In plots (b) and (c), Point 'A' occurs outside of the domain shown and is thus coloured grey; however, these flow condition details were also calculated and are provided in Appendix C

pressure (aside from its benefits of increased core flow size and test time). However, such nozzles are expensive to produce and do not necessarily possess good performance off-design, therefore they not a readily tunable parameter.

It is important to note that the sound speed buffer ratio is not met for most of the operational envelope shown in the contour plots; only for low shock tube fill pressures (where shock speeds are high) does $a_2/a_3 > 1$. This is consistent with observations by Paull and Stalker [72] that only a small range of high enthalpy conditions produced steady flow for basic expansion tubes, and was attributed to the $a_2/a_3 > 1$ acoustic buffer being present. The three scramjet flow conditions each have $a_2/a_3 \ll 1$, indicating that no acoustic buffer would be present for X2 operated in basic expansion tube mode with these driver conditions. This suggests the need for a helium secondary driver for the target scramjet flow conditions in Table 1.1 in accordance with Morgan [57].

7.7 Predicted Test Flow Properties - Expansion Tube with Secondary Driver

7.7.1 General Design Philosophy

Considering the schematic shown in Figure 3.3, the purpose of the secondary driver is twofold [57]:

1. To drive a stronger shock in the test gas.
2. For low enthalpy (for example, scramjet) conditions, to provide an acoustic buffer to prevent transmission of primary driver radial wave disturbances into the test gas [72].

In both cases, the key attribute of the secondary driver is a high sound speed; for this reason, helium is preferential due to its low molecular mass [57] (hydrogen is not used since it is difficult to handle safely). Introduction of this third slug of gas downstream of the primary driver provides an additional variable which complicates flow condition development and analysis. The basic performance plots in Section 7.6.5 can no longer be expressed in two dimensional space if the secondary driver fill pressure is treated as a continuous variable. However, it is noted that the helium driver does not need to be treated as a highly tunable variable for these performance analyses.

In terms of Item 1 above, a sufficiently low fill pressure is required to achieve a significant shock strength increase; if this increase is not appreciable, then the added complexity of the experimental arrangement, and the reduction in useful length of the shock and acceleration tubes, negates any benefit that might be achieved. Further, as will be shown

later in this section, if the secondary driver is used with high fill pressures of helium, the shock strength in the shock tube can be reduced for much of the operational envelope. Therefore, a logical approach to high enthalpy condition design is to select a sufficiently low secondary driver fill pressure to achieve significant and useful shock speed increases in the test gas.

In terms of Item 2 above, a sufficiently low fill pressure is required to ensure the shock processed secondary driver gas has a temperature rise corresponding to a sound speed in excess of the expanded primary driver gas. For the tuned driver conditions developed for this study, the combination of 80% helium / 20% argon corresponds to a fairly slow expanded primary driver gas sound speed. Consequently, a 100% helium secondary driver can be operated over a range of pressures and still achieve the desired sound speed increase across the interface; this requirement is met for a large range of fill pressures.

Considering the above, the key to configuring the secondary driver is to determine a fill pressure which generally meets performance and/or acoustic buffer requirements, and then perform condition fine tuning by adjusting the shock and acceleration tube fill pressures. In this respect, the analysis complexity is not significantly greater. The remainder of this section details the methodology used to analyse the facility with the addition of the secondary driver, and illustrates the effect of the secondary driver on facility performance, for a representative range of secondary driver fill pressures.

7.7.2 Secondary Driver Tube Shock Speed

The shock speed in the secondary driver is calculated in accordance with the methodology detailed in Section 7.6.2, using helium instead of air in the first driven tube.

7.7.3 Test Gas Tube Shock Speed

High density scramjet flow conditions can typically involve high fill pressures in the test gas tube. When a secondary driver is used, upon arrival of the shock at the secondary diaphragm, a new shock will be produced in the test gas. However, if the shock tube fill pressure (Region 1 in Figure 3.3) is sufficiently high, the velocity of the shock-processed test gas (Region 2) may be lower than the velocity of the shock-processed secondary driver gas (Region *sd2*), in which case a reflected shock will form in the secondary driver gas to slow it down; this is the scenario shown in Figure 3.3. However, for lower test gas fill pressures where the Region 2 test gas has greater velocity than the Region *sd2* secondary driver gas, an unsteady expansion must form to speed up the secondary driver gas so that velocity is matched across the Region 2/3 interface. Hence, the flow processes at the secondary diaphragm are condition- dependant, and need to be determined on a case-by-case basis. The general procedure to calculate Region 2 and 3 flow properties is as follows:

1. Start with a test gas tube shock speed just above Mach= 1, which is the minimum possible shock speed.
2. If the static pressure in Region 2 exceeds the static pressure in Region $sd2$ at this minimum shock speed, i.e. $p_2 > p_{sd2}$, then a reflected shock must occur to achieve the pressure rise observed.
3. If $p_2 \not> p_{sd2}$ in Step 2, then iterate through shock speed until shock processed test gas static pressure is equal to shock processed secondary driver gas static pressure, i.e. $p_2 = p_{sd2}$. This is the shock speed which would involve neither an unsteady expansion or a reflected shock to equalise the static pressures across the Region 3 and $sd2$ interface.
4. Compare the velocities from Step 3. If $u_2 < u_{sd2}$ - i.e. there is a velocity drop across the diaphragm - then it implies that the secondary driver gas needs to be slowed down, and that a reflected shock must form at the secondary diaphragm. If $u_2 > u_{sd2}$, then the secondary driver gas has not been sufficiently slowed down, therefore a normal shock must develop at the secondary driver.
5. Referring to Step 4, if a normal shock develops: starting with a Mach 1.0 shock in the test gas Region 1, calculate shocked test gas properties, i.e. Region 2, for a full range of shocks, with sufficient fidelity that intermediate shocked properties can be interpolated.
6. Starting with a Mach 1.0 reflected shock in the secondary driver gas, iterate through reflected shock speeds. For each u_2 , noting that $u_2 = u_3$, interpolate the corresponding p_3 from the spread of shocked properties determined in Step 5. Once $u_2 = u_3$ and interpolated $p_2 = p_3$ simultaneously, the correct reflected shock strength is known. The incident shock speed in the test gas, $u_{1,s}$, is also interpolated for the established value of $u_2 = u_3$.
7. Referring to Step 4, if an unsteady expansion develops: Start with an acceleration tube shock speed just above Mach= 1, which is the minimum possible shock speed. Use CEA2 to calculate u_2 and p_2 for the shock processed acceleration tube gas based on Region 1 known initial fill properties.
8. Using CEA2, calculate a set of self consistent flow properties for a gas expanded from known Region $sd2$ pressure and temperature, to shock processed accelerator gas pressure p_2 .
9. Calculate the velocity of the test gas once it has expanded to pressure p_2 using Equation 7.20.
10. Calculate the difference between the expanded test gas velocity, u_3 , and the shock processed accelerator gas velocity, u_2 , i.e. Δ_{u_2,u_3} .

11. Using a marching solver, incrementally increase the assumed shock speed, repeating Steps 7 and 10, until Δ_{u_2,u_3} changes sign. At the cusp of this sign change, $u_2 = u_3$ (within a pre-determined tolerance), and the corresponding shock speed is the solution.

7.7.4 Acceleration Tube Flow Processes

Referring to Figure 3.3, it is assumed that a sufficient pressure drop occurs between the shock processed test gas, Region 2, and the shock processed accelerator gas, Region 6, that an unsteady expansion forms at the tertiary diaphragm and processes the test gas. The solution process to determine the properties in Regions 6 and 7 are therefore identical to that used for the basic expansion tube Regions 2 and 3 per Section 7.6.3.

7.7.5 Results - X2 Performance Envelope - Expansion Tube with Secondary Driver

The use of a secondary driver increases the complexity of the system. However, the general effect of the secondary driver can be assessed by reference to a representative set of secondary driver fill pressures. The following calculation procedure was undertaken:

1. Consider each of the *three* driver operating conditions detailed in Table 6.7.
2. For each driver condition, calculate a full performance envelope across a representative range of shock and acceleration tube fill pressures, for each of the following *eight* secondary driver fill pressures:
 $p_{sd1} = \{25, 50, 100, 150, 200, 250, 300, 350\}$ kPa. The ratio a_2/a_3 typically exceeds 1 only for secondary driver fill pressures below $p_{sd1} = 350$ kPa, therefore there is little benefit in considering fill pressures beyond this level.
3. For each performance envelope calculated in Step 2, generally only two out of the three target parameters (M_7, u_7, p_7) can be achieved simultaneously. In this analysis, Mach number and velocity pairs from Table 1.1 were targeted. The corresponding fill pressures (p_1 and p_5) and test flow static pressure (p_7), were then solved for.
4. The above procedure constitutes $3 \times 8 = 24$ performance envelope calculations, and $3 \times 8 \times 3 = 72$ flow condition calculations.

Figure 7.3 provides an example of the procedure used to calculate one set of flow conditions (for Mach 10, 12.5, and 15.0) for driver condition X2-LWP-2.0mm-0 with secondary driver fill pressure $p_{sd1} = 150$ kPa. The procedure detailed in Figure 7.3 was similarly followed for each of the 24 performance envelope calculations, with the results shown in

Figures 7.4, 7.5, and 7.6, for the three driver conditions from Table 6.7. Results for a basic expansion tube without secondary driver are included for comparison. The data used to construct these plots are contained in Tables C.1, C.2, and C.3 in Appendix C.

It can be seen from Figures 7.4(g), 7.5(g), or 7.6(g), that in all cases the basic expansion tube (no secondary driver) has $a_2/a_3 \ll 1$ at the target flow conditions, and therefore will not provide an acoustic buffer effect with these driver conditions. However, it can be seen that with a secondary driver, $a_{sd2}/a_{sd3} > 1$ for all three driver conditions, for helium fill pressures $p_{sd1} < 200$ kPa.

Figures 7.4, 7.5, or 7.6 also show the effect of using a contoured hypersonic nozzle on target flow conditions. The result is generally to reduce test flow static pressure, p_7 , reduce the required shock tube fill pressure, p_1 , and increase the required acceleration tube fill pressure, p_5 . It is noted that the contoured nozzle is only optimised for nozzle exit test flows of $M_7 = 10$, and can interfere with flow quality at off-design Mach numbers. The higher Mach numbers of $M_7 = 12.5$ and $M_7 = 15.0$ are both materially off-design and therefore would not necessarily work with the current nozzle.

In order to achieve the target Mach number and velocity for each target flow condition, the combination of shock and acceleration tube fill pressures changes depending on the secondary driver fill pressure. Increasing p_{sd1} requires corresponding increases in p_1 and p_5 , and results in higher test flow static pressure, p_7 . Through the range of p_{sd1} considered, p_7 is significantly less than what can be achieved without the secondary driver; it is clear that the introduction of the secondary driver reduces the test flow static pressure compared to the basic expansion tube for these *target scramjet conditions*; an over-tailored secondary driver may produce a stronger shock and higher total pressure for a given shock tube fill pressure, however it also modifies the final test flow properties, and this analysis shows that for the target scramjet conditions it reduces the static pressure of the flow if target Mach number and velocity are to be matched. However, it is also clear that the secondary driver permits additional adjustment of the test flow static pressure that would otherwise require modification to the primary driver, all whilst still maintaining the acoustic buffer which the basic expansion tube fails to achieve.

7.8 Selected Flow Conditions

Based on the previous discussion, four flow conditions are considered in detail based upon the analysis in this chapter, as summarised in Table 7.4. A 100 kPa helium secondary driver fill pressure was selected since it has a significant predicted acoustic buffer sound speed ratio ($a_{sd2}/a_{sd3} = 1.33$ per Table C.2; Morgan [57] indicates the ratio should be at least 1.25).

Referring to Chapter 6, the driver condition x2-lwp-2p0mm-0 provided the best compro-

Select driver condition

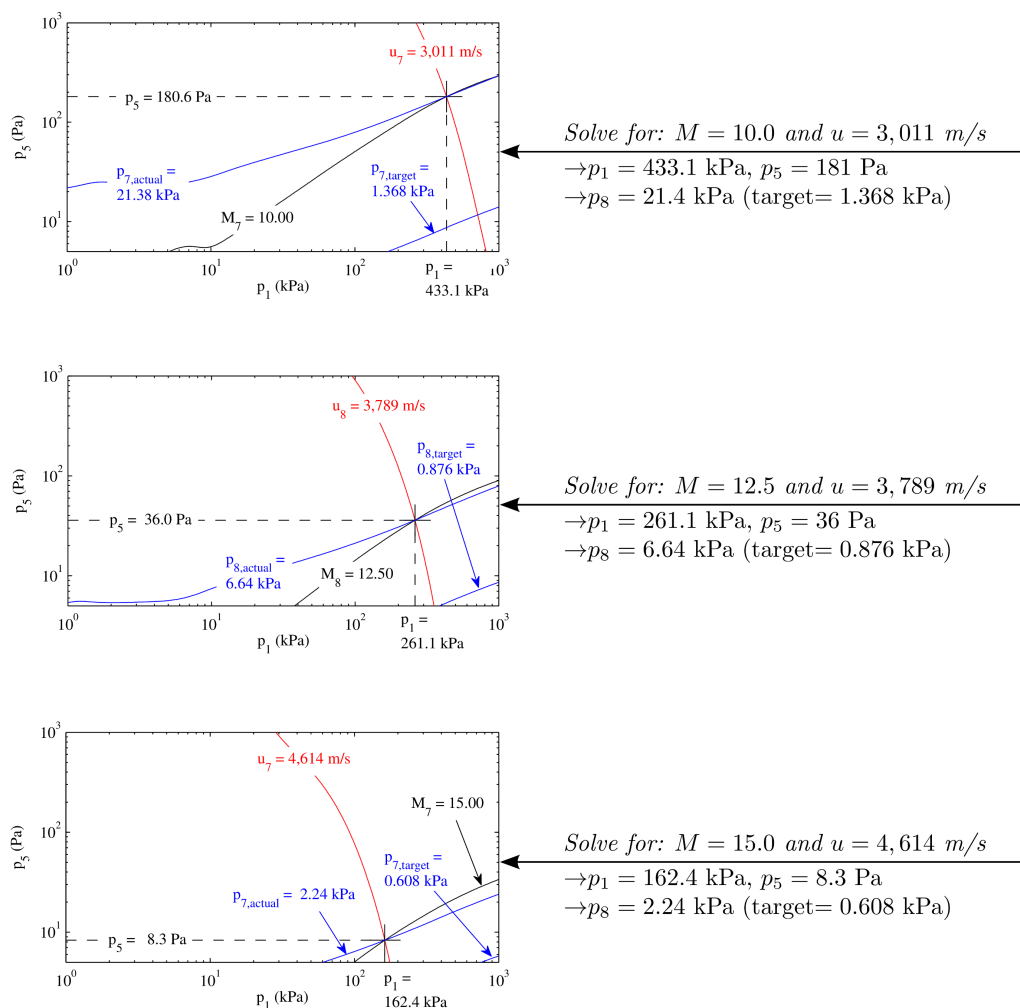
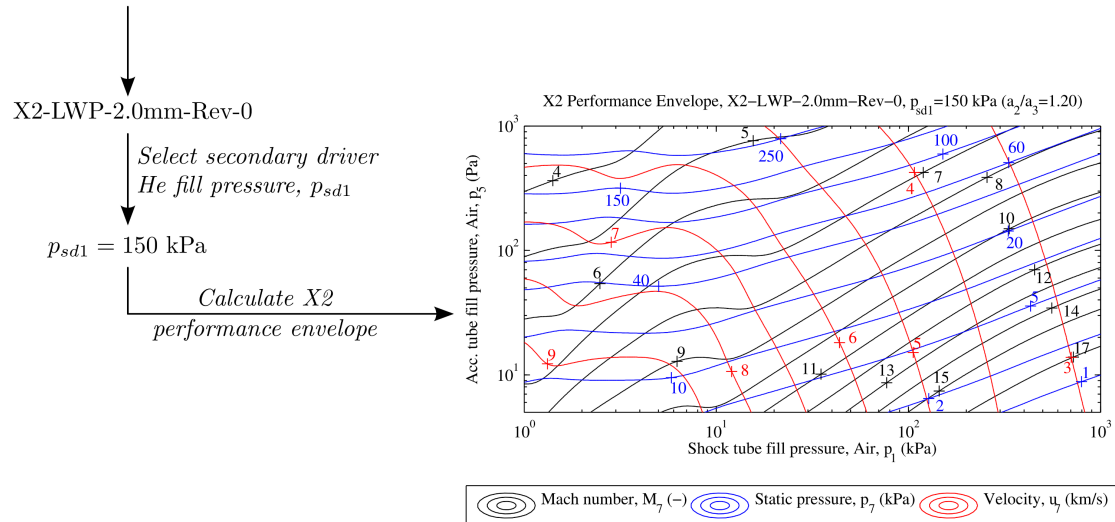


Figure 7.3: Procedure to calculate fill pressures (p_1 and p_5) and test flow static pressure (p_7) for driver condition X2-LWP-2.0mm-0 at target Mach numbers and velocities from Table 1.1.

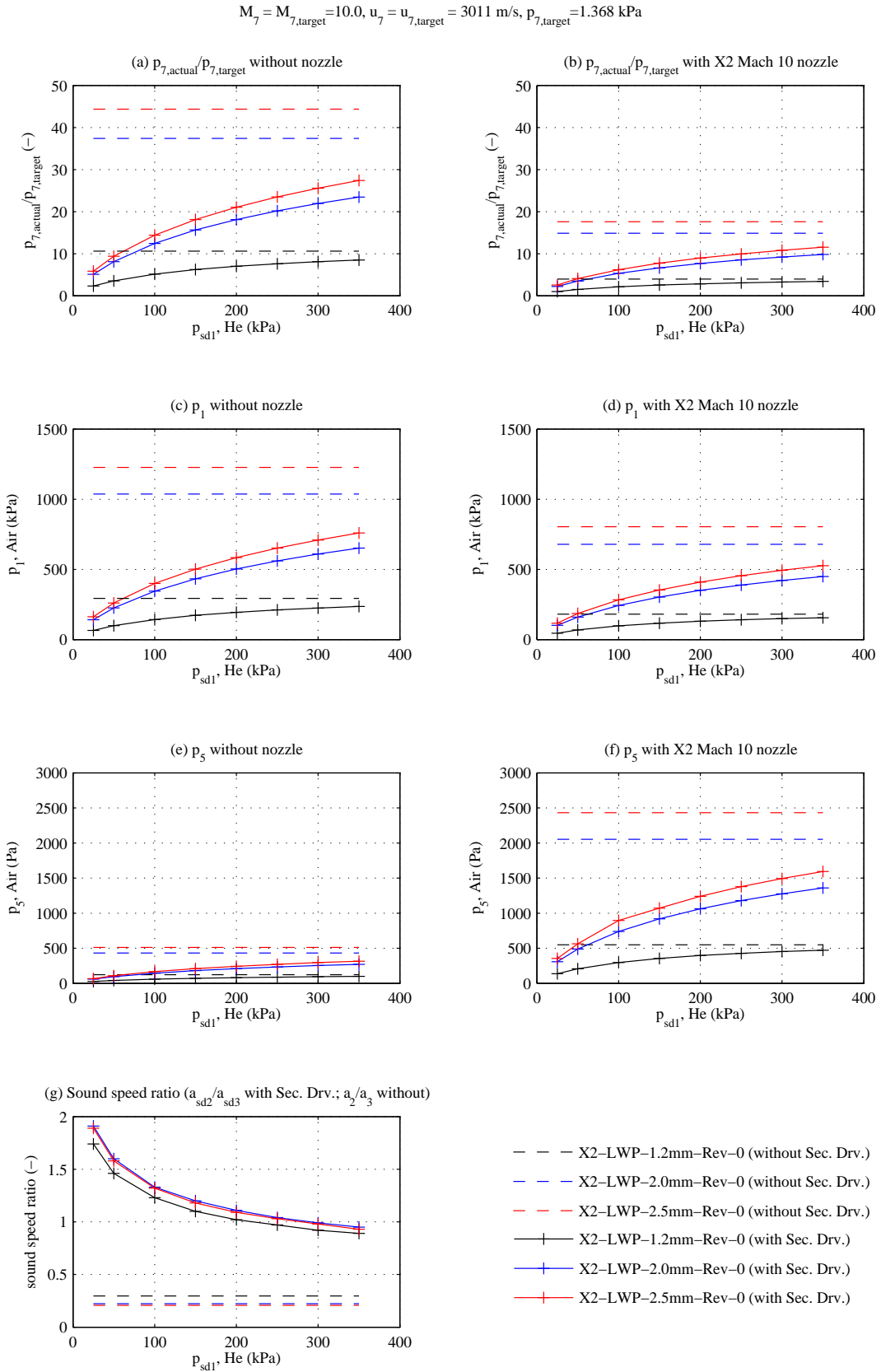


Figure 7.4: Required shock and acceleration tube fill pressures (p_1 and p_5 respectively) to achieve Mach 10 flow condition from Table 1.1. Results are for X2 using new tuned driver conditions from Table 6.7. Mach number and velocity are matched with Table 1.1; achievable test flow static pressure, p_7 , is shown. Raw data is presented in Tables C.1, C.2, and C.3.

$$M_7 = M_{7,\text{target}} = 12.5, u_7 = u_{7,\text{target}} = 3789 \text{ m/s}, p_{7,\text{target}} = 0.876 \text{ kPa}$$

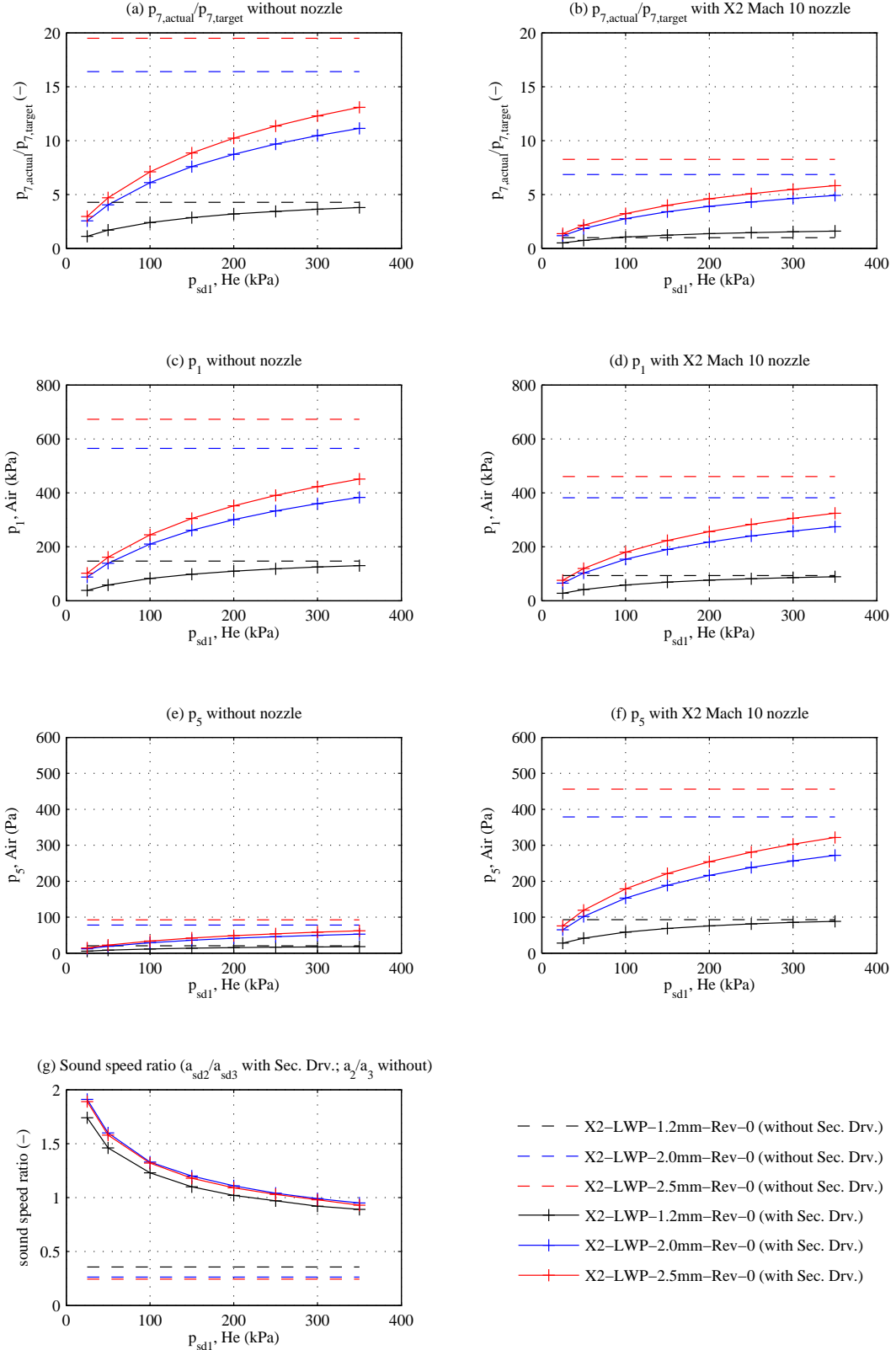


Figure 7.5: Required shock and acceleration tube fill pressures (p_1 and p_5 respectively) to achieve Mach 12.5 flow condition from Table 1.1. Results are for X2 using new tuned driver conditions from Table 6.7. Mach number and velocity are matched with Table 1.1; achievable test flow static pressure, p_7 , is shown. Raw data is presented in Tables C.1, C.2, and C.3.

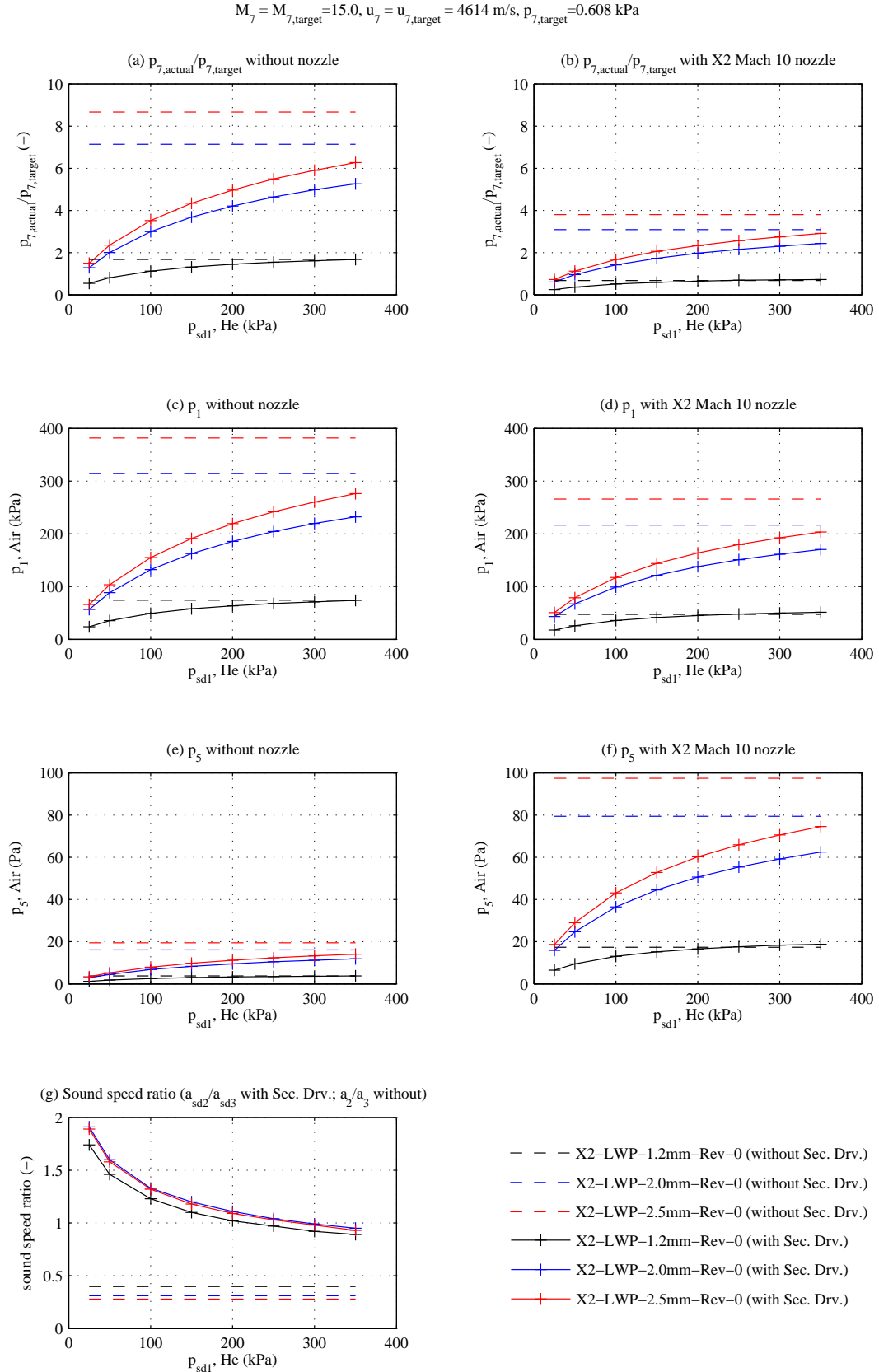


Figure 7.6: Required shock and acceleration tube fill pressures (p_1 and p_5 respectively) to achieve Mach 15 flow condition from Table 1.1. Results are for X2 using new tuned driver conditions from Table 6.7. Mach number and velocity are matched with Table 1.1; achievable test flow static pressure, p_7 , is shown. Raw data is presented in Tables C.1, C.2, and C.3.

mise between performance and smooth operation. For this reason, this driver condition is utilised for initial flow condition testing.

L1d2 [113] was used for preliminary assessment of the four proposed scramjet flow conditions detailed in Table 7.4. The L1d2 simulations predicted higher shock speeds than those produced by the equilibrium analyses detailed in Table 7.4; ‘Nominal’ shock speeds are summarised in Figures 7.9(a-d). Two key 1-D wave phenomena are potentially responsible for the discrepancy between the 0-D equilibrium and 1-D L1d2 sets of results. An L1d2 $x-t$ diagram for flow condition x2-scr-m10p0-rev-0 from Table 7.4 is shown in Figure 7.7 to illustrate these 1-D wave phenomena.

1. *Primary diaphragm offset from compression tube area change.* The primary diaphragm is located 110 mm downstream of the compression tube area change. Upon initial rupture a normal shock is formed, which begins to move downstream. The unsteady expansion initially travels upstream through the smaller diameter tube towards the area change. The initial strength of the shock is correspondingly that for a constant area tube. Eventually the unsteady expansion reaches the area change, and the capacity of the area change to drive a stronger shock is realised by the transmission of a compression wave downstream. Point (a) in Figure 7.7 indicates this compression wave. The compression wave reaches the primary shock at point (b) in Figure 7.7, whereupon there is a sudden increase in the shock speed. This occurs just before the shock reaches the primary diaphragm.

The driver performance calculations detailed in Table 7.3 are based on experimental shock speeds made in the first driven tube of X2 (for a 150 kPa helium secondary driver initial fill condition). Figure 7.8 shows the location of the shock speed measurements presented in Table 7.1; L1d2 predicted shock speed is also shown. It can be seen that the experimental shock speeds were measured within the vicinity of the shock speed increase (due to the primary diaphragm offset from the driver area change). Therefore the primary diaphragm offset from the area change is already accounted for in the driver performance calculations detailed in this section.

2. *Reflected shock at the secondary diaphragm.* For sufficiently high shock tube fill pressures, the shock processed secondary driver gas (Region $sd2$ in Figure 3.3) must slow when it reaches the high density test gas, with a corresponding increase in static pressure; this is achieved by a reflected shock (point (c) in Figure 7.7). This reflected shock propagates upstream until it encounters the interface between Regions $sd2$ and $sd3$, whereupon a compression wave forms which propagates downstream once more (point (d) in Figure 7.7). When this compression wave reaches the primary shock (point (e)), the shock speed is increased, thus part of the energy of the reflected shock is transmitted back into the primary shock.

Flow Condition ID	Driver Condition ¹ (kPa), He	p_{sd1} (kPa), air	p_1 (Pa), air	p_5 (Pa), air	$M_{7,predict}$ (-)	$u_{7,predict}$ (m/s)	$p_{7,predict}$ (kPa)	a_{s02}/a_{s03} (-)	Comments
x2-scr-m10p0-rev-0 ²	x2-lwp-2p0mm-0	100	345.4	144.1	10.0	3,011	17.04	1.33	No nozzle
x2-scr-m10p0-noz-rev-0 ²	x2-lwp-2p0mm-0	100	243.2	738.1	10.0	3,011	7.28	1.33	X2 Mach 10 nozzle
x2-scr-m12p5-rev-0 ³	x2-lwp-2p0mm-0	100	210.1	29.0	12.5	3,789	5.35	1.33	No nozzle
x2-scr-m15p0-rev-0 ⁴	x2-lwp-2p0mm-0	100	132.1	6.8	15.0	4,614	1.82	1.33	No nozzle

¹ Refer Table 6.7 for details.

² $M_{7,target} = 10.0$ (-), $u_{7,target} = 3,011$ (-), $p_{7,target} = 1,368$ (kPa) per Table 1.1.

³ $M_{7,target} = 12.5$ (-), $u_{7,target} = 3,789$ (-), $p_{7,target} = 0.876$ (kPa) per Table 1.1.

⁴ $M_{7,target} = 15.0$ (-), $u_{7,target} = 4,614$ (-), $p_{7,target} = 0.608$ (kPa) per Table 1.1.

Table 7.4: Proposed scramjet flow conditions based on equilibrium flow condition calculations. Refer Table C.2.

The increase in shock speed in Figure 7.7 is quite distinct, and is also evident in Figures 7.9(a-d); however, its strength will vary depending on the various fill conditions, it's arrival time depends on the tube lengths, and it is thus not something easily accounted for in a 0-D analysis code. It is also clear that the L1d2 shock speeds match the nominal equilibrium 0-D target speeds up until this compression wave reaches the shock. This is the primary reason that the 0-D equilibrium calculations performed in this chapter under-predict actual shock speeds.

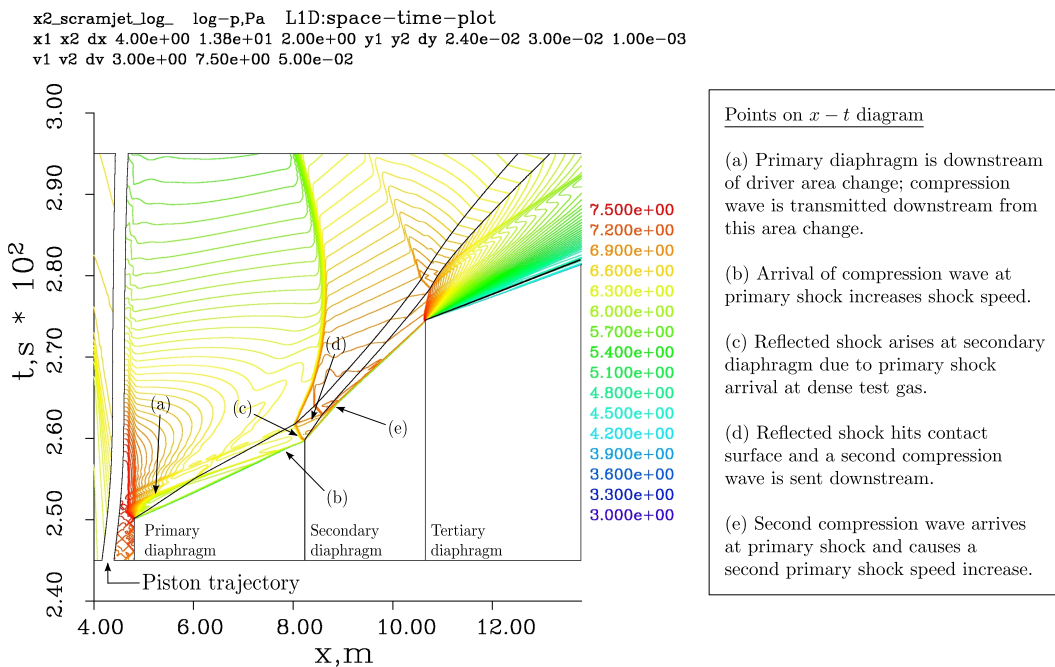


Figure 7.7: L1d2 predicted $x - t$ diagram for scramjet flow condition x2-scr-m10p0-0 per Table 7.4.

The general effect of the shock speed increase through the shock and acceleration tubes is to increase the flow speed and flow temperature. As a result, the test gas will have higher velocity but lower Mach number (due to the higher sound speed). The shock speed increase across the shock tube observed in Figures 7.9(a-d) is quite significant, therefore the flow conditions were adjusted in order to return test flow Mach number and velocity closer to target values in Table 1.1. This was achieved by equally scaling upwards both the shock and acceleration tube fill pressures. If the shock speeds are returned to target values, the same flow condition should theoretically be achieved, but with a higher static pressure. Both shock speeds could not be returned to target values precisely using this technique; instead the fill pressures were increased until the shock speeds in the shock tube were reduced to target levels. It is noted that these higher fill pressures will also generally require thicker secondary and tertiary Mylar diaphragms;

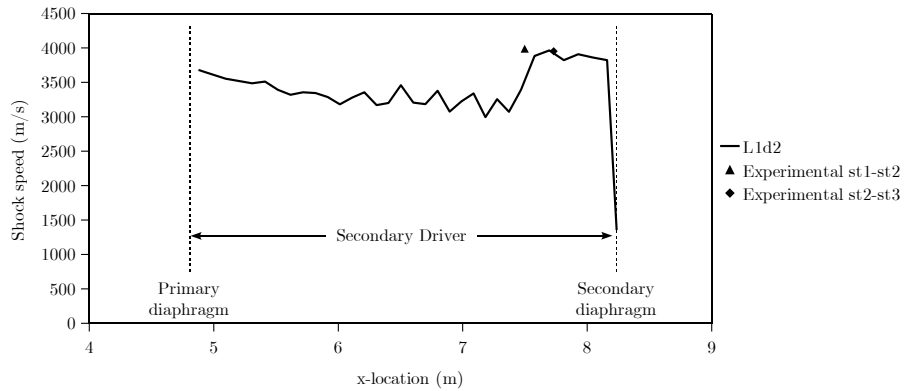


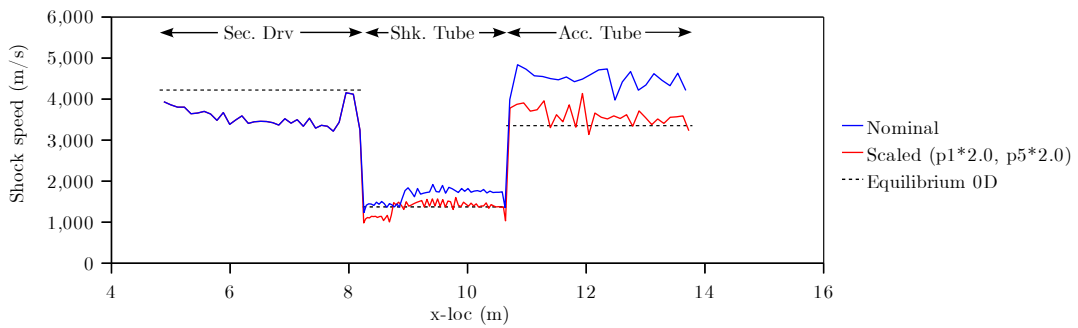
Figure 7.8: Secondary driver shocks speeds. Plot shows primary shock speed predicted by L1d2 through the secondary driver for lightweight piston driver condition LWP-2.0mm-rev-0 from Table 6.7 with a 150 kPa helium initial fill pressure secondary driver. Averaged experimental shock speeds from Table 7.1b are also shown; the x-location of each set of shock speeds is the geometric mid point between the two transducers used to calculate the shock speed. Some longitudinal offset is evident, however shock speed magnitudes are in good agreement.

the increased mass of these diaphragms will increase their disruptive effect on the related flow processes.

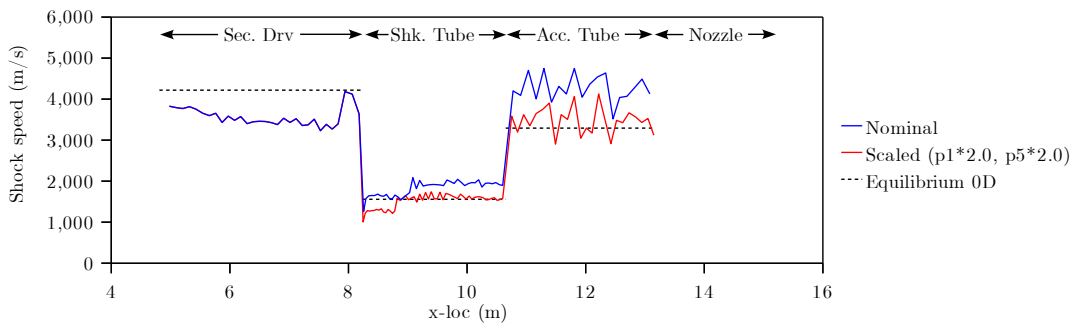
The acceleration tube shock speeds are observed to remain a bit higher than target values in Figures 7.9(a-d). However, the variation was accepted, since these are simply representative flow conditions and therefore do not need to be precisely targeted. It is also expected that factors such as Mirels effects [99, 100] and viscosity will also tend to reduce the acceleration tube shock speeds. It is finally noted that acceleration tube shock speeds are less smooth in the Mach 10 conditions; this is due to the discrete nature of the L1d2 1-D numerical model. The shock moves a shorter distance between the time steps for the Mach 10 conditions, however the time step remains very small. The shock moves in discrete steps across cells in the gas slug, which are more coarsely spaced through the acceleration tube since adaptive cell sizing has been used. At slower shock speeds, the combination of coarse cell spacing, slow shock propagation, and small time steps, results in a somewhat unsteady shock speed calculation.

7.9 Conclusion

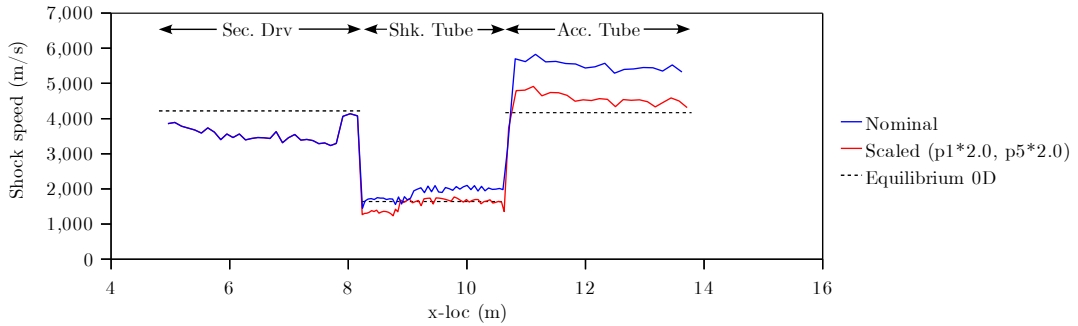
This chapter has detailed the methodology used to calculate new flow conditions for X2. The performance of the three new lightweight free-piston driver conditions (detailed in Table 6.7) was first characterised. An analytical model was then developed to calculate the performance envelope of the facility with each new driver condition. Flow conditions were identified which matched target Mach number and velocity at Mach 10, 12.5, and 15, for X2 without a nozzle, and Mach 10 for X2 with a nozzle. The new flow conditions



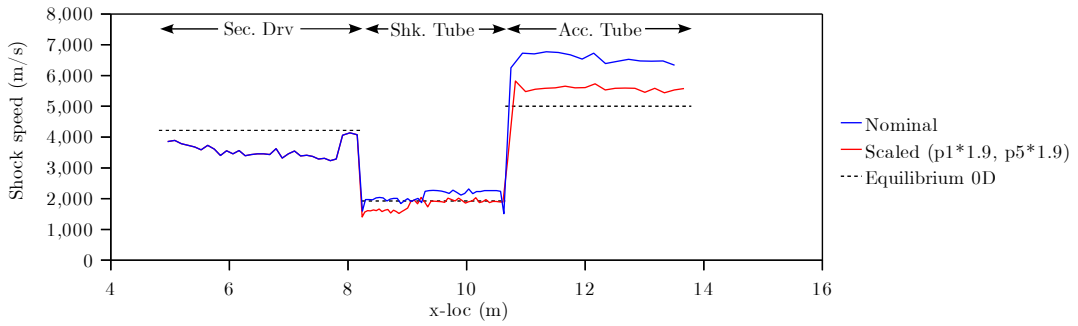
(a) Mach 10.0 without nozzle.



(b) Mach 10.0 with nozzle.



(c) Mach 12.5 without nozzle.



(d) Mach 15.0 without nozzle.

Figure 7.9: Comparison of shock speed predictions based on Equilibrium 0-D analysis, and L1d2 analysis. L1d2 has been used to calculate the scaling factor to be applied to shock and acceleration tube fill pressures, p_1 and p_5 respectively; the predicted shock speeds for the scaled results are shown.

Flow Condition ID	Driver Condition ¹	p_{sd1} (kPa), He	p_1 (kPa), air	p_5 (Pa), air	Comments
x2-scr-m10p0-rev-1 ²	x2-lwp-2p0mm-0	100	690.8	288.2	No nozzle
x2-scr-m10p0-noz-rev-1 ²	x2-lwp-2p0mm-0	100	486.4	1,476.2	X2 Mach 10 nozzle
x2-scr-m12p5-rev-1 ²	x2-lwp-2p0mm-0	100	420.2	58.0	No nozzle
x2-scr-m15p0-rev-1 ³	x2-lwp-2p0mm-0	100	251.0	12.9	No nozzle

¹ Refer Table 6.7 for details.

² Scale factor of 2.0× applied to p_1 and p_5 in Table 7.4.

³ Scale factor of 1.9× applied to p_1 and p_5 in Table 7.4.

Table 7.5: Revised scramjet flow conditions; original equilibrium flow condition calculations from Table 7.4 have been scaled following analysis with L1d2.

were finally assessed using the 1-D code L1d2, and adjusted to account for 1-D flow processes. These new flow conditions were also assessed both experimentally and using 2-D axisymmetric CFD analysis; the results are presented in Chapter 8.

Chapter 8

2-D Axisymmetric CFD Analysis using Eilmer3, and Comparison with Experimental Results

8.1 Chapter Overview

The new proposed X2 scramjet flow conditions from Table 7.5 in Chapter 7 are now assessed using the CFD code Eilmer3. A 2-D axisymmetric model of the shock and acceleration tubes was developed. An L1d2 CFD model of the facility (including full piston dynamics) was first used to calculate a 1-D inflow to the shock tube in Eilmer3. Flow condition x2-scr-m10p0-noz-rev-1, which uses the Mach 10 nozzle, was assessed by taking calculated Eilmer3 flow properties at the nozzle inlet plane, and using them as a 2-D inflow to a separate 2-D axisymmetric nozzle model. CFD calculations of test flow properties at the test section were compared to experimental observations. Wave processes computed by both L1d2 and Eilmer3 were found to closely match experiment. Eilmer3 was found to predict static pressures through the acceleration tube better than L1d2. Following difficulties measuring Pitot pressures, a cone probe was developed to experimentally measure partial impact pressures of the test flow in the test section. An equivalent pressure was calculated using Eilmer3. The Eilmer3 pressures showed poor correlation to experiment for the accelerator gas flow, but better agreement over longer time scales with the test gas and trailing unsteady expansion and driver gases. The results indicate that gigapascal total pressure steady scramjet flows are achievable. For X2, test gas core flow diameters are relatively small, and test times short, however the results indicate that the flow conditions are feasible and encourage the scaling of these conditions to a larger facility such as X3.

8.2 Previous Work

The first axisymmetric numerical simulation of an expansion tube was conducted by Jacobs [136], which examined the NASA Langley expansion tube facility. Numerical analysis was compared to experiments taken with the facility when it was located in Langley in the 1970's [137]. A primary objective of this study was to numerically investigate the effect of complex wave processes on test time and test flow quality. In particular, at the time that the study was performed, Paull and Stalker [72] had recently shown that disturbances originating in the expanded driver gas could be transmitted to the shock-processed test gas if there was a sound speed reduction across the interface between these two gases. This was identified as the cause of the significant test flow unsteadiness which had been observed across a large range of expansion tube test conditions; up until this point in time, the cause of this unsteadiness had not been understood.

Paull and Stalker [72] demonstrated that the transmitted noise is comprised only of radially dependant acoustic waves generated in the driver gas [72]; it was shown analytically and experimentally that longitudinal wave disturbances were not transmitted across this interface. This implies that transmitted driver noise cannot be simulated using a 1D code (such as L1d2), therefore a more sophisticated axisymmetric analysis is required to model this phenomenon.

Jacobs' [136] axisymmetric numerical model included the fixed volume driver, shock tube, and acceleration tube, in order to capture complex wave processes associated with driver gas expansion through the driver area change. The findings of Jacobs' numerical study generally supported Paull and Stalker [136]. Following on from Jacobs, Wilson et al. [89] also performed an axisymmetric analysis of the HYPULSE facility. HYPULSE was the name given to the NASA Langley expansion tube facility when it was moved to the General Applied Science Laboratory (GASL) [89]. The focus of the Wilson et al. study was on the effect of boundary layer development on test gas non uniformity [89], and it provided an early numerical reproduction of the Mirels effect [99, 100], a phenomenon originally identified by Duff [93] decades earlier.

UQ, with its extensive and long term experience with expansion tubes, has been involved in the majority of axisymmetric simulation work on these machines. These simulations have been performed with several purposes in mind:

1. *To fully characterise the test flow.* The process of experimentally characterising expansion tube test flows is very challenging, primarily due to short test times, harsh environmental conditions, space restrictions, and a lack of available non-invasive diagnostic techniques to make direct measurements [138]. The advanced measurement techniques which *are* available, are correspondingly expensive, however even the most advanced equipment can only reveal a small portion of the flow properties, and typically only at a few spatial locations.

2. *Development of new flow conditions.* Axisymmetric CFD is the most accurate of the *practical* tools available to predict facility response for new flow conditions. Obtaining a good estimate of the facility response permits many potential issues to be addressed prior to conducting an experimental campaign (which can be costly and is usually time constrained). Once benchmarked against an existing flow condition experiment, the code can then be used for parametric design studies [139] to improve or modify that flow condition. However, despite the utility of these codes, the experiment itself remains essential in order to establish the *actual* flow. The further away from the benchmarked conditions which the code departs, the less reliable must the computed solution be assumed to be, and correspondingly greater care must be applied to its predictions.
3. *Validation of numerical codes.* Numerical codes need to be validated against experimental results, particularly in the hypersonic flight regime [22, 45, 140, 138, 141]. Validation data may comprise, for example, pressure or heat transfer measurements on the surface of a model in the test section, Pitot pressure measurements from a probe located in the path of the test flow, spectroradiometric measurements of the flow through an observation window into the test section, and so forth. A similar ‘numerical experiment’ is then performed, and the computed flow properties are compared to the experimental measurements. In order to accurately repeat the ‘numerical experiment’, it is typically necessary to first simulate part or all of the facility flow processes upstream of the test section, so that the complex transient test flow is accurately reproduced. To otherwise assume that the test flow is 1-D and uniform may be over-simplistic, and may constitute an additional source of discrepancies between computation and experiment which then compromises the validation process.

Unlike the full facility simulation performed by Jacobs [136], most subsequent axisymmetric simulations of expansion tubes have considered flow conditions for which noise originating at the driver is not a primary focus. These studies have adopted a hybrid solution approach, whereby only the low pressure acceleration tube and dumptank are modelled two-dimensionally. An inflow condition is then defined at the secondary diaphragm (for a basic expansion tube), which is either calculated based on experimentally measured shock speeds, or calculated using a 1-D numerical code [142] (such as UQ’s L1d2 code).

Wheatley et al. [142] argue that this hybrid approach is usually acceptable for two principle reasons. Firstly, the shock tube flow typically has a relatively thin boundary layer on account of its relatively low velocity and high density. Secondly, when the secondary diaphragm ruptures, the downstream portion of the shock-processed test gas, which will eventually be the test flow, is located immediately behind the primary shock, where the

boundary layer has only just begun to develop. It is often reasonable therefore to treat the shock-processed test gas as 1-D, and restrict the 2-D axisymmetric calculation to the low pressure acceleration tube and dumptank [142]. This is the approach which has typically been adopted at UQ, for example [71, 73, 143, 144].

Wheatley et al. [142] studied rarefied superorbital flows in UQ's X1 expansion tube (which was decommissioned in 2011). Experimentally measured shock speeds were used to calculate inflow conditions to the acceleration tube. Flow in the acceleration tube and dumptank was then computed using UQ's axisymmetric solver mb_cns (the original precursor to UQ's Eilmer3 code). An earlier study by Wendt et al. [145] on the same facility used a similar approach with mb_cns, except that it is not clear whether the acceleration tube inflow conditions were calculated analytically or were based on experimental shock speeds.

More recent studies have, in contrast, used UQ's 1-D code (L1d, or its successor, L1d2) to calculate the flow in the shock tube, which has then been used as an inflow to an axisymmetric solver. In these studies the 1-D code did not include piston dynamics. Instead, the volume between the piston face and the primary diaphragm was modelled as fixed [144]. The driver pressure at primary diaphragm rupture is known; the position of the piston downstream face, and the temperature of the driver gas, are then both adjusted until shock speeds, pressure histories, peak pressures, and pulse duration, match between experiment and the 1-D calculation [144]. This approach extends the reasoning of Wheatley et al. [142] to include a time history of flow properties in the shock tube. It has been used by Jacobs et al. for X3 [144], by Scott [71], McGilvray [105], and Potter et al. [73] for X2, by McGilvray et al. [105] for the Hypervelocity Expansion Tube at the University of Illinois (using the UQ codes), and by Stewart et al. [146] for the RHYFL-X expansion tube concept (also using UQ codes).

Gollan et al. [147] used a similar approach to simulate flow in a non-reflected shock tube. However, in this instance UQ's L1d2 code was used to simulate the full piston dynamics and primary diaphragm rupture. Unlike the other hybrid analyses, this 1-D simulation was used to calculate an inflow to the *shock tube* (which was operating at a very low pressure compared to shock tubes in typical expansion tube experiments), which was then solved as a 2-D axisymmetric problem using the mb_cns2 code.

The present study is concerned with relatively high density air flow conditions, where the sound speed of the shock-processed air test gas, a_2 , will generally not exceed the sound speed of the expanded helium/argon primary driver gas, a_3 (see Figures 3.1 and 3.3 for region definitions). As previously discussed in Section 3.9.2, in a standard expansion tube arrangement (Figure 3.1) this sound speed drop across the interface will permit radial driver disturbances to penetrate the test gas [72]. Frequency focussing through the unsteady expansion to the acceleration tube will then result in unacceptable test

flow unsteadiness. A helium secondary driver has therefore been used as an ‘acoustic buffer’, as suggested by Morgan [57], which is configured such that $a_{sd2} > a_{sd3}$ (Figure 3.3). This will theoretically prevent transmission of primary driver gas noise to the test gas, in accordance with Paull and Stalker [72].

Previous expansion tube experiments using a secondary driver [62, 148, 149, 56, 150] have adopted an intermediate shock-heated tube primarily for its capability to drive a stronger shock through the test gas. While it also acts as an acoustic buffer in this configuration, its functionality in this regard has not been closely examined. In contrast to these previous studies, the present study does not utilise the secondary driver to achieve a performance gain in terms of shock strength; instead, it’s purpose is primarily to act as an acoustic buffer, and permit the use of higher values of a_4 . Furthermore, without this intermediate shock heated tube, the ‘acoustic buffer’ requirement defined in [72] will *not* be met, and the test flow would be expected to be rendered unacceptably noisy. This is in contrast to superorbital flow conditions, where even *without* a secondary driver, $a_2 > a_3$; the role of the secondary driver as an acoustic buffer is potentially redundant. These conditions belong to the class of ‘high enthalpy’ flow conditions identified by Paull and Stalker [72], which at the time were observed to have smooth test flow characteristics. A number of high enthalpy flow condition experimental studies have indeed achieved good quality test flows without a secondary driver, for example [58, 66, 71, 72, 73, 136, 76, 151, 152, 153, 154, 155, 135, 104, 144].

In the present chapter a hybrid CFD model qualitatively similar to that developed by Gollan et al. [147] is used to predict test flow properties for comparison with experimental results, for each of the four new flow conditions detailed in Table 7.5. It is noted that this modelling technique does not include the primary sources of driver gas disturbances, such as the piston compression process, or expansion of the driver gas through the area change and rupturing primary diaphragm. As such, these simulations will not provide any insight into the effectiveness of using a helium secondary driver as an acoustic buffer against transmission of primary driver disturbances to the test gas, since these disturbances will not be present in the driver gas to begin with. The effectiveness of the secondary driver is addressed separately in Chapter 9 for the Mach 10 flow condition, x2-scr-m10p0-rev-1 in Table 7.5.

In Chapter 9 a 2-D axisymmetric model of the entire facility downstream of the primary diaphragm (including the secondary driver and shock tube), and part of the primary driver itself, has been developed. Additionally, an iris-opening primary diaphragm is incorporated into the model in an attempt to make the driver gas disturbances as representative as possible (subject to the current limits of UQ’s Eilmer3 code, as well as the available computational resources). Whilst various individual aspects of this numerical analysis have previously been performed (for example, analysis of the acoustic buffer effect by Jacobs [136], or the use of iris-opening diaphragm models by Goozée [156] and

Petrie-Repair [157]), the study in Chapter 9 combines these concepts, in an expansion tube with secondary driver, for the first time.

8.3 The Eilmer3 Code

Eilmer3, developed at UQ by Jacobs et al. [114, 158], is “an integrated collection of programs for the simulation of transient, compressible flow in two and three spatial dimensions” [158]. The code, which has its origins in the early 1990’s under the name mb_cns, was originally developed for the simulation of reflected shock tunnel and expansion tube impulse facilities. Several aspects of the code make it particularly well-suited to this purpose [158]:

1. It solves the compressible Navier-Stokes equations using an upwinding approach, which can be very effective at capturing the strong shocks associated with these facilities.
2. It has multiple-block capability, which permits a reasonable solution time, using parallel processing, for models which typically are computationally very expensive.
3. It has thermochemistry and finite-rate chemistry capabilities, which are necessary for accurate predictions about the extreme flow processes which occur in these impulse facilities, particularly for superorbital flow conditions (6-15 km/s).

The Eilmer3 code was used to perform transient compressible flow analyses of the four flow conditions detailed in Table 7.5. The solutions were 2-D axisymmetric, viscous, used equilibrium chemistry, and applied the Baldwin-Lomax turbulence model. Equilibrium chemistry was considered appropriate since it is applicable to all flow regions other than immediately behind the primary shock, where finite rate processes can occur. Details of the Eilmer3 analysis model are provided in Section 8.4.

8.4 Eilmer3 2-D Axisymmetric model of X2

A 2-D axisymmetric model of the X2 shock and acceleration tubes was developed using Eilmer3. The model was comprised of 64 blocks and 481,664 cells (71 cells radially). Cells were clustered axially on either side of the tertiary diaphragm plane, and clustered radially towards the tube wall. A transient inflow to the shock tube was defined at transducer *st1*, which is located 813 mm downstream of the actual secondary diaphragm. *st1* was used since the L1d2 inflow static pressure history at this location could be compared directly to experimental measurements; it is shown later in Figures 8.13, 8.20, I.4, and J.4, that L1d2 agrees well with experiment at this location.

History data was recorded at each position in the Eilmer3 CFD model corresponding to static pressure transducer locations in the actual machine. The full length of the acceleration tube was modelled (3,129 mm including the straight tube adaptor to the dumptank). Detailed radial history data was recorded at the tube exit plane, and also at the nozzle inlet plane (when the nozzle is used, the straight tube adaptor is removed, and the nozzle interfaces with the acceleration tube along a plane 762 mm upstream of the standard tube exit). A schematic diagram of the Eilmer3 analysis geometry is shown in Figure 8.1. It is noted that the geometry used in this chapter takes the primary diaphragm axial location as $x = 0$; this is different to preceding chapters in this thesis, which define the piston upstream face as $x = 0$ (which locates the primary diaphragm at $x = 4.810$ m).

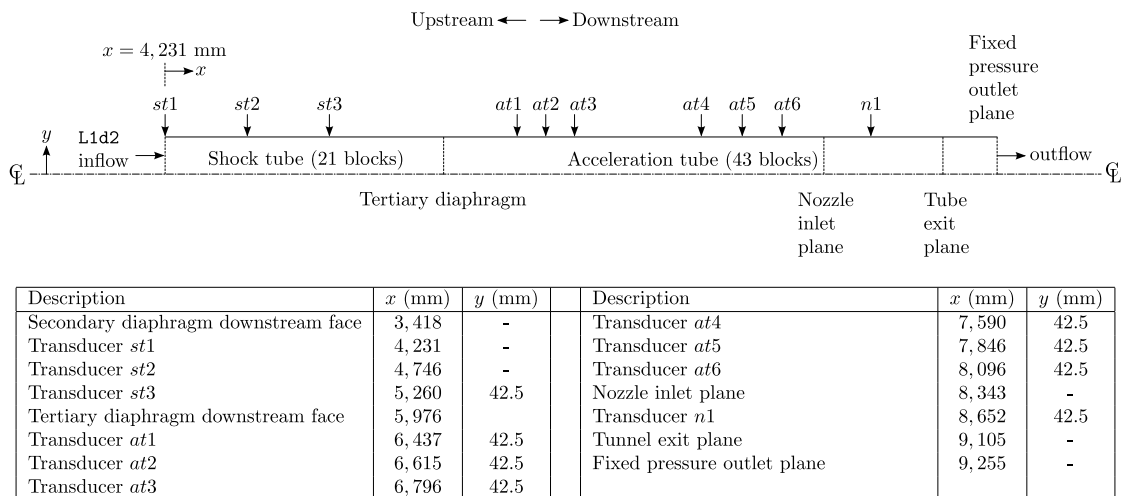


Figure 8.1: X2 2-D axisymmetric hybrid model geometry. All longitudinal positions have an uncertainty of ± 2 mm, vertical positions are to machining tolerance (assumed to be ± 0.1 mm). Vertical scale has been stretched for illustrative purposes.

An L1d2 1-D CFD model of the complete facility (including full piston dynamics) was used to calculate a 1-D inflow to the shock tube at transducer location *st1*, for each flow condition in Table 7.5. In Chapter 7 L1d2 was used as a predictive tool for the design and assessment of new flow conditions, *prior* to experimentation. However, for the present application the experimental results have been obtained separately, and can therefore be used to improve the L1d2 predictions. The average shock speed between transducers *st1* and *st3* was calculated using L1d2, and compared to the equivalent experimental measurement averaged across multiple experiments. The loss factor across the primary diaphragm in L1d2, K/L , was then adjusted until the L1d2 prediction approximately matched the experiment.

Complex 2-D and 3-D physical processes (such as flow through the launcher or area

change) cannot be directly modelled by L1d2. A pipe fitting loss is applied in order to simulate the effect of these complex flow paths. The code requires that a head loss per unit length, K/L , be specified for the portion of tube where the area contraction (for example) is present. K is dimensionless, therefore K/L has dimensions (m^{-1}). The loss is spread across a finite length to ensure that individual cells which pass across the affected region ‘see’ the loss. At each time step the loss appears in the momentum source term for each cell, as follows:

$$Q_{\text{momentum}} = -\frac{K}{L} \times \frac{1}{2} \rho u |u| \times A \times dl \quad (8.1)$$

where $K/L \neq 0$ across a loss region, and ρ , u , A , and dl , are respectively the cell density, velocity, cross-sectional area, and length. The sign of Equation 8.1 is such that the loss always acts as a ‘drag’ force on the affected cell. Q_{momentum} , which has units of force (N), is then incorporated into the momentum equation for the cell, along with pressure and wall shear stress contributions.

Representative values for K/L can only be determined from experimental data. However, the experience at UQ is that the modelling tool is quite effective once tuned for a given test condition.

The initial discrepancy between the L1d2 and experimental shock speeds is shown in Table 8.1 for the nominal primary diaphragm loss factor of $K/L = 0.7$. This is then compared to the final L1d2 shock speeds using the corrected K/L . It can be seen that the changes are not significant, and that the downstream flow is fairly insensitive to the magnitude of K/L . This insensitivity is most likely due to the fact that the subsonic pipe flow loss model used by L1d2 is not very representative of the actual sonic flow through the area change. However, these results provide closest agreement to the experimental results and should therefore improve the accuracy of the calculated inflow.

Flow condition	Experimental ¹ u_s (m/s)	L1d2 Nominal		L1d2 Adjusted	
		K/L (-)	u_s (m/s)	K/L (-)	u_s (m/s)
x2-scr-m10p0-rev-1	1,454	0.7	1,482	2.1	1,454
x2-scr-m10p0-noz-rev-1	1,621	0.7	1,639	1.5	1,621
x2-scr-m12p5-rev-1	1,684	0.7	1,705	1.7	1,683
x2-scr-m15p0-rev-1	1,952	0.7	1,945	no change	

¹ Quoted shock speed is an average value for multiple experiments at this condition.

Table 8.1: Adjustments to L1d2 primary diaphragm loss factor, K/L . Shock speeds are the average speed of the shock as it travels between transducer locations $st1$ and $st3$ (see Figure 8.1).

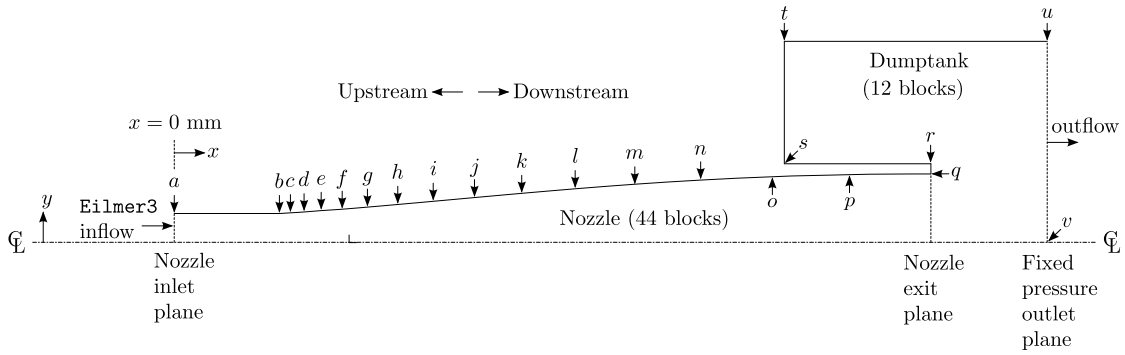
The planar inflow calculated using L1d2 was modified to include an estimate of the boundary layer development. Mirels’ theory describing the turbulent boundary layer behind a shock [100] was used in accordance with the method used previously by Jacobs [159] for axisymmetric modelling of the Drummond Tunnel at UQ. The boundary layer

was only calculated in the initial slug of air test gas. The inflow boundary layer thickness was then assumed to remain constant upon arrival of the trailing driver gases; this was a necessary simplifying assumption for this region of significantly more complex flow.

The geometry shown in Figure 8.1 applies to X2 running in expansion *tube* mode (i.e. no nozzle). The tube exit is located inside the dumptank in the actual facility; in the CFD model the dumptank is ignored, and the tube is extended 150 mm further downstream ($x = 9.255$ mm) to a fixed pressure outlet boundary condition (FixedPOutBC() per [114]), although tube exit flow properties are recorded at the nominal tube exit ($x = 9.105$ mm). The centreline boundary is modelled as a slip wall (SlipWallBC() per [114]), and the remaining external boundaries are modelled as fixed temperature boundary conditions (FixedTBC() per [114]). Cells are clustered, using a Roberts cluster function [114], vertically towards the tube wall, and horizontally towards diaphragm stations and at the driver area change. The tertiary Mylar diaphragm was modelled as a hold diaphragm [73], initially triggering when a pre-defined pressure differential is reached, and then instantaneously and completely opening 10 μ s later.

For the Mach 10 condition using the X2 contoured nozzle (x2-scr-m10p0-noz-rev-1 in Table 7.5), the same basic Eilmer3 model was used. However, history data was recorded at the upstream nozzle inlet plane (at $x = 8.359$ m per Figure 8.1), and used as an inflow to a separate nozzle axisymmetric model (see Figure 8.2 for nozzle geometry). History data was recorded at 0.5 μ s time intervals, at the radial locations of each cell centroid between the tube centreline and wall (71 cells across the 42.5 mm radius, giving an average cell spacing of approximately 0.6 mm/cell). To achieve a similarly accurate calculation, the large 201.8 mm diameter of the nozzle exit requires a larger number of cells across the radial axis than the upstream 85 mm tube. If the two components are combined in a single model, the structured grid would require that this large number of radial cells be used along the entire length of the model. This would dramatically and prohibitively increase the computational time for the model. As such, two separate models were instead adopted.

The nozzle axisymmetric model includes the dumptank, and is comprised of 56 blocks and 765,000 cells (150 cells spaced radially across the nozzle axis; this corresponds to an average cell spacing of 0.3 mm/cell at the nozzle inlet, and 0.7 mm/cell at the nozzle exit). A user-defined function (udf) was developed to interpolate the radially spaced nozzle inflow properties (calculated using the hybrid shock and acceleration tube CFD model) into the nozzle. The nozzle centreline was modelled with a slip wall boundary condition, and other solid boundaries shown in Figure 8.2 were modelled with fixed temperature boundary conditions. The dumptank is extended in the model 250 mm downstream from the nozzle exit, with the downstream face modelled as a fixed pressure outlet. The dumptank internal geometry, which includes non-axisymmetric features such as inspection windows and access panels, is ignored in the present calculation. The



Point ID	x (mm)	y (mm)	Point ID	x (mm)	y (mm)
a	0.0	42.5	l	861.5	79.0
b	226.0	42.5	m	989.8	85.7
c	249.4	43.5	n	1,131.3	91.9
d	279.0	44.7	o	1,285.3	96.7
e	315.8	46.5	p	1,450.8	99.8
f	360.8	48.8	q	1,626.0	100.8
g	415.3	51.9	r	1,626.0	115.0
h	480.2	55.8	s	1,311.0	115.0
i	556.5	60.5	t	1,311.0	297.5
j	645.1	66.0	u	2,126.0	297.5
k	746.6	72.3	v	2,126.0	0.0

Figure 8.2: X2 nozzle geometry. An inflow is supplied at the nozzle inflow plane. Nozzle radial coordinates have a machining tolerance of ± 0.1 mm; the remaining coordinates have an uncertainty of ± 2 mm except where noted otherwise in the text.

nozzle calculation was only run for long enough to calculate the test flow properties at the nozzle exit. This model does not capture the reflection of the primary shock from the rear of the dumptank, however this shock will only interact with nozzle flow *after* the useful test time has passed; disregarding the effects of this reflected shock will therefore not impact the computed test flow properties.

8.5 Conical Glancing Impact Pressure Measurements

Experimental Pitot pressure measurements can be used to evaluate the test time, the flow steadiness, and the size of the core flow. However, Pitot pressure measurements in these expansion tube scramjet flows proved to be very challenging. The test flow and follow-on gases induce high temperatures and pressures at the probe surface (after shock processing by the Pitot bow shock). Additionally, these scramjet conditions require relatively large total thicknesses of Mylar diaphragm material to contain the high initial fill pressures, and subsequently there is a large quantity of Mylar, in solid form, entrained in the flow. Adequate protection therefore needs to be applied to Pitot pressure sensors to prevent damage to the instrumentation.

Protective measures typically involve shielding the pressure transducer with a metallic cap to prevent direct impact of the flow against the transducer face. The Pitot cap has an internal volume which takes a finite time to reach the pressure on the outer surface of the cap; this increases the rise time of the sensor. The presence of this cavity can also introduce complex aerodynamic phenomena which alter the measured pressure on the transducer face and are characterised by additional signal noise. An example of this noise is Helmholtz Resonance [160]. The Pitot cap itself is often insufficient to protect the transducer face, therefore a disc of cellophane or thin brass shim may also be attached to the transducer face (typically with a thin film of o-ring grease). This disc adds mass to the transducer face, thereby increasing response time, and also increases shot-to-shot variability due to unavoidable inconsistencies in its application.

Initial attempts to measure Pitot pressures made use of 4-hole stainless steel swirl caps (see Appendix G). The swirl cap holes are designed to introduce vorticity to the flow, which is intended to dampen Helmholtz Resonance [160]. The swirl caps were manufactured from high tensile stainless steel to improve their survivability. However, initial experimentation with these caps produced very inconsistent pressure measurements. Additionally, the caps suffered severe damage shot-to-shot, particularly for initial testing where a single sheet of 0.1 mm thick Mylar was used to contain the high initial fill pressures at the secondary and tertiary diaphragm stations; Figure 8.3 shows an example of damage to one of the swirl caps from a single shot using the 0.1 mm thick Mylar. It was found that damage to the Pitot caps could be reduced by substituting several sheets of 0.025 mm thick Mylar in place of a single thicker sheet. This probably reduced the mass of individual fragments, but high speed camera footage of the test section during several experiments indicated a large mass of Mylar remained entrained in the flow; see Figure 8.4 for example.

Several different Pitot cap arrangements were trialled in the present experimental campaign, however satisfactory results were not obtained; pressure traces were inconsistent and appeared excessively unsteady/noisy. Unsuccessful arrangements included standard single-hole brass Pitot caps, the already discussed swirl caps, and vibration isolated Pitot tube assemblies from the T4 RST facility; either cellophane or brass shim was attached with o-ring grease to the PCB transducer face in each case. Figure 8.5 shows examples of the different arrangements.

A useful characteristic of the supersonic Pitot pressure measurement is that it is Mach number independent; the flow is processed by a normal shock at all supersonic Mach numbers. However, particularly for these scramjet flow conditions, this normal shock significantly increases the pressure and temperature of the flow, and the blunt face of the Pitot cap presents a large obstruction to the flow. A similar measurement can be made using a conical probe, which instead processes the flow with a conical shock. The measured pressure still reveals information about the flow density and velocity. How-



Figure 8.3: Stainless steel 4-hole swirl cap after a single Mach 12.5 shot (m12p5-2.0mm-rev-0) using 0.1 mm thick Mylar at both secondary and tertiary diaphragm stations. A new cap is shown on left, the damaged cap on the right; the ruler indicates approximate scale. A large gouge is observed on the lower left face of the damaged cap.

ever, for relatively shallow cone angles, the flow at the transducer face is significantly less severe. The disadvantage of this measurement is that it is *not* Mach number independent, however at higher Mach numbers the Mach number sensitivity reduces and useful measurements are possible. These ‘glancing impact’ pressure measurements can then be correlated back to Pitot pressure using analytical or CFD relations, so long as the experimental flow Mach number can be estimated with reasonable confidence.

Several conical probes were developed and tested in the present experimental campaign: 15 and 45 deg half angle conical probes, with 4 and 8 holes (normal to the cone surface, supplying the PCB transducer cavity). The fastest rise time, and cleanest and most reproducible traces, were observed for the 8 hole 15 deg half angle probes. A drawing for the final design is shown in Appendix H. Two different cone configurations were used. For X2 in tube mode only (no nozzle), two probes were located at the tube exit and centre around the tube centreline; see Figure 8.6. For nozzle measurements, seven probes were located at the nozzle exit, centred around the tube centreline; see Figure 8.7. Referring to Figure 8.7, two static pressure transducers at the nozzle exit were also used for the nozzle measurements.

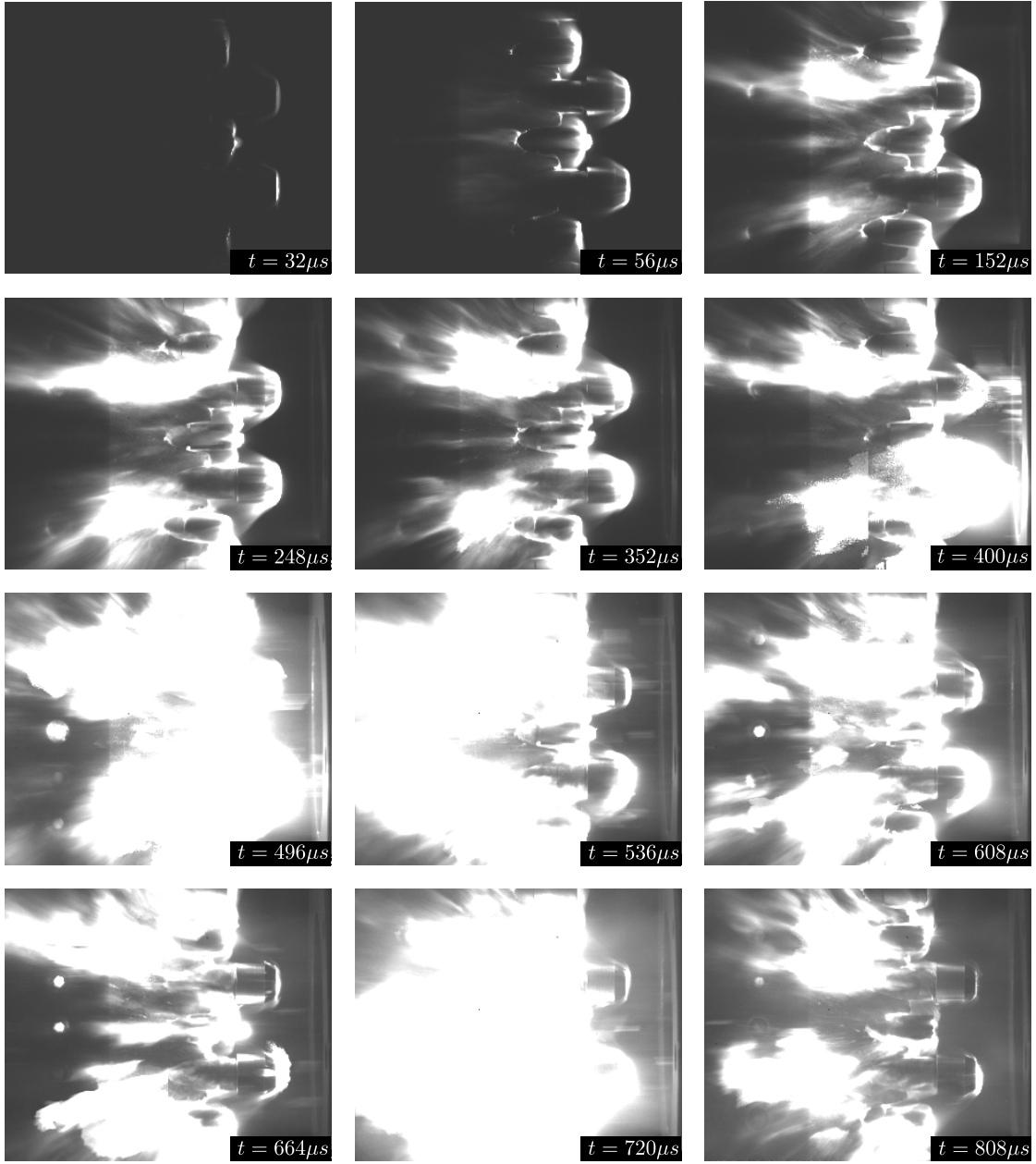


Figure 8.4: High speed camera footage of X2 expansion tube flow over two Pitot probes (T4 RST Pitot probes with 4 hole brass swirl caps). Experiment is the Mach 12.5 scramjet flow condition (x2-scr-m12p5-rev-1), shot x2s1609. Flow is from right to left. Accelerator gas is observed at $t = 32\mu s$; test gas at $t = 56\mu s$; unsteady expansion at $t = 152\mu s$; trailing secondary and primary driver gases are observed at remaining times. At $t = 400\mu s$ Mylar diaphragm fragments can be seen to arrive in test section and to impact the Pitot probes. Mylar continues to impact objects in the test section for a total duration of approximately $400\mu s$; at $t = 808\mu s$ the Mylar impact finishes. For this condition secondary and tertiary diaphragms were comprised of four and five sheets of 0.025 mm thick Mylar respectively.

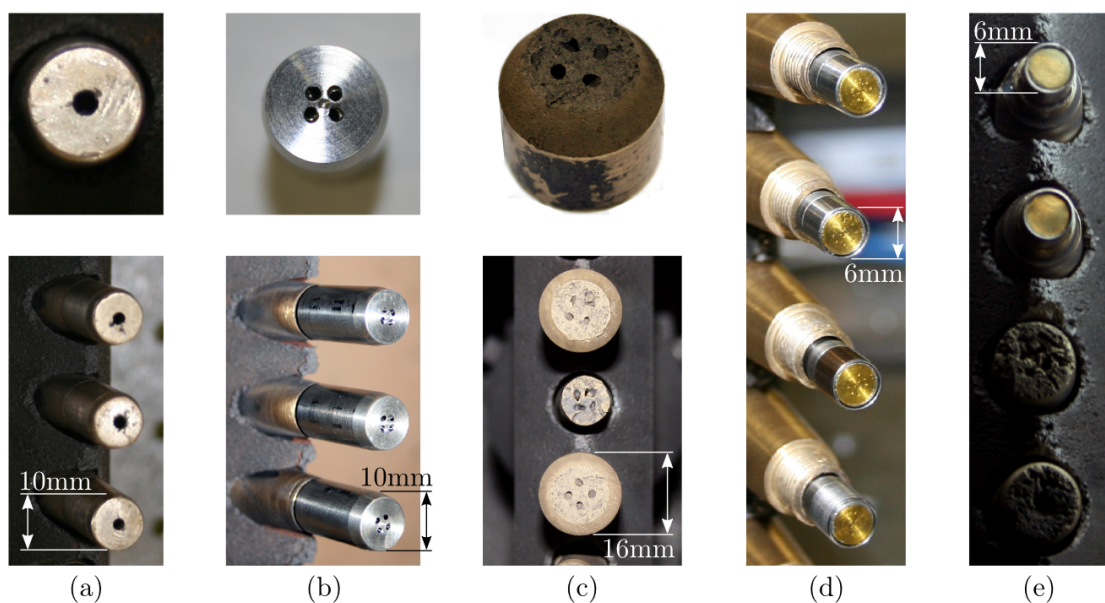


Figure 8.5: Various Pitot probe configurations. (a) Standard brass single hole cap (used with an internal brass six hole impact plate to prevent line-of-sight between flow and the PCB transducer face); (b) stainless steel 4 hole swirl cap; (c) brass T4 RST 4 hole swirl cap (vibration isolated with rubber); (d) example of cellophane protection to PCB transducer face; (e) example of 0.05 mm thick brass shim protection to PCB transducer face.

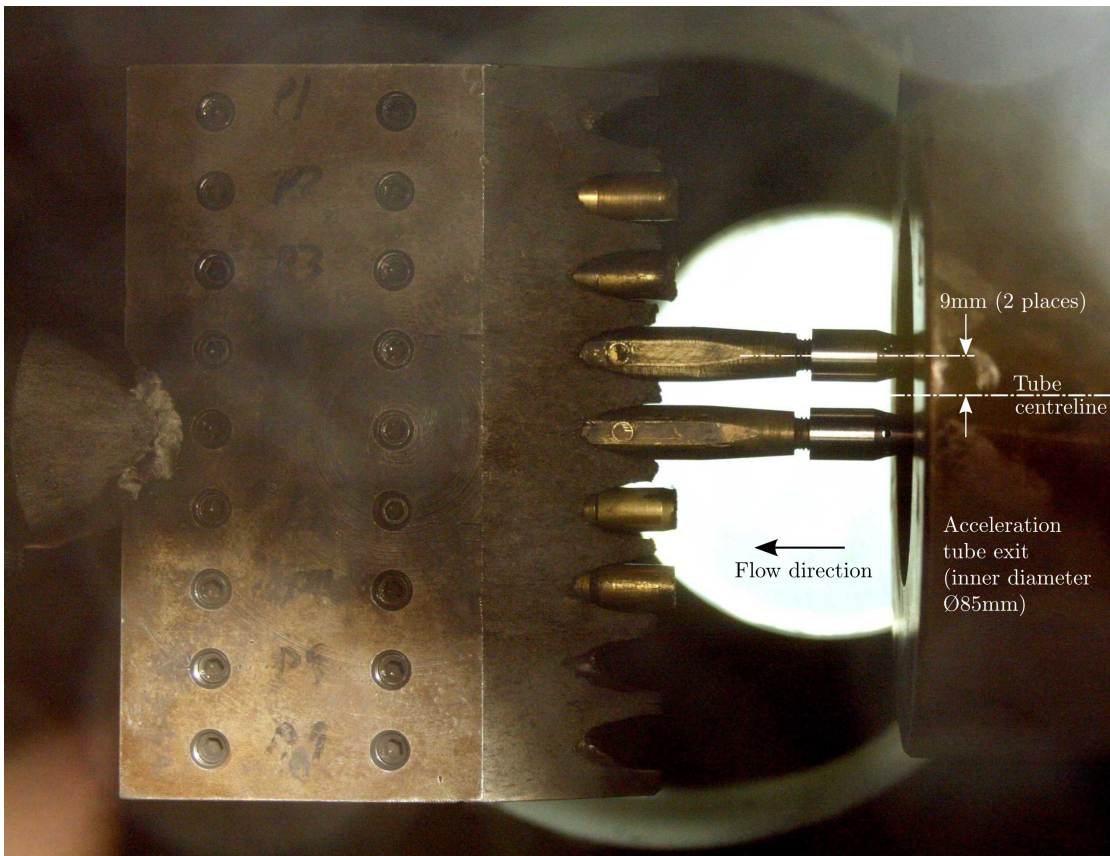


Figure 8.6: Conical probe arrangement in test section, X2 *without* nozzle.

If the test flow Mach number is known, the measured static pressure from the conical probe surface can be related back to the test flow Pitot and static pressures. Using nominal test flow properties from Table 7.5, a 2D axisymmetric model of the conical probe was simulated with Eilmer3, and used to predict static pressure on the cone surface for each flow condition. Eilmer3 includes equilibrium gas effects, which are not accounted for in analytical conical shock relations (for example [161]). The ratio of cone surface static pressure at the supply holes, to free stream Pitot pressure, is shown in Table 8.2. Ratios are calculated for both the idealised Pitot pressure (making perfect gas assumptions and assuming high Mach numbers) and also for the equilibrium air Pitot pressure; the former is used for comparison with CFD results, whereby Pitot pressure is calculated using $p_{Pitot,ideal} \approx 0.92\rho u^2$; the latter is used to determine a more accurate absolute estimate of experimental Pitot pressure. Referring to Table 8.2, it can be seen that the equilibrium gas pressure ratio reduces from 0.096 to 0.080 between Mach 6.9 and 15.0 respectively. This indicates low Mach number sensitivity, with the ratio sensitivity reducing from $\pm 3.6\%/\text{Mach}$ at Mach 6.9 to $\pm 1.0\%/\text{Mach}$ at Mach 15.

Reference ¹	Flow condition details					Eilmer3 calculations ³				
	Mach	Description	p (kPa)	T (K)	u (m/s)	p _{pitot,equl} ²	Mach angle (deg)	p _{cone} (kPa) ⁴	p _{cone} /p _{pitot,equl}	Mach sensitivity (%/Mach) ⁵
m10p0-2.0mm-nozz-rev-1	6.9	Flow at nozzle inlet	167.2	451	2,934	10,533	18.29	987.2	0.0956	-
m10p0-2.0mm-nozz-rev-1	10.0	Flow at nozzle exit	14.56	226	3,011	1,920	17.36	160.8	0.0859	3.6%
m10p0-2.0mm-rev-1	10.0	Flow at tube exit	34.08	226	3,011	4,491	17.36	376.5	0.0859	3.6%
m12p5-2.0mm-rev-1	12.5	Flow at tube exit	10.70	229	3,879	2,222	17.00	177.0	0.0823	1.7%
m15p0-2.0mm-rev-1	15.0	Flow at tube exit	3.458	235	4,614	1,040	16.76	80.57	0.0803	1.0%

¹ Refer to Table 7.5.

² Equilibrium flow properties behind bow shock were calculated using NASA code CEA [43]; total pressure was calculated using code estcipy, which solves for the static pressure at zero velocity which corresponds to the same total enthalpy and entropy as the flow behind the bow shock.

³ Eilmer3 calculations for a 2-D axisymmetric equilibrium air cone CFD model, for cone geometry based on drawing X2-PIT-003-1. Results are for a grid comprised of 64,000 cells. Calculation was shown to be grid independent at this grid spacing.

⁴ Static pressure is recorded at the intersection of the cone surface and the centreline of holes supplying air to transducer inside the actual cone.

⁵ Mach sensitivity = $|(1 - Ratio_1/Ratio_2)/(Mach_2 - Mach_1)| \times 100$

Table 8.2: Correlation factors for partial impact cone probes.

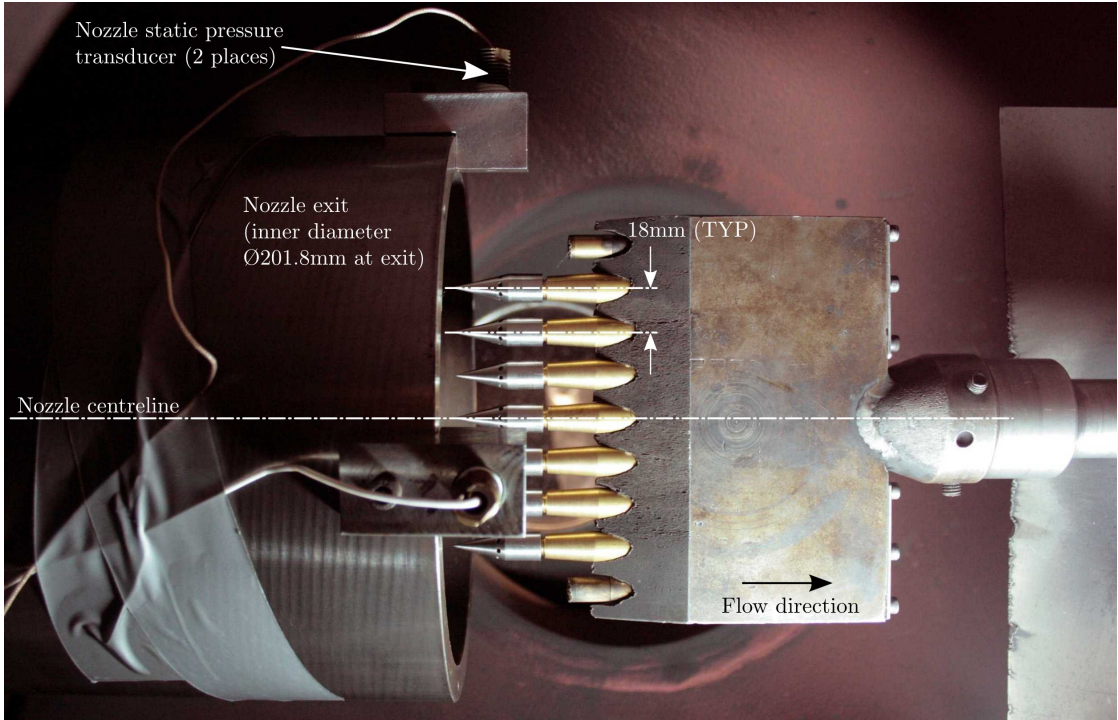


Figure 8.7: Conical probe arrangement in test section, X2 *with* nozzle.

8.6 Results and Discussion

8.6.1 Results Overview

The four new scramjet flow conditions detailed in Table 7.5 were each assessed experimentally and numerically, as follows:

1. Experimentally: Tube wall static pressure measurements along the length of the facility; cone surface static pressure measurements in the tube/nozzle exit flow.
2. 1-D L1d2 CFD: Simulation of entire facility. The loss factor K/L through the primary driver was adjusted so that the computed L1d2 average shock speeds between transducers $st1$ and $st3$ approximately matched the equivalent experimental measurement (averaged across multiple experiments) in Item (1).
3. 2-D axisymmetric Eilmer3 CFD: Simulation of shock and acceleration tubes downstream of transducer location $st1$. The experimentally tuned L1d2 simulation from Item (2) was used to calculate a planar inflow at $st1$ for the Eilmer3 simulation. Detailed flow history was recorded radially across the acceleration tube exit plane to reveal test flow properties. Detailed flow history was also recorded at $0.5\mu s$ time increments at all shock and acceleration tube static pressure transducer locations. The full flow solution was recorded at $10\mu s$ increments.

- For the Mach 10 flow condition *with* nozzle (x2-scr-m10p0-noz-rev-1), flow history across the nozzle inlet plane was recorded (upstream of the nominal acceleration tube exit plane), and used as an inflow to a separate 2-D axisymmetric model of the nozzle. The detailed flow history was recorded at cell centroid locations radially across the nozzle exit plan.

Detailed analysis for the two Mach 10 flow conditions is presented in this chapter. Section 8.6.2 presents results and analysis for the Mach 10 flow condition using X2 in tube mode (no nozzle). Section 8.6.3 considers Mach 10 flow using the contoured Mach 10 nozzle. Detailed results for the Mach 12.5 and Mach 15 flow conditions are presented in Appendices I and J respectively, with general observations summarised in Section 8.6.4. Finally, the results of a grid sensitivity analysis are presented in Section 8.6.5.

8.6.2 Mach 10 without Nozzle (x2-scr-m10p0-rev-1)

Results for the Mach 10 flow condition are summarised in Table 8.4. L1d2 and Eilmer3 shock speeds match experiment closely. Average test flow properties in the test gas core flow are also presented; the \pm limit shows the *maximum* departure, within the core flow, away from the averaged value during the test time. It is seen that Mach and velocity are well matched; static and Pitot pressures are well in excess of true flight values, which is desirable to satisfy pressure-length scaling requirements for subscale model testing.

8.6.2.1 Critical Wave Processes

An x - t diagram for the Mach 10 flow condition is shown in Figure 8.8. The basic diagram was constructed using the complete flow solution result, recorded at $10\mu s$ increments, from an L1d2 simulation of the facility. Key wave processes and other phenomena are identified in the figure. Experimental measurements of shock arrival times at transducer locations are plotted for an example shot. The experimental data has no reference to or measurement of the physical moment when the diaphragm ruptures, so the time scales have been aligned so that the experimental shock arrival times in the *secondary driver* approximately align with the L1d2 computed primary shock.

Property	True flight	Experimental	L1d2	Eilmer3
<i>Secondary driver</i>				
Shock speed between $sd1$ and $sd2$ (m/s)	-	$4,113 \pm 0.8\%$ ($\sigma = 14$ m/s)	3,365	-
Shock speed between $sd2$ and $sd3$ (m/s)	-	$4,178 \pm 0.8\%$ ($\sigma = 26$ m/s)	3,491	-
<i>Shock tube</i>				
Shock speed between $st1$ and $st2$ (m/s)	-	$1,493 \pm 0.2\%$ ($\sigma = 24$ m/s)	1,459	1,450
Shock speed between $st2$ and $st3$ (m/s)	-	$1,417 \pm 0.2\%$ ($\sigma = 16$ m/s)	1,450	1,436
<i>Acceleration tube</i>				
Shock speed between $at4$ and $at5$ (m/s)	-	$3,379 \pm 0.7\%$ ($\sigma = 44$ m/s)	3,432	3,496
Shock speed between $at5$ and $n1$ (m/s)	-	$3,264 \pm 0.2\%$ ($\sigma = 23$ m/s)	3,404	3,487
<i>Acceleration tube exit plane:</i>				
<i>Final test flow properties</i>				
Static pressure (kPa)	1.37	-	-	$35.8 \pm 15\%$
Pitot pressure (kPa)	181	-	-	$4,557 \pm 10\%$
Mach number (-)	10	-	-	$9.94 \pm 3\%$
Density (kg/m^3)	0.0221	-	-	$0.465 \pm 12\%$
Static temperature (K)	226	-	-	$268 \pm 5\%$
Velocity (m/s)	3011	-	-	$3,257 \pm 1\%$
Stagnation enthalpy (MJ/kg)	3.39	-	-	4.05
Total pressure (GPa)	0.129	-	-	3.75
Unit Reynolds number [<i>million/m</i>]	-	-	-	91.7
Core flow diameter (mm)	-	-	-	50
Test time [μs]	-	-	-	60

Table 8.3: Test flow properties for Mach 10 flow condition, x2-scr-m10p0-rev-1, X2 without nozzle. Shock speeds are averaged between the transducer locations. Each Eilmer3 test flow property is the mean value within the core flow averaged across the test time (see Section 8.6.2.4); the Eilmer ‘±’ value is the maximum departure from the mean value during the test time. The experimental shock speed ‘±’ is the experimental uncertainty. Total pressure and enthalpy are calculated based on average flow properties during the test time, and assume shifting chemical equilibrium per Chinitz et. al [41].

It can be seen that the L1d2 computed shock trajectory agrees well with the experimental measurements in the shock and acceleration tubes, in terms of both shock speed and also timing of shock arrival. Good agreement with the timing was achieved by using inertial diaphragm models for the secondary and tertiary diaphragms in L1d2. The Mylar diaphragm is modelled as a piston with a mass equal to the amount of Mylar used for the actual experiment. Upon reaching a pre-determined rupture pressure the piston is released. The subsequent piston motion is computed by integrating its acceleration due to the variable pressure force, $F(t)$, acting across its diminishing mass, $m(t)$. The piston mass is reduced exponentially until it reaches a lower mass limit, as follows [73]:

$$\frac{dm}{dt} = \begin{cases} f_{\text{decay}} \times m & \text{for } m > m_{\text{limit}} \\ 0 & \text{for } m \leq m_{\text{limit}} \end{cases} \quad (8.2)$$

The lower mass limit is imposed to prevent numerical instabilities [73] as the mass approaches zero. An obvious effect of using the inertial diaphragm model is to delay development of the transmitted shock in the downstream tube. This delay is characterised by initial curvature in the transmitted shock trajectory, evident upon close inspection of Figure 8.8 at the tertiary diaphragm location. Good agreement with shock timing was obtained by setting the time constant, f_{decay} , equal to 20,000. This corresponds to the diaphragm losing 50% of its mass within $34\mu\text{s}$, 90% of its mass within $114\mu\text{s}$, and 99% of its mass after $228\mu\text{s}$.

A strong reflected shock from the secondary diaphragm is also observed in both computed and experimental results, however the L1d2 reflected shock progresses upstream through the shock tube later than in the experiment. It is not surprising that this discrepancy exists; the strength and arrival time of the reflected shock depends on numerous critical preceding flow phenomena, including the secondary diaphragm rupture process and primary driver wave processes. Over these relatively long time scales it seems probable that imperfect modelling of these phenomena will easily lead to timing discrepancies of the order of magnitude observed.

Figure 8.9 shows the primary shock speed as the shock traverses the length of the facility. Experimental data points represent the average shock speed between adjacent transducers in the same tube. L1d2 shock speed is plotted along the entire length of the facility downstream of the primary diaphragm. Results are shown for one L1d2 model using inertial diaphragms, and a different model using hold diaphragms, which have no mass. After the hold diaphragm is triggered, the boundary is maintained for an additional $10\mu\text{s}$, and then fully opened. The Eilmer3 shock speed is only plotted downstream of $st1$, since this is where the axisymmetric calculation begins. The Eilmer3 tertiary diaphragm was also modelled as a $10\mu\text{s}$ hold diaphragm.

Observing both of the L1d2 computed shock speeds, the shock speed through the sec-

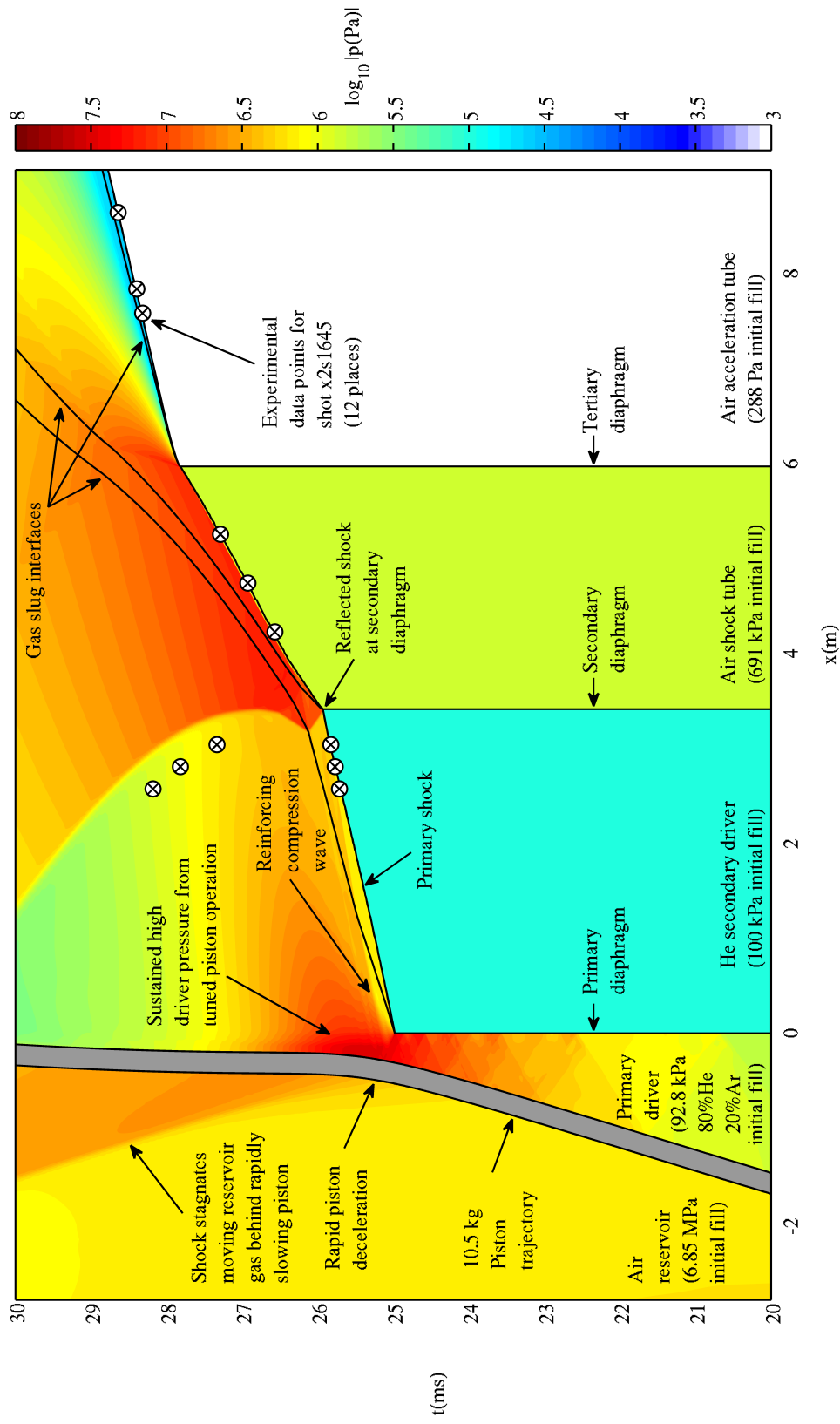


Figure 8.8: x - t diagram for Mach 10 flow condition, X2 without nozzle ($x2-scr-m10p0-rev-1$ in Table 7.5). Results are based on L1d2 calculations and experimental measurements.

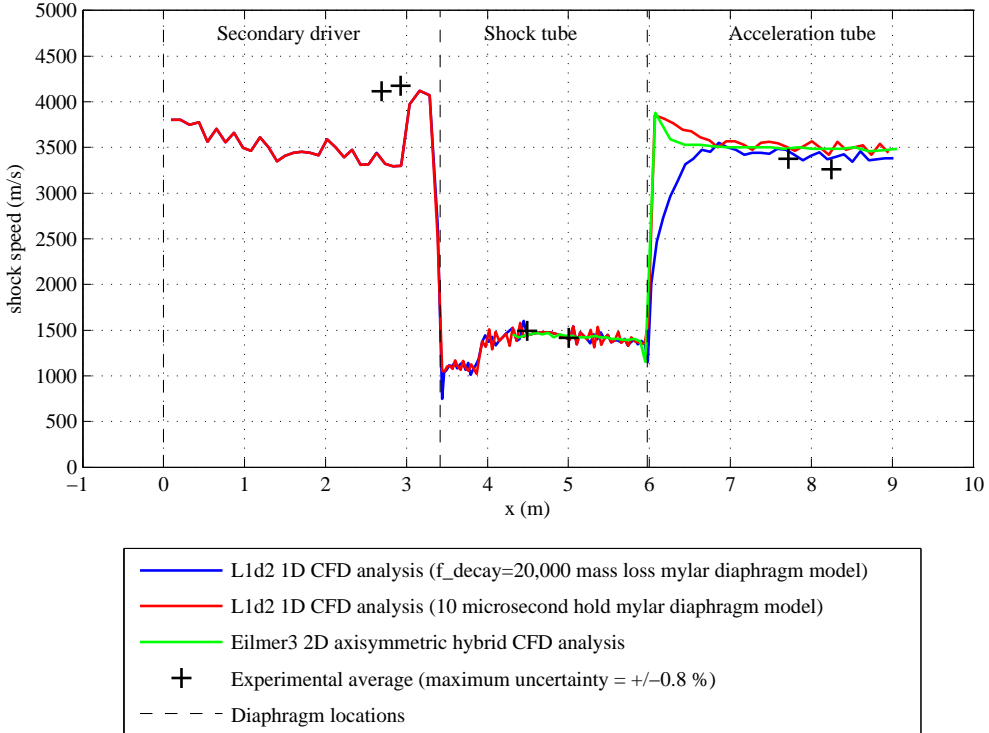


Figure 8.9: Primary shock speed vs. axial position for Mach 10 flow condition, X2 *without* nozzle (x_2 -scr-m10p0-rev-1 in Table 7.5).

ondary driver matches experiment well, however the arrival of the reinforcing compression wave from the driver (see Section 7.8, Point ‘a’) occurs slightly later than in the experiment; this explains the discrepancy between experimental and L1d2 shock speeds in the secondary driver in Table 8.4 previously. It is not surprising that the L1d2 shock speeds agree well with the experiment through the shock tube, since the L1d2 models were specifically tuned to match the average experimental shock speed between transducers *st1* and *st3* (see Section 8.4). However, it is observed that the experimental shock speed drops faster through the shock tube. This faster deceleration is not observed in the Eilmer3 shock speed, therefore it is not believed that it is due to boundary layer or 2-D effects. Instead it may be due to unsteady 2-D wave processes in the driver which are not properly captured in the L1d2 models. If this is the cause of the discrepancy, then the same behaviour would be expected in both the L1d2 and Eilmer3 models since the former is used to calculate an inflow to the latter.

The L1d2 code over-estimates the acceleration tube shock speed. This is as expected, since 2-D effects become very important in this low pressure tube. The effect of the inertial diaphragm model is evident in the corresponding L1d2 plot, whereby it can be seen that the relatively heavy diaphragm (8 sheets of 0.025 mm thick Mylar corresponding to a mass of 0.0016 kg) takes a relatively long distance to accelerate to full speed

in the low pressure acceleration tube flow. The same effect is not as obvious at the secondary diaphragm, where the much higher pressures accelerate the diaphragm to the lower maximum speed in a much shorter distance. Observing the shock trajectory for the L1d2 model using $10\mu s$ hold diaphragms, the effect of zero diaphragm mass is obvious in the acceleration tube; shock speed for the hold diaphragm model reaches a higher peak speed, in a much shorter distance, than the inertial diaphragm model.

The Eilmer3 code also models the tertiary diaphragm using a $10\mu s$ hold diaphragm, and predicts a very similar initial shock speed in the acceleration tube to the L1d2 hold diaphragm model. However, downstream of the tertiary diaphragm, the Eilmer3 shock speed drops faster than L1d2, although it then settles to a fairly constant speed which is similar to both L1d2 models, and a little higher than the experimental shock speeds.

8.6.2.2 Visualisation of Flow Development

Figure 8.10 shows the flow development predicted by Eilmer3 in the shock and acceleration tubes. The top half of each contour plot shows Mach number; the bottom half shows static pressure. The vertical scale has been increased $5\times$ for clarity, and it should be noted that this makes shocks and interfaces look more planar than they are.

Observing Figure 8.10, the primary shock (denoted by PS) arrives at the secondary diaphragm just after $t = 1.22$ ms. The diaphragm has a $10 \mu s$ hold time on it, which results in the creation of an upstream travelling reflected shock; after flow arrival this shock is approximately stationary in the laboratory frame of reference. This reflected shock is quite strong, and can still be observed $600 \mu s$ later (at $t = 1.90$ ms). When the reflected shock reaches the interface, I1 (at $t = 2.13$ ms), a series of compressive disturbances are sent downstream towards the test gas. These disturbances are difficult to identify on the figure, but are evident in an animation of the simulation. The reflected disturbances (some of which are identified by ‘DIST’ in Figure 8.10) do not reach the test section before the conclusion of the test time, and therefore do not disrupt the test flow.

Mach number was selected for the upper contour because it clearly shows the development of the test gas; the test gas is the bright red region of gas which has a Mach number of approximately 10. Observing Figure 8.10, the Mach 10 test gas arrives at the acceleration tube exit at approximately $t = 2.22$ ms. The useful portion of this gas continues for $60 \mu s$ longer until $t = 2.28$ ms, at which point the unsteady expansion arrives. Beyond this time the flow properties deviate excessively from the average test time values and the test time can therefore be assumed to have ended; see Section 8.6.2.4 for further analysis of the test flow properties.

The boundary layer is observed to be thin through the high density shock tube, but

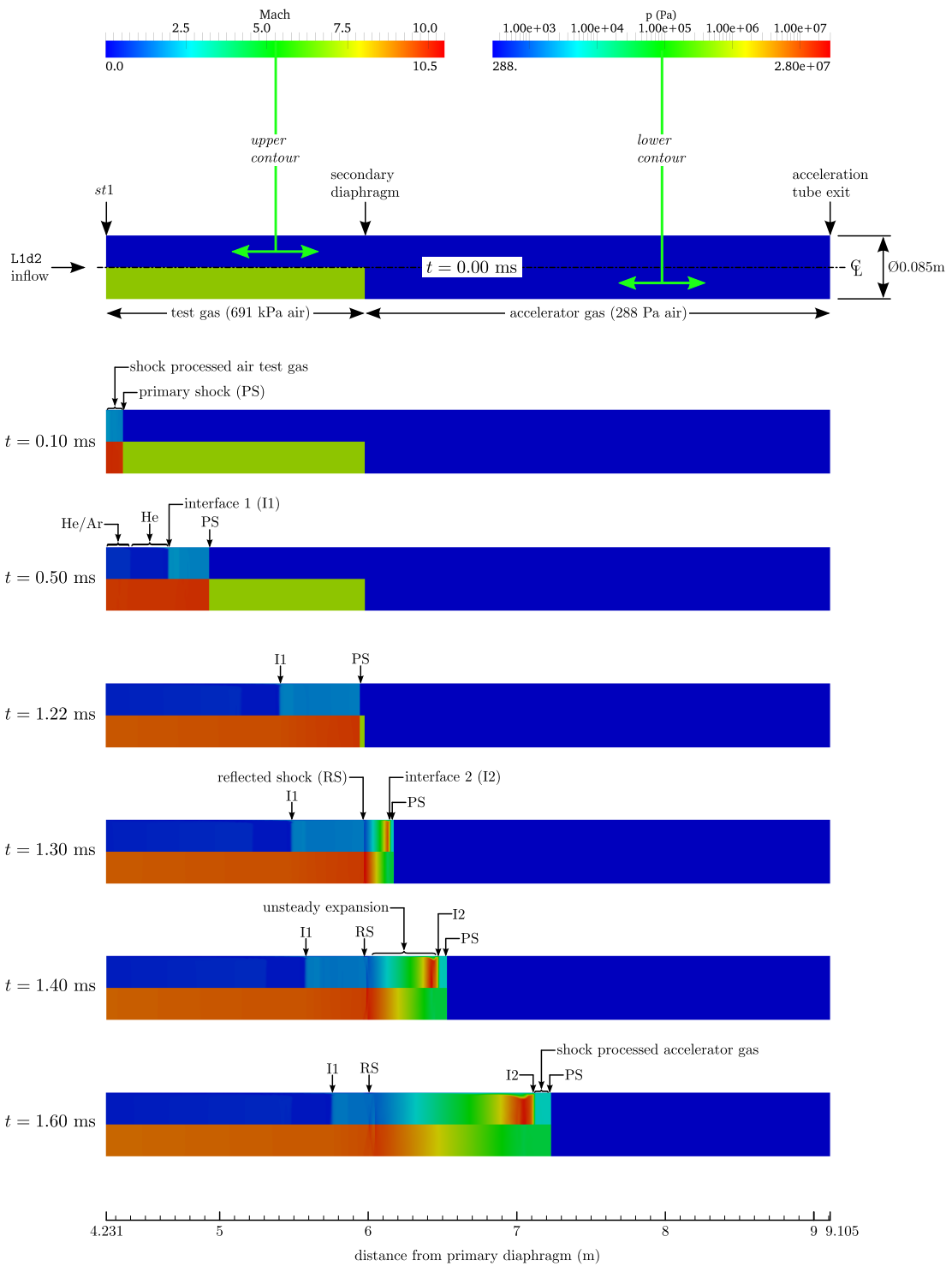


Figure 8.10: Flow development in shock and acceleration tubes (part 1 of 2), flow condition x2-scr-m10p0-rev-1.

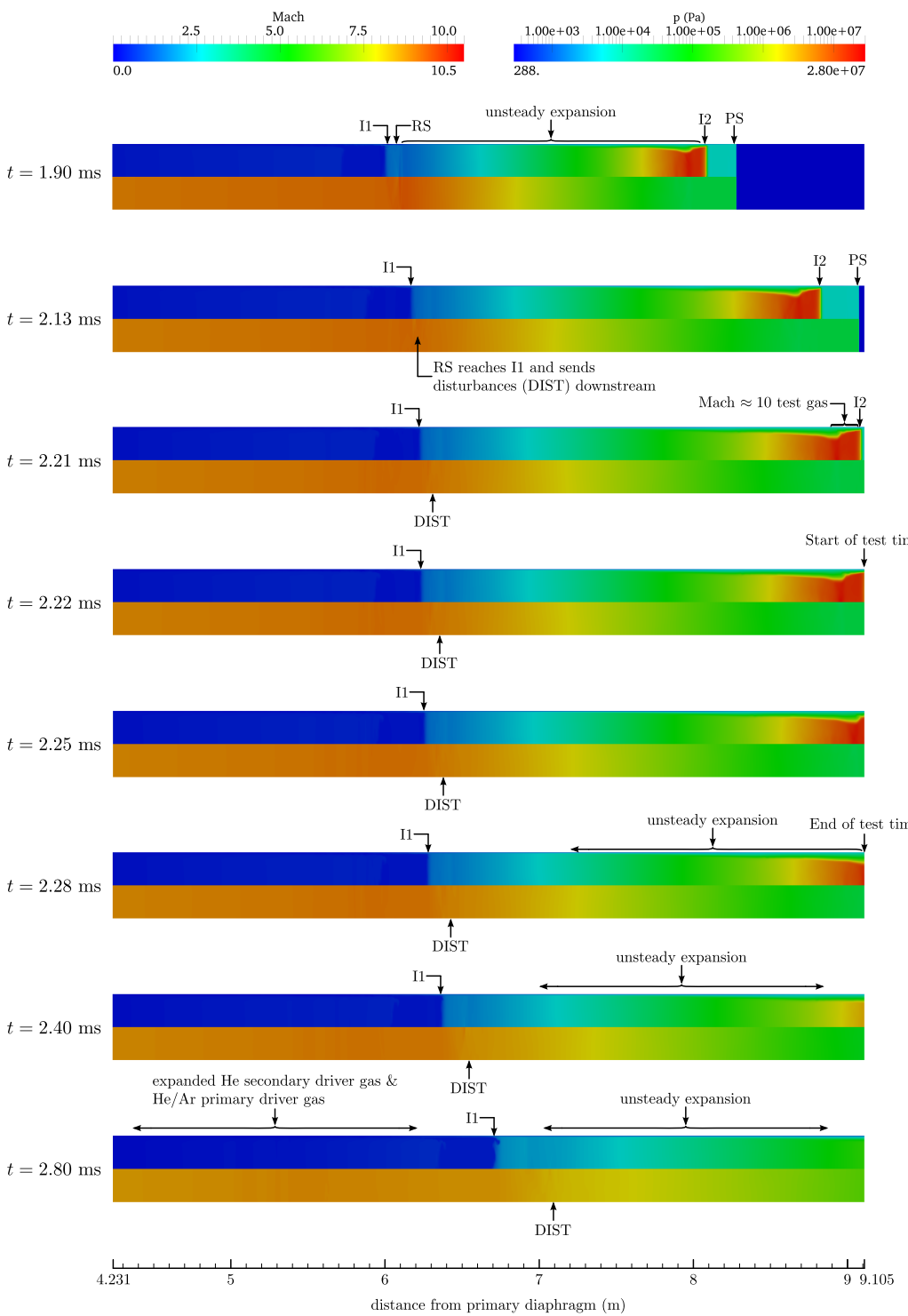


Figure 8.10: Flow development in shock and acceleration tubes (part 2 of 2), flow condition x2-scr-m10p0-rev-1. It is noted that these contours are truncated at the acceleration tube exit, however the actual Eilmer3 model extends 150 mm further downstream.

thickens substantially in the acceleration tube. Observing the test gas slug at $t = 2.22$ ms, the core diameter of the Mach 10 flow is clearly less than 70% of the tube diameter when it exits the tube. This *necking* of the Mach ≈ 10 region of test gas begins to form after tertiary diaphragm rupture occurs ($t = 1.40$ ms), and is a characteristic of the flow dynamics near the contact surface. Observing the length of the accelerator gas slug between the moment of tertiary diaphragm rupture and the arrival of the shock at the tube exit, the distance between the shock and the contact surface is continually increasing. This indicates that flow processes between the shock and the contact surface are unsteady, and that the Mirels effect (boundary layer entrainment of the flow) has not reached a steady state condition whereby the shock and contact surface move at the same velocity [99, 100]. However, the observed necking of the test gas slug is still primarily attributed to boundary layer effects.

Figure 8.11 shows the *direction* (not magnitude) of velocity vectors in the vicinity of the shock and contact surface at $t = 1.90$ ms. The velocity has been calculated in the *contact surface-steady* frame of reference. In this frame of reference, the contact surface is stationary, i.e. $\mathbf{V}_{css} = (u - u_{cs})\cdot \mathbf{i} + v\cdot \mathbf{j} + w\cdot \mathbf{k}$; the contact surface velocity at this instant of time is $u_{cs} = 3,239$ m/s. The flow processes in this region are not steady, therefore it is not appropriate to calculate particle pathlines through the flow. However, these arrows indicate which direction the flow is *tending* towards.

Observing the accelerator gas, although there is an ongoing accumulation of gas between the contact surface and the shock, gas which reaches the contact surface does tend to be swept up into the boundary layer and along the tube walls. There also appears to be an anticlockwise recirculation region of test gas between the contact surface and the necked region. This recirculation occurs due to viscous effects at the tube wall. The central region of test gas initially flows downstream towards the contact surface in order to supply mass to the boundary layer. This gas then slows as it reaches the contact surface, and is swept into the boundary layer. The pressure of this decelerating gas will tend to increase as it loses velocity. Lower pressure gas continues to progress downstream past this entrained boundary layer gas; the boundary layer expands to balance the pressure, resulting in the observed necking region. It is finally noted that to the left of Figure 8.11 the arrows change direction (point upstream). This region of flow is the unsteady expansion which has not yet expanded to the test gas velocity.

8.6.2.3 Tube Wall Static Pressure Traces

Tube wall transducer static pressure traces are shown in Figures 8.12, 8.13, and 8.14, for the secondary driver, shock, and acceleration tubes respectively. All traces have been time-referenced to initiate with the corresponding L1d2 trace, therefore these plots are not indicative of relative timing between transducers. The L1d2 timing is indicative of

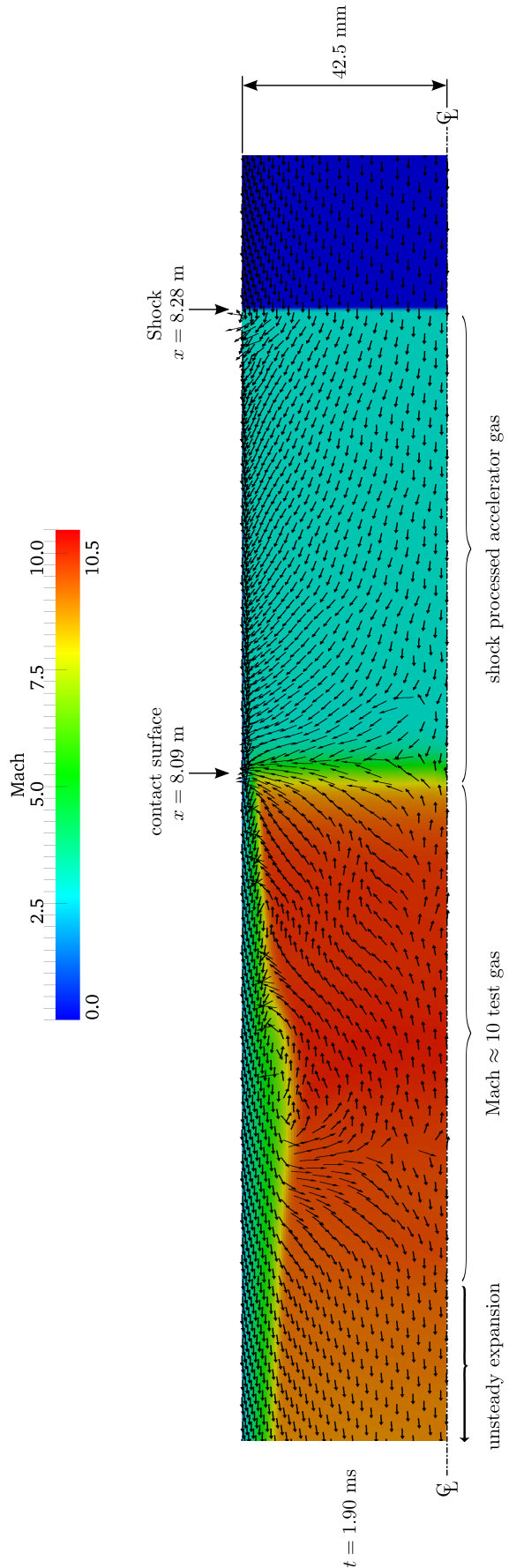


Figure 8.11: Contour plot of Mach number local to shock at $t = 1.90$ ms in the hybrid Eilmer3 simulation time, for Mach 10 flow condition, $x2\text{-scr-m10p0-rev-1}$. Vertical scale has been increased $2\times$. Arrows show the direction of velocity vectors, in the *contact surface-steady (css)* frame of reference (i.e. $\mathbf{V}_{css} = (u - u_{cs}) \cdot \mathbf{i} + v \cdot \mathbf{j} + w \cdot \mathbf{k}$, where $u_{cs} = 3,239$ m/s is the velocity of the contact surface at this instant in time). Arrows lengths are all equal and are *not* indicative of the velocity magnitude, $|\mathbf{V}_{css}|$. Discontinuities in the distribution of arrows are an artefact of the software graphical rendering.

overall event timing after piston release from the launcher.

Pressure traces from multiple experiments were averaged in order to better illustrate general behaviour; for some transducers in particular, there was excessive signal noise. Averaged curves were calculated by first manually clipping ‘obvious’ noise from the data, then zeroing and time shifting the traces to intersect at a common pressure magnitude during the rapid pressure rise phase (i.e. immediately following shock arrival), and finally averaging the traces. Aside from noise introduced by sensor and cabling problems (characterised by random spikes in the trace), the repeatability of pressure traces was excellent, including the small amplitude transient response. This is demonstrated in the plots, where each averaged pressure trace is compared to a specific trace from a sample experiment, indicating that the averaged trace is sufficiently representative. It is further noted that secondary driver experimental pressure traces are averaged across all flow conditions, since the configuration of the primary and secondary drivers was common for all flow conditions. However, these traces are truncated prior to arrival of the reflected shock; the reflected shock varies depending on the shock and acceleration tube fill pressures, and is therefore flow condition dependent.

L1d2 and Eilmer3 traces are also shown; referring to Figure 8.1, since the Eilmer3 model only computed the response downstream of *st1*, there are correspondingly no secondary driver traces.

It is finally noted that experimental pressure traces were made with PCB piezoelectric pressure sensors. The experimental pressure traces are observed to diminish more rapidly than the computed traces, and over longer time scales these traces can become negative (for example, Figure 8.12(a)). This characteristic of the piezoelectric pressure sensor traces is attributed primarily to thermal effects. As the hot flow heats the sensing diaphragm of the piezoelectric pressure sensor, the case surrounding the internal piezoelectric sensing crystals can expand. Expansion of the case results in a reduction in the pre-load force on the crystals, and can result in a negative-signal output [162]. This effect can be mitigated by applying insulating coatings to the sensing surface (for example, by applying tape across the sensing surface), although any such coating/barrier may add to the mechanical impedance of the sensor [163]. For these experiments no special efforts were made to reduce this effect; the most important flow processes occur over short time scales which are not greatly affected by thermal effects, and other important wave processes, such as the arrival time of reflected shocks, remain evident in the pressure traces even when thermal effects are present.

Secondary Driver Static Pressure Traces Referring to Figure 8.12, it can be seen that L1d2 closely matches experiment for the initial pressure rise in transducers *sd1* and *sd3*. There is a large discrepancy at *sd2*, which is unexpected since it does not follow

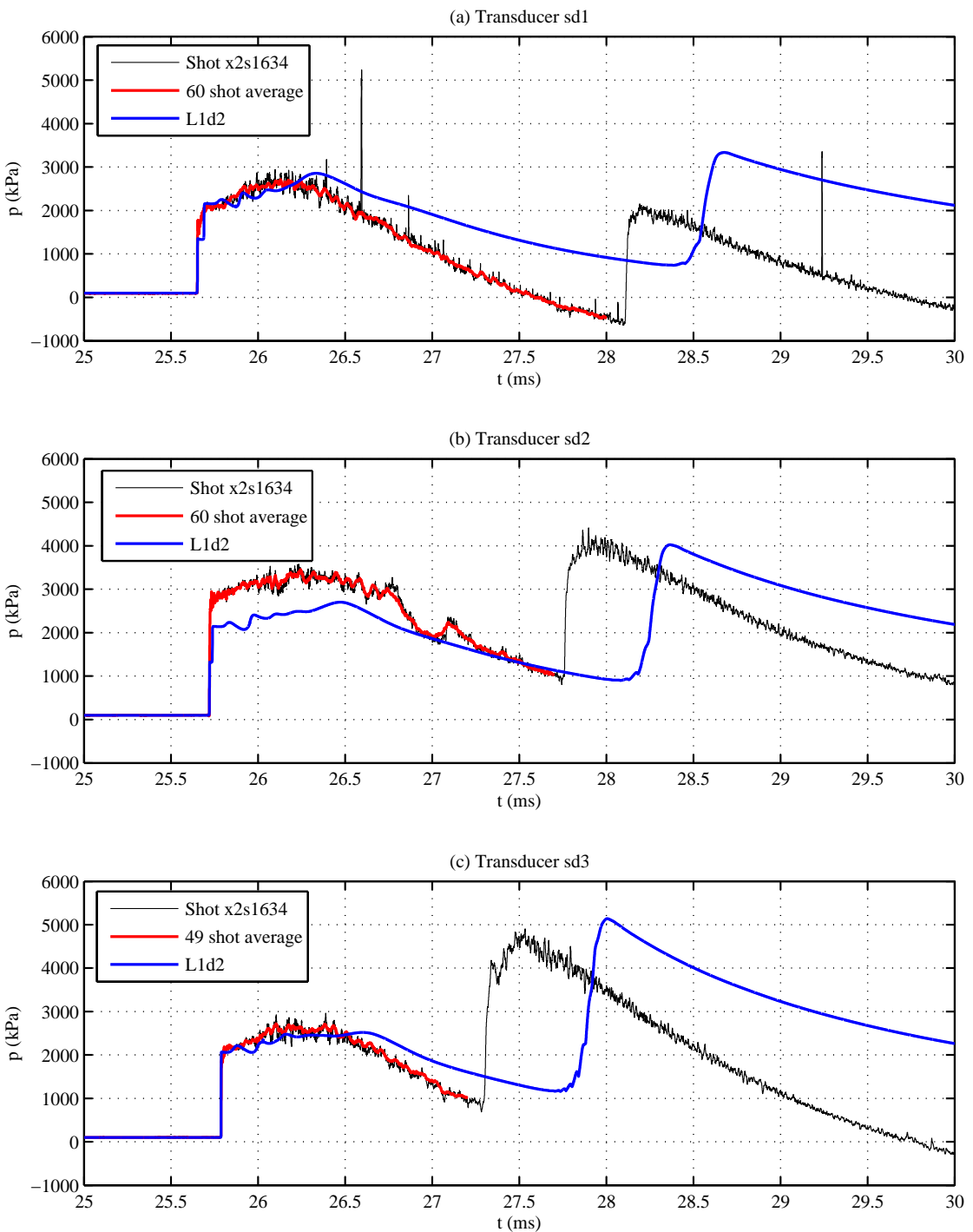


Figure 8.12: Static pressures at secondary driver transducers $sd1$, $sd2$, and $sd3$ (see Figure 8.1), flow condition x2-scr-m10p0-rev-1. All traces are time-referenced to initiate with the corresponding $L1d2$ trace. These averaged experimental traces are derived from all of the flow conditions since they all used the same primary/secondary driver configuration; the averaged traces are truncated prior to arrival of the reflected shock from the secondary diaphragm, since this shock is flow condition dependant. $2\mu s$ time averaging has been applied to experimental traces. Eilmer3 results are not shown since the Eilmer3 hybrid model does not have a secondary driver.

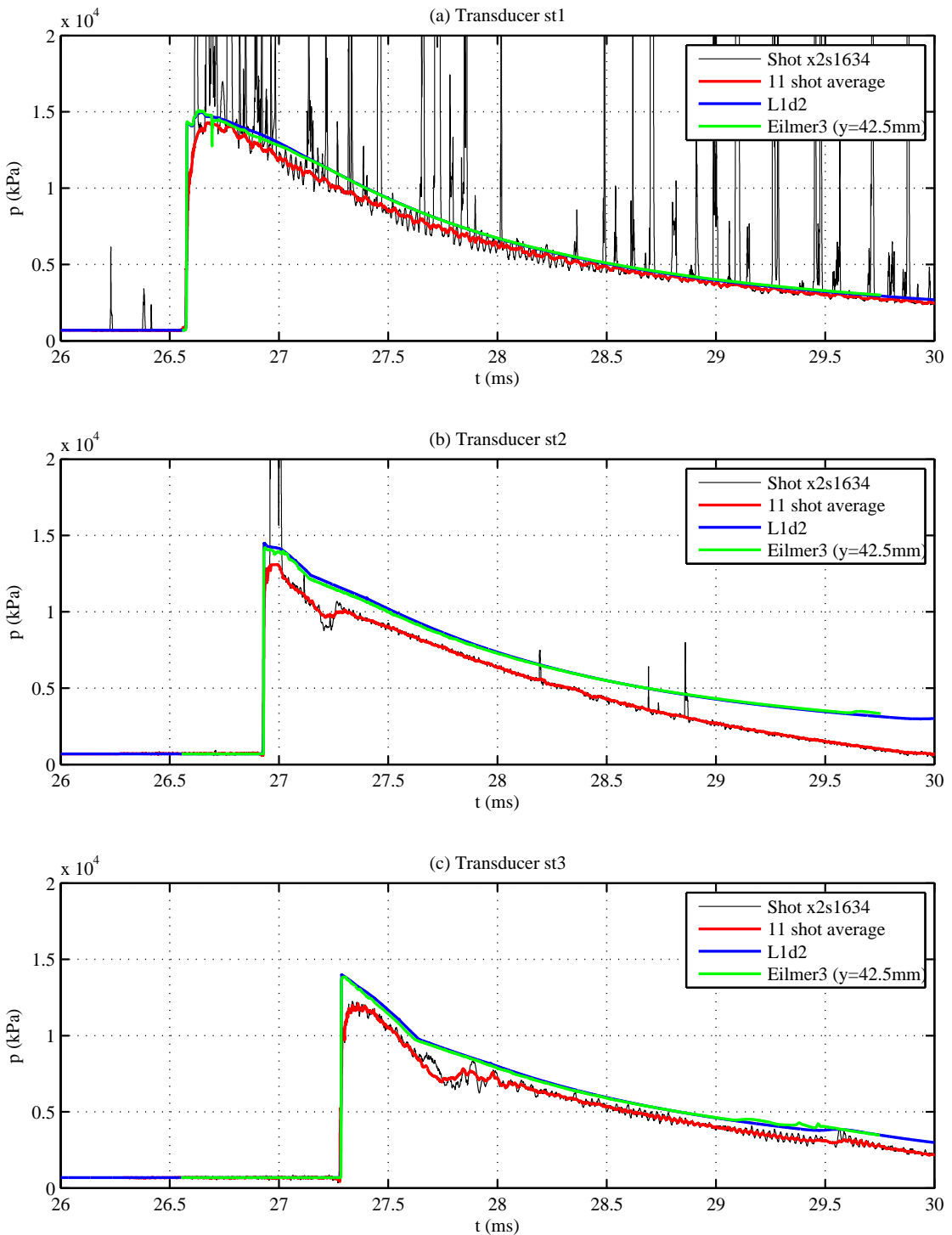


Figure 8.13: Static pressures at shock tube transducers $st1$, $st2$, and $st3$, flow condition x2-scr-m10p0-rev-1. All traces are time-referenced to initiate with the corresponding L1d2 trace. Averaged experimental traces are derived from results for this specific flow condition. $2\mu\text{s}$ time averaging has been applied to experimental traces.

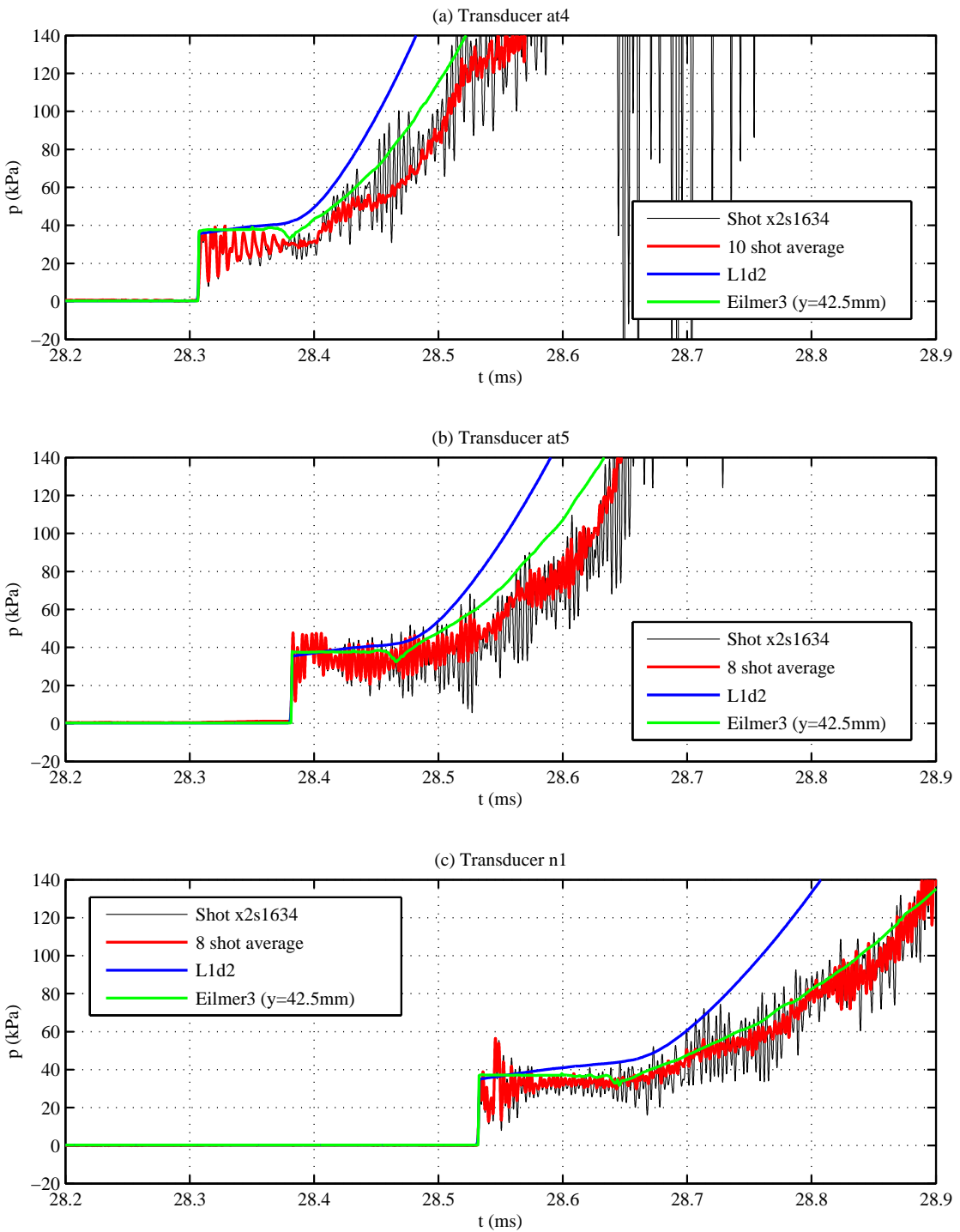


Figure 8.14: Static pressures at acceleration tube transducers *at4*, *at5*, and *n1*, flow condition x2-scr-m10p0-rev-1. All traces are time-referenced to initiate with the corresponding L1d2 trace. Averaged experimental traces are derived from results for this specific flow condition. $2\mu\text{s}$ time averaging has been applied to experimental traces.

the trend of reducing magnitude evident with $sd1$ and $sd3$, and which is predicted for $sd2$ by L1d2. However, the transducer calibration was checked at the completion of the campaign and had not deviated from its previous measurement by the magnitude apparent in the plot. The reflected shock arrives sooner in the experiment than predicted by L1d2, as was already observed in Figure 8.8. It is finally noted that since the same primary and secondary driver configuration was used for *all* flow conditions, that a large number of traces were available to calculate the experimental averages for the secondary driver.

Shock Tube Static Pressure Traces Referring to Figure 8.13, it can be seen that L1d2 and Eilmer3 are in close agreement through the shock tube. This is to be expected, since Eilmer3 uses the L1d2 inflow at $st1$, and because 2-D effects are not expected to be significant through the dense gas shock tube. It can be seen that the computed pressure exceeds the experimental pressure by an increasing amount between $st1$, $st2$, and $st3$. The lower experimental pressures reflect the lower experimentally measured shock speeds as compared to the L1d2 predictions; see Section 8.6.2.1 and Figure 8.9. Finally, a kink can be observed in both the $st2$ (Figure 8.13b) and $st3$ (Figure 8.13c) pressure traces, at $t \approx 27.1$ ms and $t \approx 27.6$ ms respectively, whereby the rate of static pressure loss reduces. These kinks signal the arrival at each transducer of the downstream running compression wave created by the reflection of the secondary diaphragm reflected shock from the primary/secondary driver gas interface. This general wave process is discussed in more detail in point (2) of Section 7.8 and point (d) of Figure 7.7. magnitude.

Acceleration Tube Static Pressure Traces Referring to Figure 8.1, there are seven static pressure transducers located in the acceleration tube wall (when the nozzle is not used): $at1$ to $at6$, and $n1$ (located in the tube-to-dumptank adaptor, and downstream of the nozzle inlet plane). During the experimental campaign satisfactory measurements could not be made with $at1$, $at2$, or $at3$, each of which produced extremely noisy pressure traces. It is thought that this was due to their close proximity to the tertiary diaphragm; at this axial location the shock may not have fully formed and separated from the unsteady expansion, and the effects of tertiary diaphragm rupture may also be prominent. Further, these transducers had rigid brass mountings, which have poor vibration isolation characteristics. The acceleration tube PCB pressure transducers need to have high sensitivity in order to measure low magnitude test flow static pressures; these transducers are correspondingly more sensitive to facility mechanical vibrations which induce inertial loads on the sensing element. These inertial loads have proportionally less effect on the stiffer sensing elements of the lower sensitivity upstream pressure transducers. Whilst mechanical vibrations were significantly reduced by incorporating a new secondary diaphragm vibration isolation arrangement (see Section 8.7), non-negligible vibrations still exist, and these will not be well isolated by the rigid mountings at these

specific transducers.

Only *at4*, *at6*, and *n1* produced usable pressure traces (*at6* was removed since the existing transducer mount was discovered to be physically protruding into the flow). Referring to Figure 8.14, it can be seen that each experimental transducer trace has a different initial unsteady response. The averaged experimental traces show that this unsteady behaviour was highly repeatable, however it is not reflected in either the L1d2 or Eilmer3 computed responses. It is believed that this initial unsteady response is due to the unique mechanical/aerodynamic interaction of each transducer to the flow. This unique response might reasonably be expected since each of these transducers had a different mounting arrangement: *at4* was suspended in a floating arrangement, using silastic, within an oversized brass mounting in the tube wall; *at5* was mounted between thin rubber o-rings in a narrow nylon mounting in the tube wall; *n1* was also mounted between thin rubber o-rings, but in a larger nylon mounting within the heavy and thick-walled tube-to-dumptank adaptor piece.

Both L1d2 and Eilmer3 predict an identical initial pressure rise due to shock arrival; this rise is marginally higher than the experimental measurement, and is consistent with the computed shock speeds being marginally higher than the experimental shock speeds. Following shock arrival, L1d2 generally over-estimates the pressure, and prematurely predicts the arrival of the unsteady expansion (characterised by the large pressure rise). However, the Eilmer3 computed response much more closely matches the experimental measurement; both in terms of predicting a generally lower pressure level following shock arrival (which very closely matches experiment), and also in terms of predicting the arrival of the unsteady expansion.

8.6.2.4 Test Flow Properties (see Table 8.3)

The black line in Figure 8.15(a) shows the Eilmer3 computed 15 deg cone surface static pressure at the acceleration tube exit, at a radial offset of $y = 9$ mm from the tube centreline. Referring to Figure 8.6, this corresponds to the experimental radial location of the 15 deg cone probes. The cone pressure was computed by first calculating the transient flow history at $y = 9$ mm along the acceleration tube exit plane, and then applying this flow history as a radially constant transient inflow to a separate cone axisymmetric Eilmer3 model. The Eilmer3 cone model consisted of an 8,000 cell viscous calculation, with equilibrium air.

The coloured curves in Figure 8.15(a) are the experimentally measured cone surface static pressures for two example experimental shots, each time-referenced to match the CFD. *cone1* is the cone above the tube centreline; *cone2* is the cone below the tube centreline. It can be seen that the experimentally measured cone pressure traces are reasonably consistent and repeatable, and over the full time scale shown eventually

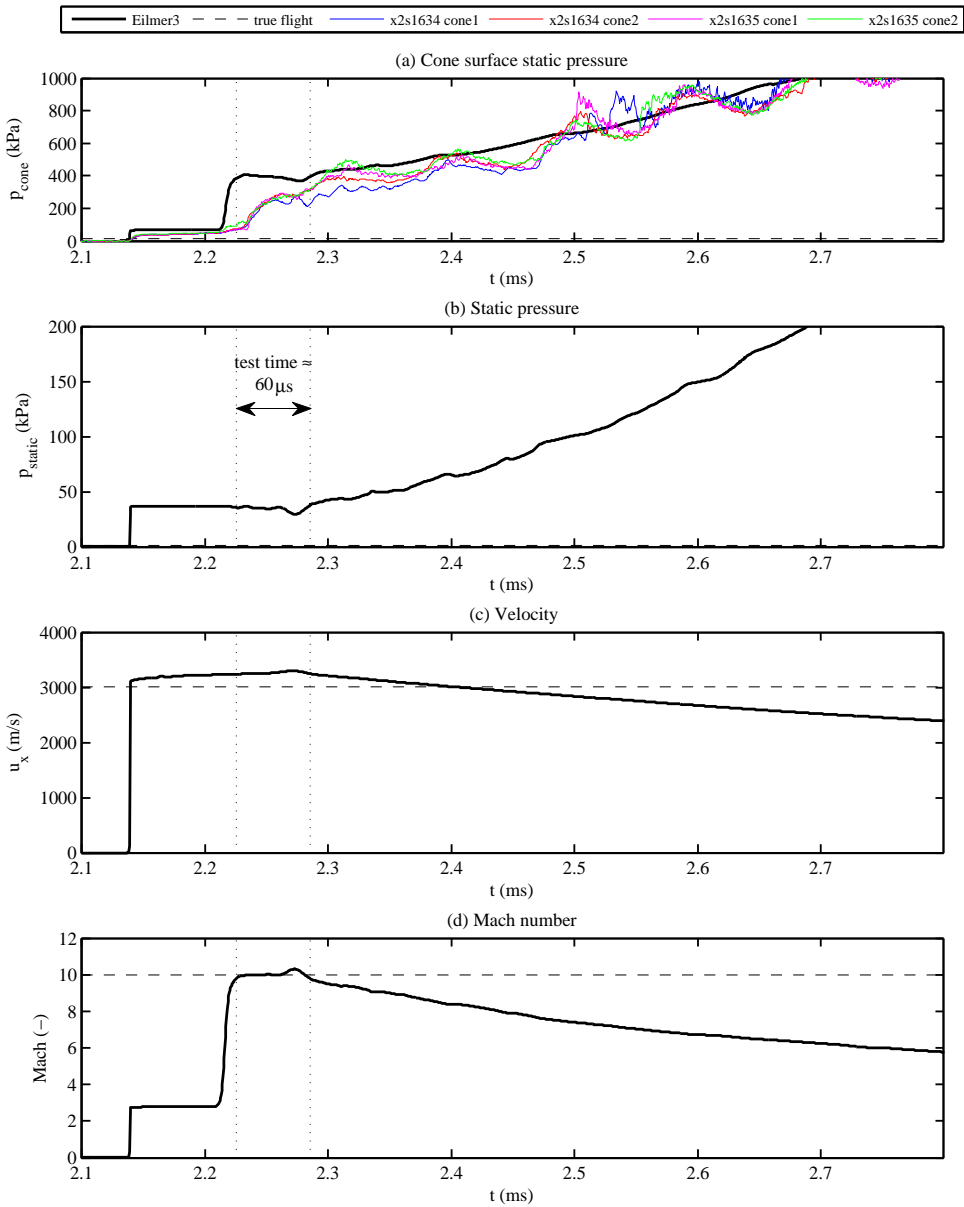


Figure 8.15: Computed and experimental test flow properties at the acceleration tube exit, at $y = 9$ mm from the tube centreline, for flow condition x2-scr-m10p0-rev-1. $t = 0$ corresponds to the beginning of the axisymmetric calculation. Experimental cone pressures in (a) were measured using 15 deg half angle cones; see Section 8.5. Computed Eilmer3 cone pressures were obtained by taking the transient flow history at the equivalent location in the axisymmetric model ($y = 9$ mm) and applying this as a planar inflow to a separate cone axisymmetric model.

match the numerically computed average pressure magnitude. However, the initial experimental response does not match the CFD well; the experimental traces appear to have very slow rise time. The initial cone pressure rise indicates the arrival of the shocked accelerator gas. The CFD predicts a steady cone pressure during this period, whereas the experimental traces are continually increasing. This may indicate a slow response time for the probes. The CFD also predicts a shorter acceleration gas slug length than was observed experimentally, probably indicating excessive loss of accelerator gas to the boundary layer in the CFD simulation.

Figures 8.15(b), (c), and (d), respectively show the computed static pressure, axial velocity, and Mach number, at $y = 9\text{ mm}$ along the acceleration tube exit plane. The dashed lines represent the true flight flow properties based on Table 1.1. Observing Figure 8.15(b), the static pressure is significantly higher than the true flight value. This is intended, since scale model testing typically requires significant pressure-length scaling. Observing plots (b-d), it can be seen that for a period of approximately $60\text{ }\mu\text{s}$ (identified on the plots), the computed Mach number and velocity match the true flight values, and the static pressure is relatively steady. This period of time is therefore identified as the useful test time for this flow condition.

Figure 8.15(a) does not show good correlation between the CFD and experiment during this time period. However, the experimental cone pressure probes may simply have an excessively slow response time and therefore be unable to fully identify the true cone surface pressure during this time. Reference to Figure 8.14 indicates that static pressure close to the tube exit very closely matches the computed prediction at the tube wall; this, combined with the good longer duration agreement between experimental and computed cone pressures, indicates that the computed flow properties are likely to be representative of the true flow in the facility. It is finally noted that there is an obvious $100\text{ }\mu\text{s}$ oscillation in the experimental cone pressure traces. The cause of this fluctuation was not identified, however the possibility of mechanical vibration in the cone support sting was excluded by undertaking measurements with a cone with no holes (i.e. with a PCB transducer sealed from the flow). This oscillation was not observed for a similar test flow after it was expanded through a nozzle; see Section 8.6.3.4. While it is expected that the probable cause of this oscillation is due to the aerodynamic response of the cone probe hole arrangement, this theory was not tested and further investigation would be beneficial.

Having used Figure 8.15 to establish that the test test time occurs between simulation times $t = 2.231\text{ ms}$ and $t = 2.291\text{ ms}$, the computed radial variation in flow properties is now analysed. Figure 8.16 shows how the computed flow properties vary between the tube centreline and tube wall. Curves are shown at 0%, 25%, 50%, 75%, and 100% of the test time. The dashed red line in each plot shows the average core flow properties during the test time, and is calculated for each plot by averaging the flow properties

across the core flow region, over the five time intervals. The black dashed line shows the true flight value for each flow property.

Referring to Figure 8.16, the core flow is observed to be the region of reasonably constant flow properties which extends from the tube centreline to a radius of approximately 25 mm. It is noted that true flight velocity and Mach number are well matched within the core flow region. True flight static and Pitot pressures are well exceeded, however this is intentional, and further, required in order to achieve pressure-length scaling. Static pressure at 100% of test time is observed to increase by approximately 10% above its mean value, and indicates arrival of the unsteady expansion. Pitot pressure correspondingly rises towards the end of the test time; velocity remains very constant and Mach number gradually drops.

While the 60 μs test time is clearly an inadequate duration for practical scramjet testing, this experimental and numerical analysis indicates that a reasonably steady Mach 10 scramjet flow at a total pressure of approximately 3.75 GPa can be achieved (per Table 8.3). The glancing impact pressure measurements using the 15 deg cones do not provide conclusive experimental verification of the numerical predictions during the test time, although they do indicate reasonable agreement over longer time scales. However, good agreement between experimental and numerical shock speeds and tube wall static measurements justifies the expectation that improved experimental Pitot measurements will show reasonable agreement with the numerical predictions.

8.6.3 Mach 10 with Nozzle (x2-scr-m10p0-noz-rev-1)

Results for the Mach 10 flow condition, using the contoured Mach 10 nozzle, are presented in Table 8.4. L1d2 and Eilmer3 shock speeds once more match experiment closely. The test flow core diameter has increased from 50 mm to 80 mm, and test time from 60 μs to 150 μs , compared to the Mach 10 flow condition without a nozzle (see Table 8.4). Static and Pitot pressures are well in excess of true flight values, by an order of magnitude, indicating suitability for pressure-length scaling. Detailed flow results are presented below.

8.6.3.1 Critical Wave Processes

Figure 8.17 shows the primary shock speed as the shock traverses the length of the facility, and includes experimental measurements and also L1d2 and Eilmer3 computed shock speeds. It is once more noted that the Eilmer3 shock speed is only plotted downstream of *st1*, since this is where the axisymmetric calculation begins. Observations for the Mach 10 condition with nozzle are qualitatively the same as for the condition *without* nozzle (see Section 8.6.2.1); the key difference is that the test gas is expanded to a lower Mach number through the acceleration tube unsteady expansion process, since it later

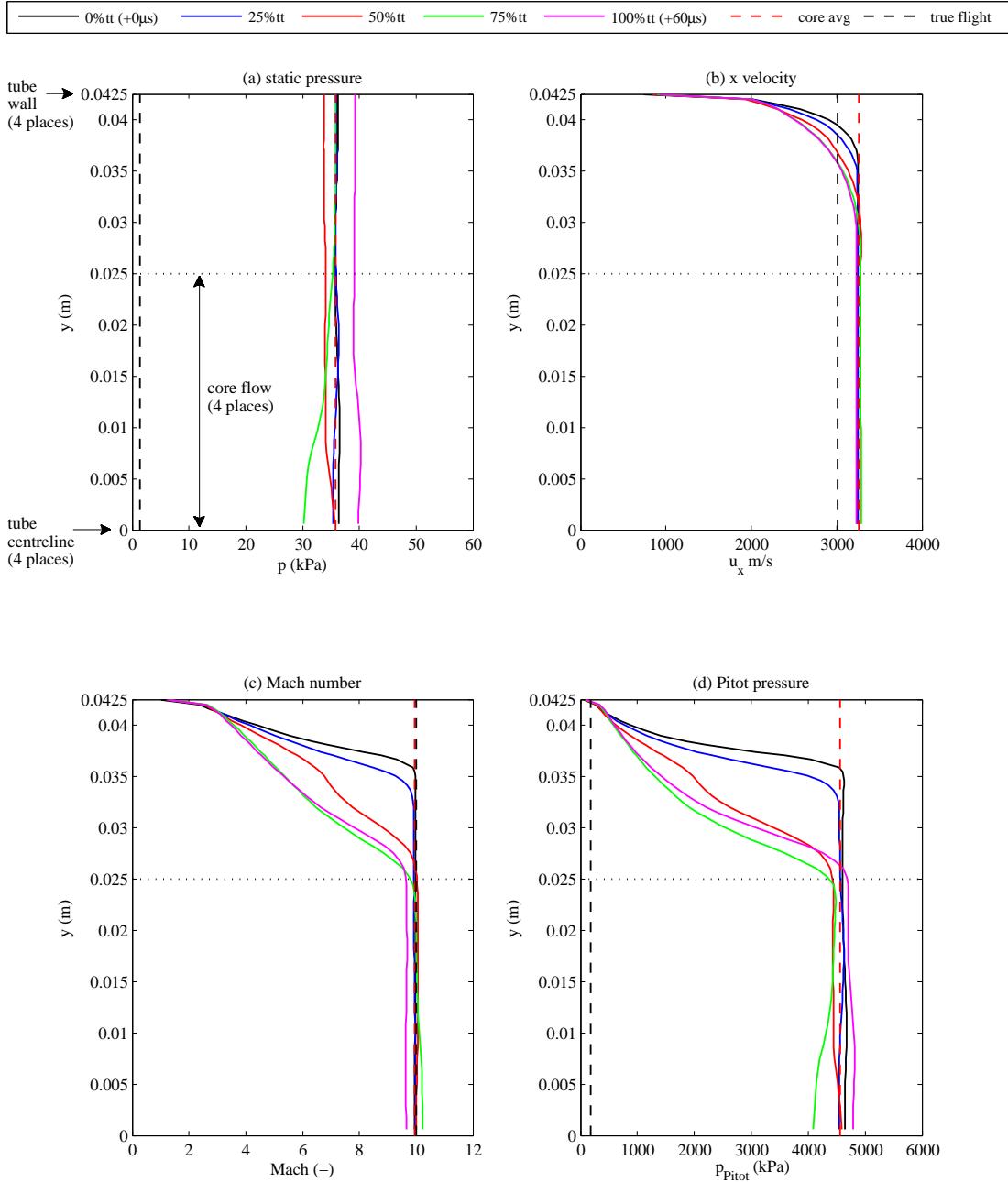


Figure 8.16: Radial variation in flow properties during the test time (denoted by *tt*), flow condition x2-scr-m10p0-rev-1. Test time is assumed to occur between simulation times $t = 2.231$ ms and $t = 2.291$ ms.

Property	True flight	Experimental	L1d2	Eilmer3
<i>Secondary driver</i>				
Shock speed between $sd1$ and $sd2$ (m/s)	-	$4,101 \pm 1\% (\sigma = 17 \text{ m/s})$	3,372	-
Shock speed between $sd2$ and $sd3$ (m/s)	-	$4,211 \pm 1\% (\sigma = 22 \text{ m/s})$	3,477	-
<i>Shock tube</i>				
Shock speed between $st1$ and $st2$ (m/s)	-	$1,655 \pm 0.3\% (\sigma = 5 \text{ m/s})$	1,611	1,601
Shock speed between $st2$ and $st3$ (m/s)	-	$1,586 \pm 0.3\% (\sigma = 4 \text{ m/s})$	1,632	1,612
<i>Acceleration tube</i>				
Shock speed between $at4$ and $at5$ (m/s)	-	$3,275 \pm 0.9\% (\sigma = 22 \text{ m/s})$	3,333	3,373
Shock speed between $at5$ and $n1$ (m/s)	-	$3,151 \pm 0.4\% (\sigma = 13 \text{ m/s})$	3,306	3,342
<i>Acceleration tube exit plane:</i>				
<i>Final test flow properties</i>				
Static pressure (kPa)	1.37	-	-	$12.0 \pm 38\%$
Pitot pressure (kPa)	181	-	-	$1,310 \pm 23\%$
Mach number (-)	10	-	-	$9.24 \pm 8\%$
Density (kg/m^3)	0.0221	-	-	$0.160 \pm 31\%$
Static temperature (K)	226	-	-	$259 \pm 8\%$
Velocity (m/s)	3,011	-	-	$2,976 \pm 3\%$
Stagnation enthalpy (MJ/kg)	3.39	-	-	3.33
Total pressure (GPa)	0.129	-	-	0.650
Unit Reynolds number [<i>million/m</i>]	-	-	-	29.9
Core flow diameter (mm)	-	-	-	80
Test time [μs]	-	-	-	200

Table 8.4: Test flow properties for Mach 10 flow condition, x2-scr-m10p0-noz-rev-1, X2 *with* nozzle. Shock speeds are averaged between the transducer locations. Each Eilmer3 test flow property is the mean value within the core flow averaged across the test time, along the nozzle exit plane (see Section 8.6.3.4); the Eilmer ‘ \pm ’ value is the maximum departure from the mean value during the test time. The experimental shock speed ‘ \pm ’ is the experimental uncertainty. Total pressure and enthalpy are calculated based on average flow properties during the test time, and assume shifting chemical equilibrium per Chinitz et. al [41].

undergoes a steady expansion to Mach 10 through the nozzle. An x - t diagram for the Mach 10 flow condition with nozzle is shown in Figure 8.18. This figure was constructed in accordance with the methodology detailed in Section 8.6.2.1 for the Mach 10 condition without nozzle. Once more the computed L1d2 shock trajectory agreed well with the experimental measurements in the shock and acceleration tubes, in terms of both shock speed and also timing of shock arrival.

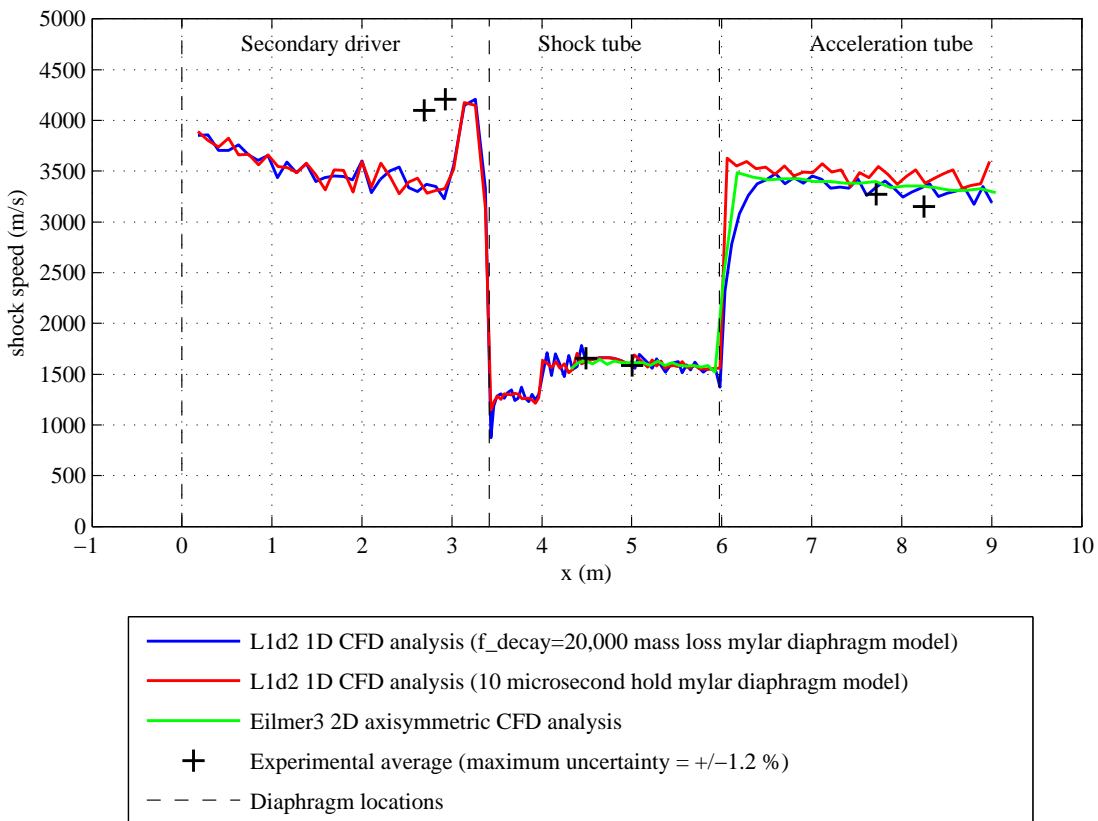


Figure 8.17: Primary shock speed vs. position for Mach 10 flow condition, X2 with nozzle (x2-scr-m10p0-noz-rev-1 in Table 7.5).

8.6.3.2 Tube Wall Static Pressure Measurements

Transducer pressure traces are shown in Figures 8.19, 8.20, and 8.21, for the secondary driver, shock, and acceleration tubes respectively. Computed pressure traces from L1d2 and Eilmer3 are also shown. All traces have been time-referenced to initiate with the corresponding L1d2 trace, which provides a global indication of event timing relative to piston launch. As in Section 8.6.2.3, pressure traces from multiple experiments have been averaged to better illustrate general behaviour, especially where excessive signal noise was present at specific transducers. Experimental repeatability was once more observed to be excellent for this condition. Besides the different observed pressure magnitudes, the static pressure traces for the Mach 10 condition using the nozzle were qualitatively similar to those without the nozzle in Section 8.6.2.3, including comparison to the numerical calculations, therefore additional comment is not required.

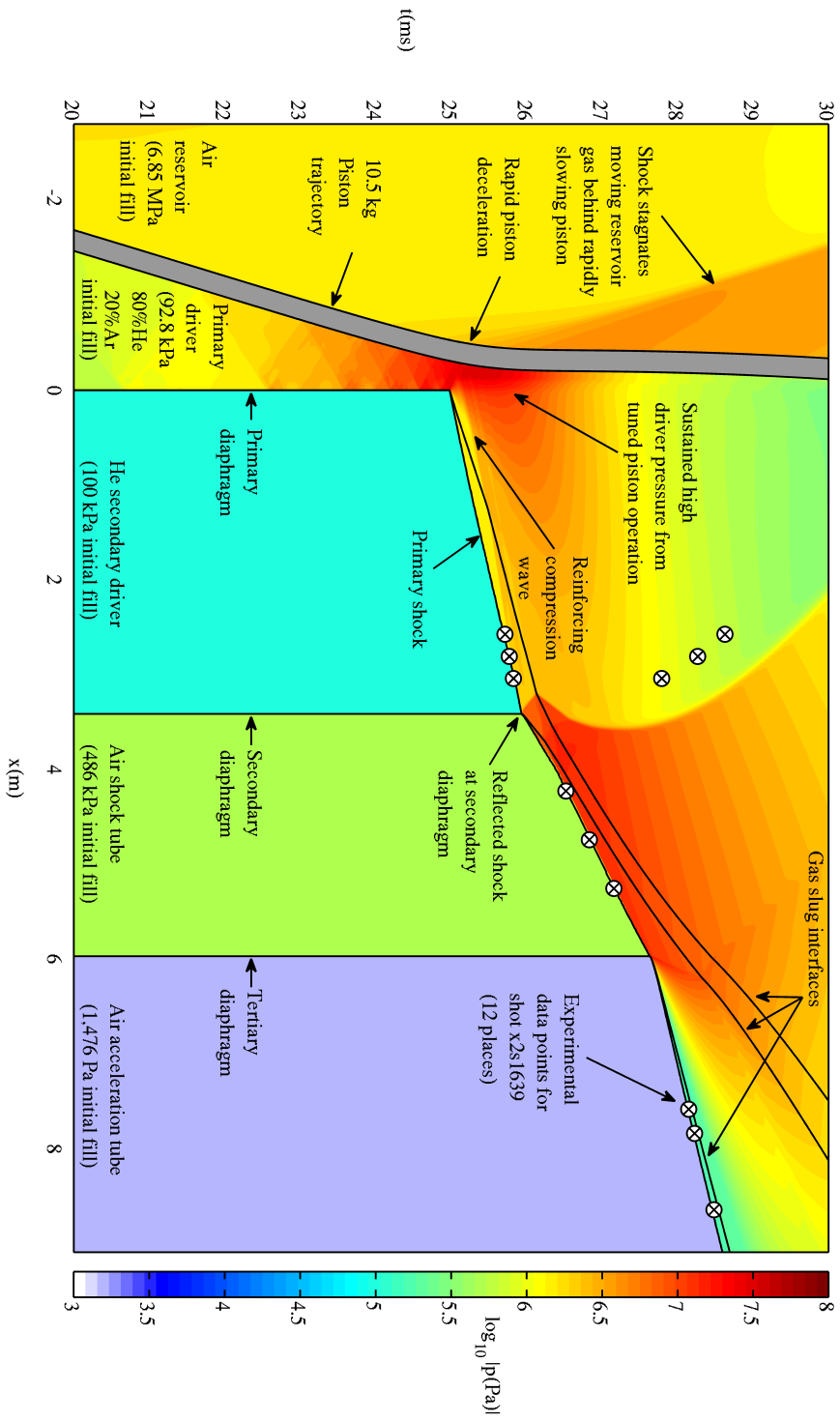


Figure 8.18: x - t diagram for Mach 10 flow condition, $X2$ with nozzle ($\times 2$ -scr-m10p0-noz-rev-1 in Table 7.5). Results are based on L1d2 calculations and experimental measurements.

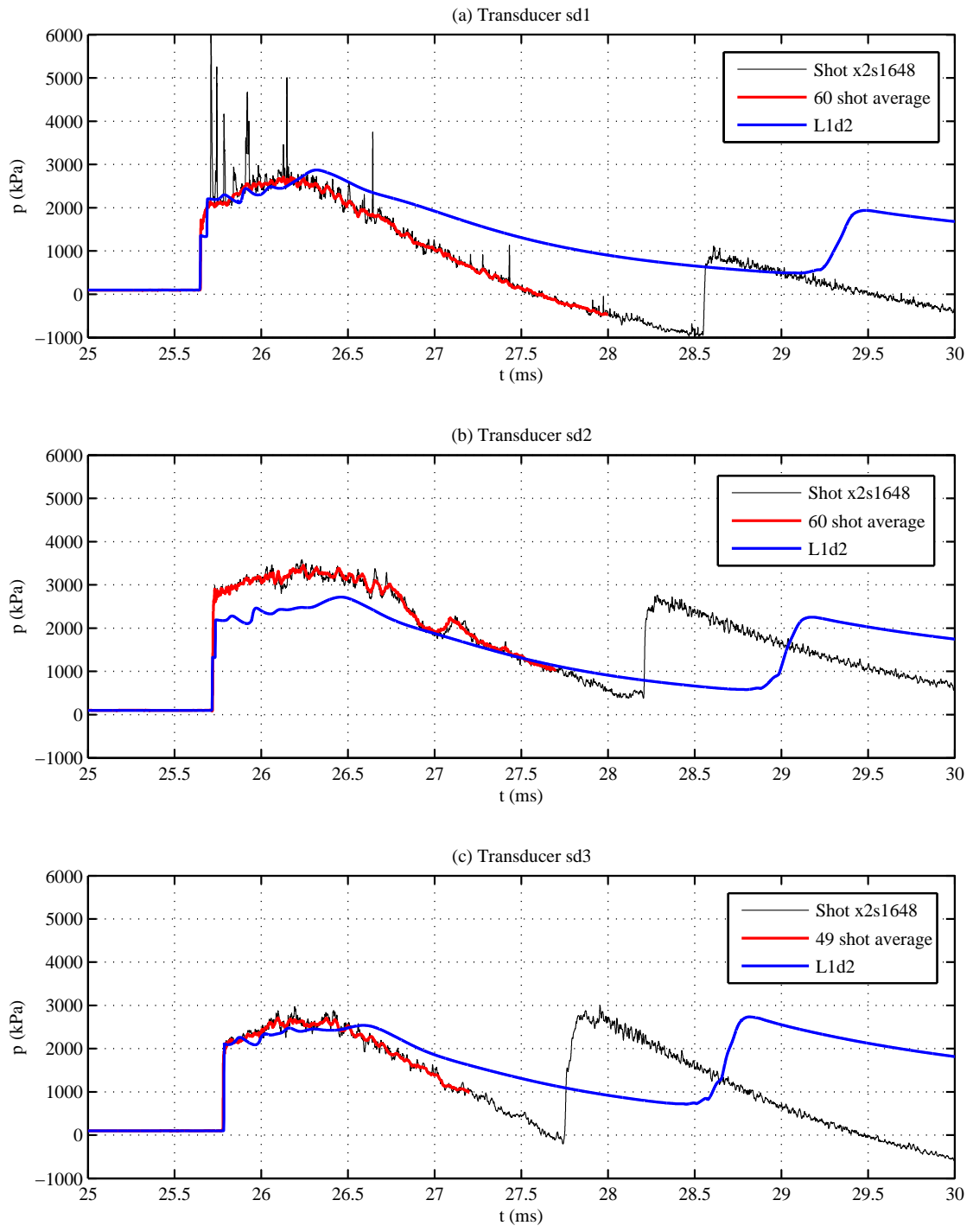


Figure 8.19: Static pressures at secondary driver transducers $sd1$, $sd2$, and $sd3$, flow condition x2-scr-m10p0-noz-rev-1. All traces are time-referenced to initiate with the corresponding L1d2 trace. Averaged experimental traces are derived from results for this specific flow condition. $2\mu s$ time averaging has been applied to experimental traces.

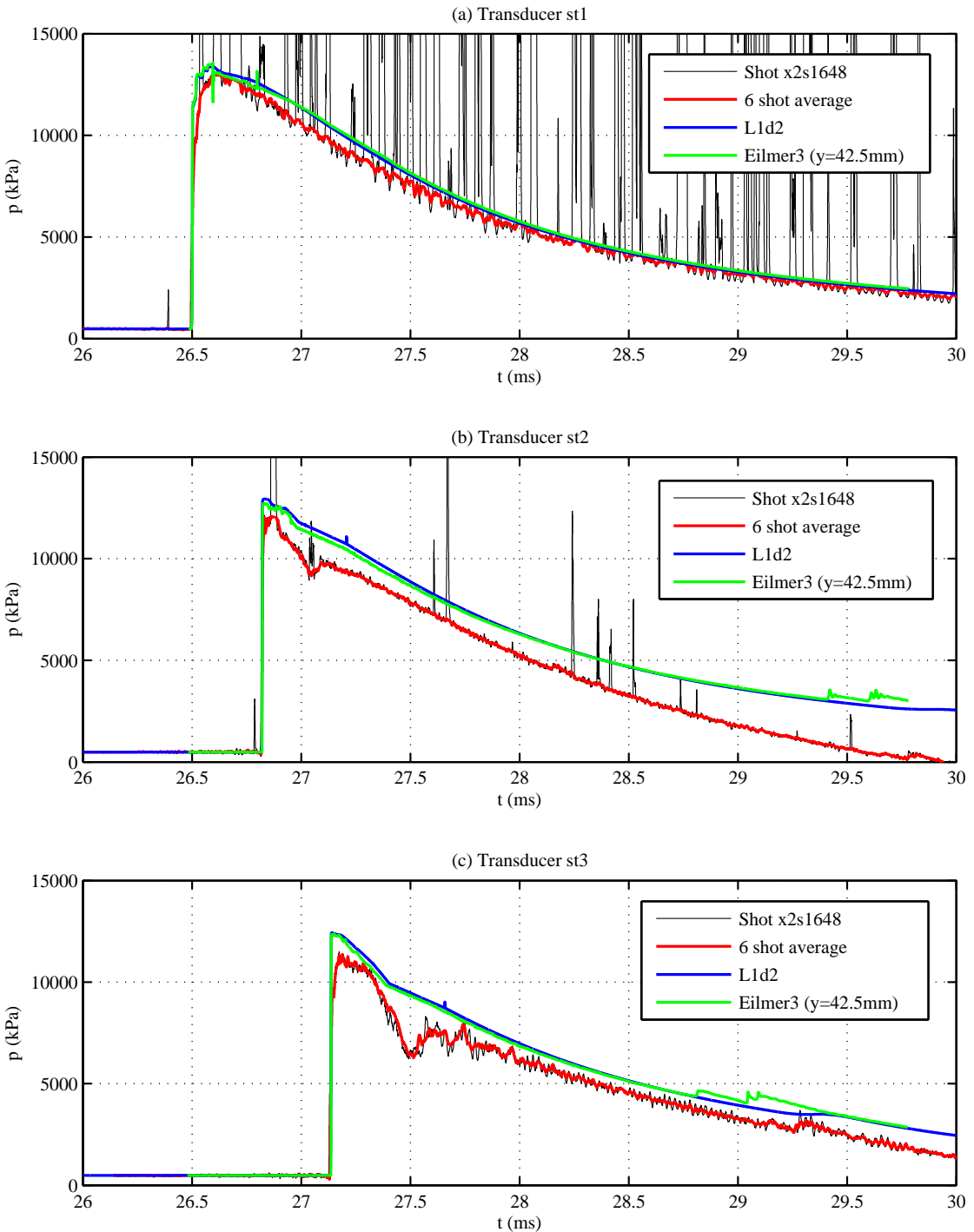


Figure 8.20: Static pressures at shock tube transducers $st1$, $st2$, and $st3$, flow condition $x2\text{-scr-m10p0-noz-rev-1}$. All traces are time-referenced to initiate with the corresponding L1d2 trace. Averaged experimental traces are derived from results for this specific flow condition. $2\mu\text{s}$ time averaging has been applied to experimental traces.

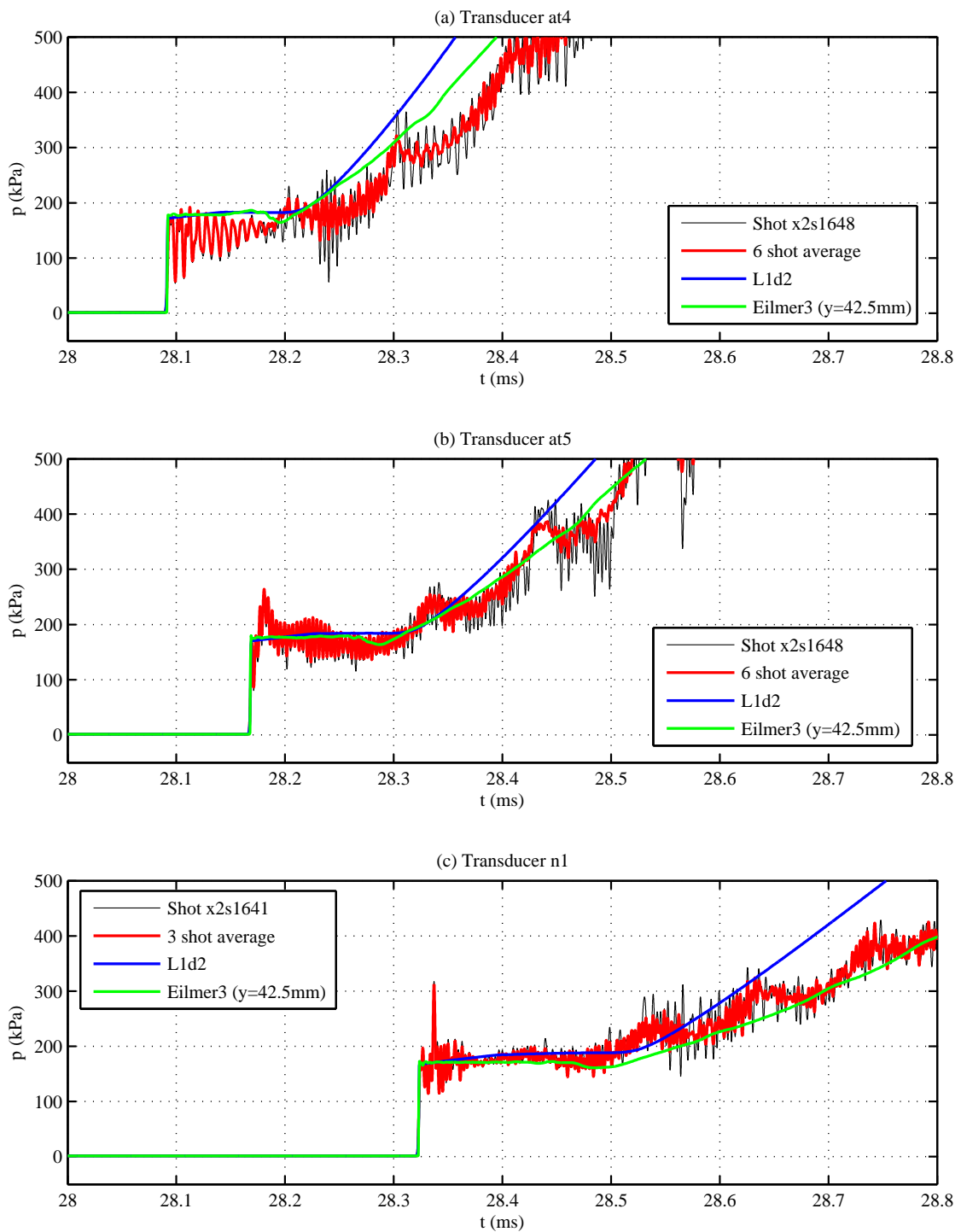


Figure 8.21: Static pressures at acceleration tube transducers *at4*, *at5*, and *n1*, flow condition x2-scr-m10p0-noz-rev-1. All traces are time-referenced to initiate with the corresponding L1d2 trace. Averaged experimental traces are derived from results for this specific flow condition. $2\mu\text{s}$ time averaging has been applied to experimental traces.

8.6.3.3 Test Flow Properties at the Nozzle Inlet

The Mach 10 flow condition experiment x2-scr-m10p0-noz-rev-1 was performed with and without the Mach 10 nozzle installed, so that cone probe pressure measurements could be taken with and without processing by the nozzle. This section examines the test flow properties at the acceleration tube exit (i.e. without the nozzle). When the nozzle is removed, a separate adaptor is used to connect the acceleration tube to the dumptank. The acceleration tube exit plane is located 536 mm downstream of the nozzle inlet plane (i.e. where the tube contour begins to change when the nozzle is installed) therefore both experimental and numerical results discussed in this section are for an axial location offset 536 mm downstream of the true nozzle inlet. However, this inconsistency is not considered important and these results are considered sufficiently representative of conditions at the nozzle inlet when the nozzle is installed.

The cone configuration for these tests was in accordance with that detailed in Figure 8.6. Figure 8.22(a) presents experimentally measured cone pressures at the nozzle inlet, at $y = \pm 9$ mm, and compares these to Eilmer3 computed 15 deg cone surface static pressure at the acceleration tube exit, at a radial offset of $y = 9$ mm from the tube centreline. The methodology used to calculate the Eilmer3 cone pressures is the same as that detailed in Section 8.6.2.4. The coloured curves on Figure 8.22(a) are the experimentally measured cone surface static pressures for two example experimental shots, each time-referenced to match the CFD. *cone1* is the cone above the tube centreline; *cone2* is the cone below the tube centreline.

The observed behaviour of the experimentally measured cone pressure traces is similar to that observed for the Mach 10 condition without nozzle in Section 8.6.2.4 - the traces are consistent and repeatable, and eventually match the average pressure magnitude computed numerically. However, once more the initial experimental response does not match the CFD, and the traces appear to have a very slow rise time. The traces show that the CFD significantly underestimates the length of the accelerator gas slug compared to the experiment, indicating excessive mass loss to the boundary layer in the calculated solution. There is also a large magnitude 10 kHz pressure oscillation which is evident after $t = 2.150$ ms. Interestingly, a similar oscillation is also observed in the experimental acceleration tube wall static pressure traces in Figure 8.21, indicating that the oscillation is most likely a feature of the unsteady expansion. It is not clear, however, why for flow condition x2-scr-m10p0-rev-1, the same oscillation is *only* observed for the Figure 8.15 cone traces, and not the Figure 8.14 tube wall static pressure traces.

Figures 8.22(b), (c), and (d), respectively show the computed static pressure, axial velocity, and Mach number, at $y = 9$ mm along the acceleration tube exit plane. True flight values are not shown since this is only an intermediate stage in the development of the flow condition prior to nozzle processing. Observing Figures 8.15(b-d), it can be

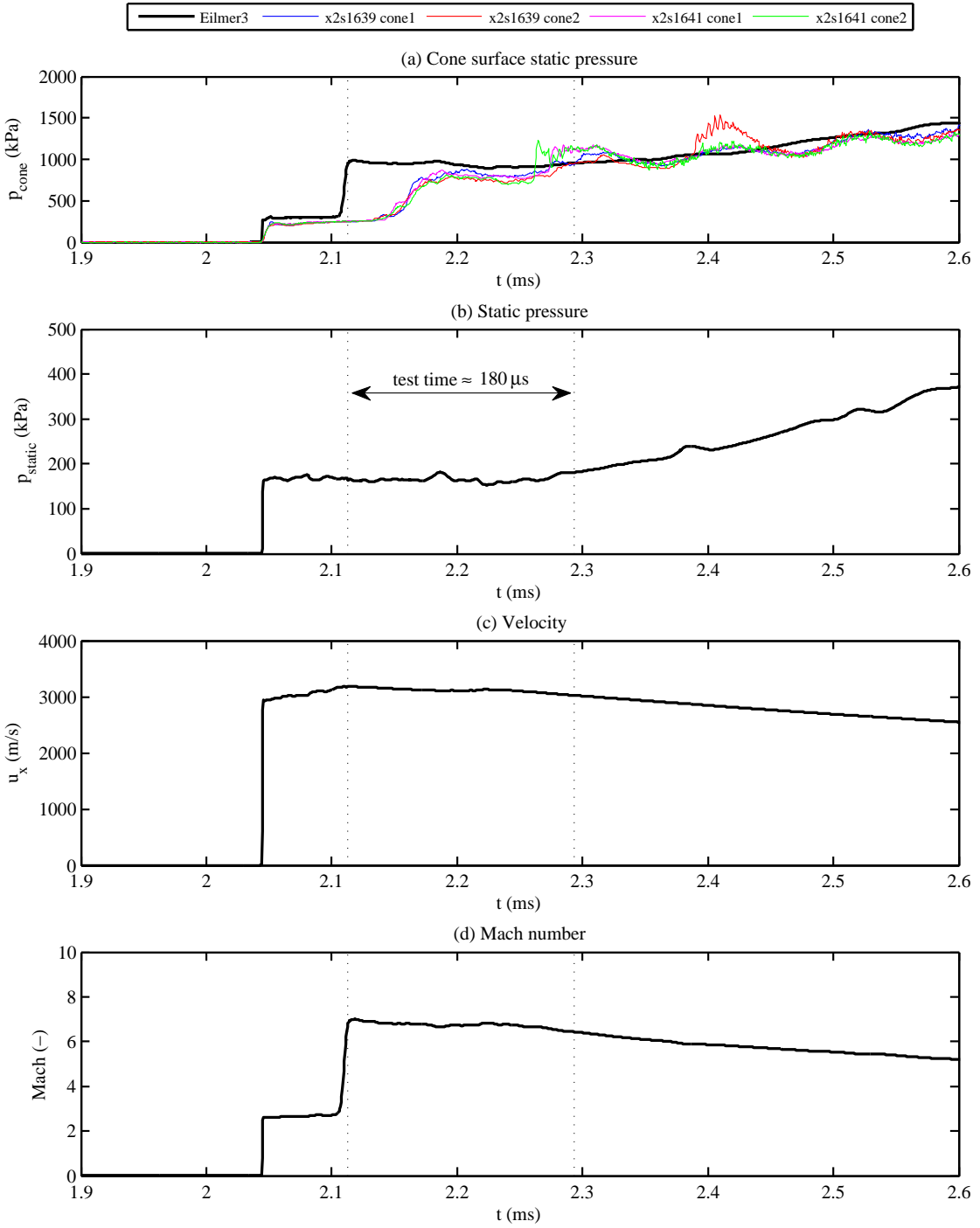


Figure 8.22: Computed and experimental test flow properties at the acceleration tube exit, at $y = 0$ mm from the tube centreline, for flow condition x2-scr-m10p0-noz-rev-1. $t = 0$ corresponds to the beginning of the axisymmetric calculation. Experimental cone pressures in (a) were measured using 15 deg half angle cones; see Section 8.5. Computed Eilmer3 cone pressures were obtained by taking the transient flow history at the equivalent location in the axisymmetric model ($y = 9$ mm) and applying this as a planar inflow to a separate cone axisymmetric model. It is finally noted that true flight cone and static pressures are much lower than experimental or numerical calculations; this indicates significant capacity for pressure-length scaling.

seen that the computed test gas has steady flow properties for a period of approximately $180 \mu\text{s}$ (identified on the plots). This period of time is therefore identified as the useful test time for this flow condition.

The computed radial variation in flow properties during the test time is now analysed (i.e. between the simulation times $t = 2.113 \text{ ms}$ and $t = 2.293 \text{ ms}$). Figure 8.23 shows how the computed flow properties vary between the tube centreline and tube wall. Curves are shown at 0%, 25%, 50%, 75%, and 100% of the test time. The dashed red line in each plot shows the average core flow properties during the test time, and is calculated for each plot by averaging the flow properties across the core flow region over the five time intervals.

Referring to Figure 8.23, the core flow is observed to have a diameter of approximately 55 mm ($2 \times 27.5 \text{ mm}$ radius). It is noted that flow properties across the core flow are reasonably constant, although static pressure does vary by approximately $\pm 5\%$ from its mean value. Prior to expansion through the nozzle, the average flow properties in summary are: 165 kPa static pressure, 9,339 kPa Pitot pressure, 3,110 m/s axial velocity, and Mach 6.65, for a duration of approximately $t = 180 \mu\text{s}$.

8.6.3.4 Test Flow Properties at the Nozzle Exit (see Table 8.4)

The Mach 10 flow condition x2-m10p0-noz-rev-1 discussed in previous Section 8.6.3.3 was run with the X2 Mach 10 nozzle installed. This section examines the test flow properties at the nozzle exit. Flow processes upstream of the nozzle inlet are identical for both sets of experiments, therefore no additional commentary is required in terms of shock speeds and tube wall static pressures. This section will subsequently only examine flow at the nozzle exit.

The cone probe configuration for nozzle exit flow tests was detailed earlier in Figure 8.7. Seven cones, radially spaced 18 mm apart, were centred around the nozzle centreline. The cones were numbered ‘2’ to ‘8’ from top to bottom respectively. Static pressure was also measured at the nozzle exit, at both the top of the nozzle, and on its side (parallel to its centreline).

Figure 8.24 shows the computed Eilmer3 centreline static pressure, velocity, and Mach number, at the nozzle exit. It is observed that a period of approximately steady conditions is observed for $200 \mu\text{s}$, between $t = 0.78 \text{ ms}$ and $t = 0.98 \text{ ms}$ (identified on the plots). The test flow Mach number varies between 9-9.5 during the test time, which is lower than the true flight target value (Mach 10). Test flow velocity is steadily falling during this period, but not significantly. Figure 8.24(a) also compares experimental nozzle wall pressure to the equivalent computed Eilmer3 solution at approximately 1 mm from the wall. It can be seen that the experimental nozzle startup takes approximately

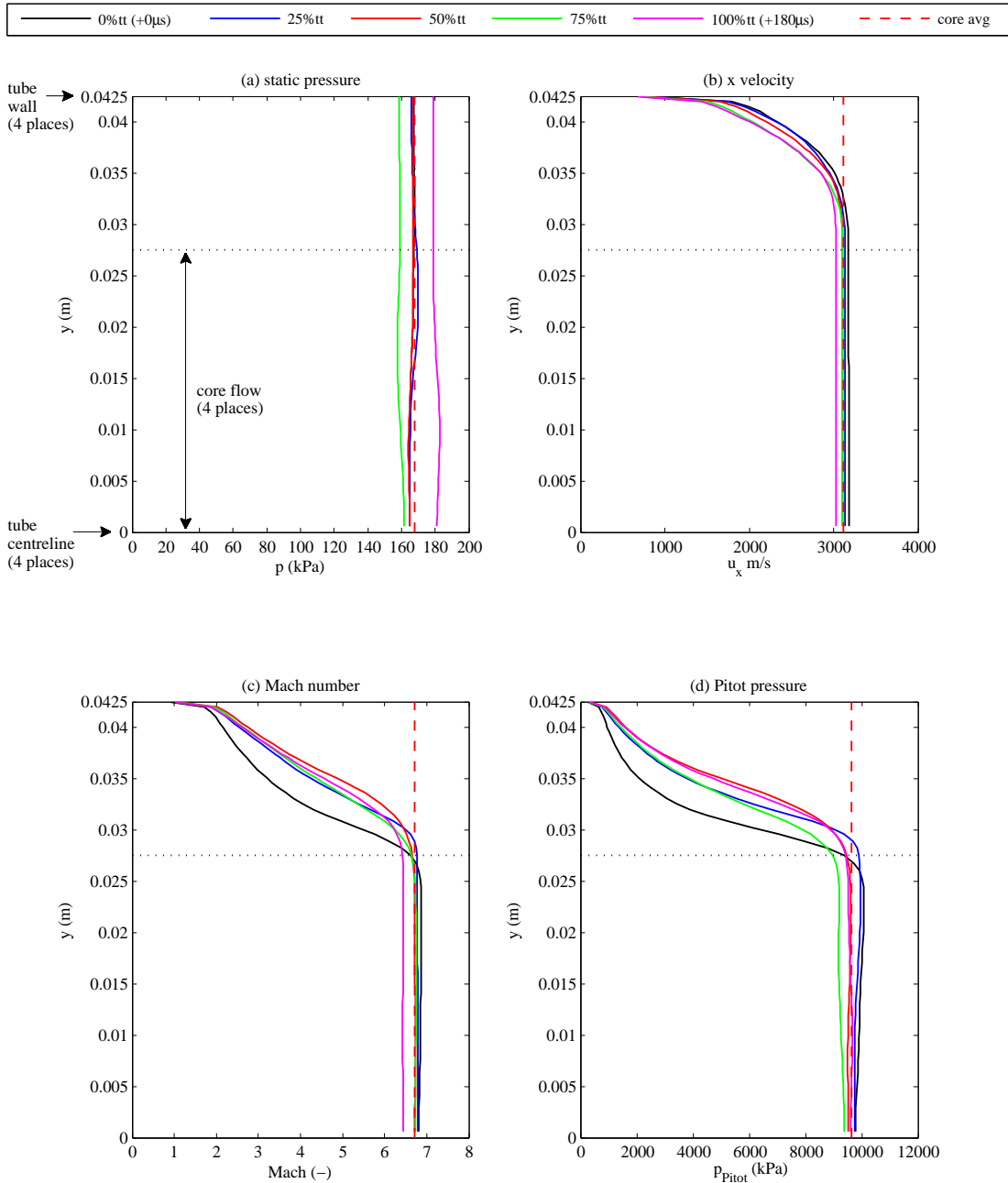


Figure 8.23: Radial variation in flow properties during the test time (denoted by tt) at the acceleration tube exit, flow condition x2-scr-m10p0-noz-rev-1. These are test flow conditions prior to nozzle expansion. Test time is assumed to occur between simulation times $t = 2.113 \mu\text{s}$ and $t = 2.293 \mu\text{s}$.

25% longer duration than in Eilmer3, however the final static pressures are very closely matched during the test time.

Figure 8.25(a-d) respectively compare experimental and numerical cone surface static pressures at radial offsets of $y = 0, \pm 18, \pm 36, \pm 54$ mm from the nozzle centreline. The initial responses compare poorly between calculation and experiment, however the longer term pressure magnitudes agree better. Once more the CFD appears to underestimate the length of the accelerator gas slug, indicating too much mass loss to the boundary layer. It is noted that the cones do not show the $100 \mu\text{s}$ oscillation which was observed at the nozzle inlet. The discrepancy between the experimental and numerical results further emphasises the need for a more reliable, but still robust, Pitot-type experimental measurement which can firmly establish the correct baseline. This is clearly an important priority for future flow development research in this field.

Based on Figure 8.24, the simulation test time was determined to occur between simulation times $t = 0.78$ ss and $t = 0.98$ ms ($200\mu\text{s}$ total). Figure 8.26 shows how the computed flow properties vary between the tube centreline and nozzle wall. Curves are shown at 0%, 25%, 50%, 75%, and 100% of the test time. The dashed red line in each plot shows the average core flow properties during the test time, and is calculated for each plot by averaging the flow properties across the core flow region over the five time intervals. The black dashed line shows the true flight value.

Referring to Figure 8.26, the core flow is observed to have a minimum diameter of approximately 80 mm (2×40 mm). Observing Figure 8.26(a), at the start of the test time (black curve) the edge of the core flow is defined by a discrete change in static pressure at $y \approx 40$ mm. At 25% and 50% of the test time (blue and red curves respectively), this discontinuity moves towards the tube wall. Referring to Figure 8.27 (shown in Section 8.6.3.5 below), this pressure discontinuity is a characteristic of the conically-shaped downstream face of the useful test gas, as it passes across the nozzle exit plane.

It is noted that flow properties across the core flow are reasonably constant, although static pressure steadily increases by approximately 30% at $y > \pm 30$ mm compared to the centreline. The average core flow properties before and after nozzle expansion are summarised in Table 8.5. Based on the variation in Mach number through the nozzle, the effective area ratio is 4.3 (using Equation 3.39 and $\gamma = 1.4$); this compares to the nozzle geometric area ratio of 5.6.

8.6.3.5 Visualisation of Flow Development Through the Nozzle

Figure 8.27 shows the flow development predicted by Eilmer3 through the nozzle. The top half of each contour plot shows Mach number; the bottom half shows static pressure. Large boundary layers are observed, which explain the relatively small diameter core

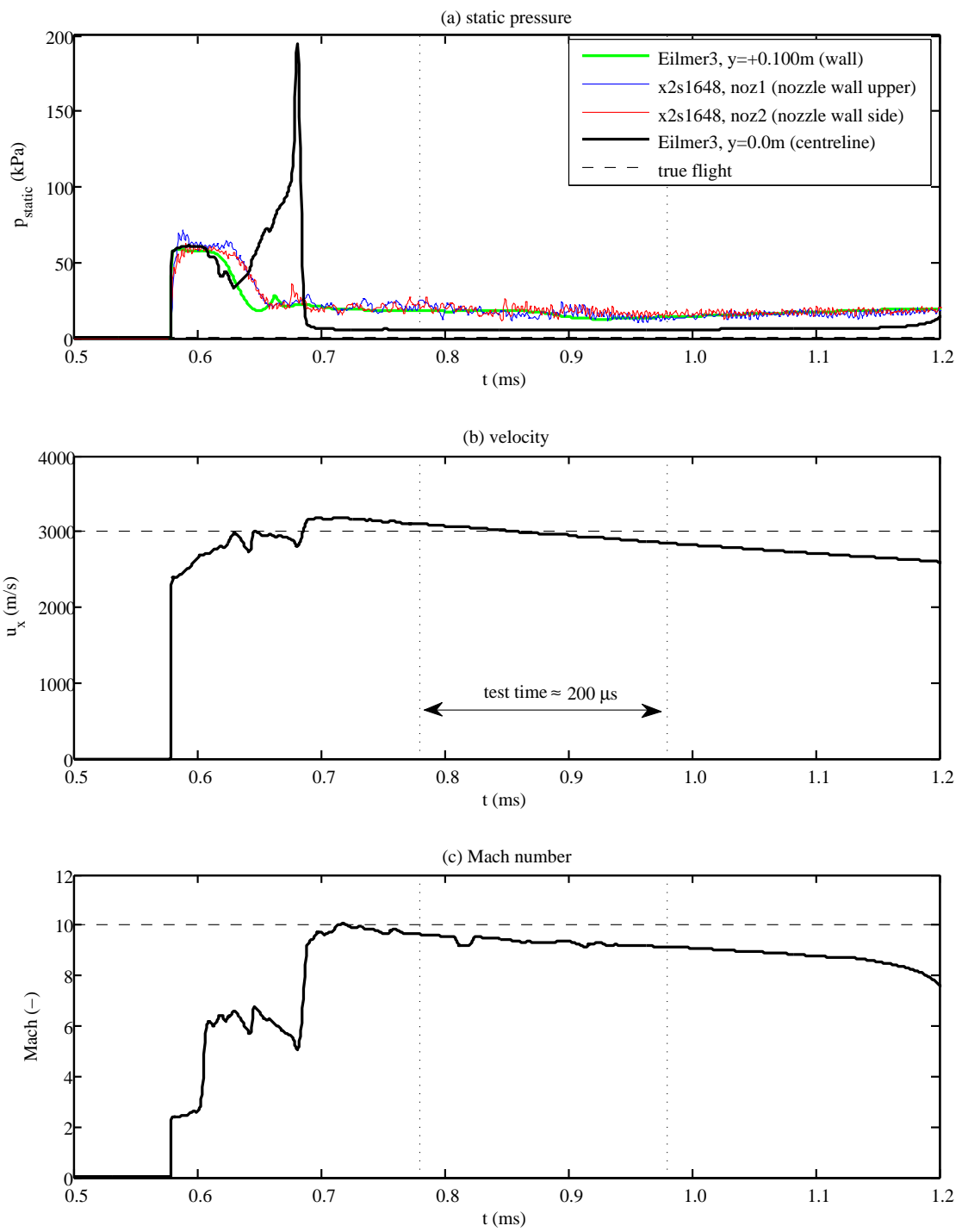


Figure 8.24: Computed and experimental test flow properties at the nozzle exit, at nozzle centreline (a-c) and nozzle wall (a only), for flow condition x2-scr-m10p0-noz-rev-1. Nozzle experimental static pressure traces are time-referenced to initiate with Eilmer3 traces.

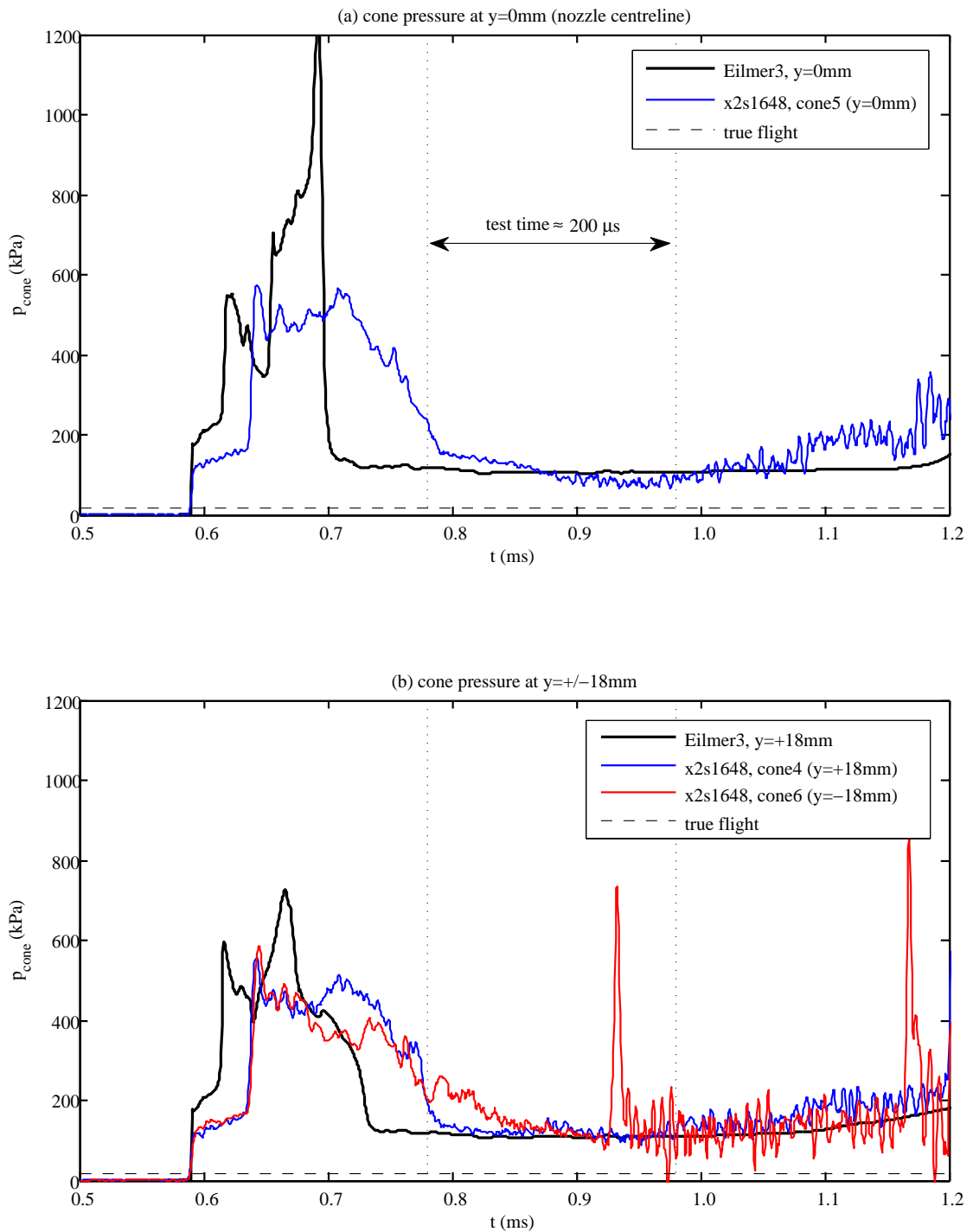


Figure 8.25: (part 1 of 2) Computed and experimental cone static pressures at the nozzle exit, at radial offsets of (a) $y = 0 \text{ mm}$, and (b) $y = \pm 18 \text{ mm}$, relative to the tube centreline, flow condition x2-scr-m10p0-noz-rev-1. Experimental cone pressures were measured using 15 deg half angle cones; see Section 8.5. Computed Eilmer3 cone pressures were obtained by taking the transient flow history at the equivalent y location in the axisymmetric model and applying this as a planar inflow to a separate cone axisymmetric model.

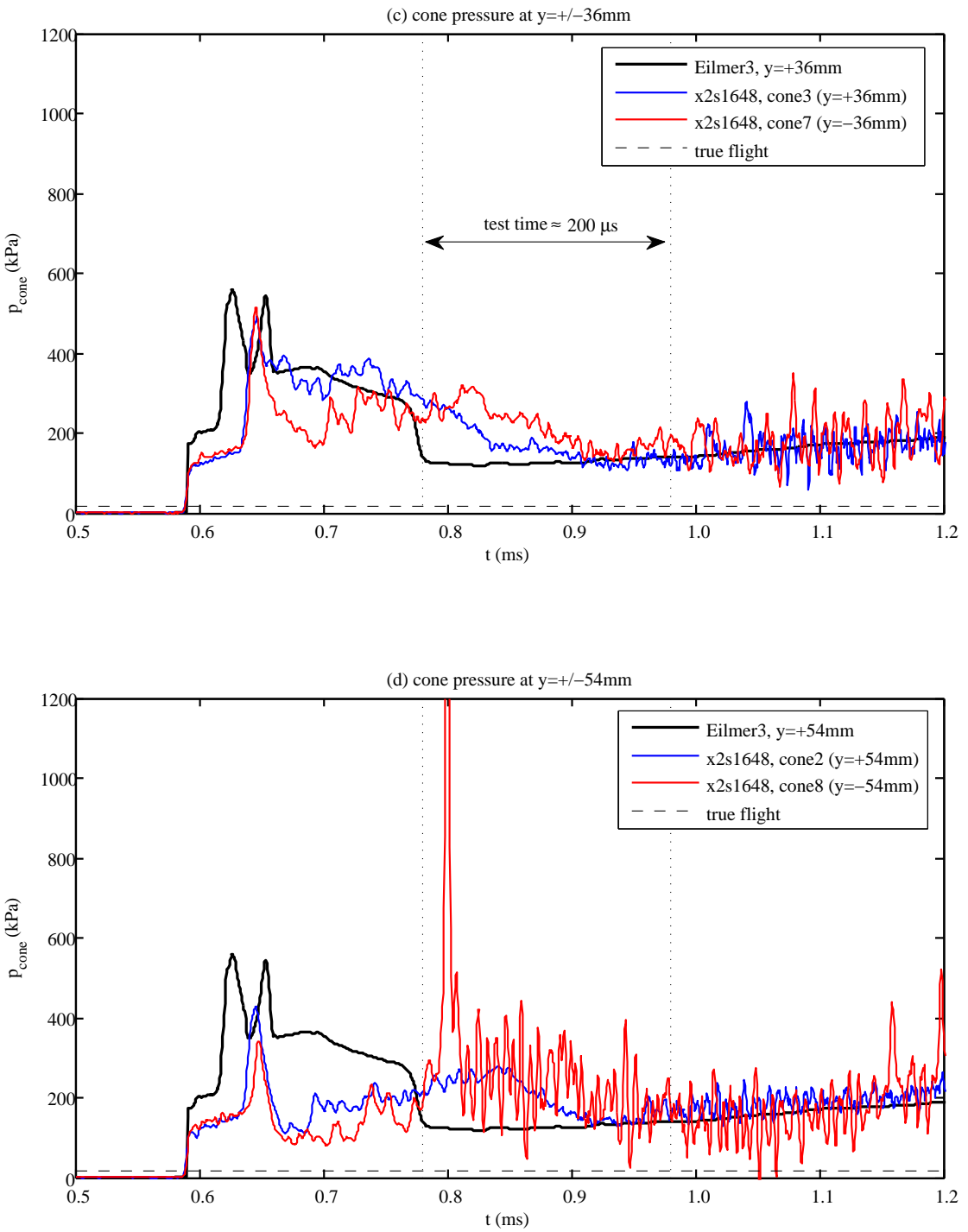


Figure 8.25: (part 2 of 2) Computed and experimental cone static pressures at the nozzle exit, at radial offsets of (a) $y = \pm 36 \text{ mm}$, and (d) $y = \pm 54 \text{ mm}$, relative to the tube centreline, flow condition x2-scr-m10p0-noz-rev-1. Experimental cone pressures were measured using 15 deg half angle cones; see Section 8.5. Computed Eilmer3 cone pressures were obtained by taking the transient flow history at the equivalent y location in the axisymmetric model and applying this as a planar inflow to a separate cone axisymmetric model.

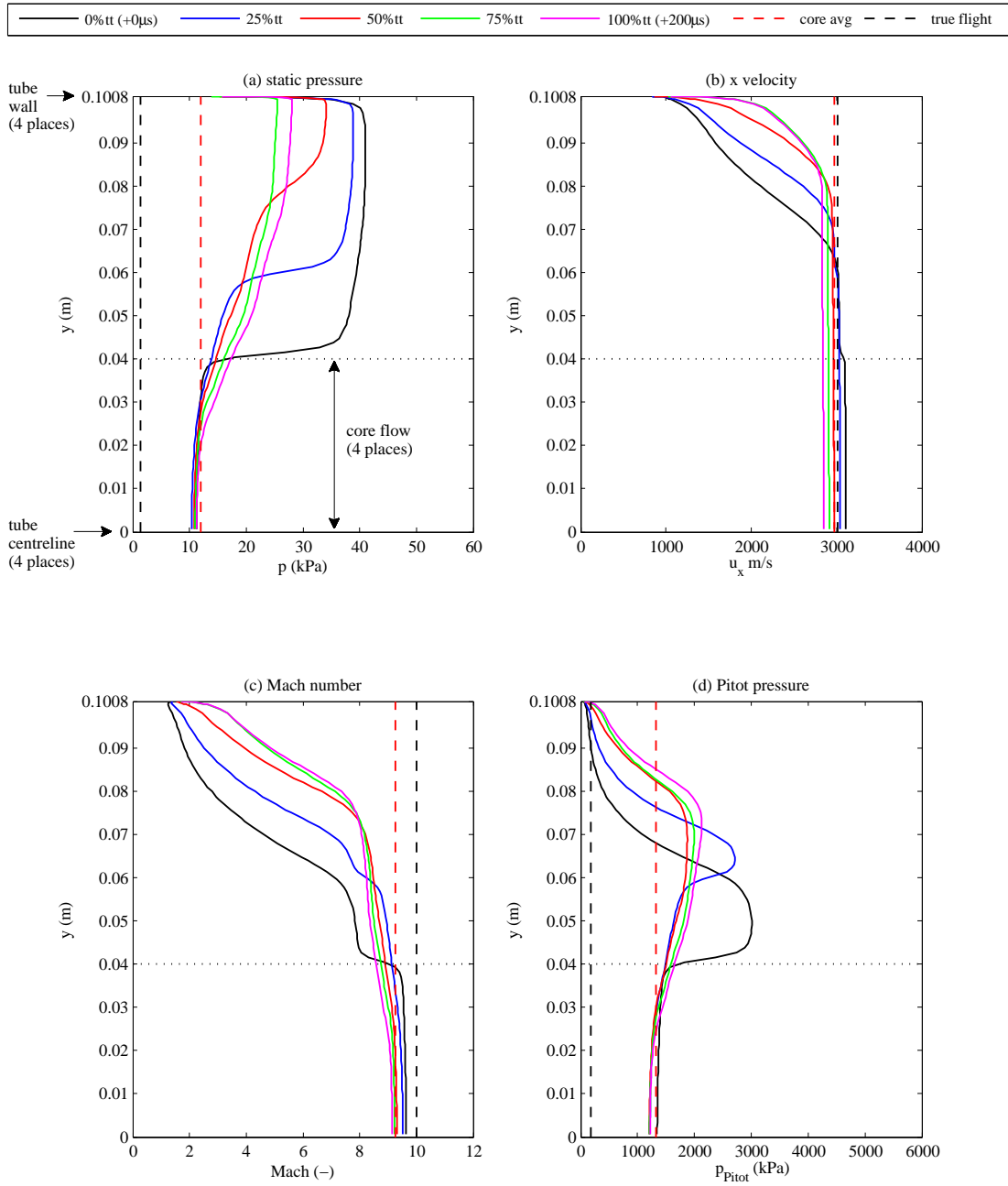


Figure 8.26: Radial variation in flow properties at nozzle exit during the test time (denoted by tt), flow condition $x2\text{-scr-m10p0-noz-rev-1}$. Test time is assumed to occur between simulation times $t = 0.00078 \mu\text{s}$ and $t = 0.00098 \mu\text{s}$.

Flow property	Nozzle inlet	Nozzle exit
Static pressure (kPa)	168	12.0
Velocity (m/s)	3,111	2,975
Mach number (-)	6.70	9.24
Density (kg/m^3)	1.07	0.163
Temperature (K)	546	258
Pitot pressure (kPa)	9,635	1,328
core flow diameter (mm)	55	80
test time (μs)	180	200

Table 8.5: Comparison of average test flow properties between nozzle inlet and exit, flow condition x2-scr-m10p0-noz-rev-1.

flow. The Mach contours clearly show the $Mach \approx 9-9.5$ test gas. The test time is identified on the figure, which is the period of time when this portion of useful gas passes across the nozzle exit plane (shown with a dashed line).

8.6.4 Mach 12.5 and 15 Flow Conditions

Numerical and experimental studies were also performed for the Mach 12.5 and Mach 15 flow conditions outlined in Table 7.5. Detailed results are included in the appendices as follows:

Mach 12.5 Flow Condition, X2 *without* Nozzle, x2-scr-m12p5-rev-1 (Appendix I)

- Summary of flow properties: Table I.1.
- $x-t$ diagram: Figure I.1.
- Shock speed vs. axial location: Figure I.2.
- Tube wall static pressure traces: Figures I.3, I.4, and I.5, respectively.
- Centreline test flow properties and test time identification: Figures I.6(a-d).
- Radial variation in test flow properties at acceleration tube exit: Figures I.7(a-d).

Mach 15.0 Flow Condition, X2 *without* Nozzle, x2-scr-m15p0-rev-1 (Appendix J)

- Summary of flow properties: Table J.1.
- $x-t$ diagram: Figure J.1.
- Shock speed vs. axial location: Figure J.2.
- Tube wall static pressure traces: Figures J.3, J.4, and J.5.

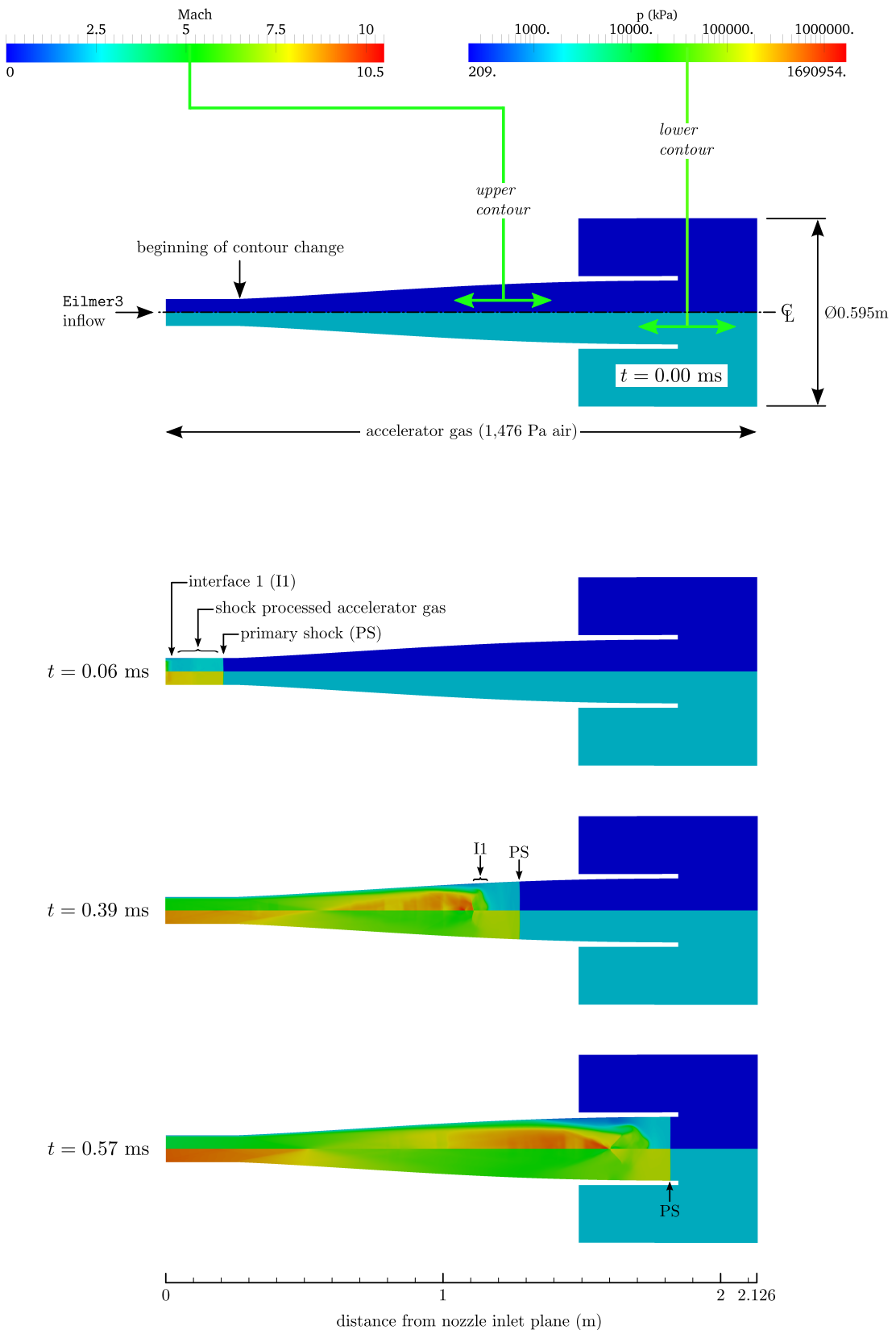


Figure 8.27: Flow development in nozzle (part 1 of 2), flow condition x2-scr-m10p0-noz-rev-1.

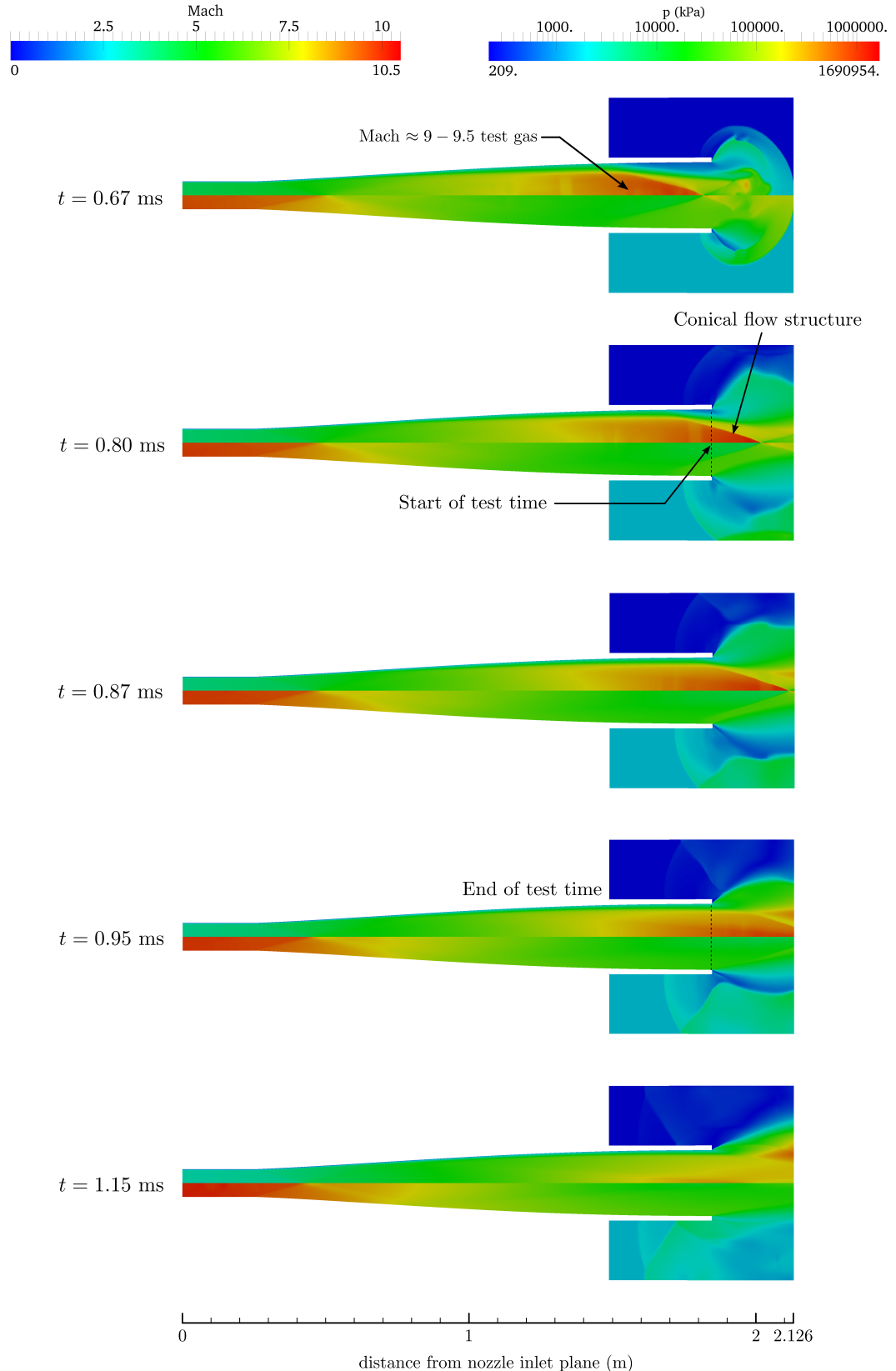


Figure 8.27: Flow development in nozzle (part 2 of 2), flow condition x2-scr-m10p0-noz-rev-1.

- Centreline test flow properties and test time identification: Figures J.6(a-d).
- Radial variation in test flow properties at acceleration tube exit: Figures J.7(a-d).

Reviewing Appendices I and J, it can be seen that the wave processes, and both secondary driver and shock tube static pressure traces, once more match closely between experiment and CFD, for both Mach 12.5 and 15 flow conditions. Observing Figures I.5 and J.5, for Mach 12.5 and 15 respectively, it can be seen that the computed acceleration tube static pressure traces match experiment reasonably well at transducer *at4*. However, for both flow conditions, the computed Eilmer3 pressure is initially higher than the experimental pressure at both *at5* and *n1*. This difference is more pronounced further downstream at *n1*.

The duration of time over which the Eilmer3 pressures are significantly higher than experiment approximately corresponds to the length of time it takes for the accelerator gas to pass the transducer location. Following arrival of the test gas and unsteady expansion, the computed pressure traces approximately align with experiment. The reason for the initial discrepancies in the Eilmer3 solutions is most likely due to the accelerator gas not being modelled well in either model, with viscous shear stresses and static pressures in the low density accelerator gas slugs being over-estimated. The grid sensitivity study in Section 8.6.5 also indicates that although average *test* flow properties calculated in this study are converged, not all flow properties are fully resolved, and boundary layer thicknesses are probably overestimated.

This discrepancy in these initial computed static pressures does not invalidate the predicted test flow properties. The accelerator gas provides a boundary condition which determines the degree of unsteady expansion of the test gas. Figures I.5 and J.5 show that the computed and experimental *test* gas static pressures are in reasonable agreement, and CFD and experimental shock speeds match closely, so there is reason to maintain confidence in the predicted test flow properties. However, it is recommended that future work would look to improve the modelling of the accelerator gas.

Observing the test flow centreline traces in Figures I.6 and J.6, at higher speeds the test time is $50\mu\text{s}$ and $40\mu\text{s}$ for Mach 12.5 and 15 flow conditions respectively (compared to $60\mu\text{s}$ for the Mach 10 condition). These plots, and the plots of core flow in Figures I.7 and J.7, also indicate that the test flow becomes more unsteady at these higher Mach numbers. While the grid sensitivity study in Section 8.6.5 indicates that the *averaged* flow properties during the test time are largely grid independent for the nominal grid used, the spatially variable transient flow properties are not fully resolved with these grids. The time and computational resources were not available to address this issue for the present study, although this would be required to more confidently predict these spatially variable transient flow properties.

Observing Figure I.6(a), it can be seen that computed cone pressure for the Mach 12.5 does not closely match the experiment. Considering J.6(a), at Mach 15 there is even less correlation between experiment and CFD. It is believed that this is due to the poor response time of the cone, however the cause of the discrepancy has not been identified, and requires further investigation.

The average core flow properties of these two test flows are presented in Table 8.6, and are compared to the Mach 10 conditions (with and without a nozzle). It is noted that the CFD predicts that the test gas is under-expanded at the higher Mach numbers. As a result, test flow temperatures are higher, and Mach numbers are correspondingly lower, than originally targeted. However, flow velocities are close to target levels, and test flow total pressures remain very high (8.79 and 10.4 GPa for Mach 12.5 and 15 flows respectively).

Flow property	x2-scr-m10p0-rev-1	x2-scr-m10p0-noz-rev-1	x2-scr-m12p5-rev-1	x2-scr-m15p0-rev-1
Mach number (-)	9.94±3%	9.24±8%	12.3±4%	13.8±8%
velocity (m/s)	3,257±1%	2,976±3%	4,130±2%	5,113±2%
static pressure (kPa)	35.8±15%	12.0±38%	11.6±20%	3.38±27%
Static temperature (K)	268±5%	259±8%	282±7%	345±21%
Pitot pressure (kPa)	4,557±10%	1,310±23%	2,246±13%	825±29%
Total pressure (GPa)	3.75	0.650	8.79	10.4
Stagnation enthalpy (MJ/kg)	4.05	3.33	6.68	10.4
Unit Reynolds number [million/m]	91.7	29.9	34.4	8.70
core flow diameter (mm)	50	80	50	40
test time (μs)	60	200	50	40

Table 8.6: Comparison of average test flow properties for flow conditions from Table 7.5.

8.6.5 Grid Sensitivity Check

The sensitivity of the solution to the grid spacing was assessed by examining two additional coarser grids. These grids were modified by increasing the nominal grid spacing by $\sqrt{2}\times$ and $2\times$ in both x and y directions, thereby reducing the total number of cells by 50% and 75% compared to the nominal grid. The results are shown in Appendix K. Convergence of shock speeds, and the average core flow properties during the test time, are shown in the following figures:

1. Figure K.1 (Mach 10 without nozzle).
2. Figure K.6 (Mach 10 with nozzle, nozzle *inlet*).
3. Figure K.11 (Mach 10 with nozzle, nozzle *exit*).
4. Figure K.15 (Mach 12.5).
5. Figure K.20 (Mach 15).

Figures (a,b) show computed shock speeds between transducer pairs; Figures (c-f) show averaged test gas core flow properties during the test time. For the nozzle CFD grid convergence plot (Figure K.11), only averaged test flow properties are shown (since this model takes an inflow from a hybrid tube model). The test time was assumed to occur for the same duration as that identified for the nominal grid, and average flow properties were calculated using an identical methodology. A least squares fit has been applied to each curve and extrapolated to a grid spacing of zero. This is a conservative ‘worst case’ estimate, since it includes the largest grid spacing.

Observing the plots, it can be seen that there is little variation in the parameters with grid spacing. The extrapolation to zero grid spacing indicates there is little to be gained from using a finer grid. While in some cases the extrapolation indicates a significantly different zero-grid spacing value for some of the plots (Figures K.6(c) and (f) for example), in such cases the two finer grid values clearly indicate the solution has actually converged. It is noted that these are *averaged* properties, which may explain why they are relatively insensitive to grid refinement. This is considered adequate for the present study, which is essentially an initial proof-of-concept study to demonstrate that it is possible to achieve this type of flow condition in an expansion tube.

Computed shock tube and acceleration wall static pressure traces for the three different grid spacings are shown in Figures K.2 (Mach 10 without nozzle), K.7 (Mach 10 with nozzle), K.16 (Mach 12.5), and K.21 (Mach 15). Observing both Mach 10 flow conditions, the static pressure histories appear to have converged for the two finer grid spacings, in terms of the shape of the pressure traces, and also the shock arrival time. For Mach 12.5 and Mach 15, the shock arrival time has not converged, but the shapes of the pressure traces are very similar. These pressure history traces indicate that shock speeds, and the time of arrival of subsequent flow processes, are consistent for the two more finely spaced grids.

The remaining figures in Appendix K show the spatial variation in flow properties across the tube exit at 25%, 50%, and 75% of the test time. The results generally indicate that the transient, spatially variable test flow properties, are not fully converged. Considering each flow condition separately:

1. Mach 10, X2 without nozzle (flow condition x2-scr-m10p0-rev-1, hybrid tube model, Figures K.27 to K.29): Mach number and velocity through the core flow is well resolved; the maximum variation between grids occurs for static pressure. The size of the boundary layer is greater at wider grid spacings in Figure K.9, which would be expected for the Baldwin-Lomax turbulence model.
2. Mach 10, X2 with nozzle, nozzle inlet (flow condition x2-scr-m10p0-noz-rev-1, hybrid tube model, Figures K.8 to K.10): The two more finely spaced grids (black

and blue curves) have very similar test flow properties, however the widest grid spacing (the red curves) diverges significantly at each of the three times.

3. Mach 10, X2 with nozzle, nozzle exit (flow condition x2-scr-m10p0-noz-rev-1, hybrid nozzle model, Figures K.12 to K.14): The solution appears to be converged at 75% of the test time (Figure K.12); at 25% and 50% of the test time, the core flow properties are very consistent for each grid spacing, however the size of the boundary layer is larger for the coarser grids. It is not clear whether this is due to the Baldwin-Lomax turbulence model over-estimating the boundary layer for the coarser grids, or whether the coarser grids simply predict later arrival of the conical flow structure which initially sweeps through the nozzle exit ahead of the test gas (see $t = 0.80$ ms in Figure 8.27). It is considered most likely to be a combination of both of these two factors.
4. Mach 12.5, X2 without nozzle (flow condition x2-scr-m12p5-rev-1, hybrid tube model, Figures K.17 and K.19): the Mach 12.5 solution is not fully converged. There are reasonably large variations between grids of the core flow static pressure, Mach number, and Pitot pressure. The boundary layer thickness is higher with the coarser grids.
5. Mach 15, X2 without nozzle (flow condition x2-scr-m15p0-rev-1, hybrid tube model, Figures K.22 and K.24): The Mach 15 results are similar to the Mach 12.5 results. The static and Pitot pressures, and Mach number, are not fully converged, and the fluctuation of these properties is generally greater than for Mach 12.5.

In conclusion, the grid sensitivity analysis in Appendix K indicates that at the finest grid spacing, the *averaged* core flow test properties, and also the static pressure histories, are both converged for all flow conditions. This satisfies the general requirements of this study. The spatially variable, transient flow properties are not fully resolved; at specific instants in the time, the results predicted by the different grid spacings do not all appear to converge. This indicates that more refined CFD analysis is required in order to fully resolve the transient flow features.

8.7 Additional Comments Regarding Acceleration Tube Transducer Signal Noise

It is noted that there is noise evident in the acceleration tube transducers which is attributed to mechanical vibration, and is not thought to be present in the actual test flow. For example, considering Figure 8.14, it can be seen that each acceleration tube signal has different high frequency characteristics. This noise is not

random, since it is very repeatable as evidenced by the consistency between individual experimental and multi-shot averaged traces. This response is most obvious in the acceleration tube transducers because they are high sensitivity compared to upstream transducers, therefore inertial loading of the sensor due to vibration constitutes a correspondingly stronger component of the measured signal.

It is believed that this noise is due to the transient response of the transducer, in its unique individual mounting arrangement, to the impact of the normal shock and trailing high speed and high pressure gases. In the present experimental campaign, the mounting arrangements for transducers *at4*, *at5*, and *n1*, were all different, which is thought to explain the qualitatively significant difference in the transient responses of the gauges. For example, *at4* was encased within silastic inside a brass holder in the tube wall; *at5* was supported by rubber o-rings in a nylon mount in the main tube wall; *n1* was supported by rubber o-rings in a nylon mount in the heavy tube-to-dumptank adaptor segment. The silastic was used for *at4* in an attempt to try to isolate the transducer from mechanical vibration; initial results indicated an improvement, and future work will seek further improvements in the transducer mounts.

Considering mechanical vibration, a potentially major source of noise is the series of stress waves originating from the free-piston compression process in the primary driver. Particularly for the high speed lightweight piston, the piston deceleration effectively applies a large axial impulse load to the tube which sends a series of stress waves downstream which can manifest themselves as significant signal noise in the sensitive acceleration tube transducers. For scramjet tests, the speed of sound in steel ($\approx 5\text{--}6 \text{ km/s}$) is greater than the average shock speed down the full length of the facility ($\approx 3\text{km/s}$), therefore the stress wave arrives before the test flow. Initial experimental results for this campaign showed unacceptably high levels of acceleration tube transducer noise before and during the test time, which rendered these transducer signals largely unusable.

To remove the effect of these stress waves from the transducer signals, a new secondary diaphragm arrangement was developed in order to mechanically decouple the tube upstream of these critical acceleration tube transducer locations. The standard arrangement for securing diaphragms in the X2 and X3 expansion tubes is to rigidly clamp the Mylar diaphragm between two tube sections. Initially the Mylar diaphragm is lightly attached to one side of the tube using a small amount of o-ring grease, the tubes are brought together, and finally a capstan is used to secure the joint. One problem with this method is that the Mylar diaphragm

can become unseated or damaged when the tube is closed, and it is often unclear the exact physical state of the diaphragm after assembly (but prior to the shot). Another problem is that in order to mechanically restrain the diaphragm from slipping when subject to high pressures, the tube join must be very tight, and even then the diaphragm may slip or leak if the tube is not perfectly aligned and applying an even clamping force.

A new diaphragm holder arrangement was developed which served the following dual purposes:

- To secure the Mylar diaphragm in a cartridge unit prior to insertion into the tube. This ensures that the diaphragm condition is known prior to assembly, that the diaphragm is very firmly clamped in the cartridge and therefore will not slip under high fill pressures, and the diaphragm will not be damaged during insertion into the tube.
- The new arrangement is located at the secondary diaphragm station, and mechanically decouples the tube at this axial position. Since the diaphragm is supported within the cartridge unit, it is not necessary to clamp the tube tightly to prevent diaphragm slippage or maintain a good seal. The new design uses sliding seals and allows relative movement of the two tube sections within the capstan joint. The two tubes are tightened around a rubber bumper. When the upstream tube section displaces suddenly due to a strong stress wave downstream, most of this displacement is taken up by the rubber, and subsequently only a small part of the stress wave is transferred to the downstream tube section.

The new design was found to very effectively isolate the mechanical noise, thus significantly cleaning up pressure traces. Detailed drawings for the design are provided in Appendix L, and the design is shown in Figures 8.28(a-d). An example of acceleration tube wall static pressure traces before and after incorporation of the new design are shown in Figures 8.29(a) and (b) respectively. The stress wave in (a), characterised by significant oscillation in the signal trace *prior* to arrival of the normal shock, is observed to be almost completely removed in (b).

8.8 Conclusion

This chapter presents results from experimental and numerical assessment of the four new scramjet flow conditions detailed in Table 7.5. Both sets of results demon-



(a) mylar diaphragm supported in cartridge unit



(b) diaphragm holder assembly



(c) X2 secondary diaphragm station open



(d) X2 secondary diaphragm station closed

Figure 8.28: New X2 diaphragm holder and buffer assembly, PNo. X2-DIA-000-0 (refer Appendix L for drawings).

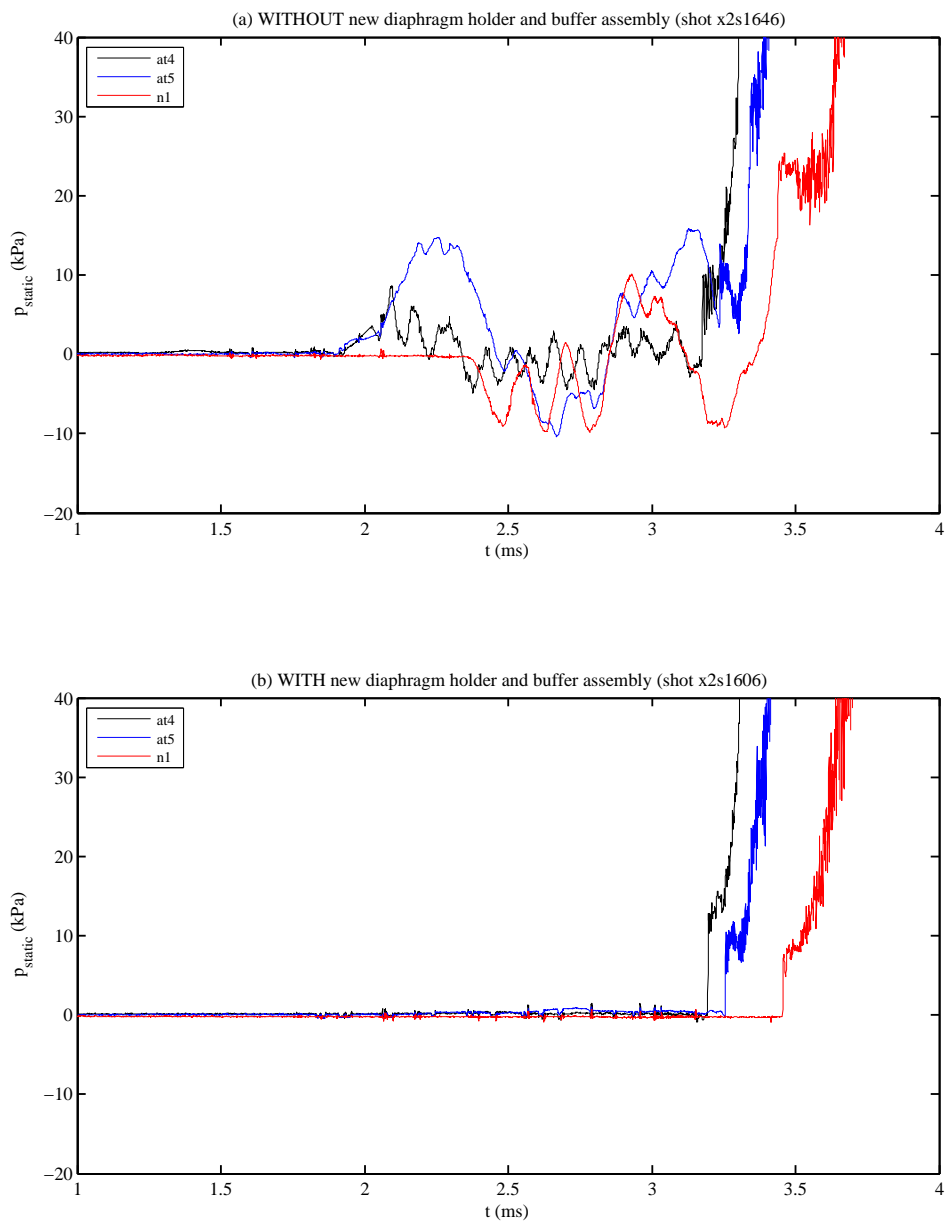


Figure 8.29: Comparison of acceleration tube transducer responses for Mach 12.5 flow condition x2-scr-m12p5-rev-1, (a) before and (b) after installation of new diaphragm holder and buffer arrangement (see Figure 8.28). Experimental configuration of both shots is otherwise identical. $2\mu\text{s}$ time averaging applied to experiment pressure traces.

strate that the primary waves processes have been achieved, indicating correct configuration of the facility at each condition, and also confirming the performance of the new tuned driver with lightweight piston.

The 2-D CFD analyses indicate that each test condition has been achieved, in terms of Mach number, velocity, and static pressure. It is predicted that maximum test flow total pressures of 3.75, 8.79, and 10.4 GPa have been achieved at Mach 10, 12.5, and 15, respectively. These total pressures are higher than any other scramjet test flow reported elsewhere.

Only limited experimental data is available for comparison with CFD results. Agreement between experimental and CFD shock speeds *has* been demonstrated. Further, experimental tube wall static pressure traces have been shown to be relatively steady, and to generally agree with CFD, especially for the Mach 10 flow conditions (with and without nozzle). Satisfactory Pitot measurements were not, however, obtained. An attempt to yield a comparable measurement was made by using 15 degree partial impact cone pressure probes. Whilst experimental cone pressure traces showed reasonable agreement with CFD after test flow arrival, they generally appear to have a slow response time.

At Mach 12.5 and Mach 15 the computed wave processes matched experiment closely, however the experimental acceleration tube wall static pressure traces were generally lower than the computed pressures until the arrival of the test gas. This is attributed to inadequacies in the numerical modelling of the accelerator gas flow processes, and it is recommended that future work examine this problem in more detail. It was also found that the cone probes performed poorly at Mach 12.5 and 15, and conclusive experimental partial impact pressure measurements were not achieved for these two flow conditions.

Clearly it is necessary to obtain more reliable Pitot pressure measurements; this is an important future task. But the results provide reason to be confident that useful scramjet test flows, at total pressures an order-of-magnitude higher than previous tests, can be achieved with expansion tubes. For X2, test gas core flow diameters are small, and test times short, however the results indicate that the flow conditions are feasible and encourage scaling these conditions to a larger facility such as X3.

Chapter 9

Test Flow Disturbances Originating at the Primary Driver

9.1 Chapter Overview

The CFD analyses performed in Chapter 8 used the 1-D code L1d2 to calculate a radially uniform inflow to the shock tube, which was then assessed downstream to the test section using an axisymmetric Eilmer3 model. This methodology is not capable of modelling 2-D disturbances originating in the primary driver, which can be transferred to the test gas for some expansion tube flows, and were the justification for using a secondary driver for these new scramjet flow conditions. The present chapter aims to examine if the secondary driver is effective by introducing representative driver-induced noise into the upstream flow for Mach 10 flow condition x2-scr-m10p0-rev-1 from Table 7.5. Since Eilmer3 is not currently able to model piston dynamics, a fixed volume driver, initially at constant pressure and temperature, has been selected which produces a similar flow condition in the test section to the hybrid analysis. The rest of the facility downstream of the driver is included in the model. The primary diaphragm is modelled as an iris opening diaphragm, and secondary and tertiary Mylar diaphragms are modelled as 10 μs hold diaphragms. A detailed analysis of the computed flow processes is presented.

9.2 Fixed Volume Primary Driver Model

Eilmer3 is currently unable to model piston dynamics, although this is a capability which is intended to be added in future. Therefore the X2 free-piston driver was modelled as a fixed volume driver. A 2-D axisymmetric model of the X2 facility

was developed using Eilmer3, including a fixed volume driver and all of the driven tubes. The primary diaphragm is modelled as an iris opening diaphragm (see Section 9.3), and secondary and tertiary Mylar diaphragms are modelled as $10 \mu\text{s}$ hold diaphragms. The model was comprised of 96 blocks and 1.1 million cells (71 cells radially in the driven tube). Cells were clustered axially on either side of each diaphragm plane, and clustered radially towards the tube wall. History data was recorded at each position in the CFD model corresponding to static pressure transducer locations in the actual machine. Detailed radial history data was recorded at the acceleration tube exit plane. A schematic diagram of the Eilmer3 analysis geometry is shown in Figure 9.1.

Referring to Figure 9.1, this representation includes the expansion of driver gas through the area reduction, therefore it should induce the fundamental radial disturbances associated with this flow path. This representation does not capture driver gas unsteadiness due to piston dynamics. However, it is believed that in combination with the iris opening diaphragm (see Section 9.3), sufficiently representative driver gas noise can be induced in order to assess the effectiveness of the acoustic buffer. That is to say, if the acoustic buffer prevents transmission of this noise in the analytical model, then it would also be expected to prevent transmission of other *characteristically similar* noise sources which the model may fail to include.

The initial temperature and pressure of the driver gas were calculated using an iterative approach with L1d2. To begin with, an L1d2 model of the Mach 13 reference flow condition from Table 4.1 was run with driver condition LWP-2.0mm-Rev-0 from Table 6.7, with full piston dynamics; this is the same model that was used in Section 6.8.2. Figure 6.7 shows the driver pressure and piston response during the simulation. Rupture is observed at the primary diaphragm, which is represented by the red curve which shows predicted driver pressure 10 mm upstream of the primary diaphragm (where the area has reduced to 85 mm). It can be seen that driver pressure towards the start of the area change, 175 mm upstream, is approximately 15% less. Both traces are compared since L1d2 tends to focus compression waves through the driver area change, thus overestimating pressure oscillatory behaviour at the diaphragm.

The temperature and pressure in the driver gas were extracted at the moment of diaphragm rupture ($t = 25.060\text{ms}$) and are shown in Figure 9.2. The horizontal axis in Figure 9.2 represents the longitudinal position of L1d2 cells in the driver gas slug. The left hand edge represents the piston boundary; the right

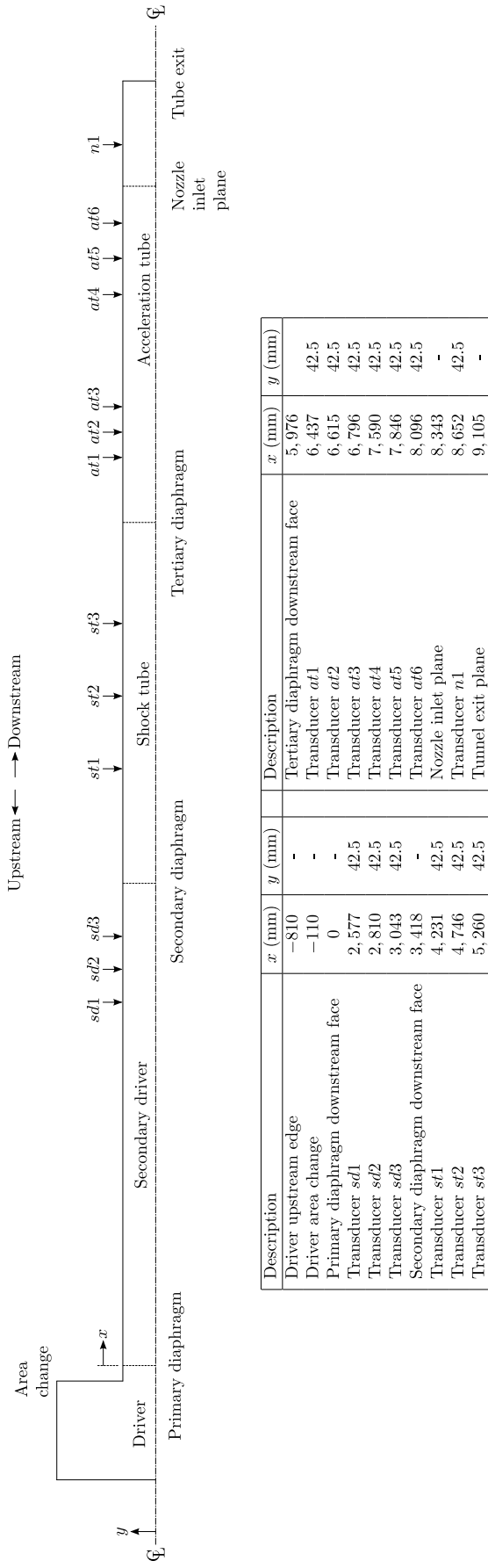


Figure 9.1: X2 2-D axisymmetric fixed volume driver model geometry. All longitudinal positions have an uncertainty of ± 2 mm, vertical positions are to machining tolerance (assumed to be ± 0.1 mm). Vertical scale has been stretched to fit image onto page.

hand edge represents the diaphragm, which is just rupturing at this moment. The unsteady nature of the compression process results in a variation in temperature and pressure across the length of the slug of driver gas, evident in the plot. Mean values have been calculated across the slug and are also shown. It is observed that although the nominal diaphragm rupture pressure (27.9 MPa) occurs at the primary diaphragm (initiating rupture and subsequent driven tube flow processes), the pressure across most of the rest of the driver gas slug is less, with the mean pressure being 23.51 MPa. The mean temperature at rupture was similarly calculated to be 2,657 K.

The driver gas average pressure and temperature calculated in Figure 9.2 serve as a starting point for a fixed volume representation of the driver gas. However, given the complexity of the unsteady processes occurring in the driver and driven tubes during the diaphragm rupture process, directly using these averaged values in the axisymmetric simulation is likely to result in shock speeds which are not ideally matched to the L1d2 model incorporating the piston dynamics. Therefore, these averaged values were adjusted using an L1d2 simulation with a fixed volume driver. The shock speeds from both L1d2 models (one with full piston dynamics, the other with a fixed volume driver) were compared. The average pressure in the fixed volume driver was increased incrementally, and the temperature was varied assuming an isentropic compression, until the shock speeds in the downstream tubes most closely matched the shock speeds calculated with the full piston dynamics. The scale factor applied to the temperature, SF_T , is related to the scale factor applied to the pressure, SF_P by Equation 9.1:

$$SF_T = SF_P^{\frac{\gamma-1}{\gamma}} \quad (9.1)$$

where γ is for helium/argon. It was found that a pressure scaling factor of $1.15\times$ produced the closest fit between shock speeds. For $\gamma = 5/3$, the corresponding temperature scaling factor calculated using Equation 9.1 was $1.06\times$. Good agreement was obtained through the driven tube (secondary driver), however shock speeds further downstream (through the shock and acceleration tubes) were under-predicted.

The size of the fixed volume driver was selected such that there would be sufficient driver gas to avoid a strong $u + a$ wave prematurely reflecting from the piston face upon arrival of the unsteady expansion in the driver gas. The actual driver gas volume at rupture is quite small, therefore the unsteady expansion reaches the piston face very early. However, the high piston speed, fundamental

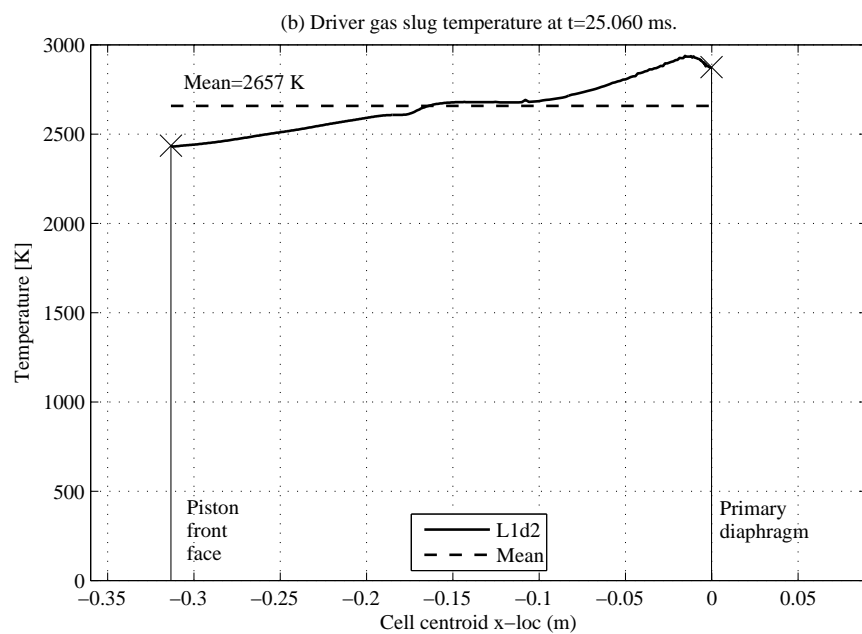
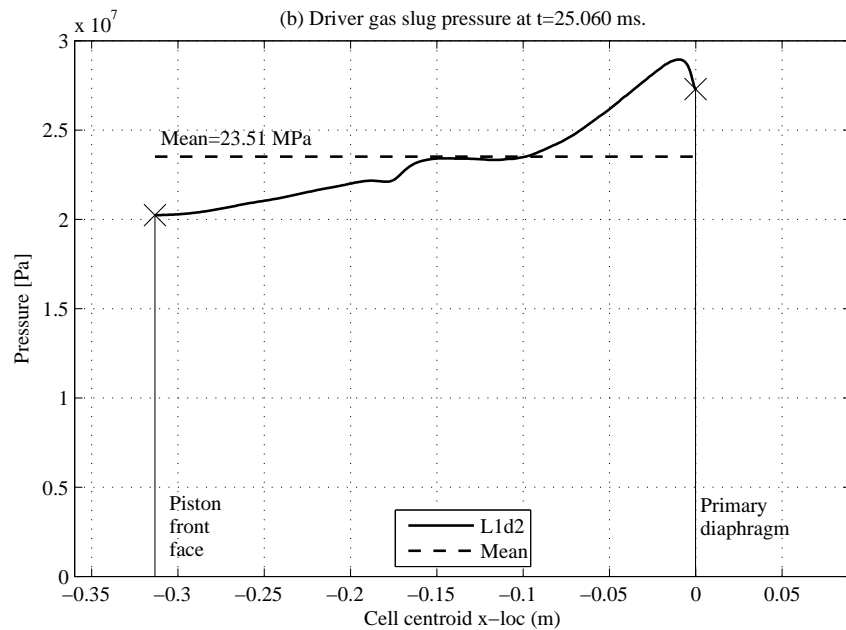


Figure 9.2: L1d2 predictions of X2 pressure and temperature in the driver gas slug at the moment of diagram rupture ($t = 25.060$ ms), for driver condition x2-lwp-2.0mm-0. The horizontal axis represents the centroidal location for each driver gas slug cell; the upper and lower vertical axes represent (a) the driver pressure [Pa], and (b) the driver temperature [K], respectively.

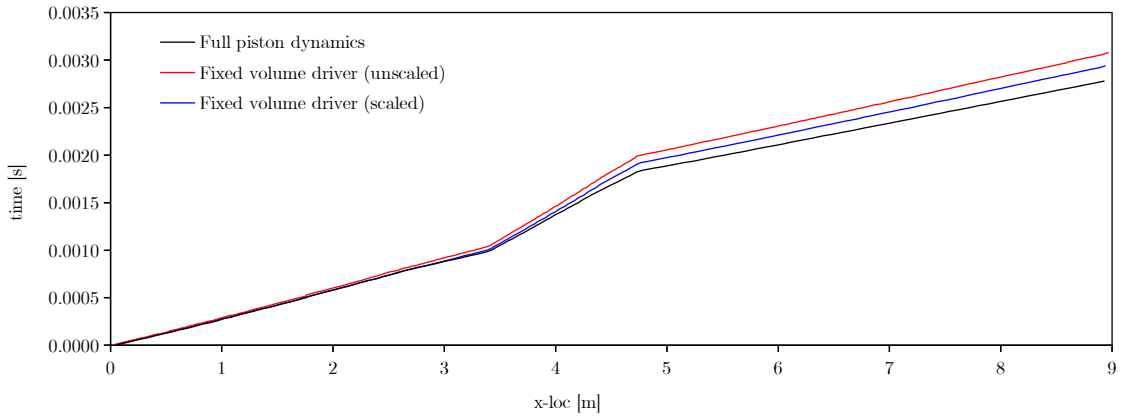


Figure 9.3: x - t diagram calculated using L1d2, for flow condition x2-scr-m10p0-rev-1. The black curve represents an L1d2 simulation incorporating full piston dynamics; the red curve represents an L1d2 simulation using a fixed volume driver with mean temperature and pressure per Figure 9.2; the blue curve also represents an L1d2 simulation with a fixed volume driver, except that mean pressure and temperature from Figure 9.2 have been scaled upwards (pressure by $1.15\times$ and temperature by $1.06\times$). The scaled fixed volume solution achieves good agreement through the first driven tube (the secondary driver), and therefore is used for the axisymmetric driver study.

to tuned driver operation, significantly weakens this series of expansion waves for a relatively long duration after diaphragm rupture. The resulting effect is similar to making the driver gas tube longer. otherwise occur undisturbed with a tuned driver.

The driver length has therefore to be correspondingly increased to delay transmission of the reflected $u + a$ characteristic so that downstream flow processes are not prematurely interrupted. Referring to Figure 9.4, driver length was varied between 0.2 m and 0.6 m (this length includes the area change, and is the axial distance between the piston front face and the primary diaphragm). It can be seen that there is progressively less shock attenuation with increasing driver length. For the 0.6 m driver length, the shock traverses the entire length of the facility without attenuation. For the axisymmetric model, the length of the driver gas fixed volume was conservatively set to a slightly longer length of 0.81 m.

In summary, the above analysis indicated that X2 driver condition x2-lwp-2.0mm-0 can be approximated in L1d2 by a fixed volume driver with the piston face fixed at 0.81 m upstream from the primary diaphragm, an initial driver pressure of 27.04 MPa, and an initial driver temperature of 2,810 K. Figure 9.5 shows sound speed mapped over an x - t diagram for this condition. It can be seen that there is a large increase in sound speed across the primary-driver-gas/secondary-driver-gas interface, indicating that the acoustic buffer has been established per [72]. This

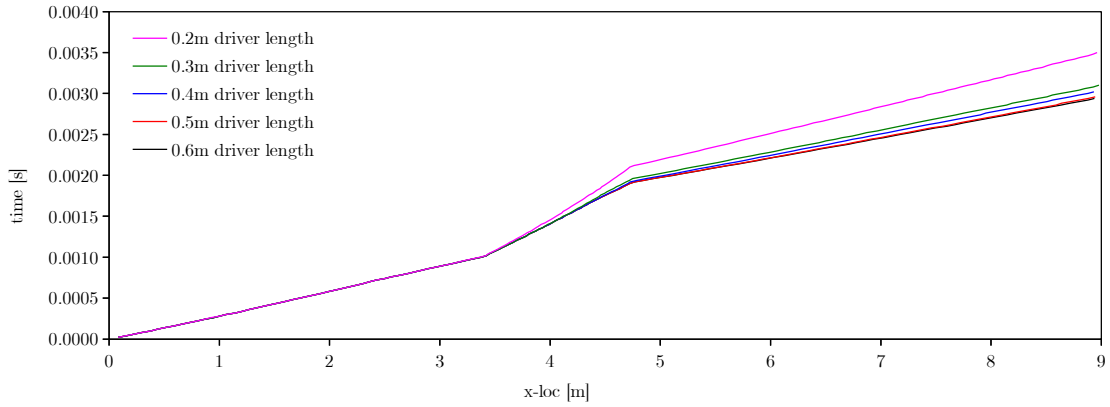


Figure 9.4: x - t diagram comparing shock speeds for different assumed driver lengths of a fixed volume driver, calculated with L1d2 for flow condition x2-scr-m10p0-rev-1.

also exceeds the minimum ratio of $a_{sd2}/a_{sd3} > 1.25$ later suggested by Morgan [57] following experimental and analytical experience using this type of configuration. These results are for the original Mach 13 condition, where the secondary driver has a 150 kPa helium initial fill pressure. For the new flow conditions detailed in Table 7.5, the initial fill pressure is 100 kPa; therefore, the shock through the secondary driver will be faster, and the ratio a_{sd2}/a_{sd3} will be even greater.

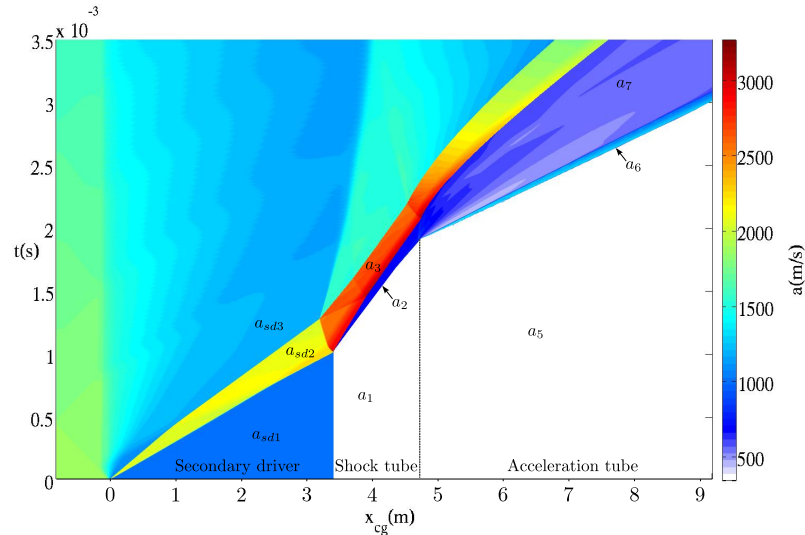


Figure 9.5: x - t diagram with sound speed mapped for flow condition x2-scr-m10p0-rev-1, calculated with L1d2 assuming a fixed volume driver.

9.3 Iris Opening Primary Diaphragm Model

In order to generate representative primary driver acoustic noise using numerical simulation techniques, the primary diaphragm rupturing process must be modelled with sufficient fidelity to recreate key flow processes. An understanding of the diaphragm rupture mechanism and its effect on flow development is therefore required.

Analytical techniques typically assume that diaphragm removal is instantaneous. However, in reality diaphragm rupture occurs over a finite time period of time, and this has been found to affect subsequent flow processes. White [164] first attempted to quantify the effect of diaphragm opening time on the shock formation process, and showed that a finite opening time increased the distance for shock formation. Various later studies [165, 166, 167, 168] have determined experimentally and analytically that opening time affects initial acceleration of the shock wave and distance to maximum shock strength/velocity; creates non-uniformity in driven gas density and causes mixing between driving and driven gases at the interface; and generally introduces non-one-dimensional characteristics to the flow.

Attempts to quantify the opening time have been both experimental and analytical. Analytical studies have typically considered a pre-scored diaphragm which initially ruptures at its centre. Individual petals form as the diaphragm tears along the score lines. Ignoring bulging prior to rupture, the key physical characteristics are the linear width at the base of the petals (L), the diaphragm density (ρ), the diaphragm thickness away from the score (τ), and p_r is the diaphragm rupture pressure; refer Figure 9.6. Several studies [169, 167, 170, 171, 170, 172] make the assumption that the petal behaves as a rigid mass about a free hinge at its base, which is then accelerated through an arc by the driver pressure force. Volkov et al. [173] took a similar approach, except the diaphragm is modelled as a chain of discrete masses in order to capture the effect of mass distribution. Each study arrived at an equation with the following form:

$$R.T. = K \left(\frac{L\rho\tau}{p_r} \right)^{1/2} \quad (9.2)$$

The constant K varies between studies, depending on additional assumptions and also empirical correlations:

- $K = 0.91$ per Simpson et al. [169].
- $K = 0.95$ per Duntsova et al. [167].

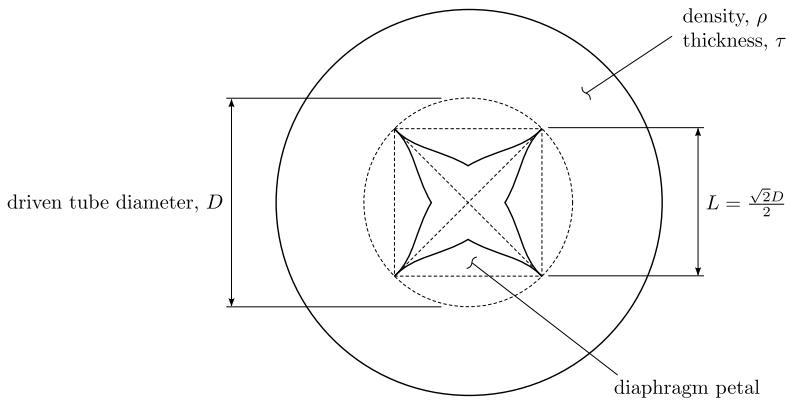


Figure 9.6: Schematic of rupturing diaphragm.

- $K \approx 0.6$ per Volkov et al. [173], which accounted for non-uniform mass along the length of the petal by modelling it as a chain of lumped masses.
- $K = 1.5$ per Yamaki and Rooker [171]. A $2\times$ factor was applied to their initial analytical derivation of $K = 0.75$ to account for significant discrepancy with test data, attributed to (1) the large period of time required for initial opening, (2) the free hinge assumption at the base of the petal which ignores its bending stiffness, (3) the unsteady nature of the driver pressure force, and (4) the assumption of no back pressure on the petal.
- $K = 0.93$ per Drewry and Walenta [170] (making appropriate unit conversions). [170] also indicates that a $2\times$ factor should be applied to this number to account for discrepancies with their own experimental results, again attributed to significant simplifying assumptions use in their analysis.
- $K = 1.38$ per Curzon and Phillips [172], which assumes a free hinged petal, but reduces the average applied pressure to 80% based on an empirical correlation for thin (< 0.020 in) Aluminium and Brass diaphragms.
- Hickman et al. [174] applied their analysis to thick diaphragms where bending stiffness could not be ignored and the hinged assumption is no longer valid; the stiffness term varies with displacement and therefore the final solution was iterative and not amenable to a simple formula. Zeitoun et al. [175] performed a 1-D calculation using both the Hickman et al. [174] and Simpson et al. [169] models, suggesting that both models produce similar results, with the Simpson et al. [169] model being simpler to run since it is only time dependant.

The large variation in values for K in Equation 9.2, and the application of large correction factors by [170] and [171], all indicate the difficulty that exists in establishing a simple analytical tool to predict diaphragm rupture time. Rothkopf and Low [176] did not attempt to predict rupture time accurately, but instead attempted to characterise the rupturing behaviour. Rothkopf and Low [176] made several observations:

1. The deformed (bulged) shape of the diaphragm prior to bursting is a function of ductility only, with thickness affecting strength.
2. The initial tearing process at the onset of rupture may take up to 50% of the total opening time. This was also observed by [168, 170, 167].
3. Neglecting the initial tearing process, and measuring diaphragm opening in terms of total aperture area, after about 5% of the aperture is open, the remaining rupture process proceeds at a steady rate (in terms of aperture area) until the diaphragm is approximately fully open. Normalised curves shown in Figure 9.7 indicate the linear behaviour of this opening process.

Point (3) above is the most relevant finding from [176] to the current analysis. It indicates that the rate of diaphragm opening, when measured in terms of aperture area, is approximately constant after the initial rupture has occurred.

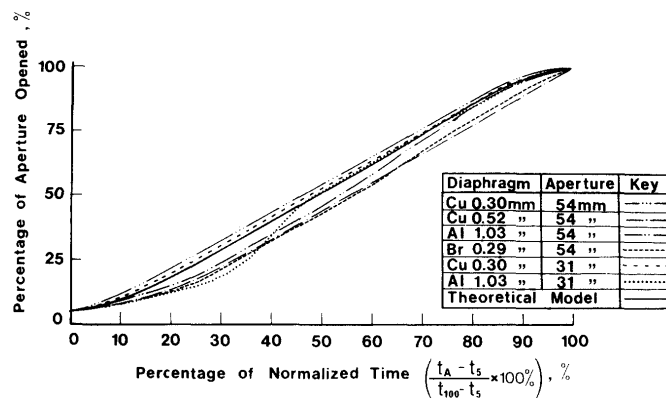


Figure 9.7: Diaphragm opening time curves (taken from [176]). Time at any given moment, T_A , is normalised against the experimentally measured times at 5% and 100% opening, measured in terms of current aperture area of the diaphragm compared to the tube diameter.

Previous studies have investigated the effect of finite diaphragm rupture time on flow development using 1-D analysis [175, 177], two-dimensional analysis [177, 178], and axisymmetric flow [179, 180, 157, 181, 156]. Of these studies, [157, 181, 156]

are most relevant, largely since they are most recent, use similar numerical tools to that available with Eilmer3, and use the iris model for the rupturing diaphragm.

Petrie-Repar [157] performed an axisymmetric analysis of the Langley expansion tube using an unstructured finite volume code, modelling the rupturing diaphragm as an opening iris with area increasing linearly with time (based on the observations of Rothkopf and Low [176]). Diaphragm rupture time was nominally assumed to be $200\mu\text{s}$ in accordance with Miller and Jones [165], which involved experimentation on the same facility. The effect of assuming other rupture times was also considered. The intact diaphragm was initially modelled by enforcing a boundary between driver and driven gas cells, modelled using a line of ignored cells. Opening of the diaphragm was achieved by incrementally changing ignored cells to flow cells, at a rate such that iris opening area increased linearly with time. Diaphragm opening was achieved in 48 discrete steps; the resolution of this operation is limited by the cell density, but it is preferable to make it as continuous as possible. A comparison of numerical and physical jetting through the opening diaphragm is made by [157]. Numerical jetting was observed to increase with increasing grid resolution, or increasing cell aspect ratio.

Goozée [156] simulated UQ’s Drummond Reflected Shock Tunnel using an axisymmetric code designed for parallelisation. The same basic iris diaphragm concept was adopted as that used by Petrie-Repair [157], however Goozée implemented the model into the structured MB_CNS code, which was a precursor to the Eilmer3 code used in the present study. A $200\mu\text{s}$ rupture time was nominally assumed for the Drummond Tunnel aluminium diaphragms, rupturing to a diameter of 57 mm (compared to the 62.2 mm diameter of the tube). This rupture time was compared to $100\mu\text{s}$ and $400\mu\text{s}$ times. Simulations were run with both an idealised diaphragm rupture (instantaneous removal of the entire diaphragm) and with the finite time iris rupturing diaphragm model. It was found that the iris model was able to reproduce experimental results well, whereas the idealised model failed to do so. The shock development is inherently stable, since compression waves rapidly coalesce to produce a planar shock. However, the slow initial opening of the diaphragm results in jetting of driver gas and a complex interaction at the interface [156]. Goozée [156] observed that shock and contact surface speeds far downstream of the diaphragm were relatively unaffected by opening time, however the characteristics of the contact surface were quite significantly affected by non-ideal rupture, and initiation of these flow processes was correspondingly delayed by increasing rupture time. Goozée [156] found that the flow processes associated

with an opening iris diaphragm rupture were not particularly sensitive to mesh resolution. Finally, the iris opening diaphragm was shown to introduce the acoustic radial waves which are associated with the test flow unsteadiness described by Paull and Stalker [72].

Gaetani et al. [181] have investigated partial diaphragm rupture experimentally, analytically, and numerically using an axisymmetric model. They assessed the reduction in shock strength due to incomplete rupture, and also the introduction of post-shock pressure oscillations to the flow. They found that individual peculiarities of diaphragm dynamics do not affect the final flow field since all initial perturbations coalesce into the leading shock wave. The amplitude of post-shock pressure oscillations was found to decrease with distance from the diaphragm, and was inversely proportional to the diameter of the opening section of the diaphragm [181].

Based on the preceding review of work on this topic, it becomes apparent that an accurate analytical model predicting the diaphragm rupturing mechanism is not available. The most reliable approach would be to conduct an extensive experimental characterisation of the rupturing process for each specific application (for example, in this instance, to systematically measure the rupturing of 2.0 mm cold rolled steel diaphragms in X2 using available modern techniques, but essentially similar to Rothkopf and Low [176]). However, numerical studies such as those of Petrie-Repar [157] or Goozée [156] indicate that this level of sophistication is unnecessary for the present application. The iris opening model incorporated by both of these studies captures the complex flow processes at the contact surface, and has been shown by Goozée [156] to introduce the radial disturbances first described by Paull and Stalker [72] which are a focus of the present study. The rupture time is a variable which is still poorly defined, however this only affects the timeline and magnitude of downstream flow process development, not the fundamental characteristics of the flow. An iris opening model with a constant rate of area increase was thus used for the present analysis. The rupture time was estimated using Simpson et al. [169]. Considering driver condition x2-lwp-2.0mm-0, rupture time for a 2 mm steel diaphragm is calculated by substituting relevant parameters into Equation 9.2:

$$R.T. = 0.91 \times \left(\frac{0.060 \times 7,850 \times 0.002}{27.9 \times 10^6} \right)^{1/2} = 167 \mu \text{s} \quad (9.3)$$

$L = \sqrt{2} \times 0.085/2 = 0.060$ mm, which assumes the final diameter is equal to the tube diameter, and ignores the tube circular curvature.

It can be shown that for an constant rate of increase in iris opening area at the primary diaphragm, between an initial radius, r_0 , a final radius, R , and where total opening time is equal to t_f , that radius must vary with time as follows:

$$r = \sqrt{r_0^2 + \frac{t}{t_f} (R^2 - r_0^2)} \quad (9.4)$$

Primary diaphragm rupture is modelled as a finite time opening iris in accordance with the methodology previously investigated by Petrie-Repar [157] and Goozée [156]. This methodology was shown by Goozée [156] to produce acoustic radial waves similar to those observed experimentally. Goozée [156] performed an axisymmetric numerical simulation of the Drummond Reflected Shock Tunnel at UQ using the code mb_cns (the original precursor code to Eilmer3). An iris model of the primary diaphragm was opened over a finite time, resulting in generation of oblique waves in the driver gas. It was found that when a nitrogen driver gas was used to drive a nitrogen test gas, and was configured to have an increase in sound speed across the driver-test gas interface, driver gas noise was prevented from entering the driven gas. When the driver gas was changed to helium, with a correspondingly much higher sound speed (higher than the driven gas), the test gas was observed to have significantly greater noise levels, with acoustic characteristics very similar to those observed in the driver gas. These numerically simulated noise predictions were then compared with noise measured experimentally in the Drummond Tunnel nozzle. The experimentally measure noise was observed to have frequencies between 10 and 50 kHz, which closely matched the numerical simulation predictions [156].

9.4 Results and Discussion

This section presents CFD results for the Mach 10 flow condition x2-scr-m10p0-rev-1 from Table 7.5, for X2 operating with a straight tube adaptor to the test section (i.e. no nozzle). This flow condition is the same one analysed using the hybrid L1d2/Eilmer3 model in Section 8.6.2. Table 9.1 summarises the predicted flow properties using the full facility model, and compares them to the hybrid CFD model, and also L1d2 and experimental results where applicable. Both the hybrid and full Eilmer3 models compare fairly closely. The same period of test time was assumed for both (timed following shock arrival at the tube exit), and the general magnitude and fluctuation in the test gas core flow properties is similar in terms of Mach number, temperature, velocity, and static pressure. This essentially indi-

cates that the fixed volume driver was appropriately configured to produce similar test gas properties. However, given the complexity of the flow processes, closer agreement is not required nor expected, since this is known to be an approximate model which cannot fully replicate all of the flow processes. Instead, the purpose of this analysis is to investigate the effect of driver flow processes on the test gas during the test time. The analysis will therefore qualitatively focus on the test flow characteristics for the fixed volume driver full facility model CFD, and investigate if and how the driver gas expansion through both the area change at the driver, and the iris opening primary diaphragm, affect the test flow.

Property	Experimental	L1d2	Eilmer3 hybrid	Eilmer3 full
<i>Secondary driver</i>				
Shock speed between $sd1$ and $sd2$ (m/s)	$4,113 \pm 0.8\%$	3,365	-	3,461
Shock speed between $sd2$ and $sd3$ (m/s)	$4,117 \pm 0.8\%$	3,491	-	3,500
<i>Shock tube</i>				
Shock speed between $st1$ and $st2$ (m/s)	$1,492 \pm 0.2\%$	1,459	1,360	1,350
Shock speed between $st2$ and $st3$ (m/s)	$1,416 \pm 0.2\%$	1,450	1,357	1,353
<i>Acceleration tube</i>				
Shock speed between $at4$ and $at5$ (m/s)	$3,377 \pm 0.7\%$	3,432	3,325	3,325
Shock speed between $at5$ and $n1$ (m/s)	$3,264 \pm 0.2\%$	3,404	3,332	3,324
<i>Acceleration tube exit plane:</i>				
<i>Final test flow properties</i>				
Static pressure (kPa)	-	-	$35.8 \pm 15\%$	$34.8 \pm 15\%$
Pitot pressure (kPa)		-	$4,557 \pm 10\%$	$4,205 \pm 14\%$
Mach number (-)	-	-	$9.94 \pm 3\%$	$9.68 \pm 4\%$
Density (kg/m^3)	-	-	$0.465 \pm 12\%$	$0.471 \pm 13\%$
Static temperature (K)	-	-	$268 \pm 5\%$	$257 \pm 1\%$
Velocity (m/s)	-	-	$3,257 \pm 1\%$	$3,110 \pm 1\%$
Stagnation enthalpy (MJ/kg)	-	-	4.05	3.664
Total pressure (GPa)	-	-	3.75	2.81
Unit Reynolds number [<i>million/m</i>]	-	-	91.7	91.8
Core flow diameter (mm)	-	-	50	50
Test time [μs]		-	60	60

Table 9.1: Test flow properties for Mach 10 flow condition, x2-scr-m10p0-rev-1, X2 *without* nozzle, full facility CFD model. Shock speeds are averaged between the transducer locations. Each Eilmer3 test flow property is the mean value within the core flow averaged across the test time (see Section 9.4.2.2); the Eilmer ‘ \pm ’ value is the maximum departure from the mean value during the test time. The experimental shock speed ‘ \pm ’ is the experimental uncertainty. Total pressure and enthalpy are calculated based on average flow properties during the test time, and assume shifting chemical equilibrium per Chinitz et. al [41].

9.4.1 Critical Wave Processes

Figure 9.8 compares experimental and computed shock speeds downstream of the primary diaphragm. The L1d2 shock speed, which was calculated using a model incorporating full piston dynamics, compares well with experiment through all of the tubes. The *hybrid* Eilmer3 model from Chapter 8 only computes the flow downstream of transducer *st1*, using a 1-D inflow from the L1d2 model. It can be seen that the shock speed closely matches the L1d2, although Eilmer3 predicts a slightly higher shock speed through the acceleration tube.

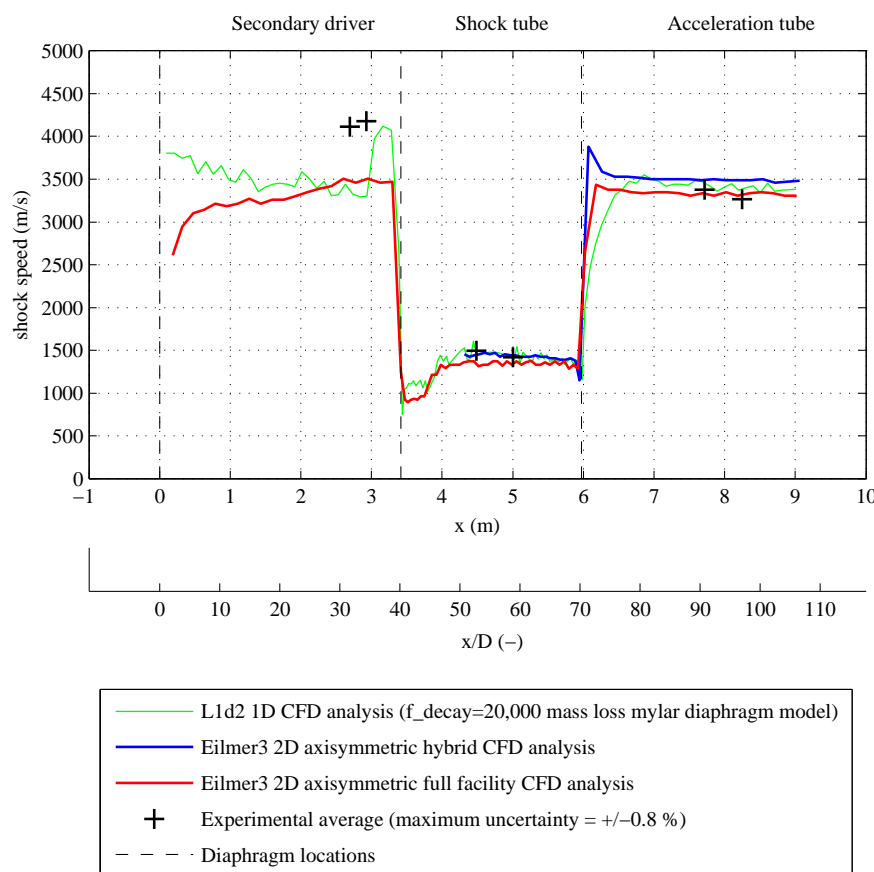


Figure 9.8: Primary shock speed vs. position for Mach 10 flow condition, X2 *without* nozzle (*x2-scr-m10p0-rev-1* in Table 7.5), full facility simulation.

The computed shock speed for the *full facility* Eilmer3 model, which is the subject of the present chapter, is shown for the entire length of the facility downstream of the primary diaphragm. It can be seen that the initial shock speed is significantly lower than the L1d2 prediction, but that it steadily rises across the secondary driver and eventually exceeds L1d2 downstream of $x \approx 2.5$ m. However,

the reinforcing compression wave from the driver area change (see Section 4.2.4 or Section 7.8), which is evident in both the L1d2 and experimental results, is not obvious in the full facility Eilmer3 model.

The initial acceleration of the full facility Eilmer3 shock between approximately $x = 0$ and $x = 1$ m is attributed to the gradual opening of the iris diaphragm, and would be expected to be observed in the actual experiment if several transducers were located at the start of the secondary driver tube. However, the distance over which the shock attains full speed obviously depends on the diaphragm opening time, and also the true 3-D diaphragm rupture characteristics, therefore the predicted Eilmer3 length scale cannot be assumed to be representative of the true event. A general rule-of-thumb states that a planar shock forms across a distance of $x/D \approx 6$, where D is the diameter of the tube. Observing Figure 9.8, x/D is also shown on the horizontal axis; it can be seen that by $x/D = 6$ the shock has almost reached full strength. This indicates that the formation distance is probably reasonable, and therefore the calculated opening time would not be expected to greatly influence overall shock development. However, diaphragm opening remains a potential source of radial disturbances, which is why it has been modelled here.

The absence of an obvious reinforcing wave in the full facility Eilmer3 model between $x = 2.5$ and $x = 3.5$ m is expected to be due to a ‘smearing’ of the compression wave through the iris opening primary diaphragm. An increase in shock speed is evident across the secondary driver, however the shock speed increase is not discrete like the L1d2 or experimental shock speeds. If the iris diaphragm model is excessively damping out this reinforcing compression wave, then this could indicate that the total opening time ($167\mu s$) is too long. Since the fixed volume driver model is already a significant simplification of the actual driver, investigating shorter opening times was not considered beneficial in the present investigation. However, once piston dynamics are incorporated into Eilmer3, one method of estimating diaphragm opening time would be to identify which opening time most successfully predicted the shock speed increase due to the reinforcing compression wave.

Another reason that the full facility Eilmer3 model does not successfully predict the reinforcing compression wave may be due to nature of the fixed volume driver itself. This driver model produces a fairly steady supply of driver gas. This compares to the actual free-piston driver, which fundamentally relies on a fluctuating driver pressure to achieve its tuned/over-driven operating condition. The rise in shock speed due to the arrival of the reinforcing compression wave, in both

the experiment and L1d2, may therefore be particularly abrupt due to transient effects in the driver.

The full facility Eilmer3 model successfully predicts the initial drop in shock speed due to the reflected shock at the secondary diaphragm, although the shock speed is slightly lower than the experimental and L1d2 shock speeds across transducer locations $st1$ to $st3$. Towards the end of the shock tube, the full facility Eilmer3 shock speed eventually matches the computed L1d2 and hybrid L1d2/Eilmer3 shock speeds. Finally, across the acceleration tube, of the three computed solutions, the full facility Eilmer3 shock speed most closely matches experiment.

In summary, the full facility Eilmer3 computed shock speeds do not closely match experiment along the secondary driver tube or the upstream length of the shock tube, for the reasons stated above. However, the selected initial properties of the fixed volume driver *do* produce shock speeds which closely match experiment towards the tertiary diaphragm and along the acceleration tube, therefore the computed test flow for the full facility Eilmer3 model is suitable for comparison with the other experimental and numerical results. Since the fixed volume driver model also incorporates the effects of the driver area change and iris opening primary diaphragm in its simulation flow processes, the effects of these driver processes on the test flow can now be assessed.

9.4.2 Visualisation of Flow Development

Figure 9.9 shows the flow development predicted by Eilmer3 from the fixed volume driver through to the acceleration tube exit. The top half of each contour plot shows Mach number; the bottom half shows the log of static pressure. The vertical scale has been increased $5\times$ for clarity, however it should be remembered that this will make shocks and interfaces look more planar than they are. A detailed 1:1 view of the diaphragm opening process is also shown in Figure 9.10.

Observing Figures 9.9 and 9.10, the iris diaphragm is observed to be in the process of opening between $t = 0.0$ ms and $t = 0.16$ ms. A planar shock is rapidly established, however as observed previously in Figure 9.8, the shock does not develop full strength immediately.

Referring to 9.9, oblique shock waves begin to form at the area change at $t = 0.48$ ms, and remain for the duration of critical flow processes. The finite opening time of the iris diaphragm leads to some mixing at the interface between

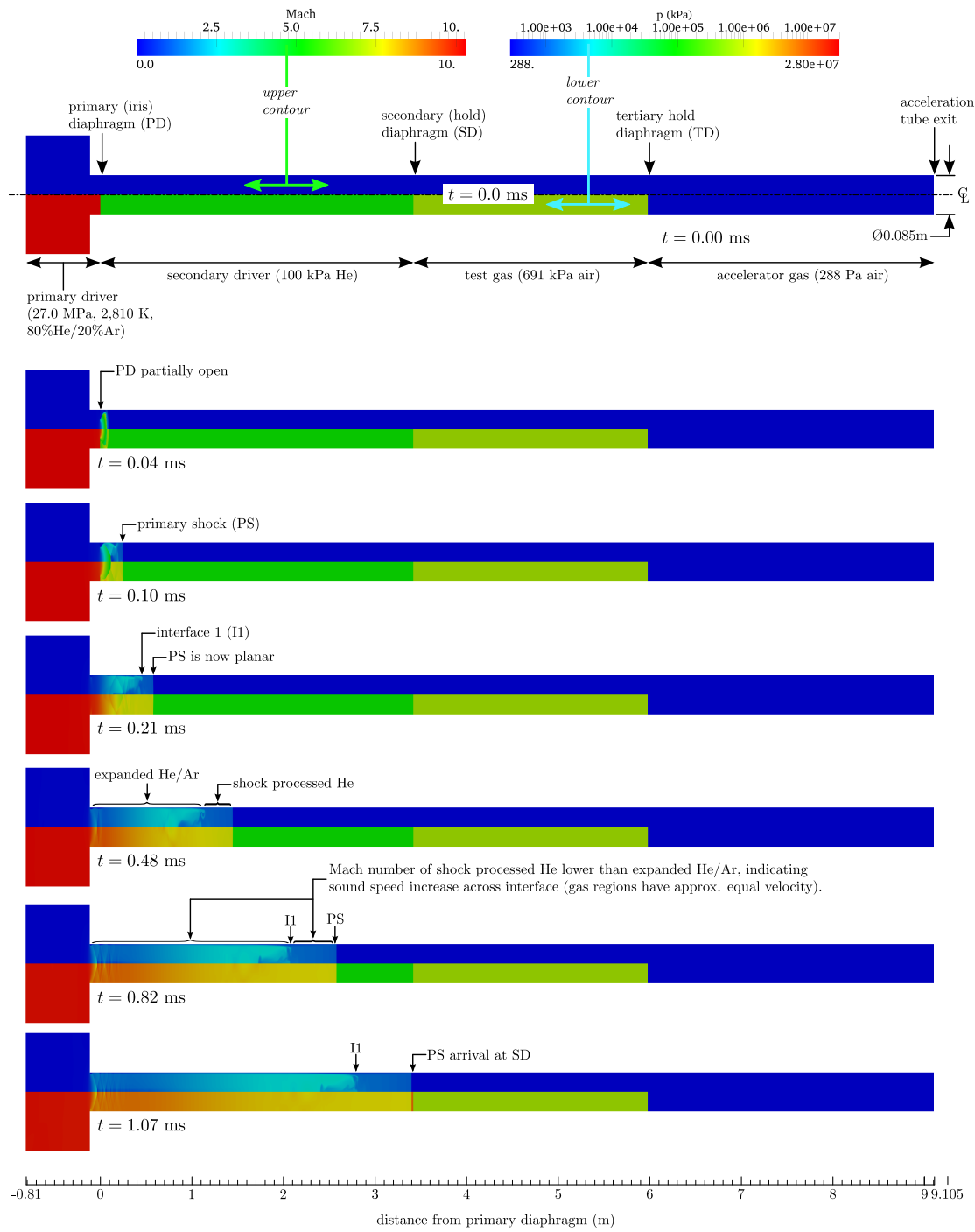


Figure 9.9: Flow development in secondary driver, shock, and acceleration tubes (part 1 of 2).

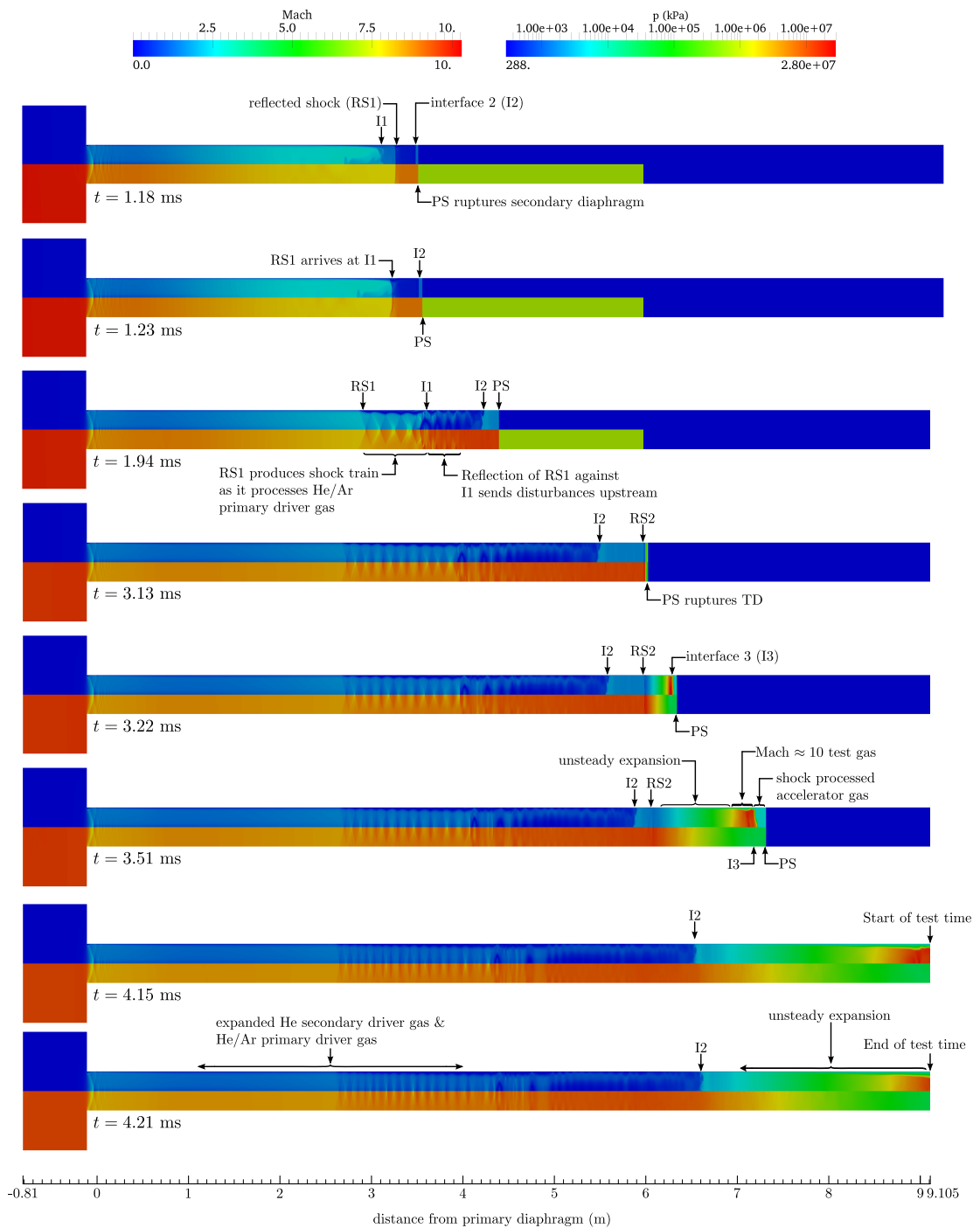


Figure 9.9: Flow development in secondary driver, shock, and acceleration tubes (part 2 of 2). It is noted that these contours are truncated at the acceleration tube exit, however the actual Eilmer3 model extends 150 mm further downstream.

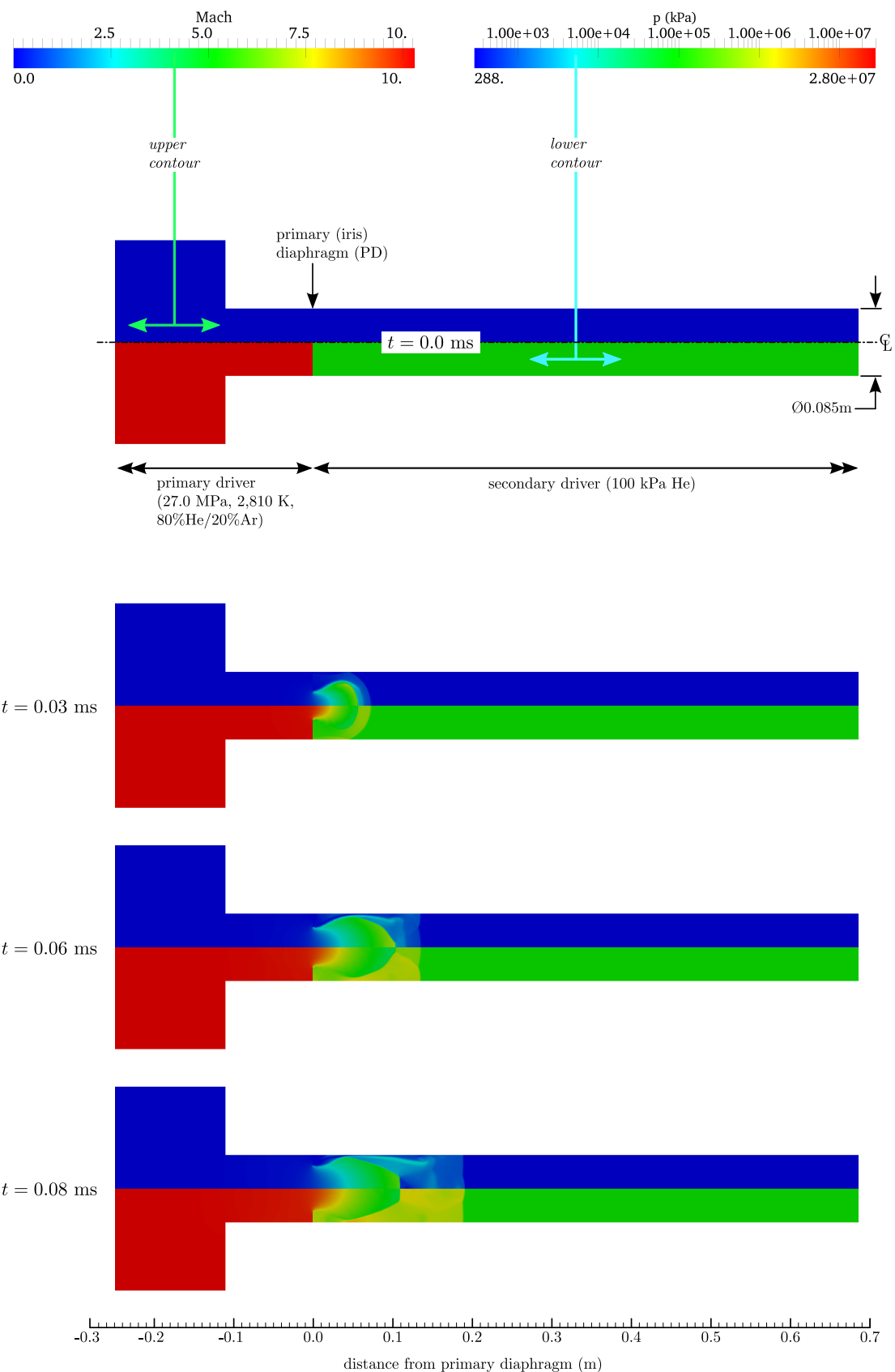


Figure 9.10: Detail view of primary diaphragm opening process (part 1 of 2). Scale is 1:1.

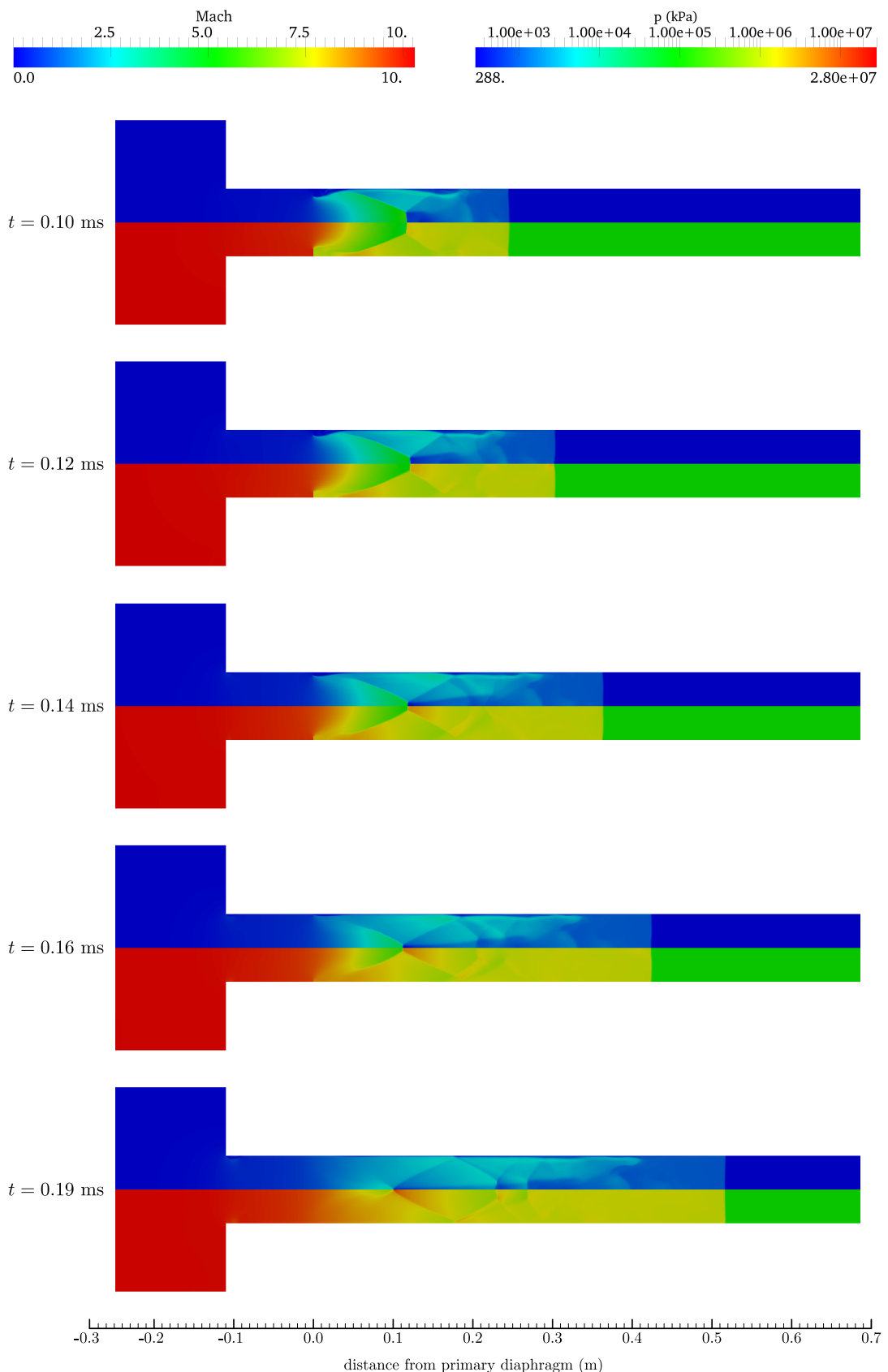


Figure 9.10: Detail view of primary diaphragm opening process (part 2 of 2). Scale is 1:1.

the He/Ar primary and He secondary driver gases, however the downstream slug of shock-processed helium has reasonably steady Mach number and pressure.

When the shock arrives at the secondary diaphragm, the shock processed helium collides with the very dense (691 kPa initial fill) air test gas, and a strong reflected shock (RS1) forms. This reflected shock first processes the relatively steady portion of helium gas (refer $t = 1.18$ ms), producing a correspondingly steady region of double shock-processed helium secondary driver gas. However, when the reflected shock reaches the He/Ar primary driver gas interface, a compression wave reflects downstream and disturbs this steady region of helium secondary driver gas. As the reflected shock processes the He/Ar primary driver gas, a complex shock train develops which remains present through to completion of the test time.

When the primary shock arrives at the tertiary diaphragm, the $10\mu s$ hold time results in a second reflected shock (RS2). This is an upstream running shock, however in the laboratory frame of reference it is approximately stationary over these time scales. Following diaphragm rupture the primary shock enters the acceleration tube. Observing the Mach contours from $t = 3.22\mu s$ onwards, the test gas undergoes an unsteady expansion to the target Mach number of approximately 10, and can be identified as the red region of gas. Upon arrival of this region of gas at the acceleration tube exit, the test time begins (at $t = 4.15\mu s$). The test time ends when the useful portion of this gas passes the exit $60\mu s$ later at $t = 4.21\mu s$.

Comparing these contours, for the full facility model, with those for the hybrid model (Figure 8.10 in Chapter 8), it can be seen that the shape of the Mach 10 region of test gas is generally similar for both models. This suggests that the constitution of the test gas slug is primarily dependant on flow processes in the shock and acceleration tubes, and not on the upstream flow processes. Observing Figure 9.9 it is also evident that complex unsteady 2-D flow processes arise due to the expansion of the primary driver gas through the area change and iris opening primary diaphragm. However, the effects of this unsteady flow do not appear to affect the test gas, during the test time, on the large scale displayed in this contour plot.

9.4.2.1 Tube Wall Static Pressure Traces

Transducer pressure traces are shown in Figures 9.11, 9.12, and 9.13, for the secondary driver, shock, and acceleration tubes respectively. All traces have been time-referenced to initiate with the corresponding L1d2 trace, therefore these plots are not indicative of absolute timing.

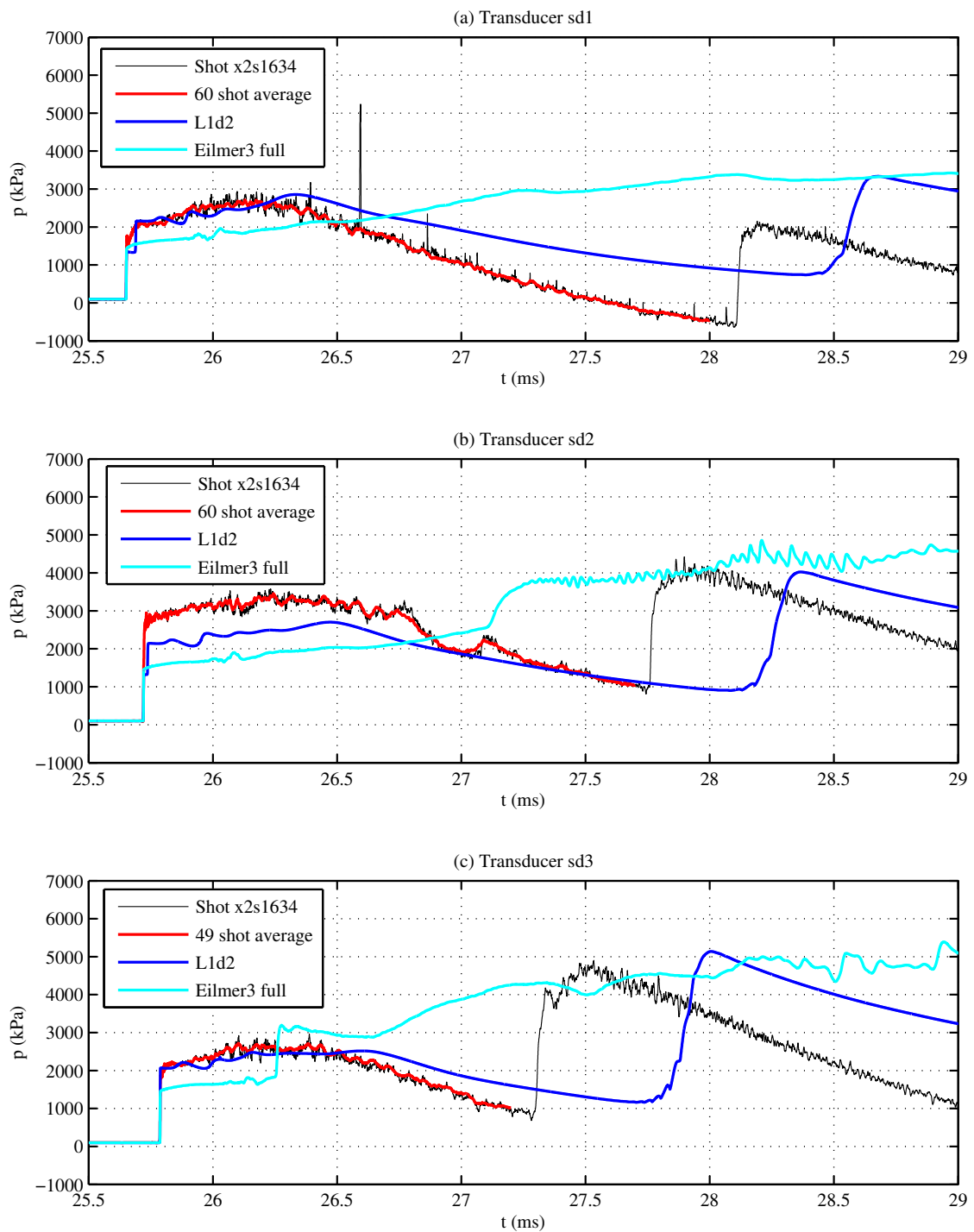


Figure 9.11: Static pressures at secondary driver transducers $sd1$, $sd2$, and $sd3$, for flow condition x2-scr-m10p0-rev-1.

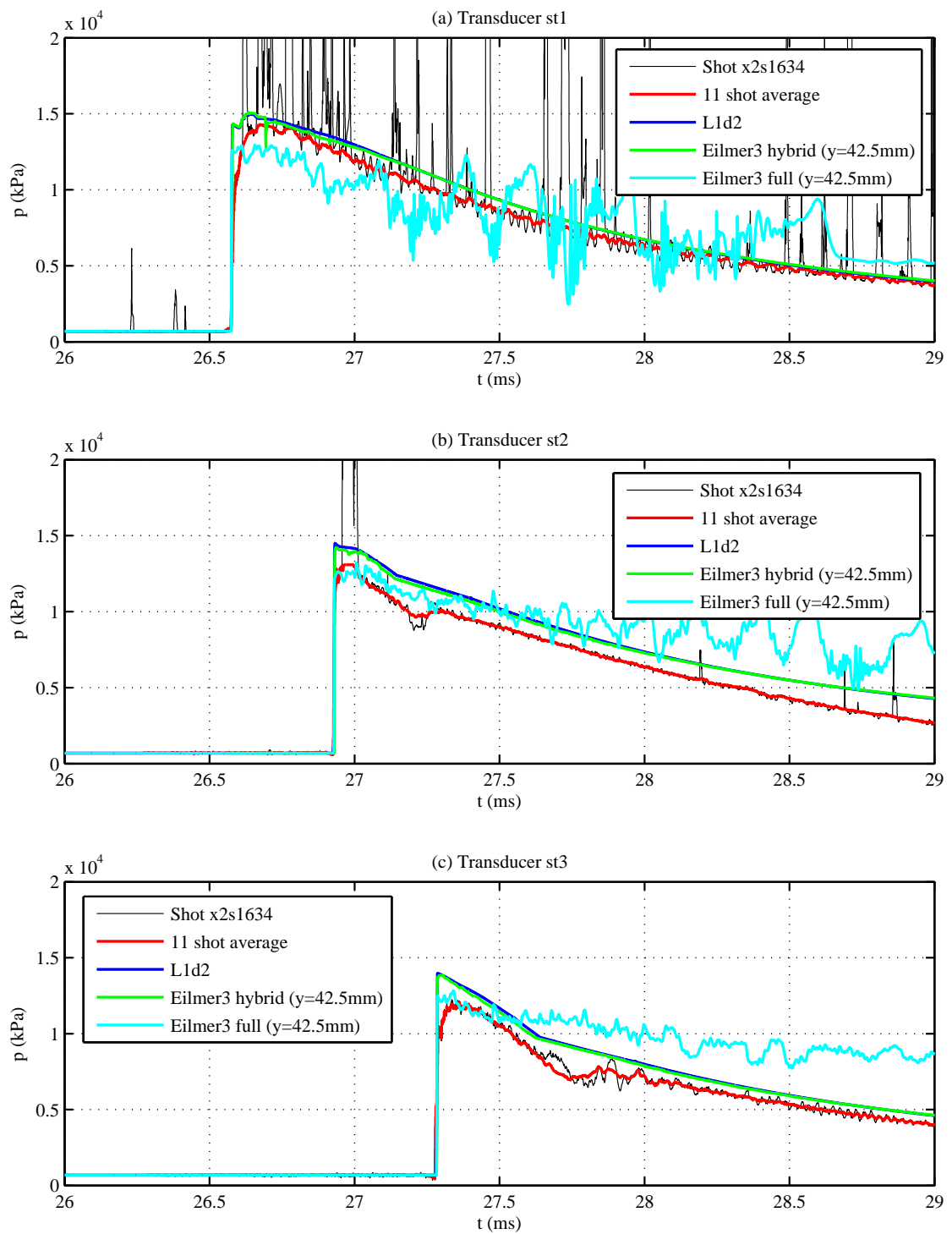


Figure 9.12: Static pressures at shock tube transducers $st1$, $st2$, and $st3$, for flow condition x2-scr-m10p0-rev-1.

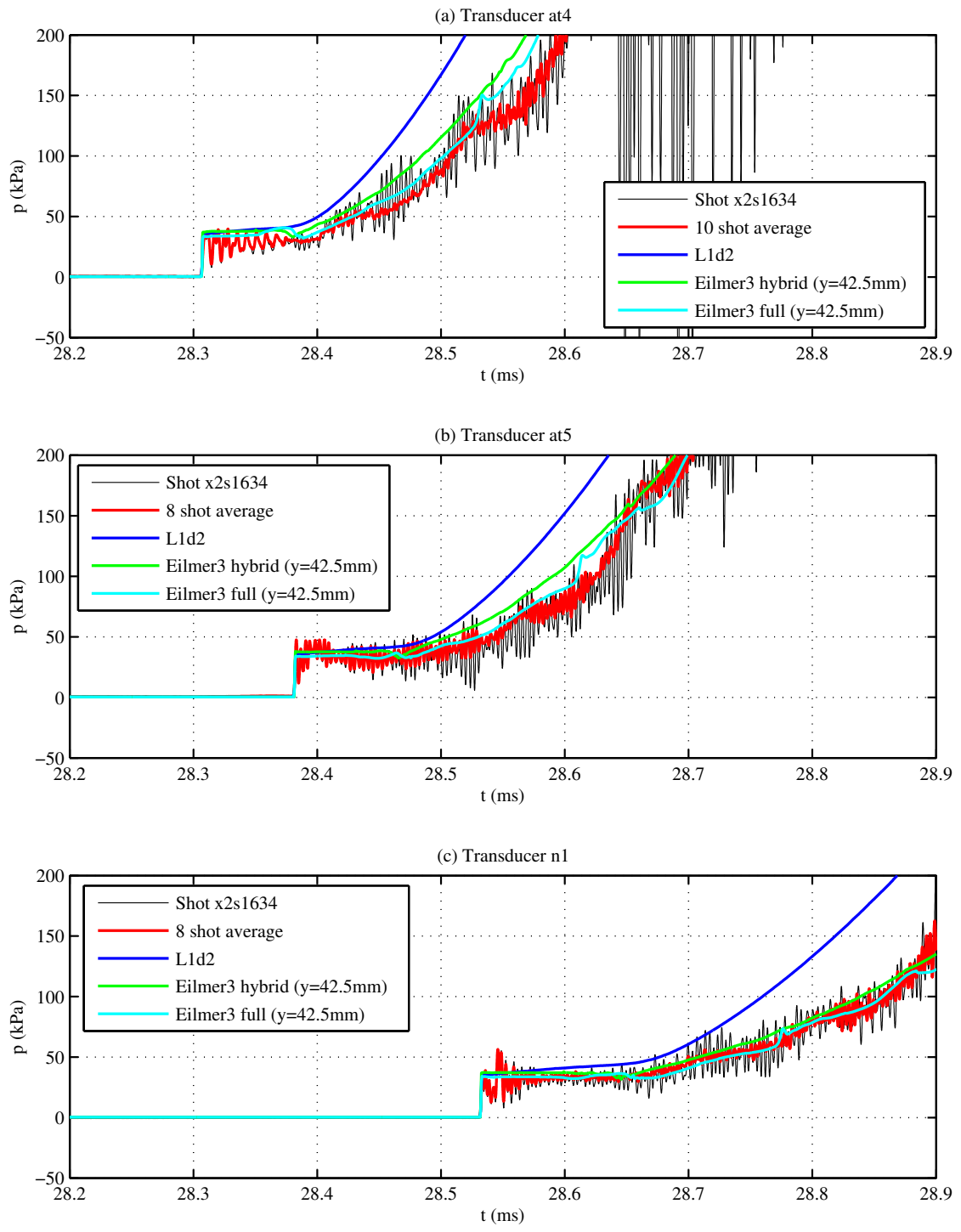


Figure 9.13: Static pressures at acceleration tube transducers *at4*, *at5*, and *n1*, for flow condition x2-scr-m10p0-rev-1.

Observing Figures 9.11(a-c), the full facility Eilmer3 static pressure traces are initially significantly lower than the L1d2 and experimental traces (no results are shown for the hybrid Eilmer3 model since this model does not include the secondary driver). This is consistent with the low initial shock speeds in the secondary driver tube for the full facility model (see Figure 9.8). The reflected shock from the secondary diaphragm is observed in Figures 9.11(b) and (c); the shock arrives at $sd3$ first since it is travelling upstream from the secondary diaphragm. The general behaviour of the full facility Eilmer3 model differs from the L1d2 and experimental results; the former model computes static pressure traces which are steadily rising over time due to flow establishment in the large volume fixed driver; the latter results indicate a transient pressure rise then fall due to the free-piston compression process. Agreement between the results is not expected, and the discrepancy is due to the simplified driver model used in the full facility Eilmer3 analysis.

Observing Figures 9.12(a-c), the full facility Eilmer3 computed static pressures at transducers $st1$, $st2$, and $st3$, are more representative of the experimental traces through the shock tube, and match the hybrid Eilmer3 and L1d2 results more closely. The full facility computed pressure is initially lower than the other results at $st1$, and in-between experiment and hybrid Eilmer3 and L1d2 models at $st2$ and $st3$. This is consistent with the relative shock speeds observed in Figure 9.8 for the various numerical models and experimental results.

One important characteristic observed in the full facility Eilmer3 shock tube static pressure traces is the larger magnitude noise. Since $st1$ is located close to the secondary diaphragm, the slug of shock processed test gas which passes the transducer is short, and the trailing secondary He and primary He/Ar driver gases arrive soon after shock arrival. In Figure 9.12(a) this is characterised by significant unsteadiness following $t \approx 27$ ms. The length of the test gas slug increases as the primary shock reaches $st2$ and $st3$; this is observed in the plots as an increasing delay in arrival of the unsteady driver gases. It is finally noted that the unsteadiness in the initial test gas is qualitatively similar to that observed in the experiment, although the fluctuations are of a greater magnitude. The pressure fluctuations in the trailing driver gases are much greater than those observed experimentally, indicating that the fixed volume driver model does not predict unsteady behaviour in the driver gases well.

Observing Figures 9.13(a-c), the full facility and hybrid Eilmer3 models predict very similar static pressure traces in the acceleration tube, although the full facility

model most closely matches the experimental results. The full facility Eilmer3 model predicts a large pressure fluctuation at $at4$ (Figure 9.13(a)) between $t = 28.3$ ms and $t = 28.4$ ms, which reduces in magnitude between $at5$ (Figure 9.13(b)) and $n1$ (Figure 9.13(b)), and appears to coincide with the arrival of the unsteady expansion.

Importantly, observing Figure 9.13(c), the full facility Eilmer3 static pressure trace at $n1$ agrees closely with experiment, and indicates steady flow. This implies that the unsteady upstream driver flow processes, which are observed in the secondary driver and shock tube, do not interfere with the test gas during the test time. This indicates that the secondary driver is proving to be effective in acting as an acoustic buffer between the test gas and primary driver disturbances.

9.4.2.2 Test Flow Properties

Figure 9.14 compares computed 15 deg cone surface static pressures at the acceleration tube exit, at a radial offset of $y = 9$ mm from the tube centreline, for both the full facility (red curve) and hybrid (black curve) Eilmer3 models. Referring to Figure 8.6, this corresponds to the experimental radial location of the 15 deg cone probes. The cone pressure is computed by first calculating the transient flow history at $y = 9$ mm along the acceleration tube exit plane, and then applying this flow history as a radially constant transient inflow to a separate cone axisymmetric Eilmer3 model. The Eilmer3 cone model consisted of an 8,000 cell grid, viscous calculation with equilibrium air. Sample experimental results are also shown for shot x2s1635 (blue and green curves).

The two Eilmer3 results compare closely in Figure 9.14. The full facility model predicts a slightly lower velocity, which is consistent with the computed shock speeds in Figure 9.8. The experimental results for this condition were previously discussed in Section 8.6.2.4, and the full facility results do not present anything new in this regard.

Observing Figure 9.14(a), one interesting feature of the full facility CFD model cone pressure trace (coloured red) is the presence of an oscillation in the cone pressure following arrival of the unsteady expansion. Whilst this oscillation does not directly match the oscillation observed in the experimental cone traces, it is characteristically similar. Further, it is not observed in the hybrid CFD model pressure trace, indicating that this oscillatory behaviour may originate in the driver as a 2D disturbance.

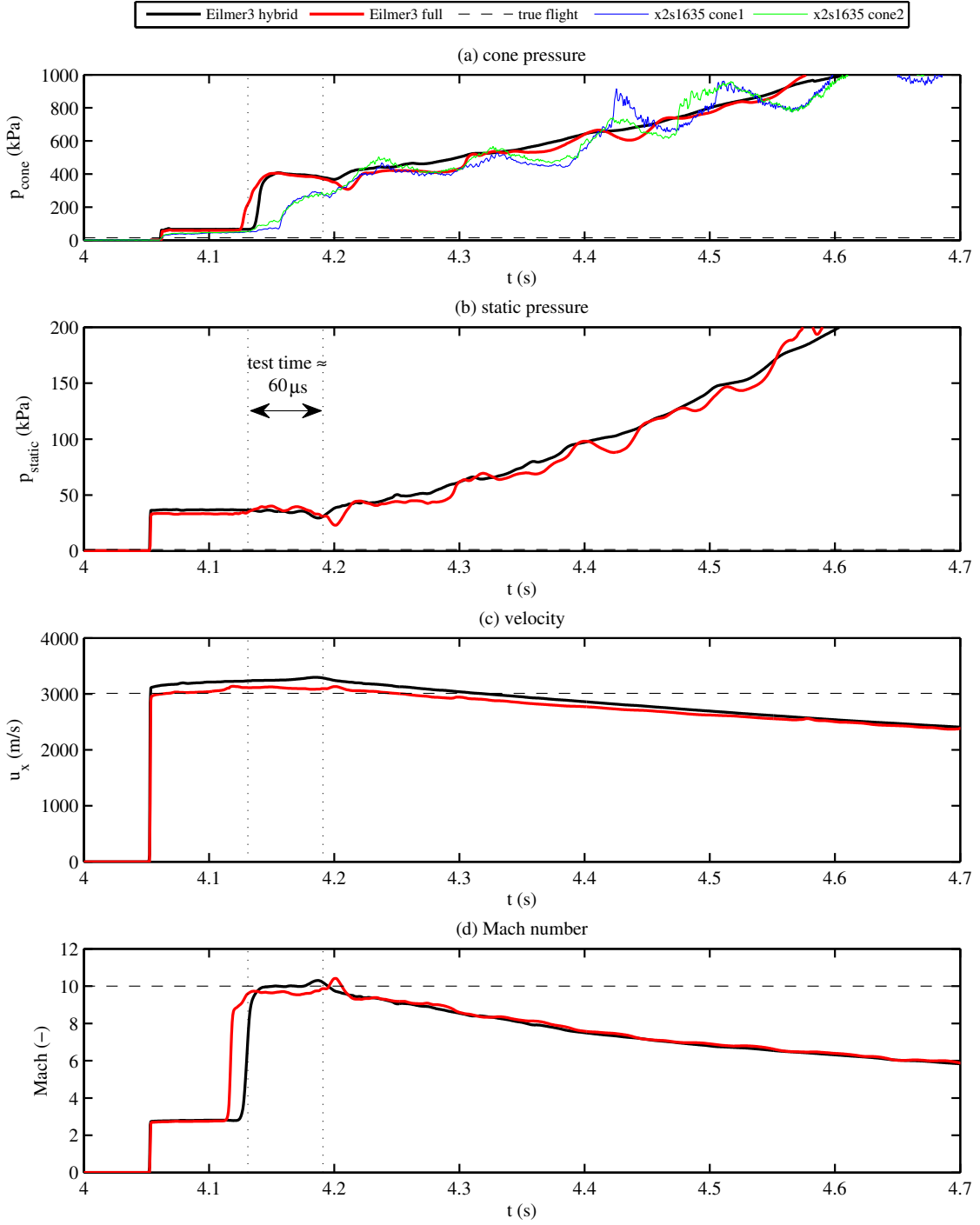


Figure 9.14: Computed and experimental test flow properties at the acceleration tube exit, at $y = 0$ mm from the tube centreline. All traces time-referenced to initiate with *full facility* Eilmer3 traces. Experimental cone pressures in (a) were measured using 15 deg half angle cones; see Section 8.5. Computed Eilmer3 cone pressures were obtained by taking the transient flow history at the equivalent location in the axisymmetric model ($y = 9$ mm) and applying this as a planar inflow to a separate cone axisymmetric model. It is finally noted that true flight cone and static pressures are much lower than experimental or numerical calculations; this indicates significant capacity for pressure-length scaling.

Both hybrid and full facility Eilmer3 models underpredict the length of the accelerator gas slug; this is evidenced by the computed cone pressure traces rising ahead of the experimental trace upon arrival of the test gas; see Figure 9.14(a). The shorter slug length predicted by the CFD is most likely due to excess entrainment of flow into the boundary layer.

It is further noted that the full facility CFD model predicts a shorter accelerator gas slug length than the hybrid model. The full facility CFD model has a radially coarser grid than the hybrid model; this was necessary to enable computation of its larger geometry within a reasonable time frame. The Baldwin-Lomax turbulence model tends to over-estimate boundary layer thickness with under-resolved grids, so the shorter accelerator gas slug length of the full facility model is consistent with it having a coarser grid.

Figure 9.15 shows how the computed flow properties vary between the tube centreline and tube wall for the full facility Eilmer3 model. Curves are shown at 0%, 25%, 50%, 75%, and 100% of the test time identified in Figure 9.14. The dashed red line in each plot shows the average core flow properties during the test time, and is calculated for each plot by averaging the flow properties across the core flow region over the five time intervals. The black dashed line shows the true flight value for each flow property. Comparing these results to those for the hybrid Eilmer3 model in Figure 8.16, the results are generally similar. The fluctuation in flow properties is slightly greater for the full facility model, especially at 75% of the test time. It is not clear whether this fluctuation is a true characteristic of the flow, or a simulation discrepancy.

9.5 Grid Sensitivity Check

The sensitivity of the solution to the grid spacing was assessed by examining two additional coarser grids. These grids were modified by increasing the nominal grid spacing by $\sqrt{2}\times$ and $2\times$ in both x and y directions, thereby reducing the total number of cells by 50% and 75% compared to the nominal grid. The results are shown in Appendix K.

Convergence of shock speeds, and the average core flow properties during the test time, are shown in Figure K.25. Figures K.25(a-c) show computed shock speeds between transducer pairs; Figures K.25(d-f) show averaged test gas core flow properties during the test time. The test time was assumed to occur over the same simulation time as that identified for the nominal grid, and average flow

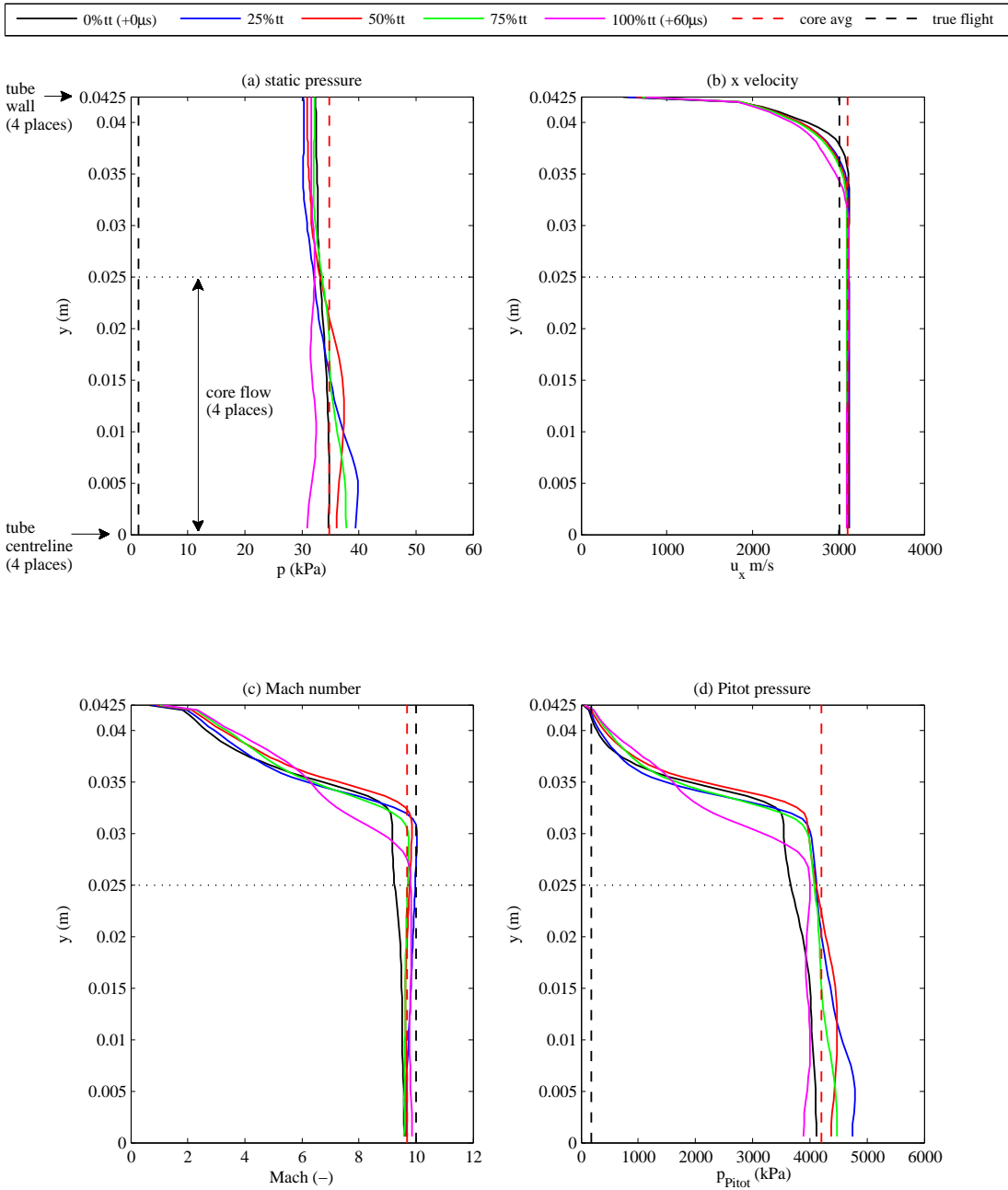


Figure 9.15: Radial variation in flow properties during the test time (denoted by *tt*). Test time is assumed to occur between simulation times $t = 0.004131 \mu\text{s}$ and $t = 0.004191 \mu\text{s}$.

properties were also calculated using an identical methodology. A least squares fit has been applied to each curve and extrapolated to a grid spacing of zero. This is considered a conservative ‘worst case’ estimate, since it includes the largest grid spacing. Referring to Figure K.25, it can be seen that there is little variation in the parameters with grid spacing. The extrapolation to zero grid spacing indicates that these *averaged* flow properties are approximately converged.

Computed shock tube and acceleration wall static pressure traces for the three different grid spacings are shown in Figures K.26. Interestingly, for each parameter the ‘noisiness’ of the pressure history appears to generally increase with finer grid spacing. This is particularly evident with the acceleration tube static pressure traces (Figure K.26(d-f)). Although the general shape and timing of the curves appears to converge (i.e. the blue and black curves), some of the transient features do not converge.

Figures K.27, K.28, and K.29 show the spatial variation in flow properties across the tube exit at 25%, 50%, and 75% of the test time. These transient, spatially variable test flow properties, do not fluctuate wildly for the different grid spacings, however neither do they obviously converge.

In conclusion, the grid sensitivity analysis in Appendix K indicates that at the finest grid spacing, the *averaged* core flow test properties are fully converged. The static pressure histories are converged in terms of timing and overall shape, however some transient features are not resolved. The spatially variable, transient flow properties are not fully resolved, however the variation in computed flow properties does not vary significantly between different grid spacings. A more refined CFD analysis is required in order to fully resolve these transient flow features.

9.6 Conclusion

Chapter 8 used a hybrid 1-D L1d2/2-D Eilmer3 CFD model to compute the test flow properties for a range of new scramjet flow conditions. However, this modelling technique did not account for complex 2-D primary and secondary driver flow processes upstream of the shock tube, which are known to interfere with test flow steadiness for some expansion tube flows. Although a helium secondary driver was used in experiments to act as an acoustic buffer against these disturbances, the hybrid model cannot reveal whether this acoustic buffer is actually likely to have been effective.

Ideally a full facility axisymmetric model would include the piston dynamics,

however Eilmer3 does not presently have this capability. Therefore the driver was modelled as a fixed volume driver. The driver length and initial fill properties were selected, using an iterative approach with L1d2, to achieve similar shock speeds to an equivalent full piston dynamics model in L1d2. This is a large simplification, however this simplified full facility model still captured the expansion of driver gas through the area change, and subsequent expansion of this gas through an iris opening primary diaphragm. The objective was to introduce *characteristically* similar disturbances into the driver gas, and configure this driver gas to eventually produce approximately similar flow processes in the shock and acceleration tubes. This is considered a good first step to qualitatively establish if driver disturbances are transferred to the test gas; a more representative full piston dynamics model is required in order to actually quantify this effect.

The results from this chapter indicate that expansion of the driver gas through the area change, and across the iris opening primary diaphragm, does indeed produce complex unsteady flow processes in the primary and secondary driver gases. This unsteadiness manifests itself as noisier computed static pressure traces in the secondary driver and shock tubes, although the full facility Eilmer3 model over-estimated the magnitude of this unsteadiness compared to experiment. However, in the acceleration tube the full facility model produces very similar test flow properties to the hybrid Eilmer3 model (which does not account for any driver-induced disturbances). There is more unsteadiness in the full facility CFD test flow, however this is not the high frequency noise that might be expected if it was due to noise originating in the driver gas.

The computed secondary driver shock speeds in the full facility model indicate that the primary diaphragm opening time may be excessive, with the partially open diaphragm damping out the effects of the reinforcing compression wave from the driver area change. In addition to diaphragm opening time, the discrepancy may also be due to the assumption of a constant volume driver. 3-D diaphragm rupture processes ignored in the iris diaphragm model may also account for part of the discrepancy, however good agreement between the 1-D L1d2 and experimental shock speeds indicates this effect is likely to be only of secondary importance.

A fixed volume driver was used which was shown to reproduce the dynamics of the driver process sufficiently accurately to model the macroscopic flow development in the tunnel well. By introducing a source of transverse disturbances, it was able to model the operation of the secondary driver as a means of noise filtering. The logical next step is to incorporate full piston dynamics into Eilmer3, which

will be necessary to achieve quantitative agreement with experimental results in the secondary driver and shock tube.

Chapter 10

Conclusion

The objective of this thesis was to use X2 to produce the high Mach number and high total pressure scramjet flow conditions associated with access to space. Initial experimental attempts to produce a Mach 13 condition indicated that the existing free-piston driver arrangement, based on a 35 kg piston and 100% helium driver gas, did not produce high pressure driver gas for sufficient duration; see Chapter 4. Following expansion of the driver gas, the expansion wave processing the driver gas reflected off the piston face, sending a strong $u + a$ expansion wave downstream. This $u + a$ wave interfered with the test gas prior to its arrival in the test section; the result was significant attenuation of the primary shock prior to its arrival in the test section. It was determined that a tuned driver condition could provide a significantly longer duration of high pressure driver gas, and achieving this operating condition subsequently became the first major task of this investigation.

Tuned operation involves configuring the driver so that the piston is moving sufficiently fast following primary diaphragm rupture that the piston displacement compensates for driver gas loss to the driven tube. This can result in approximately constant driver pressures for a relatively long duration of time. An analysis of the free-piston driver in Chapter 4 indicated that for X2's relatively short (4.5 m) compression tube, tuned operation requires a very lightweight piston (≈ 10 kg). The tuned piston must be light so that it can be first accelerated to a high speed (>200 m/s), and then brought to rest, over the short compression tube length. A new 10.5 kg lightweight piston for X2 was developed, which is detailed in Chapter 5.

A series of three new tuned driver conditions were developed for X2 using the new lightweight piston. The commissioning of the new driver is detailed in Chapter

6. Tuned operation was achieved, involving maximum piston speeds of up to 240 m/s, whilst simultaneously achieving soft landing at the buffer. The duration of high pressure driver gas supply was increased by an order of magnitude, thus eliminating any problems of shock attenuation due to driver pressure loss.

The new tuned driver conditions require a lower driver gas sound speed, by the addition of 20% argon, since it is not feasible to run X2's new lightweight piston fast enough to match the mass loss of pure helium to the driven tube. Further, lower compression ratios are required in order to provide enough time/distance to bring the piston to rest after diaphragm rupture, resulting in a further reduction in the driver gas sound speed. For a given rupture pressure, this reduced sound speed results in a weaker driven shock. However, for scramjet conditions the performance of the new driver remained sufficient, and operation at higher rupture pressures partially compensated for the slower driver gas sound speed. As a result, the driver was now capable of driving the scramjet flow conditions targeted by this investigation.

The theoretical performance envelope of X2 with the new driver was investigated in Chapter 7, and a set of new scramjet flow conditions were proposed for X2. Initial calculations used analytical relations with equilibrium gas properties. The proposed flow conditions were then assessed using the 1-D CFD code L1d2, which includes full piston dynamics, and were adjusted to account for 1-D effects not considered in the original analytical calculations.

The final task in this study was to assess the new flow conditions both experimentally in X2, and numerically using a hybrid 1-D L1d2/2-D axisymmetric Eilmer3 CFD model. Four flow conditions were considered: Mach 10, 12.5, and 15 conditions in X2 without a nozzle, and a Mach 10 condition with a nozzle. Both the experimental and numerical results indicated that the predicted primary wave processes were achieved. The detailed CFD analysis further predicted that the target test flow Mach number, velocity, temperature, and static pressure, were all achieved at each condition. Computations show that the maximum test flow total pressures were 3.75, 8.79, and 10.4 GPa, at Mach 10, 12.5, and 15 respectively. At these relatively low enthalpies (4.05, 6.68, and 10.4 MJ/kg respectively), these are the highest total pressure scramjet flows that have been reported in the literature.

This investigation did not yield definitive Pitot pressure measurements; pressure traces were inconsistent, and conventional Pitot probes were continually being damaged by the harsh test flows. In order to obtain a similar measurement with less damage to the probe, a new 15 deg cone probe was developed to take a partial

impact pressure measurement. While the cone surface static pressure is not totally Mach number independent, at these high Mach numbers the sensitivity to Mach number is relatively low, and a comparison pressure can be calculated using CFD. These cone pressures were more repeatable, and showed reasonable agreement with the CFD over longer time scales. However, the cones had a slow response time, and cone pressures exhibited some unsteadiness.

Reliable Pitot or partial impact pressure measurements are required to verify that the predicted CFD test flow properties are representative of the true flow. Whilst conclusive measurements have not been achieved in the present investigation, there are reasons to be confident that better measurements will demonstrate that agreement exists with the experiment. This is based on a) matched wave processes, b) matched and steady tube wall static pressure measurements, c) correlation with cone probe pressure measurements, and d) the high fidelity of the CFD simulations. Considering the last point, a separate full facility 2-D axisymmetric simulation was performed in Chapter 9 for the Mach 10 condition without a nozzle, purely to assess whether complex driver flow processes are likely to interfere with test flow properties. This more sophisticated simulation predicted a similar test flow to the hybrid analysis, increasing confidence that the hybrid model results were representative of the true flow.

Two other obvious limiting features of these test flows are the short test times and small core flow diameters (40-80 mm). X2 is a medium sized facility, and test time and core flow size are directly dependent on tube length and diameter. The purpose of this investigation was to demonstrate proof of concept, and it is shown that this has been achieved. UQ's X3 facility is much larger than X2, and when these conditions are scaled upwards it is expected that test flow duration and core flow diameter will correspondingly increase to meet the requirements for scramjet testing.

In summary, this study has shown, for the first time, that an expansion tube *can* be configured to achieve the high Mach number, GPa total pressure, flow conditions associated with scramjet access to space. Several challenges certainly remain for future ground testing of scramjet engines at these extreme conditions; chief amongst these is the need for accurate and reliable Pitot pressure measurements in these harsh flows. The CFD also predicts some unsteadiness in these test flows; in the worst case, future testing may simply need to adapt to these imperfect test flows, since no ground testing technique, other than the expansion tube, is currently conceived which can produce flows even close to these total pressures.

One of ground testing's most important functions is validation of CFD models, and these test flows can provide experimental data which permit validation of CFD models very close to the true flight conditions.

Chapter 11

Recommendations for Further Work

In regards to expansion tubes in general, and simulating scramjet test flows specifically, recommendations for further work include the following:

- *Develop improved Pitot measurement techniques.* High Mach number scramjet test flows present a very harsh environment for Pitot pressure measurements. Improvements need to be made in terms of probe survivability, response time, and consistency. Mechanical/aerodynamic effects specific to the probe need to be identified and quantified, so that the true test flow properties can be determined. Even if very high quality Pitot measurements are not practical for routine measurements (in terms of both cost and effort), it would be of immense benefit to achieve some ‘gold standard’ measurements which could be used as a calibration basis for other probes. This could possibly end the ongoing conjecture about how much measured unsteadiness should be attributed to the probe, as opposed to the test flow itself.
- *Incorporate full piston dynamics in the 2-D axisymmetric CFD.* The CFD results can only be considered truly representative if they include all of the important flow processes. The Eilmer3 code currently does not include piston dynamics, however this capability will be incorporated in future. In combination with increasing computing power, eventually full facility CFD models, including full piston dynamics, should be used to compute the expansion tube test flows. Although 3-D flow processes may also be important, it is not considered practical to attempt 3-D expansion tube CFD analysis in the foreseeable future.
- *Run finer grid CFD simulations to resolve boundary layers and transient flow features.* The present study has demonstrated reasonable convergence of average test core flow properties during the test time. However, it has not been

demonstrated that the nominal grid has fully resolved the boundary layers or transient flow features, and the computed accelerator gas static pressures were inconsistent with experimental measurements at Mach 12.5 and 15. Future studies could make use of inevitable future improvements in computing power to perform improved CFD calculations which have converged transient and spatial flow properties.

- *Conduct further analysis of computed flow properties outside of the core flow.* Chapters 8 and 9 do not present detailed analyses of predicted flow properties *within* the large boundary layer of the acceleration tube, including boundary layer transition, and further work could entail examining the numerical results in more detail in this region of the flow.
- *Develop an accurate CFD primary diaphragm rupture model.* This investigation did not undertake a detailed quantitative investigation of the primary diaphragm rupture process as applied to impulse facility flows. It is expected that a better diaphragm rupture model can be developed once full piston dynamics are included in the Eilmer3 code. Finer resolution experimental shock speed measurements in the vicinity of the primary diaphragm would be essential for validation of such a model.
- *Develop a Mylar-free secondary and tertiary diaphragm.* Scramjet test flows have high initial fill pressures, and as such, require relatively large amounts of Mylar at the secondary and tertiary diaphragm stations. This Mylar aerodynamically interferes with the flow processes, contaminates the flow, and introduces a large amount of debris which eventually impact the test section. A major development in expansion tubes would be a secondary/tertiary diaphragm station which did not contaminate or introduce debris to the test flow, nor present excessive aerodynamic interference with flow processes.
- *Develop a lightweight piston for the X3 expansion tube.* The X3 free-piston driver currently comprises a 200 kg aluminium piston and a Ø500 mm, 14.5 m long compression tube. In order to achieve high performance tuned free-piston driver conditions, a much lighter piston will be required. A filament wound carbon composite piston with foam core is planned for X3, with $m_p \approx 50$ kg. To permit a broader range of operating conditions, the piston may have brakes incorporated into it. In the shorter term the existing aluminium piston will be used. It is estimated that its mass can be reduced to $m_p \approx 120$ kg. In combination with orifice plates at the driver area change, this should permit improved levels of performance prior to commissioning of the

composite piston.

It is also noted that Chapter 5 did not attempt a detailed analysis of the dynamic loading of X2’s lightweight piston. It is recommended that the future stress analysis of X3’s piston would examine the dynamic load case in more detail. This might start by using a simple 1-D analytical model in order to establish the relationship between the loading history and peak stresses for the dynamic loading case. These results could then be compared to a more accurate analysis using an explicit finite element code.

- *Test scramjets in the X3 expansion tube.* Following the successful achievement of high Mach number scramjet flows in X2, the next step is to scale up these conditions to the X3 expansion tube facility. The larger size of X3 should increase the test times and core flow diameter to the levels required for scramjet testing.
- *Develop new hypersonic nozzles.* The present study used the X2 Mach 10 nozzle, which is designed to expand a Mach 7.3 inlet flow to Mach 10 at the nozzle exit. Contoured hypersonic nozzles are optimised for a single Mach number, and subsequently their performance can increasingly deteriorate at off-design conditions. Further, the size of the expanded flow depends on the area ratio of the nozzle; to achieve a bigger core flow, a larger area ratio is required. For these reasons future work may involve designing new nozzles for X2 and X3 for different exit Mach numbers.

References

- [1] D. Andreadis. Scramjet Engines Enabling the Seamless Integration of Air and Space Operations. *The Industrial Physicist*, Aug/Sep 2004.
- [2] W.H. Heiser and D.T. Pratt. *Hypersonic Airbreathing Propulsion*. AIAA education series. American Institute of Aeronautics and Astronautics, Washington, D.C., 1994.
- [3] E.T. Curran. Scramjet Engines: The First Forty Years. *Journal of Propulsion and Power*, 17(6):1138–1148, 2001.
- [4] M.R. Tetlow and C.J. Doolan. Comparison of Hydrogen and Hydrocarbon-Fuelled Scramjet Engines for Orbital Insertion. *Journal of Spacecraft and Rockets*, 44(2):365–373, 2007.
- [5] D.L. Kors. Design considerations for combined air breathing-rocket propulsion systems. *AIAA 2nd International Aerospace Planes Conference, 29-31 Oct 1990, Orlando, FL*, pages 12–1 to 12–13, 1990.
- [6] F.S. Billig. Research on Supersonic Combustion. *Journal of Propulsion and Power*, 9(4):499–514, 1993.
- [7] A. Kumar, J.P. Drummond, C.R. McClinton, and J.L. Hunt. Research in Hypersonic Airbreathing Propulsion at the NASA Langley Research Center. In *ISABE-2001: Invited Lecture 4. Presented at the Fifteenth International Symposium on Airbreathing Engines, Bangalore, India, Sep 2-7*, 2001.
- [8] R.T. Voland, L.D. Huebner, and C.R. McClinton. X-43A Hypersonic Vehicle Technology Development. *Acta Astronautica*, 59(1-5):181–191, 2006.
- [9] C.R. McClinton. X-43 Scramjet Power Breaks the Hypersonic Barrier, Dryden Lectureship in Research for 2006. In *44th AIAA Aerospace Sciences Meeting and Exhibit, 9 - 12 Jan, Reno, Nevada*, AIAA 2006-1, 2006.

- [10] M.K. Smart and M.R. Tetlow. Orbital Delivery of Small Payloads Using Hypersonic Airbreathing Propulsion. *Journal of Spacecraft and Rockets*, 46(1):117–125, 2009.
- [11] E.C. Semple. Trajectory and Performance of an Expendable Scramjet Powered Launcher. In *The Institution of Engineers, Australia, Seventh National Space Engineering Symposium, Canberra, 21-26 Sep*, 1992.
- [12] P. L. Moses, K. A. Bouchard, R. F. Vause, S. Z. Pinckney, S. M. Ferlemann, C. P. Leonard, L. W. Taylor III, J. S. Robinson, J. G. Martin, D. H. Petley, and J. L. Hunt. An Airbreathing Launch Vehicle Design with Turbine-Based Low-Speed Propulsion and Dual Mode Scramjet High-Speed Propulsion. In *9th International Space Planes and Hypersonic Systems and Technologies Conference and 3rd Weakly Ionized Gases Workshop, Nov 1-5, Norfolk, VA*, 1999.
- [13] C.E. Cockrell Jr., A.H. Auslender, R.W. Guy, C.R. McClinton, and S.S. Welch. Technology Roadmap for Dual-Mode Scramjet Propulsion to Support Space-Access Vision Vehicle Development. In *11th AIAA/AAAF International Space Planes and Hypersonic Systems and Technologies Conference 29 Sep - 4 Oct, Orleans, France*, AIAA 2002-5188, 2002.
- [14] K. Itoh, H. Tanno, T. Sunami, and N. Chinzei. HyShot Scramjet Engine Test. Technical report, JAXA Ramjet Propulsion Center, 2003.
- [15] M. Smart. Scramjets. *The Aeronautical Journal of the Royal Aeronautical Society*, 111(1124):605–619, 2007.
- [16] M. A. Dornheim. Mach 10, But Now What?
 $\cdot \text{http://www.aviationweek.com/aw/jsp_includes/articlePrint.jsp?headLine=}$
 $\text{NASA\%27s\%20X-43A\%20Hyper-X\%20Reaches\%20Mach\%2010t\&storyID=}$
 $\text{news/11224wna.xml (downloaded Nov 28, 2008)}$, Nov 23, 2004.
- [17] Anonymous. Revolutionary jet engine tested.
 $\text{http://news.bbc.co.uk/go/pr/fr/-/2/hi/science/nature/4832254.stm}$
 $(\text{downloaded 19/12/2011})$, 2006.
- [18] High speed success at Woomera (DSTO Media Release Number: PARLSEC57/07). $\text{http://www.dsto.defence.gov.au/news/5118/}$ ($\text{downloaded 19/12/2011}$), 2007.

- [19] HyShot. <http://www.uq.edu.au/hypersonics/?page=19501> (*downloaded 19/12/2011*), 2011.
- [20] K. Barnstorff. X-51A Makes Longest Scramjet Flight. <http://www.nasa.gov/topics/aeronautics/features/X-51A.html> (*downloaded Feb 1, 2010*), May 28, 2010.
- [21] G. Warwick. X-51A Team Eyes Results Of Scramjet Flight. http://www.aviationweek.com/aw/generic/story_generic.jsp?channel=awst&id=news/awst/2010/05/31/AW_05_31_2010_p27-230271.xml (*downloaded Feb 1, 2010*), Jun 1, 2010.
- [22] G. Anderson, A. Kumar, and J. Erdos. Progress in Hypersonic Combustion Technology with Computation and Experiment. In *AIAA Second International Aerospace Planes Conference, 29-31 Oct, Orlando, FL*, AIAA-90-5254, 1990.
- [23] M.J. Lewis. Significance of Fuel Selection for Hypersonic Vehicle Range. *Journal of Propulsion and Power*, 17(6):8, 2001.
- [24] L .H. Townend. The domain of the scramjet. *Phil. Trans. R. Soc. Lond.*, 357(1759):2317–2334, 1999.
- [25] P.J. Waltrup. Upper Bounds on the Flight Speed of Hydrocarbon-Fuelled Scramjet-Powered Vehicles. *Journal of Propulsion and Power*, 17(6):1199–1204, 2001.
- [26] D.W. Bogdanoff. Advanced Injection and Mixing Techniques for Scramjet Combustors. *Journal of Propulsion and Power*, 10(2):183–190, 1994.
- [27] J.M. Seiner, S.M. Dash, and D.C. Kenzakowski. Historical Survey on Enhanced Mixing in Scramjet Engines. *Journal of Propulsion and Power*, 17(6):1273–1286, 2001.
- [28] A.D. Gardner, A. Paull, and T.J. McIntyre. Upstream porthole injection in a 2-D scramjet model. *Shock Waves*, 11(5):369–375, 2002.
- [29] J.L. Hunt and J.G. Martin. *Rudiments and Methodology for Design and Analysis of Hypersonic Air-Breathing Vehicles*. In: *Scramjet Propulsion*, volume 189 of *Progress in Astronautics and Aeronautics*, chapter 15, pages 939–978. AIAA, Reston, Virginia, 2000.

- [30] J.W. Hicks. Flight Testing of Airbreathing Hypersonic Vehicles. *NASA-TM-4524*, 1993.
- [31] T. Kimura and K. Sawada. Three-Stage Launch System with Scramjets. *Journal of Spacecraft and Rockets*, 36(5):675–680, 1999.
- [32] M. Ardema, J.V. Bowles, and T. Whittaker. Optimal Trajectories for Hypersonic Launch Vehicles. *Dynamics and Control*, 4(4):337–347, 1994.
- [33] J.R. Olds and I.A. Budianto. Constant Dynamic Pressure Trajectory Simulation with POST. In *36th Aerospace Sciences Meeting & Exhibit, Jan 12-15, Reno, NV*, pages 1–12, AIAA 98-0302, 1998.
- [34] A. Ferri. Mixing-Controlled Supersonic Combustion. *Annual Review of Fluid Dynamics*, 5(1):301–338, Jan 1973.
- [35] R.G. Morgan. A Practical Flight Plan for an Aerospaceplane. *Proceedings of the Fifth National Space Engineering Symposium, Canberra, 27 Nov - 1 Dec*, 1989.
- [36] M.R. Tetlow and C.J. Doolan. Orbital Payload Delivery Using Hydrogen and Hydrocarbon Fuelled Scramjet Engines. In *IEEEAC paper #1058*, 2006.
- [37] J.D. Anderson Jr. *Introduction to Flight*. McGraw-Hill Book Company, New York, U.S.A., 5th edition, 2004.
- [38] H.G. Hornung. 28th Lanchester Memorial Lecture - Experimental real-gas hypersonics. *Aeronautical Journal of Fluid Mechanics*, 92(920):379–389, 1988.
- [39] R.J. Stalker and M. Pulsonetti. Experiments on Scaling of Supersonic Combustion. *Research Report No: 2004/13*, The University of Queensland, 2004.
- [40] R.J. Stalker, A. Paull, D.J Mee, R.G. Morgan, and P.A. Jacobs. Scramjets and shock tunnels - The Queensland experience. *Progress in Aerospace Sciences*, 41(6):471–513, 2005.
- [41] W. Chinitz, J.I. Erdos, O. Rizkalla, G.Y. Anderson, and D. Bushnell. Facility Opportunities and Associated Stream Chemistry Considerations for Hypersonic Air-Breathing Propulsion. *Journal of Propulsion and Power*, 10(1):6–17, 1994.
- [42] U.S. Standard Atmosphere, 1976.

- [43] S. Gordon and B.J. McBride. Computer Program for Calculation of Complex Chemical Equilibrium Compositions and Applications. *NASA Reference Publication 1311*, Oct, 1994.
- [44] J.I. Erdos and R. Bakos. Prospects For a Quiet Hypervelocity Shock-Expansion Tunnel. In *18th AIAA Aerospace Ground Testing Conference, Jun 20-23, Colorado Springs, CO*, AIAA Paper 94-2500, 1994.
- [45] G.Y. Anderson, C.R. McClinton, and J.P. Weidner. *Scramjet Propulsion*, chapter Scramjet Performance. Progress in Astronautics and Aeronautics, Editors: E.T. Curran and S.N.B. Murthy. AIAA, Reston, Virginia, 2000.
- [46] C.R. McClinton. High Speed/Hypersonic Aircraft Propulsion Technology Development. *NATO Report RTO-EN-AVT-150*, 2008.
- [47] M.R. Gruber and M.A. Hagenmaier. Simulating Inlet Distortion Effects in a Direct-Connect Scramjet Combustor. In *42nd AIAA/ASME/SAE/ASEE Joint Propulsion Conference & Exhibit, 9 - 12 Jul 2006, Sacramento, California*, AIAA 2006-4680, 2006.
- [48] F.K. Lu and D.E. Marren. *Advanced Hypersonic Test Facilities*, volume 198 of *Progress in Astronautics and Aeronautics*. AIAA, Reston, Virginia, 2002.
- [49] M.S. Holden. *Flight Experiments for Hypersonic Vehicle Development. Educational Notes RTO-EN-AVT-130, Paper 1*. Neuilly-sur-Seine, France, chapter Aero thermal and Propulsion Ground Testing That Can Be Conducted to Increase Chances for Successful Hypervelocity Flight Experiments, pages 1-1 to 1-36. 2007.
- [50] R.J. Bakos, J. Tamagno, O. Rizkalla, M.V. Pulsonetti, W. Chinitz, and J.I. Erdos. Hypersonic Mixing and Combustion Studies in the Hypulse Facility. *Journal of Propulsion and Power*, 8(4):900–906, Jul-Aug 1992.
- [51] Benjamin S. Stewart. *Predicted scramjet testing capabilities of the proposed RHYFL-X expansion tube*. PhD thesis, Centre for Hypersonics, Department of Mechanical Engineering, University of Queensland, 2004.
- [52] K.E. Fischer and K.E. Rock. Calculated Effects of Nitric Oxide Flow Contamination on Scramjet Performance. In *AIAA/ASME/SAE/ASEE Joint Propulsion Conference and Exhibit, Jul 10-12, San Diego, CA*, AIAA 95-2524, 1995.

- [53] DCSCTF Brochure. http://hapb-www.larc.nasa.gov/Public/Documents/DCSCTF_Brochure_V1.0.pdf (downloaded 19/12/2011).
- [54] S. Borrelli and C. Bruno. SCIROCCO Air-Breathing Propulsion Simulation Capabilities. In *4th European Symposium on Aerothermodynamics for Space Applications, 15-18 Oct, Capua, Italy*, 2001.
- [55] John D. Anderson. *Modern Compressible Flow with Historical Perspective*. McGraw Hill, 3rd edition, 2003.
- [56] R.G. Morgan. A review of the use of expansion tubes for creating superorbital flows. In *35th Aerospace Sciences Meeting & Exhibit, Reno, NV*, AIAA 97-0279, 1997.
- [57] R.G. Morgan. *Handbook of Shock Waves, Volume 1*, chapter 4.3 Free-Piston Driven Expansion Tubes, pages 603–622. Academic Press, 2001.
- [58] M. McGilvray. *The use of expansion tube facilities for scramjet testing*. PhD thesis, Centre for Hypersonics, Department of Mechanical Engineering, University of Queensland, Jan 2008.
- [59] K. Itoh. *Advanced Hypersonic Test Facilities*, volume 198 of *Progress in Astronautics and Aeronautics*, chapter Characteristics of the HEST and its Applicability for Hypersonic Aerothermodynamic and Scramjet Research, pages 239–253. AIAA, 2002.
- [60] Benjamin S. Stewart, Richard G. Morgan, and Peter A. Jacobs. Rocketdyne Hypersonic Flow Laboratory as High-Performance Expansion Tube for Scramjet Testing. *Journal of Propulsion and Power*, 19(1):98–103, Jan-Feb 2003.
- [61] R.J. Bakos and J.I. Erdos. Options for Enhancement of the Performance of Shock-Expansion Tubes and Tunnels. In *33rd Aerospace Sciences Meeting and Exhibit, Jan 9-12, Reno, NV*, AIAA 95-0799, 1995.
- [62] R.G. Morgan and R.J. Stalker. Double Diaphragm Driven Free Piston Expansion Tube. In *18th International Symposium on Shock Waves, Jul 21-26, Sendai, Japan*, 1991.
- [63] A. Paull and R.J. Stalker. *Scramjet Testing in the T3 and T4 Hypersonic Impulse Facilities*. In: *Scramjet Propulsion*, chapter 1, pages 1–46. AIAA, 2000.

- [64] K. Itoh, S. Ueda, H. Tanno, T. Komuro, and K. K. Sato. Hypersonic aerothermodynamic and scramjet research using high enthalpy shock tunnel. *Shock Waves*, 12(2):93–98, 2002.
- [65] R.J. Bakos, R.G. Morgan, and J. Tamagno. Effects of Oxygen Dissociation on Hypervelocity Combustion Experiments. In *AIAA 17th Aerospace Ground Testing Conference, Jul 6-8, Nashville, TN*, AIAA-92-3964, 1992.
- [66] O. Rizkalla, Robert J. Bakos, Wallace Chinitz, Maria V. Pulsonetti, and John I. Erdos. Use of an Expansion Tube to Examine Scramjet Combustion at Hypersonic Velocities. In *AIAA/ASME/SAE/ASEE 25th Joint Propulsion Conference, Jul 10-12, Monterey, CA*, AIAA 89-2536, 1989.
- [67] C.J. Jachimowski. An Analysis of Combustion Studies in Shock Expansion Tunnels and Reflected Shock Tunnels. *NASA TP-3224*, NASA Langley Research Center, Hampton, VA 23665-5225, Jul, 1992.
- [68] R.J. Bakos, A. Castrogiovanni, J.F. Calleja, L. Nucci, and J.I. Erdos. Expansion of the Scramjet Ground Test Envelope of the HYPULSE Facility. *Proceedings of the 7th International Space Planes and Hypersonic Systems and Technologies Conference, Norfolk, VA, November 18-22*, 1996.
- [69] M. McGilvray, R. Kirchhartz, and T. Jazra. Comparison of mach 10 scramjet measurements from different impulse facilities. *AIAA Journal*, 48(8):1647–1651, 2010.
- [70] Robert L. Trimpli. A preliminary theoretical study of the expansion tube, a new device for producing high-enthalpy short-duration hypersonic gas flows. *NASA Technical Report R-133*, 1962.
- [71] Michael Paul Scott. *Development and Modelling of Expansion Tubes*. PhD thesis, Centre for Hypersonics, Department of Mechanical Engineering, University of Queensland, 2006.
- [72] A. Paull and R.J. Stalker. Test flow disturbances in an expansion tube. *Journal of Fluid Mechanics*, 245:493–521, 1992.
- [73] Daniel F. Potter, Rowan J. Gollan, Troy Eichmann, Tim J. McIntyre, Richard G. Morgan, and Peter A. Jacobs. Simulation of CO₂-N₂ expansion tunnel flows for the study of radiating shock layers. In *46th AIAA Aerospace Sciences Meeting and Exhibit 7-10 Jan, Reno, Nevada*, AIAA 2008-1280, 2008.

- [74] Con Doolan and Richard Morgan. Test-time Optimization of a Large Scale Hypervelocity Expansion Tunnel. In *Eighth National Space Engineering Symposium, Barton, ACT*, 1993.
- [75] R. Morgan. *Handbook of Shock Waves, Volume 1*, chapter 4.2 Free Piston-Driven Reflected Shock Tunnels, pages 587–601. Academic Pres, 2001.
- [76] C.J. Doolan and R.G. Morgan. A two-stage free-piston driver. *Shock Waves*, 9(4):239–249, 1999.
- [77] R. J. Stalker. Modern developments in hypersonic wind tunnels. *The Aeronautical Journal*, 110(1103):21–39, 2006.
- [78] M. Holden. Calibration and Validation Studies in the LENS Facility. *Technical Report AFOSR-TR 94 0161*, Calspan-UB Research Center Buffalo NY, 1994.
- [79] R.A. Alpher and D.R. White. Flow in shock tubes with area change at the diaphragm section. *Journal of Fluid Mechanics*, 3(5):457–470, 1958.
- [80] B.D. Henshall. The Use of Multiple Diaphragms in Shock Tubes. *A.R.C. Technical Report C.P. No. 291*, Ministry of Supply, Aeronautical Research Council, 1956.
- [81] R.J. Stalker and D.L. Plumb. Diaphragm-type Shock Tube for High Shock Speeds. *Nature*, 218(5143):789–790, May 1968.
- [82] P.A. Jacobs, R.C. Rogers, E.H. Weidner, and R.D. Bittner. Flow Establishment in a Generic Scramjet Combustor. *Journal of Propulsion and Power*, 8(4):890–899, 1992.
- [83] Margaret Wegener, Mark Sutcliffe, and Richard Morgan. Optical study of a light diaphragm rupture process in an expansion tube. *Shock Waves*, 10(3):167–178, 2000.
- [84] R.J. Bakos and R.G. Morgan. Chemical Recombination in an Expansion Tube. *AIAA Journal Technical Note*, 32(6):4, 1994.
- [85] T. Furukawa, T. Aochi, and Akihiro Sasoh. Expansion Tube Operation with Thin Secondary Diaphragm. *AIAA Journal*, 45(1):214–217, 2007.
- [86] J.L. Shinn and C.G. Miller III. Experimental Perfect-Gas Study of Expansion-Tube Flow Characteristics. *NASA Technical Paper 1317*, 1978.

- [87] G.T. Roberts, M.A. Kendall, and R.G. Morgan. Shock-diaphragm interaction in expansion tubes. In *21st International Symposium on Shock Waves, Jul 20-25, Great Keppel Island, Australia*, 1997.
- [88] K.J. Weilmuenster. A Self-Opening Diaphragm for Expansion Tubes and Expansion Tunnels. *AIAA Journal*, 8(3):573–574, 1970.
- [89] G.J. Wilson, M.A. Sussman, and R.J. Bakos. Numerical Simulations of the Flow in the HYPULSE Expansion Tube. *NASA Technical Memorandum 110357*, NASA Ames Research Center, Moffett Field, California, Jun, 1995.
- [90] P.A. Jacobs. L1d: A computer program for the simulation of transient-flow facilities. *Report 1/99*, Department of Mechanical Engineering, The University of Queensland, 1999.
- [91] C.D. Donaldson and R.D. Sullivan. The effect of wall friction on the strength of shock waves in tubes and hydraulic jumps in channels. Technical Report NACA-TN-1942, NASA Langley Research Center, 1949.
- [92] R.N. Hollyer Jr. A Study of Attenuation in the Shock Tube. Technical report, University of Michigan Eng. Research Inst. Rept. Project M720-4, 1953.
- [93] R.E. Duff. Shock-Tube Performance at Low Initial Pressure. *The Physics of Fluids*, 2(2):207–216, 1959.
- [94] H. Mirels. Laminar Boundary Layer Behind Shock Advancing into Stationary Fluid. *NACA Technical Report TN 3401*, 1955.
- [95] H. Mirels. Attenuation in a Shock Tube Due to Unsteady-Boundary-Layer Action. *NACA Technical Report 1333*, 1957.
- [96] H. Mirels. Laminar Boundary Layer Behind a Strong Shock Moving Into Air. *NASA Technical Report TN D-291*, Feb, 1961.
- [97] H. Mirels. Boundary Layer Behind Shock or Thin Expansion Wave Moving Into Stationary Fluid. *NACA Technical Report TN 3712*, 1956.
- [98] H. Mirels and W.H. Braun. Nonuniformities in Shock-Tube Flow Due to Unsteady-Boundary-Layer Action. *NACA Technical Report TN 4021*, 1957.
- [99] H. Mirels. Test Time in Low-Pressure Shock Tubes. *The Physics of Fluids*, 6(9):1201–1214, 1963.

- [100] H. Mirels. Shock Tube Test Time Limitation Due to Turbulent-Wall Boundary Layer. *AIAA Journal*, 2(1):84–93, 1963.
- [101] E.L. Petersen and R.K. Hanson. Improved Turbulent Boundary-Layer Model for Shock Tubes. *AIAA Journal*, 41(7):1314–1322, 2003.
- [102] A. Paull and R.J. Stalker. Theoretical and Experimental Test Times Available in an Expansion Tube. In *10th Australasian Fluid Mechanics Conference, Melbourne, Australia*, 1990.
- [103] F.R. Livingstone. Experimentally Measured Effects of the Wall Boundary Layer on Shock-Tube Performance. *Technical Report No. 32-714*, Jet Propulsion Laboratory, California Institute of Technology, Pasadena, California, 1965.
- [104] A. Ben-Yakar and R.K. Hanson. Characterization of Expansion Tube Flows for Hypervelocity Combustion Studies. *Journal of Propulsion and Power*, 18(4):943–952, 2002.
- [105] M. McGilvray, J.M. Austin, M. Sharma, P.A. Jacobs, and R.G. Morgan. Diagnostic modelling of an expansion tube operating condition. *Shock Waves*, 19(1):59–66, 2009.
- [106] R.J. Bakos, J.F. Calleja, J.I. Erdos, A.H. Auslender, M.A. Sussman, and G.J. Wilson. Design, Calibration and Analysis of a Tunnel Mode of Operation for the HYPULSE Facility. In *19th AIAA Advanced Measurement and Ground Testing Technology Conference, Jun 17-20, New Orleans, LA*, AIAA 96-2194, 1996.
- [107] B.S. Stewart, P.A. Jacobs, and R.G. Morgan. The Starting Process of an Expansion Tube Nozzle. In *23rd International Symposium on Shock Waves, 23-27 Jul, The University of Texas at Arlington, USA*, 2001.
- [108] R.S.M. Chue, R.J. Bakos, C.-Y. Tsai, and A. Betti. Design of a shock-free expansion tunnel nozzle in HYPULSE. *Shock Waves*, 13(4):261–270, 2003.
- [109] N.E. Hass, A.T. Shih, and R.C. Rogers. Mach 12 & 15 Scramjet Test Capabilities of the HYPULSE Shock-Expansion Tunnel. In *43rd AIAA Aerospace Sciences Meeting and Exhibit, 10-13 Jan, Reno, Nevada*, AIAA 2005-690, 2005.

- [110] Michael G. Davey. A Hypersonic Nozzle for the X3 Expansion Tube. Bachelor of Engineering Thesis, Department of Mechanical Engineering, University of Queensland, 2006.
- [111] M.P. Scott, R.G. Morgan, and P.A. Jacobs. A New Single Stage Driver for the X2 Expansion Tube. In *43rd AIAA Aerospace Sciences Meeting and Exhibition, 10-13 Jan, Reno, Nevada*, AIAA-2005-697, 2005.
- [112] M.P. Scott, P.A. Jacobs, and R.G. Morgan. Nozzle development for an expansion tunnel. In *International Symposium on Shock Waves, Jul 11-16, Beijing*, 2004.
- [113] Peter A. Jacobs. Shock Tube Modelling with L1d. *Research Report 13/98*, Department of Mechanical Engineering, The University of Queensland, Nov 1998.
- [114] P.A. Jacobs and R.J. Gollan. The Eilmer3 Code: User Guide and Example Book. *Mechanical Engineering Report 2008/07*, University of Queensland, 2009.
- [115] P.A. Jacobs. MB_CNS: A computer program for the simulation of transient compressible flows. *Report 10/96*, Department of Mechanical Engineering, The University of Queensland, Dec 18, 1996.
- [116] E. Zitzler, M. Launmanns, and S. Bleuler. *A Tutorial on Evolutionary Multi-objective Optimization*, chapter Lecture Notes in Economics and Mathematical Systems - Metaheuristics for Multiobjective Optimisation, pages 3–38. Springer-Verlag, 2004.
- [117] V. Stark. Implementation of simulated annealing optimization method for aplac circuit simulator. Master’s thesis, Electrical Engineering, Helsinki University of Technology, Espoo, Finland, 1996.
- [118] D. Gildfind. X2 Lightweight Piston Experimental Test Campaign, November 2009 to February 2010, Analysis and Observations. *Departmental Report Number 2010/04*, Division of Mechanical Engineering, School of Engineering, The University of Queensland, Australia, 2010.
- [119] R.J. Stalker. Use of Argon in a Free Piston Shock Tunnel. In *AIAA Plasmadynamics Conference, Monterey, California, Mar 2-4*, AIAA Paper No. 66-169, 1966.

- [120] R.J. Stalker. A Study of the Free-Piston Shock Tunnel. *AIAA Journal*, 5(12):2160–2165, 1967.
- [121] K. Itoh, S. Ueda, T. Komuro, K. Sato, M. Takahashi, H. Myajima, H. Tanno, and H. Muramoto. Improvement of a free piston driver for a high-enthalpy shock tunnel. *Shock Waves*, 8(4):215–233, 1998.
- [122] H. Tanno, K. Itoh, T. Komuro, and K. Sato. Experimental study on the tuned operation of a free piston driver. *Shock Waves*, 10(1):1–7, 2000.
- [123] H.G. Hornung and J. Belanger. Role and Techniques of Ground Testing for Simulation of Flows up to Orbital Speed. In *AIAA 16th Aerodynamic Ground Testing Conference, Seattle, WA*, AIAA 90-1377, 1990.
- [124] H.G. Hornung. The Piston Motion in a Free-Piston Driver for Shock Tubes and Tunnels. *GALCIT Report FM 88-1*, Graduate Aeronautical Laboratories, California Institute of Technology, Jan 1988.
- [125] R. J. Stalker. Personal communication, 27.04.2009.
- [126] C. Dennis. X2 Single Driver Solid Edge Drawing Set, Centre for Hypersonics, University of Queensland, Jul 2002.
- [127] David Gildfind. Stress Analysis of a New Lightweight Piston for X2. *Departmental Report Number 2009/16*, Division of Mechanical Engineering, School of Engineering, The University of Queensland, Australia, 2009.
- [128] U.S. Department of Defense - Military Handbook - MIL-HDBK-5G - Metallic Materials and Elements for Aerospace Vehicle Structures. 1998.
- [129] W.C. Young and R.G. Budynas. *Roark's Formulas for Stress and Strain*. McGraw Hill, Singapore, 7th edition, 2002.
- [130] D.S. Griffin. Inelastic and Creep Buckling of Circular Cylinders due to Axial Compression, Bending, and Twisting. Technical report, Westinghouse Electric Corporation, Advanced Reactors Division, Pittsburgh, P.A., 1973.
- [131] W. Johnson. *Impact Strength of Materials*. Edward Arnold, London, 1st edition, 1972.
- [132] R. Smerd, A.S. Winkler, C. Salisbury, M. Worswick, D. Lloyd, and M. Finn. High strain rate tensile testing of automotive aluminum alloy sheet. *International Journal of Impact Engineering*, 32(1-4):514–560, 2005.

- [133] Yunus A. Çengel and Michael A. Boles. *Thermodynamics: an engineering approach*. McGraw Hill, USA, 4th edition, 2002.
- [134] J.M. Gere and S.P. Timoshenko. *Mechanics of Materials*. Fourth S.I. Edition, Stanley Thornes, 1999.
- [135] T.J. McIntyre, I. Lourel, T.N. Eichmann, R.G. Morgan, P.A. Jacobs, and A.I. Bishop. An experimental expansion tube study of the flow over a toroidal ballute. *Mechanical Engineering Research Report No. 2001/06*, Centre for Hypersonics, The University of Queensland, Nov 15, 2001.
- [136] P. A. Jacobs. Numerical Simulation of Transient Hypervelocity Flow in an Expansion Tube. *Computers Fluids*, 23(1):77–101, 1994.
- [137] C.G. Miller. Operational Experience in the Langley Expansion Tube With Various Test Gases. *NASA Technical Memorandum 78637*, NASA Langley Research Center, Dec 1977.
- [138] R. Hillier, R.R. Boyce, S.A. Creighton, A. Fiala, A.P. Jackson, S.G. Mallinson, A.H. Sheikh, S. Soltani, and S. Williams. Development of some hypersonic benchmark flows using CFD and experiment. *Shock Waves*, 12(5):375–384, 2003.
- [139] C.J. Roy, W.L. Oberkampf, and M.A. McWherter-Payne. Verification and Validation for Laminar Hypersonic Flow Fields, Part 2: Validation. *AIAA Journal*, 41(10):1944–1954, 2003.
- [140] G.V. Candler and I. Nompelis. CFD Validation for Hypersonic Flight: Real Gas Flows. *Proceedings of the 40th AIAA Aerospace Sciences Meeting and Exhibit, Reno, NV, 14-17 Jan*, (RTO-TR-AVT-007-V3; AIAA 2002-0434), 2002.
- [141] J.G. Marvin. A CFD Validation Roadmap For Hypersonic Flows. *NASA Technical Memorandum 103935*, Ames Research Center, Moffett Field, California, 1992.
- [142] V. Wheatley, H.S. Chiu, P.A. Jacobs, M.N. Macrossan, D.J. Mee, and R.G. Morgan. Rarefied, superorbital flows in an expansion tube. *International Journal of Numerical Methods for Heat & Fluid Flow*, 14(4):512–537, 2004.
- [143] R.G. Morgan, T.J. McIntyre, P.A. Jacobs, D.R. Buttsworth, M.N. Macrossan, R.J. Gollan, B.R. Capra, A.M. Brandis, D. Potter, T. Eichmann,

C.M. Jacobs, M. McGilvray, D. van Diem, and M.P. Scott. Impulse facility simulation of hypervelocity radiating flows. *Proceedings of the 2nd International Workshop on Radiation of High Temperature Gases in Atmospheric Entry, 6-8 Sep, Rome, Italy*, 2007.

- [144] P.A. Jacobs, T.B. Silvester, R.G. Morgan, M.P. Scott, R.J. Gollan, and T.J. McIntyre. Superorbital expansion tube operation: Estimates of flow conditons via numerical simulation. *Proceedings of the 43rd AIAA Aerospace Sciences Meeting, 10-13 Jan, Reno, NV*, AIAA-2005-0694, 2005.
- [145] M. Wendt, M. Macrossan, P. Jacobs, and D. Mee. Pilot study for a rarefied hypervelocity test facility. *Proceedings of the 13th Australasian Fluid Mechanics Conference, Monash University, Melbourne, Australia, 13-18 Dec, 1998*.
- [146] B. Stewart, R.G. Morgan, P.A. Jacobs, and M. Hayne. Flow Establishment in Large-Scale High-Performance Expansion Tubes. *Proceedings of the AIAA/AAAF 11th International Space Planes and Hypersonic Systems and Technologies Conference, 29 Sep - 4 Oct, Orleans, France*, Paper No. 5239, 2002.
- [147] R.J. Gollan, C.M. Jacobs, P.A. Jacobs, R.G. Morgan, T.J. McIntyre, M.N. Macrossan, D.R. Buttsworth, T.N. Eichmann, and D.F. Potter. A simulation technique for radiating shock tube flows. *Proceedings of the 26th International Symposium on Shock Waves, Gottingen, Germany, Jul*, pages pp. 465–470, Springer, 2009, 2007.
- [148] A.J. Neely and R.G. Morgan. Flow Measurements and Calibration of a Superorbital Expansion Tube. *Proceedings of the 11th Australasian Fluid Mechanics Conference, University of Tasmania, Hobart, Australia, 14-18 Dec, 1992*.
- [149] A.J. Neely and R.G. Morgan. The Superorbital Expansion Tube concept, experiment and analysis. *Aeronautical Journal*, 98:97–105, 1994.
- [150] R.G. Morgan. Superorbital expansion tubes. *Proceedings of the 21st International Symposium on Shock Waves, Great Keppel Island, Australia, Jul 20-25, 1997*.

- [151] A.J. Neely and R.J. Stalker. Hypervelocity flows of argon produced in a free piston driven expansion tube. *Proceedings of the 18th International Symposium on Shock Waves, Sendai, Japan, 21-26 Jul*, 1991.
- [152] A.J. Neely, R.J. Stalker, and A. Paull. High enthalpy, hypervelocity flows of air and argon in an expansion tube. *Aeronautical Journal*, 95(946):175–186, Jun/Jul, 1991.
- [153] M.A. Sutcliffe. *The Use of an Expansion Tube to Generate Carbon Dioxide Flows Application to Martian Atmospheric Entry Simulation*. PhD thesis, The Department of Mechanical Engineering, the University of Queensland, 1999.
- [154] A. Sasoh, R.G. Morgan, B.N. Littleton, T.J. McIntyre, and A.I. Bishop. High-Enthalpy Expansion Tube Experiments with Gas Injection. *AIAA Journal*, 38(12):2253–2259, 2000.
- [155] B.R. Capra. *Aerothermodynamic Simulation of Subscale Models of the FIRE II and Titan Explorer Vehicles in Expansion Tubes*. PhD thesis, Division of Mechanical Engineering, School of Engineering, The University of Queensland, 2006.
- [156] Richard J. Goozée. *Simulation of a Complete Shock Tunnel Using Parallel Computer Codes*. PhD thesis, Division of Mechanical Engineering, the University of Queensland, 2003.
- [157] Paul Petrie-Repar. *Numerical Simulation of Diaphragm Rupture*. PhD thesis, Mechanical Engineering Department, University of Queensland, Dec 1997.
- [158] P.A. Jacobs, R.J. Gollan, A.J. Denman, B.T. O’Flaherty, D.F. Potter, P.J. Petrie-Repar, and I.A. Johnston. Eilmer’s Theory Book: Basic Models for Gas Dynamics and Thermochemistry. *Mechanical Engineering Report 2010/09*, The University of Queensland, Department of Mechanical and Mining Engineering, 2010.
- [159] P.A. Jacobs. Personal communication "Inflow for Drummond Shock-Reflection", Sep 2011.
- [160] M. McGilvray, P.A. Jacobs, R.G. Morgan, R.J. Gollan, and C.M. Jacobs. Helmholtz Resonance of Pitot Pressure Measurements in Impulsive Hypersonic Test Facilities. *AIAA Journal*, 47(10):2430–2439, Oct 2009.

- [161] Ames Research Staff. Equations, tables, and charts for compressible flow. *NACA Report 1135*, NACA Ames Aeronautical Laboratory, Moffett Field, Calif., 1953.
- [162] PCB Piezotronics. PCB pressure transducer technical information. http://wwwpcb.com/techsupport/tech_pres.php (downloaded 1 Feb 2012), 2012.
- [163] P.L. Walkter. Introduction to Air Blast Measurements. Part III: Guaranteeing that Validated Pressure Measurements are Acquired. *Technical Note TN-18, PRS-TN-18-1005*, http://wwwpcb.com/techsupport/docs/prs/TN_18_1005_Air_Blast_Part_3.pdf (downloaded 1 Feb 2012), 2005.
- [164] D.R. White. Influence of diaphragm opening time on shock-tube flows. *Journal of Fluid Mechanics*, 4(6):585–599, 1958.
- [165] C.G. Miller and J.J. Jones. Incident shock-wave characteristics in air, argon, carbon dioxide, and helium in a shock tube with unheated driver. *NASA TN D-8099*, Dec, 1975.
- [166] E.M. Rothkopf and W. Low. Shock formation distance in a pressure driven shock tube. *The Physics of Fluids*, 19(12):1885–1888, Dec 1976.
- [167] Zh. S. Duntsova, I. V. Ershov, V. T. Kireev, and E. I. Ruzavin. Calculation of Shock Wave Motion and Flow Parameters for a Noninstantaneous Shock Tube Diaphragm Opening. *Fluid Dynamics*, 4(2):81–87, Mar 1969.
- [168] G.A. Campbell, G.M. Kimber, and D.H. Napier. Bursting of diaphragms as related to the operation of shock tubes. *J. Sci. Instrum.*, 42:381–384, 1965.
- [169] C.J.S. Simpson, T.R.D. Chandler, and K.B. Bridgman. Effect on Shock Trajectory of the Opening Time of Diaphragms in a Shock Tube. *The Physics of Fluids*, 10(9):1894–1896, 1967.
- [170] J.E. Drewry and Z.A. WalentaDre. Determination of Diaphragm Opening-Times and Use of Diaphragm Particle Traps in a Hypersonic Shock Tube. *UTIAS Technical Note No. 90*, University of Toronto Institute for Aerospace Studies, 1965.

- [171] Y. Yamaki and J.R. Rooker. Experimental Investigation of Circular, Flat, Grooved and Plain Steel Diaphragms Bursting into a 30.5-Centimeter-Square Section. *NASA TM X-2549*, May, 1972.
- [172] F.L. Curzon and M.G.R. Phillips. Low attenuation shock tube: driving mechanism and diaphragm characteristics. *Canadian Journal of Physics*, 49(15):1982–1993, 1971.
- [173] V.A. Volkov, V.N. Parmon, and B.K. Tkachenko. Process of opening of an inelastic diaphragm in a shock tube. *PMTF - Zhurnal Prikladnoi Mekhaniki i Tekhnicheskoi Fiziki*, 18(4):509–509, Jul-Aug 1977.
- [174] R.S. Hickman, L.C. Farrar, and J.B. Kyser. Behavior of burst diaphragms in shock tubes. *The Physics of Fluids*, 18(10):1249–1252, Oct 1975.
- [175] D. Zeitoun, R. Brun, and M.-J. Valetta. Shock-tube flow computation including the diaphragm and boundary-layer effects. In *Shock Tubes and Waves - Proceedings of the 12th international Symposium on Shock Tubes and Waves, Jeryusalem, Jul 16-19*, 1979.
- [176] E.M. Rothkopf and W. Low. Diaphragm opening process in shock tubes. *The Physics of Fluids*, 17(6):1169–1173, Jun 1974.
- [177] E. Outa and K. Hayakawa K. Tajima. Shock tube flow influenced by diaphragm opening (two-dimensional flow near the diaphragm). In *10th International Symposium on Shock Waves and Shock Tubes, Kyoto Univ., Kyoto*, pages 312–319, 1975.
- [178] E.I. Vasil'ev and E.V. Danil'chuk. Numerical Solution of the Problem of Shock Tube Flow Development with Transverse Diaphragm Withdrawal. *Fluid Dynamics*, 29(2):270–276, 1994.
- [179] N. Satofuka. A Numerical Study of Shock Formation in Cylindrical and Two-Dimensional Shock Tubes. *Technical Report 451*, Institute of Space and Aeronautical Science, University of Tokyo, Japan, 1970.
- [180] J.-L. Cambier, S. Tokarcik, and D.K. Prabhu. Numerical simulations of unsteady flow in a hypersonic shock tunnel facility. In *AIAA 17th Aerospace Ground Testing Conference, Nashville, TN, Jul 6-8*, 1992.
- [181] P. Gaetani, A. Guardone, and G. Persico. Shock tube flows past partially opened diaphragms. *J. Fluid Mech.*, 602:267–286, 2008.

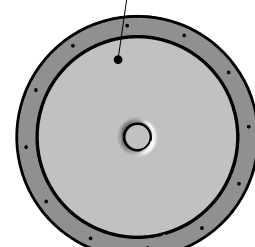
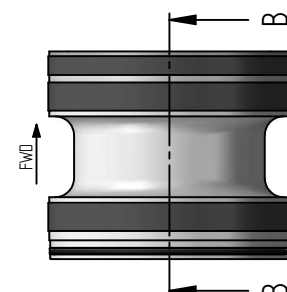
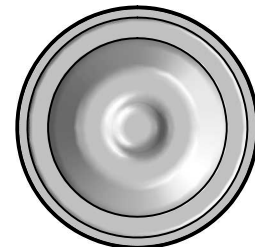
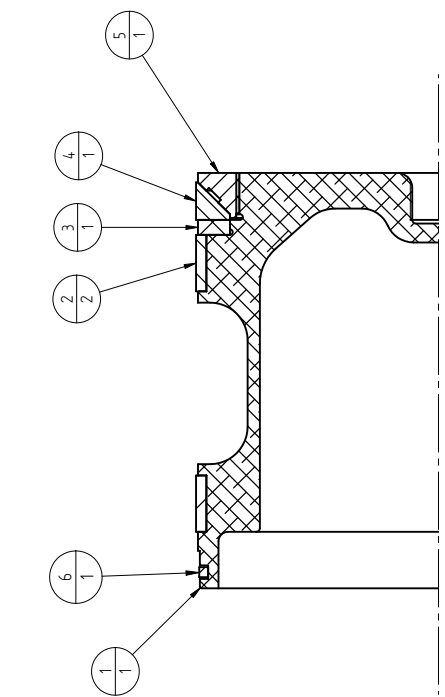
- [182] *Copper and copper alloys. 1st ed. ASM Speciality Handbook, ed. J.R. Davis.* 2001, USA: ASM International.
- [183] Material properties: Quadrant EPP Nylatron® LIG Nylon, Type 6, oil filled, cast. URL: <http://www.matweb.com/search/DataSheet.aspx?MatGUID=cf96115e154048048aa16c3035ef2761> (downloaded 19/06/2009).
- [184] J.R. Taylor. *An Introduction to Error Analysis - The Study of Uncertainties in Physical Measurements.* University Science Books, 1982.
- [185] C. Doolan. *A two-stage free-piston driver for hypervelocity expansion tubes.* PhD thesis, University of Queensland, St Lucia, Australia, 1997.
- [186] M. Hayne. *Hypervelocity flow over rearward facing steps.* PhD thesis, The University of Queensland, St Lucia, Australia, 2004.
- [187] D. Mee. Uncertainty analysis of the conditions in the test section of the T4 shock tunnel. *Departmental Report 4/93,* The University of Queensland, St Lucia, Australia, 1993.

Appendices

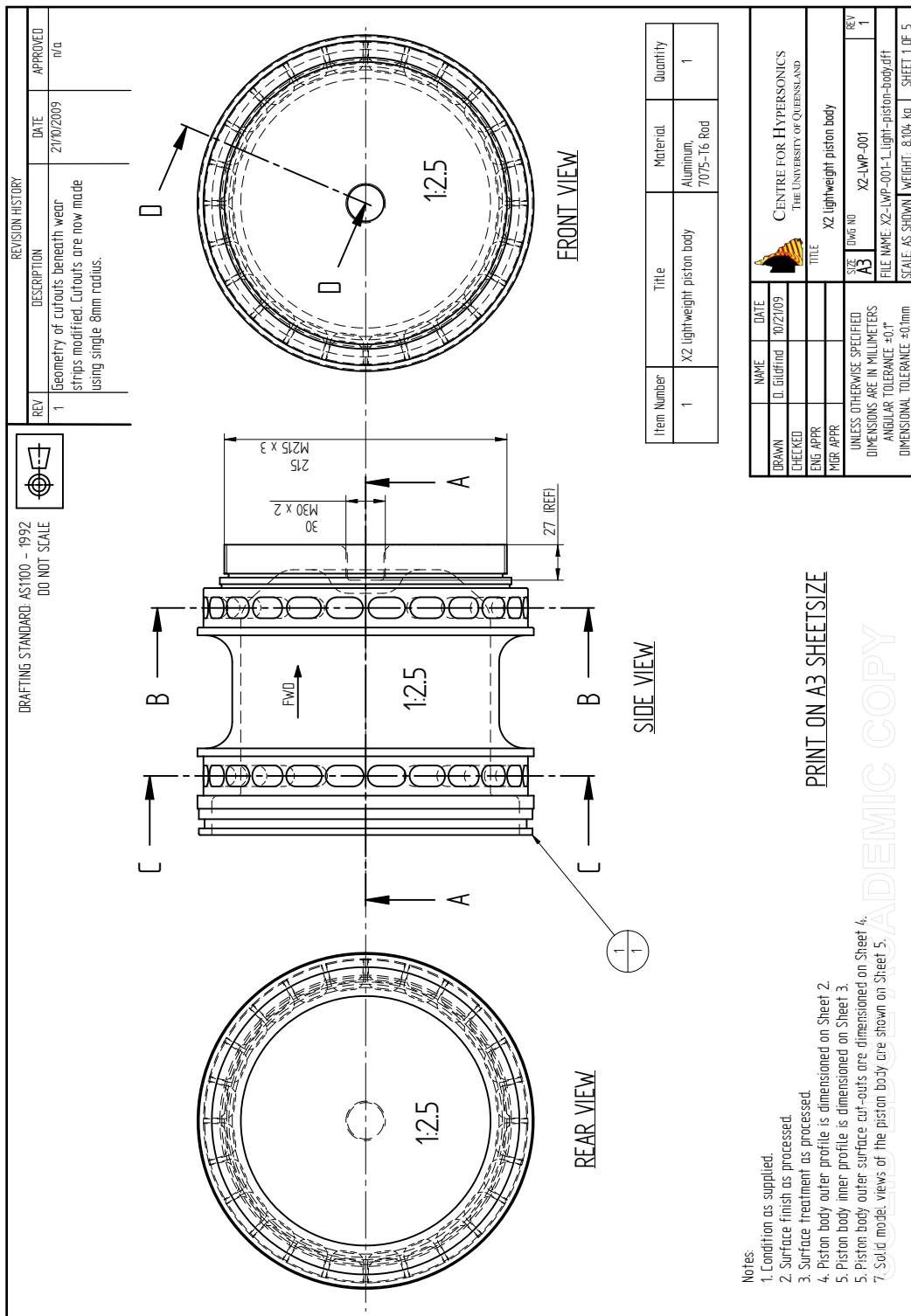
Appendix A

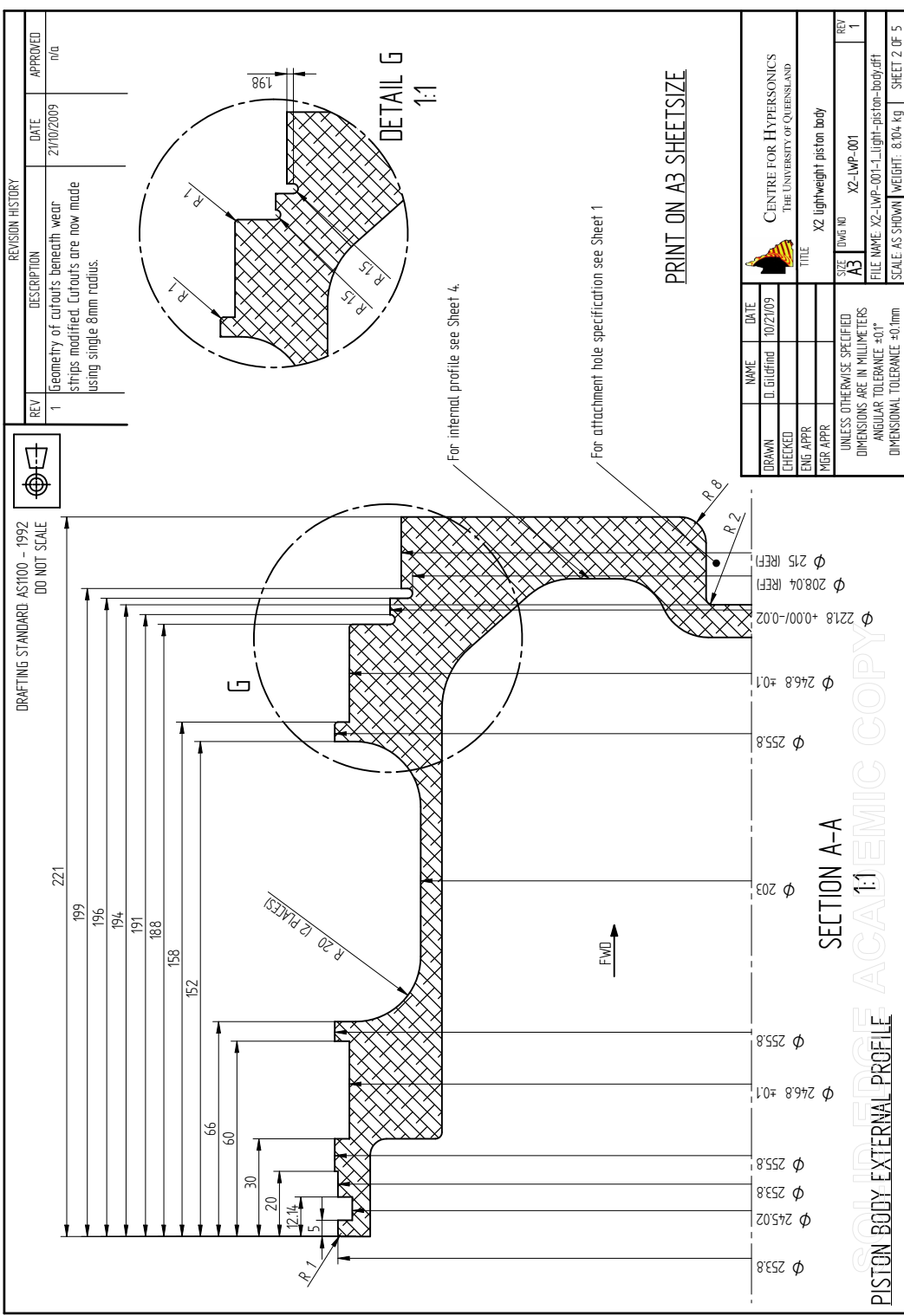
X2 Lightweight Piston Drawing Set

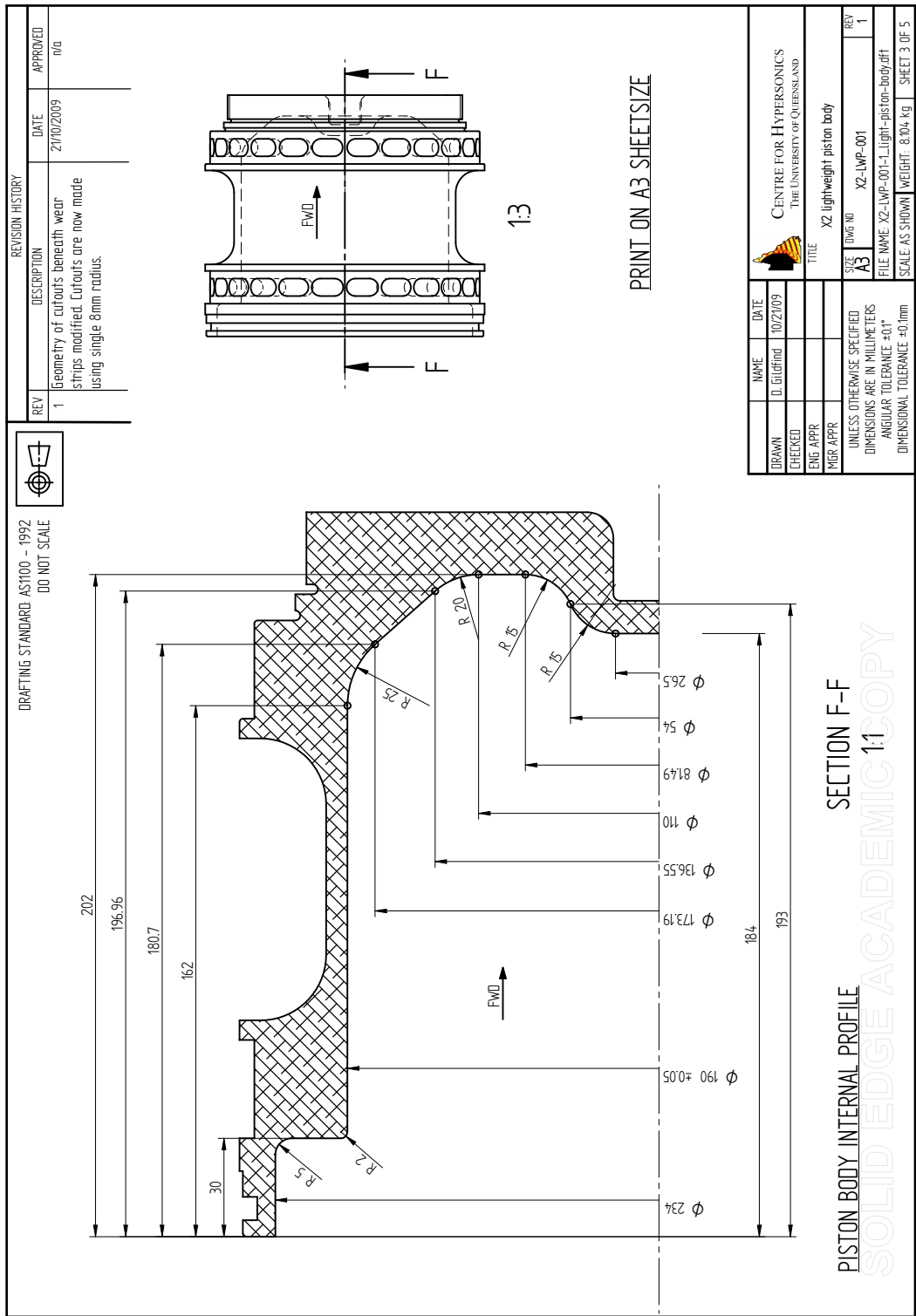
A.1 X2-LWP-000-1: X2 Lightweight Piston Assembly

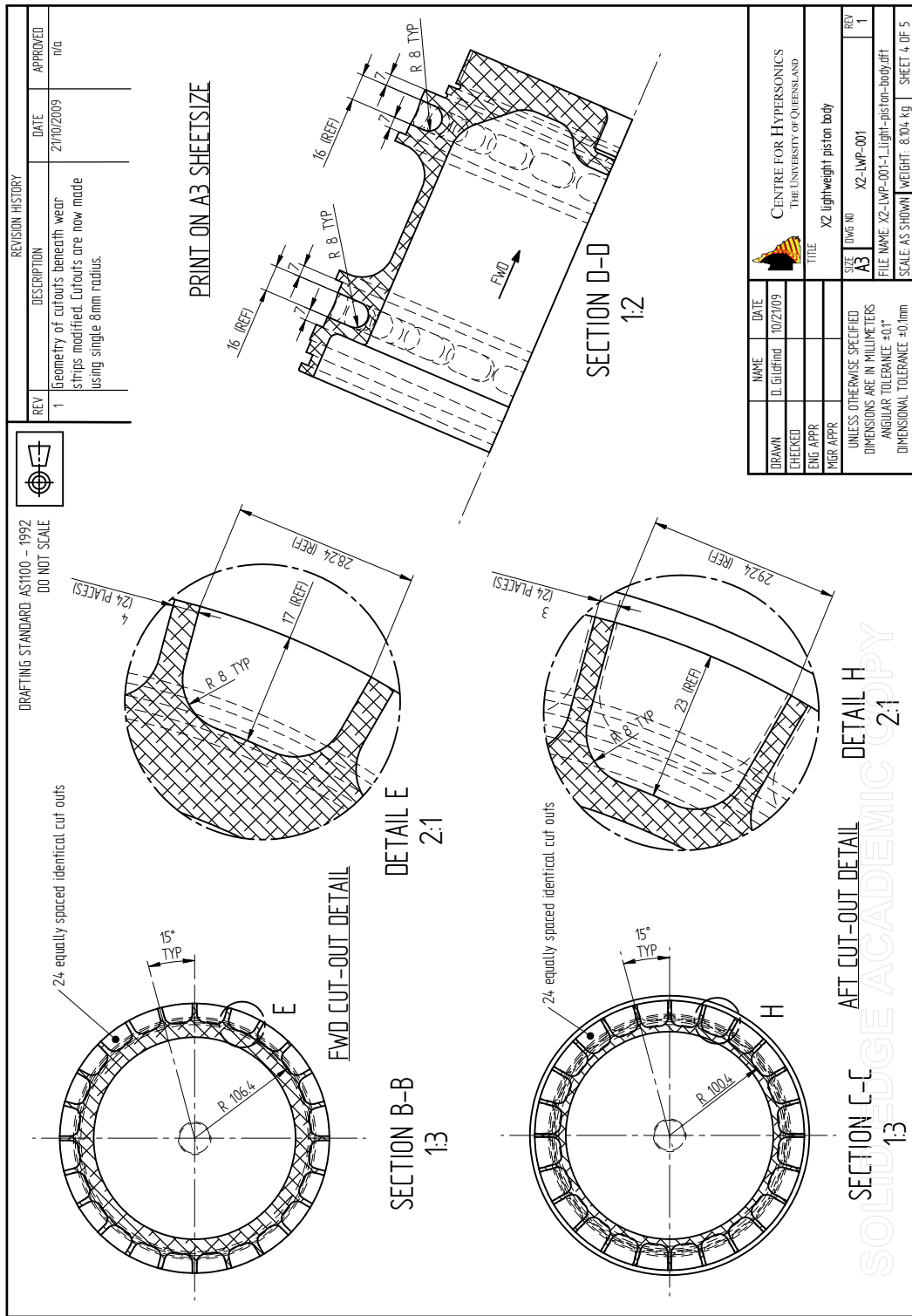
REVISION HISTORY																																																				
REV	DESCRIPTION	DATE	APPROVED																																																	
1	PNo. X2-LWP-001-0 changed to X2-LWP-001-1. Change involves modified cutout geometry. See drawing X2-LWP-001-1 for details.	21/10/2009	n/a																																																	
PRINT ON A3 SHEETSIZE																																																				
 <p>FRONT VIEW</p> <p>Machine to diameter which results in 0.1mm clearance within X2 tunnel (nominal $\varnothing 256.8$). Refer Note 3.</p>																																																				
 <p>SIDE VIEW</p> <p>B</p> <p>Fwd</p>																																																				
 <p>REAR VIEW</p> <p>B</p>																																																				
<p>Notes:</p> <ol style="list-style-type: none"> Assemble Items 1 to 6 as shown. If necessary, Item 2 (fwd and aft wear rings) may be installed by first cutting a 45° deg diagonal split in the ring. The split ring can then be located at the correct position on the piston and bonded together using commercial araldite. Item 2 (wear rings) and Item 4 (chevron seal) are nominally oversized by 1mm diameter compared to the nominal X2 tunnel bore diameter of 256.8mm. Following assembly of the piston, the wear rings and chevron seal are to be machined to a diameter which results in 0.1mm total diametrical clearance of the piston within the actual X2 tunnel. The piston should have a secure fit but still be able to slide freely within the tunnel. 																																																				
<table border="1"> <thead> <tr> <th>Item Number</th> <th>Document Number</th> <th>Revision</th> <th>Title</th> <th>Material</th> <th>Quantity</th> <th>Mass</th> </tr> </thead> <tbody> <tr> <td>1</td> <td>X2-LWP-001</td> <td>1</td> <td>X2 lightweight piston body</td> <td>Aluminum, 7075-T6 Rod</td> <td>1</td> <td>8104 kg</td> </tr> <tr> <td>2</td> <td>X2-LWP-002</td> <td>0</td> <td>Wear ring</td> <td>Oil Filled Nylon 6, Cast</td> <td>2</td> <td>0.297 kg</td> </tr> <tr> <td>3</td> <td>X2-LWP-003</td> <td>0</td> <td>Load ring</td> <td>Commercial Aluminum</td> <td>1</td> <td>0.285 kg</td> </tr> <tr> <td>4</td> <td>X2-LWP-004</td> <td>0</td> <td>Chevron seal</td> <td>Oil Filled Nylon 6, Cast</td> <td>1</td> <td>0.188 kg</td> </tr> <tr> <td>5</td> <td>X2-LWP-005</td> <td>0</td> <td>Bronze holder</td> <td>Aluminum Bronze C95810</td> <td>1</td> <td>1.789 kg</td> </tr> <tr> <td>6</td> <td>BS375</td> <td>n/a</td> <td>BS series o-ring</td> <td>Nitrile</td> <td>1</td> <td>0.020 kg</td> </tr> </tbody> </table>				Item Number	Document Number	Revision	Title	Material	Quantity	Mass	1	X2-LWP-001	1	X2 lightweight piston body	Aluminum, 7075-T6 Rod	1	8104 kg	2	X2-LWP-002	0	Wear ring	Oil Filled Nylon 6, Cast	2	0.297 kg	3	X2-LWP-003	0	Load ring	Commercial Aluminum	1	0.285 kg	4	X2-LWP-004	0	Chevron seal	Oil Filled Nylon 6, Cast	1	0.188 kg	5	X2-LWP-005	0	Bronze holder	Aluminum Bronze C95810	1	1.789 kg	6	BS375	n/a	BS series o-ring	Nitrile	1	0.020 kg
Item Number	Document Number	Revision	Title	Material	Quantity	Mass																																														
1	X2-LWP-001	1	X2 lightweight piston body	Aluminum, 7075-T6 Rod	1	8104 kg																																														
2	X2-LWP-002	0	Wear ring	Oil Filled Nylon 6, Cast	2	0.297 kg																																														
3	X2-LWP-003	0	Load ring	Commercial Aluminum	1	0.285 kg																																														
4	X2-LWP-004	0	Chevron seal	Oil Filled Nylon 6, Cast	1	0.188 kg																																														
5	X2-LWP-005	0	Bronze holder	Aluminum Bronze C95810	1	1.789 kg																																														
6	BS375	n/a	BS series o-ring	Nitrile	1	0.020 kg																																														
 <p>SECTION B-B</p> <p>1:4</p>																																																				
<table border="1"> <tr> <td>DRAWN</td> <td>I. Gurdind</td> <td>NAME</td> <td>DATE</td> <td colspan="2">CENTRE FOR HYPERSONICS</td> </tr> <tr> <td>CHEKED</td> <td></td> <td></td> <td>10/21/09</td> <td colspan="2">THE UNIVERSITY OF QUEENSLAND</td> </tr> <tr> <td>ENG APPR</td> <td></td> <td></td> <td></td> <td colspan="2">TITLE</td> </tr> <tr> <td>MGR APPR</td> <td></td> <td></td> <td></td> <td colspan="2">X2 Lightweight Piston Assembly</td> </tr> <tr> <td colspan="6">UNLESS OTHERWISE SPECIFIED</td> </tr> <tr> <td colspan="6">DIMENSIONS ARE IN MILLIMETERS</td> </tr> <tr> <td colspan="6">ANGULAR TOLERANCE: $\pm 0.1^\circ$</td> </tr> <tr> <td colspan="6">DIMENSIONAL TOLERANCE: $\pm 0.1\text{mm}$</td> </tr> </table>				DRAWN	I. Gurdind	NAME	DATE	CENTRE FOR HYPERSONICS		CHEKED			10/21/09	THE UNIVERSITY OF QUEENSLAND		ENG APPR				TITLE		MGR APPR				X2 Lightweight Piston Assembly		UNLESS OTHERWISE SPECIFIED						DIMENSIONS ARE IN MILLIMETERS						ANGULAR TOLERANCE: $\pm 0.1^\circ$						DIMENSIONAL TOLERANCE: $\pm 0.1\text{mm}$						
DRAWN	I. Gurdind	NAME	DATE	CENTRE FOR HYPERSONICS																																																
CHEKED			10/21/09	THE UNIVERSITY OF QUEENSLAND																																																
ENG APPR				TITLE																																																
MGR APPR				X2 Lightweight Piston Assembly																																																
UNLESS OTHERWISE SPECIFIED																																																				
DIMENSIONS ARE IN MILLIMETERS																																																				
ANGULAR TOLERANCE: $\pm 0.1^\circ$																																																				
DIMENSIONAL TOLERANCE: $\pm 0.1\text{mm}$																																																				
<table border="1"> <tr> <td>SIZE</td> <td>A3</td> <td>FILE NAME</td> <td>X2-LWP-000-1.Light-piston-asv.dwg</td> <td>REV</td> <td>1</td> </tr> <tr> <td>SCALE AS SHOWN</td> <td></td> <td>SCALE</td> <td>AS SHOWN</td> <td>WEIGHT</td> <td>0.683 kg</td> </tr> <tr> <td colspan="6">SHEET 1 OF 1</td> </tr> </table>				SIZE	A3	FILE NAME	X2-LWP-000-1.Light-piston-asv.dwg	REV	1	SCALE AS SHOWN		SCALE	AS SHOWN	WEIGHT	0.683 kg	SHEET 1 OF 1																																				
SIZE	A3	FILE NAME	X2-LWP-000-1.Light-piston-asv.dwg	REV	1																																															
SCALE AS SHOWN		SCALE	AS SHOWN	WEIGHT	0.683 kg																																															
SHEET 1 OF 1																																																				

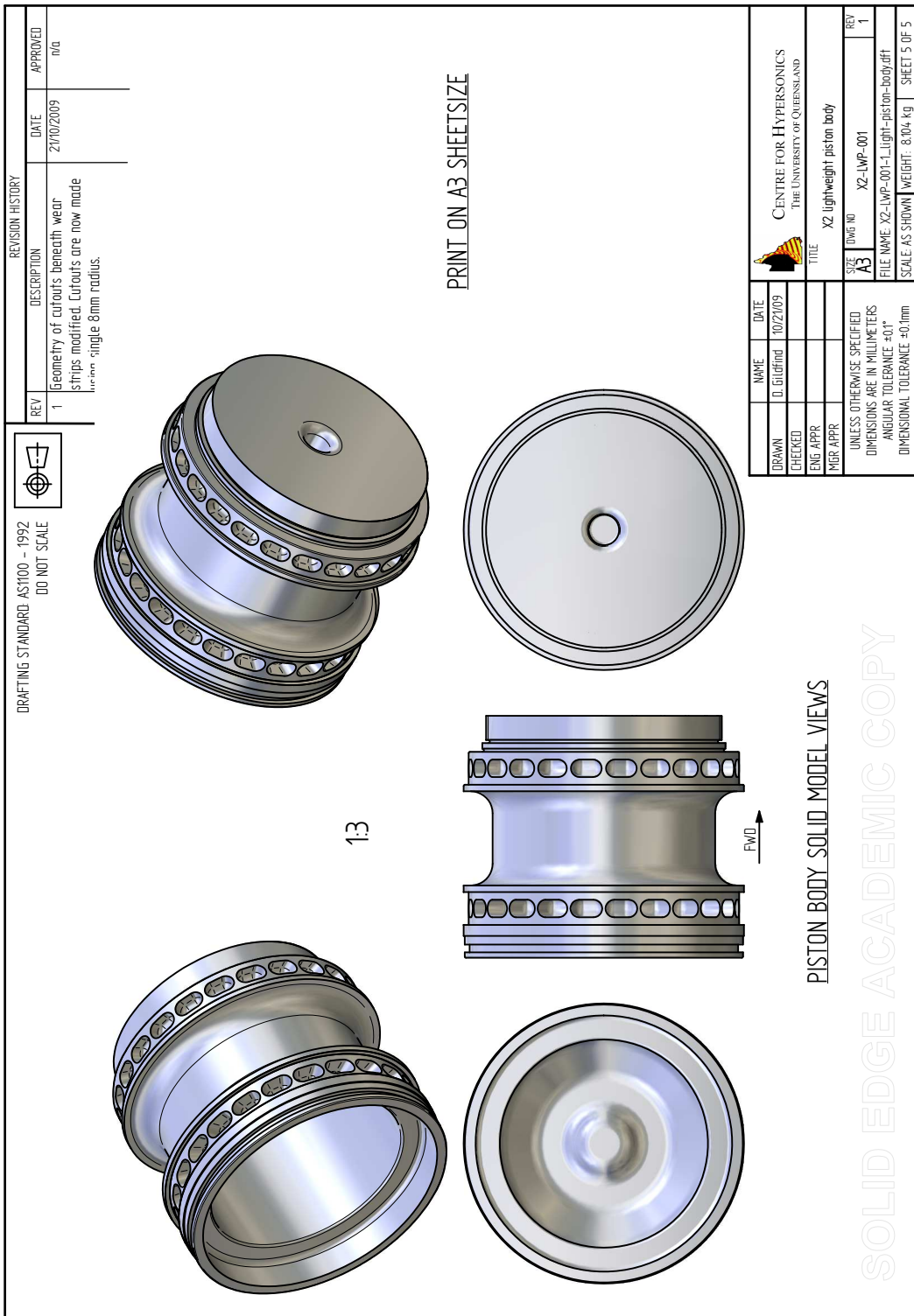
A.2 X2-LWP-001-1: X2 Lightweight Piston Body



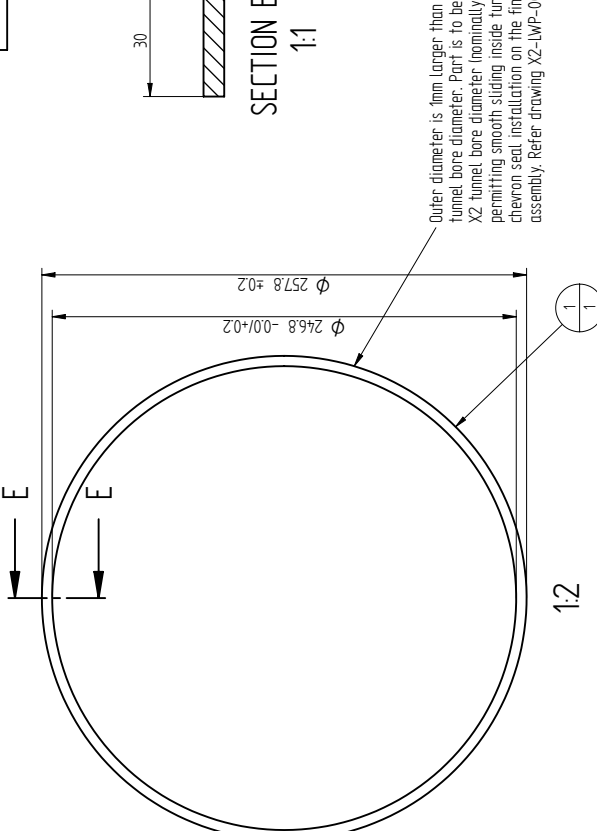
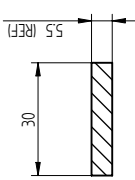




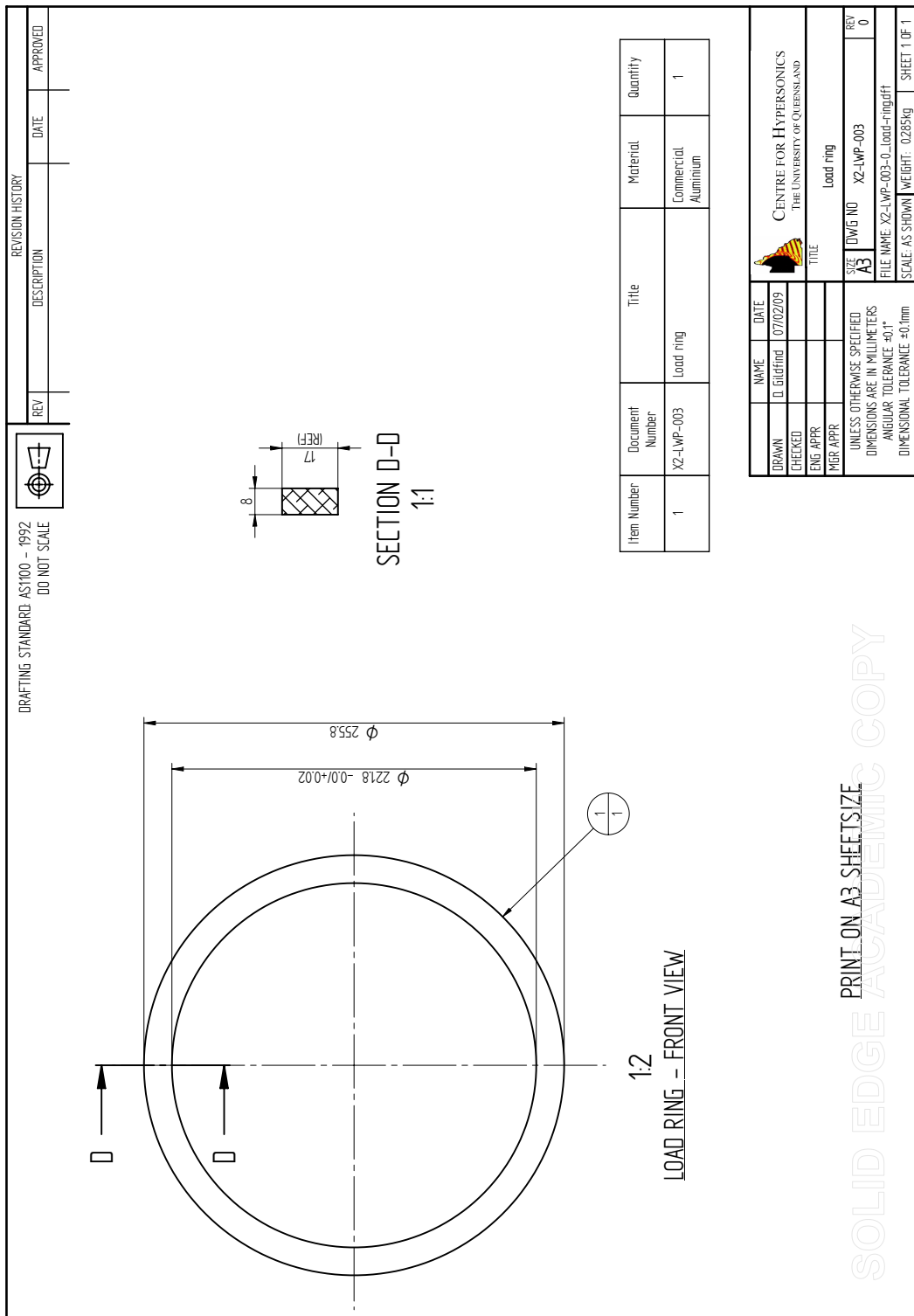




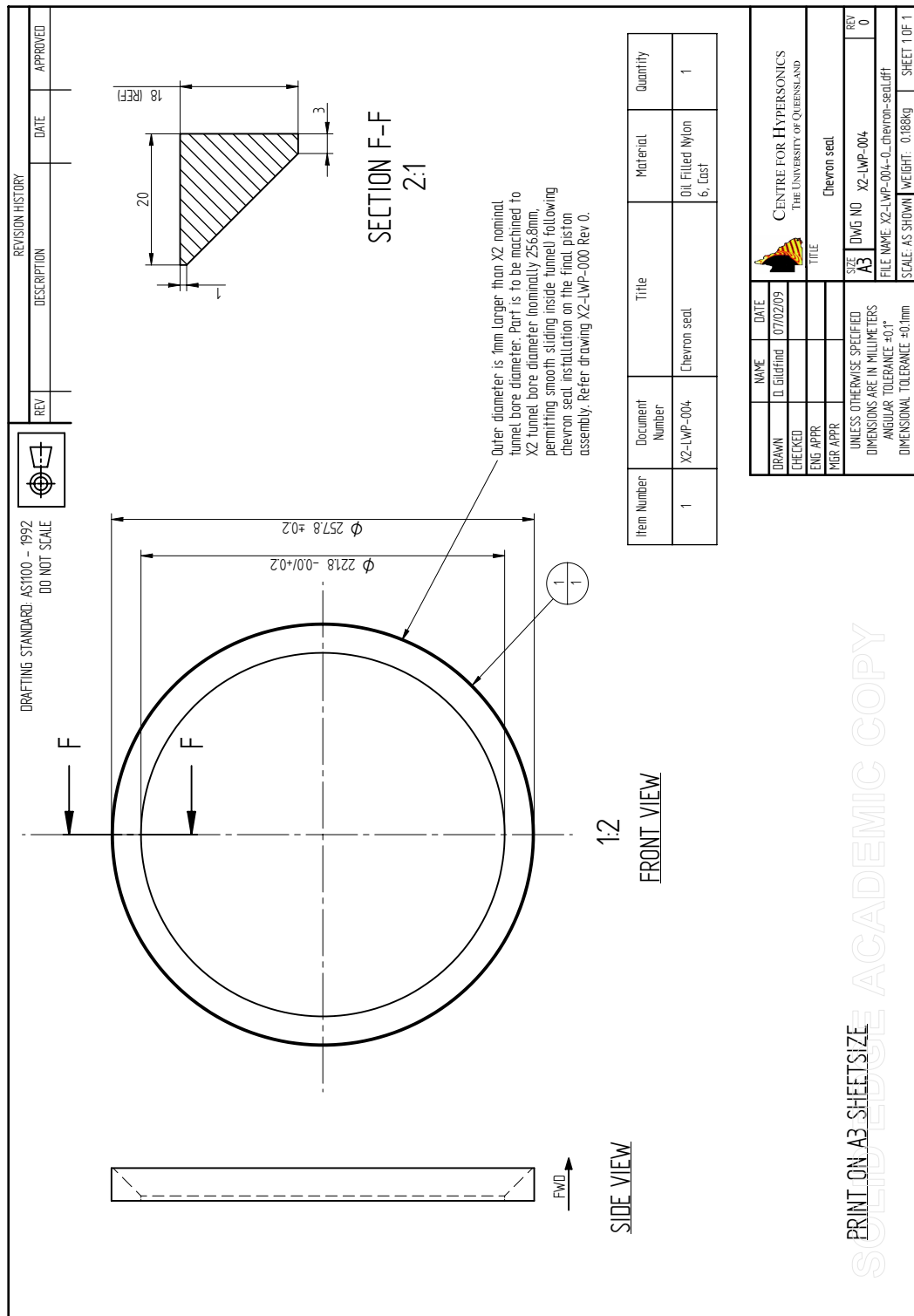
A.3 X2-LWP-002-0: Wear Ring

DRAFTING STANDARD AS1100 - 1992	DO NOT SCALE	REV	REVISION HISTORY		DATE	APPROVED																																																																														
SECTION E-E																																																																																				
1:1																																																																																				
 <p>Outer diameter is 1mm larger than X2 nominal tunnel bore diameter. Part is to be machined to X2 tunnel bore diameter (nominally 256.8mm), permitting smooth sliding inside tunnel following chevron seal installation on the final piston assembly. Refer drawing X2-LWP-000 Rev 0.</p>																																																																																				
WEAR RING - FRONT VIEW																																																																																				
1:2																																																																																				
																																																																																				
<table border="1" style="width: 100%; border-collapse: collapse;"> <thead> <tr> <th>Item Number</th> <th>Document Number</th> <th>Title</th> <th>Material</th> <th>Quantity</th> </tr> </thead> <tbody> <tr> <td>1</td> <td>X2-LWP-002</td> <td>Wear ring</td> <td>Oil Filled Nylon 6, Last</td> <td>1</td> </tr> </tbody> </table>							Item Number	Document Number	Title	Material	Quantity	1	X2-LWP-002	Wear ring	Oil Filled Nylon 6, Last	1																																																																				
Item Number	Document Number	Title	Material	Quantity																																																																																
1	X2-LWP-002	Wear ring	Oil Filled Nylon 6, Last	1																																																																																
<table border="1" style="width: 100%; border-collapse: collapse;"> <tr> <td>DRAWN</td> <td>NAME</td> <td>DATE</td> <td colspan="3">CENTRE FOR HYPERSONICS</td> </tr> <tr> <td>0. Gilding</td> <td></td> <td>07/02/09</td> <td colspan="3">THE UNIVERSITY OF QUEENSLAND</td> </tr> <tr> <td>CHEKED</td> <td></td> <td></td> <td colspan="3"></td> </tr> <tr> <td>ENG APPR</td> <td></td> <td></td> <td colspan="3"></td> </tr> <tr> <td>MGR APPR</td> <td></td> <td></td> <td colspan="3"></td> </tr> <tr> <td colspan="3"></td> <td>SIZE</td> <td>DRAW NO</td> <td>REV</td> </tr> <tr> <td colspan="3"></td> <td>A3</td> <td>X2-LWP-002</td> <td>0</td> </tr> <tr> <td colspan="3"></td> <td colspan="3">UNLESS OTHERWISE SPECIFIED</td> </tr> <tr> <td colspan="3"></td> <td colspan="3">DIMENSIONS ARE IN MILLIMETERS</td> </tr> <tr> <td colspan="3"></td> <td colspan="3">ANGULAR TOLERANCE: ±0.1°</td> </tr> <tr> <td colspan="3"></td> <td colspan="3">DIMENSIONAL TOLERANCE: ±0.1mm</td> </tr> <tr> <td colspan="3"></td> <td colspan="3">SCALE AS SHOWN WEIGHT: 0.148g</td> </tr> <tr> <td colspan="3"></td> <td colspan="3">SHEET 1 OF 1</td> </tr> </table>							DRAWN	NAME	DATE	CENTRE FOR HYPERSONICS			0. Gilding		07/02/09	THE UNIVERSITY OF QUEENSLAND			CHEKED						ENG APPR						MGR APPR									SIZE	DRAW NO	REV				A3	X2-LWP-002	0				UNLESS OTHERWISE SPECIFIED						DIMENSIONS ARE IN MILLIMETERS						ANGULAR TOLERANCE: ±0.1°						DIMENSIONAL TOLERANCE: ±0.1mm						SCALE AS SHOWN WEIGHT: 0.148g						SHEET 1 OF 1		
DRAWN	NAME	DATE	CENTRE FOR HYPERSONICS																																																																																	
0. Gilding		07/02/09	THE UNIVERSITY OF QUEENSLAND																																																																																	
CHEKED																																																																																				
ENG APPR																																																																																				
MGR APPR																																																																																				
			SIZE	DRAW NO	REV																																																																															
			A3	X2-LWP-002	0																																																																															
			UNLESS OTHERWISE SPECIFIED																																																																																	
			DIMENSIONS ARE IN MILLIMETERS																																																																																	
			ANGULAR TOLERANCE: ±0.1°																																																																																	
			DIMENSIONAL TOLERANCE: ±0.1mm																																																																																	
			SCALE AS SHOWN WEIGHT: 0.148g																																																																																	
			SHEET 1 OF 1																																																																																	
PRINT ON A3 SHEET SIZE																																																																																				
SOLID EDGE ACADEMIC COPY																																																																																				

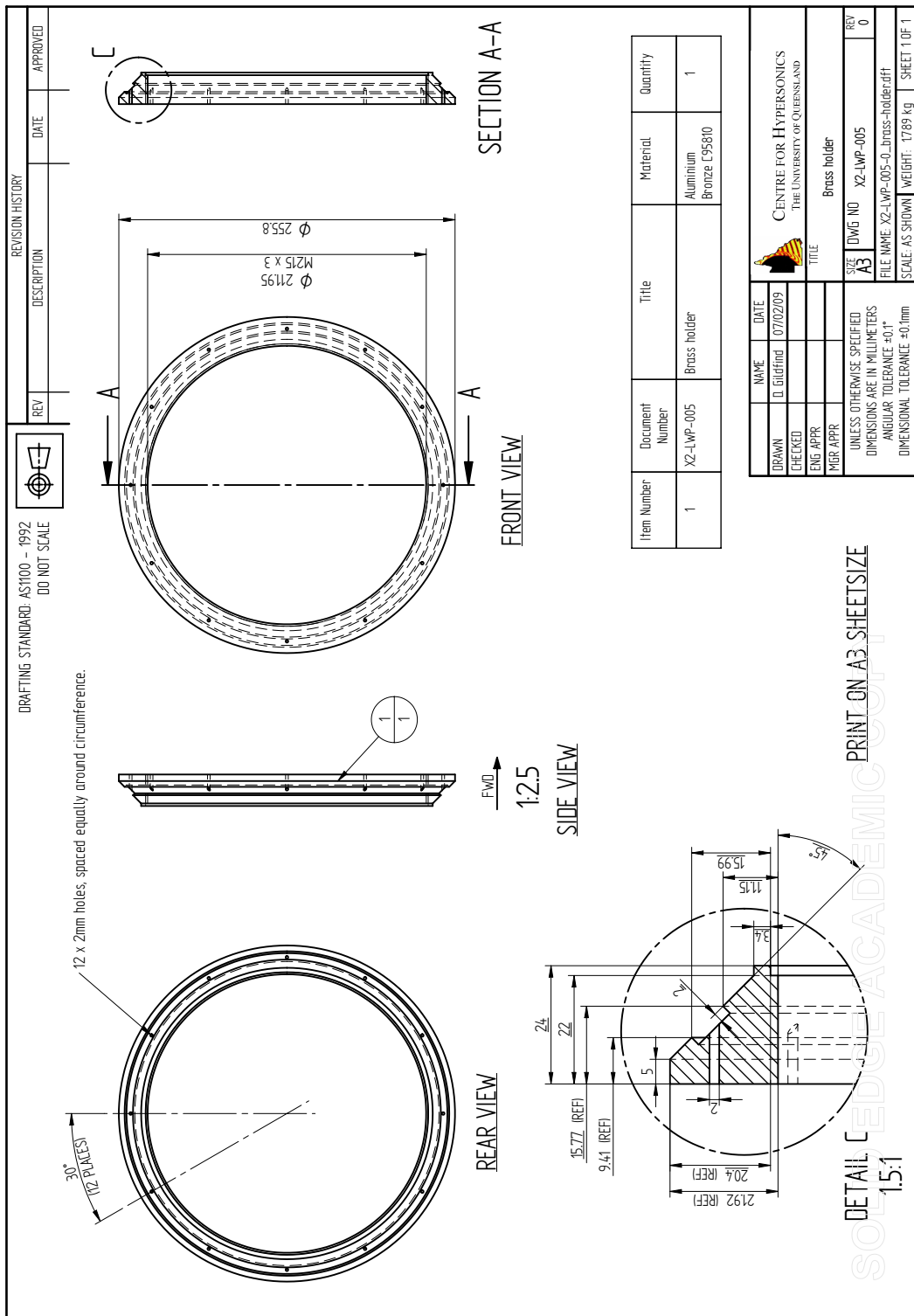
A.4 X2-LWP-003-0: Load Ring



A.5 X2-LWP-004-0: Chevron Seal



A.6 X2-LWP-005-0: Brass Holder



Appendix B

Material and Physical Properties

B.1 7075-T6 Aluminium Alloy Rod

The tangent modulus is calculated assuming constant modulus between material yield and failure, which is reasonable for this type of aluminium alloy which tends to plastically deform at a constant rate until failure.

Property	Description	Empirical	Metric	Notes
F_{tu}	Ultimate tensile strength	69 ksi	476 MPa	A-basis, L-T value, 3.001-4.000" DIA.
F_{ty}	Yield tensile strength	60 ksi	414 MPa	A-basis, L-T value, 3.001-4.000" DIA.
F_{cy}	Yield compressive strength	64 ksi	441 MPa	A-basis, L value.
F_{su}	Ultimate shear strength	46 ksi	317 MPa	A-basis.
e	Strain at failure	0.07(7%)	0.07(7%)	A-basis.
E	Young's modulus	10,300 ksi	71.0 GPa	Smaller of E and E_c .
E_t	Tangent modulus	140 ksi	965 MPa	$E_t = (F_{tu} - F_{ty})/(e - F_{ty}/E)$.
G	Shear modulus	3,900 ksi	26.9 GPa	
μ	Poisson's ratio	0.33	0.33	
ρ	Density	0.101 lb/in ³	71.0 kg/m ³	Smaller of E and E_c .

Table B.1: Mechanical and physical properties of 7075-T6 rod [128].

B.2 C95800 Copper Alloy

Property	Description	Metric	Notes
E	Young's modulus	110 GPa	Tension direction.
μ	Poisson's ratio	0.32	
ρ	Density	7,640 kg/m ³	

Table B.2: Mechanical and physical properties of C95800 copper alloy [182].

B.3 Nylon 6 Oil Filled Cast

Property	Description	Metric	Notes
E	Young's modulus	2.28 GPa	Per [183], compression direction, since these are bearing components.
μ	Poisson's ratio	0.4	Per [134], Table H-1, for nylon.
ρ	Density	1,135 kg/m ³	Per [183].

Table B.3: Mechanical and physical properties of Nylon 6 oil filled cast.

Appendix C

X2 Equilibrium Gas Operational Envelope - Results

X2 with driver condition X2-LWP-1.2mm-Rev-0

P_{sd1} (kPa)	M_7 (-)	u_7 (m/s)	$P_{7,target}$ (kPa)	Without X2 Mach 10 nozzle				With X2 Mach 10 nozzle					
				$P_{7,actual}$ (kPa)	P_1 (kPa)	P_5 (Pa)	a_2/a_3 (-)	a_{sd2}/a_{sd3} (-)	$P_{7,actual}$ (kPa)	P_1 (kPa)	P_5 (Pa)	a_2/a_3 (-)	a_{sd2}/a_{sd3} (-)
Expansion tube, no secondary driver.													
n/a	10.0	3,011	1.37	14.49	293.6	122.6	0.30		5.42	181.1	550.2	0.34	
	12.5	3,789	0.88	3.74	147.1	20.3	0.36	n/a	0.88	93.5	92.9	0.40	n/a
	15.0	4,614	0.61	1.02	74.1	3.8	0.40		0.41	47.4	17.4	0.48	
Expansion tube, with secondary driver.													
25	10.0	3,011	1.37	3.19	64.6	27.1			1.35	45.1	137.5		
	12.5	3,789	0.88	0.98	38.7	5.4	n/a	1.74	0.44	28.0	27.9	n/a	1.74
	15.0	4,614	0.61	0.33	23.9	1.2			0.15	17.7	6.5		
50	10.0	3,011	1.37	4.86	98.5	41.3			2.04	68.0	207.6		
	12.5	3,789	0.88	1.48	58.1	8.0	n/a	1.46	0.65	41.7	41.5	n/a	1.46
	15.0	4,614	0.61	0.49	35.4	1.8			0.22	25.9	9.5		
100	10.0	3,011	1.37	7.05	142.8	59.8			2.91	97.2	295.9		
	12.5	3,789	0.88	2.10	82.6	11.4	n/a	1.23	0.92	58.5	58.2	n/a	1.23
	15.0	4,614	0.61	0.68	49.2	2.5			0.31	35.6	13.1		
150	10.0	3,011	1.37	8.50	172.3	72.0			3.48	116.3	353.9		
	12.5	3,789	0.88	2.50	98.5	13.6	n/a	1.10	1.08	69.0	68.6	n/a	1.10
	15.0	4,614	0.61	0.80	57.8	3.0			0.36	41.4	15.2		
200	10.0	3,011	1.37	9.57	194.0	81.1			3.90	130.1	396.0		
	12.5	3,789	0.88	2.80	109.8	15.2	n/a	1.02	1.20	76.3	75.8	n/a	1.02
	15.0	4,614	0.61	0.88	63.7	3.3			0.39	45.2	16.6		
250	10.0	3,011	1.37	10.41	211.1	88.2			4.21	140.6	427.8		
	12.5	3,789	0.88	3.01	118.5	16.4	n/a	0.97	1.28	81.7	81.2	n/a	0.97
	15.0	4,614	0.61	0.94	68.0	3.5			0.42	48.0	17.6		
300	10.0	3,011	1.37	11.08	224.6	93.8			4.46	148.9	452.8		
	12.5	3,789	0.88	3.18	125.1	17.3	n/a	0.92	1.35	85.8	85.3	n/a	0.92
	15.0	4,614	0.61	0.98	71.1	3.6			0.43	49.9	18.4		
350	10.0	3,011	1.37	11.62	235.8	98.4			4.66	155.5	472.7		
	12.5	3,789	0.88	3.32	130.3	18.0	n/a	0.89	1.40	89.0	88.4	n/a	0.89
	15.0	4,614	0.61	1.02	73.7	3.8			0.44	51.3	18.8		

Table C.1: Required shock and acceleration tube fill pressures (p_1 and p_5 respectively) to achieve target flow conditions from Table 1.1. Results are for X2 using new tuned driver condition X2-LWP-1.2mm-0 from Table 6.7. Mach number and velocity are matched with Table 1.1; achievable test flow static pressure, p_7 , is shown.

X2 with driver condition X2-LWP-2.0mm-Rev-0													
P_{sd1} (kPa)	M_7 (-)	u_7 (m/s)	$P_{7,target}$ (kPa)	Without X2 Mach 10 nozzle					With X2 Mach 10 nozzle				
				$P_{7,actual}$ (kPa)	P_1 (kPa)	P_5 (Pa)	a_2/a_3 (-)	a_{sd2}/a_{sd3} (-)	$P_{7,actual}$ (kPa)	P_1 (kPa)	P_5 (Pa)	a_2/a_3 (-)	a_{sd2}/a_{sd3} (-)
Expansion tube, no secondary driver.													
n/a	10.0	3,011	1.37	51.16	1037.4	431.0	0.22	n/a	20.31	678.2	2051.7	0.25	n/a
	12.5	3,789	0.88	14.36	565.0	77.8	0.26	n/a	6.00	381.9	378.5	0.29	n/a
	15.0	4,614	0.61	4.34	314.5	16.1	0.31	n/a	1.88	216.6	79.4	0.34	n/a
Expansion tube, with secondary driver.													
25	10.0	3,011	1.37	6.97	141.2	59.1	n/a	1.91	3.03	101.0	307.6	n/a	1.91
	12.5	3,789	0.88	2.24	87.9	12.1	n/a	n/a	1.03	65.4	65.0	n/a	n/a
	15.0	4,614	0.61	0.78	56.7	2.9	n/a	n/a	0.37	43.3	15.9	n/a	n/a
50	10.0	3,011	1.37	11.11	225.3	94.1	n/a	1.60	4.80	160.3	487.4	n/a	1.60
	12.5	3,789	0.88	3.54	138.9	19.2	n/a	n/a	1.61	102.7	102.1	n/a	n/a
	15.0	4,614	0.61	1.22	88.5	4.5	n/a	n/a	0.58	67.2	24.7	n/a	n/a
100	10.0	3,011	1.37	17.04	345.4	144.1	n/a	1.33	7.28	243.2	738.1	n/a	1.33
	12.5	3,789	0.88	5.35	210.1	29.0	n/a	n/a	2.42	153.8	152.7	n/a	n/a
	15.0	4,614	0.61	1.82	132.1	6.8	n/a	n/a	0.86	99.2	36.5	n/a	n/a
150	10.0	3,011	1.37	21.38	433.1	180.6	n/a	1.20	9.07	303.0	918.3	n/a	1.20
	12.5	3,789	0.88	6.64	261.1	36.0	n/a	n/a	2.98	189.9	188.5	n/a	n/a
	15.0	4,614	0.61	2.24	162.4	8.3	n/a	n/a	1.05	121.2	44.5	n/a	n/a
200	10.0	3,011	1.37	24.79	502.8	209.3	n/a	1.11	10.50	350.4	1062.5	n/a	1.11
	12.5	3,789	0.88	7.65	300.8	41.5	n/a	n/a	3.42	217.6	216.0	n/a	n/a
	15.0	4,614	0.61	2.56	185.7	9.5	n/a	n/a	1.20	137.8	50.6	n/a	n/a
250	10.0	3,011	1.37	27.61	560.1	233.1	n/a	1.04	11.65	388.7	1178.2	n/a	1.04
	12.5	3,789	0.88	8.48	333.2	45.9	n/a	n/a	3.77	240.0	238.0	n/a	n/a
	15.0	4,614	0.61	2.82	204.3	10.5	n/a	n/a	1.31	150.9	55.4	n/a	n/a
300	10.0	3,011	1.37	30.02	609.1	253.4	n/a	n/a	12.61	421.1	1275.6	n/a	0.99
	12.5	3,789	0.88	9.16	360.2	49.6	n/a	n/a	4.06	258.5	256.5	n/a	n/a
	15.0	4,614	0.61	3.03	219.6	11.2	n/a	n/a	1.40	161.4	59.2	n/a	n/a
350	10.0	3,011	1.37	32.10	651.3	270.8	n/a	n/a	13.45	448.8	1360.2	n/a	0.95
	12.5	3,789	0.88	9.75	383.4	52.8	n/a	n/a	4.31	274.3	272.1	n/a	n/a
	15.0	4,614	0.61	3.20	232.3	11.9	n/a	n/a	1.48	170.3	62.5	n/a	n/a

Table C.2: Required shock and acceleration tube fill pressures (p_1 and p_5 respectively) to achieve target flow conditions from Table 1.1. Results are for X2 using new tuned driver condition X2-LWP-2.0mm-0 from Table 6.7. Mach number and velocity are matched with Table 1.1; achievable test flow static pressure, p_5 , is shown.

X2 with driver condition X2-LWP-2.5mm-Rev-0

				Without X2 Mach 10 nozzle				With X2 Mach 10 nozzle					
p _{sd1} (kPa)	M ₇ (-)	u ₇ (m/s)	p _{7,target} (kPa)	p _{7,actual} (kPa)	p ₁ (kPa)	p ₅ (Pa)	a ₂ /a ₃ (-)	a _{sd2} /a _{sd3} (-)	p _{7,actual} (kPa)	p ₁ (kPa)	p ₅ (Pa)	a ₂ /a ₃ (-)	a _{sd2} /a _{sd3} (-)
Expansion tube, no secondary driver.													
n/a	10.0	3,011	1.37	60.66	1226.3	510.6	0.21	n/a	24.09	803.8	2431.2	0.23	n/a
	12.5	3,789	0.88	17.07	672.8	92.4	0.25		7.23	460.4	456.0	0.27	
	15.0	4,614	0.61	5.27	381.7	19.5	0.28		2.31	265.9	97.5	0.32	
Expansion tube, with secondary driver.													
25	10.0	3,011	1.37	8.01	162.5	67.9	n/a	1.89	3.50	116.8	355.7	n/a	1.89
	12.5	3,789	0.88	2.59	101.8	14.1			1.20	76.1	75.7		
	15.0	4,614	0.61	0.91	66.0	3.4			0.44	50.7	18.7		
50	10.0	3,011	1.37	12.84	260.2	108.7	n/a	1.58	5.56	185.6	563.8	n/a	1.58
	12.5	3,789	0.88	4.11	161.4	22.3			1.88	119.7	119.0		
	15.0	4,614	0.61	1.43	103.6	5.3			0.68	79.0	29.0		
100	10.0	3,011	1.37	19.68	399.3	166.3	n/a	1.32	8.48	283.0	895.3	n/a	1.32
	12.5	3,789	0.88	6.22	244.7	33.7			2.83	180.1	178.8		
	15.0	4,614	0.61	2.14	155.1	7.9			1.02	117.2	43.1		
150	10.0	3,011	1.37	24.77	502.3	209.2	n/a	1.18	10.60	353.6	1072.3	n/a	1.18
	12.5	3,789	0.88	7.75	304.9	42.0			3.50	223.1	221.3		
	15.0	4,614	0.61	2.64	191.4	9.8			1.25	143.8	52.8		
200	10.0	3,011	1.37	28.80	583.9	243.1	n/a	1.09	12.25	408.9	1239.4	n/a	1.09
	12.5	3,789	0.88	8.96	352.2	48.6			4.03	256.4	254.3		
	15.0	4,614	0.61	3.02	219.3	11.2			1.42	163.8	60.2		
250	10.0	3,011	1.37	32.12	651.7	271.1	n/a	1.03	13.62	454.7	1377.5	n/a	1.03
	12.5	3,789	0.88	9.94	390.8	53.8			4.44	283.0	280.6		
	15.0	4,614	0.61	3.34	241.9	12.4			1.56	179.7	65.9		
300	10.0	3,011	1.37	34.99	709.5	295.2	n/a	0.98	14.77	493.1	1494.0	n/a	0.98
	12.5	3,789	0.88	10.77	423.4	58.3			4.80	305.4	302.7		
	15.0	4,614	0.61	3.59	260.2	13.3			1.67	192.5	70.6		
350	10.0	3,011	1.37	37.48	759.7	316.1	n/a	0.93	15.77	526.2	1594.0	n/a	0.93
	12.5	3,789	0.88	11.46	450.9	62.1			5.10	324.5	321.6		
	15.0	4,614	0.61	3.81	276.1	14.1			1.77	203.5	74.6		

Table C.3: Required shock and acceleration tube fill pressures (p_1 and p_5 respectively) to achieve target flow conditions from Table 1.1. Results are for X2 using new tuned driver condition X2-LWP-2.5mm-0 from Table 6.7. Mach number and velocity are matched with Table 1.1; achievable test flow static pressure, p_5 , is shown.

Appendix D

L1d2 Validation of Hornung Free-Piston Dynamics Model

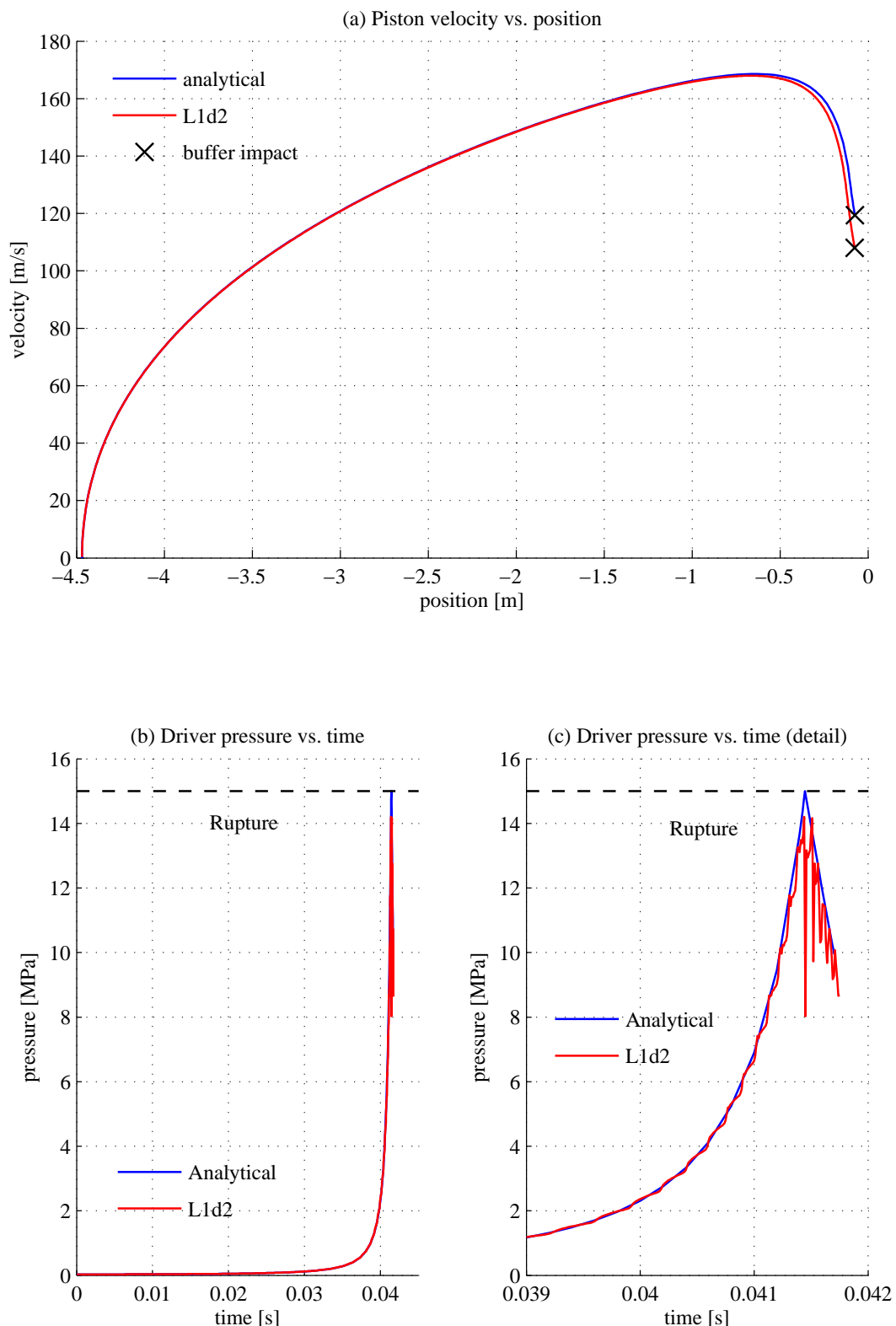


Figure D.1: Analytical piston dynamics model validation test case 1 $p_{A,0} = 1.5 \text{ MPa}$, $p_{D,0,H_e} = 30.0 \text{ kPa}$, $p_{D,0,Ar} = 0.0 \text{ kPa}$, $p_r = 15.0 \text{ MPa}$

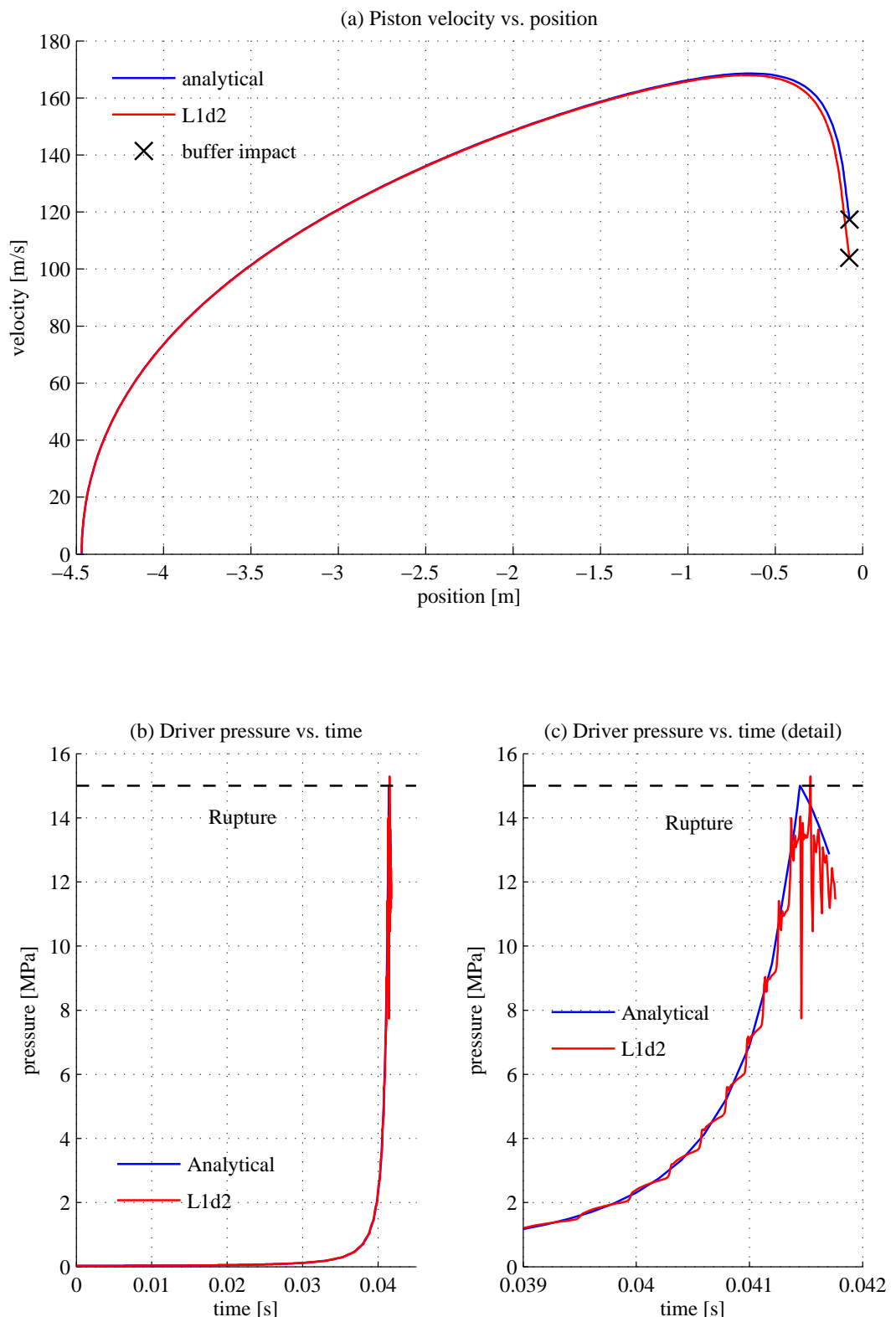


Figure D.2: Analytical piston dynamics model validation test case 2 ($p_{A,0} = 1.5 \text{ MPa}$, $p_{D,0,He} = 27.0 \text{ kPa}$, $p_{D,0,Ar} = 3.0 \text{ kPa}$, $p_r = 15.0 \text{ MPa}$)

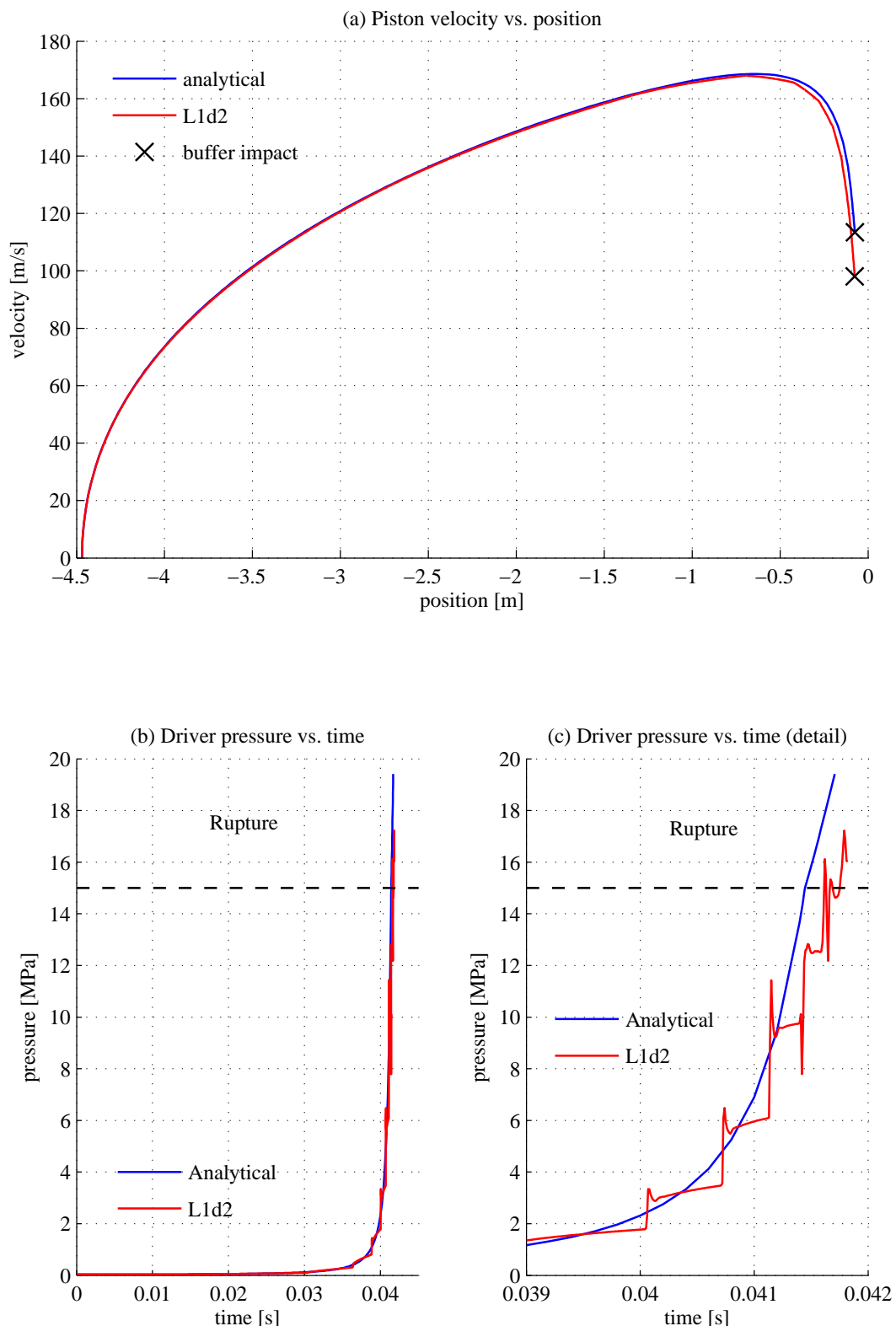


Figure D.3: Analytical piston dynamics model validation test case 3 ($p_{A,0} = 1.5 \text{ MPa}$, $p_{D,0,H_e} = 0.0 \text{ kPa}$, $p_{D,0,A_r} = 30.0 \text{ kPa}$, $p_r = 15.0 \text{ MPa}$)

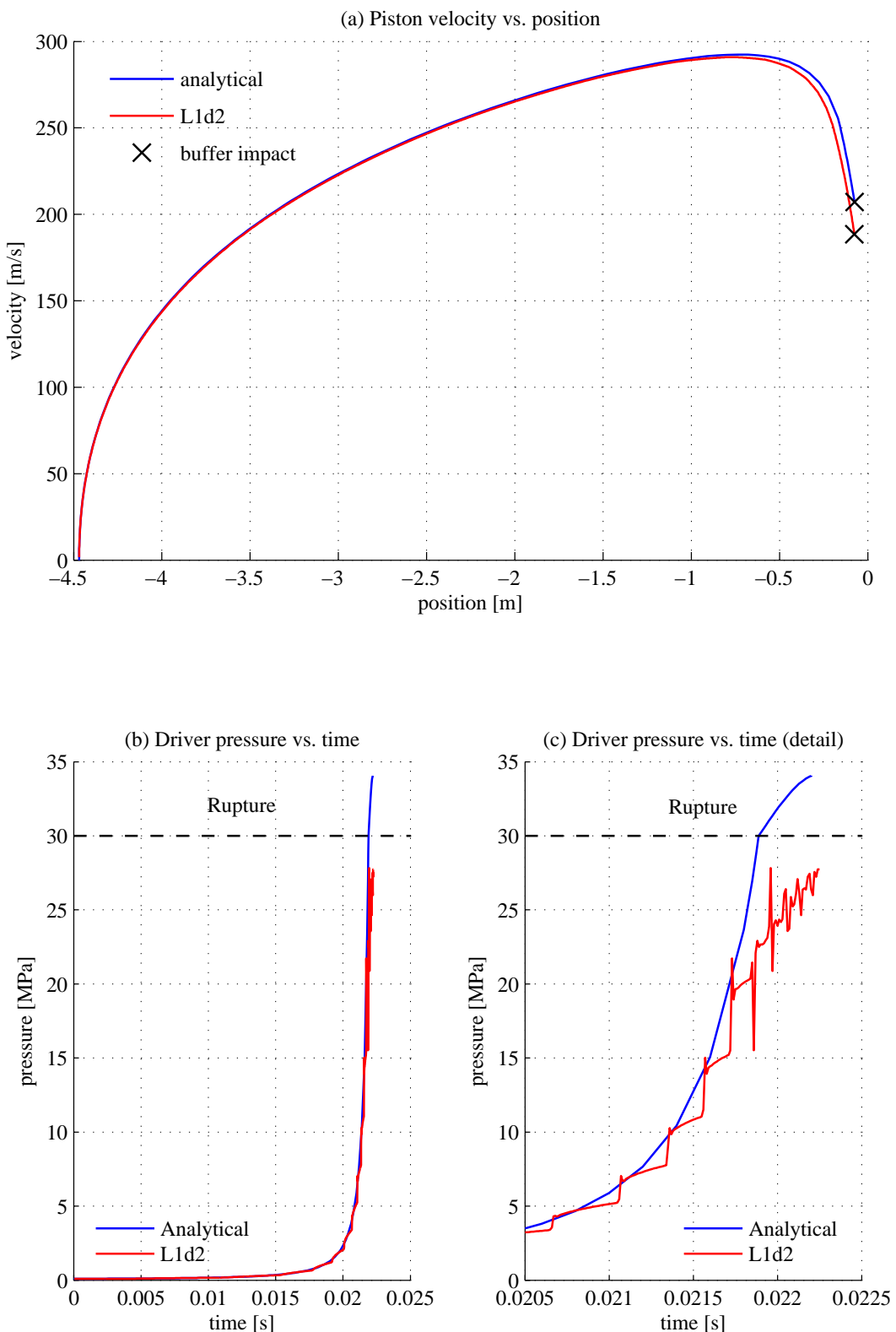


Figure D.4: Analytical piston dynamics model validation test case 4 ($p_{A,0} = 7.0$ MPa, $p_{D,0,He} = 30.0$ kPa, $p_{D,0,Ar} = 0.0$ kPa, $p_r = 30.0$ MPa)

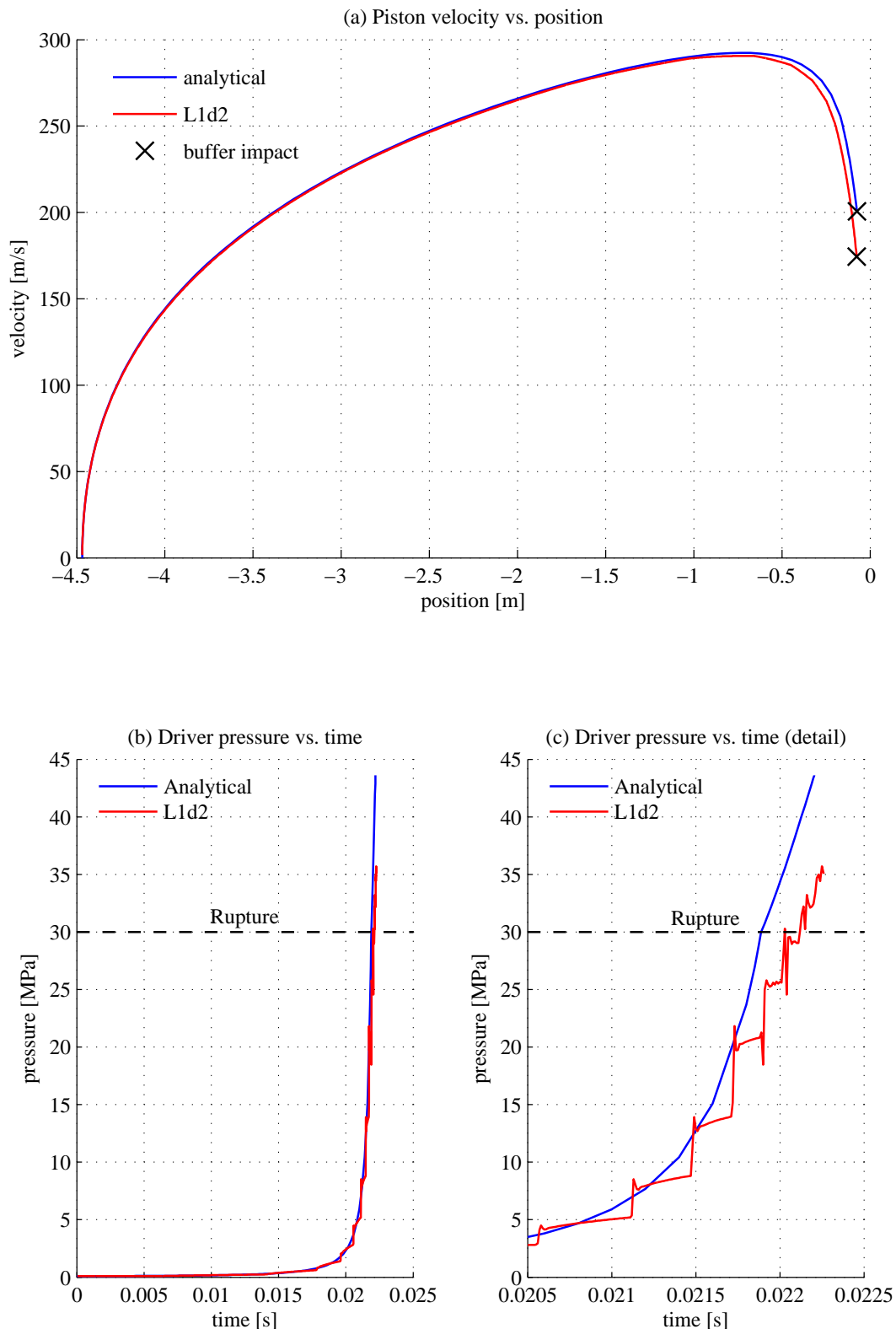


Figure D.5: Analytical piston dynamics model validation test case 5 ($p_{A,0} = 7.0 \text{ MPa}$, $p_{D,0,H_e} = 27.0 \text{ kPa}$, $p_{D,0,Ar} = 3.0 \text{ kPa}$, $p_r = 30.0 \text{ MPa}$)

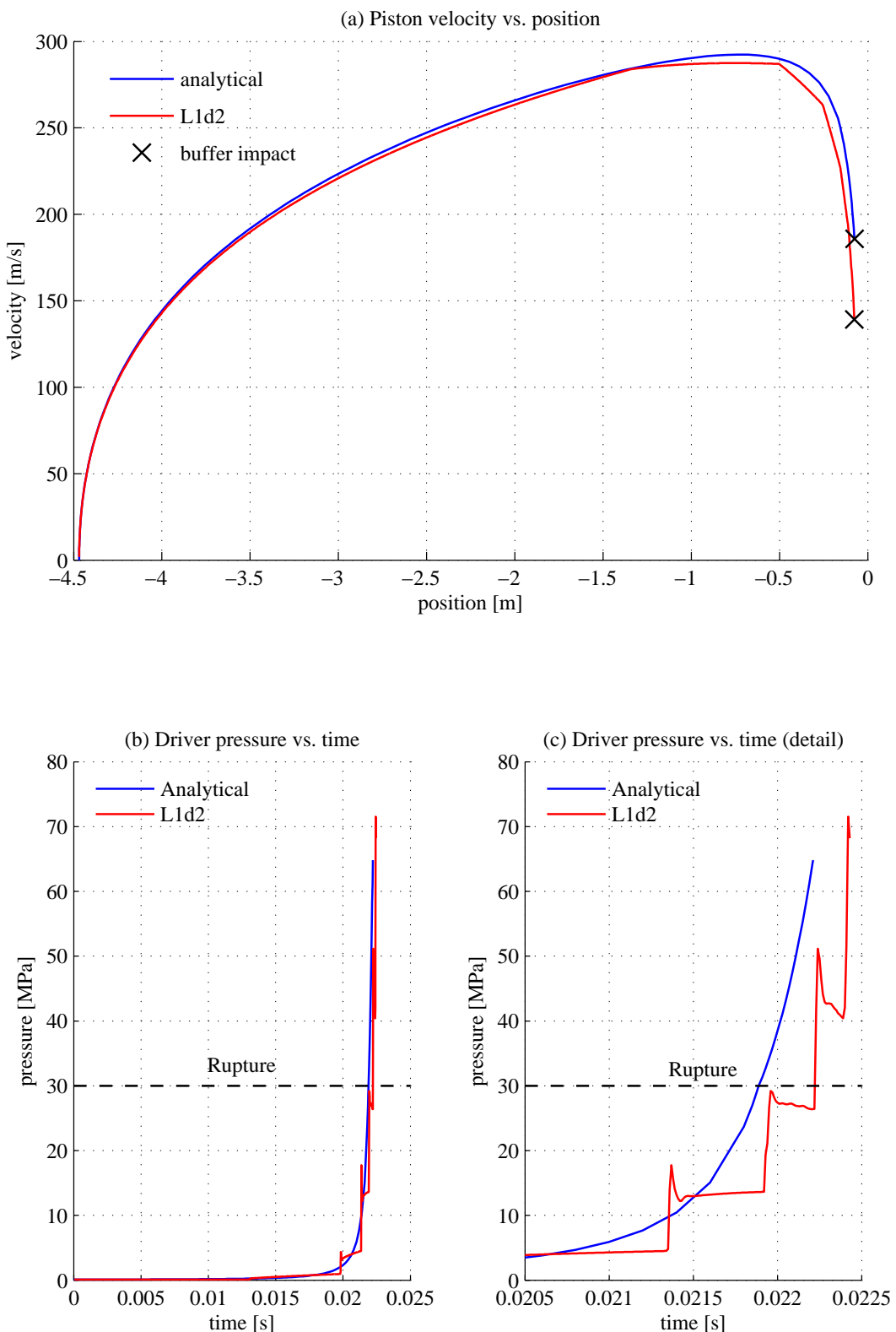


Figure D.6: Analytical piston dynamics model validation test case 6 ($p_{A,0} = 1.5 \text{ MPa}$, $p_{D,0,H_e} = 0.0 \text{ kPa}$, $p_{D,0,Ar} = 30.0 \text{ kPa}$, $p_r = 30.0 \text{ MPa}$)

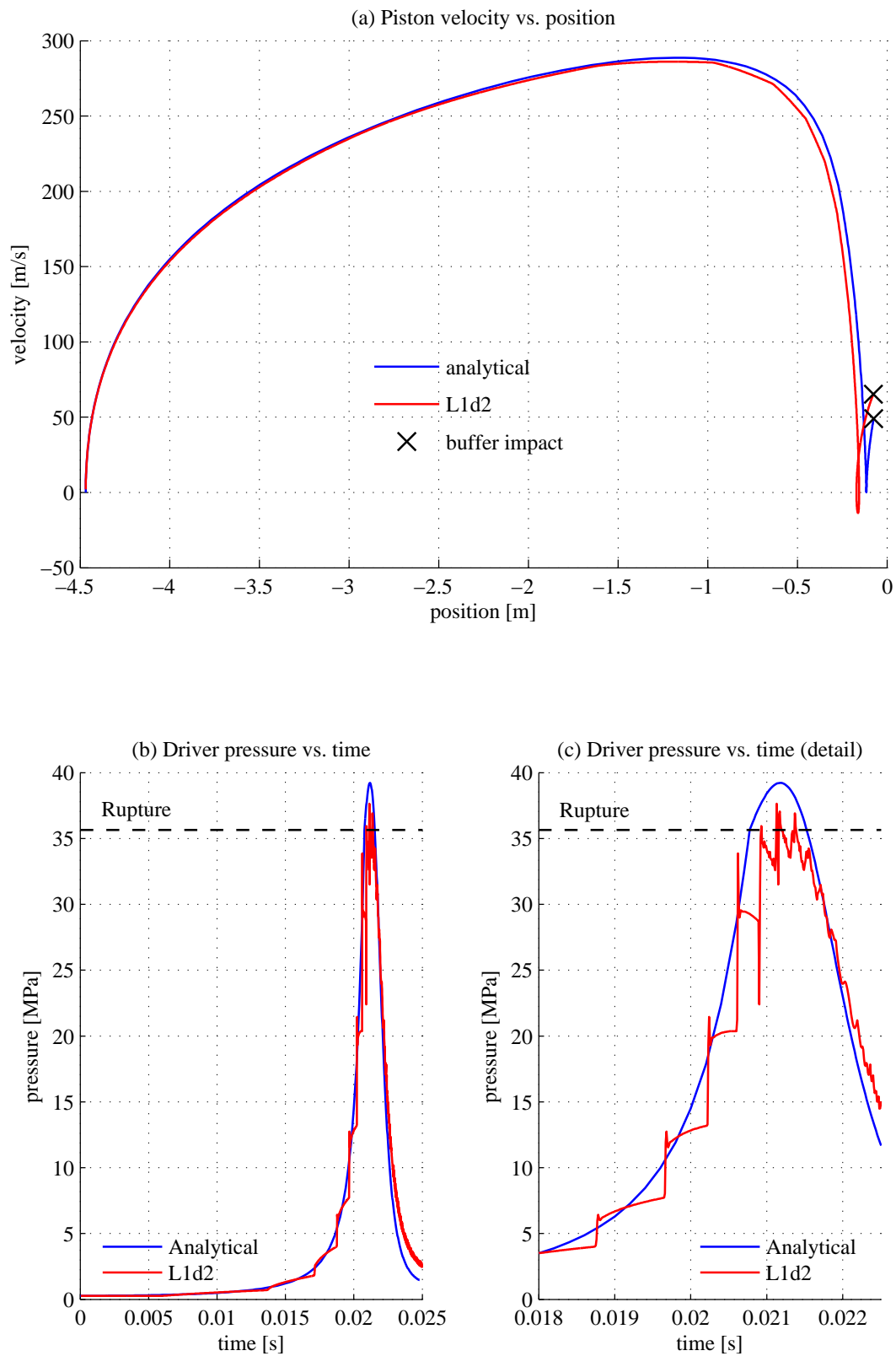


Figure D.7: Analytical piston dynamics model validation test case 7 ($p_{A,0} = 8.6 \text{ MPa}$, $p_{D,0,He} = 242.1 \text{ kPa}$, $p_{D,0,Ar} = 26.9 \text{ kPa}$, $p_r = 35.65 \text{ MPa}$)

Appendix E

X2 Compression Ratio Volumetric Correction Factors

This section summarises corrections which were applied to the calculation of volumetric compression ratio. It considers interpretation of L1d2 results, and experimental results, in different sections.

E.1 Driver Volume: No Buffer

Figure E.1 shows the internal geometry of the space enclosed between the front face of the piston, and the primary diaphragm, with no buffer in place. The volume of driver gas is determined in Equation E.1 for piston position L in Figure E.1.

$$\begin{aligned} V_{Drv,NoBuffer} &= \pi \frac{0.085^2}{4} \times 0.110 + \pi \frac{0.2568^2}{4} \times L \\ &= 0.0518L + 0.000624 \text{ m}^3, \text{ for } L \geq 0.0 \text{ m} \end{aligned} \quad (\text{E.1})$$

E.2 Driver Volume: Rubber Buffer

Figure E.2 shows internal geometry of the space enclosed between the front face of the piston, and the primary diaphragm, with the standard rubber buffer in place. A typical buffer was measured using vernier callipers to give the dimensions shown. Variation of a couple of millimetres from the dimensions shown is considered possible for any given buffer, however this accuracy is considered adequate for the current application. The rubber buffer has been used for blanked

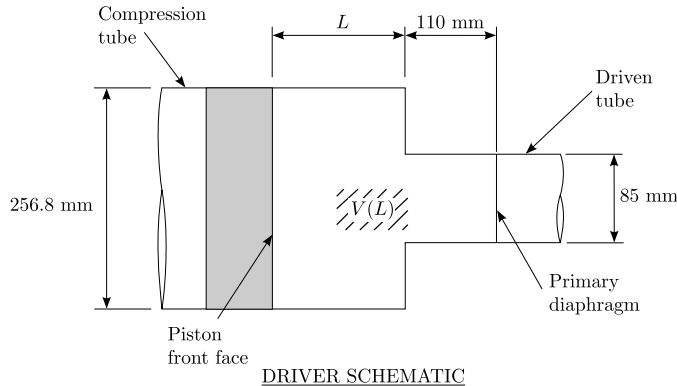


Figure E.1: Driver geometry - no buffer.

off shots with the lightweight piston. Compared to the driver gas, the rubber is effectively incompressible, and therefore should be accounted for in driver gas volume calculations. Equation E.1 calculates the volume of the axisymmetric buffer using Pappus' Centroid Theorem. The volume of driver gas is then determined in Equation E.2 for piston position L in Figure E.2.

$$\begin{aligned}
 V_{Buffer} &= \sum 2\pi A\bar{r} = 2\pi \times 0.033 \times 0.027 \times \left(\frac{0.192}{2} - \frac{0.027}{2} \right) \\
 &\quad + 2\pi \times 0.012 \times (0.048 - 0.033) \times \left(\frac{0.192}{2} - \frac{0.012}{2} \right) \\
 &\quad + 2\pi \times \frac{0.015^2}{4} \times \left(\frac{0.192}{2} - 0.012 - \frac{4 \times 0.015}{3\pi} \right) \\
 &= 0.000650 \text{ m}^3
 \end{aligned} \tag{E.1}$$

$$\begin{aligned}
 V_{Drv, Buffer} &= \pi \frac{0.085^2}{4} \times 0.110 \\
 &\quad + \pi \frac{0.2568^2}{4} \times L \\
 &\quad - 0.000650 \\
 &= 0.0518L - 0.0000258 \text{ m}^3, \text{ for } L \geq 0.048 \text{ m}
 \end{aligned} \tag{E.2}$$

E.3 Driver Volume: Nylon Stud Buffer

Figure E.3 shows internal geometry of the space enclosed between the front face of the piston, and the primary diaphragm, when 6×5 cm diameter nylon studs, of

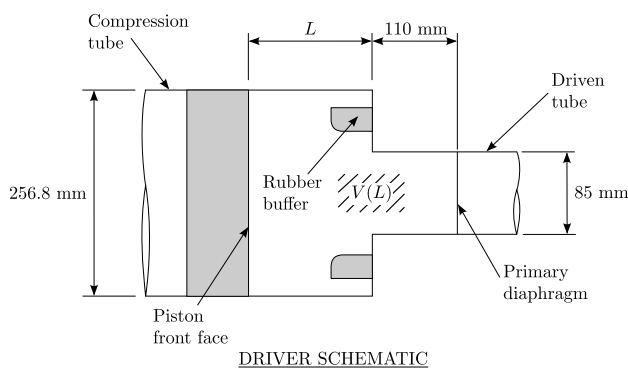
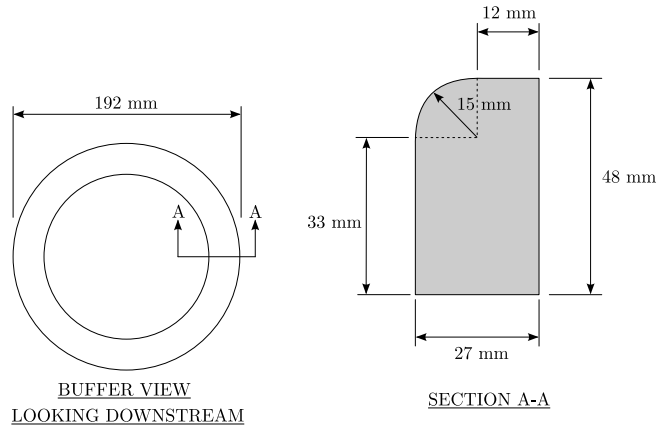


Figure E.2: Buffer geometry - rubber buffer.

length L_s , are installed. The nylon studs are used for actual diaphragm rupturing shots. Compared to the driver gas, the nylon studs are effectively incompressible, and therefore should be accounted for in driver gas volume calculations. The volume of driver gas is determined in Equation E.1 for piston position L , and nylon stud length L_s , in Figure E.3.

$$\begin{aligned}
 V_{Drv,Nylon} &= \pi \frac{0.085^2}{4} \times 0.110 \\
 &\quad + \pi \frac{0.2568^2}{4} \times L \\
 &\quad - 6 \times \pi \times \frac{0.050^2}{4} \times L_s \\
 &= 0.000624 + 0.0518L - 0.0118L_s \text{ m}^3, \text{ for } L \geq L_s \quad (\text{E.1})
 \end{aligned}$$

Where piston position is desired to coincide with the edge of the studs (i.e. $L = L_s$):

$$V_{Drv,Nylon} = 0.000624 + 0.0518L_s - 0.0118L_s^2 = 0.000624 + 0.0400L_s \text{ m}^3, \text{ for } L_s \in \mathbb{R}$$

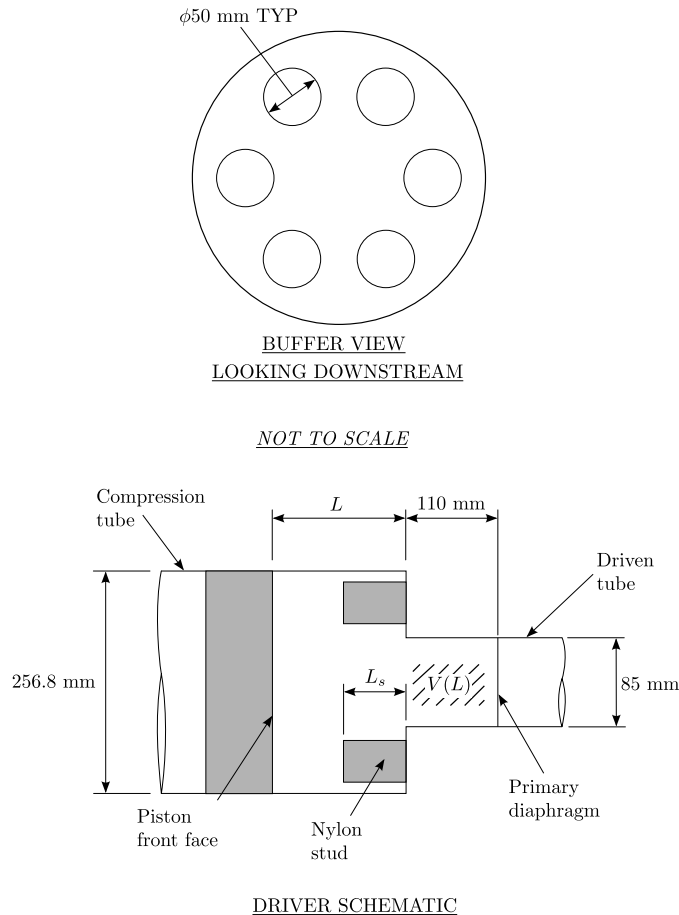


Figure E.3: Buffer geometry - nylon studs.

E.4 Driver Volume: L1d2 Buffer

Equation E.1 shows the L1d2 representation used to model the internal geometry of the space enclosed between the front face of the piston and the primary diaphragm. Since L1d2 is quasi one-dimensional, it cannot handle abrupt area changes along the tube's length. A gradual area change is thus used, however this representation is a departure from the actual geometry, and therefore must be accounted for when interpreting the results. It is assumed that the L1d2 predictions regarding driver gas will be comparable with the actual geometry if identical volumes are compared. For example, a given piston position in L1d2 can be transformed to

the actual geometry if the volume of driver gas in front of the piston is kept equal. Therefore the volume of driver gas is now determined for piston position L in Figure E.4. It will be assumed that there is no buffer installed, and that the piston may move to the beginning of the minimum area cross section. The driver volume therefore depends on whether the piston is in the transition region (Equations E.1 and E.3) or not (Equations E.2 and E.4).

$$\begin{aligned} D_L &= 0.085 + \left(\frac{0.2568 - 0.085}{0.100 - 0} \right) L \\ &= 0.085 + 1.718L, \text{ for } L < 0.100 \text{ m} \end{aligned} \quad (\text{E.1})$$

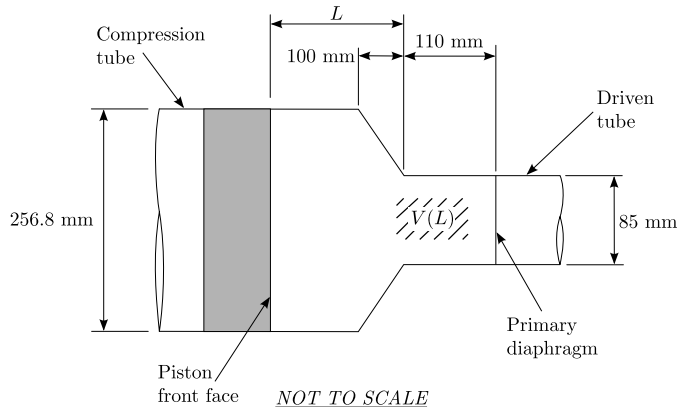
$$D_L = 0.2568, \text{ for } L \geq 0.100 \text{ m} \quad (\text{E.2})$$

$$\begin{aligned} V_{Drv,L1d2} &= \pi \frac{0.085^2}{4} \times 0.110 \\ &\quad + \frac{\pi}{3} \left[\frac{0.085^2}{4} + \frac{0.085}{2} \times \frac{0.085 + 1.718L}{2} + \frac{(0.085 + 1.718L)^2}{4} \right] \times L \\ &= 0.000624 + 0.00567L + 0.115L^2 + 0.773L^3 \text{ m}^3, \text{ for } L < 0.100 \text{ m} \end{aligned} \quad (\text{E.3})$$

$$\begin{aligned} V_{Drv,L1d2} &= \pi \frac{0.085^2}{4} \times 0.110 \\ &\quad + \frac{\pi}{3} \left(\frac{0.085^2}{4} + \frac{0.085}{2} \times \frac{0.2568}{2} + \frac{0.2568^2}{4} \right) \times 0.100 \\ &\quad + \pi \frac{0.2568^2}{4} \times (L - 0.100) \\ &= 0.0518L - 0.00207 \text{ m}^3, \text{ for } L \geq 0.100 \text{ m} \end{aligned} \quad (\text{E.4})$$

E.5 Driver Volume: Correction Factors

The preceding driver gas volume calculations have been made in order to permit sensible use of piston position data from L1d2 calculations. A given piston position in L1d2 will be used to calculate a corresponding position in the tunnel, with either nylon rods or rubber buffer, by equating volumes of driver gas between the piston



L1d2 SCHEMATIC

Figure E.4: Buffer geometry - L1d2.

front face and the primary diaphragm (these calculations are only relevant prior to primary diaphragm rupture).

Consider a piston position from L1d2, x_{mid} , which defines the midpoint position of the piston. The piston has a length of 0.221 m, therefore the position of the front face is given by the following:

$$x_{ff} = x_{mid} + 0.221/2 = x_{mid} + 0.111 \text{ m} \quad (\text{E.1})$$

The assumed length of the compression tube, from the rear of the piston, to the area change, is 4.700 m. Therefore, the length between the area change and the front face of the piston, calculated in L1d2, is as follows:

$$L_{L1d2} = 4.700 - x_{ff} = 4.700 - x_{mid} - 0.111 = 4.590 - x_{mid} \text{ m} \quad (\text{E.2})$$

E.5.1 No Buffer Correction

The conversion for length from L1d2, L_{L1d2} , to an equivalent length with no buffer present, is now calculated by equating volumes.

$$V_{Drv,NoBuffer} = V_{Drv,L1d2} \quad (\text{E.3})$$

For $L_{L1d2} < 0.100 \text{ m}$,

$$0.0518L + 0.000624 = 0.000624 + 0.00567L_{L1d2} + 0.115L_{L1d2}^2 + 0.773L_{L1d2}^3 \\ \rightarrow L_{Corr,NoBuffer} = 0.109L_{L1d2} + 2.22L_{L1d2}^2 + 14.9L_{L1d2}^3 \text{ m (E.4)}$$

For $L_{L1d2} \geq 0.100$ m,

$$0.0518L + 0.000624 = 0.0518L_{L1d2} - 0.00207 \\ \rightarrow L_{Corr,NoBuffer} = L_{L1d2} - 0.00269 \text{ m (E.5)}$$

E.5.2 Rubber Buffer Correction

The conversion for length from L1d2, L_{L1d2} , to an equivalent length with rubber buffer is now calculated by equating volumes.

$$V_{Drv,Buffer} = V_{Drv,L1d2} \text{ (E.6)}$$

For $L_{L1d2} < 0.100$ m,

$$0.0518L - 0.0000258 = 0.000624 + 0.00567L_{L1d2} + 0.115L_{L1d2}^2 + 0.773L_{L1d2}^3 \\ \rightarrow L_{Corr,Buffer} = 0.0125 + 0.109L_{L1d2} + 2.22L_{L1d2}^2 + 14.9L_{L1d2}^3 \text{ m (E.7)}$$

For $L_{L1d2} \geq 0.100$ m,

$$0.0518L - 0.0000258 = 0.0518L_{L1d2} - 0.00207 \\ \rightarrow L_{Corr,Buffer} = L_{L1d2} - 0.0395 \text{ m (E.8)}$$

E.5.3 Nylon Stud Correction

The conversion for length from L1d2, L_{L1d2} , to an equivalent length of nylon stud, L_s , is also calculated by equating volumes.

$$V_{Drv,Nylon} = V_{Drv,L1d2} \text{ (E.9)}$$

For $L_{L1d2} < 0.100$ m,

$$0.000624 + 0.0518L - 0.0118L_s = 0.000624 + 0.00567L_{L1d2} + 0.115L_{L1d2}^2 + 0.773L_{L1d2}^3 \\ \rightarrow L_{Corr,Nylon} = 0.228L_s + 0.109L_{L1d2} + 2.22L_{L1d2}^2 + 14.9L_{L1d2}^3 \quad (\text{E.10})$$

Where it is desirable to size the nylon stud to coincide with piston position, set $L_{Corr,Nylon} = L_s$:

$$L_{Corr,Nylon} = L_s = 0.228L_s + 0.109L_{L1d2} + 2.22L_{L1d2}^2 + 14.9L_{L1d2}^3 \text{ m} \quad (\text{E.11})$$

$$\rightarrow L_s = 0.141L_{L1d2} + 2.88L_{L1d2}^2 + 19.3L_{L1d2}^3 \text{ m} \quad (\text{E.12})$$

For $L_{L1d2} \geq 0.100$ m,

$$0.000624 + 0.0518L - 0.0118L_s = 0.0518L_{L1d2} - 0.00207 \\ \rightarrow L_{Corr,Nylon} = 0.228L_s + L_{L1d2} - 0.00269 \text{ m} \quad (\text{E.13})$$

Once again, where it is desirable to size the nylon stud to coincide with piston position, set $L_{Corr,Nylon} = L_s$:

$$L_{Corr,Nylon} = L_s = 0.228L_s + L_{L1d2} - 0.00269 \text{ m} \quad (\text{E.14})$$

$$\rightarrow L_s = 1.30L_{L1d2} - 0.00348 \text{ m} \quad (\text{E.15})$$

Appendix F

Nylon Studs: Allowable Piston Impact Speed

Consider n nylon studs evenly spaced around the X2 buffer attachment plate, each with length, L_s , and diameter, D_s . An example of such a buffer is shown in Figure F.1. The interfacing area of each stud is as follows:

$$A_s = \frac{\pi D_s^2}{4} \quad (\text{F.1})$$



Figure F.1: Example of a buffer comprised of 6×50 mm DIA nylon studs.

It is assumed that the studs fail plastically at constant volume and constant pressure. Considering a single stud with original length L_s , area A_s , and resisting a pressure σ_{av} as it deforms, the total work required, W_s , to induce a deformation

of length, x , can be calculated. Assuming constant volume, the cross-sectional area for a change in stud length, x , is as follows:

$$A_{s,x} = \frac{A_s L_s}{L_s - x} \quad (\text{F.2})$$

The work required to deform the stud by length, x , is therefore as follows:

$$W_s = \int_0^x \sigma_{av} A_{s,x} dx = \int_0^x \sigma_{av} \left(\frac{A_s L_s}{L_s - x} \right) dx \quad (\text{F.3})$$

Evaluating the integral in Equation F.3, and setting $u = (L_s - x)$:

$$W_s = -\sigma_{av} A_s L_s \int_{L_s}^{(L_s-x)} \left(\frac{1}{u} \right) du = -\sigma_{av} A_s L_s \ln \left| \frac{L_s - x}{L_s} \right| \quad (\text{F.4})$$

Setting the total work to deform n studs equal to the kinetic of the piston at impact:

$$nW_s = -n\sigma_{av} A_s L_s \ln \left| \frac{L_s - x}{L_s} \right| = \frac{1}{2} m_p u_{imp}^2 \quad (\text{F.5})$$

Substituting Equation F.1 into Equation F.5 and rearranging the result, the maximum piston impact speed that can be absorbed for a given nylon stud configuration is therefore as follows:

$$u_{imp} = \left[-n\sigma_{av} \frac{\pi D_s^2}{2m_p} L_s \ln \left| \frac{L_s - x}{L_s} \right| \right]^{\frac{1}{2}} \quad (\text{F.6})$$

Noting the above analysis, it is essential that there is sufficient free space adjacent to the nylon studs to ensure they have room to increase diameter. If they become constrained from deforming radially (due to contact with the tunnel walls, or with the other studs) then the stiffness of the nylon studs will increase by orders of magnitude since further displacement will require actual volumetric reduction as opposed to plastic redistribution.

Therefore, the crushed area of the studs must not exceed the cross-sectional area of the tube. Setting the total crushed area, Equation F.2, for n studs, equal to the compression tube area:

$$nA_{s,max} = n \frac{A_s L_s}{L_s - \Delta L_{s,max}} = \frac{\pi D^2}{4} \quad (\text{F.7})$$

Also, setting $x = \Delta L_{s,max}$ in Equation F.7, and substituting Equation F.1:

$$n \frac{\pi D_s^2}{4} \frac{L_s}{L_s - \Delta L_{s,max}} = \frac{\pi D^2}{4} \quad (\text{F.8})$$

Solving for maximum stud crush displacement, $\Delta L_{s,max}$, in Equation F.8:

$$\Delta L_{s,max} = L_s \left[1 - n \left(\frac{D_s}{D} \right)^2 \right] \quad (\text{F.9})$$

Also, setting $x = \Delta L_{s,max}$ in Equation F.6, maximum permissible impact velocity is determined as follows:

$$u_{imp,max} = \left(-n\sigma_{av} \frac{\pi D_s^2}{2m_p} L_s \ln \left| \frac{L_s - \Delta L_{s,max}}{L_s} \right| \right)^{\frac{1}{2}} \quad (\text{F.10})$$

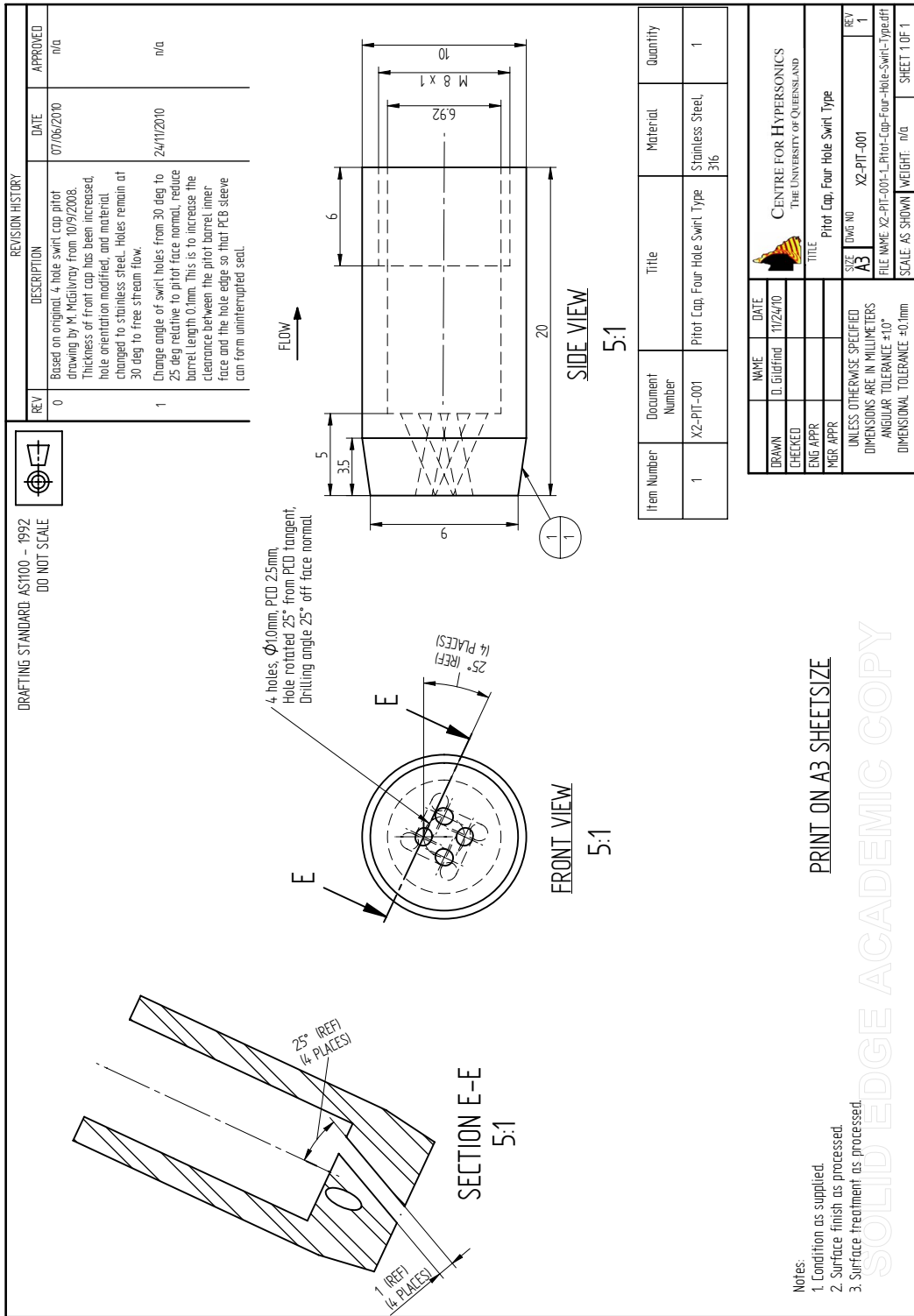
Substituting Equation F.9 into Equation F.10 and simplifying, the maximum permissible impact velocity for a given stud and tunnel configuration may be estimated:

$$u_{imp,max} = \left(-n\sigma_{av} \frac{\pi D_s^2}{2m_p} L_s \ln \left| n \left(\frac{D_s}{D} \right)^2 \right| \right)^{\frac{1}{2}} \quad (\text{F.11})$$

Equation F.11 estimates maximum impact speed based on the assumption that the piston volume is completely filled by the plastically deforming nylon studs; beyond this point the flowing nylon will be volumetrically constrained and the interface pressure will rise substantially. In reality, the nylon will be extruded through the area change into the driven tube, and therefore will never become fully blocked. However, it is not desirable to operate the driver at conditions that would push the mechanism to these limits.

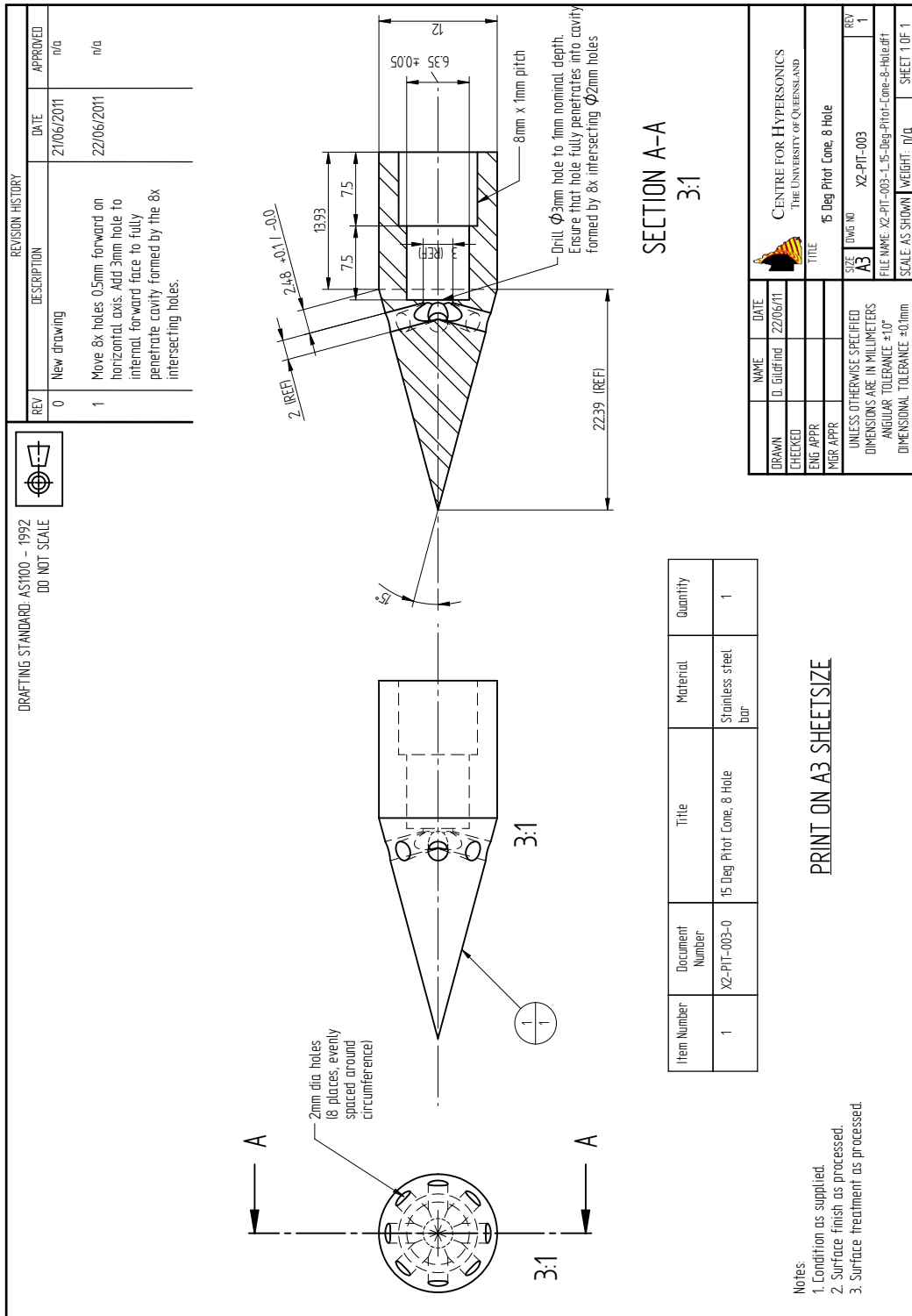
Appendix G

Stainless Steel Pitot Cap Drawing



Appendix H

15 Deg Half Angle Conical Glancing Impact Pressure Probe Drawing



Appendix I

**Results, Mach 12.5 Flow Condition,
X2 *without* Nozzle,
(x2-scr-m12p5-rev-1 in Table 7.5)**

Property	Experimental	L1d2	Eilmer3
<i>Secondary driver</i>			
Shock speed between $sd1$ and $sd2$ (m/s)	$4,112 \pm 0.5\%$ ($\sigma = 23$ m/s)	3,372	-
Shock speed between $sd2$ and $sd3$ (m/s)	$4,210 \pm 0.5\%$ ($\sigma = 38$ m/s)	3,478	-
<i>Shock tube</i>			
Shock speed between $st1$ and $st2$ (m/s)	$1,708 \pm 0.1\%$ ($\sigma = 12$ m/s)	1,666	1,609
Shock speed between $st2$ and $st3$ (m/s)	$1,659 \pm 0.1\%$ ($\sigma = 10$ m/s)	1,699	1,680
<i>Acceleration tube</i>			
Shock speed between $at4$ and $at5$ (m/s)	$4,197 \pm 0.5\%$ ($\sigma = 44$ m/s)	4,347	4,303
Shock speed between $at5$ and $n1$ (m/s)	$4,042 \pm 0.1\%$ ($\sigma = 53$ m/s)	4,342	4,253
<i>Acceleration tube exit plane:</i>			
<i>Final test flow properties</i>			
Static pressure (kPa)	-	-	$11.6 \pm 20\%$
Pitot pressure (kPa)	-	-	$2,246 \pm 13\%$
Mach number (-)	-	-	$12.3 \pm 4\%$
Density (kg/m^3)	-	-	$0.143 \pm 17\%$
Static temperature (K)	-	-	$282 \pm 7\%$
Velocity (m/s)	-	-	$4,130 \pm 2\%$
Stagnation enthalpy (MJ/kg)	-	-	6.68
Total pressure GPa	-	-	8.79
Unit Reynolds number [<i>million/m</i>]	-	-	34.4
Core flow diameter (mm)	-	-	50
Test time [μs]	-	-	50

Table I.1: Test flow properties for Mach 12.5 flow condition, x2-scr-m12p5-rev-1, X2 *without* nozzle. Shock speeds are averaged between the transducer locations. Each Eilmer3 test flow property is the mean value within the core flow averaged across the test time (see Figure I.7); the Eilmer ‘±’ value is the maximum departure from the mean value during the test time. The experimental shock speed ‘±’ is the experimental uncertainty. Total pressure and enthalpy are calculated based on average flow properties during the test time, and assume shifting chemical equilibrium per Chinitz et. al [41].

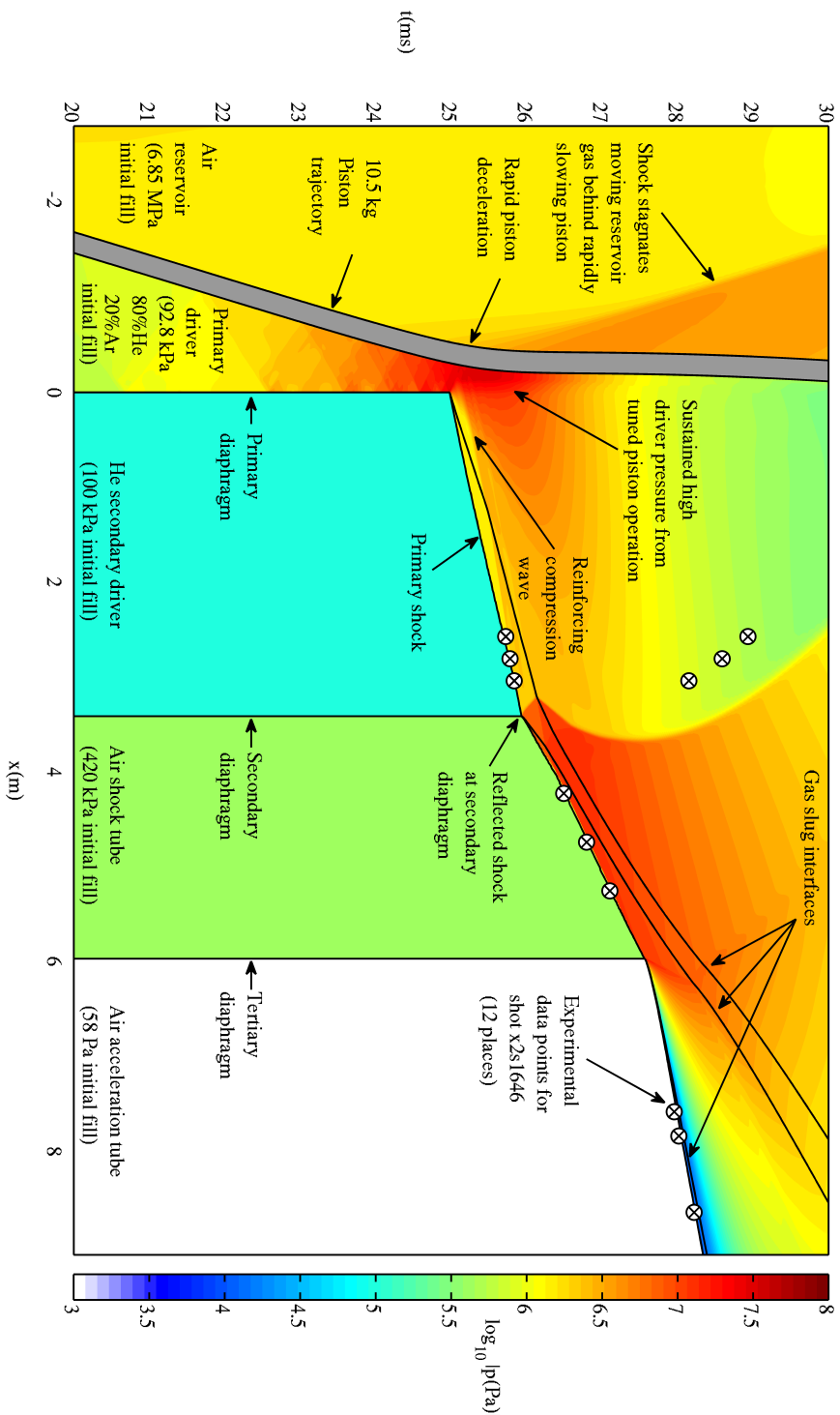


Figure I.1: x - t diagram for Mach 12.5 flow condition, X2 without nozzle (flow condition $\times 2$ -scr-m12p5-rev-1 in Table 7.5). Results are based on L1d2 calculations and experimental measurements.

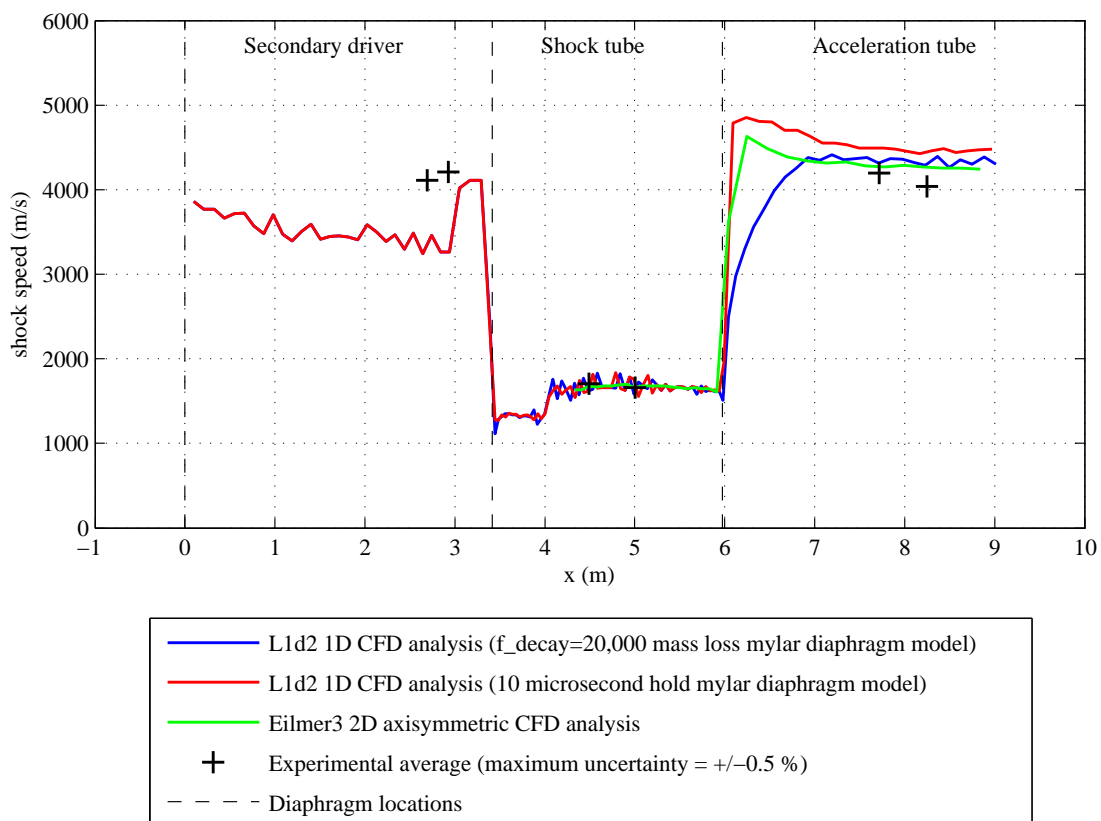


Figure I.2: Primary shock speed vs. position for Mach 12.5 flow condition, X2 *without* nozzle (flow condition x2-scr-m12p5-rev-1 in Table 7.5).

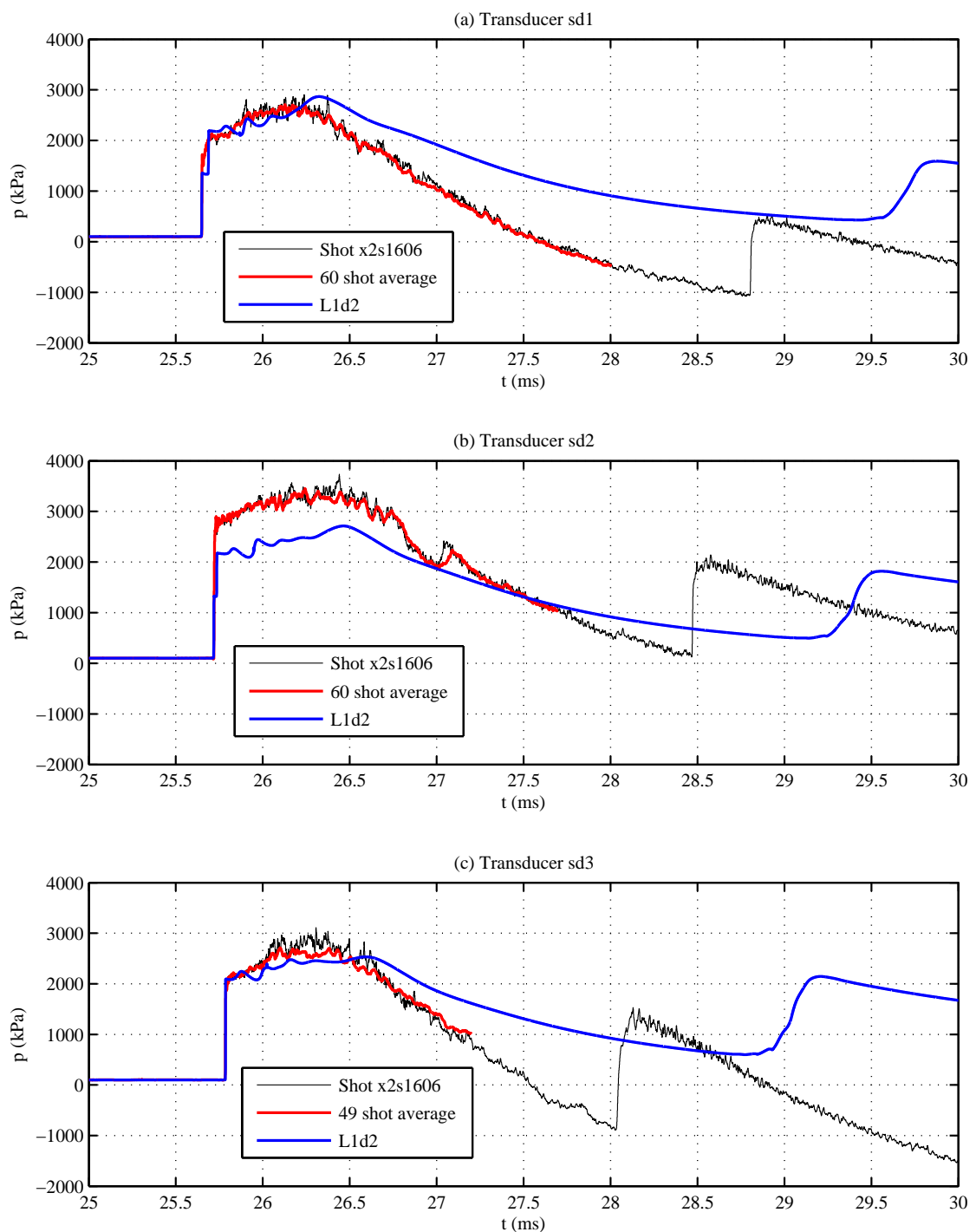


Figure I.3: Static pressures at secondary driver transducers $sd1$, $sd2$, and $sd3$ (flow condition $x2$ -scr-m12p5-rev-1 in Table 7.5).

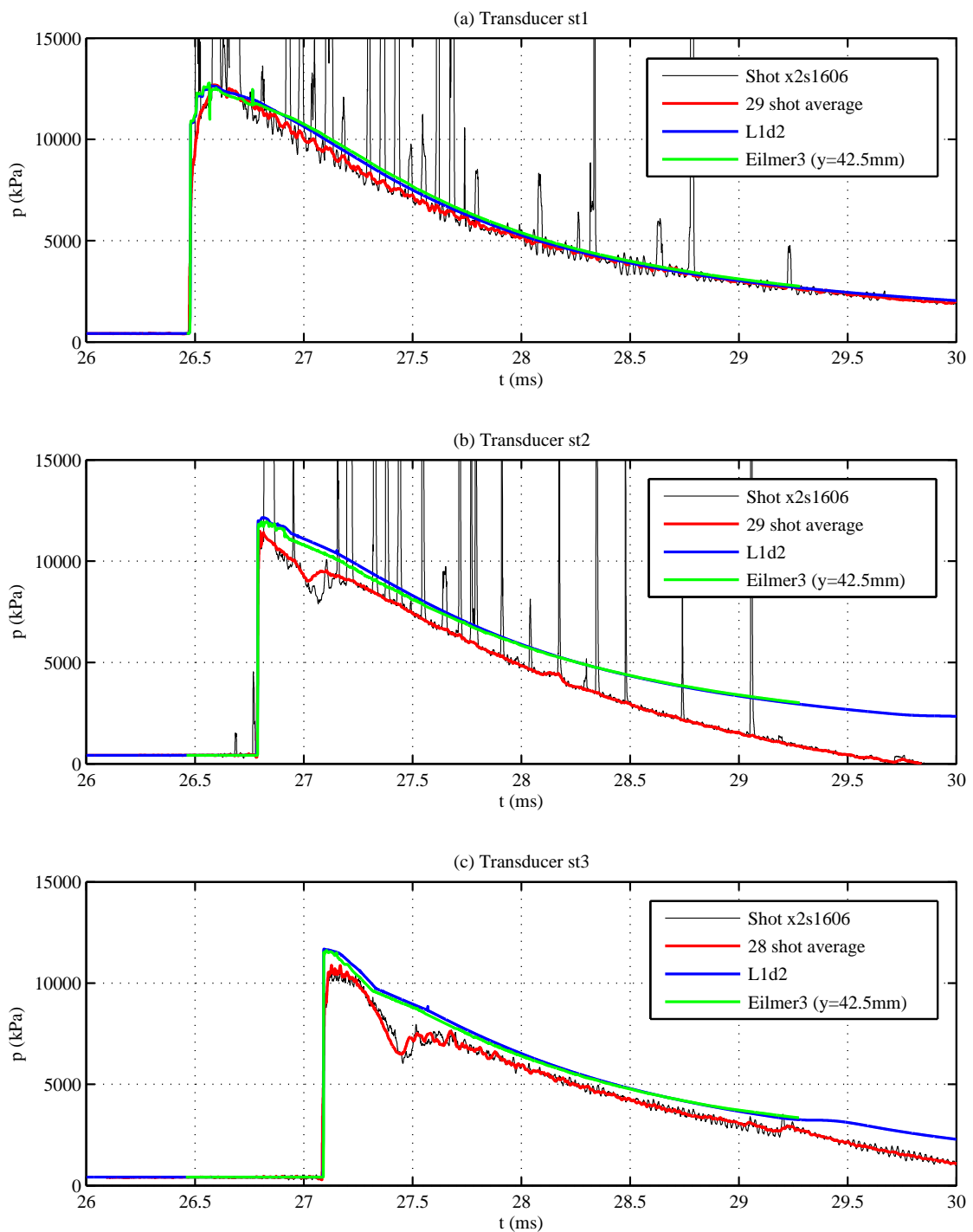


Figure I.4: Static pressures at shock tube transducers $st1$, $st2$, and $st3$ (flow condition $x2\text{-scr-m12p5-rev-1}$ in Table 7.5).

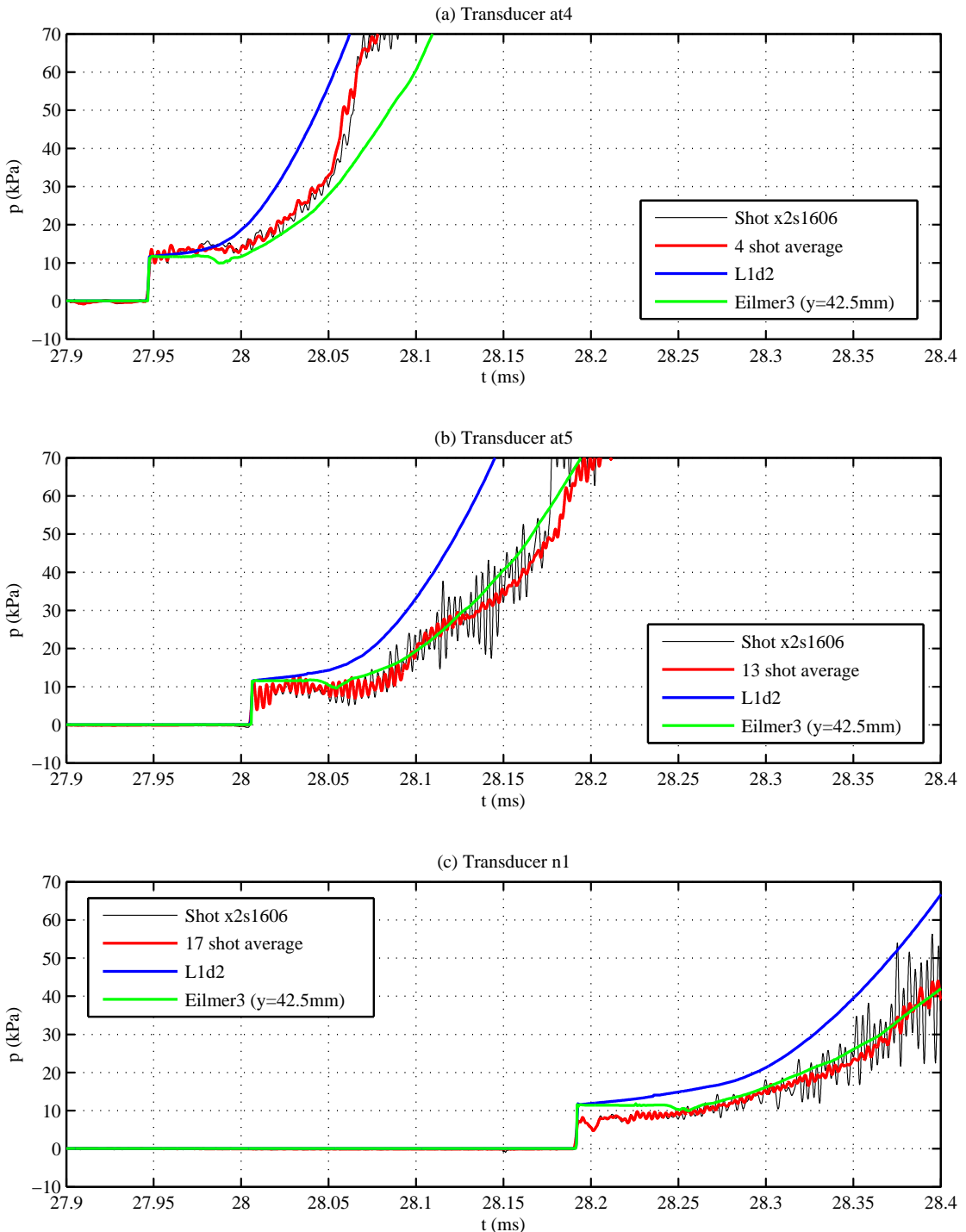


Figure 1.5: Static pressures at acceleration tube transducers *at4*, *at5*, and *n1* (flow condition *x2-scr-m12p5-rev-1* in Table 7.5).

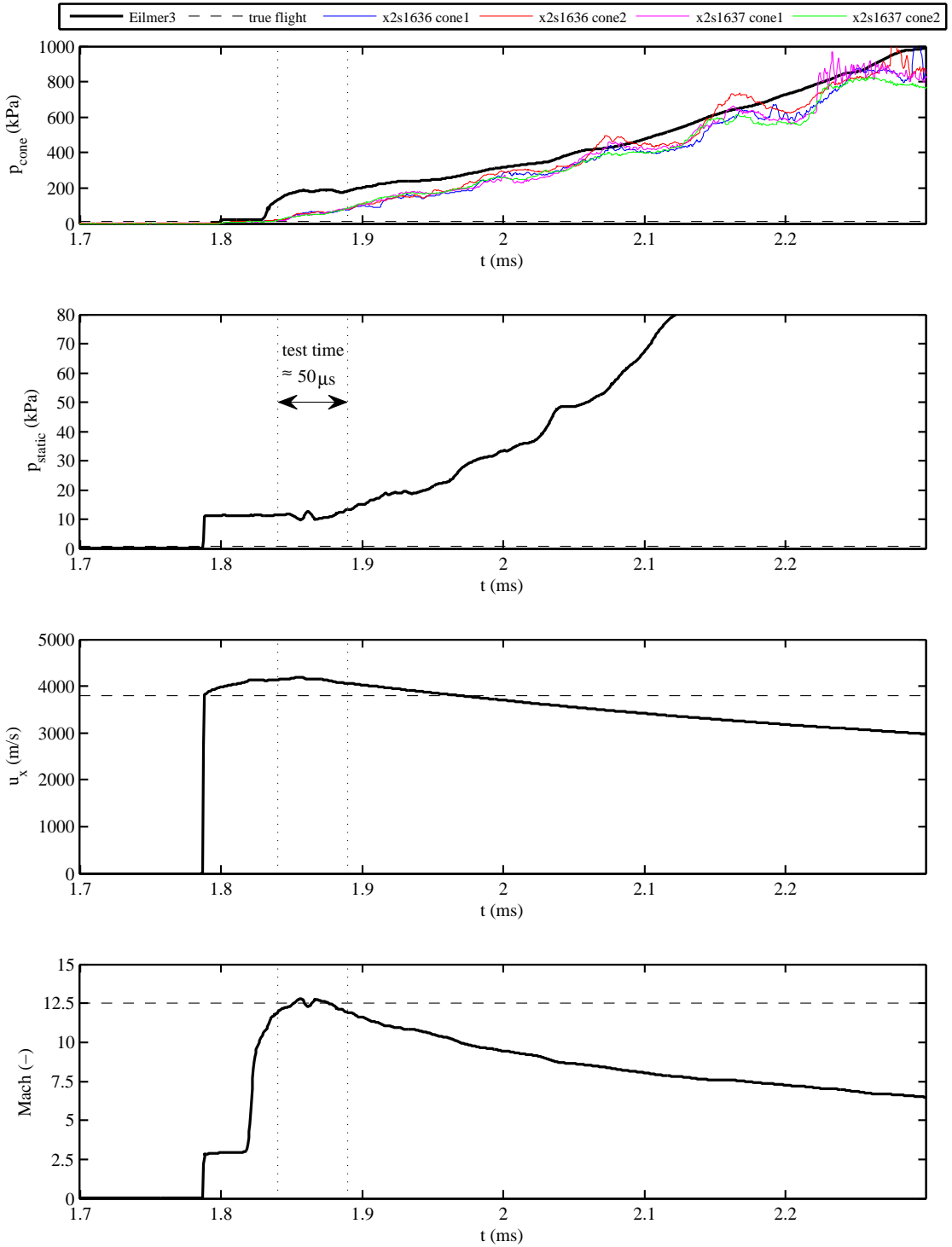


Figure I.6: Computed and experimental test flow properties at the acceleration tube exit, at $y = 0$ mm from the tube centreline (flow condition x2-scr-m12p5-rev-1 in Table 7.5). $t = 0$ corresponds to the beginning of the axisymmetric calculation. Experimental cone pressures in (a) were measured using 15 deg half angle cones; see Section 8.5. Computed Eilmer3 cone pressures were obtained by taking the transient flow history at the equivalent location in the axisymmetric model ($y = 9$ mm) and applying this as a planar inflow to a separate cone axisymmetric model. It is finally noted that true flight cone and static pressures are much lower than experimental or numerical calculations; this indicates significant capacity for pressure-length scaling.

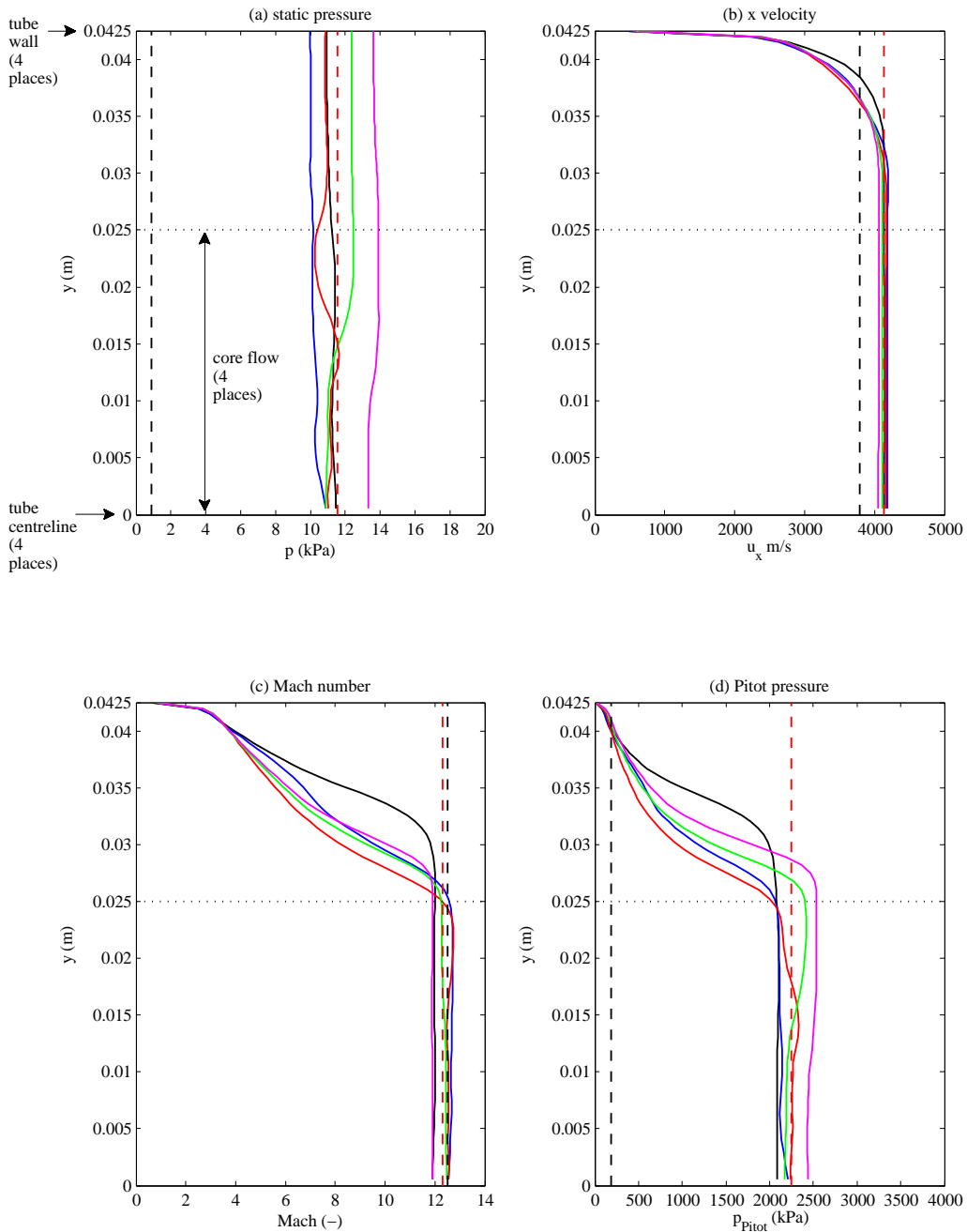


Figure I.7: Radial variation in flow properties during the test time (denoted by tt ; flow condition x2-scr-m12p5-rev-1 in Table 7.5). Test time is assumed to occur between simulation times $t = 0.001840 \mu\text{s}$ and $t = 0.001890 \mu\text{s}$.

Appendix J

**Results, Mach 15.0 Flow Condition,
X2 *without* Nozzle,
(x2-scr-m15p0-rev-1 in Table 7.5)**

Property	Experimental	L1d2	Eilmer3
<i>Secondary driver</i>			
Shock speed between $sd1$ and $sd2$ (m/s)	$4,113 \pm 0.7\% (\sigma = 20 \text{ m/s})$	3,348	-
Shock speed between $sd2$ and $sd3$ (m/s)	$4,195 \pm 0.8\% (\sigma = 28 \text{ m/s})$	3,362	-
<i>Shock tube</i>			
Shock speed between $st1$ and $st2$ (m/s)	$2,044 \pm 0.2\% (\sigma = 42 \text{ m/s})$	1,907	1,895
Shock speed between $st2$ and $st3$ (m/s)	$1,864 \pm 0.2\% (\sigma = 41 \text{ m/s})$	1,969	1,957
<i>Acceleration tube</i>			
Shock speed between $at4$ and $at5$ (m/s)	$5,287 \pm 0.8\% (\sigma = 71 \text{ m/s})$	5,333	5,172
Shock speed between $at5$ and $n1$ (m/s)	$5,096 \pm 0.3\% (\sigma = 70 \text{ m/s})$	5,268	5,111
<i>Acceleration tube exit plane:</i>			
<i>Final test flow properties</i>			
Static pressure (kPa)	-	-	$3.38 \pm 27\%$
Pitot pressure (kPa)	-	-	$825 \pm 29\%$
Mach number (-)	-	-	$13.8 \pm 8\%$
Density (kg/m^3)	-	-	$0.0343 \pm 32\%$
Static temperature (K)	-	-	$345 \pm 21\%$
Velocity (m/s)	-	-	$5,113 \pm 2\%$
Stagnation enthalpy (MJ/kg)	-	-	10.4
Total pressure GPa	-	-	10.4
Unit Reynolds number [<i>million/m</i>]	-	-	8.70
Core flow diameter (mm)	-	-	40
Test time [μs]	-	-	40

Table J.1: Test flow properties for Mach 15.0 flow condition, x2-scr-m15p0-rev-1, X2 *without* nozzle. Shock speeds are averaged between the transducer locations. Each Eilmer3 test flow property is the mean value within the core flow averaged across the test time (see Figure J.7); the Eilmer ‘±’ value is the maximum departure from the mean value during the test time. The experimental shock speed ‘±’ is the experimental uncertainty. Total pressure and enthalpy are calculated based on average flow properties during the test time, and assume shifting chemical equilibrium per Chinitz et. al [41].

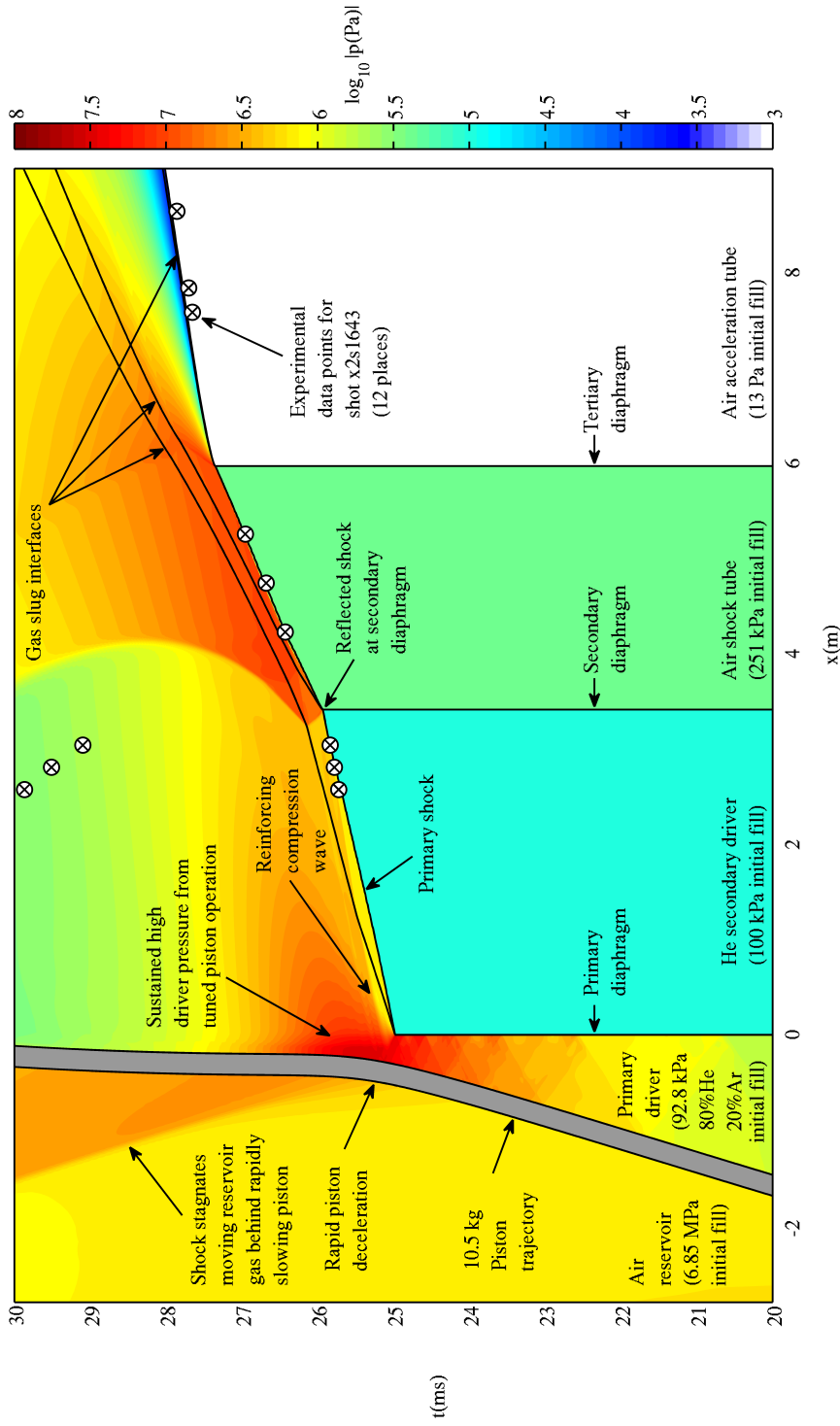


Figure J.1: x - t diagram for Mach 15.0 flow condition, X2 without nozzle (x2-scr-m15p0-rev-1 in Table 7.5). Results are based on L1d2 calculations and experimental measurements.

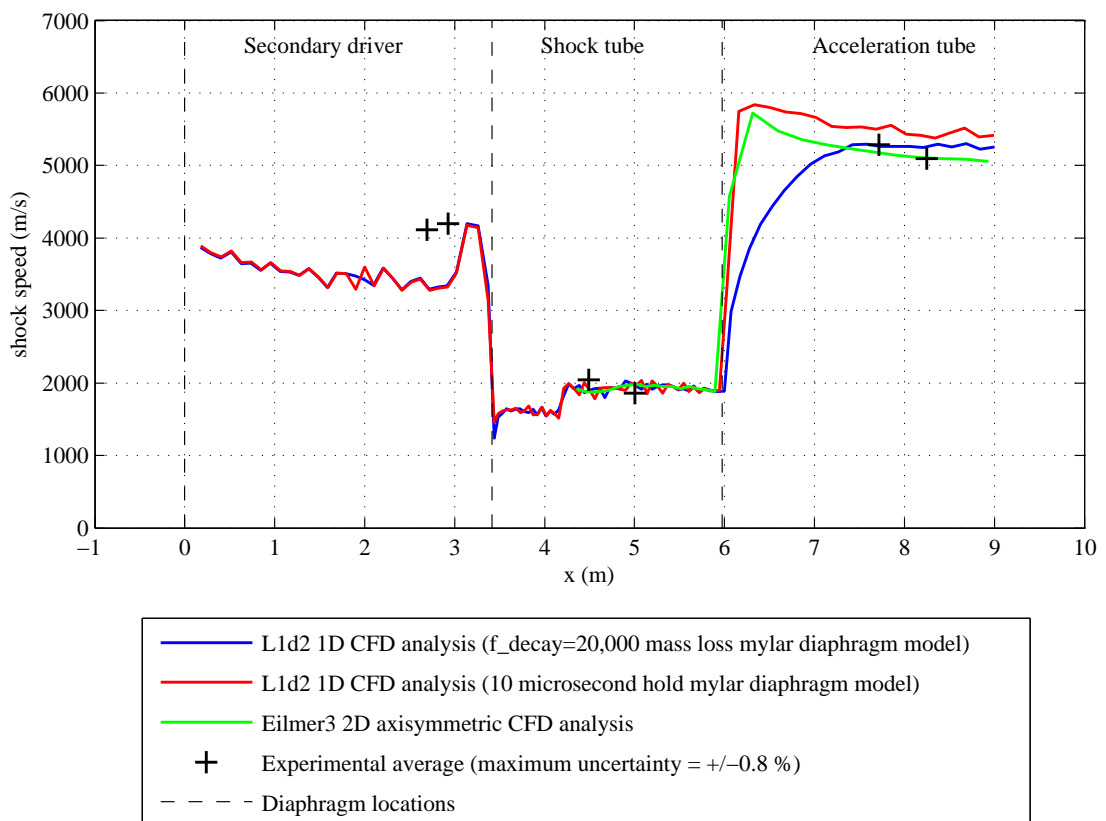


Figure J.2: Primary shock speed vs. position for Mach 15.0 flow condition, X2 *without* nozzle (x2-scr-m15p0-rev-1 in Table 7.5).

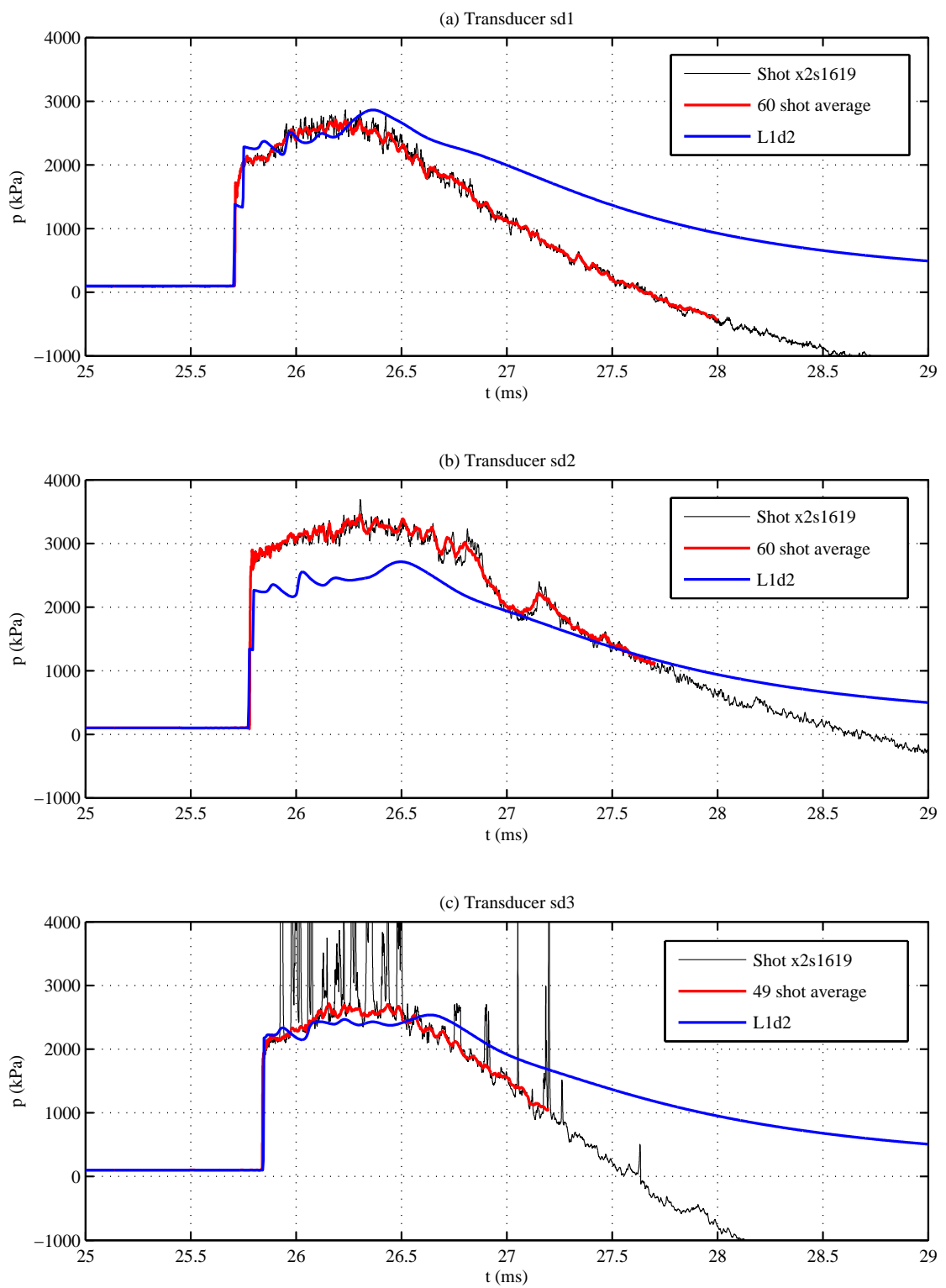


Figure J.3: Static pressures at secondary driver transducers $sd1$, $sd2$, and $sd3$ (flow condition x2-scr-m15p0-rev-1 in Table 7.5).

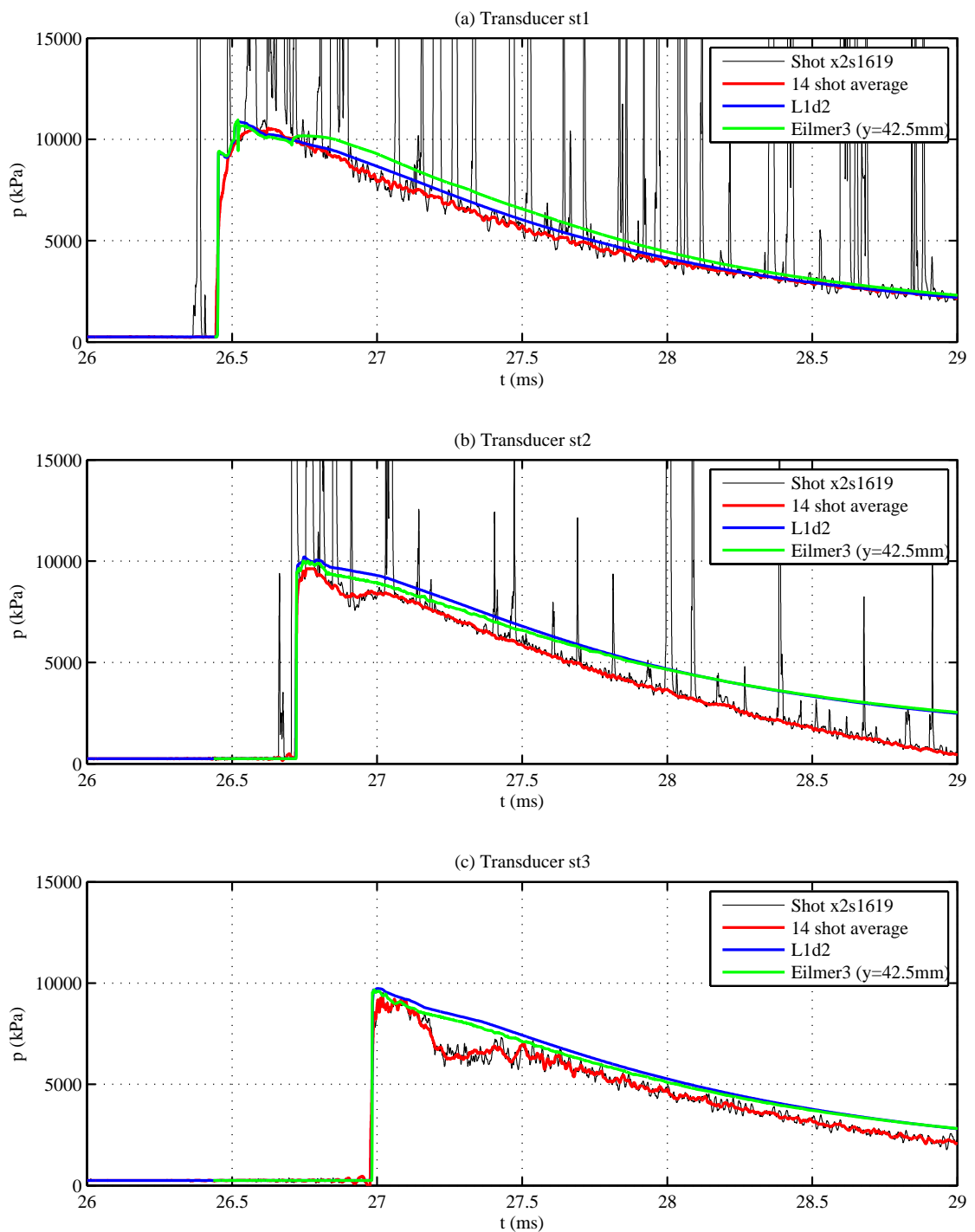


Figure J.4: Static pressures at shock tube transducers $st1$, $st2$, and $st3$ (flow condition x2-scr-m15p0-rev-1 in Table 7.5).

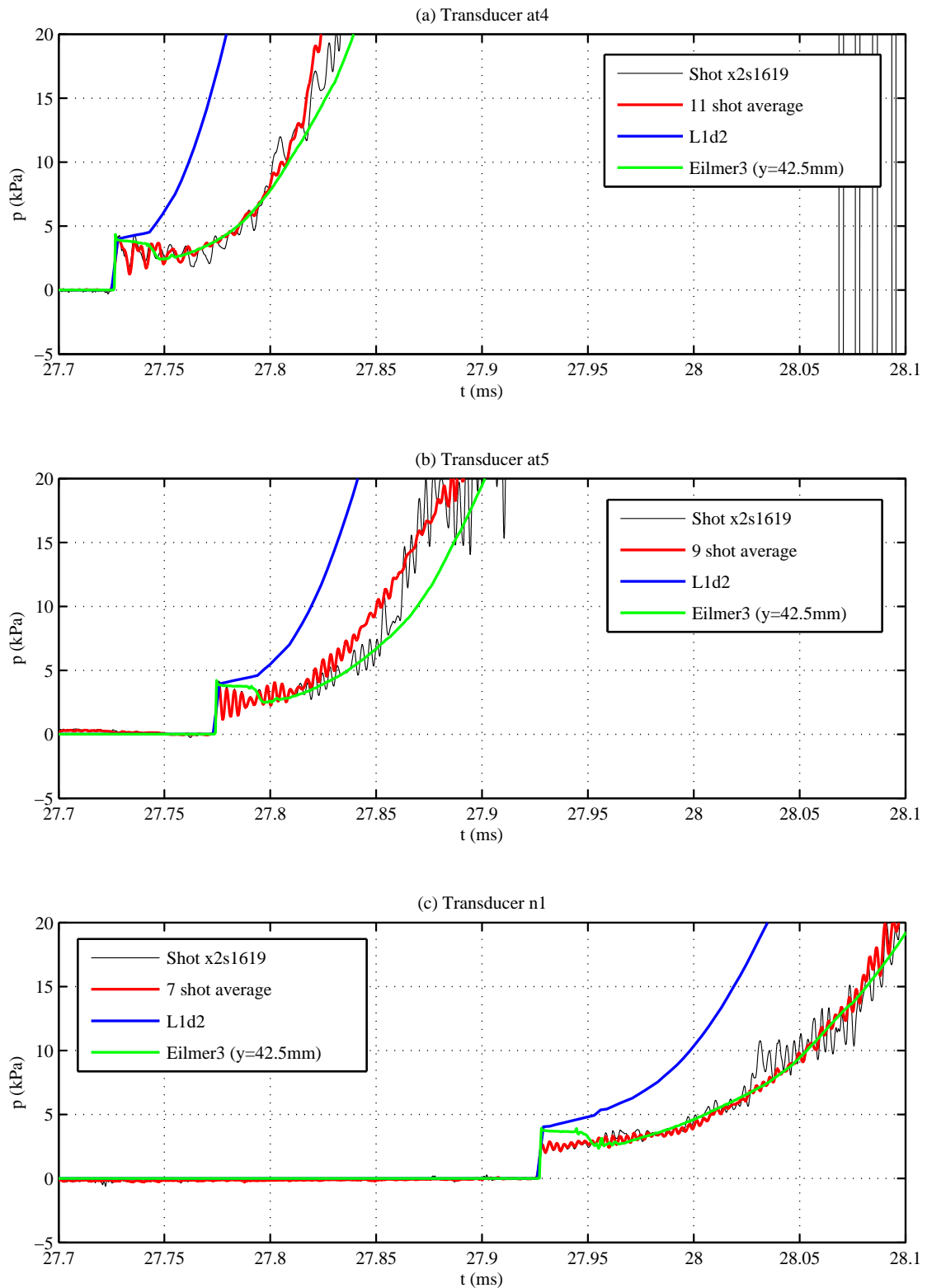


Figure J.5: Static pressures at acceleration tube transducers *at4*, *at5*, and *n1* (flow condition x2-scr-m15p0-rev-1 in Table 7.5).

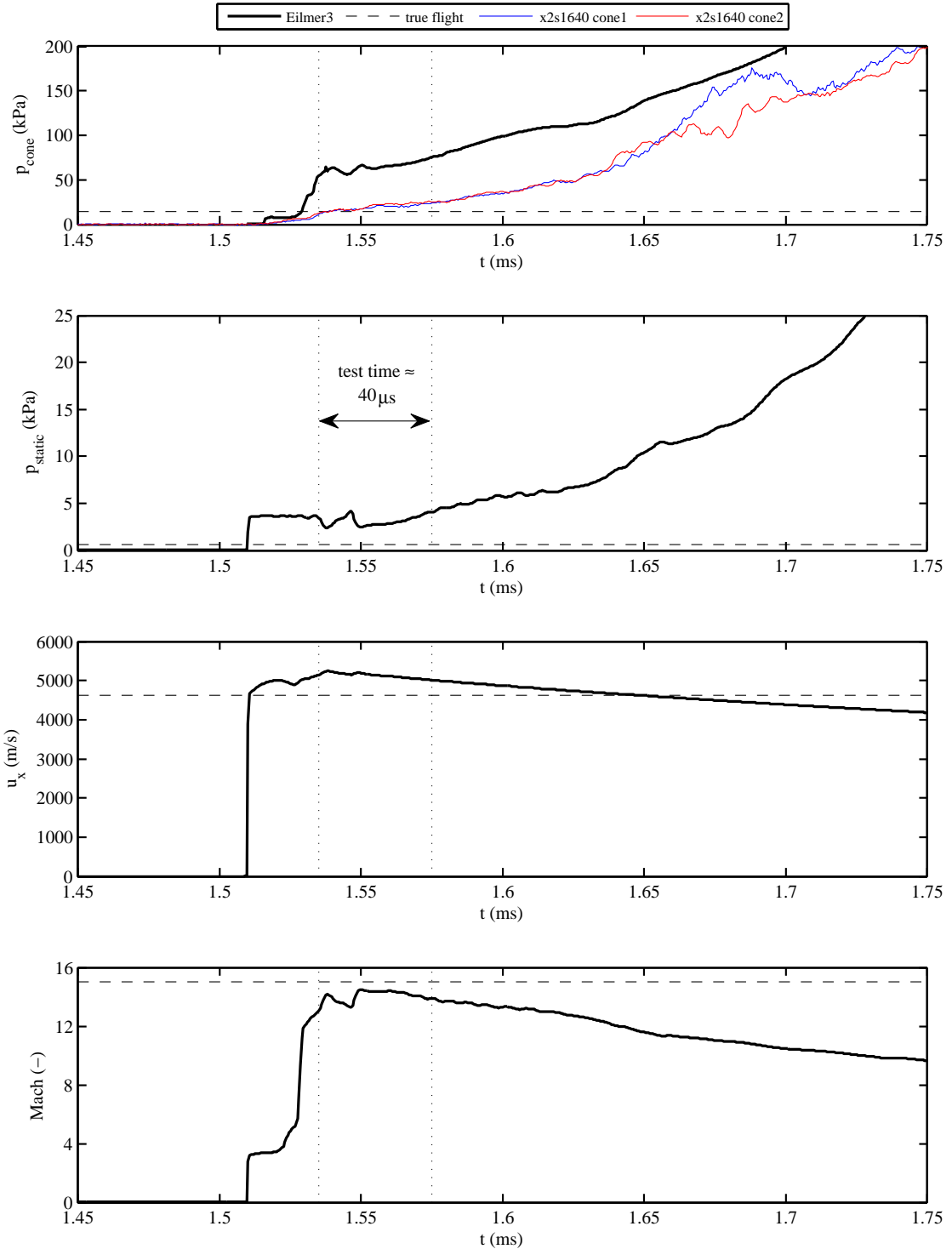


Figure J.6: Computed and experimental test flow properties at the acceleration tube exit, at $y = 0$ mm from the tube centreline, flow condition x2-scr-m15p0-rev-1 in Table 7.5. $t = 0$ corresponds to the beginning of the axisymmetric calculation. Experimental cone pressures in (a) were measured using 15 deg half angle cones; see Section 8.5. Computed Eilmer3 cone pressures were obtained by taking the transient flow history at the equivalent location in the axisymmetric model ($y = 9$ mm) and applying this as a planar inflow to a separate cone axisymmetric model. It is finally noted that true flight cone and static pressures are much lower than experimental or numerical calculations; this indicates significant capacity for pressure-length scaling.

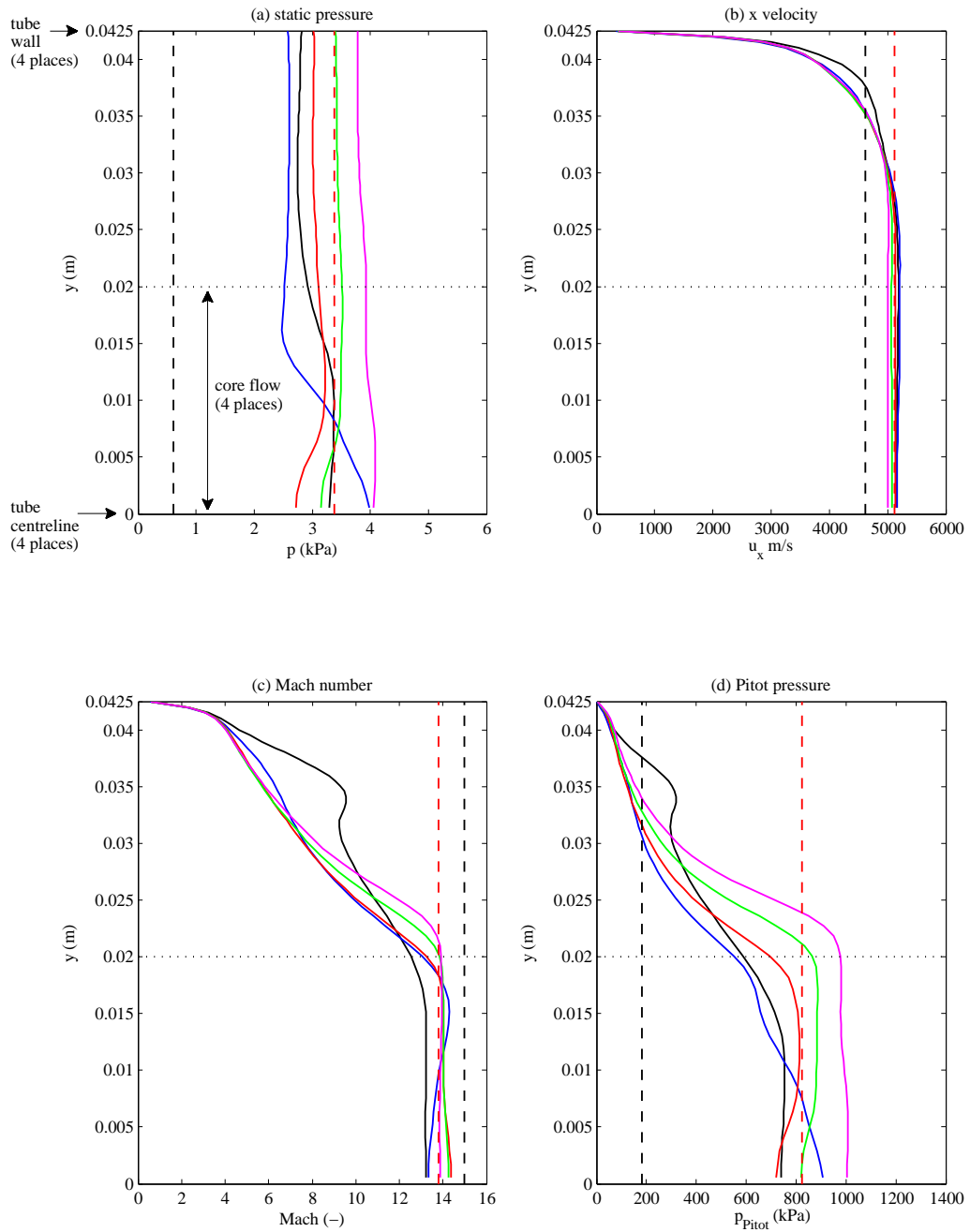


Figure J.7: Radial variation in flow properties during the test time (denoted by tt ; flow condition x2-scr-m15p0-rev-1 in Table 7.5). Test time is assumed to occur between simulation times $t = 0.001535 \mu\text{s}$ and $t = 0.001575 \mu\text{s}$.

Appendix K

Grid Sensitivity Analysis

M10 Hybrid 1D/2D CFD Model, x2-scr-m10p0-rev-1

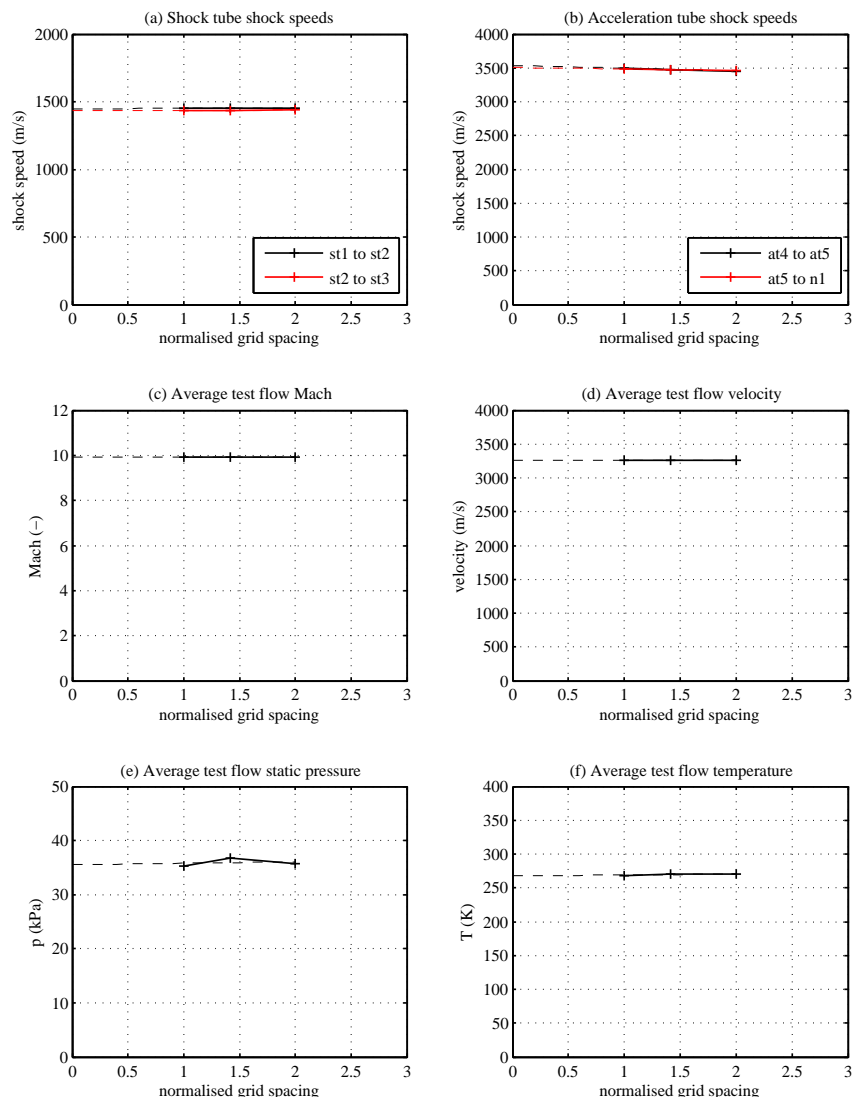


Figure K.1: Variation of selected computed flow properties with normalised grid spacing, flow condition x2-scr-m10p0-rev-1, hybrid CFD model. Normalised grid spacing of 1.0 is that used to produce the results presented in this document. Normalised grid spacings of $\sqrt{2}$ and 2 correspond to 50% and 75% fewer cells compared to the nominal grid used to compute results in Chapter 8.

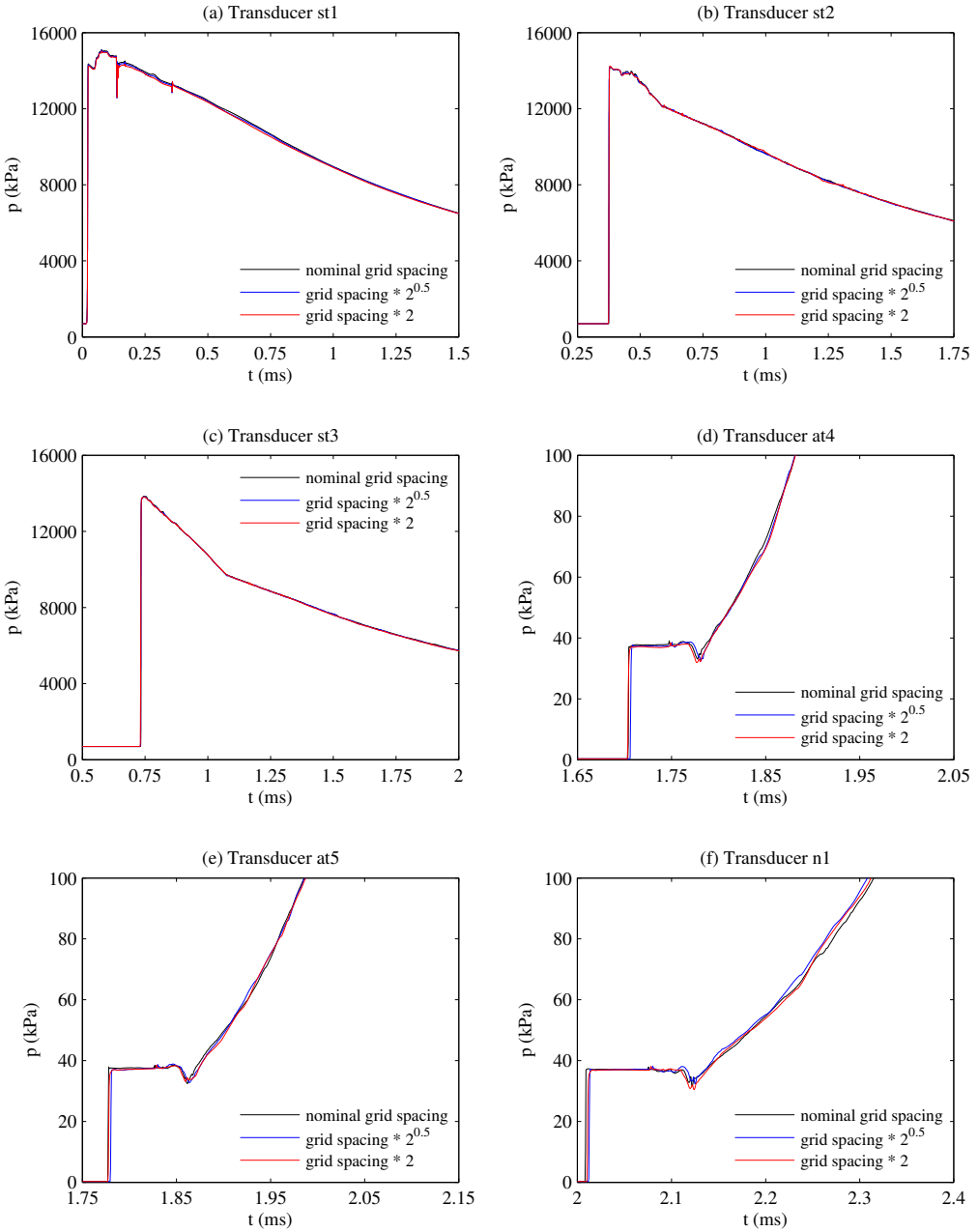


Figure K.2: Comparison of transducer pressure histories for different grid spacings, for flow condition x2-scr-m10p0-rev-1, hybrid CFD model. Normalised grid spacing of 1.0 is that used to produce the results presented in this document. Normalised grid spacings of $\sqrt{2}$ and 2 correspond to 50% and 75% fewer cells compared to the nominal grid used to compute results in Chapter 8.

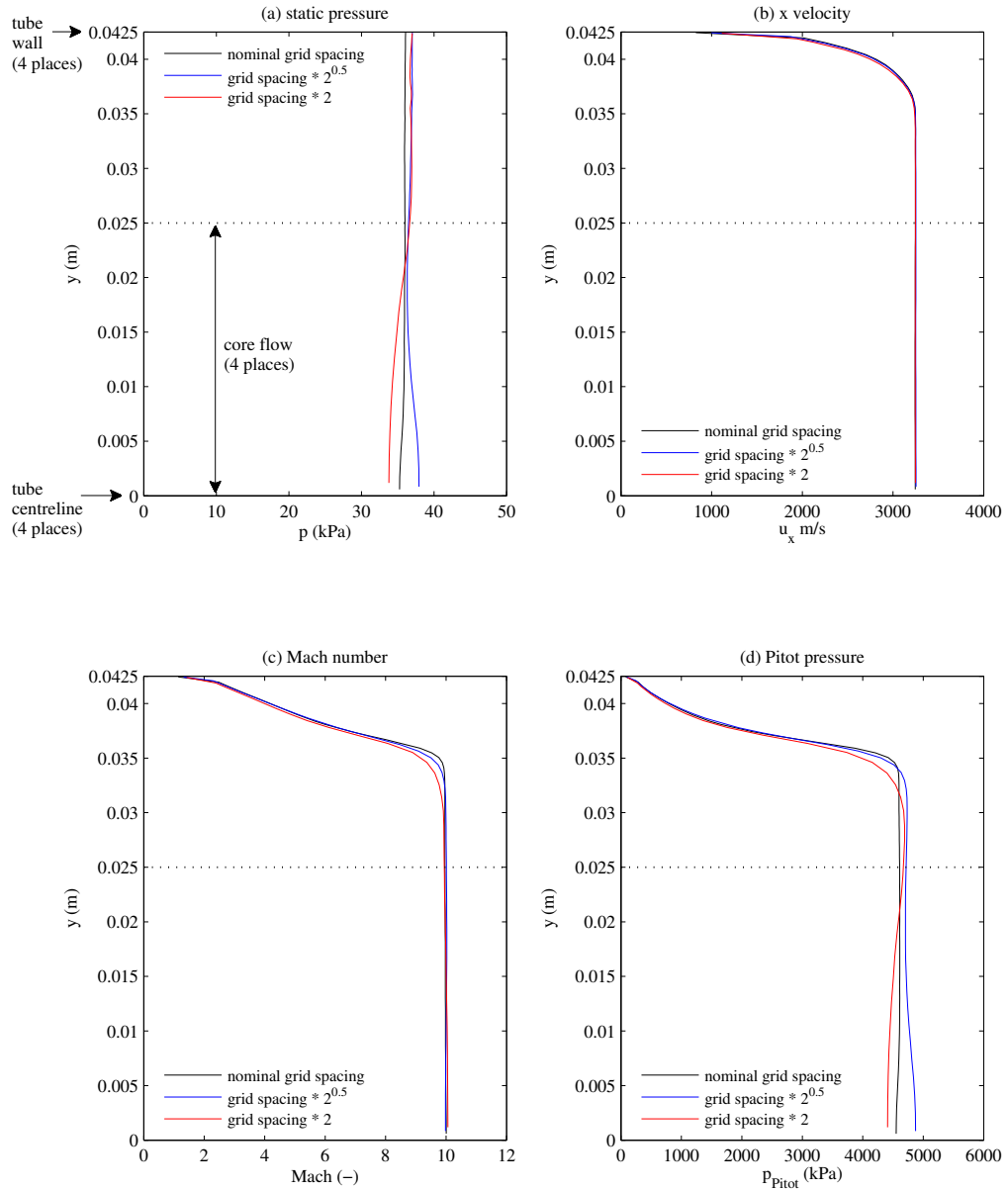


Figure K.3: Comparison of radial variation in flow properties across tube exit, at 25% of test time, for different grid spacings, for flow condition x2-scr-m10p0-rev-1, hybrid CFD model. Normalised grid spacing of 1.0 is that used to produce the results presented in this document. Normalised grid spacings of $\sqrt{2}$ and 2 correspond to 50% and 75% fewer cells compared to the nominal grid used to compute results in Chapter 8.

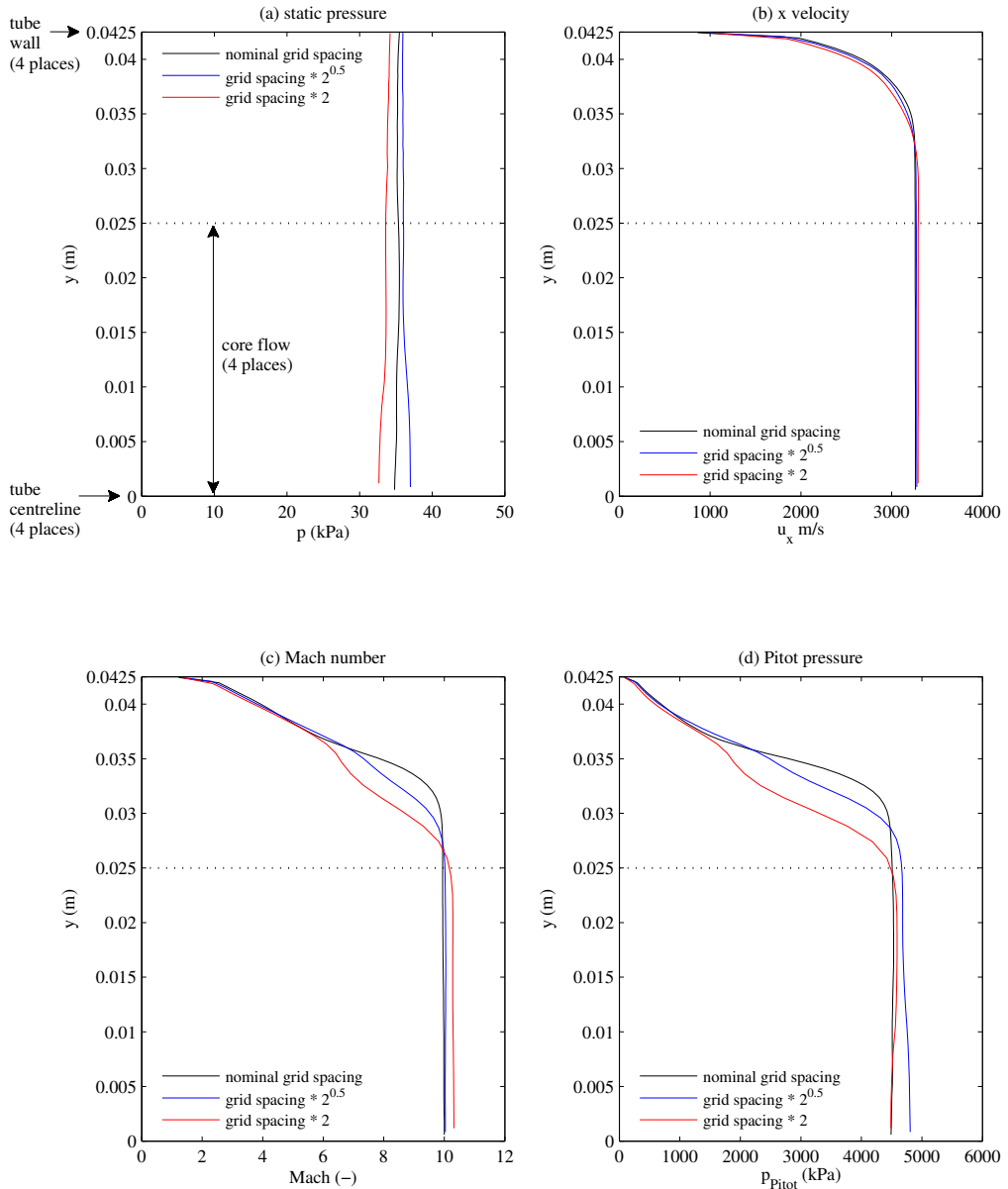


Figure K.4: Comparison of radial variation in flow properties across tube exit, at 50% of test time, for different grid spacings, for flow condition x2-scr-m10p0-rev-1, hybrid CFD model. Normalised grid spacing of 1.0 is that used to produce the results presented in this document. Normalised grid spacings of $\sqrt{2}$ and 2 correspond to 50% and 75% fewer cells compared to the nominal grid used to compute results in Chapter 8.

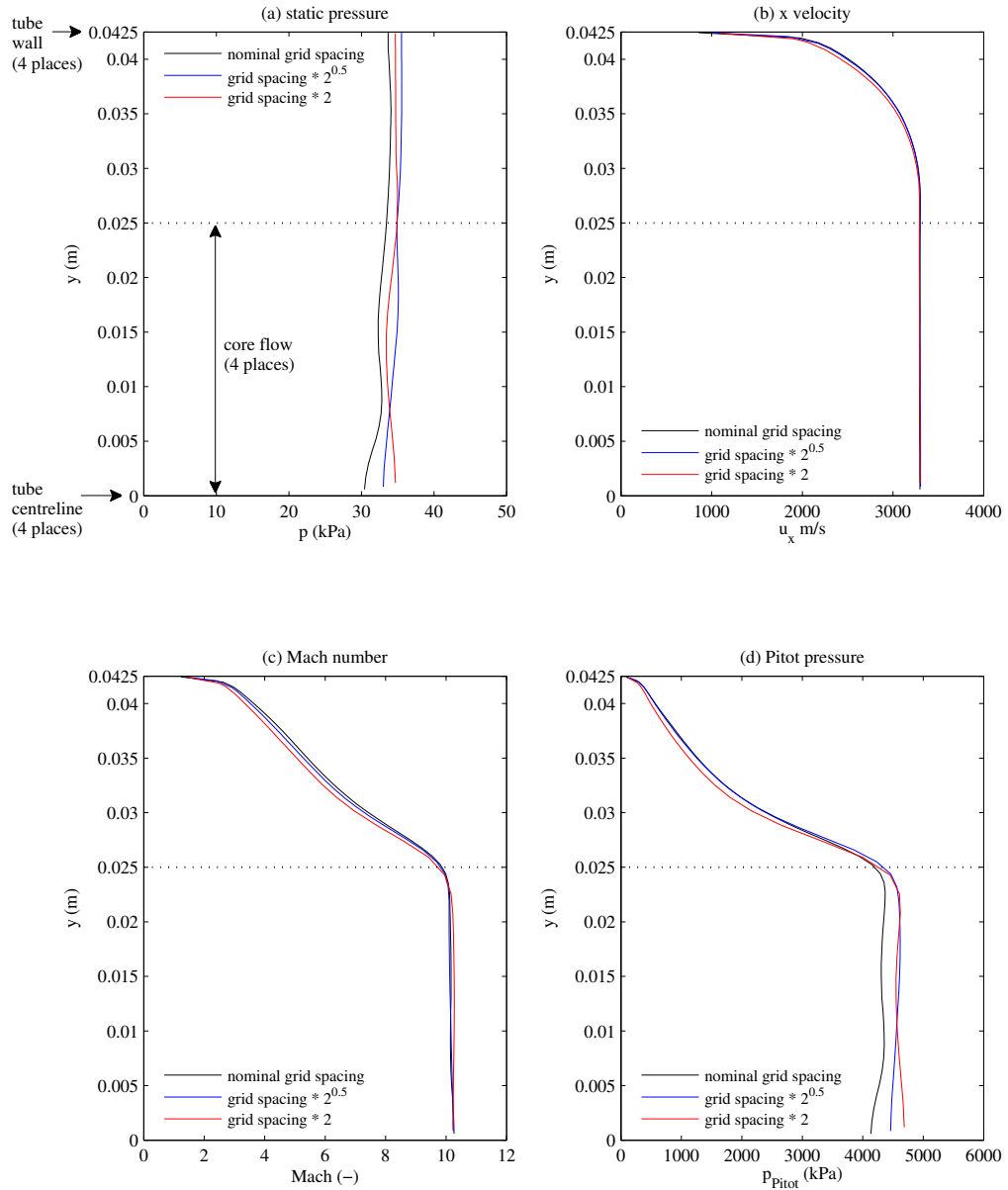


Figure K.5: Comparison of radial variation in flow properties across tube exit, at 75% of test time, for different grid spacings, for flow condition x2-scr-m10p0-rev-1, hybrid CFD model. Normalised grid spacing of 1.0 is that used to produce the results presented in this document. Normalised grid spacings of $\sqrt{2}$ and 2 correspond to 50% and 75% fewer cells compared to the nominal grid used to compute results in Chapter 8.

M10 Hybrid 1D/2D CFD Model, x2-scr-m10p0-noz-rev-1

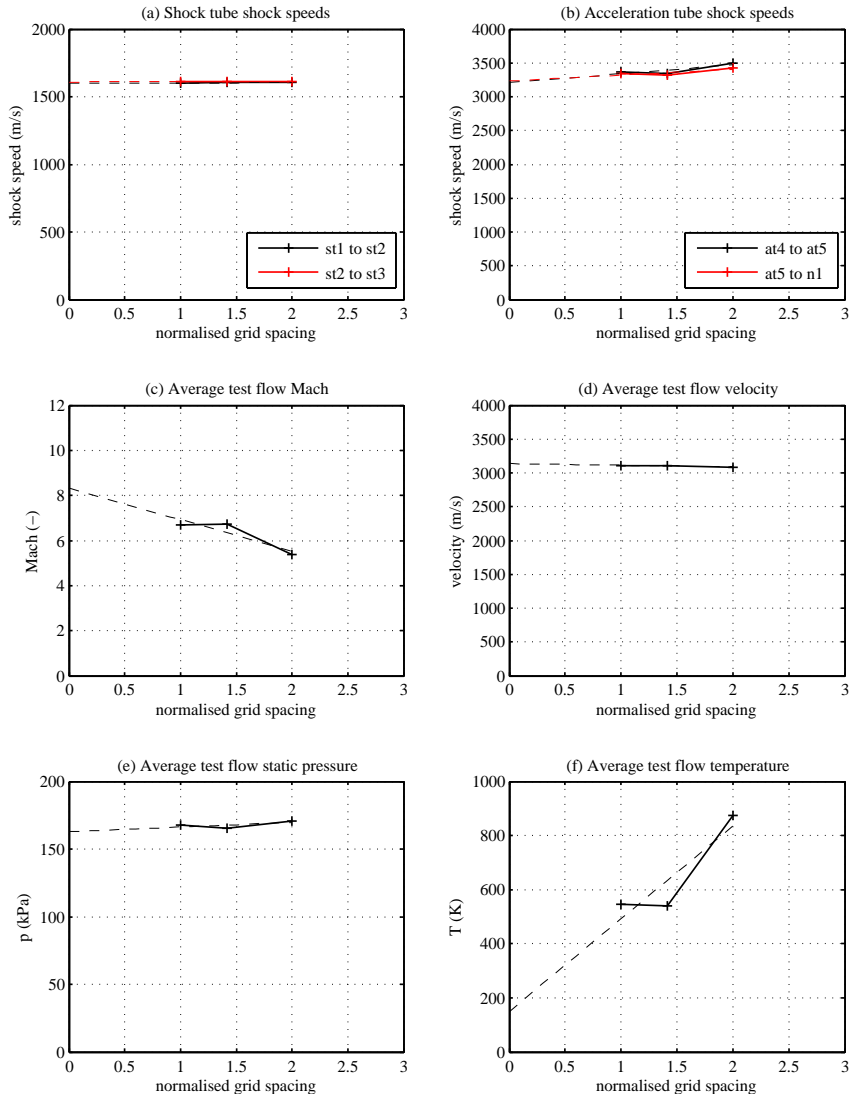


Figure K.6: Variation of selected computed flow properties with normalised grid spacing, flow condition x2-scr-m10p0-noz-rev-1, hybrid CFD model, flow at nozzle *inlet*. Normalised grid spacing of 1.0 is that used to produce the results presented in this document. Normalised grid spacings of $\sqrt{2}$ and 2 correspond to 50% and 75% fewer cells compared to the nominal grid used to compute results in Chapter 8.

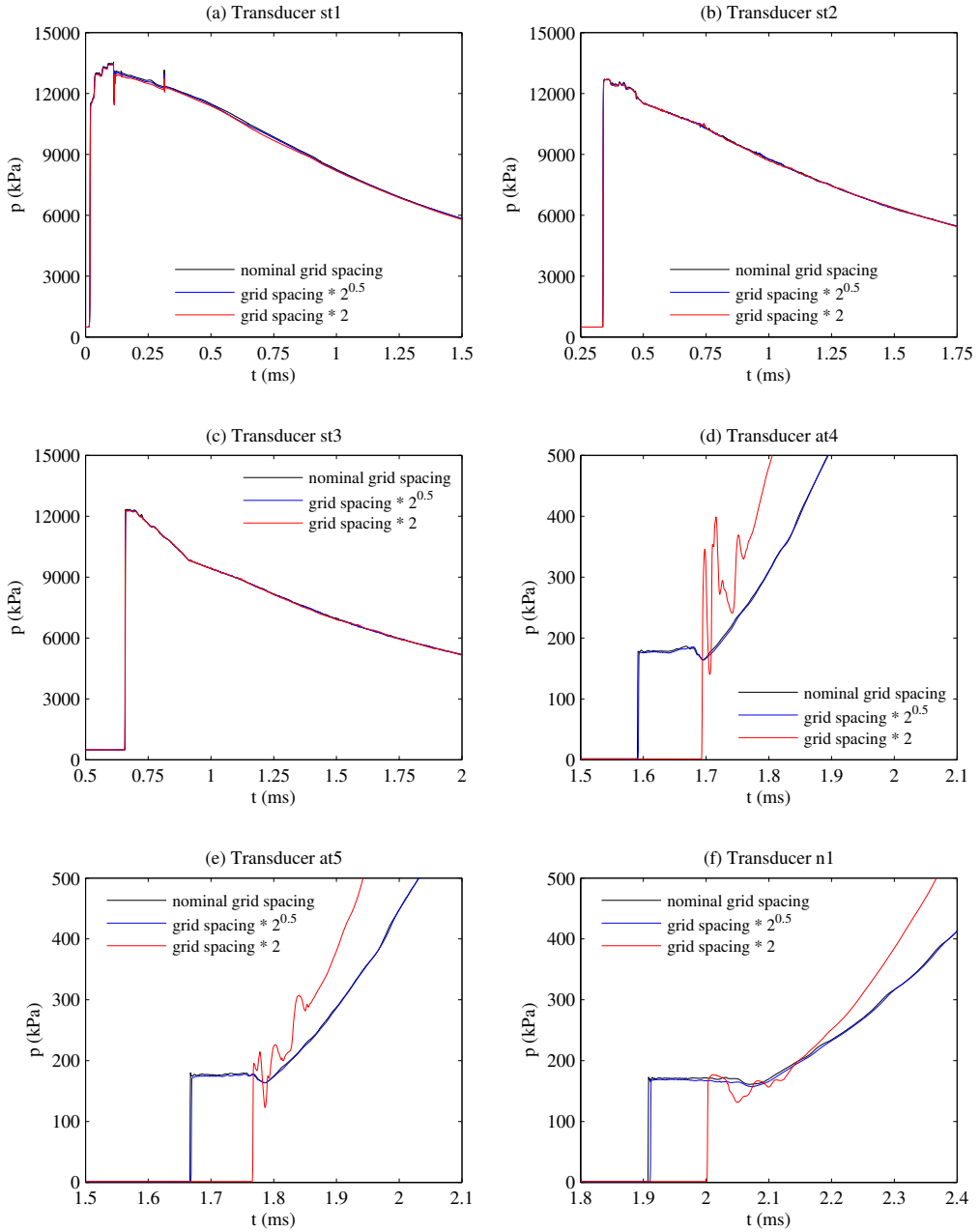


Figure K.7: Comparison of transducer pressure histories for different grid spacings, for flow condition x2-scr-m10p0-noz-rev-1, hybrid CFD model, flow at nozzle *inlet*. Normalised grid spacing of 1.0 is that used to produce the results presented in this document. Normalised grid spacings of $\sqrt{2}$ and 2 correspond to 50% and 75% fewer cells compared to the nominal grid used to compute results in Chapter 8.

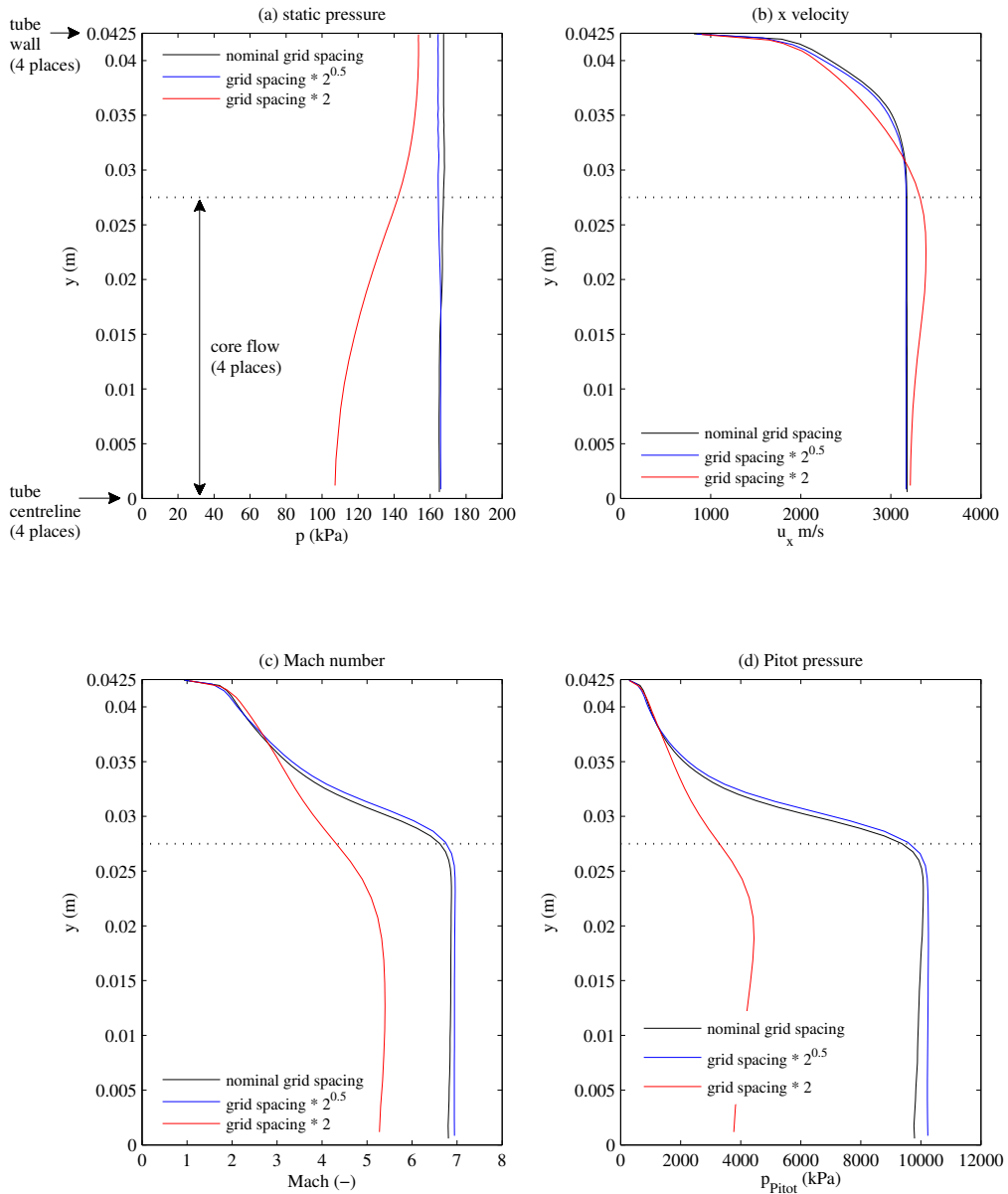


Figure K.8: Comparison of radial variation in flow properties across nozzle *inlet*, at 25% of test time, for different grid spacings, for flow condition x2-scr-m10p0-noz-rev-1, hybrid CFD model. Normalised grid spacing of 1.0 is that used to produce the results presented in this document. Normalised grid spacings of $\sqrt{2}$ and 2 correspond to 50% and 75% fewer cells compared to the nominal grid used to compute results in Chapter 8.

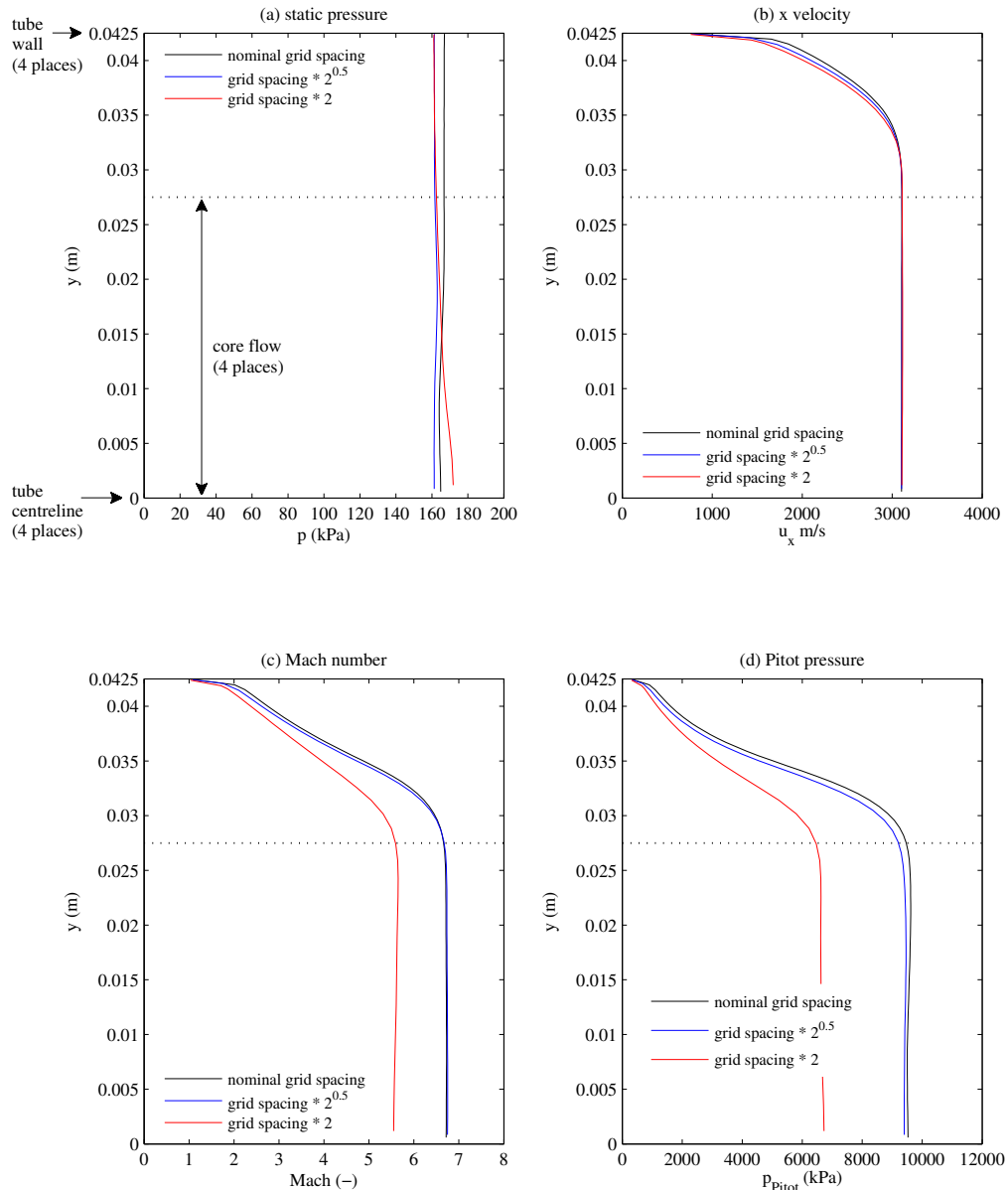


Figure K.9: Comparison of radial variation in flow properties across nozzle *inlet*, at 50% of test time, for different grid spacings, for flow condition x2-scr-m10p0-noz-rev-1, hybrid CFD model. Normalised grid spacing of 1.0 is that used to produce the results presented in this document. Normalised grid spacings of $\sqrt{2}$ and 2 correspond to 50% and 75% fewer cells compared to the nominal grid used to compute results in Chapter 8.

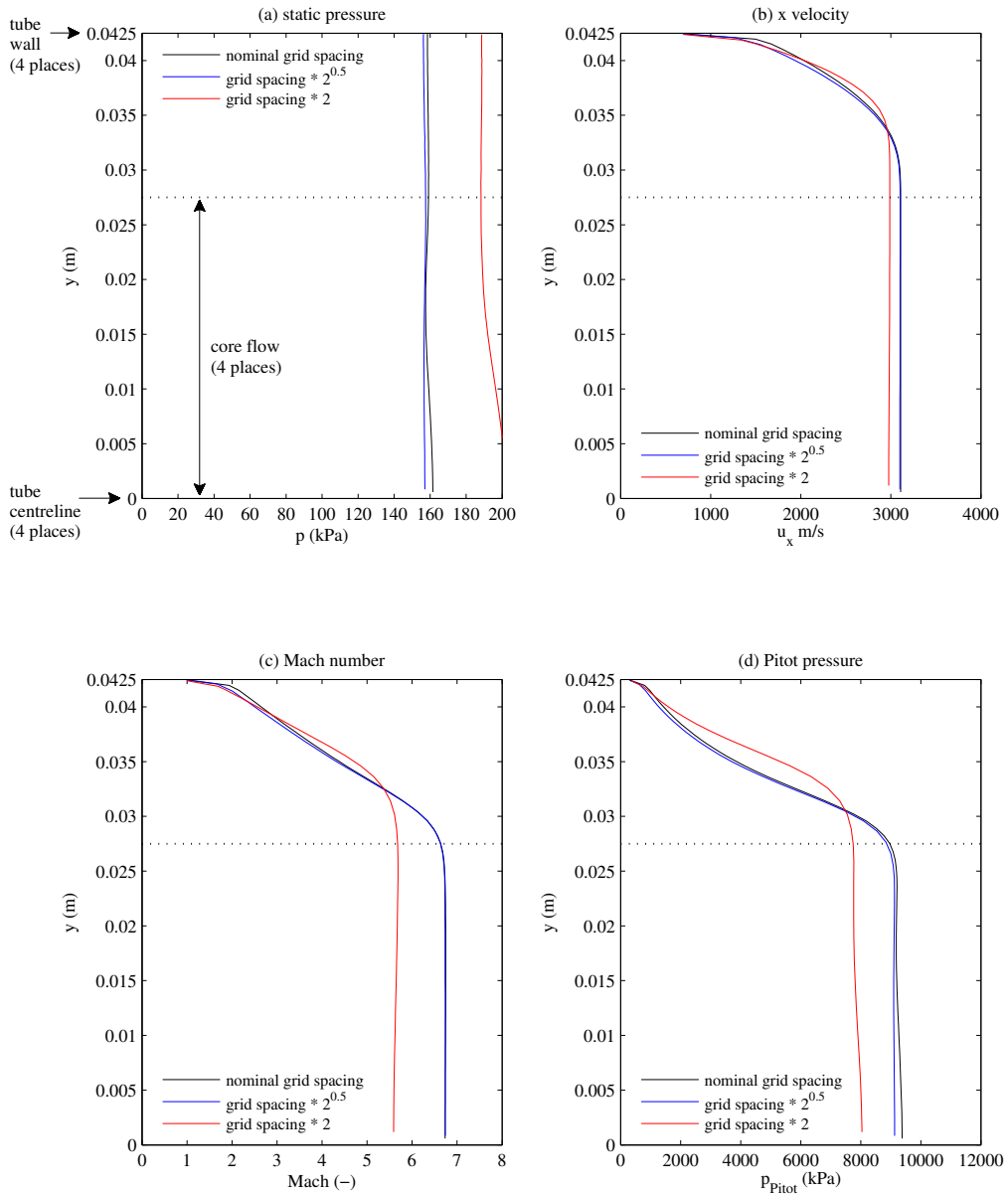


Figure K.10: Comparison of radial variation in flow properties across nozzle *inlet*, at 75% of test time, for different grid spacings, for flow condition x2-scr-m10p0-noz-rev-1, hybrid CFD model. Normalised grid spacing of 1.0 is that used to produce the results presented in this document. Normalised grid spacings of $\sqrt{2}$ and 2 correspond to 50% and 75% fewer cells compared to the nominal grid used to compute results in Chapter 8.

M10 Nozzle CFD Model, x2-scr-m10p0-noz-rev-1

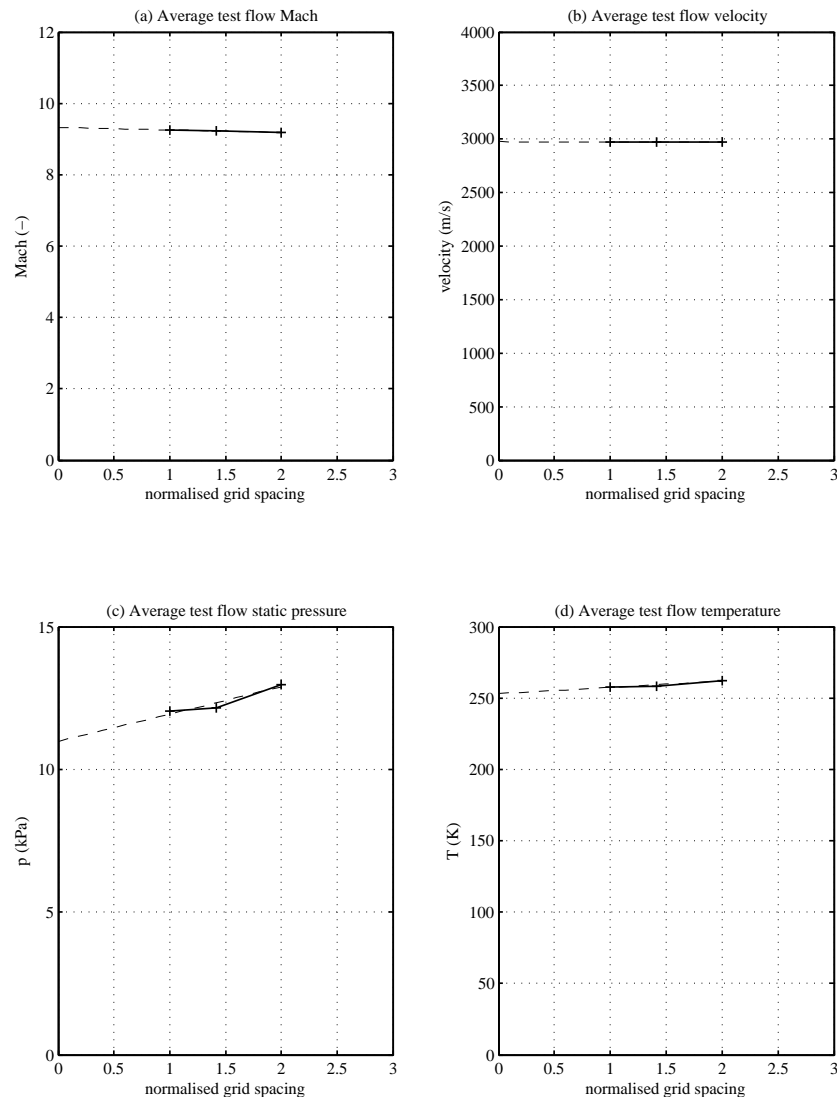


Figure K.11: Variation of selected computed flow properties with normalised grid spacing, flow condition x2-scr-m10p0-noz-rev-1, nozzle CFD model, flow at nozzle exit. Inflow is calculated using a nominal grid for M10 Hybrid 1D/2D CFD Model, x2-scr-m10p0-noz-rev-1. Normalised grid spacing of 1.0 is that used to produce the results presented in this document. Normalised grid spacings of $\sqrt{2}$ and 2 correspond to 50% and 75% fewer cells compared to the nominal grid used to compute results in Chapter 8.

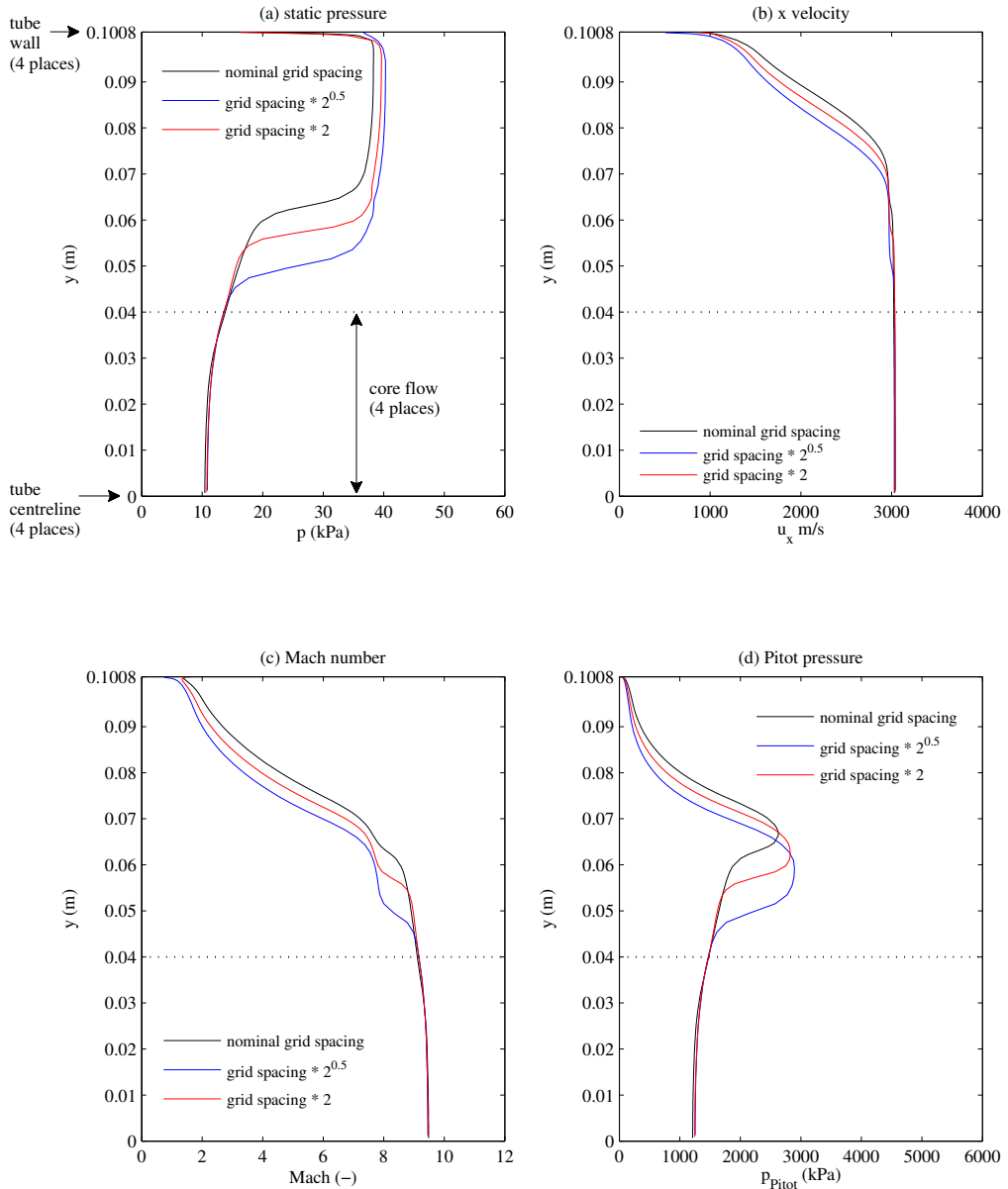


Figure K.12: Comparison of radial variation in flow properties across nozzle exit, at 25% of test time, for different grid spacings, for flow condition x2-scr-m10p0-noz-rev-1, hybrid CFD model. Normalised grid spacing of 1.0 is that used to produce the results presented in this document. Normalised grid spacings of $\sqrt{2}$ and 2 correspond to 50% and 75% fewer cells compared to the nominal grid used to compute results in Chapter 8.

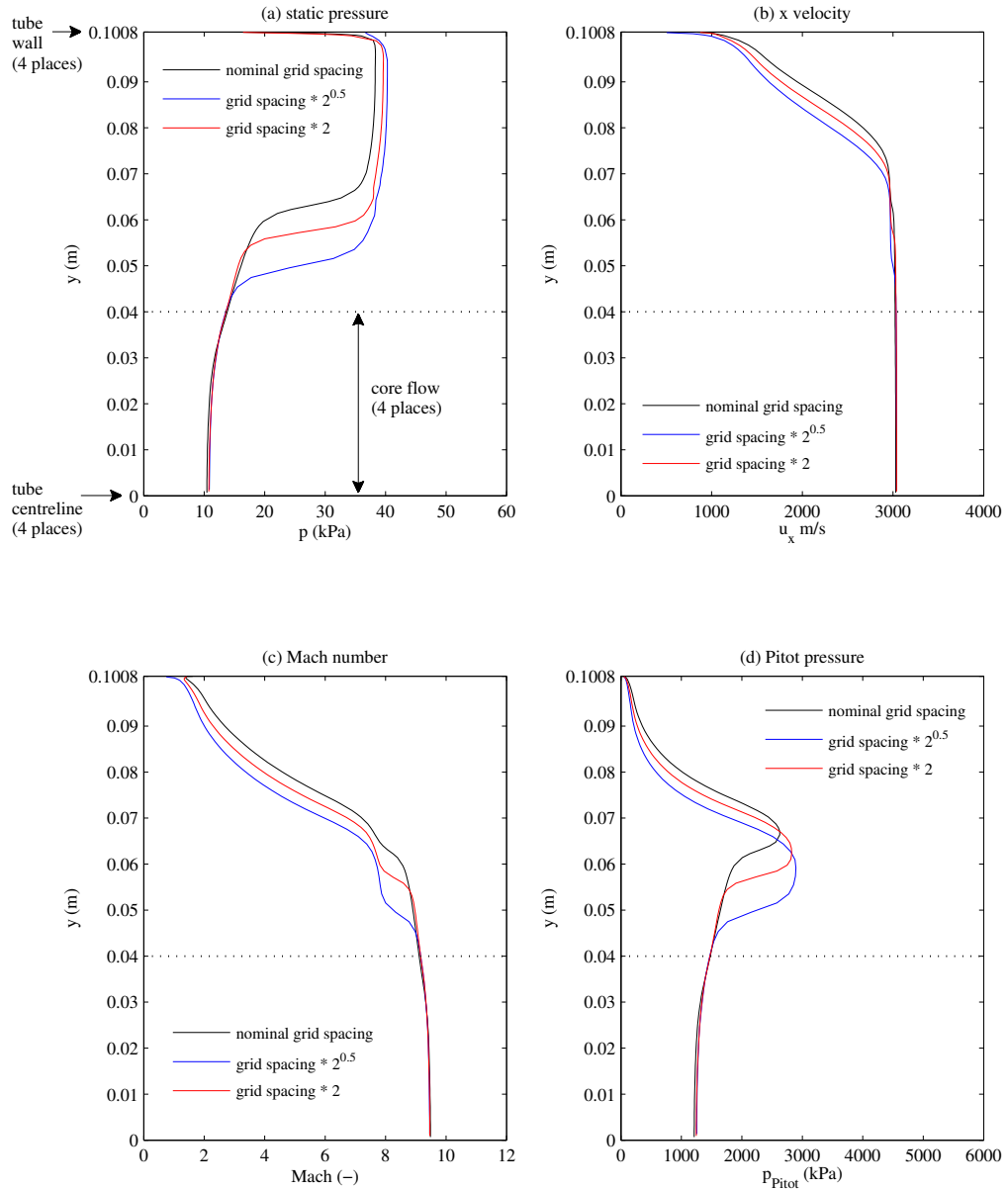


Figure K.13: Comparison of radial variation in flow properties across nozzle exit, at 50% of test time, for different grid spacings, for flow condition x2-scr-m10p0-noz-rev-1, hybrid CFD model. Normalised grid spacing of 1.0 is that used to produce the results presented in this document. Normalised grid spacings of $\sqrt{2}$ and 2 correspond to 50% and 75% fewer cells compared to the nominal grid used to compute results in Chapter 8.

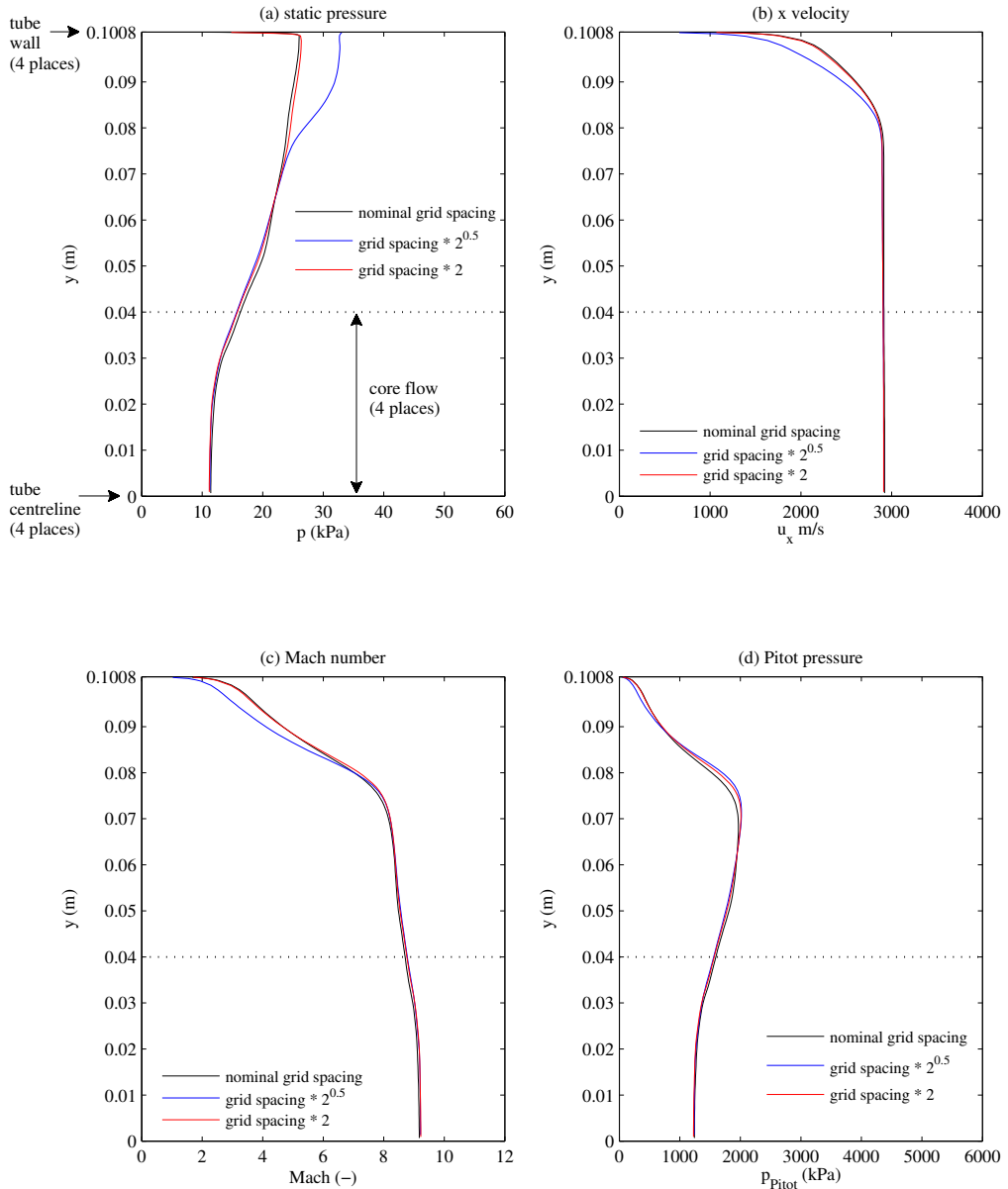


Figure K.14: Comparison of radial variation in flow properties across nozzle exit, at 75% of test time, for different grid spacings, for flow condition x2-scr-m10p0-noz-rev-1, hybrid CFD model. Normalised grid spacing of 1.0 is that used to produce the results presented in this document. Normalised grid spacings of $\sqrt{2}$ and 2 correspond to 50% and 75% fewer cells compared to the nominal grid used to compute results in Chapter 8.

M12.5 Hybrid 1D/2D CFD Model, x2-scr-m12p5-rev-1

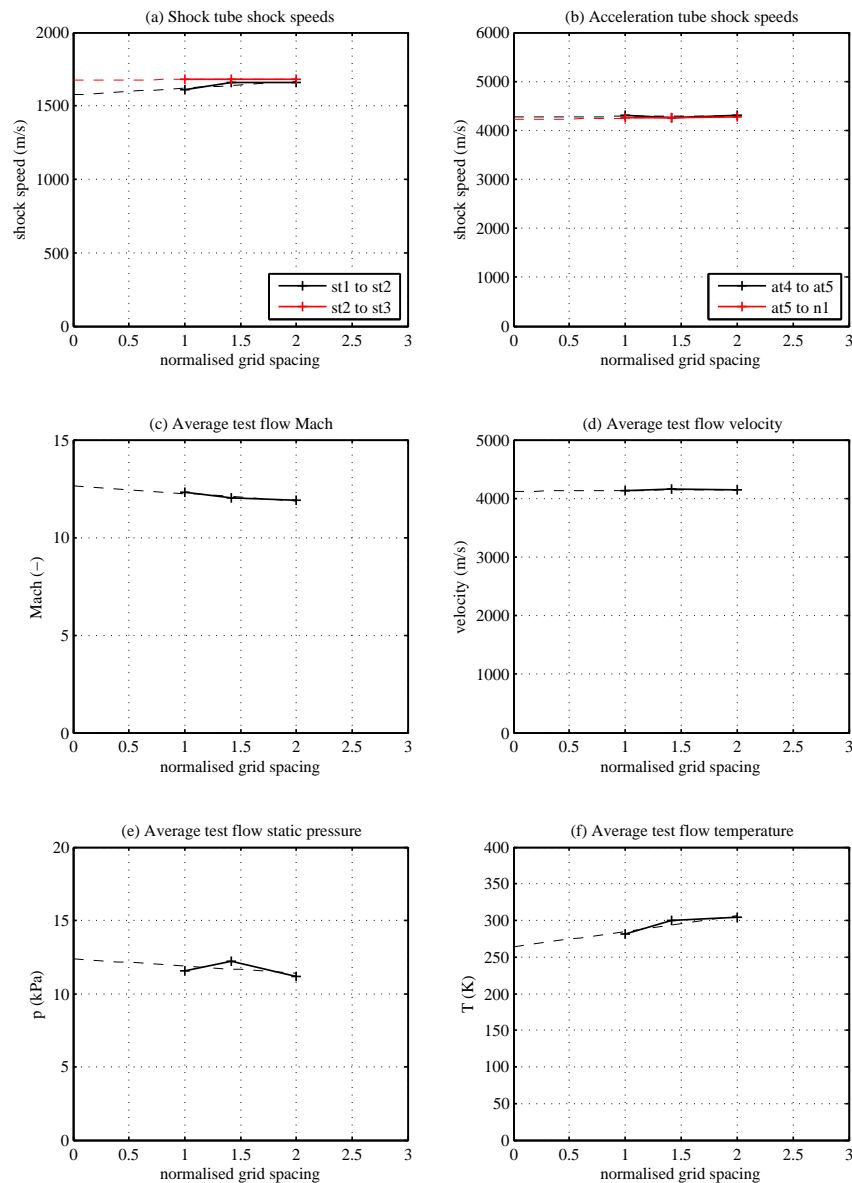


Figure K.15: Variation of selected computed flow properties with normalised grid spacing, flow condition x2-scr-m12p5-rev-1, hybrid CFD model. Normalised grid spacing of 1.0 is that used to produce the results presented in this document. Normalised grid spacings of $\sqrt{2}$ and 2 correspond to 50% and 75% fewer cells compared to the nominal grid used to compute results in Chapter 8.

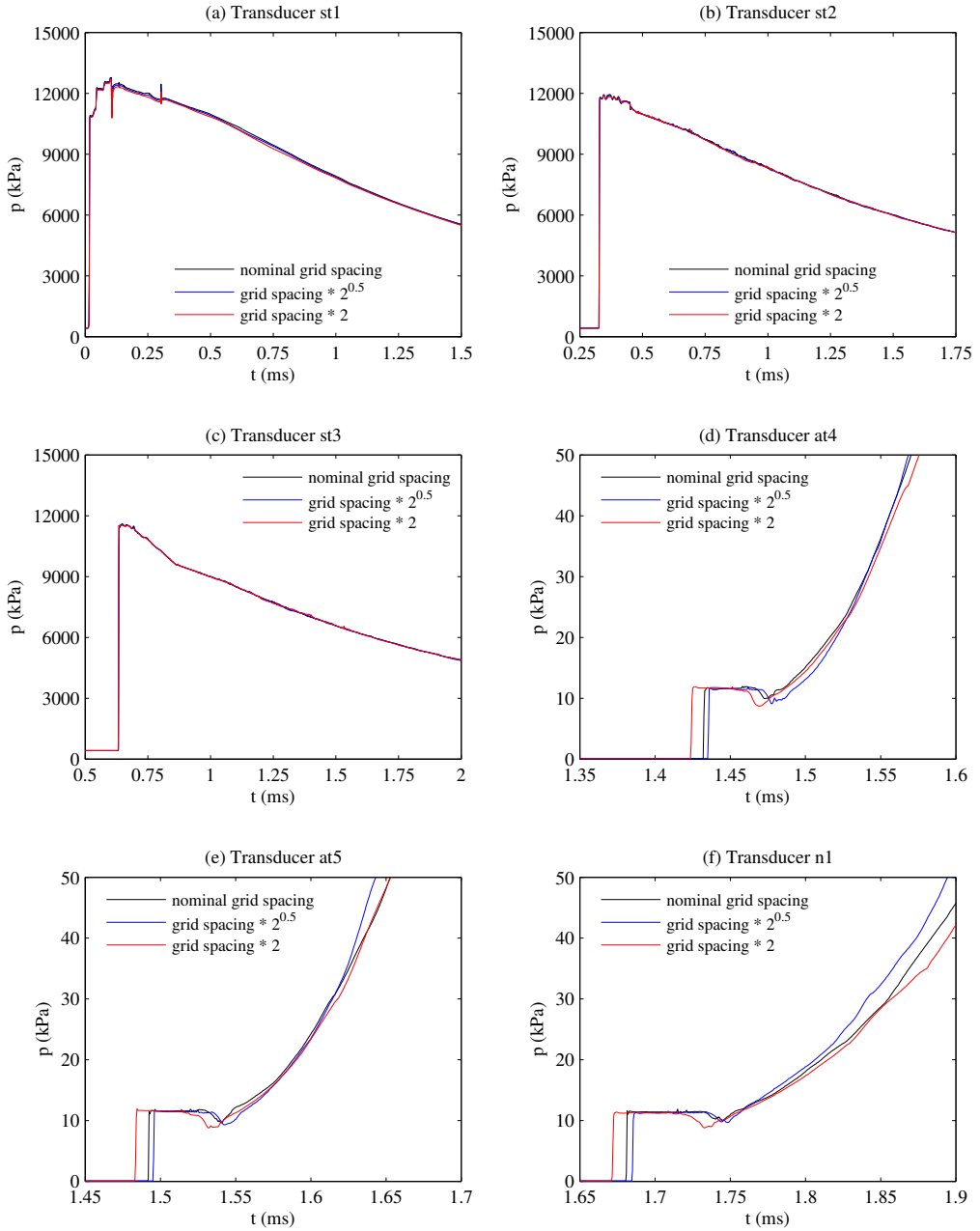


Figure K.16: Comparison of transducer pressure histories for different grid spacings, for flow condition x2-scr-m12p5-rev-1, hybrid CFD model. Normalised grid spacing of 1.0 is that used to produce the results presented in this document. Normalised grid spacings of $\sqrt{2}$ and 2 correspond to 50% and 75% fewer cells compared to the nominal grid used to compute results in Chapter 8.

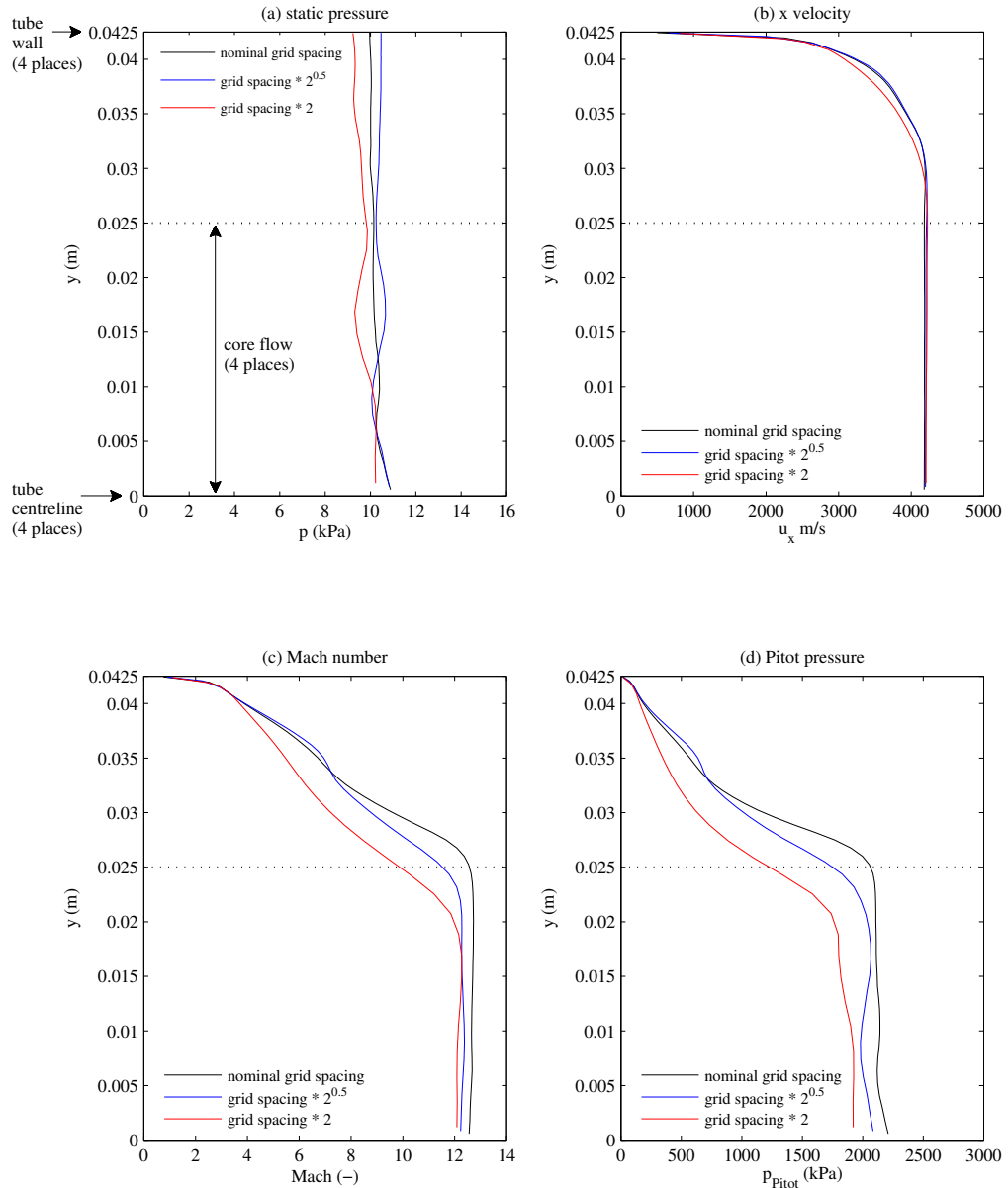


Figure K.17: Comparison of radial variation in flow properties across tube exit, at 25% of test time, for different grid spacings, for flow condition x2-scr-m12p5-rev-1, hybrid CFD model. Normalised grid spacing of 1.0 is that used to produce the results presented in this document. Normalised grid spacings of $\sqrt{2}$ and 2 correspond to 50% and 75% fewer cells compared to the nominal grid used to compute results in Chapter 8.

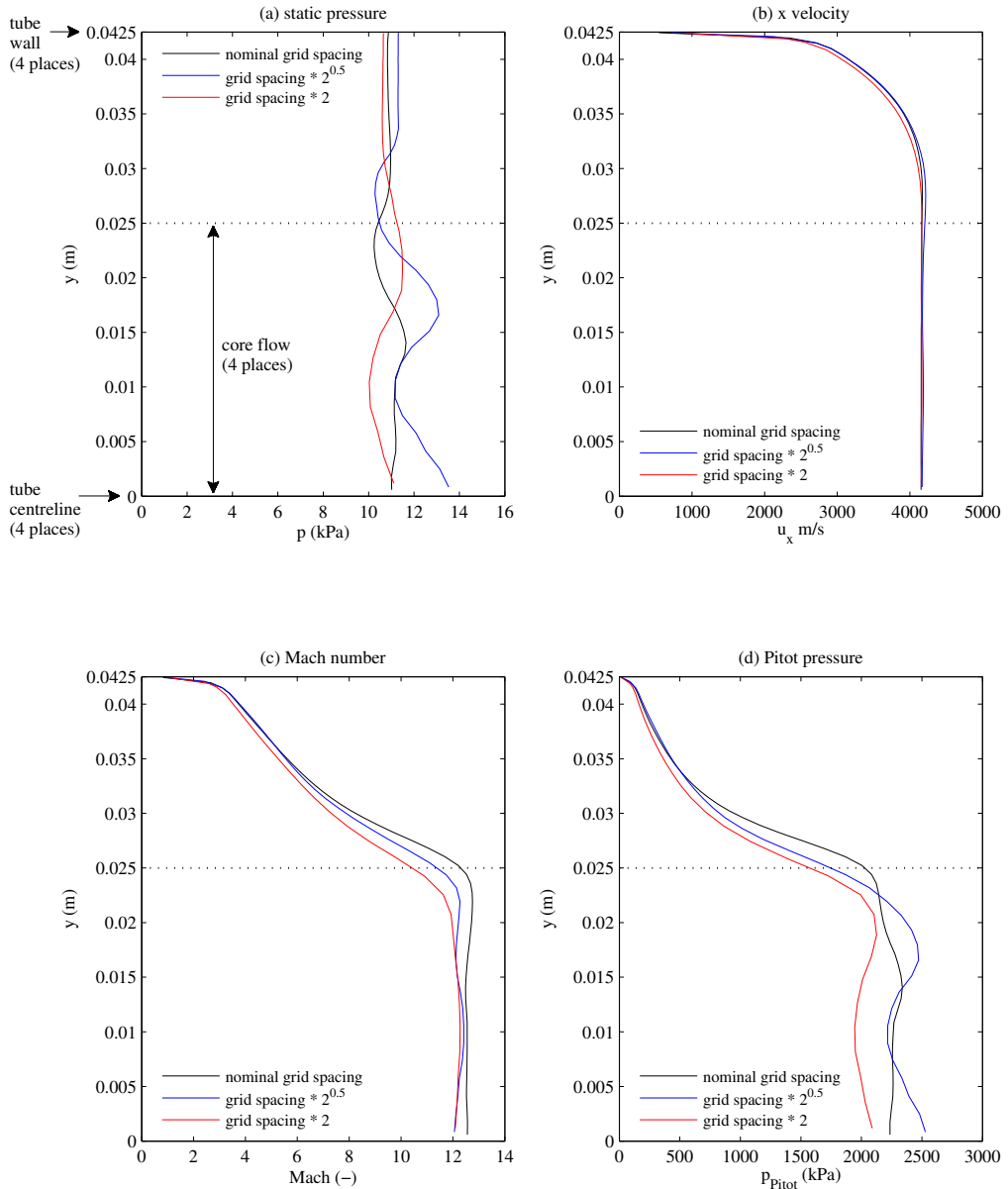


Figure K.18: Comparison of radial variation in flow properties across tube exit, at 50% of test time, for different grid spacings, for flow condition x2-scr-m12p5-rev-1, hybrid CFD model. Normalised grid spacing of 1.0 is that used to produce the results presented in this document. Normalised grid spacings of $\sqrt{2}$ and 2 correspond to 50% and 75% fewer cells compared to the nominal grid used to compute results in Chapter 8.

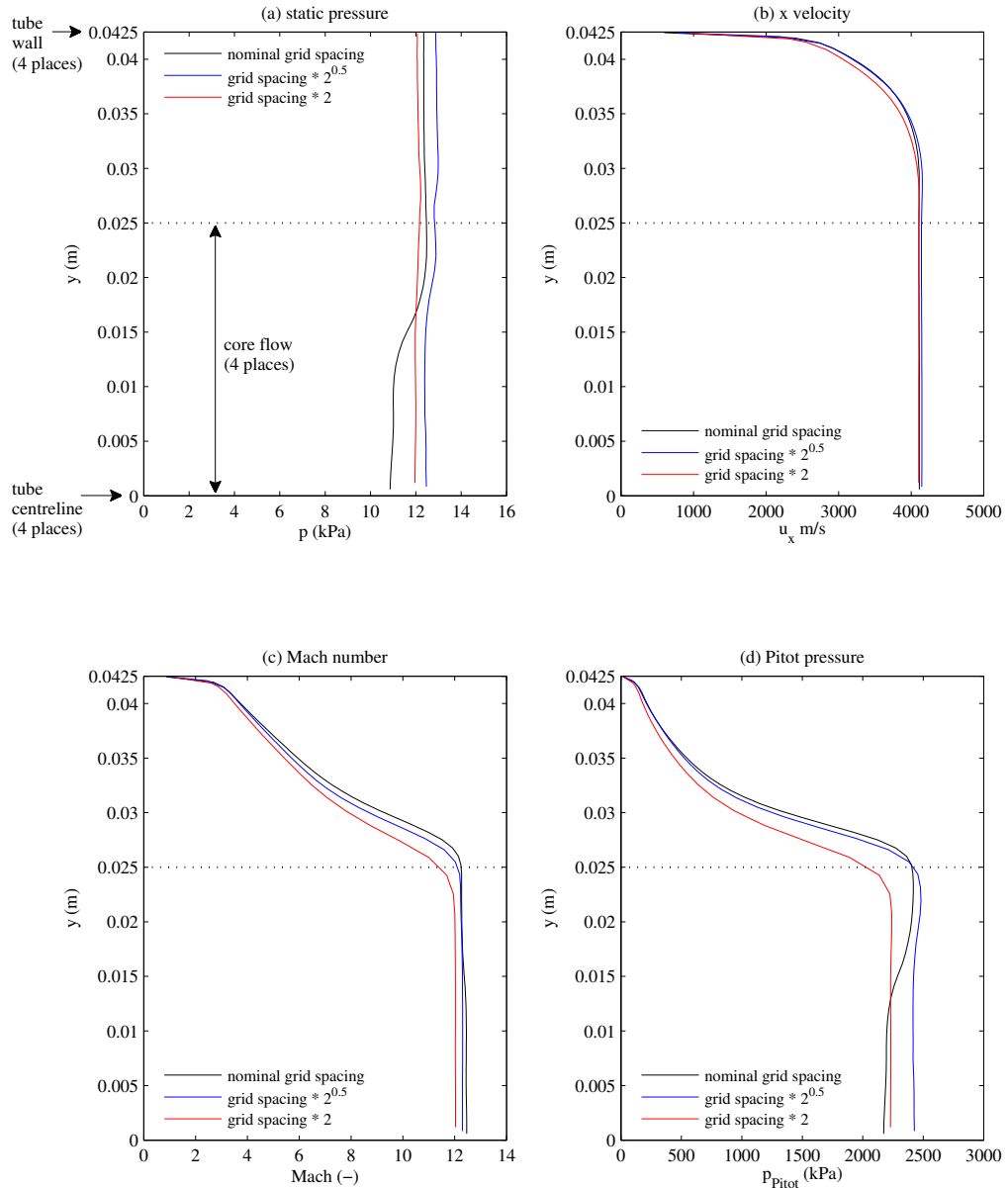


Figure K.19: Comparison of radial variation in flow properties across tube exit, at 75% of test time, for different grid spacings, for flow condition x2-scr-m12p5-rev-1, hybrid CFD model. Normalised grid spacing of 1.0 is that used to produce the results presented in this document. Normalised grid spacings of $\sqrt{2}$ and 2 correspond to 50% and 75% fewer cells compared to the nominal grid used to compute results in Chapter 8.

M15 Hybrid 1D/2D CFD Model, x2-scr-m15p0-rev-1

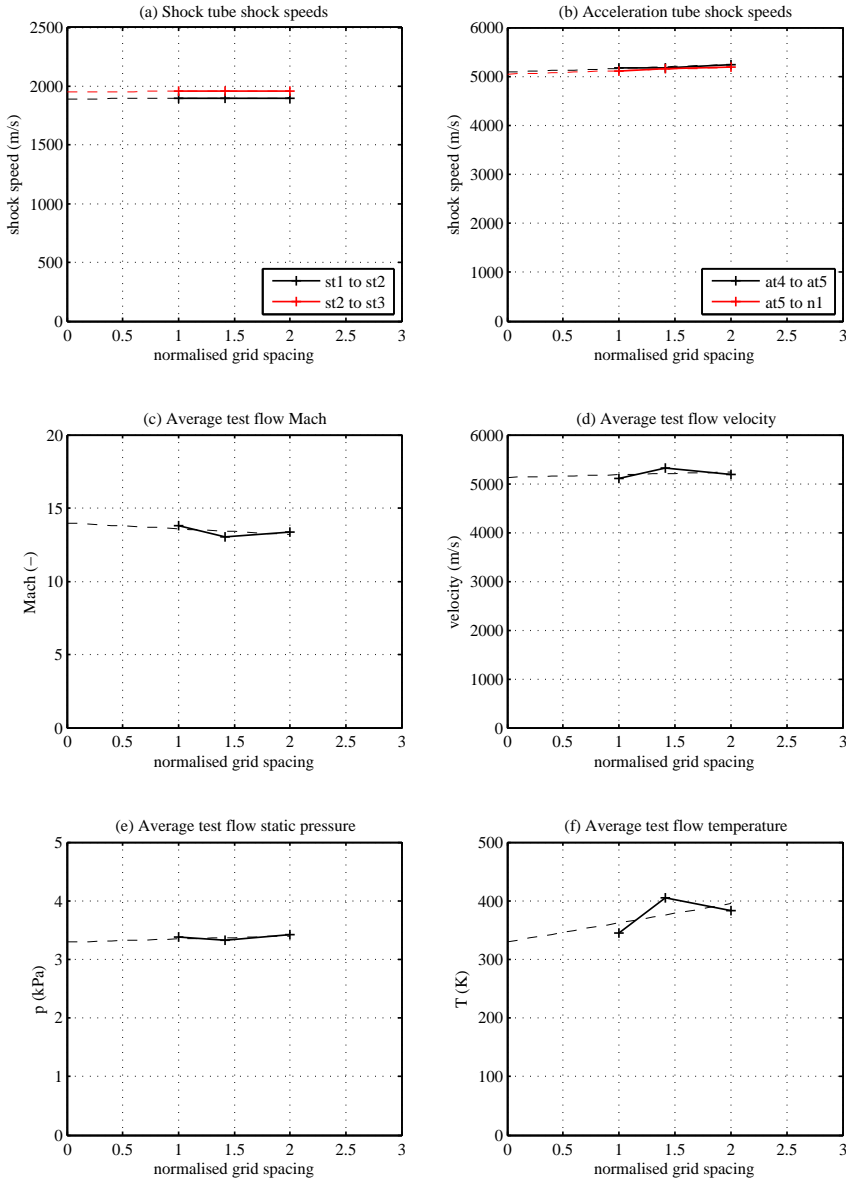


Figure K.20: Variation of selected computed flow properties with normalised grid spacing, flow condition x2-scr-m15p0-rev-1, hybrid CFD model. Normalised grid spacing of 1.0 is that used to produce the results presented in this document. Normalised grid spacings of $\sqrt{2}$ and 2 correspond to 50% and 75% fewer cells compared to the nominal grid used to compute results in Chapter 8.

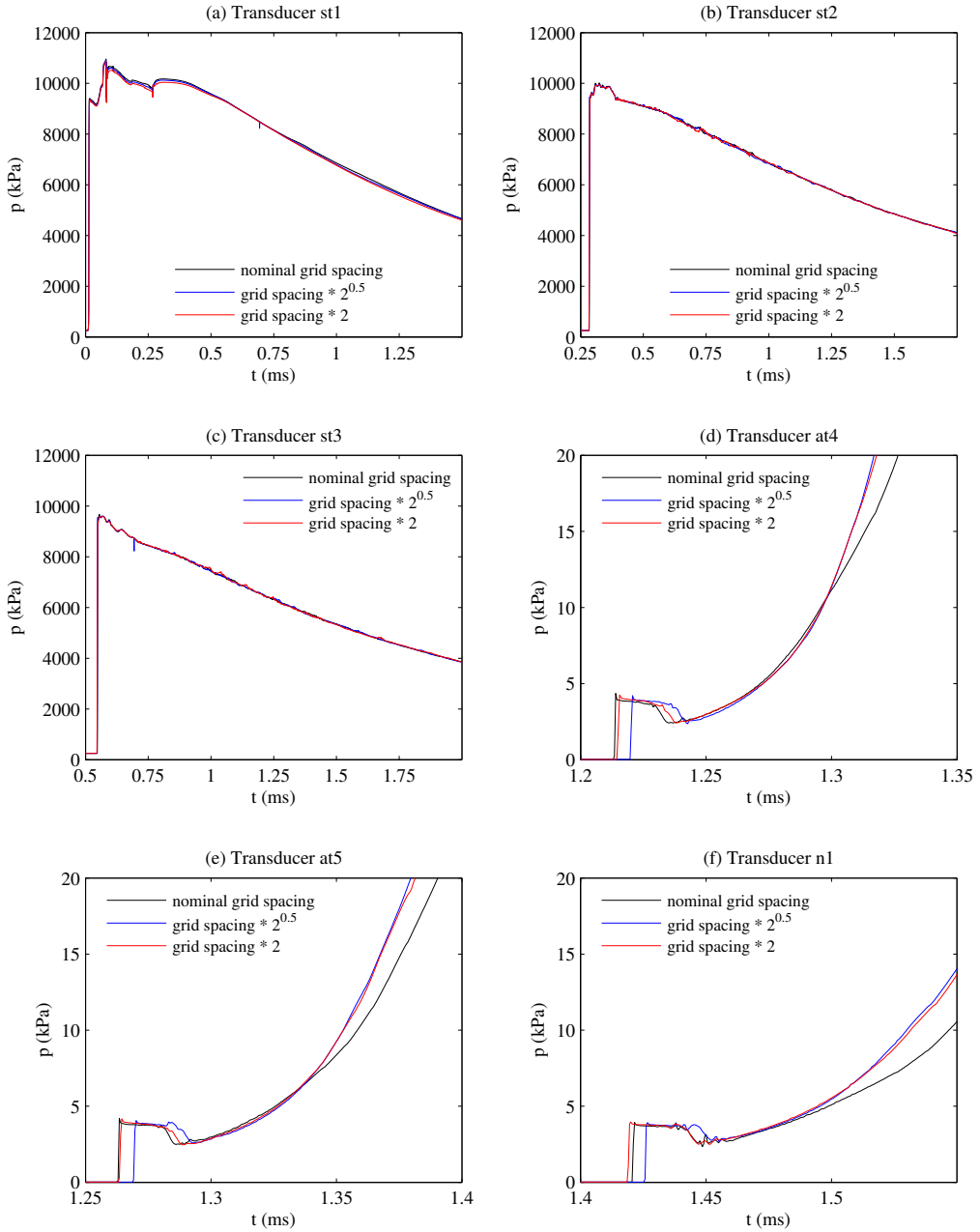


Figure K.21: Comparison of transducer pressure histories for different grid spacings, for flow condition x2-scr-m15p0-rev-1, hybrid CFD model. Normalised grid spacing of 1.0 is that used to produce the results presented in this document. Normalised grid spacings of $\sqrt{2}$ and 2 correspond to 50% and 75% fewer cells compared to the nominal grid used to compute results in Chapter 8.

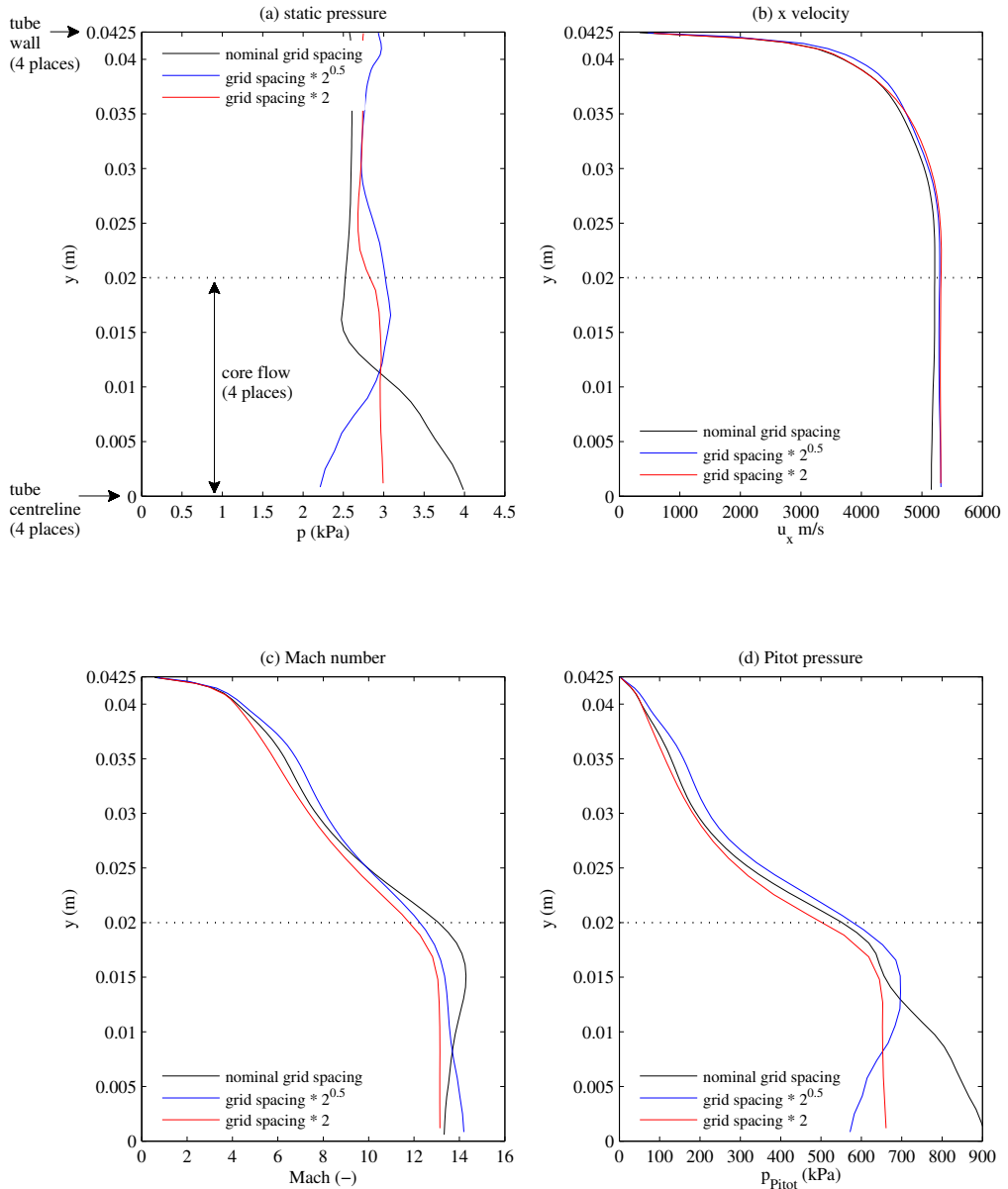


Figure K.22: Comparison of radial variation in flow properties across tube exit, at 25% of test time, for different grid spacings, for flow condition x2-scr-m15p0-rev-1, hybrid CFD model. Normalised grid spacing of 1.0 is that used to produce the results presented in this document. Normalised grid spacings of $\sqrt{2}$ and 2 correspond to 50% and 75% fewer cells compared to the nominal grid used to compute results in Chapter 8.

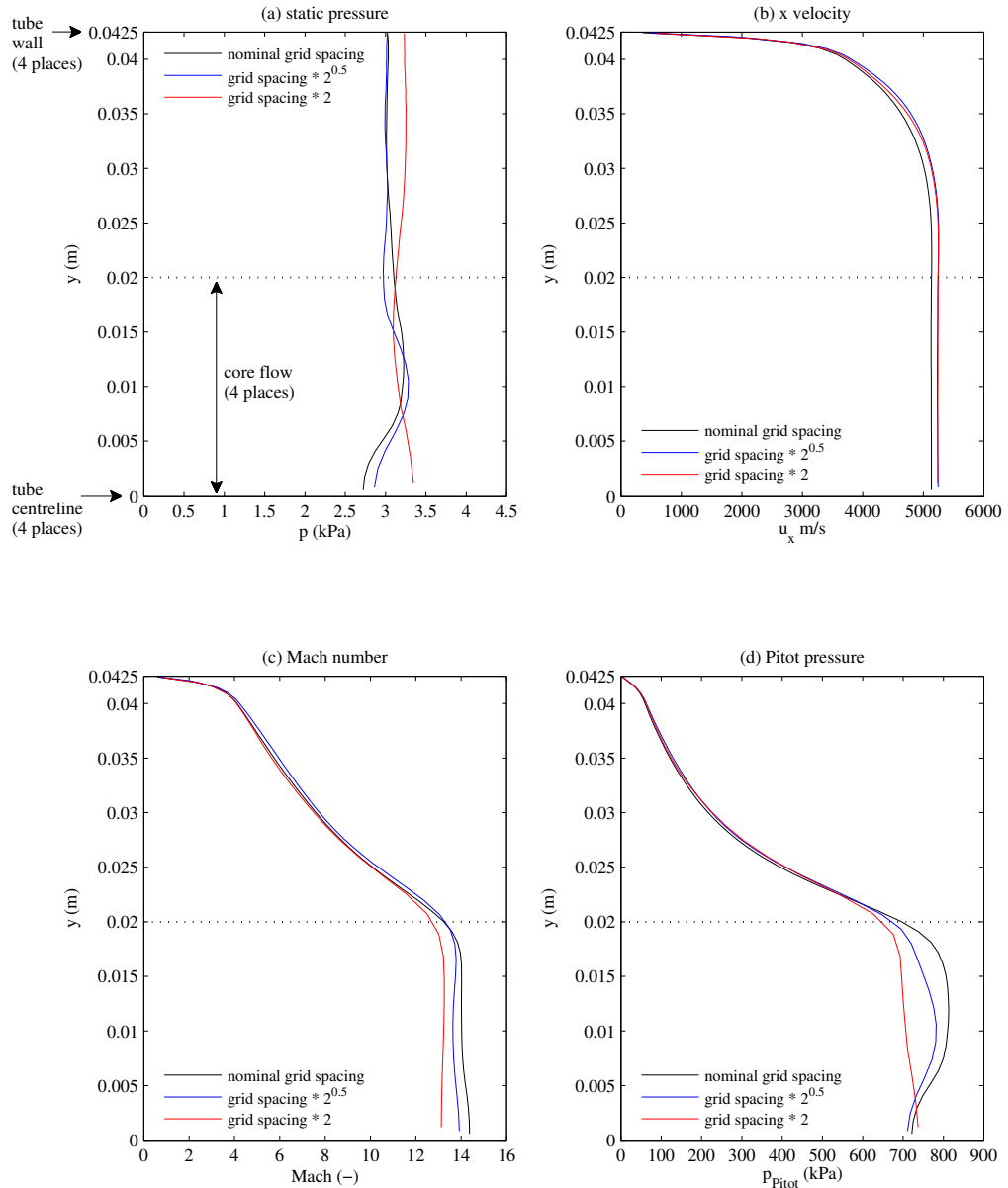


Figure K.23: Comparison of radial variation in flow properties across tube exit, at 50% of test time, for different grid spacings, for flow condition x2-scr-m15p0-rev-1, hybrid CFD model. Normalised grid spacing of 1.0 is that used to produce the results presented in this document. Normalised grid spacings of $\sqrt{2}$ and 2 correspond to 50% and 75% fewer cells compared to the nominal grid used to compute results in Chapter 8.

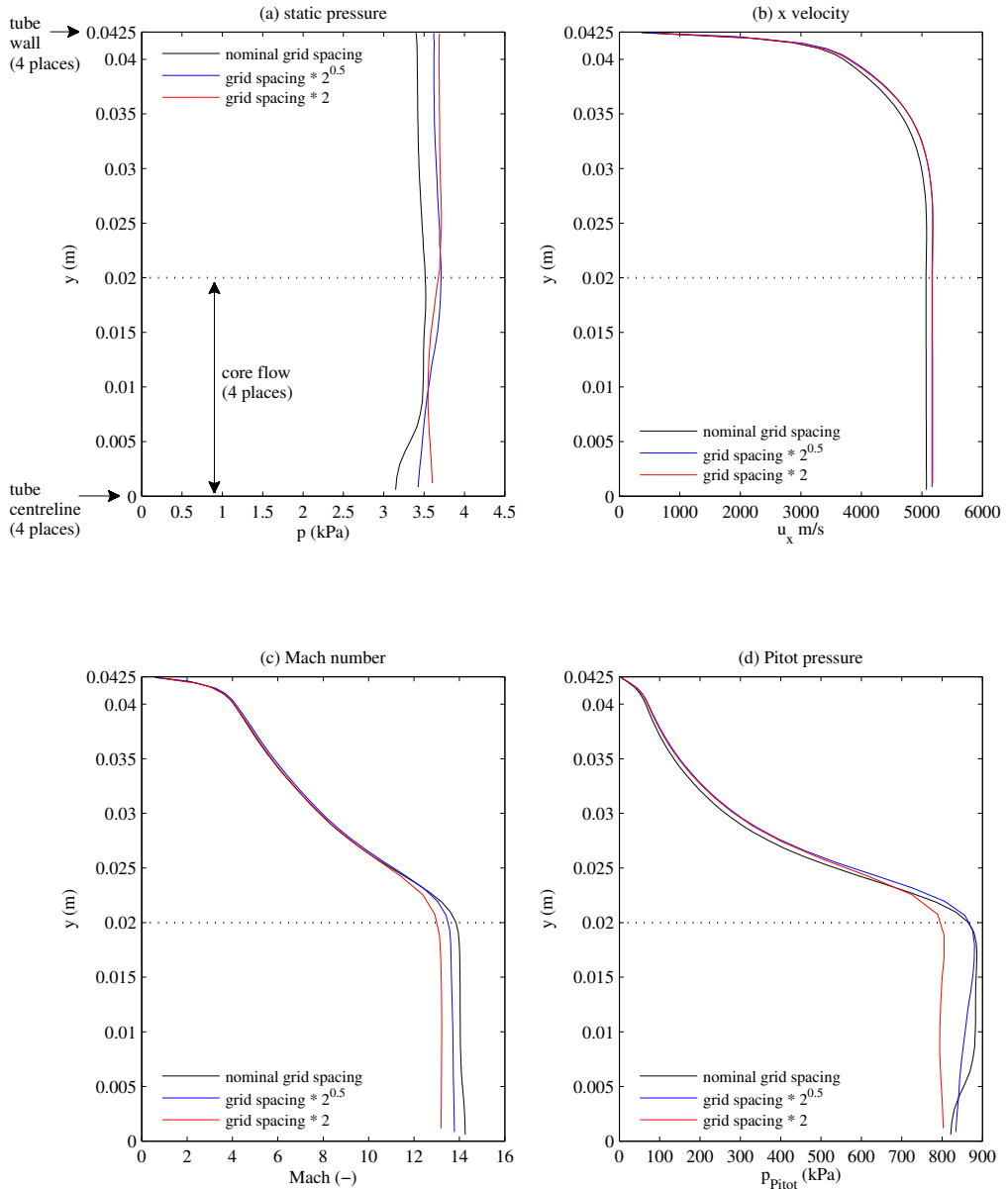


Figure K.24: Comparison of radial variation in flow properties across tube exit, at 75% of test time, for different grid spacings, for flow condition x2-scr-m15p0-rev-1, hybrid CFD model. Normalised grid spacing of 1.0 is that used to produce the results presented in this document. Normalised grid spacings of $\sqrt{2}$ and 2 correspond to 50% and 75% fewer cells compared to the nominal grid used to compute results in Chapter 8.

M10 Full Facility CFD Model, x2-scr-m10p0-rev-1

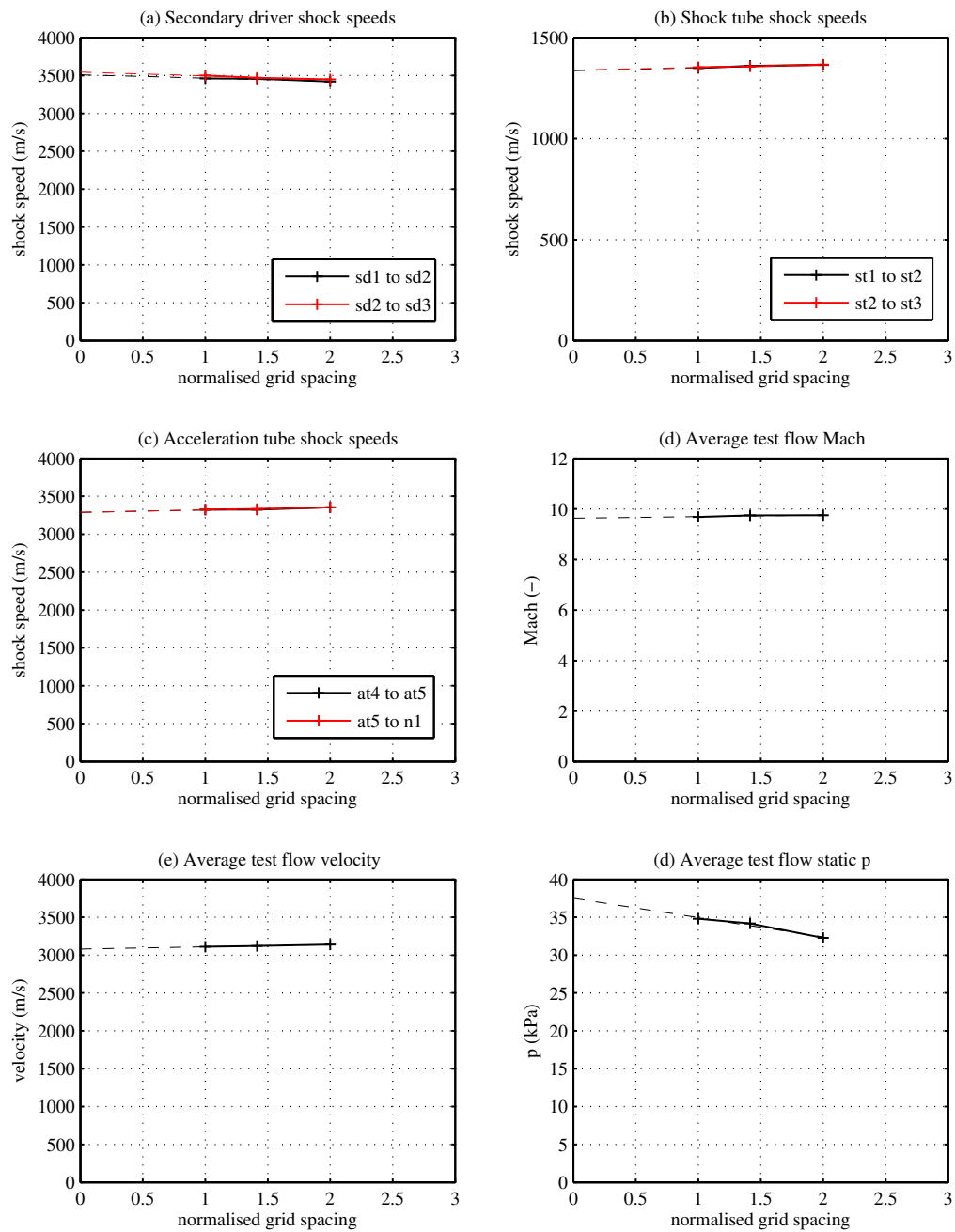


Figure K.25: Variation of selected computed flow properties with normalised grid spacing, flow condition x2-scr-m10p0-rev-1, full facility CFD model. Normalised grid spacing of 1.0 is that used to produce the results presented in this document. Normalised grid spacings of $\sqrt{2}$ and 2 correspond to 50% and 75% fewer cells compared to the nominal grid used to compute results in Chapter 9.

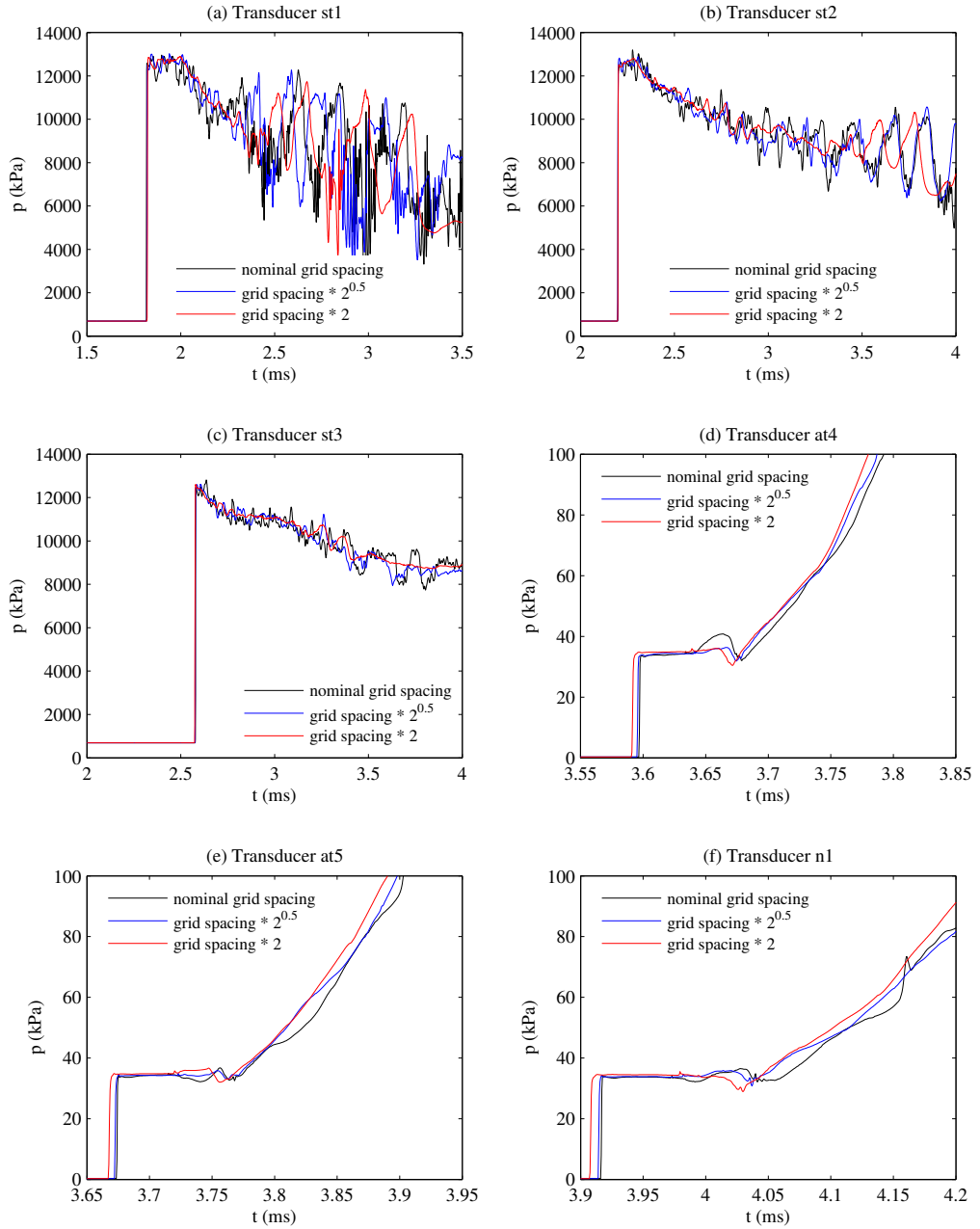


Figure K.26: Comparison of transducer pressure histories for different grid spacings, for flow condition x2-scr-m10p0-rev-1, full facility CFD model. Normalised grid spacing of 1.0 is that used to produce the results presented in this document. Normalised grid spacings of $\sqrt{2}$ and 2 correspond to 50% and 75% fewer cells compared to the nominal grid used to compute results in Chapter 9.

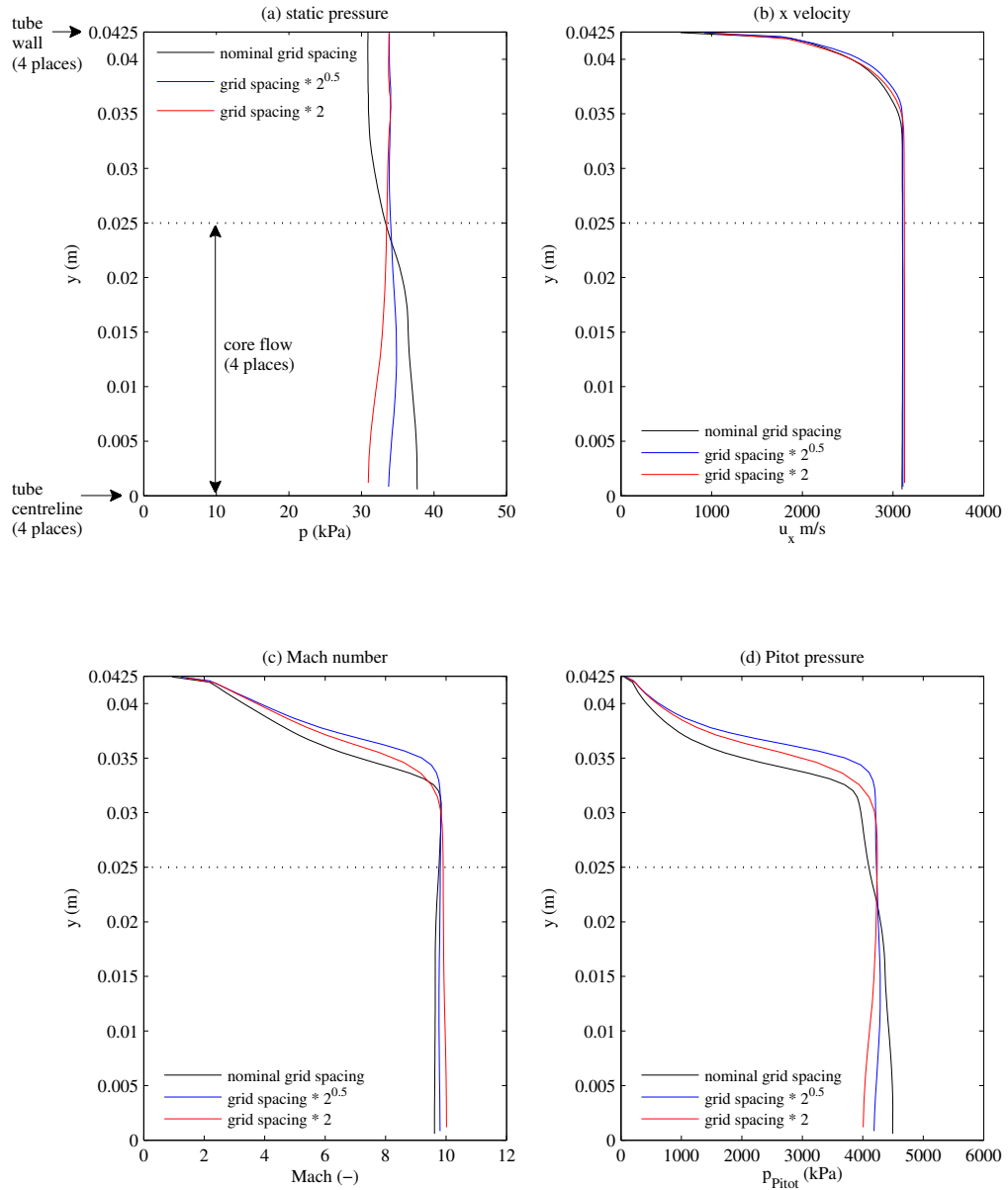


Figure K.27: Comparison of radial variation in flow properties across tube exit, at 25% of test time, for different grid spacings, for flow condition x2-scr-m10p0-rev-1, full facility CFD model. Normalised grid spacing of 1.0 is that used to produce the results presented in this document. Normalised grid spacings of $\sqrt{2}$ and 2 correspond to 50% and 75% fewer cells compared to the nominal grid used to compute results in Chapter 9.

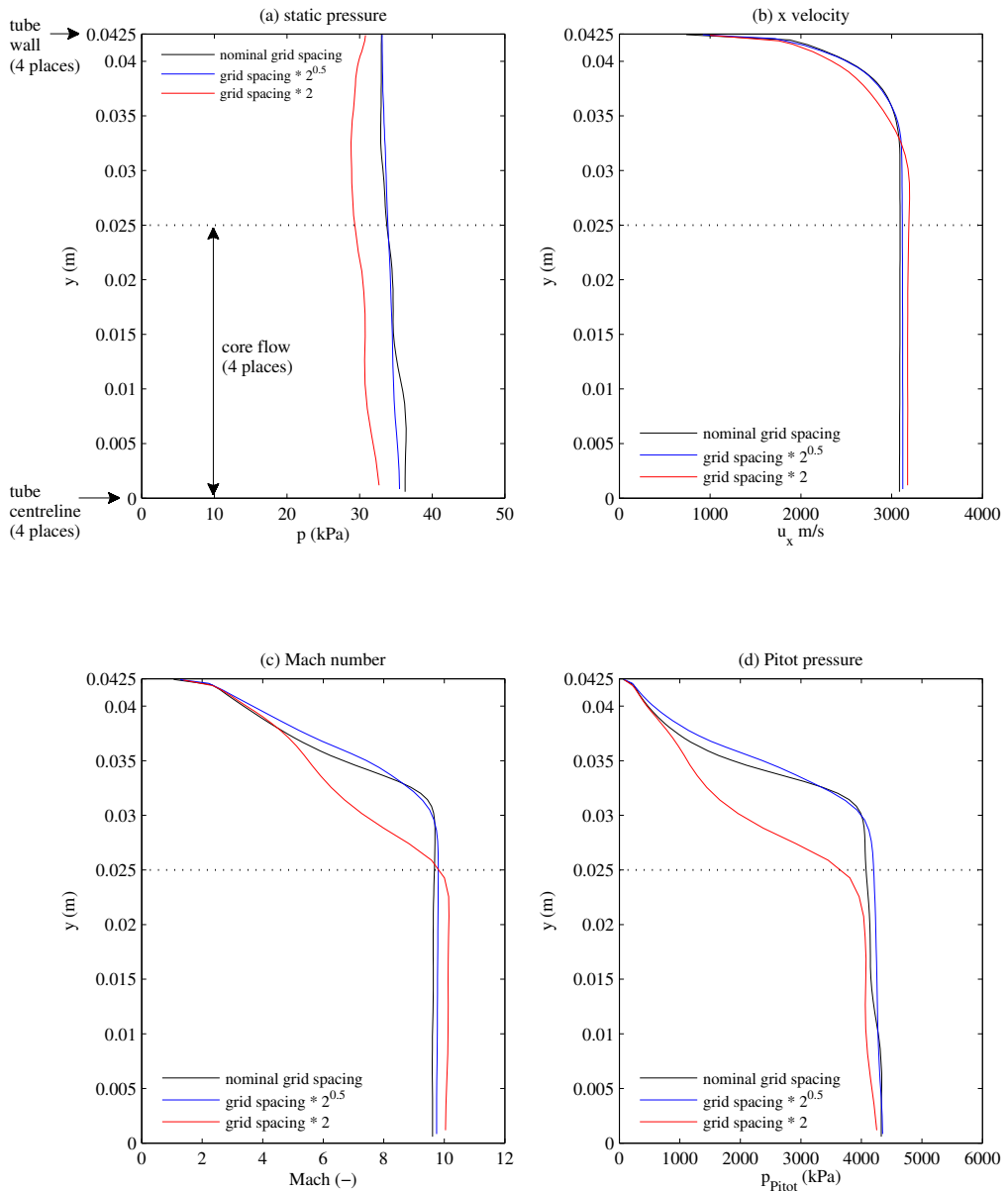


Figure K.28: Comparison of radial variation in flow properties across tube exit, at 50% of test time, for different grid spacings, for flow condition x2-scr-m10p0-rev-1, full facility CFD model. Normalised grid spacing of 1.0 is that used to produce the results presented in this document. Normalised grid spacings of $\sqrt{2}$ and 2 correspond to 50% and 75% fewer cells compared to the nominal grid used to compute results in Chapter 9.

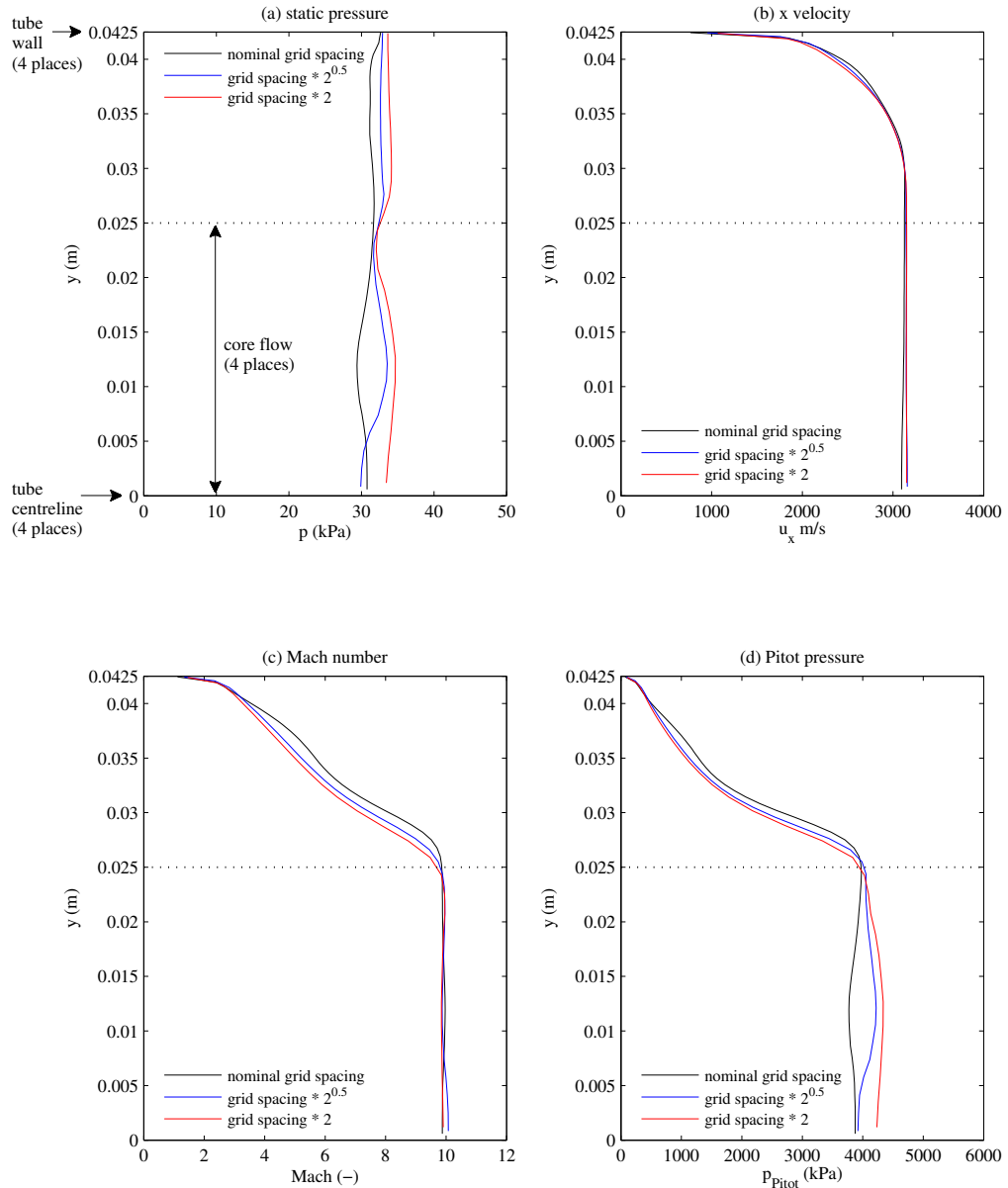
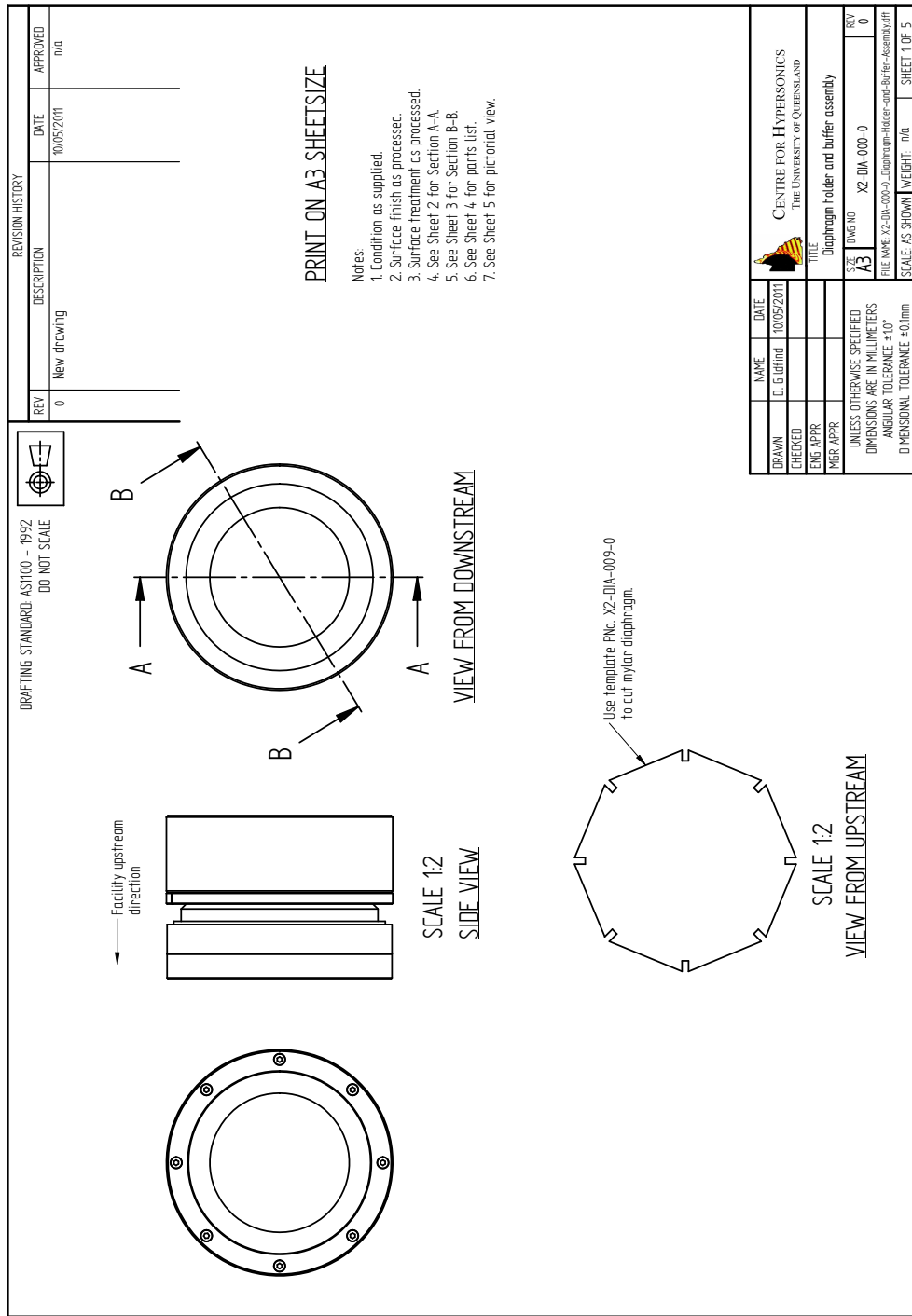


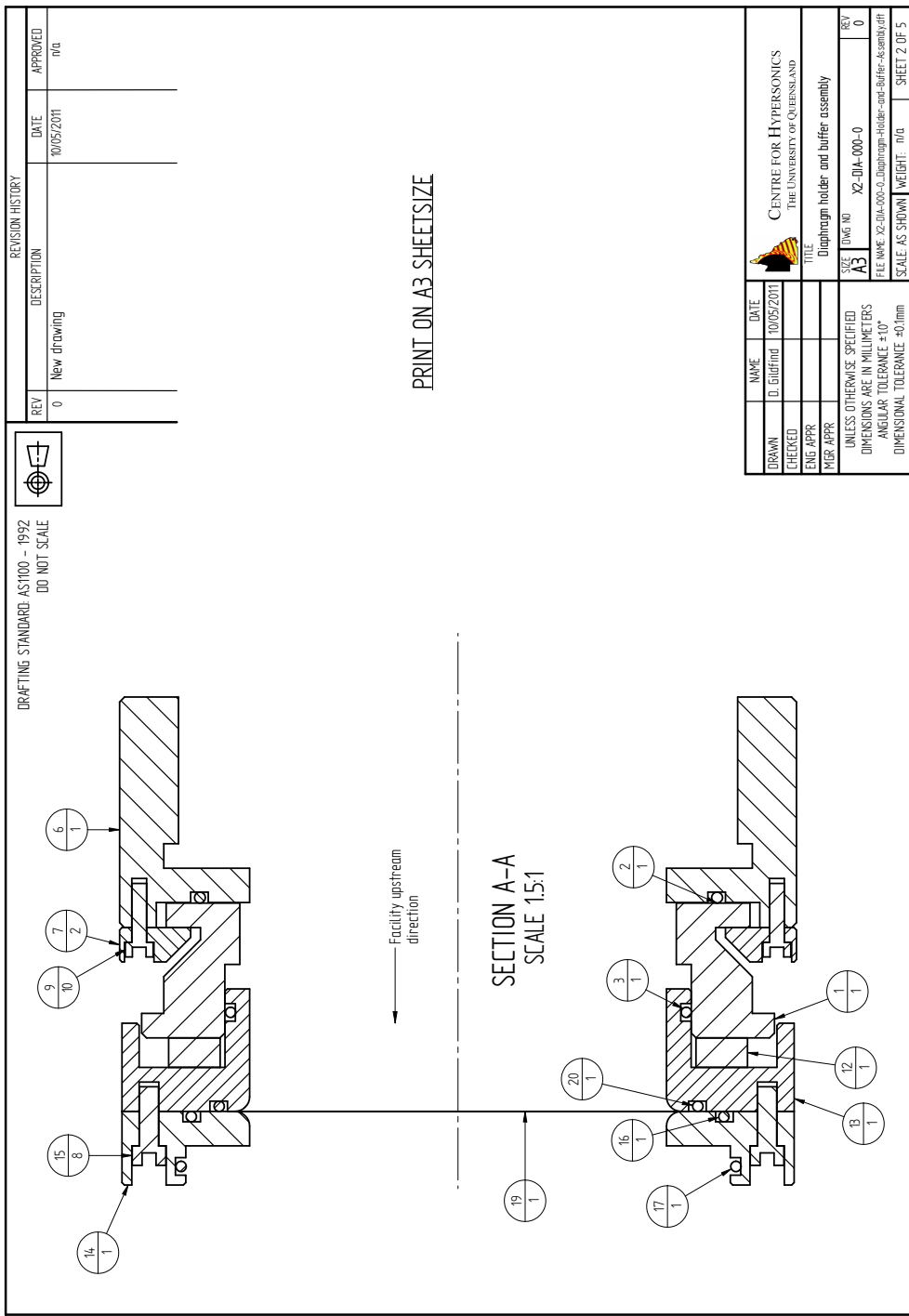
Figure K.29: Comparison of radial variation in flow properties across tube exit, at 75% of test time, for different grid spacings, for flow condition x2-scr-m10p0-rev-1, full facility CFD model. Normalised grid spacing of 1.0 is that used to produce the results presented in this document. Normalised grid spacings of $\sqrt{2}$ and 2 correspond to 50% and 75% fewer cells compared to the nominal grid used to compute results in Chapter 9.

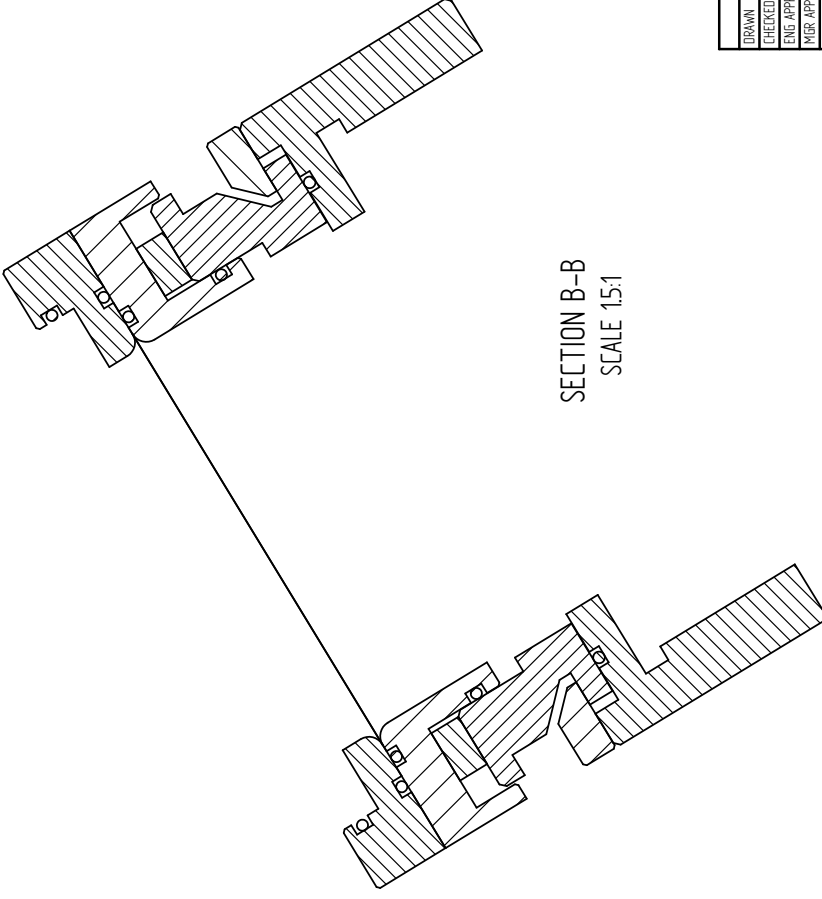
Appendix L

X2 Diaphragm Holder and Buffer Drawing Set

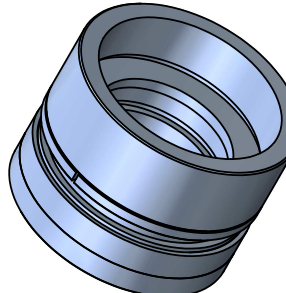
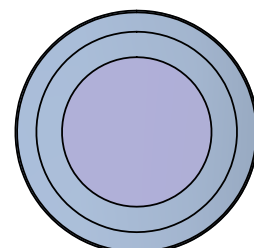
L.1 X2-DIA-000-0: Diaphragm Holder and Buffer Assembly



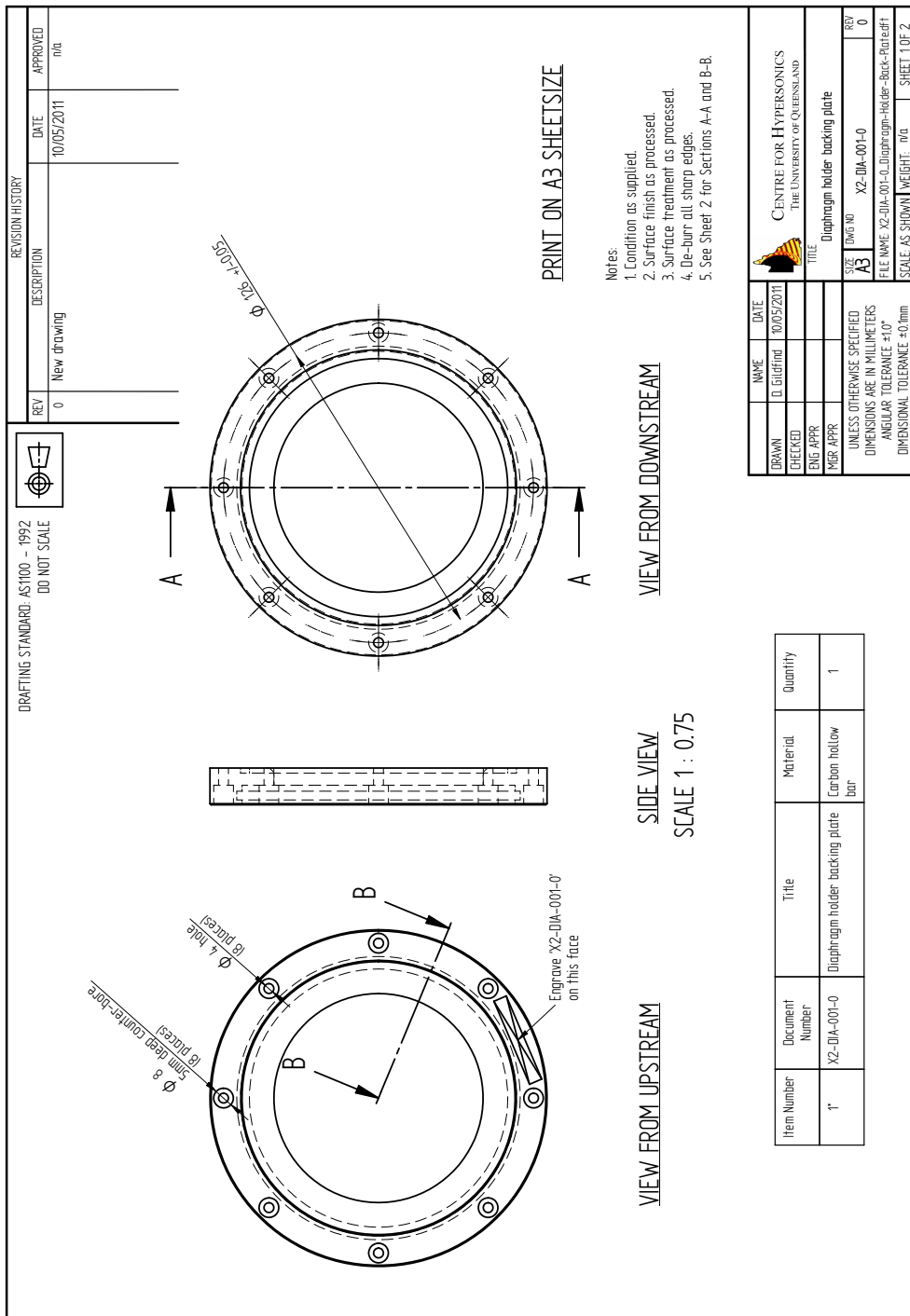


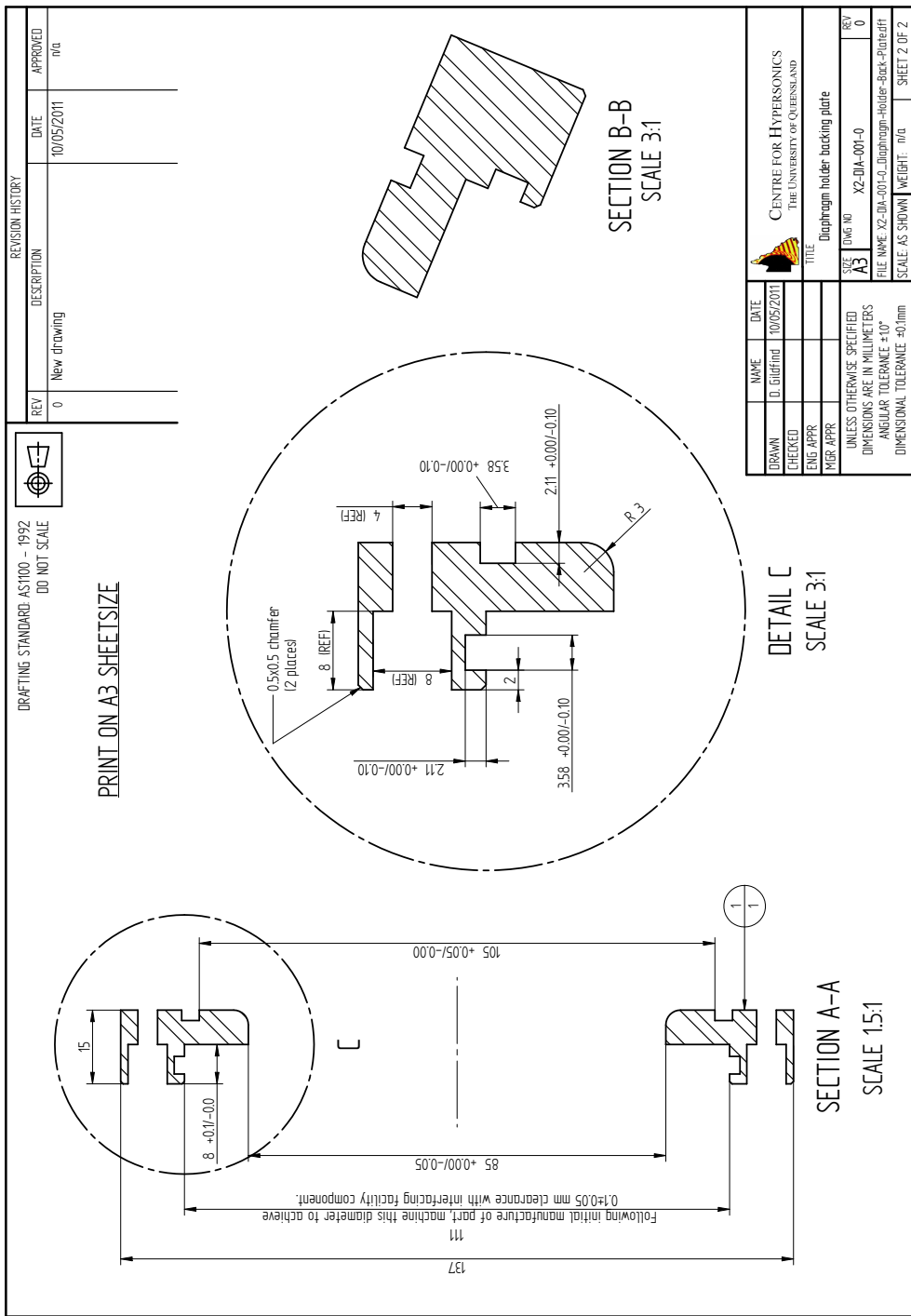
DRAFTING STANDARD AS1000 - 1992 DO NOT SCALE																																							
REV 0 New drawing																																							
DESCRIPTION																																							
DATE 10/05/2011																																							
APPROVED n/a																																							
REVISION HISTORY																																							
PRINT ON A3 SHEET SIZE																																							
																																							
<table border="1"> <tr> <td>DRAWN</td> <td>NAME</td> <td>DATE</td> </tr> <tr> <td>D. Gifford</td> <td></td> <td>10/05/2011</td> </tr> <tr> <td>CHEKED</td> <td></td> <td></td> </tr> <tr> <td>EUG APPR</td> <td></td> <td></td> </tr> <tr> <td>MGR APPR</td> <td></td> <td></td> </tr> <tr> <td colspan="3">UNLESS OTHERWISE SPECIFIED</td> </tr> <tr> <td colspan="3">DIMENSIONS ARE IN MILLIMETERS</td> </tr> <tr> <td colspan="3">ANGULAR TOLERANCE $\pm 10^\circ$</td> </tr> <tr> <td colspan="3">DIMENSIONAL TOLERANCE $\pm 0.1\text{mm}$</td> </tr> <tr> <td>SIZE A3</td> <td>DOC NO X2-DIA-000-0</td> <td>REV 0</td> </tr> <tr> <td colspan="3">FILE NAME X2-DIA-000-0_Diaphragm-Holder-and-Buffer-Assembly.dwg</td> </tr> <tr> <td>SCALE AS SHOWN</td> <td>WEIGHT n/a</td> <td>SHEET 3 OF 5</td> </tr> </table>				DRAWN	NAME	DATE	D. Gifford		10/05/2011	CHEKED			EUG APPR			MGR APPR			UNLESS OTHERWISE SPECIFIED			DIMENSIONS ARE IN MILLIMETERS			ANGULAR TOLERANCE $\pm 10^\circ$			DIMENSIONAL TOLERANCE $\pm 0.1\text{mm}$			SIZE A3	DOC NO X2-DIA-000-0	REV 0	FILE NAME X2-DIA-000-0_Diaphragm-Holder-and-Buffer-Assembly.dwg			SCALE AS SHOWN	WEIGHT n/a	SHEET 3 OF 5
DRAWN	NAME	DATE																																					
D. Gifford		10/05/2011																																					
CHEKED																																							
EUG APPR																																							
MGR APPR																																							
UNLESS OTHERWISE SPECIFIED																																							
DIMENSIONS ARE IN MILLIMETERS																																							
ANGULAR TOLERANCE $\pm 10^\circ$																																							
DIMENSIONAL TOLERANCE $\pm 0.1\text{mm}$																																							
SIZE A3	DOC NO X2-DIA-000-0	REV 0																																					
FILE NAME X2-DIA-000-0_Diaphragm-Holder-and-Buffer-Assembly.dwg																																							
SCALE AS SHOWN	WEIGHT n/a	SHEET 3 OF 5																																					

DRAFTING STANDARD AS1000 - 1992																																									
DO NOT SCALE			REV 0																																						
			DESCRIPTION		DATE APPROVED																																				
			New drawing		10/05/2011 n/a																																				
PRINT ON A3 SHEET SIZE																																									
Item Number	Document Number	Title	Material	Quantity																																					
1	X2-DIA-005-0	Diaphragm holder bumper	Carbon steel hollow bar	1																																					
2	BS555	BS55 o-ring	Nitrile rubber	1																																					
3	BS53	BS53 o-ring	Nitrile rubber	1																																					
6	X2-DIA-006-0	Diaphragm holder front tube adapter	Carbon steel hollow bar	1																																					
7	X2-DIA-007-0	Diaphragm holder fixing ring	Carbon steel hollow bar	2																																					
9	M3-15	M3x15 hi-strength steel bolt	NA	10																																					
12	X2-DIA-004-0	Diaphragm holder buffer	Rubber	1																																					
3	X2-DIA-002-0	Diaphragm holder front plate	Carbon steel hollow bar	1																																					
14	X2-DIA-001-0	Diaphragm holder buckling plate	Carbon steel hollow bar	1																																					
15	M4-15	M4x15 hi-strength steel bolt	NA	8																																					
16	BS556	BS55 o-ring	Nitrile rubber	1																																					
17	BS557	BS55 o-ring	Nitrile rubber	1																																					
19	n/a	Mylar diaphragm	Mylar	1																																					
20	BS555	BS55 o-ring	Nitrile rubber	1																																					
<table border="1" style="width: 100%;"> <tr> <td>DRAWN</td> <td>NAME</td> <td>DATE</td> </tr> <tr> <td>D. Gifford</td> <td></td> <td>10/05/2011</td> </tr> <tr> <td colspan="3">CENTRE FOR HYPERSONICS</td> </tr> <tr> <td colspan="3">THE UNIVERSITY OF QUEENSLAND</td> </tr> <tr> <td colspan="3" style="text-align: center;">TITLE</td> </tr> <tr> <td colspan="3" style="text-align: center;">Diaphragm holder and buffer assembly</td> </tr> <tr> <td>APPR</td> <td>APPR</td> <td>REV</td> </tr> <tr> <td>ENG APPR</td> <td>MGR APPR</td> <td>0</td> </tr> <tr> <td colspan="3" style="text-align: center;">UNLESS OTHERWISE SPECIFIED</td> </tr> <tr> <td colspan="3" style="text-align: center;">DIMENSIONS ARE IN MILLIMETERS</td> </tr> <tr> <td colspan="3" style="text-align: center;">ANGULAR TOLERANCE: ±1°</td> </tr> <tr> <td colspan="3" style="text-align: center;">DIMENSIONAL TOLERANCE: ±0.1mm</td> </tr> </table>						DRAWN	NAME	DATE	D. Gifford		10/05/2011	CENTRE FOR HYPERSONICS			THE UNIVERSITY OF QUEENSLAND			TITLE			Diaphragm holder and buffer assembly			APPR	APPR	REV	ENG APPR	MGR APPR	0	UNLESS OTHERWISE SPECIFIED			DIMENSIONS ARE IN MILLIMETERS			ANGULAR TOLERANCE: ±1°			DIMENSIONAL TOLERANCE: ±0.1mm		
DRAWN	NAME	DATE																																							
D. Gifford		10/05/2011																																							
CENTRE FOR HYPERSONICS																																									
THE UNIVERSITY OF QUEENSLAND																																									
TITLE																																									
Diaphragm holder and buffer assembly																																									
APPR	APPR	REV																																							
ENG APPR	MGR APPR	0																																							
UNLESS OTHERWISE SPECIFIED																																									
DIMENSIONS ARE IN MILLIMETERS																																									
ANGULAR TOLERANCE: ±1°																																									
DIMENSIONAL TOLERANCE: ±0.1mm																																									
<table border="1" style="width: 100%;"> <tr> <td>REF</td> <td>DOC NO</td> <td>FILE NAME</td> </tr> <tr> <td>A3</td> <td>X2-DIA-000-0</td> <td>X2-DIA-000-0</td> </tr> <tr> <td colspan="3">SCALE AS SHOWN WEIGHT: n/a</td> </tr> <tr> <td colspan="3">SHEET 4 OF 5</td> </tr> </table>						REF	DOC NO	FILE NAME	A3	X2-DIA-000-0	X2-DIA-000-0	SCALE AS SHOWN WEIGHT: n/a			SHEET 4 OF 5																										
REF	DOC NO	FILE NAME																																							
A3	X2-DIA-000-0	X2-DIA-000-0																																							
SCALE AS SHOWN WEIGHT: n/a																																									
SHEET 4 OF 5																																									

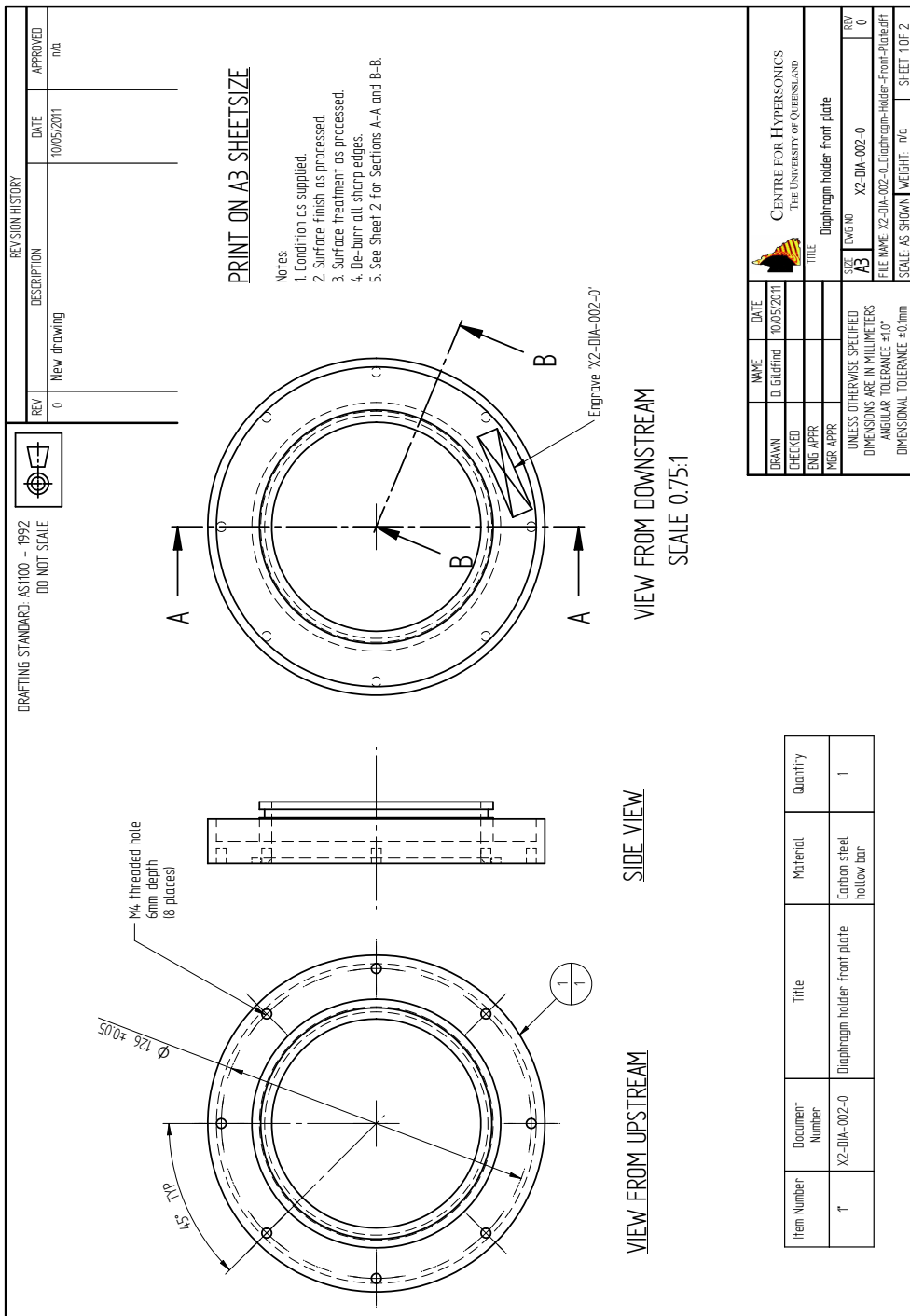
<p>DRAFTING STANDARD AS1000 - 1992 DO NOT SCALE</p> 	<p>REV 0 New drawing</p>	<p>DESCRIPTION</p>	<p>DATE 10/05/2011</p>	<p>APPROVED n/a</p>
<p>PRINT ON A3 SHEETSIZE</p>				
				
<p>SCALE 1:2</p>				
				
<p>VIEW FROM DOWNSTREAM</p>				
				
<p>SIDE VIEW</p>				
<p>VIEW FROM UPSTREAM</p>				
<p>→ Facility upstream direction</p>				
<p>CENTRE FOR HYPERSONICS THE UNIVERSITY OF QUEENSLAND</p>				
<p>TITLE: Diaphragm holder and buffer assembly</p>				
<p>DRAWN D. Gifford DATE 10/05/2011</p>				
<p>CHEKED</p>				
<p>ENG APPR</p>				
<p>MGR APPR</p>				
<p>UNLESS OTHERWISE SPECIFIED DIMENSIONS ARE IN MILLIMETERS ANGULAR TOLERANCE $\pm 10^\circ$ DIMENSIONAL TOLERANCE ± 0.1mm</p>				
<p>FILE NAME: X2-DIA-000-0_Diaphragm-Holder-and-Buffer-&semitight.dwg SCALE AS SHOWN WEIGHT: n/a SHEET 5 OF 5</p>				

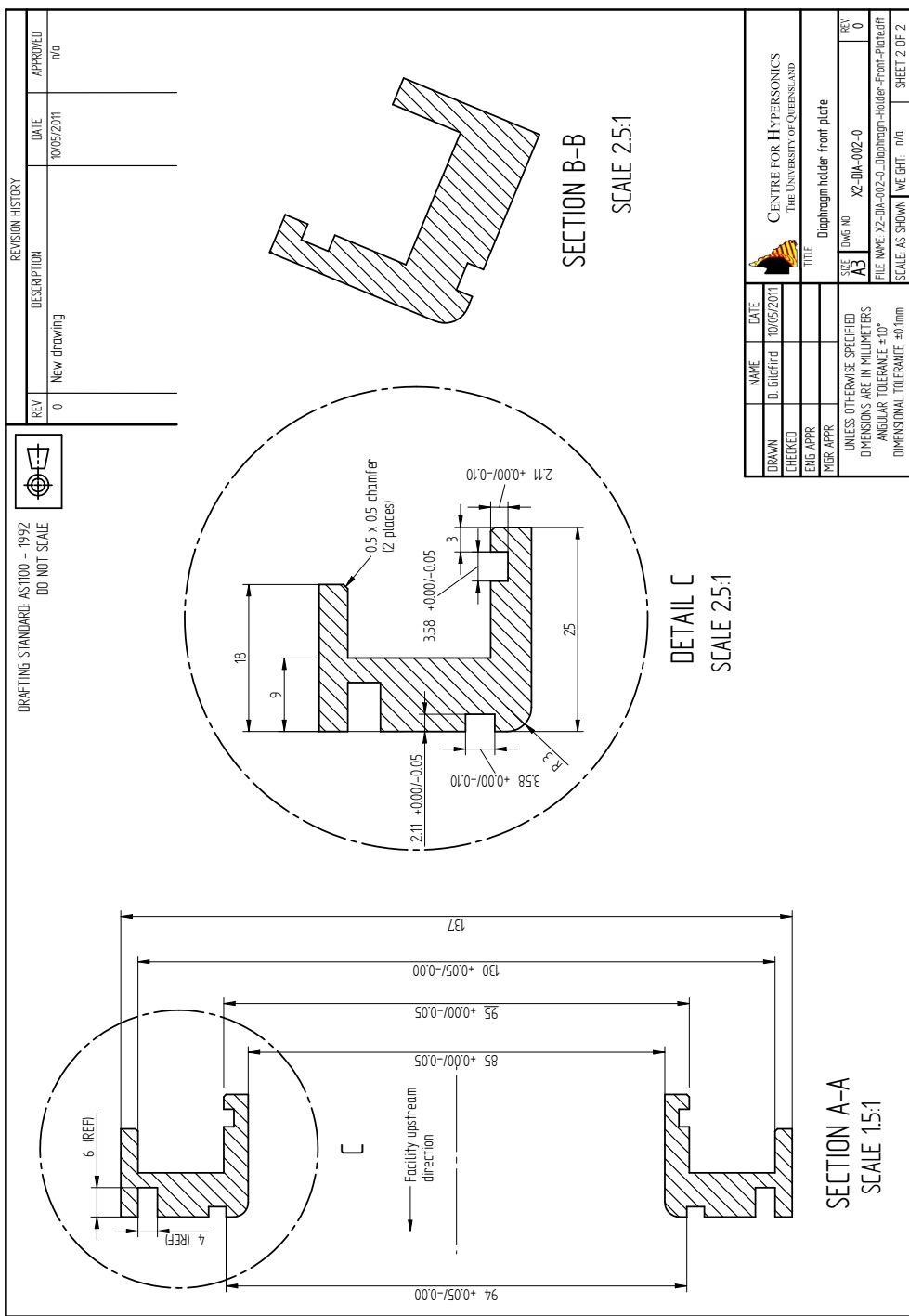
L.2 X2-DIA-001-0: Diaphragm Holder Back Plate



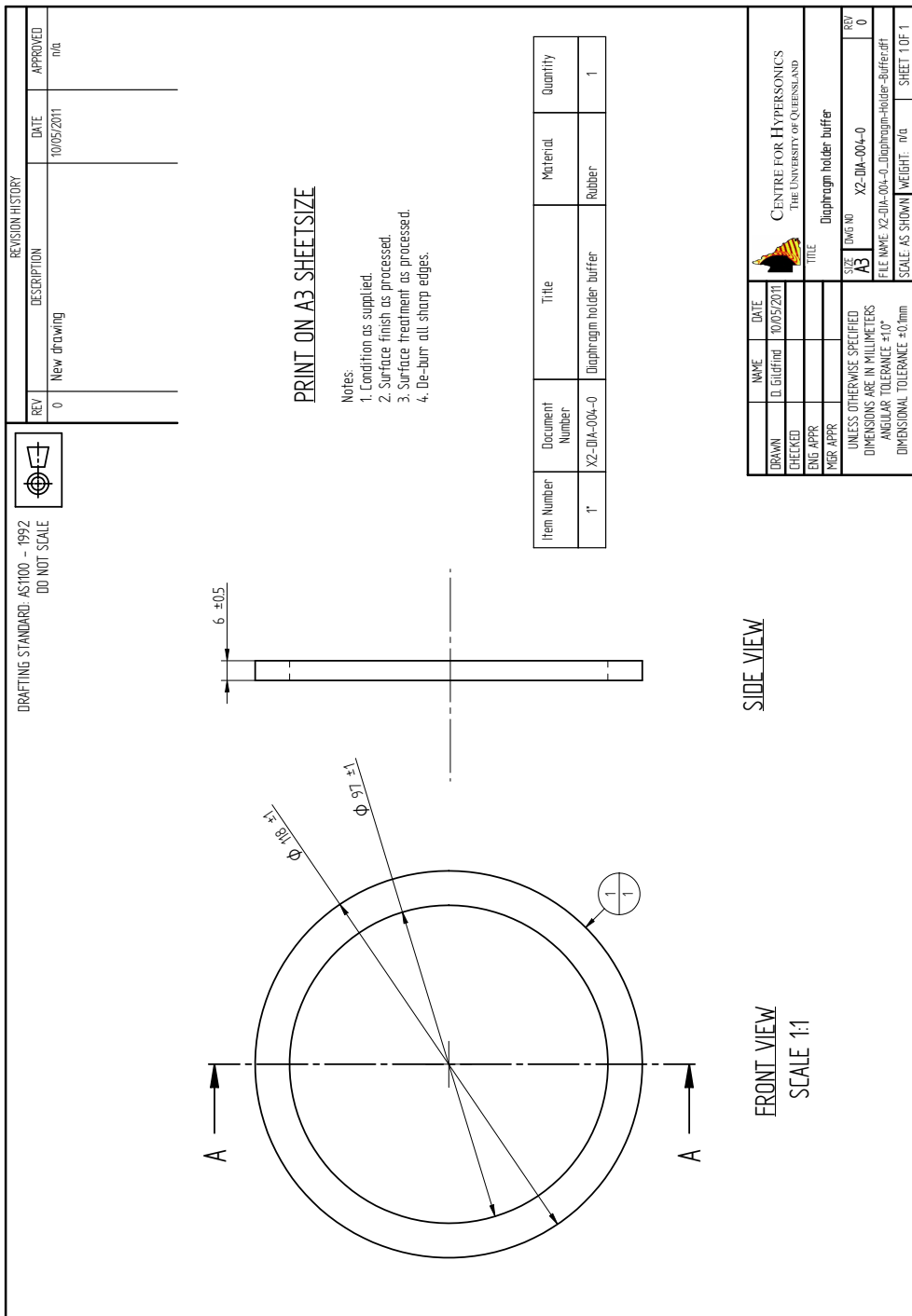


L.3 X2-DIA-002-0: Diaphragm Holder Front Plate

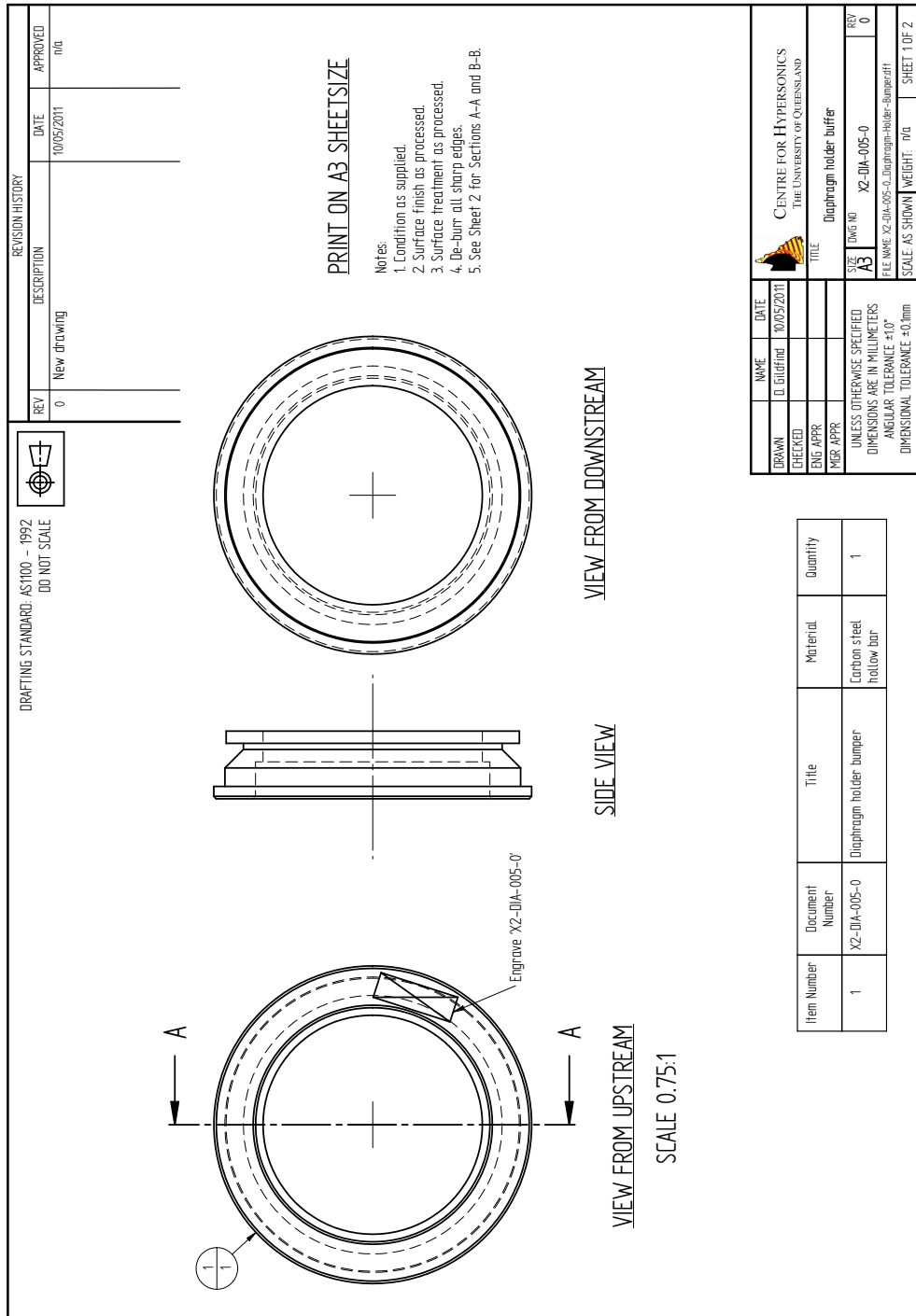


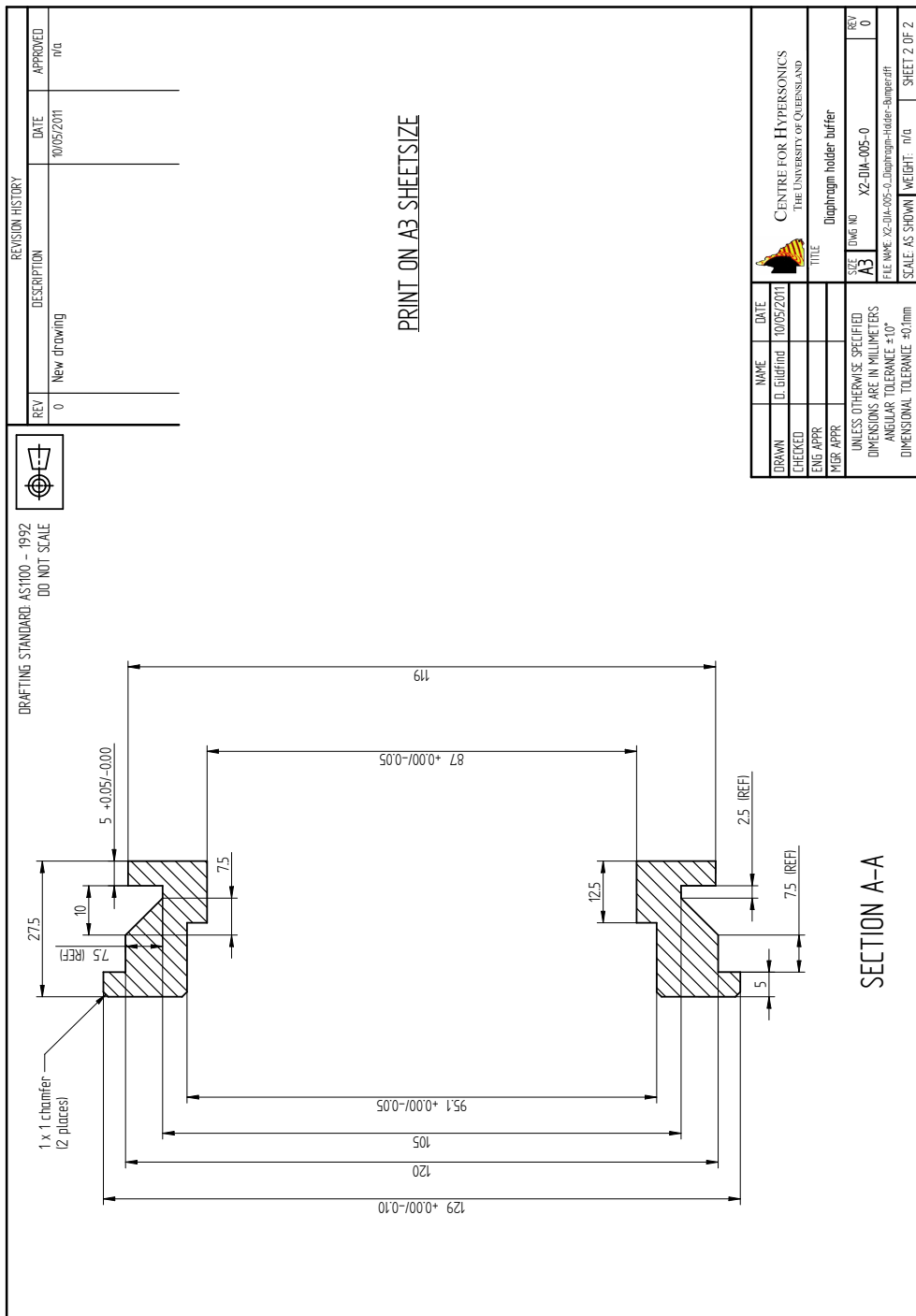


L.4 X2-DIA-004-0: Diaphragm Holder Buffer

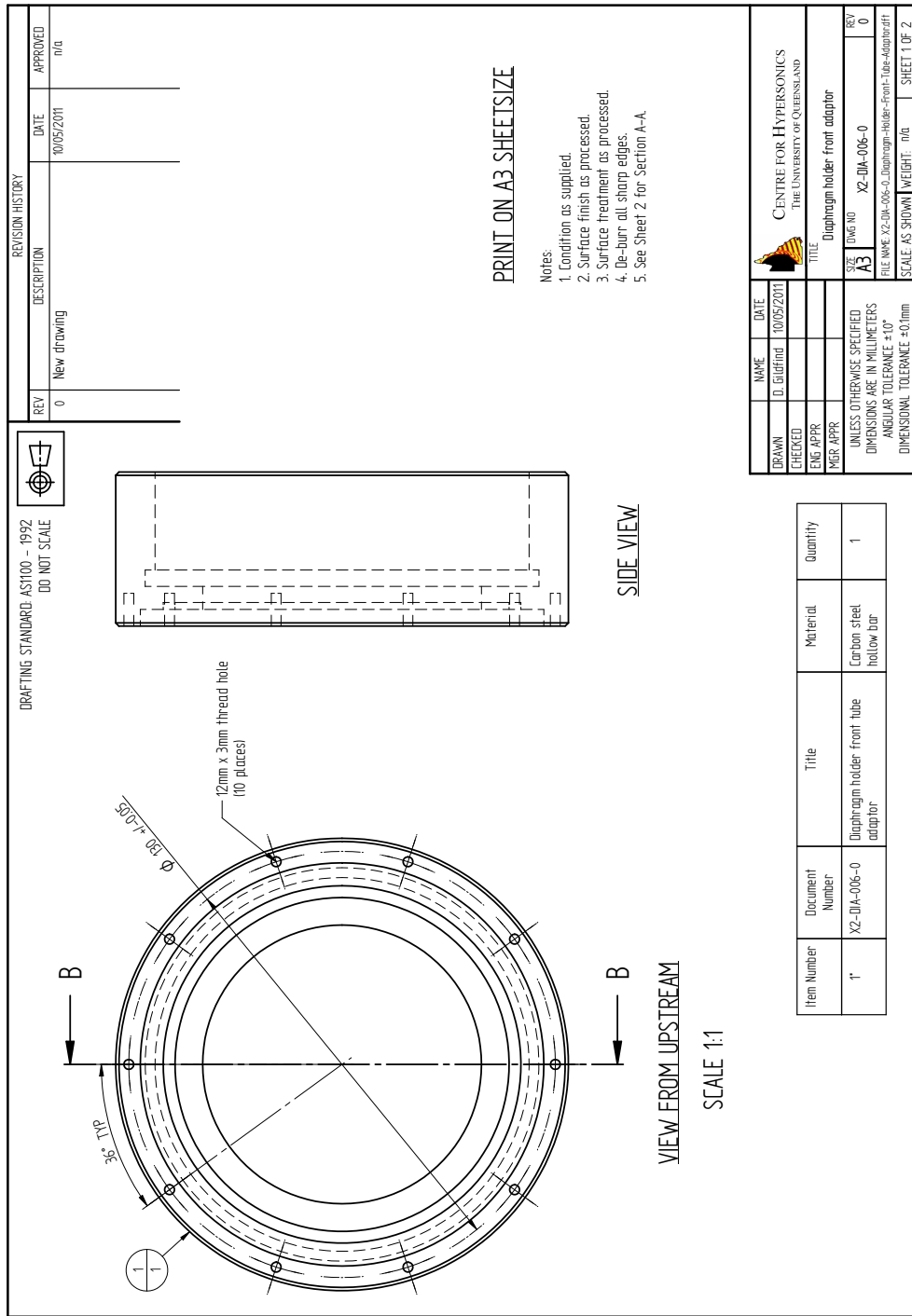


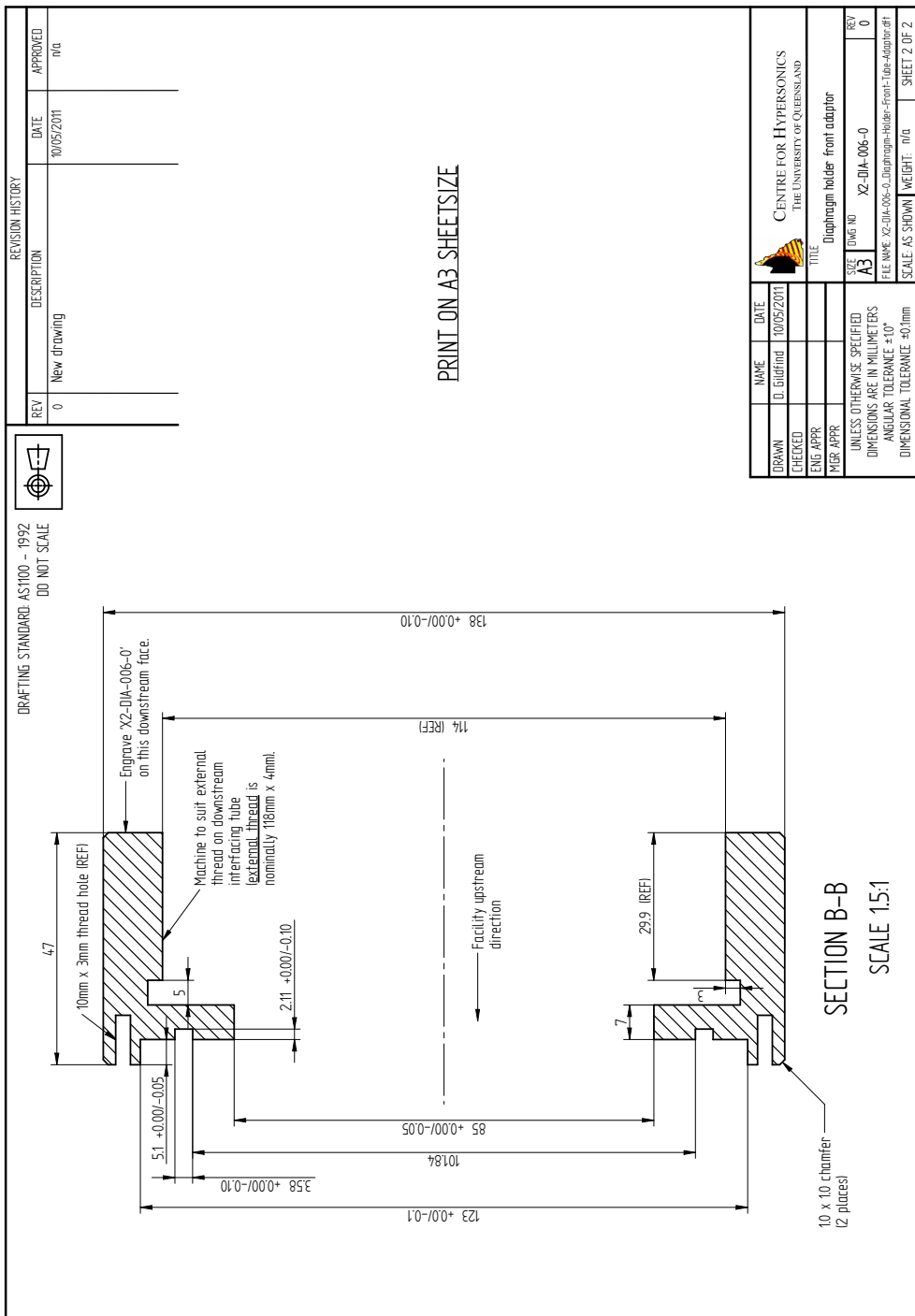
L.5 X2-DIA-005-0: Diaphragm Holder Bumper



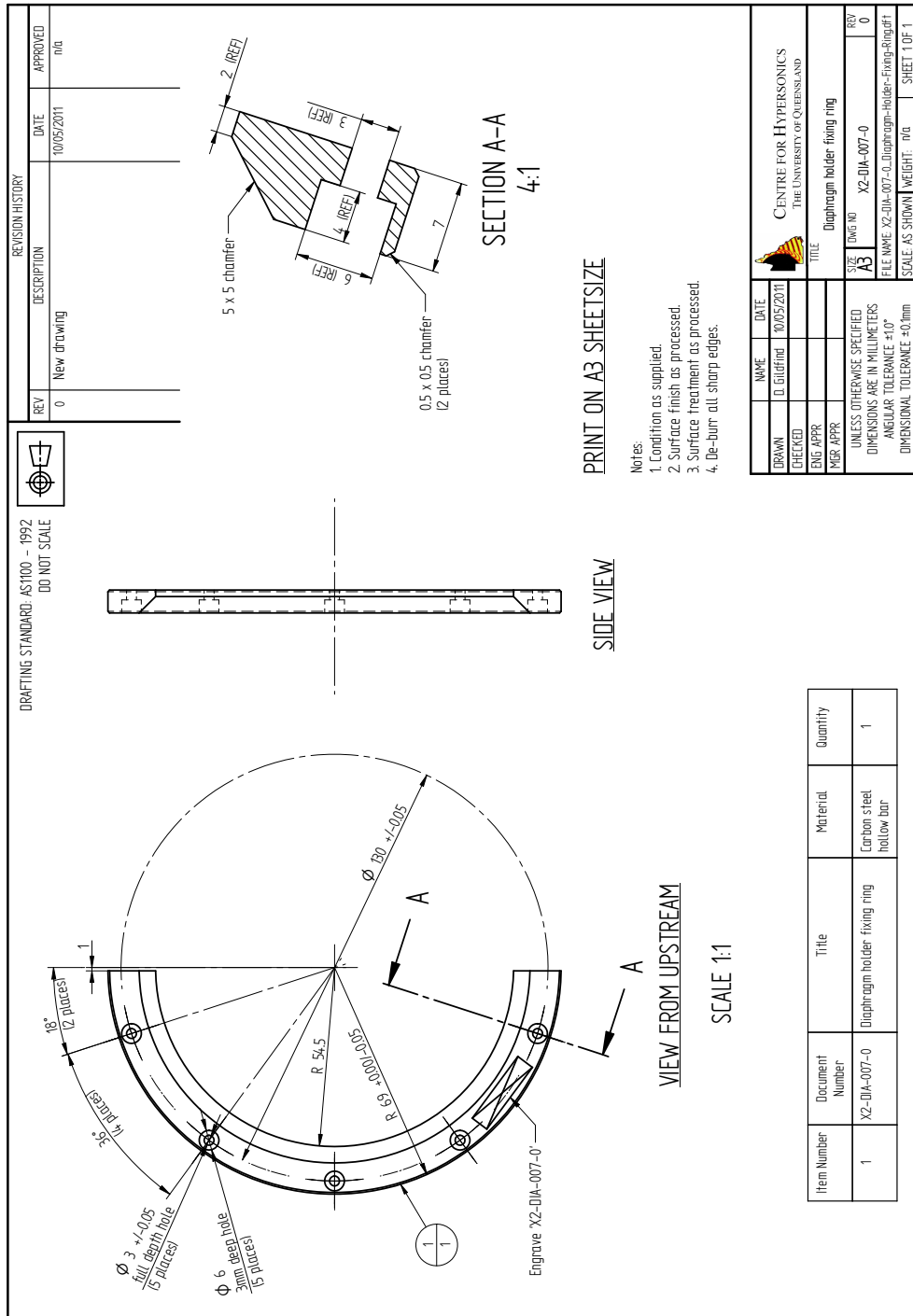


L.6 X2-DIA-006-0: Diaphragm Holder Front Tube Adaptor





L.7 X2-DIA-007-0: Diaphragm Holder Fixing Ring



L.8 X2-DIA-008-0: Diaphragm Holder Buffer Template

REVISION HISTORY			
REV	DESCRIPTION	DATE	APPROVED
0	New drawing	10/05/2011	Ma

PRINT ON A3 SHEETSIZE

FRONT VIEW

SCALE 1:1

2 [tolerance as supplied]

Notes:

1. Condition as supplied.
2. Surface finish as processed.
3. Surface treatment as processed.
4. De-burr all sharp edges.

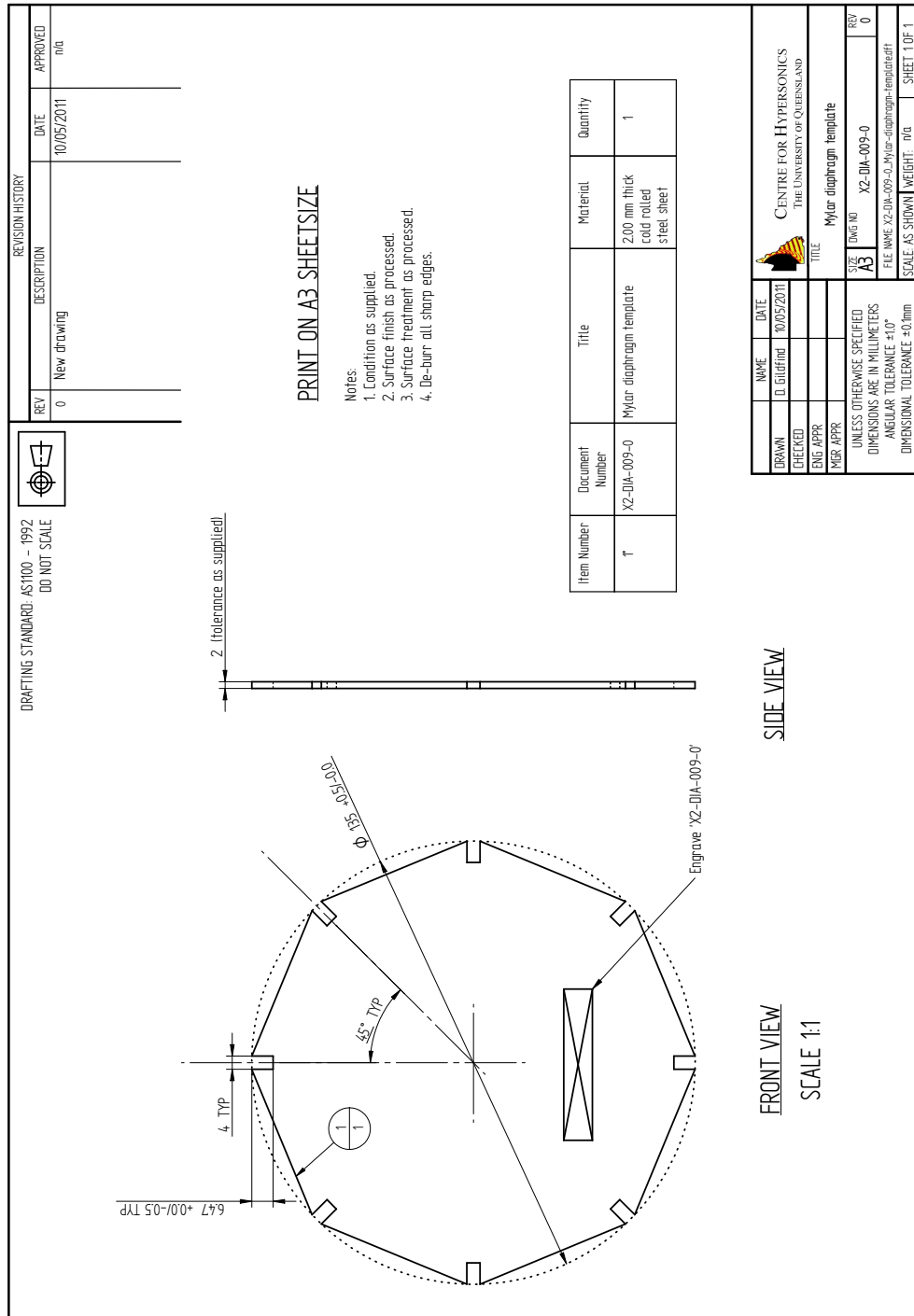
SIDE VIEW

Item Number	Document Number	Title	Material	Quantity
1'	X2-DIA-008-0	Diaphragm holder buffer template	2.0mm thick Cold rolled Steel sheet	1

REV A3

DRAWN	NAME D. Griffith	DATE 10/05/2011	REV 0
CHECKED	CENTRE FOR HYPERSONICS THE UNIVERSITY OF QUEENSLAND		
ENG APPR			
MGR APPR			
UNLESS OTHERWISE SPECIFIED		DIMENSIONS ARE IN MILLIMETERS	
		ANGULAR TOLERANCE ±1°	
		DIMENSIONAL TOLERANCE ±0.1mm	
FILE NAME: X2-DIA-008-0 Diaphragm-Holder-Buffer-Template.dwg		SCALE AS SHOWN WEIGHT: n/a SHEET 1 OF 1	

L.9 X2-DIA-009-0: Mylar diaphragm template



Appendix M

Uncertainty Analysis

M.1 Introduction

Referring to Taylor [184], let x, \dots, z be measurements with corresponding uncertainties $\delta x, \dots, \delta z$, which are used to compute a function $q(x, \dots, z)$. If the uncertainties are independent and random, then the uncertainty in q is given by Equation M.1. Otherwise, the uncertainty in q is never larger than that given by Equation M.2.

$$\delta q = \sqrt{\left(\frac{\delta q}{\delta x} \delta x\right)^2 + \dots + \left(\frac{\delta q}{\delta z} \delta z\right)^2} \quad (\text{M.1})$$

$$\delta q \leq \left| \frac{\delta q}{\delta x} \right| \delta x + \dots + \left| \frac{\delta q}{\delta z} \right| \delta z \quad (\text{M.2})$$

For uncertainty calculations in this thesis, it is assumed that uncertainties are independent and random, therefore Equation M.1 has been used. Various measurements which were made for this thesis are now considered separately. Identification of these uncertainties was largely based on the previous uncertainty analyses of Doolan [185], Hayne [186], and McGilvray [58], which themselves were largely based on the method presented by Mee [187].

M.2 Facility Geometry

Tube inner diameters were assumed to have an uncertainty of ± 0.1 mm compared to their original drawing specification. If the diameter has changed since manufacture, it is most likely that the diameter may have increased due to erosion of the inner surface of the tube by the severe flows produced during experiments. While

this is possible, sample measurements of the tube diameter at its ends with a ruler (with uncertainty of $\approx \pm 0.5$ mm) indicated that the nominal diameters are still valid.

The axial location of tube geometric features, such as diaphragm stations, pressure transducers, and so forth, was measured during the experimental campaign. A steel tape was aligned with the tube centreline, and bonded to the laboratory floor. A plumb-bob was used to measure all relevant axial locations. It was determined that these measurements had a maximum uncertainty of ± 2 mm, which has conservatively been assumed to apply for all axial measurements. Note: transducer locations quoted in this thesis refer to the axial location of the centre of the transducer.

M.3 Reservoir Fill Pressure

The reservoir fill pressure was measured with a Solfrunt 1981 10 MPa gauge. This gauge has an accuracy of $\pm 0.5\%$ of full scale, which corresponds to ± 50 kPa.

M.4 Compression Tube Fill Pressure

The compression tube fill pressure was measured with a Varian WV100-2 multiple-range vacuum gauge with digital display. This gauge has an accuracy of $\pm 1\%$ of reading, or ± 2 mbar, whichever is higher.

M.5 Secondary Driver Fill Pressure

The secondary driver fill pressure was measured with a Varian WV100-2 multiple-range vacuum gauge with digital display. This gauge has an accuracy of $\pm 1\%$ of reading, or ± 2 mbar, whichever is higher.

M.6 Shock Tube Fill Pressure

The shock tube fill pressure was measured with a Solfrunt 1981 1,600 kPa gauge. This gauge has an accuracy of $\pm 0.5\%$ of full scale, which corresponds to ± 8 kPa. Calibration against the dead weight calibration apparatus indicated that this gauge had a $+10$ kPa offset across the entire range that these experiments would use it

for, therefore this offset was added to all fill pressures to ensure the correct *actual* pressure was used.

M.7 Acceleration Tube Fill Pressure

The following barocell pressure gauges were used to measure acceleration tube fill pressures:

1. Mach 10 flow conditions (with and without nozzle): BOC Edwards 600B TRANS 10MB NW16, PNo. W6D022611, SNo. 020815481. Accuracy of $\pm(0.15 \text{ of reading} + 0.01 \text{ of full scale})$
2. Mach 12.5 and Mach 15 flow conditions: BOC Edwards 655 Trans 1TORR NW-16, PNo W65511811, Serial No. 8023023. Accuracy of $\pm(0.15 \text{ of reading} + 0.01 \text{ of full scale})$

M.8 Primary Diaphragm Rupture Pressure

The primary diaphragm rupture pressures were estimated by scaling the value measured in previous hydraulic rupture tests on 1.2 mm (with 0.2 mm score) cold rolled steel diaphragms (the same type of steel). Whilst the assumed rupture pressure produces results consistent with experiment in L1d2 analyses, its uncertainty has not been established. A conservative upper limit on this uncertainty is estimated to be no greater than $\pm 20\%$. For tuned piston conditions, following diaphragm rupture the pressure in the driver is primarily affected by the piston dynamics and the choked conditions across the area change, therefore this uncertainty is not expected to significantly influence predicted flow processes.

M.9 Mylar Diaphragm Rupture Pressures

Several combinations of Mylar secondary and tertiary diaphragms were used in this investigation. Burst pressures must be specified for these diaphragms in the numerical simulations. A series of pop tests were performed to measure the rupture pressure.

Figure M.1 shows rupture pressures for different Mylar diaphragm arrangements. Interestingly, it is observed that multiple sheets of Mylar rupture at more consistent pressures than single sheets, and that the largest uncertainties exist for

the rupture of a single sheet of the thinnest Mylar. During the actual experimental campaign, most experiments used multiple thin sheets of 0.025 mm thick Mylar. The rupture pressure for several sheets of this material was estimated based on the average rupture pressure of a single sheet (136 kPa per Figure M.1).

M.10 Tube Fill Temperatures

All numerical analyses assume a fill temperature in each tube of 300 K prior to each shot. In reality, the gas temperature will depend on the initial temperature and subsequent flow path of a tube fill gas from its initial source, and also the amount of time between filling the tube and firing the facility. Each fill gas has a different source:

1. Reservoir: compressed air bottle bank.
2. Compression tube: G-size cylinders of helium and argon.
3. Secondary driver tube: G-size cylinder of helium.
4. Shock tube: G-size cylinder of air.
5. Acceleration tube: laboratory ambient air.

Consistent with Hayne [186], it is assumed that laboratory temperature varied between 293 and 303 K, indicating that the assumed 300 K temperature conservatively has an accuracy of $\pm 3\%$.

M.11 Piston Maximum Displacement Measurement

Referring to Section 6.9.2, for blanked-off driver tests the piston maximum displacement was measured using a staggered arrangement of soft welding rods (see Figures 6.12, 6.13, and 6.14). These rods were sized at approximately 10 mm intervals. An impacted rod can be identified by its deformed condition, however it is not certain how much the rod may have sprung back from its displaced position, or else deformed past its displaced position due to its inertia. On the other hand, a rod which has *not* been impacted obviously remains unaffected. Comparison of deflected and undeflected rods permits a fairly accurate assessment of the piston maximum displacement during the compression stroke, and an uncertainty of ± 5 mm is therefore assumed for this measurement.

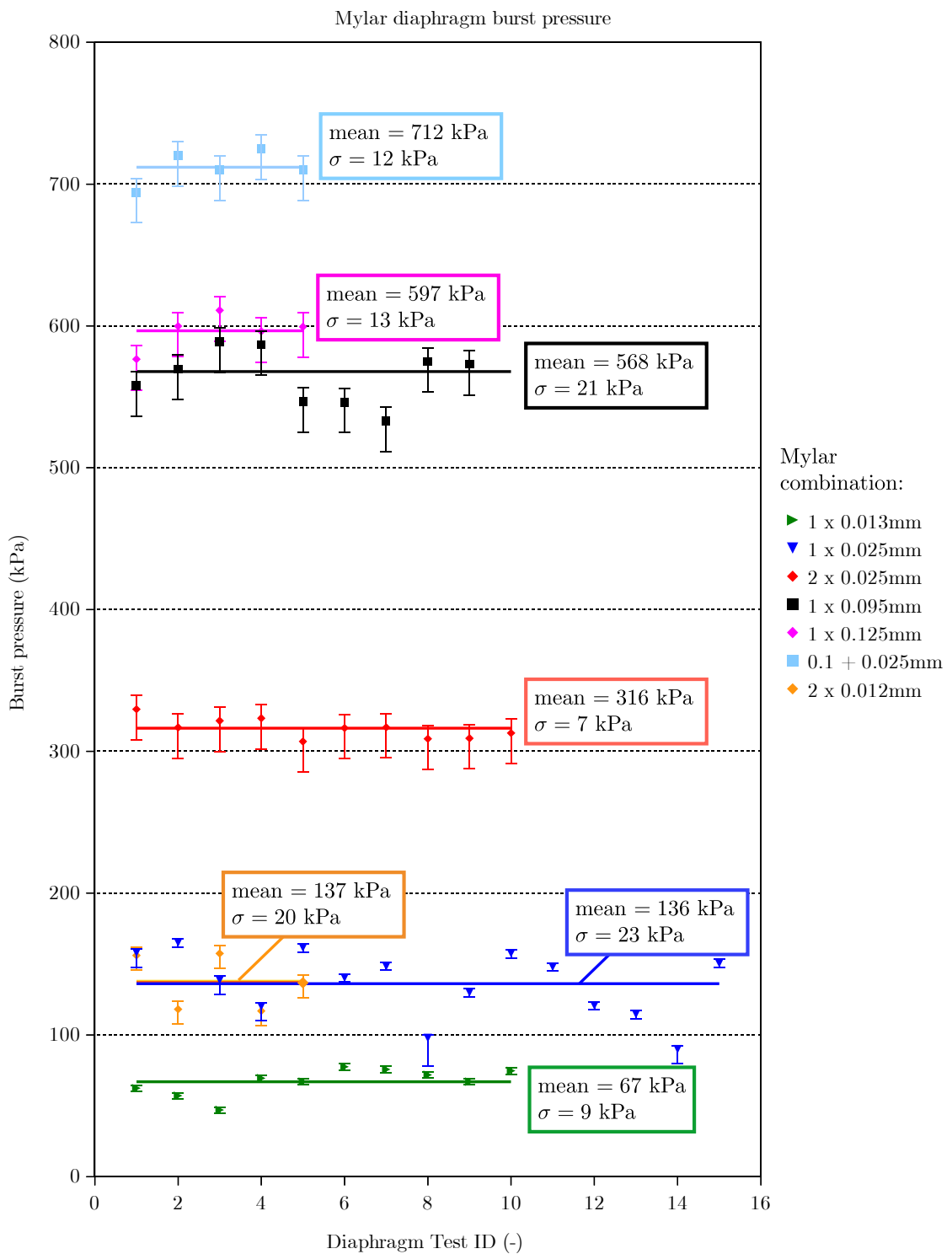


Figure M.1: Rupture pressures for different combinations of Mylar diaphragms. Diaphragms were assembled in the secondary diaphragm station of X2. Tube inner diameter was 85 mm. Error bars were calculated for each test based on estimated uncertainties at time of diaphragm rupture, and were calculated using Equation M.1.

M.12 Shock Speeds

Shock speeds were calculated by measuring the time of arrival of the shock at two transducers, measuring the distance between the two transducers, and calculating the average speed. Referring to Section M.2, axial location of transducers was measured to an accuracy of ± 2 mm. Data sampling of pressures was performed at a minimum 1 MHz. Based on these uncertainties, and using Equation M.1, uncertainties for individual shock speeds, and shock speeds averaged across multiple experiments, were calculated. Clearly the distance between transducers, and the number of shots at each condition, both vary. Therefore, the uncertainty associated with each shock speed calculation is unique, and quoted uncertainties are therefore presented for each shock speed where applicable.

M.13 PCB Transducer Sensitivities

PCB sensitivities were all measured using either the air-based or oil-based calibration rigs, respectively for low and high pressure magnitude measurements. Results for the calibration are shown in Table M.1. Details are provided in Sections M.13.1 and M.13.2. Referring to Table M.1, the maximum uncertainty is $\approx \pm 2\%$. This is assumed to apply to all PCB sensitivities.

M.13.1 Air Rig Calibrations

The apparatus used to conduct a compressed air-based pressure calibration of the PCB pressure transducers is shown in Figure M.2. The procedure to calibrate the pressure gauges was as follows:

- Apply impulsive pressure load simultaneously to PCB transducers and to calibration gauge. This is achieved using a solenoid valve, which exposes the transducer manifold, originally at ambient pressure, to a reservoir of selected pressure. PCB and calibration pressure gauge responses are recorded using National Instruments data collection hardware integrated into a computer running Labview software. A proportion of the recorded signal is comprised of pre-trigger data samples. The calibration transducer is used to trigger data recording.
- The data is loaded into a computer spreadsheet. For each pressure trace, a proportion of the pre-trigger samples (typically approximately 100 samples)

PCB ID	Nominal Range (psi)	Calibration Method	Calibration Range (psi)	Calculated Sensitivity (V/kPa)	Manufacturer Sensitivity (mV/psi)	Manufacturer Sensitivity (V/kPa)	Manufacturer Range (psi)
111A22-11406	0-5,000	Oil rig (March 2011)	0-4,685	0.000145 ± 0.000003	0.9711	0.000141	0-500
111A22-8487	0-5,000	Oil rig (March 2011)	0-4,685	0.000148 ± 0.000003	1.02	0.000148	0-5000
111A22-9533	0-5,000	Oil rig (March 2011)	0-4,685	0.000139 ± 0.000003	1.01	0.000146	0-5000
111A22-9535	0-5,000	Oil rig (March 2011)	0-4,685	0.000139 ± 0.000003	0.986	0.000143	0-5000
111A24-9906	0-1,000	Air rig (March 2011)	29-102	0.000655 ± 0.000006	4.99	0.000724	0-1000
		Oil rig (March 2011)	0-1,639	0.00069 ± 0.00004			
111A26-7430	0-500	Air rig (March 2011)	29-102	0.00128 ± 0.00001	9.98	0.00145	0-500
		Air rig (April 2011)	29-87	0.00128 ± 0.00001			
111A26-7432	0-500	Air rig (March 2011)	29-102	0.00130 ± 0.00001	9.62	0.00140	0-500
111A26-7441	0-500	Air rig (March 2011)	29-102	0.00169 ± 0.00002	10.23	0.00148	0-500
111A26-7442	0-500	Air rig (March 2011)	29-102	0.00143 ± 0.00001	10.6	0.00154	0-500
		Air rig (April 2011)	29-87	0.00142 ± 0.00002			
111A26-7448	0-500	Air rig (March 2011)	29-102	0.00148 ± 0.00001	10.18	0.00148	0-500
111A26-7453	0-500	Air rig (March 2011)	29-102	0.00155 ± 0.00001	10.51	0.00152	0-500
		Air rig (April 2011)	29-87	0.00152 ± 0.00002			
112A22-10635	0-50	Air rig (March 2011)	15-87	0.0142 ± 0.0002	115.4	0.01674	0-50
112A22-15292	0-50	Air rig (March 2011)	15-87	0.0120 ± 0.0002	104.8	0.01520	0-50
112A22-19127	0-50	Air rig (March 2011)	29-87	0.0136 ± 0.0001	97.46	0.01414	0-50
112A22-19276	0-50	Air rig (March 2011)	15-87	0.0127 ± 0.0002	97.97	0.01421	0-50
112A22-19279	0-50	Air rig (March 2011)	15-87	0.0141 ± 0.0002	101.3	0.01469	0-50
112A22-21210	0-50	Air rig (March 2011)	29-87	0.0134 ± 0.0001	98.6	0.01430	0-50
112A22-9593	0-50	Air rig (March 2011)	15-87	0.0133 ± 0.0002	115.6	0.01677	0-50
112A22-9597	0-50	Air rig (March 2011)	29-87	0.0135 ± 0.0001	112.8	0.01636	0-50
112A22-9608	0-50	Air rig (March 2011)	15-87	0.0113 ± 0.0002	113.2	0.01642	0-50
		Air rig (April 2011)	29-87	0.0115 ± 0.0001			
112A22-9609	0-50	Air rig (March 2011)	29-87	0.0127 ± 0.0001	109.1	0.01582	0-50
		Air rig (April 2011)	29-87	0.0133 ± 0.0001			
113A21-11061	0-200	Air rig (March 2011)	29-102	0.00161 ± 0.00001	24.5	0.00355	0-200
		Air rig (April 2011)	29-87	0.00162 ± 0.00002			
113A21-9570	0-200	Air rig (March 2011)	29-102	0.00327 ± 0.00003	29.44	0.00427	0-200
113A24-2676	0-1,000	Air rig (March 2011)	29-102	0.000682 ± 0.000006	4.77	0.000692	0-1000
		Oil rig (March 2011)	0-2,074	0.00068 ± 0.00004			
113B24-22531	0-1,000	n/a	n/a	n/a	-	0.0007264	-
113B24-22373	0-1,000	n/a	n/a	n/a	-	0.0007589	-
113B26-22554	0-500	n/a	n/a	n/a	-	0.001463	-
113B24-22372	0-1,000	n/a	n/a	n/a	-	0.0007448	-
113B26-22553	0-500	n/a	n/a	n/a	-	0.001464	-
113B24-22371	0-1,000	n/a	n/a	n/a	-	0.0007512	-
113B24-22374	0-1,000	n/a	n/a	n/a	-	0.0007344	-

Table M.1: Summary of experimentally measured PCB sensitivities. The PCBs with ‘n/a’ noted against their calibration method were newly purchased items. For these gauges the manufacturer’s sensitivity was used, which have an accuracy ±1% according to the manufacturer specification.

are averaged and subtracted from all values of that trace. This is to zero the trace.

- The zeroed PCB trace is then divided by the calibration gauge trace, to produce a sensitivity curve for each PCB trace.
- The rise time of the calibration gauge exceeds that of the PCB transducer. Further, the PCB pressure trace begins to lag immediately following its impulsive loading. Therefore the optimal time to record the PCB sensitivity is immediately after peak pressure is recorded (and is held steady) in the calibration gauge, and before the PCB response indicates lag.
- The sensitivity is recorded using this technique at a number of different

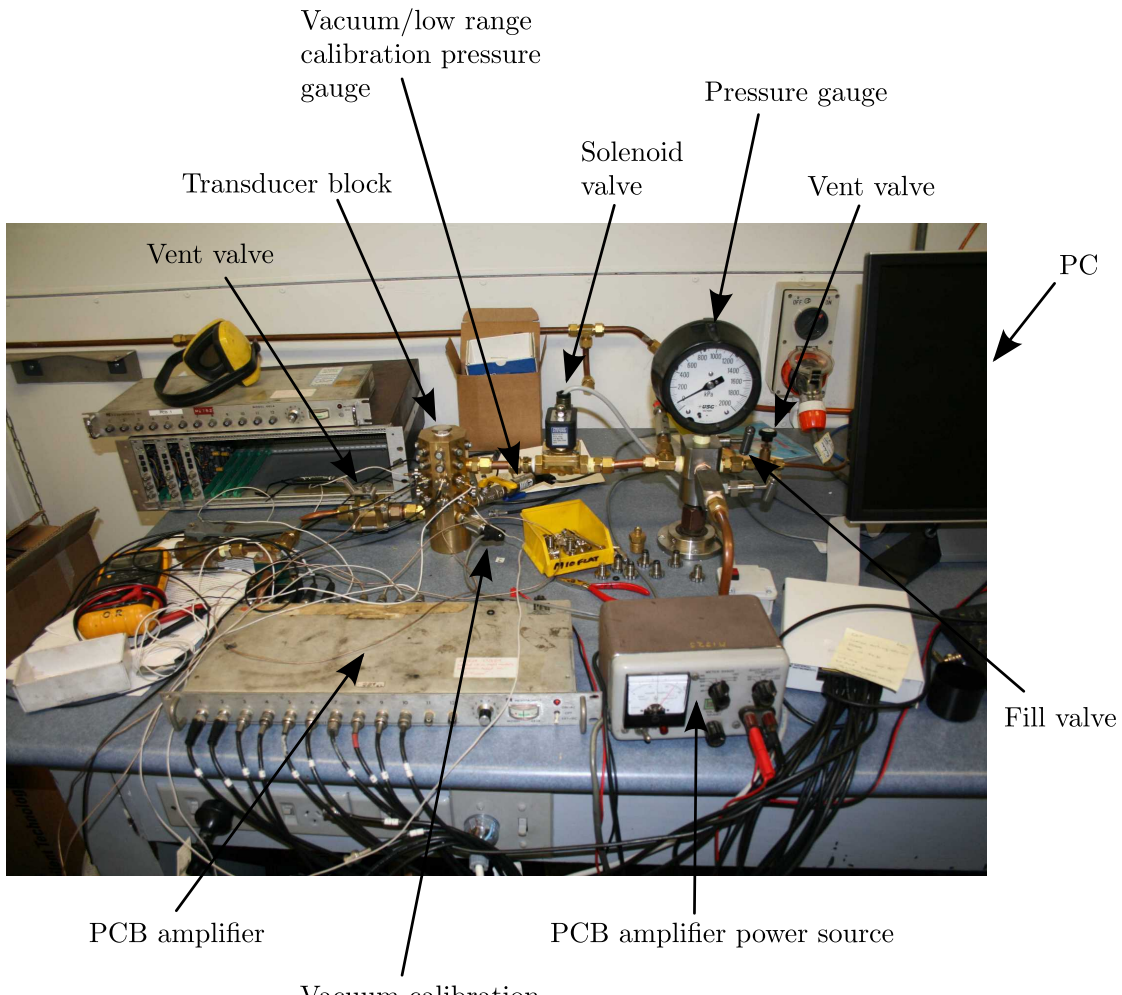


Figure M.2: Compressed air calibration apparatus.

manifold pressures (within the pressure range of the calibration rig, typically 200-600 kPa). This is repeated for each pressure level a number of times.

- The key uncertainty is the pressure measurement from the Omegadyne px319 200A5V 0-200psi calibration gauge ($\pm 0.25\%$ of full scale, = 3.4 kPa), therefore the percentage uncertainty is higher at lower pressures. The final sensitivity is established by calculating the mean sensitivity:

$$S = \frac{\sum_{i=1}^n \frac{V_i}{p_i}}{n} = \frac{\sum_{i=1}^n \frac{V_i}{p_i}}{n} = \frac{\sum_{i=1}^n S_i}{n} \quad (\text{M.1})$$

- The uncertainty at each pressure measurement level is calculated based on the assumption that the uncertainty in the voltage measurement is negligible.

Δp is the fixed uncertainty of the calibration gauge:

$$\Delta S_i = \frac{\Delta p}{p_i} \frac{V_i}{p_i} \quad (\text{M.2})$$

- The uncertainty ΔS for an averaged sensitivity measurement, where i indicates measurements for each calibration sample, is calculated conservatively by assuming that uncertainties are systematic:

$$\Delta S = \frac{1}{n} \sum_{i=1}^n \left[\frac{\Delta p}{p_i} \frac{V_i}{p_i} \right] \quad (\text{M.3})$$

M.13.2 Oil Rig Calibrations

The apparatus used to conduct an oil-based pressure calibration of the PCB pressure transducers is shown in Figure M.3. The oil-based calibration apparatus is used to measure PCB transducer sensitivities for transducers designed to operate at higher pressures (typically >10 MPa). The procedure to calibrate the oil gauge was as follows:



Figure M.3: Hydraulic oil calibration apparatus.

- A PCB is exposed to an oil reservoir which can be pressurised to a specified pressure using a hand-operated screw jack pump. Pressure is measured

using a SOLFRUNT 80 MPa pressure gauge (Model 1981), which has been calibrated against a dead weight calibration apparatus.

- At the specified pressure, a ball valve is opened, which rapidly relieves the oil pressure. The drop in pressure induces a negative voltage response in the PCB. The voltage drops temporarily, and then begins to climb back to zero level.
- A pre-defined drop in the PCB voltage is used to trigger a Labview-based data acquisition PC. The single PCB transducer response is recorded in Labview.
- The PCB trace is zeroed by subtracting the average of a set of initial pre-trigger samples from the trace.
- The calibration pressure gauge has a correction applied to it based on the results of its calibration against the dead-weight calibration apparatus.
- There should be a period of time during the PCB trace, whereby the voltage drops and then stays relatively constant, before rising again. The point where the voltage is a minimum is assumed to be the point where the manifold oil pressure is ambient, but the PCB trace hasn't drifted yet. This point is used to calculate the PCB sensitivity. The subsequent rise in the PCB voltage trace is the PCB drift, which initiates immediately upon impulse pressure loading.
- The above process is repeated for a range of oil pressures. The sensitivity of the PCB is calculated at each pressure level. The final sensitivity of the PCB is determined by calculating a least-squares fit through the data points of sensitivity vs. pressure level. The uncertainty of this value is calculated assuming it is actually a mean value, according to Equation M.3. The voltage uncertainty is once again neglected; the pressure measurement uncertainty is based on the SOLFRUNT gauge specification (0.5% of maximum scale, which is $0.5/100 \times 80 = 0.4$ MPa)